

**Surface bonding of a functionalized aromatic molecule:
Adsorption configurations of PTCDA
on coinage metal surfaces**

DISSERTATION

zur Erlangung des Doktorgrades (Dr. rer. nat.)

der Mathematisch-Naturwissenschaftlichen Fakultät

der Rheinischen Friedrich-Wilhelms-Universität Bonn

vorgelegt von

OLIVER BAUER

aus Siegburg

Bonn, Oktober 2014

Angefertigt mit Genehmigung der Mathematisch-Naturwissenschaftlichen Fakultät der Rheinischen Friedrich-Wilhelms-Universität Bonn.

1. Gutachter:	Prof. Dr. M. Sokolowski
2. Gutachter:	Prof. Dr. C. Kumpf
Fachnaher Gutachter:	Prof. Dr. T. Bredow
Fachfremder Gutachter:	Priv.-Doz. Dr. C. Busse

Tag der Promotion:	30.04.2015
Erscheinungsjahr:	2015

Diese Dissertation ist auf dem Hochschulschriftenserver der Universitäts- und Landesbibliothek Bonn (ULB, http://hss.ulb.uni-bonn.de/diss_online) elektronisch publiziert.

Die vorliegende Arbeit wurde im Zeitraum von September 2007 bis März 2014 unter Anleitung von Herrn Professor Dr. Moritz Sokolowski am Institut für Physikalische und Theoretische Chemie der Rheinischen Friedrich-Wilhelms-Universität Bonn angefertigt.

Diese Arbeit wurde bereits auszugsweise veröffentlicht in folgenden Publikationen:

1. A. Hauschild, R. Temirov, S. Soubatch, **O. Bauer**, A. Schöll, B. C. C. Cowie, T.-L. Lee, F. S. Tautz, and M. Sokolowski, *Normal-incidence x-ray standing-wave determination of the adsorption geometry of PTCDA on Ag(111): Comparison of the ordered room-temperature and disordered low-temperature phases*, Physical Review B **81**, 125432 (2010).
2. **O. Bauer**, G. Mercurio, M. Willenbockel, W. Reckien, C. H. Schmitz, B. Fiedler, S. Soubatch, T. Bredow, F. S. Tautz, and M. Sokolowski, *Role of functional groups in surface bonding of planar π -conjugated molecules*, Physical Review B **86**, 235431 (2012).
3. G. Mercurio, **O. Bauer**, M. Willenbockel, N. Fairley, W. Reckien, C. H. Schmitz, B. Fiedler, S. Soubatch, T. Bredow, M. Sokolowski, and F. S. Tautz, *Adsorption height determination of nonequivalent C and O species of PTCDA on Ag(110) using x-ray standing waves*, Physical Review B **87**, 045421 (2013).
4. G. Mercurio, **O. Bauer**, M. Willenbockel, B. Fiedler, T. Sueyoshi, C. Weiss, R. Temirov, S. Soubatch, M. Sokolowski, and F. S. Tautz, *Tuning and probing interfacial bonding channels for a functionalized organic molecule by surface modification*, Physical Review B **87**, 121409(R) (2013).

Kurzzusammenfassung

Ziel der vorliegenden Arbeit ist die Entwicklung eines schlüssigen Modells für den Bindungsmechanismus der Adsorption des prototypischen organischen Moleküls 3,4,9,10-Perylentetracarbonsäure-3,4:9,10-dianhydrid (PTCDA; siehe Abb. 1) auf Münzmetalloberflächen. Aufgrund seines chemischen Aufbaus ermöglicht es das PTCDA-Molekül, die Auswirkungen sowohl des ausgedehnten π -Systems als auch der Gegenwart funktioneller Gruppen mitsamt deren Heteroatomen auf die Grenzflächenbindung zu untersuchen. Grundsätzlich ist der Oberflächenbindungsmechanismus für große π -konjugierte Moleküle von immensm Interesse für das Verständnis sowohl struktureller als auch elektronischer Eigenschaften von dünnen organischen Filmen [1]. Einblicke in die relevanten Wechselwirkungskanäle und deren relativen Beitrag zur Gesamtbindung können gewonnen werden durch die Bestimmung der Bindungskonfiguration, inklusive der Positionen aller relevanten Atome, ein und desselben Moleküls auf verschiedenen Flächen chemisch verwandter (oder identischer) Substrate.

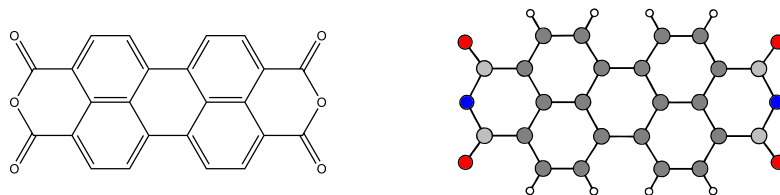


ABB. 1. Valenzstrichformel (links) und Kugel-Stab-Modell (rechts) des PTCDA-Moleküls. Die Kohlenstoffatome innerhalb des Perylenrumpfes und innerhalb der funktionellen Gruppen sind hellgrau (C_{peryl}) bzw. dunkelgrau (C_{funct}) dargestellt, während die chemisch nicht-äquivalenten Sauerstoffatome rot (O_{carb}) bzw. blau (O_{anhyd}) dargestellt sind. Wasserstoffatome sind weiß dargestellt.

Im Rahmen der vorliegenden Arbeit wurden die geometrischen Adsorptionskonfigurationen von PTCDA auf der $\text{Cu}_3\text{Au}(111)$ -, der $\text{Ag}(100)$ -, der $\text{Ag}(110)$ - sowie der $\text{K}:\text{Ag}(110)$ -Oberfläche [d.h. einer Kalium-modifizierten, rekonstruierten $\text{Ag}(110)$ -Oberfläche] mit Hilfe der Absorption im stehenden Röntgenwellenfeld (x-ray standing waves, XSW) unter senkrechtem Einfall untersucht. Im Zuge dessen wurde die Serie früherer XSW-Ergebnisse über die Adsorptionskonfigurationen von PTCDA auf Münzmetall-(111)-Oberflächen, nämlich auf $\text{Au}(111)$ [2], $\text{Ag}(111)$ [3] und $\text{Cu}(111)$ [4], ergänzt. Zusätzlich wurden die Beugung niederenergetischer Elektronen (low-energy electron diffraction, LEED) und Rastertunnelmikroskopie (scanning tunneling microscopy, STM) in Verbindung mit Röntgenphotoelektronenspektroskopie (x-ray photoelectron spectroscopy, XPS) und Ultraviolettphotoelektronenspektroskopie (ultraviolet photoelectron spectroscopy, UPS) sowie theoretischen Rechnungen [auf Dichtefunktionaltheorie-Niveau (density functional theory, DFT)] zur Aufklärung der lateralen geometrischen Strukturen sowie der elektronischen Eigenschaften an den Metall-/Organik-Grenzflächen eingesetzt, um frühere Ergebnisse zu ergänzen [5, 6, 7, 8, 9].

Die Adsorptionshöhe des PTCDA-Moleküls verringert sich in der Serie $\text{Au}(111)$, $\text{Cu}_3\text{Au}(111)$ (im initialen, eher Au-analogen und im finalen, eher Cu-analogen Adsorptionszustand), $\text{Cu}(111)$,

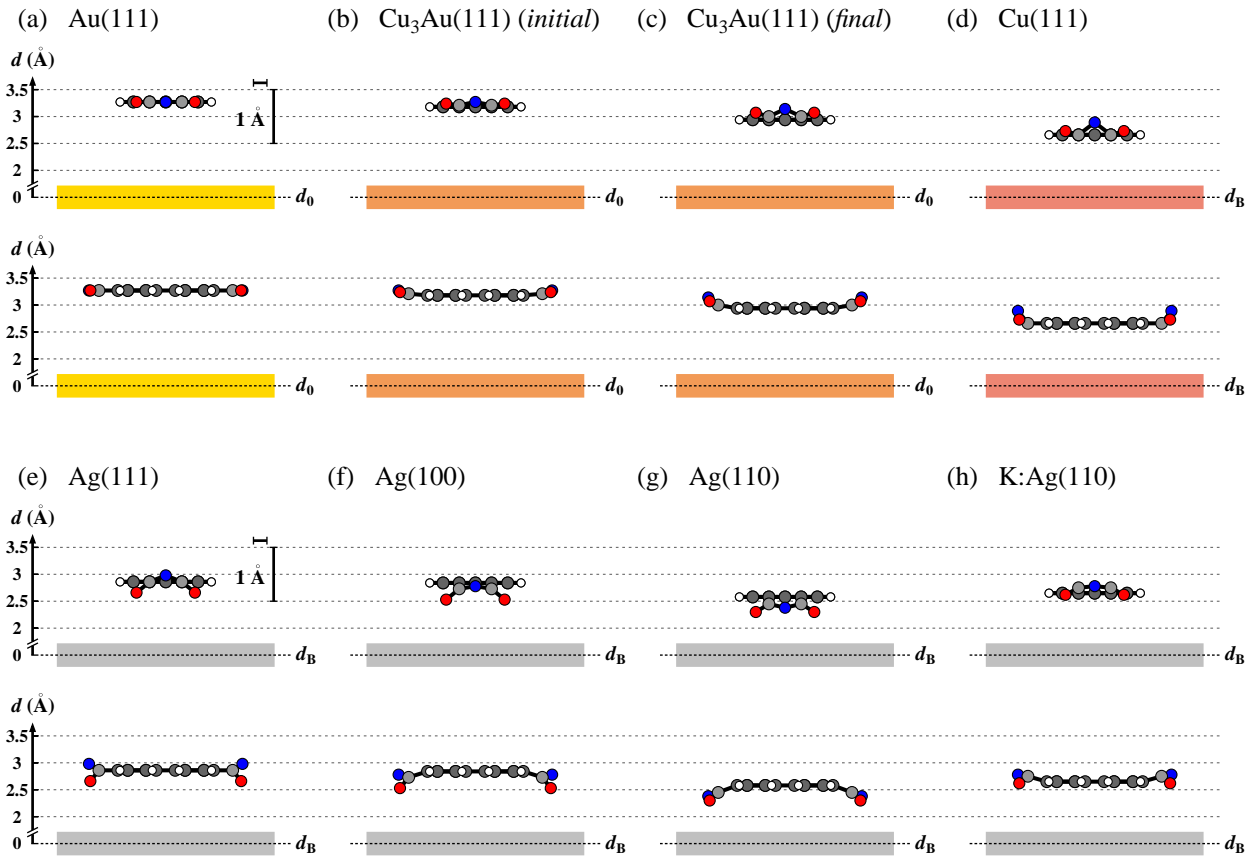


ABB. 2. Adsorptionskonfigurationen von PTCDA auf verschiedenen Münzmetalloberflächen, nämlich auf (a) Au(111) [2], (b) Cu₃Au(111) im initial state, (b) Cu₃Au(111) im final state, (d) Cu(111) [4], (e) Ag(111) [3], (f) Ag(100), (g) Ag(110) und (h) K:Ag(110). K:Ag(110) bezeichnet hier die (110)-Oberfläche von Ag, die durch eine Submonolage K-Atome modifiziert worden ist. Die oberen Zeilen zeigen jeweils Seitenansichten entlang der langen Molekülachse, während die unteren Zeilen jeweils Seitenansichten entlang der kurzen Molekülachse zeigen. H-Atome sind in weiß dargestellt, C_{funct}- und C_{peryl}-Atome in hellgrau bzw. dunkelgrau sowie O_{carb}- und O_{anhyd}-Atome in rot bzw. blau. Die einzelnen Oberflächen sind als farbige Regionen dargestellt. d bezeichnet die vertikale Adsorptionshöhe; die vertikale Skala ist um einen Faktor 4 überhöht und bezogen auf die Braggenebene (gestrichelte Linie, d_B) oder die (gemittelte) Position der relaxierten Oberfläche (gestrichelte Linie, d_0). Man beachte, dass für PTCDA/Au(111) die O-Atome auf derselben Höhe dargestellt sind wie die C_{funct}- und C_{peryl}-Atome, obwohl deren Positionen aus experimentellen Gründen nicht bekannt sind [2]. Man beachte weiterhin, dass die C_{funct}- und C_{peryl}-Atome für PTCDA auf Au(111) [2], Cu(111) [4] und Ag(111) [3] experimentell nicht unterschieden werden konnten. Im Fall von PTCDA auf Cu(111) ist aus den vorhandenen Daten jedoch gefolgert worden, dass C_{peryl} und C_{funct} innerhalb der experimentellen Genauigkeit dieselben d -Werte aufweisen [4].

Ag(111), Ag(100) und Ag(110), wie die XSW-Ergebnisse gezeigt haben (siehe Abb. 2). Zusätzlich weisen die intrinsisch planaren PTCDA-Moleküle im adsorbierten Zustand Verzerrungen auf, die sich je nach Oberfläche unterscheiden. Auf der Au(111)-Oberfläche wird PTCDA als im Wesentlichen planar angenommen [2], während auf Cu₃Au(111) und Cu(111) [4] PTCDA eine bootartige Verzerrung aufweist. Dabei ist der Perylenrumpf des Moleküls näher an der Oberfläche als die Atome innerhalb der funktionellen Gruppen. Anders verhält sich die Situation auf den kanonischen Ag-Oberflächen. Auf Ag(111) ist die Verzerrung sattelartig bzw. auf Ag(100) sowie Ag(110) gewölbeartig, wobei hier die Kohlenstoff- und Sauerstoff-Atome in den funktionellen Gruppen näher an der Oberfläche sind als der Perylenrumpf. Die Verzerrung des Perylenrückgrates nimmt für PTCDA/Ag(*hkl*) mit abnehmender Koordinationszahl der Oberflächenatome zu. Auf K:Ag(110) adsorbiert PTCDA ebenfalls in einer sattelartigen Konfiguration.

Ausgehend von unseren strukturellen und spektroskopischen Ergebnissen wird ein allgemeingültiger Bindungsmechanismus für die Adsorption von PTCDA auf Münzmetalloberflächen vorgeschlagen. Dieser Bindungsmechanismus besteht aus mehreren Komponenten (Bindungskanälen). Abgesehen von van der Waals-Wechselwirkungen (vdW), die immer vorliegen, sind die Hauptbindungskanäle (a) ein Metall-zu-Molekül Ladungstransfer sowie (b) lokale O—M Bindungen (M = Ag, K) an den Anhydridgruppen; (c) in einigen Fällen – insbesondere im Falle starker chemischer Bindung – können auch lokale C—M Bindungen (M = Ag, Cu) ausgebildet werden. Man beachte, dass diese Bindungskanäle (a)–(c) chemischer Natur sind, d.h. es werden tatsächliche chemische Bindungen zwischen der Oberfläche bzw. einzelnen Oberflächenatomen und den Adsorbatmolekülen ausgebildet.

Der Metall-zu-Molekül Ladungstransfer verstärkt sich mit der Reaktivität der Substrat-Oberfläche, wobei die Reaktivität hier anhand der Austrittsarbeit der sauberen Oberfläche bemessen wurde. In sehr guter Näherung wird ein linearer Zusammenhang zwischen der Gesamt-Adsorptionshöhe *d* des Moleküls (hier gegeben durch die Adsorptionshöhe des Perylenrumpfes) und der Austrittsarbeit Φ (die ebenfalls in der oben genannten Reihenfolge sinkt) gefunden. Für kleinere Werte von Φ nimmt der Ladungstransfer, d.h. die Elektronendonation, über die Grenzfläche hinweg zu, woraus ausgeprägtere elektrostatische Wechselwirkungen und somit kleinere *d*-Werte resultieren. Das Vorliegen des Metall-zu-Molekül Ladungstrfers konnte sowohl anhand der beobachteten Verschiebungen im XPS und UPS als auch durch DFT-Rechnungen gezeigt werden. Beispielsweise zeigen die beobachteten Verschiebungen der XPS-Levels des PTCDA hin zu niedrigeren Bindungsenergien eine erhöhte Elektronendichte auf dem Molekül an. Weiterhin wurde mit UPS das (partielle) Füllen des ehemals niedrigsten unbesetzten Molekülorbitals (former lowest unoccupied molecular orbital, F-LUMO) für PTCDA auf Cu(111) [9] und auf den Ag-Oberflächen beobachtet [8].

Das (partielle) Füllen des PTCDA (F-)LUMO erhöht die Flexibilität des molekularen Rückgrates, da dieses Orbital in Bezug auf einige intramolekulare Bindungen antibindend ist (z.B. in Bezug auf die C_{funct}=O_{carb} Doppelbindungen). Dadurch favorisiert der Metall-zu-Molekül Ladungstransfer die molekularen Verzerrungen. In den Fällen, in denen sich potentielle Bindungspartner – C- und, vor allem, O-Atome innerhalb des PTCDA-Moleküls auf der einen Seite und Oberflächenatome auf der anderen Seite – in gegenseitiger Nähe befinden, bilden sich lokale Bindungen aus, die zu den oben genannten, sattel- oder gewölbeartigen Adsorptionskonfigurationen führen. Dies gilt insbesondere für eine wohl-definierte, kommensurable Registratur zwischen der Adsorbatlage und der Substratoberfläche, d.h. für PTCDA auf den Ag-Oberflächen. Aus den beobachteten Adsorptionskonfigurationen sowie den daraus abgeleiteten Bindungslängen kann auf das Vorliegen kovalenter, dativer O—Ag Bindungen bzw. ionischer O—K Bindungen geschlossen werden. Diese dativen Bindungen stellen im Fall von O—Ag eine Rückdonation von Ladung

(Elektronen) dar. Sie sind umso kürzer, je offener die Oberfläche ist, und führen sogar lokal zu repulsiven Wechselwirkungen zwischen dem Perylenrumpf und der Oberfläche. Dies zeigt sich, den DFT-Rechnungen zufolge, anhand der spürbaren Wellung der Oberfläche unter PTCDA-Adsorption. Im Fall von O—K führen diese ionischen Bindungen zu einer erhöhten Elektronendichte auf dem Molekül. In beiden Fällen ist die Grenzflächenbindung verstärkt, wie sich an den (relativ betrachtet) kürzeren Bindungslängen zeigt (Man beachte, dass die Größe der beteiligten Atome hier berücksichtigt werden muss). Daher lässt sich an dieser Stelle schlussfolgern, dass diese beiden Bindungskanäle, Metall-zu-Molekül Ladungstransfer und lokale O—M Bindungen (M = Ag, K), in synergistischer Art und Weise gekoppelt sind.

Im Rahmen dieser Arbeit wird ein schlüssiges Bild des komplexen, synergistischen Bindungsmechanismus präsentiert, welches die vertikale Verzerrung des adsorbierten PTCDA im Detail erklärt. Es ist davon auszugehen, dass der hier vorgeschlagene Mechanismus mit seinen relevanten Komponenten (Bindungskanälen) von allgemeiner Bedeutung ist und dementsprechend auch für die Adsorption anderer, π -konjugierter und funktionalisierter Moleküle auf (Metall-)Oberflächen gilt.

Referenzen

- [1] H. Klauk (Ed.), *Organic Electronics: Materials, Manufacturing and Applications*, Wiley-VCH, Weinheim, Germany (2006).
- [2] S. K. M. Henze, O. Bauer, T.-L. Lee, M. Sokolowski, F. S. Tautz, *Vertical bonding distances of PTCDA on Au(111) and Ag(111): Relation to the bonding type*, *Surface Science* **601**, 1566–1573 (2007).
- [3] A. Hauschild, R. Temirov, S. Soubatch, O. Bauer, A. Schöll, B. C. C. Cowie, T.-L. Lee, F. S. Tautz, and M. Sokolowski, *Normal-incidence x-ray standing-wave determination of the adsorption geometry of PTCDA on Ag(111): Comparison of the ordered room-temperature and disordered low-temperature phases*, *Physical Review B* **81**, 125432 (2010).
- [4] A. Gerlach, S. Sellner, F. Schreiber, N. Koch, and J. Zegenhagen, *Substrate-dependent bonding distances of PTCDA: A comparative x-ray standing-wave study on Cu(111) and Ag(111)*, *Physical Review B* **75**, 045401 (2007).
- [5] K. Glöckler, C. Seidel, A. Soukopp, M. Sokolowski, E. Umbach, M. Böhringer, R. Berndt, and W.-D. Schneider, *Highly ordered structures and submolecular scanning tunnelling microscopy contrast of PTCDA and DM-PBDCI monolayers on Ag(111) and Ag(110)*, *Surface Science* **405**, 1–20 (1998).
- [6] L. Kilian, E. Umbach, and M. Sokolowski, *A refined structural analysis of the PTCDA monolayer on the reconstructed Au(111) surface—“Rigid or distorted carpet?”*, *Surface Science* **600**, 2633–2643 (2006).
- [7] J. Ikononov, O. Bauer, M. Sokolowski, *Highly ordered thin films of perylene-3,4,9,10-tetracarboxylic acid dianhydride (PTCDA) on Ag(100)*, *Surface Science* **602**, 2061–2068 (2008).
- [8] Y. Zou, L. Kilian, A. Schöll, T. Schmidt, R. Fink, and E. Umbach, *Chemical bonding of PTCDA on Ag surfaces and the formation of interface states*, *Surface Science* **600**, 1240–1251 (2006).
- [9] S. Duhm, A. Gerlach, I. Salzmann, B. Bröker, R. L. Johnson, F. Schreiber, N. Koch, *PTCDA on Au(111), Ag(111) and Cu(111): Correlation of interface charge transfer to bonding distance*, *Organic Electronics* **9**, 111–118 (2008).

Abstract

The present work aims at establishing a comprehensive model for the bonding mechanism for the adsorption of the organic prototype molecule 3,4,9,10-perylenetetracarboxylic 3,4:9,10-dianhydride (PTCDA; see Fig. 1) on coinage metal surfaces. Due to its chemical constitution, the PTCDA molecule allowed studying the effects of both the π -conjugated system and the presence of functional groups, including heteroatoms, on the interfacial bonding. As a basic principle, the surface bonding mechanism of large π -conjugated molecules is of immense interest for understanding the structural and electronic properties of organic thin films [1]. Insight into relevant interaction channels and their relative contribution to the bonding can be obtained from a detailed determination of the bonding configuration of the same molecule on different crystal faces of chemically related substrates (or one substrate), including the positions of all relevant atoms.

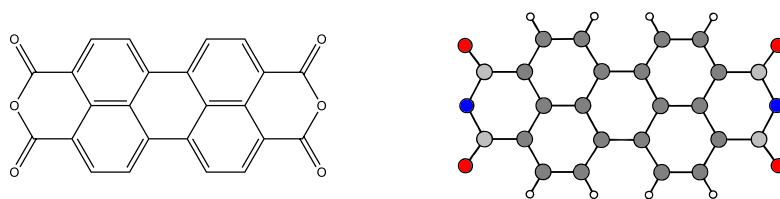


FIG. 1. Valence bond structure (left) and ball-and-stick model (right) of the PTCDA molecule. The carbon atoms within the perylene core and within the functional groups are shown in dark gray (C_{peryl}) and light gray (C_{funct}), respectively, while the chemically nonequivalent oxygen atoms are shown in red (O_{carb}) and blue (O_{anhyd}). Hydrogen atoms are depicted in white.

Within the context of the present work, we have investigated the geometric adsorption configurations of PTCDA on the $\text{Cu}_3\text{Au}(111)$, the $\text{Ag}(100)$, the $\text{Ag}(110)$, and the $\text{K}:\text{Ag}(110)$ surface [i.e., a potassium-modified, reconstructed $\text{Ag}(110)$ surface] with the x-ray standing waves (XSW) technique under normal incidence. Thereby, we have amended the series of earlier XSW results on the adsorption configurations of PTCDA on coinage metal (111) surfaces, namely, on $\text{Au}(111)$ [2], $\text{Ag}(111)$ [3], and $\text{Cu}(111)$ [4]. In addition, we have employed low-energy electron diffraction (LEED) and scanning tunneling microscopy (STM) in combination with x-ray photoelectron spectroscopy (XPS) and ultraviolet photoelectron spectroscopy (UPS) as well as theoretical calculations [at density functional theory (DFT) level] for clarifying both the lateral geometric structures and the electronic properties at the metal/organic interfaces, complementing earlier results [5, 6, 7, 8, 9].

The adsorption height of the PTCDA molecules decreases in the series $\text{Au}(111)$, $\text{Cu}_3\text{Au}(111)$ (in the initial, more Au-analogous and the final, more Cu-analogous adsorption state), $\text{Cu}(111)$, $\text{Ag}(111)$, $\text{Ag}(100)$, and $\text{Ag}(110)$, as was revealed by XSW (see Fig. 2). In addition, the intrinsically planar PTCDA molecules exhibit distortions in the adsorbed state which alter from one surface to the next. On the $\text{Au}(111)$ surface, PTCDA is concluded to be essentially undistorted [2] while on

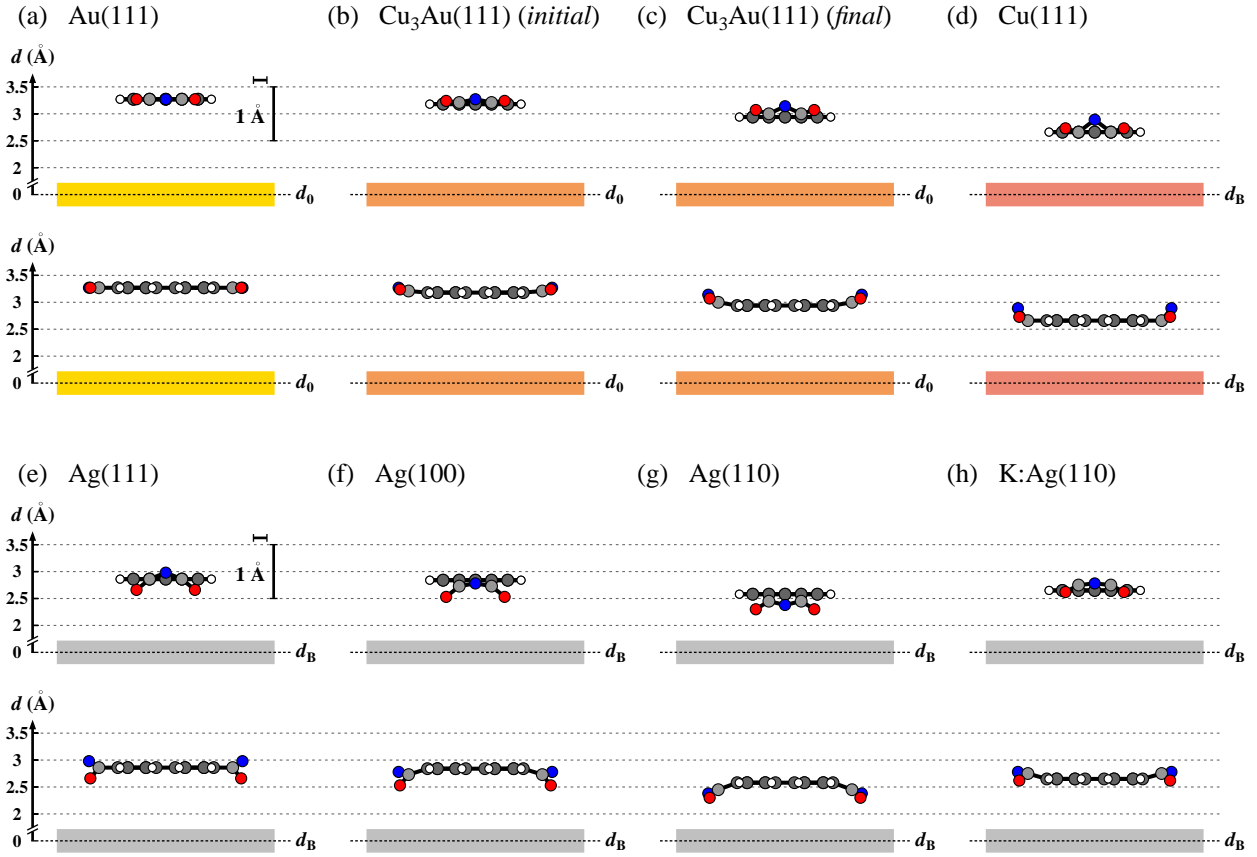


FIG. 2. Adsorption configurations of PTCDA on various coinage metal surfaces, namely, of PTCDA on (a) Au(111) [2], (b) Cu₃Au(111) in the initial state, (c) Cu₃Au(111) in the final state, (d) Cu(111) [4], (e) Ag(111) [3], (f) Ag(100), (g) Ag(110), and (h) K:Ag(110). K:Ag(110) denotes the (110) surface of Ag which has been modified by a submonolayer of K atoms. The top rows show side views along the long molecular axis while the bottom rows show side views along the short molecular axis. H atoms are shown in white, C_{funct} and C_{peryl} atoms in light gray and dark gray, and O_{carb} and O_{anhyd} atoms in red and blue, respectively. The individual surfaces are depicted as colored regions. d denotes the vertical adsorption height; the vertical scale is enlarged by a factor of 4 and referenced against the Bragg plane (dashed line, d_B) or the (averaged) position of the relaxed surface (dashed line, d_0), respectively. Note that for PTCDA/Au(111) the O atoms are depicted at the same adsorption height as the C_{funct} and C_{peryl} atoms although their positions are not known for experimental reasons [2]. Note further that the C_{funct} and C_{peryl} atoms could not be distinguished experimentally for PTCDA on Au(111) [2], Cu(111) [4], and Ag(111) [3]. In the case of PTCDA on Cu(111), however, C_{peryl} and C_{funct} were concluded to exhibit the same d values within the experimental resolution [4].

Cu₃Au(111) and Cu(111) [4] PTCDA exhibits a boat-like distortion with the perylene core of the molecule being closer to the surface than the atoms within the functional groups. On the canonical Ag surfaces, however, the situation is reversed. The distortion of the PTCDA molecule is saddle-like on Ag(111) [3] and arch-like on Ag(100) and Ag(110), respectively, with the carbon and the oxygen atoms within the functional groups being closer to the surface than the perylene core now. The distortion of the molecular C backbone increases with decreasing surface atom coordination number for PTCDA/Ag(*hkl*). On K:Ag(110), PTCDA adsorbs in a saddle-like configuration, too.

On the basis of our structural and spectroscopic results, we propose a universal bonding mechanism for the adsorption of PTCDA on coinage metal surfaces. This bonding mechanism is composed of several constituents (bonding channels). Besides the inevitable van der Waals (vdW) interactions, the main bonding channels are (a) a metal-to-molecule charge transfer and (b) local O—M bonds (M = Ag, K) on the anhydride groups; (c) in some cases—especially in the case of strong surface bonding—, local C—M bonds (M = Ag, Cu) may evolve, too. Note that these bonding channels (a)–(c) are of chemical nature, that is, actual chemical bonds are formed between the surface (atoms) and the adsorbate molecules.

The metal-to-molecule charge transfer intensifies with the reactivity of the substrate surface, for which we have employed the work function of the clean surface as the relevant measure. In very good approximation, we find a linear correlation between the overall molecular adsorption height *d* (as given by the adsorption height of the perylene core) and the work function Φ (which decreases in the above-noted series, as well). With decreasing values of Φ , the charge donation, i.e., the electron donation, across the interface increases which results in more pronounced electrostatic interactions and thus in smaller *d* values. The presence of the metal-to-molecule charge transfer has been proven by the observed shifts in both XPS and UPS as well as by DFT calculations. For example, the observed shifts of the XPS levels towards lower binding energies for PTCDA in the monolayer regime indicated an increased electron density on the molecule. In addition, a (partial) filling of the former lowest unoccupied molecular orbital (F-LUMO) was observed in UPS for PTCDA on Cu(111) [9] and the Ag surfaces [8].

The (partial) filling of the PTCDA (F-)LUMO enhances the flexibility of the molecular backbone because this orbital is antibonding with respect to several intramolecular bonds (for example, with respect to the C_{funct}=O_{carb} double bonds). Thereby, the metal-to-molecule charge transfer favors the molecular distortions. In those cases where potential binding partners—C and, in particular, O atoms within the PTCDA molecule on the one hand and surface atoms on the other hand—are in close proximity, local interactions evolve, leading to the above noted saddle- or arch-like adsorption configurations. This is true for a well-defined, commensurate registry between the adsorbate layer and the substrate surface, namely, for PTCDA on the Ag surfaces. From the observed adsorption heights and the bond length deduced thereof, the presence of covalent, dative O—Ag bonds and ionic O—K bonds can be anticipated. These dative bonds represent an electron back-donation in the case of O—Ag. They are the shorter the more open the surface is, and lead even to partly repulsive interactions between the perylene core and the surface. This is expressed by a significant buckling of the Ag surfaces upon PTCDA adsorption according to DFT. In the case of O—K, these ionic bonds result in an increased electron density on the molecule. In both cases, however, the interfacial bonding is intensified, as is expressed by (relatively) shorter bond lengths (Note that the size of the involved atoms has to be considered, too). Thus, it must be concluded that these two main bonding channels, metal-to-molecule charge transfer and local O—M bonds (M = Ag, K), are coupled in a synergistic manner.

Within this work, we present a conclusive picture of the complex, synergistic bonding mechanism that explains the out-of-plane distortion of the adsorbed PTCDA in detail. We further suggest

that our proposed bonding mechanism with its relevant constituents (bonding channels) is of general validity and also applies to the adsorption of other organic, π -conjugated and functionalized molecules on (metal) surfaces.

References

- [1] H. Klauk (Ed.), *Organic Electronics: Materials, Manufacturing and Applications*, Wiley-VCH, Weinheim, Germany (2006).
- [2] S. K. M. Henze, O. Bauer, T.-L. Lee, M. Sokolowski, F. S. Tautz, *Vertical bonding distances of PTCDA on Au(111) and Ag(111): Relation to the bonding type*, *Surface Science* **601**, 1566–1573 (2007).
- [3] A. Hauschild, R. Temirov, S. Soubatch, O. Bauer, A. Schöll, B. C. C. Cowie, T.-L. Lee, F. S. Tautz, and M. Sokolowski, *Normal-incidence x-ray standing-wave determination of the adsorption geometry of PTCDA on Ag(111): Comparison of the ordered room-temperature and disordered low-temperature phases*, *Physical Review B* **81**, 125432 (2010).
- [4] A. Gerlach, S. Sellner, F. Schreiber, N. Koch, and J. Zegenhagen, *Substrate-dependent bonding distances of PTCDA: A comparative x-ray standing-wave study on Cu(111) and Ag(111)*, *Physical Review B* **75**, 045401 (2007).
- [5] K. Glöckler, C. Seidel, A. Soukopp, M. Sokolowski, E. Umbach, M. Böhringer, R. Berndt, and W.-D. Schneider, *Highly ordered structures and submolecular scanning tunnelling microscopy contrast of PTCDA and DM-PBDCI monolayers on Ag(111) and Ag(110)*, *Surface Science* **405**, 1–20 (1998).
- [6] L. Kilian, E. Umbach, and M. Sokolowski, *A refined structural analysis of the PTCDA monolayer on the reconstructed Au(111) surface—“Rigid or distorted carpet?”*, *Surface Science* **600**, 2633–2643 (2006).
- [7] J. Ikononov, O. Bauer, M. Sokolowski, *Highly ordered thin films of perylene-3,4,9,10-tetracarboxylic acid dianhydride (PTCDA) on Ag(100)*, *Surface Science* **602**, 2061–2068 (2008).
- [8] Y. Zou, L. Kilian, A. Schöll, T. Schmidt, R. Fink, and E. Umbach, *Chemical bonding of PTCDA on Ag surfaces and the formation of interface states*, *Surface Science* **600**, 1240–1251 (2006).
- [9] S. Duhm, A. Gerlach, I. Salzmänn, B. Bröker, R. L. Johnson, F. Schreiber, N. Koch, *PTCDA on Au(111), Ag(111) and Cu(111): Correlation of interface charge transfer to bonding distance*, *Organic Electronics* **9**, 111–118 (2008).

Contents

	Page
Chapter 1 Introduction	1
Chapter 2 Review of the literature	5
2.1 Surface bonding of small molecules	5
2.1.1 Blyholder model	5
2.1.2 Newns-Anderson model	6
2.1.3 Hoffmann model	8
2.1.4 Hammer-Nørskov model	9
2.2 Properties of PTCDA	10
2.2.1 Crystal structures of PTCDA	11
2.2.2 PTCDA on coinage metal surfaces	12
Chapter 3 Theoretical Background of experimental methods	19
3.1 The x-ray standing wavefield absorption technique	19
3.1.1 Dynamical theory of x-ray diffraction	20
3.1.2 Intensity of the x-ray standing wavefield and determination of perpendicular positions	22
3.1.3 Asymmetric Bragg reflections	27
3.1.4 Dipole approximation of the photoemission process and its limitations	29
3.2 Additional experimental methods	32
3.2.1 Low energy electron diffraction	32
3.2.2 Scanning tunneling microscopy	36
3.2.3 X-ray photoelectron spectroscopy	37
3.2.4 Ultraviolet photoelectron spectroscopy	40
Chapter 4 Experimental	43
4.1 Experimental setups	43
4.1.1 SPA-LEED setup	43
4.1.2 XSW setups I and II	44
4.2 Sample preparation	47
4.3 Experimental data acquisition and treatment	48
4.3.1 LEED data	48
4.3.2 XPS data	50
4.3.3 XSW data	59
4.3.4 STM data	65
4.3.5 UPS data	65
Chapter 5 PTCDA on Cu(111)	67
5.1 Review of the literature	67
5.2 Experimental procedure	69

5.3	Results	70
5.3.1	Ordered PTCDA structures	72
5.3.2	Surface reconstruction	80
5.4	Concluding Discussion	82
Chapter 6	PTCDA on Cu₃Au(111)	87
6.1	Review of the literature	87
6.2	Experimental procedure	90
6.3	Results for the clean Cu ₃ Au(111) surface	93
6.3.1	Lateral structure	93
6.3.2	Surface composition	100
6.3.3	Vertical structure	102
6.4	Concluding Discussion, part I: the clean Cu ₃ Au(111) surface	108
6.5	Results for the PTCDA-covered Cu ₃ Au(111) surface	114
6.5.1	Lateral structure	114
6.5.2	Surface composition	115
6.5.3	Vertical structure	116
6.6	Results for PTCDA on the Cu ₃ Au(111) surface	119
6.6.1	Lateral structure and growth	119
6.6.2	Electronic structure of the core levels in PTCDA	137
6.6.3	XSW photoelectron yield curves	147
6.6.4	Adsorption configurations	151
6.7	Concluding Discussion, part II: PTCDA on Cu ₃ Au(111)	159
Chapter 7	Overview on the experimental results and general discussion	177
7.1	PTCDA on coinage metal surfaces: a review of the lateral structures and adsorption configurations	177
7.2	DFT calculations of PTCDA on Ag surfaces: theoretical methods	187
7.3	Surface bonding via the perylene core: charge transfer and the Newns-Anderson model	190
7.4	Evidences for metal-to-molecule charge transfer from photoemission and DFT	197
7.5	Surface bonding via the functional groups: relevance of local interactions	208
7.6	Interplay of the bonding channels	214
7.7	Manipulation of bonding channels	224
7.8	Final general conclusions	229
7.9	Outlook	229
Chapter 8	Summary	233
Appendix A	XSWAVES: An x-ray standing wavefield absorption data evaluation routine for Origin 8	237
A.1	Purpose of XSWAVES	237
A.2	Installation and operation	238
A.3	Computational algorithm	246
A.4	Source codes	258
A.4.1	Fitting algorithm for Reflectivity data (XSWAVES_ReflectivityFit_v2_5.fdf)	258

A.4.2	Fitting algorithm for XSW Absorption Profile data (XSWAVES_AbsorptionProfileFit_v_2_5.fdf)	266
A.4.3	Fitting algorithm for XSW Absorption Profile data: ‘special fit model’ (XSWAVES_AbsorptionProfileFit_Special_v_2_5.fdf)	275
A.5	Exemplary input files	285
A.5.1	Exemplary Substrate Parameters input file (*.txt)	285
A.5.2	Exemplary Reflectivity input file (*.txt)	286
A.5.3	Exemplary XSW Absorption Profile input file (*.txt)	287
Appendix B	Calculation of structure factors and Debye-Waller factors	289
B.1	Structure factor	289
B.2	Debye-Waller factor	293
Appendix C	PTCDA on Ag(100) and Ag(110)	295
C.1	Review of the literature	295
C.2	Experimental procedure	297
C.3	Results	299
C.3.1	Lateral structure	299
C.3.2	Electronic structure of the valence bands in PTCDA	306
C.3.3	Electronic structure of the core levels in PTCDA	307
C.3.4	XSW photoelectron yield curves	316
C.4	Adsorption site determination of PTCDA on Ag(100) by means of XSW	327
Appendix D	Coadsorption of K and PTCDA on Ag(110)	337
D.1	Review of the literature	337
D.2	Experimental procedure	338
D.3	Results	339
D.3.1	Lateral structure	339
D.3.2	Electronic structure of the core levels in PTCDA	347
D.3.3	XSW photoelectron yield curves	353
D.4	Simulation of the one-dimensional SPA-LEED scans for PTCDA/K:Ag(110)	358
D.4.1	Computational details	358
D.4.2	Source code	359
Appendix E	Influence of the nondipolar parameters on the XSW fitting results	365
Appendix F	Validity of the computational algorithm of XSWAVES, version 2.5	369
Bibliography		375
List of Abbreviations		431
List of Figures		441
List of Tables		447
Acknowledgments		451
List of publications		453

1

Introduction

The present work describes an experimental investigation on the bonding of the model molecule 3,4,9,10-perylenetetracarboxylic 3,4:9,10-dianhydride (PTCDA) on different coinage metal surfaces performed by the normal incidence x-ray standing wavefield absorption technique (NIXSW) over the last years. The surface bonding mechanism of atomic and molecular adsorbates, in general and in particular that of large π -conjugated, organic molecules, is a subject of intense experimental and theoretical research,^{1,2} especially when the organic molecules carry functional groups.^{3,4} A detailed picture of the surface bonding is the key to the understanding of fundamental processes at the metal/organic interface as well as to the development of possible technological applications, for example, in heterogeneous catalysis or in organic electronic devices.^{1,5–8} Such fundamental processes may be the formation of new geometric and electronic structures, or surface reactions, i.e., the formation and cleavage of chemical bonds.^{1,5} Since electronic properties of adsorbate layers and the chemical behavior of the molecules on the surface are influenced by their geometric structures, precise knowledge of adsorbate structures is the basis for a deeper insight into the surface bonding mechanism.⁹ In turn, the adsorbate structure in the monolayer depends on the—sometimes very delicate—balance between all relevant interfacial interactions and hence may serve to discern the details of these.¹

On the one hand, detailed bonding concepts are discussed for the chemisorption of *small* molecules on metal surfaces.^{1,10–15} On the other hand, the bonding in coordination complexes, also with extended ligands, is also well understood in gas- and liquid-phase chemistry.^{16–18} To some extent, concerning the charge transfer between the binding partners at the surface or in the metal complex, for example, the models utilize very similar concepts, although the situations are very different at a first glance.^{12,13,19} In the latter case of coordination complexes, only a single metal center or only a small number of metal atoms is coordinated by atomic or molecular ligands. Here, the picture of overlapping atomic orbitals is employed for the bond formation.^{19,20} In the former case of interface bonding, however, the metal atoms form an ordered structure in the bulk phase and at the surface. Thus, the electronic properties need to be described in a band-structure picture.^{21,22} Evidently, this may complicate the characterization of the bonding mechanism. In addition, multiple interaction sites might be present due to the complex structure of the molecule/substrate interface consisting of the long-range ordered metal surface and the large functional molecules. Since the available surface bonding concepts pertain to small molecules, their application to the adsorption of large organic molecules is demanding and deserves interest.

The detailed knowledge about the adsorption geometry of molecules on surfaces provides insight into the relevant interfacial interactions. In general, the bonding cannot be explained by one particular type of interaction alone, e.g., van der Waals (vdW), electrostatic, or covalent interactions. We will refer to locally confined interactions of a specific physical or chemical type as “bonding channels” in the following. Most interesting is the situation when several compet-

ing bonding channels are involved. Although theoretical decomposition schemes exist,^{23–27} it is difficult then to clarify their particular role since any variation of the molecular structure or the substrate leads to combined modifications. In a first step, however, insight can be obtained from a detailed determination of the bonding configuration of the *same* molecule on *one* crystal face of *different* substrate elements and, in a second step, on *different* crystal faces of *one* substrate, including the positions of all relevant atoms.

In the present work, the adsorption geometry of the functionalized organic molecule 3,4,9,10-perylenetetracarboxylic 3,4:9,10-dianhydride (PTCDA) on coinage metal^{a)} surfaces was investigated with the x-ray standing wavefield absorption technique (XSW) under normal incidence (NIXSW).^{28,29} PTCDA consists of an aromatic perylene core and two functional anhydride groups. Here, the PTCDA molecule serves as a testing probe for the relevant bonding channels on every surface. In principle, two major bonding channels may be anticipated: one via the perylene core and a second one via the functional groups, in particular via the heteroatoms. This is due to the, by tendency, contrastive characters of the different moieties within the PTCDA molecule, namely, the electron-poor/-accepting character of the perylene core and the electron-rich/-donating character of the O atoms within the functional groups.³⁰ Because of these contrastive characters of the (spatially separated) molecular moieties *within* the molecule and also because of the complex structure of the metal/organic interface, the description of the surface bonding of *large* molecules solely in the framework of (one of) the already-available bonding concepts for atoms and *small* molecules may not be possible, therefore requiring an advanced picture of the surface bonding mechanism.

With the XSW technique, adsorption heights, adsorption sites, and possible distortions of molecules in (sub-)monolayers on surfaces (of single-crystalline substrates) can in principle be determined with high accuracy.^{28,29,31,32} This method has so far been used to investigate a variety of adsorbed organic molecules, ranging from small molecules^{33–37} over native and perfluorinated pentacene (Pen, PFP),^{38,39} quinones,⁴⁰ 1,4,5,8-naphthalenetetracarboxylic 1,8:4,5-dianhydride (NTCDA),^{41,42} PTCDA,^{32,43} and native and metallated phthalocyanines (Pc, MPc)^{44–50} to fullerenes,^{51–53} for example. However, a conclusive picture of surface bonding of broad validity has not yet been obtained. Therefore, we have systematically studied the influence of several parameters on the surface bonding, namely, of:

- (a) the chemical nature and the composition of the surface,
- (b) the coordination number of the surface atoms,
- (c) the presence of several bonding channels, and
- (d) the coadsorption of reactive metal atoms.

So far, the adsorption geometries of PTCDA on Au(111),⁵⁴ Ag(111),^{32,55} and Cu(111)⁴³ have been reported. On the Ag(111) and the Cu(111) surfaces, a distortion of the intrinsically planar molecules upon adsorption was found. In the former case, the molecules adopt a saddle-like configuration where some of the O atoms are closer to the surface than the perylene core,^{32,55} while, in the latter case, the perylene core of the molecule is found closer to the surface than the O atoms within the functional groups.⁴³ In both cases, the adsorption heights are below the sum of the vdW radii of the atoms at the interface. Within the context of the present work, the length of a bond, i.e., the value of the vertical adsorption height or atom-atom distances across the metal/organic interface derived thereof, have been taken as a measure for the strength of the chemical bond:^{56,57} shorter bonds indicate stronger attractive interactions which overcompensate inevitable Pauli repulsion. Hence, the experimental findings indicate a chemisorptive nature of the interfacial

^{a)}The term “coinage metals” refers to the elements Cu, Ag, and Au (group 11 of the periodic table of the elements).²⁰

interactions for PTCDA on Ag(111) and Cu(111), whereas on the Au(111) surface physisorption is present.⁵⁴ In conjunction with spectroscopic results, where a charge transfer from the metal to the molecule has been proven,^{58–60} the so-far determined adsorption configurations have been interpreted such that the interaction with the perylene core plays the dominant role for surface bonding of PTCDA.^{4,58} However, the partial bending of the O atoms in PTCDA on Ag(111) towards the surface is indicative of the significance of that particular bonding channel,³² in contrast to the situation on Cu(111).⁴³ Thus, the role of the functional groups in surface bonding needs to be clarified.

As already noted, the adsorption heights and configurations of PTCDA on various coinage metal surfaces have been studied systematically with XSW in the present work, addressing the above-mentioned points. The XSW investigations have been complemented by structural data from spot profile analysis low energy electron diffraction (SPA-LEED) and scanning tunneling microscopy (STM), and also by data from x-ray and ultraviolet photoelectron spectroscopy (XPS, UPS). In addition, density functional theory (DFT) has been employed to shine light on the relevant interactions leading to the observed adsorption geometries for PTCDA on Ag surfaces. Note that in the course of the present work the expressions “adsorption geometry” and “adsorption configuration” of the molecule are used synonymously. In the strict chemical sense, configuration may be discerned from conformation. In the latter case, a molecule can interchange between different geometries without bond cleavage.²⁰ In the first case, however, bonds have to be cleaved and (re-)formed for the structural transformation. Since any change in the molecular structure requires a minimum activation energy, configuration and conformation of a molecule differ from each other only in the height of the energy barrier between the different structures.²⁰ Because the crossover from conformation to configuration is smooth,²⁰ and also because we anticipate an influence by the presence of the substrate via the surface bonding, the differentiation between the two terms is disregarded here.

As outlined above, the chemical nature of the surface, i.e., the chemical element, influences the surface bonding and thereby the adsorption configuration. The configurations of PTCDA on Au(111) and Cu(111) are quite contrary. While on the more noble Au(111) surface⁶¹ PTCDA is physisorbed, it is chemisorbed on the more reactive Cu(111) surface.^{54,60} Since Au and Cu form stable intermetallic compounds,²⁰ the idea of the present work was also to investigate the adsorption configuration on such an intermetallic surface where both elements are present in parallel. The structural characterization of PTCDA on Cu₃Au(111), where in principle the Cu : Au ratio is 3 : 1, clarifies (**ad a**) the impact of the different substrate elements on the overall bonding, and (**ad c**) the relevance of multiple bonding channels, also for the pure systems.

The surface reactivity not only depends on the chemical element,^{b)} but also on the packing density and thus on the coordination number of the surface atoms.⁶² Therefore, when (**ad b**) changing the crystal face of the substrate element, changes in the adsorption geometry may be expected. Also, since (**ad c**) several plausible bonding channels are present, their coupling and relative importance might be altered. In the present work this aspect was investigated for PTCDA on the more open Ag(100) and the most open Ag(110) surfaces, complementing the knowledge about the surface bonding of PTCDA on the densely packed Ag(111) surface.³² Since the work function decreases in the series Ag(111), Ag(100), and Ag(110),⁶³ we expected a strengthening of the surface

^{b)}The reactivity of chemical elements may be classified by their standard electrode potentials E° , for example. For the elements of interest in the present work, the E° values amount to -2.925 V for K/K⁺, $+0.521$ V for Cu/Cu⁺, $+0.340$ V for Cu/Cu²⁺, $+0.7991$ V for Ag/Ag⁺, $+1.390$ V for Ag/Ag²⁺, $+1.691$ V for Au/Au⁺, and $+1.401$ V for Au/Au³⁺, respectively, in acid solution with pH = 0.²⁰ Hence, the reactivity of these elements decreases in the sequence K, Cu, Ag, and Au.

bonding and thus decreasing adsorption heights accompanied with qualitatively and quantitatively different molecular distortions of PTCDA in the same sequence which was to be tested.

Lastly, the relevance of the metal–perylene core interaction was further probed by **(ad d)** the coadsorption of K atoms. Potassium is reactive,²⁰ and the K atoms on the surface may, in principle, also donate charge to the PTCDA molecules, in competition to the Ag surface atoms. Besides, as alkali metals are known to interact with the O atoms in PTCDA,^{64,65} **(ad c)** an influence on the adsorption configuration via this bonding channel is also conceivable. If we assume both bonding channels to be relevant in the surface bonding, their potential interplay can be probed at that point. Either way, a modified adsorption configuration can be rationalized as an indicator of the relevant interactions at the interface. Moreover, the coadsorption of a carefully chosen reactive element might give an opportunity to specifically tune the surface bonding.

The present thesis is organized as follows: Chapter 2 gives a review of the literature concerning both the bonding models for molecular adsorbates in general as well as the knowledge about surface bonding of PTCDA on coinage metal surfaces in particular. In Chapter 3, the theoretical foundations of the experimental techniques are outlined, with special emphasis on XSW. The experimental procedures are described in Chapter 4, while the results of the experimental investigations are presented in Chapter 5 for PTCDA on Cu(111), Chapter 6 for PTCDA on Cu₃Au(111), Appendix C for PTCDA on Ag(100) and Ag(110), and Appendix D for PTCDA coadsorbed with K on Ag(110). Note that the experimental results for the latter three systems, that is, for PTCDA on the Ag(100) and Ag(110) surfaces—also with K being coadsorbed in the latter case—, have largely been published already (see Refs. 66, 67, and 68, respectively) and thus are described only briefly in the appendix for reasons of completeness. Chapter 7 gives a general discussion, bringing together the experimental findings to a detailed picture of the surface bonding mechanism for PTCDA on the various coinage metal surfaces. In the course of this chapter, also theoretical results for PTCDA on the low-index Ag surfaces obtained from DTF are presented. They support the conclusions drawn from the corresponding experimental results. This work concludes with a summary in Chapter 8.

2

Review of the literature

This chapter briefly reviews the knowledge about the bonding of adsorbates to well-defined metal surfaces that has been gained over the past decades. In particular, the surface bonding of atomic or small molecular adsorbates is well described in the framework of several models. These models range from a qualitative to a quantitative description of the bonding. An overview on these fundamental concepts is found in Sec. 2.1. Although their statements are helpful in the discussion of the surface bonding of a large organic molecule later in this work, direct application is challenging because the real situation may be much more complex due to the higher number of involved atoms and molecular moieties/functional groups.

Recently, there have been strong experimental as well as theoretical efforts towards the understanding of the surface bonding of large organic molecules. In particular, the aromatic model compound PTCDA has been employed for probing the relevant effects at the metal/organic interface. The properties of this molecule, which was also used in the present work, as well as the literature about the bonding of PTCDA to coinage metal surfaces are introduced in Sec. 2.2.

2.1 Surface bonding of small molecules

The chemisorption of atoms and small molecules on metal surfaces has been studied intensely over the last decades.¹ One of the most prominent examples is the bonding mechanism of carbon monoxide (CO).⁵ In the following section, four bonding models will be highlighted which describe the surface bonding of various atoms and small molecules, such as H, CO and ammonia (NH₃).¹ All models originate from theoretical work, but have been supported by experimental findings. The ideas used in the discussion of the surface bonding of PTCDA bear similarities to their basic concepts. Also, analogies between the different models can be made out.

2.1.1 Blyholder model

The model introduced by Blyholder in 1964 describes the chemisorption of CO on transition metal surfaces on the basis of the Hückel molecular orbital method,¹⁰ employing also the frontier orbital concept.^{69,70} This model has been developed on the basis of experimental findings regarding the vibrational properties of adsorbed CO in comparison to those of CO in metal-carbonyl complexes.^{10,71} The Blyholder model is known to be oversimplified since it only considers frontier orbitals to be relevant for the surface bonding and neglects the contributions from lower-lying orbitals of CO to the bonding.⁷² Nonetheless, it is still helpful for a qualitative understanding of the bonding mechanism and the intramolecular responses to the surface bond formation.

The Blyholder model involves a donor–acceptor mechanism between the two binding partners, namely, the CO molecule and the metal surface, and thus a charge transfer across the interface,

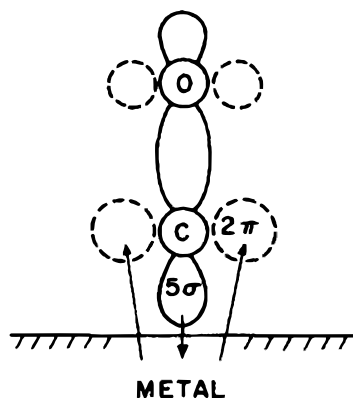


FIG. 2.1. Blyholder model for CO chemisorption on metal surfaces. Charge donation (bonding) from the 5σ orbital of CO (solid lines) to the metal and backdonation (backbonding) from the metal to the 2π orbitals of CO (dashed lines) are indicated by arrows. Taken from Ref. 73.

as is depicted in Fig. 2.1.^{10,73–75} Two synergistic bonding channels are part of the interfacial bond formation. On the one hand, a coordinative or dative σ -bond forms through the overlap of the highest occupied molecular orbital (HOMO) of CO and a suitable acceptor orbital of a metal atom, e.g., a d orbital. The donor state in this case is the 5σ orbital of CO which is mainly localized at the C atom.^{10,18} Note again that the Blyholder model is oversimplified and that the σ -donation has recently been shown to cause a repulsive instead of an attractive interaction, in fact.^{72,76,77} On the other hand, backbonding occurs via the electron donation from occupied metal states (d orbitals) to the lowest unoccupied molecular orbital (LUMO) of CO, namely, the 2π orbitals, by a coordinative π -bond.¹⁰

Because the 2π orbitals in CO are antibonding with respect to the bond between carbon and oxygen, the electron backdonation from the metal weakens the CO bond strength and increases the CO bond length.^{10,73} As a result, the C–O stretching frequency is lowered.^{10,75} The 5σ orbital is also of antibonding character,^{18,72} but the effect of removing electron density from this orbital upon adsorption on the CO bond strength is small.^{10,73} Note that the Blyholder model also bears similarities to the Dewar-Chatt-Duncanson model which describes the bonding in metal π -complexes.^{17,18,78–80}

2.1.2 Newns-Anderson model

In the model by Newns from 1969, which is based on the work of Anderson in 1961, chemisorption is treated in the Hartree-Fock approximation.^{11,81} In this model, the interaction strength between a specific electronic state $|a\rangle$ of the adsorbate with energy ϵ_a and a one-electron metal state $|k\rangle$ with energy ϵ_k is given by the coupling matrix element V_{ak} .^{14,72,82} Two limiting cases may be discerned which are shown in Fig. 2.2(a).^{14,72} In the first case, V_{ak} is much smaller than the width of the (featureless) metal band. Due to the finite lifetime of an electron in the adsorbate state, the interaction leads to a broadened resonance-level in the projected density of states on the adsorbate. The bottom of the resonance reflects more bonding character while the top resembles more antibonding character. In the second case, however, when the band width is much smaller than V_{ak} , the interaction can be considered a two-level problem where sharp bonding and antibonding states are formed above and below the two original states. The latter scenario is usually the case for *strong* chemisorption or upon interaction with the more localized metal d states while the former scenario applies to *weak* chemisorption or to the interaction with the delocalized metal sp states.^{14,72}

For a given surface and adsorbate, the energetic position of the resonance state critically depends on the distance d of the adsorbate from the surface.^{14,83} This is illustrated in Fig. 2.2(b) for an acceptor state of an electronegative adsorbate in the weak chemisorption regime. The depicted acceptor state, also called affinity level, of a molecular adsorbate is the lowest unoccupied molec-

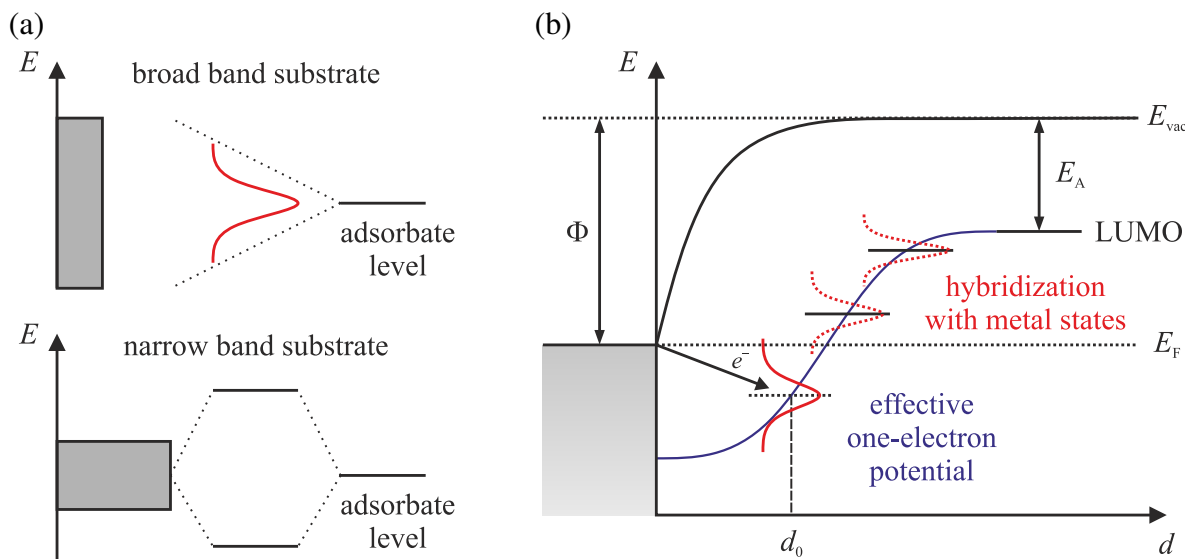


FIG. 2.2. Schematic representation of chemisorption in the Newns-Anderson model. (a) Local density of states at an adsorbate in the Newns-Anderson model in the two limiting cases when (top) the band width of the substrate (gray) is large, and when (bottom) the band width is small compared to the coupling matrix element. The adsorbate level is indicated by a black line while the red curve illustrates the broadening upon adsorption. Own representation based on Fig. 2.3 in Ref. 72 (p. 64). (b) Development of the molecule acceptor state (LUMO) with decreasing distance d from the metal surface. E_{vac} denotes the vacuum level, E_{F} the Fermi energy, Φ the work function, and E_{A} the electron affinity. The acceptor state is lowered in energy because it follows the effective one-electron potential (blue solid line), and hybridization with metal states leads to a broadening (schematically depicted in red). Electrons from the metal populate the acceptor state for $E \leq E_{\text{F}}$. Own representation based on Ref. 4.

ular orbital (LUMO) whose energy is defined by the electron affinity E_{A} .⁸⁴ With decreasing d the energetic position of this state is lowered because it follows the effective one-electron potential of the clean surface.^{14,83} This potential may be envisaged as the image potential felt by a (fictive) negative charge in the affinity level.¹⁴ When the affinity level crosses the Fermi energy E_{F} of the substrate, i.e., for $E \leq E_{\text{F}}$, it is filled by electrons from the metal substrate. Thus, a charge transfer across the interface occurs by analogy with the Blyholder model in Sec. 2.1.1. In addition, the acceptor state hybridizes with metal states which leads to a broadening. Note that in the course of the present work the term “hybridization” is used also for the mixing of electronic states on *different* atoms, although, in the strict chemical sense, it refers to the linear combination of atomic orbitals (AO) on *one* atom only.⁸⁵

The highest occupied molecular orbital (HOMO) is also lowered in energy with decreasing d .⁸⁶ The downward shift, however, is much smaller, resulting in a decreased HOMO–LUMO gap of the adsorbate.⁸⁶ The exact shape of the effective one-electron potential depends on the conduction band width of the metal substrate.^{83,87} For metals with a wide conduction band, like high-density metals, the potential is steeper than for low-density metals with a narrow conduction band.^{83,87} For the high-density metals, however, the Pauli-repulsive contribution to the overall interface interaction is higher which in sum leads to larger equilibrium distances d_0 between the adsorbate and the surface.^{83,87}

In the particular case of transition metal substrates, the chemisorption consists of a contribution due to the interference of the adsorbate electrons with the metal sp electrons, and an additional con-

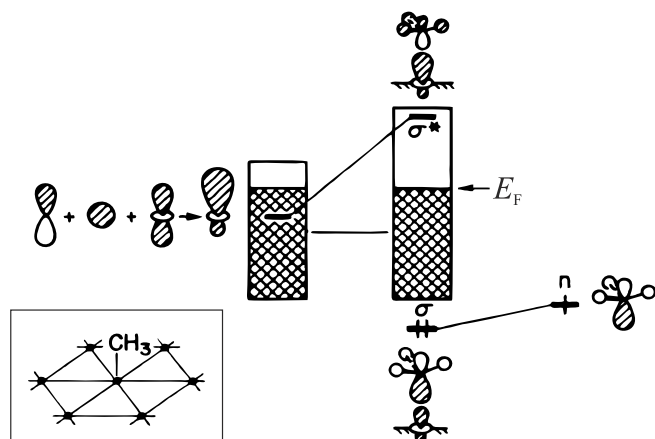


FIG. 2.3. Hoffmann model for chemisorption on a metal surface. A neutral methyl radical adsorbs in an on-top position on a hexagonal surface (see inset). The CH_3 frontier orbital, a carbon-based directed radical lobe (right, n), overlaps with a metal hybrid orbital which is a linear combination of s , p , and d_{z^2} atomic orbitals (left), yielding a fully occupied bonding orbital (σ) and an empty antibonding orbital (σ^*). E_F denotes the Fermi energy. Adapted from Ref. 13.

tribution from the interference with the d electrons.^{14,83} Depending on the nature of the transition metal and the packing density of the surface atoms, both scenarios of weak and strong chemisorption may occur.^{14,83} However, with higher filling of the substrate d -band, the d -band contribution to the chemisorption becomes less important since not only the resulting bonding states but also the antibonding states are occupied.⁸³

2.1.3 Hoffmann model

The Hoffmann model from 1985,⁸⁸ which is reviewed in Refs. 12, 13, 89, is similar to the Blyholder model described in Sec. 2.1.1. It also employs the frontier orbital concept,^{69,70} but—contrary to the Blyholder model—in the framework of the extended Hückel theory which is, unlike the classical Hückel method, not restricted to π orbitals only.⁹⁰ Although delocalized band structures are present in the bulk state and also at the surface, the Hoffmann model aims at interpreting the surface bonding with frontier-orbital arguments, that is, with the formation of localized bonds.^{12,13} Figure 2.3 shows an example of the chemisorption of methyl in an on-top position on a metal surface of hexagonal symmetry.¹³ The singly occupied molecular orbital (SOMO) of the neutral methyl radical overlaps with a metal hybrid orbital. The latter is a linear combination of s , p , and d_{z^2} atomic orbitals of the metal. The newly formed bonding state, i.e., the σ orbital, is now fully occupied by charge transfer in the form of a metal electron.¹³ Hence, as in the other models described before, the concept of charge transfer is also present here.

Note that the energy of the bonding state is lowered with respect to the two original orbitals whereas the antibonding state σ^* is raised in energy and remains empty since it is located above the Fermi level. The stabilization energy ΔE is given by the perturbation theory expression for the interaction of two orbitals of energies E_i^0 and E_j^0 :^{12,13,91}

$$\Delta E = \frac{|H_{ij}|^2}{E_i^0 - E_j^0}, \quad (2.1)$$

where H_{ij} denotes the off-diagonal Hamiltonian matrix element. Regarding the example in Fig. 2.3, ΔE describes the energetic lowering of the bonding state σ with respect to the lower of the two original orbitals, n . Since H_{ij} is taken to be proportional to the overlap integral S_{ij} ,^{90,92} the stabilization is largest for large spatial overlap and small separation in energy of the two orbitals.^{12,13} Note that the first investigation of chemisorption within the Hoffmann model was performed on the adsorption of CO on transition metal surfaces.⁸⁸ With the interpretative constructs of this model

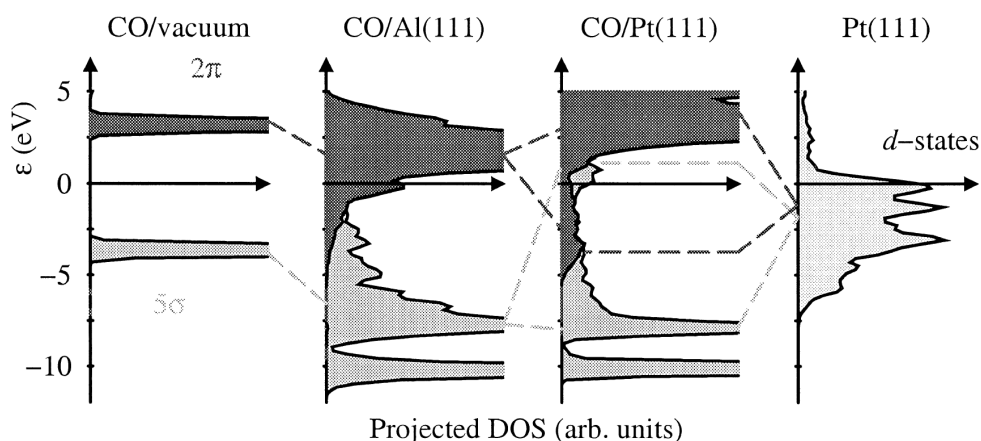


FIG. 2.4. Hammer-Nørskov model for chemisorption of CO on metal surfaces. The self-consistent electronic DOS is projected onto the 5σ (dark gray) and 2π (black) orbitals of CO: in vacuum and on Al(111) and Pt(111) surfaces. Also shown is the DOS from the d -bands in the Pt(111) surface (light gray). Dashed lines illustrate the contributions of the valence states of free CO and of the metal d states to the hybrid states in the adsorbed systems. The sharp states of CO in vacuum are seen to broaden into resonances and shift down in energy on the simple metal surface (mixing with the 4σ state causes additional structure in the 5σ resonance). On the transition metal surfaces the CO resonances further hybridize with the metal d states. This leads to shifts in the 5σ and 2π levels and to antibonding 5σ - d states at the top of the d bands and bonding 2π - d states at the bottom. These states have low weight in the 5σ and 2π projections shown. Adapted from Ref. 93.

at hand, namely, decomposition or projection of the density of states (DOS) and crystal orbital overlap population (COOP) analysis,^{12,13} the conclusions drawn from the Blyholder model were verified and enhanced.⁸⁸

2.1.4 Hammer-Nørskov model

The model by Hammer and Nørskov from 1995/1996, also referred to as d -band model, builds on the Newns-Anderson model (see Sec. 2.1.2) and correlates the strength of a chemisorptive bond on a transition metal surface with the center of the d -band, ϵ_d , and the coupling matrix element V_{ad} , i.e., the overlap, between the metal d -band state(s) $|d\rangle$ (with energy ϵ_d) and the adsorbate orbital $|a\rangle$ (with energy ϵ_a).^{15,82,93,94} The d -band model employs density functional theory (DFT) within the generalized gradient approximation (GGA).^{15,93} By taking the example of CO on a close-packed fcc (111) surface of both a simple metal and a transition metal, Fig. 2.4 illustrates the influence of the d -bands on the surface bonding with the help of the projected densities of states.^{15,93} Clearly the two regimes, which have already been described in the context of the Newns-Anderson model above (see Fig. 2.2), can be distinguished. Upon interaction with the metal sp -band, the adsorbate frontier orbitals broaden into resonance and are lowered in energy while further hybridization with the metal d states leads to the formation of bonding and antibonding states.^{15,93} The interaction with the sp -band can be considered to be the same for all transition metals.^{15,93} Thus, in this case, the strength of the surface bonds arises from the degree of hybridization with the d states and the filling of the bonding hybrid states.⁹⁴

In case of weak coupling ($V_{ad} \ll |\epsilon_d - \epsilon_a|$), the energy $E_{d\text{-hyb}}$ which is gained by the hybridization of a *filled* adsorbate level with the metal d -bands is given by:^{15,94,95}

$$E_{d\text{-hyb}} = -2(1 - f_d) \frac{V_{ad}^2}{|\epsilon_d - \epsilon_a|} + 2(1 + f_d)\alpha V_{ad}^2, \quad (2.2)$$

where f_d is the fractional filling of the metal d -bands and α is an adjustable parameter common to all metals that only weakly depends on the nature of the adsorbate.¹⁵ In the above equation, the second term describes the orthogonalization energy cost and thus the Pauli repulsion.^{15,61,82,93} Note that $f_d = 1$ applies to the coinage metals. Hence, only the repulsive part of the d -band interaction contributes to the surface bonding here. In general, V_{ad} increases from right to left and from top to bottom across the transition metals in the periodic table.^{15,61,82} In turn, ϵ_d decreases from left to right and from top to bottom.^{15,82} Also, ϵ_d is higher for the more open surfaces, i.e., for lower coordination numbers of the surface atoms, while the band width decreases.^{82,93} In addition, the position of the the d -band center may be influenced by surface alloying.^{82,93,96}

In a more general form, Eq. (2.2) is often stated as:^{15,96}

$$E_{d\text{-hyb}} = -C(f_a, f_d) \frac{V_{ad}^2}{|\epsilon_d - \epsilon_a|} + \alpha V_{ad}^2, \quad (2.3)$$

where the parameter $C(f_a, f_d)$ only depends on the number of electrons in both the adsorbate state (via the fractional filling of the adsorbate level, f_a) and the metal d -bands (via f_d). Note that, in contrast to Eq. (2.2), this equation also holds if incompletely filled adsorbate levels, e.g., the LUMO in the case of molecular adsorbates, are involved.

2.2 Properties of PTCDA

In the present work, the organic molecule 3,4,9,10-perylenetetracarboxylic 3,4:9,10-dianhydride (PTCDA) on coinage metal surfaces is used as a testing probe for the relevant interactions at different metal/organic interfaces. PTCDA is one of the experimentally best-characterized adsorbates and has been investigated with numerous spectroscopic techniques and structural clarification methods.⁴ Besides, theoretical investigations have been undertaken.⁹⁷ In the following, the knowledge concerning the surface bonding mechanism is reviewed, already in the light of the above-mentioned models for the chemisorption of small molecules. First, however, the molecular properties as well as the bulk structures of PTCDA are introduced since these information will be needed in the discussion of the so-far obtained results as well as for the interpretation of the results presented in this work.

PTCDA is a π -conjugated, planar organic molecule (symmetry point group D_{2h}^{99}) with the chemical formula $C_{24}H_8O_6$ and a molar mass of $392.32 \text{ g mol}^{-1}$.¹⁰⁰ The PTCDA molecule consists of a perylene core (C_{peryl}) and two functional anhydride groups containing C atoms (C_{funct}) and chemically nonequivalent O atoms, namely, double-bound carbonyl (O_{carb}) and single-bound, bridging anhydride O atoms (O_{anhyd}). The valence bond structure and a ball-and-stick model of PTCDA are shown in Fig. 2.5. PTCDA carries a quadrupole moment because of its electronegative functional groups.⁴ Due to the extended π system, PTCDA is an organic semiconductor of n -type.¹⁰¹ Also, because of its high electron affinity of $E_A = 4.12(10) \text{ eV}^{102, a)}$, the PTCDA molecule

^{a)}Note that, in the course of the present work, the sign convention for the reported E_A values is chosen such that positive values refer to a release of energy upon electron attachment.⁸⁵

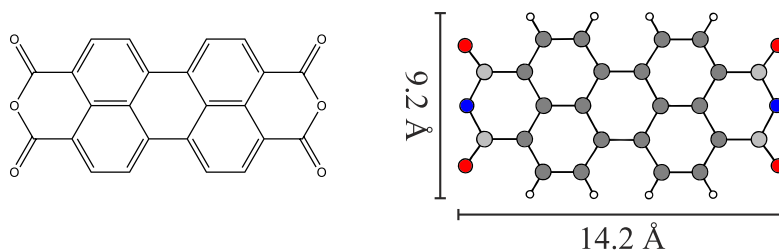


FIG. 2.5. Valence bond structure (left) and ball-and-stick model (right) of the PTCDA molecule. The carbon atoms within the perylene core and within the functional groups are shown in dark gray (C_{peryl}) and light gray (C_{funct}), respectively, while the chemically nonequivalent oxygen atoms are shown in red (O_{carb}) and blue (O_{anhyd}). Hydrogen atoms are depicted in white. The molecular dimensions, taking into account also the van der Waals radii, are indicated.⁹⁸

is an electron acceptor. PTCDA is a thermally stable, dark red powder and is commercially available as Pigment Red 224 which is used in industrial applications, for example, in the production of automotive paint.^{100,101,103} Due to its low vapor pressure (below 10^{-10} mbar at room temperature)¹⁰⁴ and its high melting point (above 300° at atmospheric pressure),¹⁰⁰ PTCDA is easy to handle under vacuum conditions.

2.2.1 Crystal structures of PTCDA

Two polymorphic crystal structures of PTCDA are known, namely, the α and the β modification (see Fig. 2.6), which were characterized with x-ray diffraction^{104–109} and electron diffraction.^{107,110} Both modifications crystallize in the monoclinic space group $P2_1/c$ (number 14) with 2 molecules per unit cell.^{107,110} The lattice parameters are summarized in Table 2.1. In both modifications, the PTCDA molecules are arranged in a *herringbone* motif in the (102) lattice plane, with an enclosed angle near 90° between the long molecular axes ($\approx 80^\circ$, to be more precise, in both modifications^{108,109}) and with only slight inclinations, i.e., out-of-plane rotations.^{105,110} This arrangement is energetically favored by intermolecular hydrogen bonding and quadrupole interactions.^{4,111} Therefore, the herringbone structure is often found also for PTCDA on surfaces.⁴

The lattice plane spacing d_{102} is close to the layer spacing found in graphite (3.35 \AA)²⁰ for both polymorphs (see Table 2.1). However, the α and the β modifications differ in the stacking of the (102) cross sections of the unit cell. While for the α modification the lateral shift between two

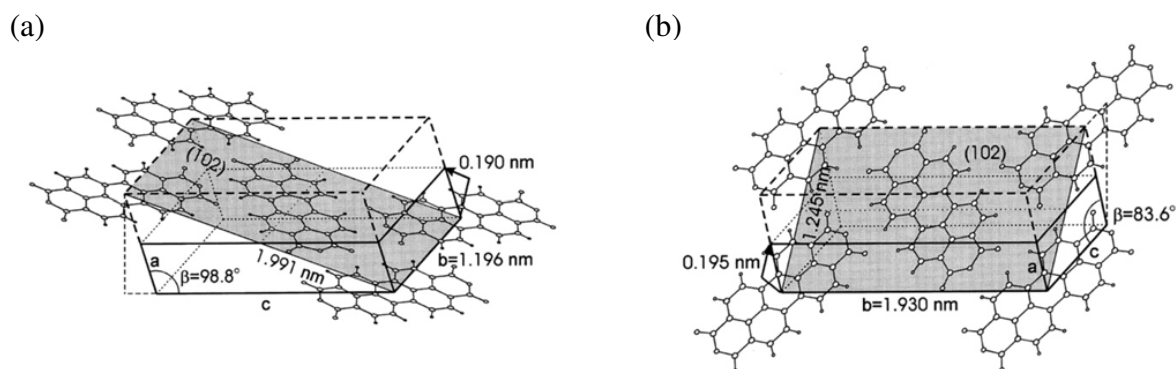


FIG. 2.6. Crystal structures of PTCDA: (a) α and (b) β modification. Solid black lines indicate the respective monoclinic unit cells. The (102) planes are colored in gray. Taken from Refs. 4, 110.

Modification	α	β
Space group	$P2_1/c$	$P2_1/c$
a (Å)	3.74	3.78
b (Å)	11.96	19.30
c (Å)	17.34	10.77
β (°)	98.8	83.6
Volume (Å ³)	766.5	780.8
(102) plane, [010] (Å)	11.96	19.30
(102) plane, [$\bar{2}01$] (Å)	19.91	12.45
Area of unit mesh in (102) plane (Å ²)	238.12	240.3
Angle between a axis and (102) plane (°)	30.6	30.7
d_{102} (Å)	3.22	3.25

TABLE 2.1. Lattice parameters of the α and β modifications of bulk PTCDA.^{105–107} In addition, the lattice parameters of the unit meshes in the respective (102) planes (the corresponding crystallographic directions are given in square brackets) as well as the corresponding lattice plane spacings d_{102} are given.^{105–107}

adjacent (102) planes occurs along the direction of the long vector of the rectangular unit mesh within the (102) plane, the shift is along the short vector for the β modification (see Fig. 2.6).^{107,110} From the higher density of the former, it can be rationalized that the α modification is the thermodynamically more stable polymorph.^{112,113}

2.2.2 PTCDA on coinage metal surfaces

Here the fundamental results for PTCDA monolayers on coinage metal surfaces are reviewed. The focus will be on spectroscopic data, adsorption configurations and theoretical investigations while the monolayer structures are only briefly mentioned. The lateral structures will be introduced in more detail later in this work when our experimental results are presented. In short, PTCDA forms *herringbone* structures in the monolayer regime on the Au(111),¹¹⁴ Ag(111),¹¹³ and Cu(111) surfaces,¹¹⁵ which are favored by intermolecular hydrogen bond-like interactions as well as by quadrupole interactions. The same holds for PTCDA on the Au(100) surface.¹¹⁶ On the more open and thus more reactive surfaces of both Ag and Cu, however, the intermolecular arrangement of the herringbone structure is lost stepwise in the sequence (111), (100), and (110), indicating an increasing importance of the molecule/substrate interactions.^{117–119} For example, on Ag(100) a *T-shape* arrangement of the PTCDA molecules is found,¹²⁰ while on Ag(110) a *brick-wall* motif is present.⁹⁸ In all cases, the molecular plane is oriented parallel to the surface.^{4,121}

As has already been pointed out in Chapter 1, at least two different bonding channels are conceivable of the PTCDA on coinage metal surfaces, that is, one via the central perylene core and another one via the functional groups, in particular via the O atoms (see Fig. 2.5 above). The following review summarizes the available data with this regard. The experimental and theoretical results have indeed evidenced substantial modifications of the electronic and geometric properties of the adsorbed PTCDA in the monolayer regime, at least on the more reactive surfaces, in comparison to the free molecule and/or PTCDA in condensed (thicker) films. So far, these findings have mainly been interpreted such that the perylene-core bonding is the prevailing bonding channel, as will be described below.

Electronic and vibrational structure

The increased impact of the metal/molecule interactions for the more reactive surfaces is not only expressed in the lateral structures of the adsorbate monolayers but also in the electronic and vibrational properties. Most intensely, the properties of PTCDA on the the (111) surfaces of Au, Ag, and Cu have been investigated,^{59,60,122} but data is also available for PTCDA/Ag(110).^{59,123} First, the electronic properties of the valence states are discussed.

In ultraviolet photoelectron spectroscopy (UPS), a peak corresponding to the LUMO of PTCDA is observed for Ag(111) and Cu(111),^{59,60} whereas a LUMO peak is not observed in the UP spectrum of PTCDA/Au(111).⁶⁰ The former indicates hybridization of molecular states with metal states, resulting in the observed energetic lowering of the LUMO orbital below E_F .^{59,60} Thus, on Ag(111) and Cu(111), the surface bonding is of chemisorptive nature and charge transfer occurs from the metal to the molecule.^{59,60} The effect is more pronounced for Cu(111) than for Ag(111), indicating a stronger metal/molecule interaction.⁶⁰ For Ag(111), the *former* LUMO (F-LUMO in the following) peak is located at a binding energy E_b of 0.3 eV and cut by the Fermi level.⁵⁹ Hence, the F-LUMO is only partly filled.⁵⁹ For Cu(111), however, the F-LUMO peak is located at 0.8 eV below E_F and fully occupied.⁶⁰ In contrast, energetic lowering and filling of the LUMO does not occur for PTCDA physisorbed on the Au(111) surface.⁶⁰ The same trends have been shown by scanning tunneling spectroscopy (STS).^{124–126} Note in this context that the LUMO of the free molecule is primarily located on the perylene core of PTCDA (see Fig. 7.5 in Sec. 7.2, page 188, of the present work for a representation of the frontier orbitals of PTCDA).⁹⁷

Since the peak which is assigned to the HOMO is shifted towards lower binding energies, i.e., upward in energy, compared to the HOMO peak of the PTCDA multilayer, the HOMO–(F-)LUMO gap is strongly reduced for PTCDA on Ag(111) and Cu(111), being smaller for PTCDA/Cu(111) (1.3 eV and 0.9 eV, respectively,^{59,60} compared to values from 3.8 eV to 4.0 eV for the bulk-like phase^{127–129}). A similar observation was made for PTCDA/Ag(110) where the band gap amounts to 1.2 eV and the F-LUMO is located at 0.6 eV below E_F , also being fully occupied.⁵⁹ Evidently, the metal/molecule interaction is strengthened for the more open (110) surface in comparison to Ag(111).⁵⁹ Angle-resolved UPS (ARUPS) has shown that the observed shifts of the F-LUMO peak on Ag surfaces are caused by a hybridization of the PTCDA LUMO with the metal *s*-band (or *sp*-band⁵⁹) where the metal contribution to the hybrid state is about 10%.¹²³ The HOMO, however, may only show admixture of Ag4*d* states⁵⁹ and is essentially not involved in the surface bonding.¹²³ These findings of a hybridization of the PTCDA LUMO with metal *sp* states while significant mixing of the PTCDA HOMO with Ag states does not occur have recently been confirmed by the ARUPS and DFT results of Wießner *et al.*¹³⁰

In addition, combined STM/STS investigations as well as time- and angle-resolved two-photon photoemission (2PPE) experiments for PTCDA/Ag(111) have proven the existence of an unoccupied state 0.6 eV above E_F with a short lifetime.^{131,132} This interface state is identified as the LUMO+1 getting in resonance with the Shockley surface state, which is shifted upward in energy and depopulated.^{4,131–134} Since the shift of the Shockley surface state is strongly dependent on the distance of the adsorbate molecules from the metal surface as well as on their surface density,¹³⁵ it can be regarded as a measure for the adsorption height and thus for the strength of the metal/molecule interaction.

We now turn to the vibrational structure of adsorbed PTCDA. High-resolution electron energy loss spectroscopy (HREELS) has revealed that the vibrational properties of a PTCDA on Au(111) are essentially identical for the monolayer and the multilayer regime, indicating only weak interaction of physisorptive nature at the interface.¹²² For PTCDA/Ag(111), in contrast, vibrational modes become active which are intrinsically only Raman-active and thus should not be present in

an HREEL spectrum.^{58,136} The vibrational modes in question can be ascribed to breathing modes of the central carbon ring in PTCDA.^{58,136} They become infrared-active due to dynamical charge transfer, i.e., charge is pumped back and forth between the metal surface and the molecule on their excitation.^{58,136} This is caused by atomic displacements in the molecule and the ensuing redistribution of electron probability densities within the half-filled LUMO.⁵⁸ From these findings, the center of the perylene core is made out as the reactive center for chemisorption of the PTCDA molecule because it couples strongly to the substrate.^{58,122} The anhydride groups, however, are not directly involved in the surface bonding but lead to an enhanced interaction.¹²²

The altering of the vibrational structure of PTCDA is even stronger when going from the close-packed (111) surface to the more open (100) and (110) Ag surfaces.^{137–139} Vibrational modes are shifted due to modifications of the molecular structure upon chemisorption.^{137–139} Most striking is the substantial shift of the C=O stretching frequency towards lower wavenumbers.^{137–139} For PTCDA/Ag(110) in the submonolayer regime, for example, the corresponding peak is found at 1568 cm^{-1} ,¹³⁸ being about 150 cm^{-1} to 200 cm^{-1} below the value for PTCDA multilayers.¹³⁷ Hence, a lowering of the bond order and a weakening of the C—O bond can be concluded.¹³⁸ Yet, this has not been interpreted as an indication for a direct interaction between the carbonyl groups and the substrate.^{137,138}

Adsorption configurations

Now the question arises whether the degree of metal/molecule interactions, which may be deduced from the changes in the spectroscopic features of adsorbed PTCDA, also manifests in the vertical structure of the molecule on the surface, that is, in the adsorption configuration. Those adsorption configurations which are known to the literature are presented in the following. At the beginning of the investigations presented in this work, only the adsorption configurations of PTCDA on the (111) surfaces of Cu, Ag, and Au had been known. In the course of the present work, the knowledge was amended by four additional adsorption configurations of PTCDA on different coinage metal surfaces. Because the aspects of interest for these particular systems, which have been investigated here, originated, among others, from the observed trends regarding the adsorption configurations on the (111) surfaces, the observed trends are outlined in the following.

Figure 2.7 illustrates the adsorption configurations of PTCDA on Au(111),⁵⁴ Ag(111),^{32,55,140} and Cu(111).⁴³ In addition, Table 2.2 summarizes the explicit adsorption heights obtained with XSW. Distinct differences can be recognized. In the first place, the overall adsorption height of the PTCDA molecule, which is taken to be equal to that of the molecular C backbone, $d(\text{C total})$, decreases in the series Au(111), Ag(111), and Cu(111), proving an increased interaction. Taking into account the size of the respective atoms (see Table 2.3), one finds that the adsorption height for PTCDA/Au(111), $d_{\text{Au}(111)}(\text{C total}) = 3.27(2)\text{ \AA}$,⁵⁴ is close (within 5 %) to the sum of the van der Waals (vdW) radii of Au and C, which amounts to 3.41 \AA .¹⁴¹ In contrast, for PTCDA/Ag(111) as well as for PTCDA/Cu(111), the adsorption heights are lowered to 82 % [$d_{\text{Ag}(111)}(\text{C total}) = 2.86(1)\text{ \AA}$]⁵⁵ and 84 % [$d_{\text{Cu}(111)}(\text{C total}) = 2.66(2)\text{ \AA}$]⁴³ of the sum of the vdW radii, being 3.47 \AA and 3.15 \AA , respectively. Hence, the adsorption heights are indicative of physisorption of PTCDA on Au(111) and chemisorption on the Ag(111) and Cu(111) surfaces.^{43,54,55}

Secondly, the PTCDA molecule, which is intrinsically planar, distorts upon adsorption on the more reactive (111) coinage metal surface (see Fig. 2.7). For PTCDA on Au(111), the exact adsorption configuration is not known,⁵⁴ but due to the weak interaction with the substrate (see also UPS and HREELS data above) the intramolecular structure may be assumed to remain almost uninfluenced. On Cu(111), however, PTCDA adopts a *boat*-like configuration, with all O atoms being *above* the C backbone of the molecule. As opposed to this, the PTCDA molecules are in

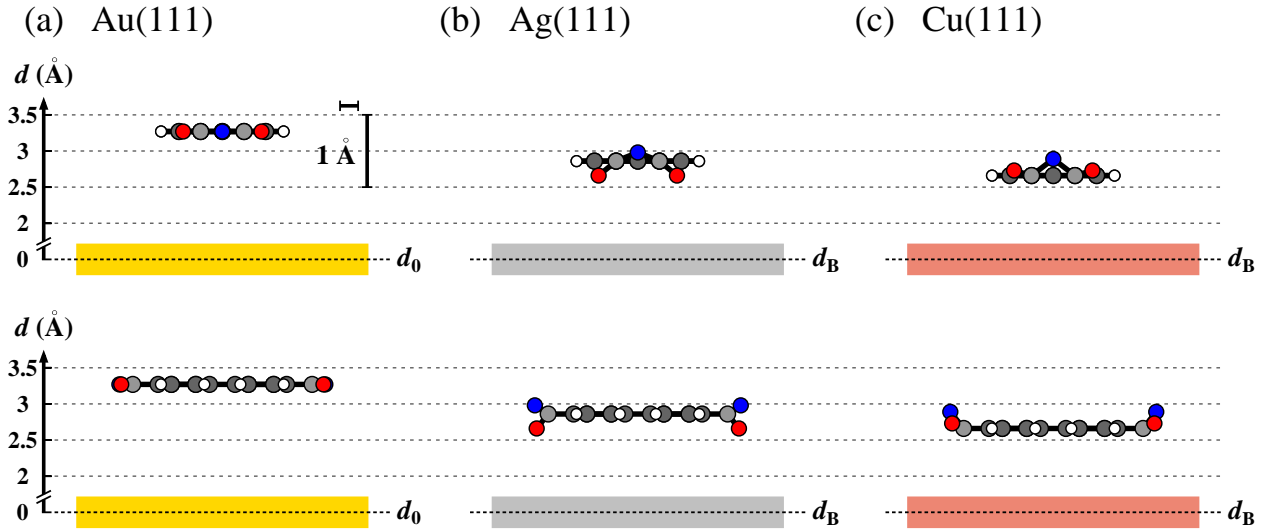


FIG. 2.7. Adsorption configurations of PTCDA on the (111) surfaces of (a) Au,⁵⁴ (b) Ag,⁵⁵ and (c) Cu.⁴³ The top row shows side views along the long molecular axis while the bottom row shows side views along the short molecular axis. H atoms are shown in white, C_{funct} and C_{pery} atoms in light gray and dark gray, and O_{carb} and O_{anhyd} atoms in red and blue, respectively. The individual surfaces are depicted as colored regions. d denotes the vertical adsorption height; the vertical scale is enlarged by a factor of 4 and referenced against the Bragg plane (dashed line, d_B) or the (averaged) position of the relaxed surface (dashed line, d_0), respectively. Note that for PTCDA/Au(111) the O atoms are depicted at the same adsorption height as C_{funct} and C_{pery} although their positions are not known for experimental reasons.⁵⁴ Note further that C_{funct} and C_{pery} atoms could not be distinguished experimentally.^{43,54,55} In the case of PTCDA on Cu(111), however, C_{pery} and C_{funct} were concluded to exhibit the same d values within the experimental resolution.⁴³

TABLE 2.2. Values for averaged vertical distances d of the carbon and oxygen atoms for PTCDA and NTCDA adsorbed on different coinage metal (111) surfaces. LT means low temperature and denotes the metastable disordered phase of PTCDA on Ag(111) which can be prepared at $T < 150$ K.¹⁴⁰ $\Delta d = d_{\max} - d_{\min}$ is the absolute (overall) vertical distortion of the (intrinsically planar) PTCDA molecule, and $\Delta d(\text{O}) = d(\text{O}_{\text{anhyd}}) - d(\text{O}_{\text{carb}})$ is the vertical displacement of the O atoms. Note that for PTCDA/Au(111) the O positions were not measured for experimental reasons (n.d. = not determined).⁵⁴

	PTCDA				NTCDA
	Au(111) (Ref. 54)	Ag(111) (Ref. 55)	Ag(111), LT (Ref. 55)	Cu(111) (Ref. 43)	Ag(111) (Ref. 41)
$d(\text{C total})$ (Å)	3.27(2)	2.86(1)	2.81(2)	2.66(2)	3.00(2)
$d(\text{O total})$ (Å)	n.d.	2.86(2)	2.67(3)	2.81(3)	2.87(1)
$d(\text{O}_{\text{carb}})$ (Å)	n.d.	2.66(3)	2.50(4)	2.73(6)	2.75(3)
$d(\text{O}_{\text{anhyd}})$ (Å)	n.d.	2.98(8)	2.83(4)	2.89(6)	3.00(2)
Δd (Å)	n.d.	0.32(11)	0.33(8)	0.23(6)	0.25(4)
$\Delta d(\text{O})$ (Å)	n.d.	0.32(11)	0.33(8)	0.16(8)	0.25(4)

TABLE 2.3. Radii of the elements of interest in the present work. r_a is the atomic radius, r_m the metallic radius, r_{cov} the covalent radius, r_{vdW} the van der Waals radius, and r_{ion} the ionic radius, respectively. The latter strongly depends on both the oxidation state and the coordination number (CN) which are given in parentheses. Note that the values for r_m refer to a (hypothetical) dense sphere packing of the metal atoms, i.e., to CN = 12 (n.a. = not applicable).¹⁴²

	r_a (Å) (Ref. 143)	r_m (Å) (Ref. 142)	r_{cov} (Å) (Ref. 144)	r_{vdW} (Å) (Ref. 141)	r_{ion} (Å) (Ref. 145) ^a
H	0.25	n.a.	0.31	1.00 ^b	-0.24, -0.04 (+I, CN 1,2)
C	0.70	n.a.	0.73 ^c	1.75 ^d	0.06–0.30 (+IV, CN 3–6)
O	0.60	n.a.	0.66	1.65 ^e	1.21–1.28 (–II, CN 2–8)
K	2.20	2.37	2.03	2.75	1.51–1.78 (+I, CN 4–12)
Cu	1.35	1.28	1.32	1.40	0.60–0.91 (+I, CN 2–6)
Ag	1.60	1.44	1.45	1.72	0.81–1.42 (+I, CN 2–8)
Au	1.35	1.44	1.36	1.66	1.51 (+I, CN 6)

^aSee also Ref. 146 for a reprint of the tabulated values from Ref. 145.

^bValid for H atoms in aromatic compounds, such as benzene; $r_{\text{vdW}}(\text{H}) = 1.20 \text{ \AA}$ for H atoms in aliphatic compounds.¹⁴¹

^cValid for sp^2 -hybridized C atoms; else 0.76 \AA (sp^3) or 0.69 \AA (sp), respectively.¹⁴⁴

^dValid for C atoms (sp^2 hybridization) in perylene, perpendicular to the molecular plane.¹⁴¹ $r_{\text{vdW}}(\text{C}) = 1.70 \text{ \AA}$ for aliphatic C atoms.¹⁴¹

^eAveraged value for O atoms (sp^2 hybridization) in double bonds, normal to the bond axis, where values in the range of 1.6 \AA to 1.7 \AA are found in general.¹⁴¹ $r_{\text{vdW}}(\text{O}) \approx 1.50 \text{ \AA}$ for single-bound O atoms and for double-bound O atoms, parallel to the bond axis.¹⁴¹

a *saddle*-like configuration on Ag(111) where the O_{carb} atoms are found *below* the C backbone and thus are closest to the surface.⁵⁵ Hence, the existence of (weak) local $\text{O}_{\text{carb}}-\text{Ag}$ bonds was concluded, in addition to the primary chemisorptive bond via the perylene core.³² As judged from the adsorption configurations, analogous $\text{O}_{\text{carb}}-\text{Cu}$ bonds are not formed on the Cu(111) surface.

The interpretation of the bonding channel on the perylene core as being of primary importance has been further corroborated by the results for the structurally similar, but smaller molecule NTCDA on Ag(111).^{41,42} Although the adsorption geometry is qualitatively similar to that of PTCDA on Ag(111), the C backbone is lifted away from the surface by $0.14(3) \text{ \AA}$ (see Table 2.2). At the same time, $d_{\text{Ag}(111)}(\text{O}_{\text{carb}})$ is increased by $0.09(4) \text{ \AA}$. Apparently, the chemisorptive bonding on the Ag(111) surface is weakened for NTCDA in comparison to PTCDA.⁴² This may be ascribed to the smaller π system of NTCDA (naphthalene versus perylene) and the smaller electron affinity E_A [in magnitude; see also footnote a) on page 10 of this chapter] of NTCDA.^{147–149}

So far, the influence of *inter*-molecular, i.e., lateral, interactions, besides the interfacial (vertical) metal/molecule interactions, on the adsorption configuration have been neglected. As pointed out above, quadrupole as well as hydrogen bond-like interactions play a role in the lateral structure formation of PTCDA on surfaces. However, intermolecular interactions also contribute to the surface bonding mechanism, as has been shown exemplarily for the *disordered* low-temperature (LT) phase of PTCDA on Ag(111), which is formed for $T < 150 \text{ K}$.^{55,140} Here, the adsorption heights for both C and O atoms in PTCDA are lowered in comparison to the room temperature phase (see Table 2.2).^{55,140} Several aspects play a role here. The absence of $\text{C}_{\text{funct}}-\text{O}\cdots\text{H}-\text{C}_{\text{peryl}}$ hydrogen bonds may lead to an increased charge density on the O atoms and hence to a strengthening of the $\text{O}_{\text{carb}}-\text{Ag}$ bonds, for instance.^{55,140} Also, the (intermolecular) charge transfer which is usually

associated with the formation of hydrogen bonds may be compensated for by an increased charge transfer from the substrate^{55,140} in the LT phase. The latter point is supported by UPS and STS data which reveal a higher binding energy of the F-LUMO ($E_B = 0.6$ eV) in comparison to the RT phase.¹⁴⁰

In summary, the spectroscopic and structural results are consistent. A stronger altering of the electronic structure (see above) is correlated with a smaller adsorption height and vice versa. The metal–perylene core interaction is identified as the primary bonding channel, whereas possible oxygen/metal interactions (on a local scale) are considered to be a secondary effect.³² However, several questions remain unanswered in this context. What is the reason behind the different adsorption configurations of PTCDA on Ag(111) and Cu(111)? If the $O_{\text{carb}}-\text{Ag}$ bonds are only a second-order effect, why are the O_{carb} atoms closer to the Ag surface than the perylene core? Is the metal–perylene core interaction influenced by the presence of local O–M bonds (M = coinage metal atom)? May (potential) local O–M bonds, in particular the $O_{\text{carb}}-\text{Ag}$ bonds, be modified, for example, via the chemical composition of the surface or structural aspects? The present work aims at providing an answer to these questions, as will be discussed in general in Chapter 7. Before our experimental work is described in detail, theoretical investigations, which are available for some of the systems mentioned above, are reviewed. They address the relevance of different bonding channels to the overall surface bonding mechanism, in particular.

Theoretical investigations of the bonding mechanism

The theoretical investigations have mainly focused on PTCDA adsorption on the coinage metal (111) surfaces, employing density functional theory (DFT) either in the local density approximation (LDA) or in the generalized gradient approximation (GGA).^{32,97,150–153} Besides, the bonding of PTCDA to the Ag(110) surface has been investigated with second-order Møller-Plesset (MP2) perturbation theory.¹⁵⁴ MP2 has the advantage of including vdW interactions, but it is limited to small systems.^{154,155} When using DFT, however, dispersion corrections have to be applied in order to take into account also the vdW interactions which play a major role in the surface bonding mechanism of PTCDA.¹⁵⁵

In some cases, the experimentally determined adsorption configurations may not be reproduced correctly, depending on the level of theory.^{32,150,151,153} For example, DFT-GGA predicts an *arch*-like adsorption configuration for PTCDA on the Ag(111) surface (instead of a *saddle*-like adsorption configuration) with an adsorption height of 3.40 Å for the C backbone, which is too high by more than 0.5 Å in comparison to the experimental result.^{32,150,151} Also, in the case of PTCDA/Cu(111), *saddle*-like or *arch*-like adsorption configurations have been found by the DFT calculations, as opposed to the experimentally observed *boat*-like configuration.¹⁵³ Nonetheless, essential features of the bonding mechanism for PTCDA on Ag and Cu may be recognized from the theoretical findings: (a) Not only the frontier orbitals themselves, i.e., HOMO and LUMO, but also lower-lying occupied molecular orbitals (MO) as well as higher-lying unoccupied molecular orbitals hybridize with metal states,^{97,152–154} mainly with metal *sp* states and, to some extent, also with metal *d* states.^{32,152} (b) Metal-to-molecule charge transfer leads to a partial [Ag(111)]^{97,152,153} or complete filling [Cu(111) and Ag(110)]^{153,154} of the F-LUMO. (c) Despite the filling of the F-LUMO, the net (negative) charge Δq per adsorbed PTCDA molecule is about $-0.5 e$ only, because electrons are also donated from the PTCDA to the substrate via the hybridization of the occupied molecular orbitals with metal states.^{97,153,154} (d) Charge accumulates in the entire plane between the adsorbed molecule and the surface, indicating the presence of *both*, metal–perylene core bond and $O_{\text{carb}}-\text{Ag}$ bonds.^{32,97,151–154} (e) An altering of the intramolecular structure is ob-

served as a consequence of the chemisorptive bonding, for example, the lengthening of the C=O bond.^{97,153}

On the Au(111) surface, however, metal-to-molecule charge transfer does not occur due to the larger adsorption height accompanied with only a small energetic lowering of the PTCDA LUMO, which stays above E_F .¹⁵³ As a result, the surface bonding of PTCDA on Au(111) is considered to be of physisorptive nature.¹⁵³ Thus, the theoretical results are in general accordance with the experimentally observed electronic structures and adsorption configurations for PTCDA on coinage metal surfaces. However, a neat picture of the complex bonding mechanism at the interface is still not available and requires further investigations. For example, the influence of the surface-atom coordination number (CN) has not yet been addressed by a detailed experimental analysis of the realized PTCDA adsorption configuration(s). Our experimental data concerning this point, among others, are discussed in the course of the present work.

Preliminary conclusions

Shifts of spectroscopic features, e.g., peak shifts in UPS towards higher binding energies,^{59,60} and shorter bonding distances are often understood as being indicative of a stronger bonding.^{56,57} Thus, concluding so far, the following aspects of the surface bonding of PTCDA adsorbed on coinage metals may already be rationalized:

- (a) UPS data have revealed an increasing shift of the PTCDA LUMO peak below the Fermi edge, i.e., towards higher binding energies, indicating an intensified surface bonding in the series Au(111), Ag(111), and Cu(111), that is, with increasing surface reactivity. Following the bonding models for small molecules introduced above, the reason behind this may be an increasing $E_{i,\text{metal}}^0$ (according to the Hoffmann model, see Sec. 2.1.3) or ϵ_d , respectively, and a decreasing V_{ad} (according to the Hammer-Nørskov model, see Sec. 2.1.4) in this sequence.¹⁵⁶
- (b) Decreasing vertical adsorption heights of the perylene core in PTCDA on coinage metal substrates have been determined with XSW in the series Au(111), Ag(111), and Cu(111). Again, this finding corroborates the conclusion of a stronger surface bonding with increasing surface reactivity.
- (c) The metal/molecule interaction is stronger for the more open surfaces, where ϵ_d is higher in energy. This can be deduced from the more pronounced changes in the vibrational features of PTCDA on Ag surfaces observed in HREELS.
- (d) The surface bonding is explained primarily via the metal–perylene core interaction. The anhydride groups are influenced upon chemisorption, but a direct interaction of the O atoms, for example, with the surface could not be concluded from the HREELS data. Only in the case of PTCDA/Ag(111), a local interaction of the atoms with the surface metal atoms may be inferred from the realized adsorption configuration.
- (e) Mainly metal sp states contribute to the surface bonding, as ARUPS investigations have exemplarily shown for the case of PTCDA/Ag(110).

We will present further experimental results in the course of the present work which will eventually allow to postulate a conclusive picture of the surface bonding mechanism for PTCDA on coinage metal surfaces (see Chapter 7).

3

Theoretical Background of experimental methods

In this chapter the theoretical background of the experimental techniques which were used in the present work is described. Different types of experiments have been performed. They yield information on both the structural and electronic nature of the investigated metal/organic interfaces. The geometric structures were examined by means of the normal incidence x-ray standing wavefield absorption technique (see Sec. 3.1), low energy electron diffraction (Sec. 3.2.1) and, to a small extent, with scanning tunneling microscopy (Sec. 3.2.2). The latter two methods are well established in surface science, and thus, they are only briefly introduced. The x-ray standing wavefield absorption technique, however, is described in more detail since its physical foundations are complex.

The electronic structure of the PTCDA layers was investigated employing the x-ray as well as the ultraviolet photoelectron spectroscopy, respectively. In particular, x-ray photoelectron spectroscopy was used to gain detailed insight into the chemical state of the atoms at the interface and their chemical environment. Also, it allowed for the exact quantification of the interface composition, as is demonstrated in Sec. 3.2.3. Ultraviolet photoelectron spectroscopy was used for deriving the valence band structure of the adsorbed molecular layers which may provide evidence on the chemical nature of the interfacial bonding (see Sec. 3.2.4).

3.1 The x-ray standing wavefield absorption technique

With the x-ray standing wavefield absorption (XSW) technique the position of atoms relative to the Bragg planes of a substrate lattice can be determined with chemical sensitivity.^{28,29,157-159} Thus, the adsorption height and the adsorption geometry of molecules on surfaces may be identified by XSW with intramolecular resolution. Usually, accuracies of 0.1 Å to 0.01 Å are obtained in the experiment.

The physical foundations of XSW are presented in this section merely to the extent required for the understanding of the data analysis that was done within the present work. The XSW technique combines the principle of x-ray diffraction from single-crystalline substrates with spectroscopic methods. Upon the interference of the incoming and the Bragg-reflected x-ray beam, a standing wavefield evolves which extends several micrometers into the bulk material and also well into the vacuum region above the surface.²⁹ This effect is described in the framework of the dynamical theory of x-ray diffraction (see Sec. 3.1.1). The periodicity of the standing wavefield is determined by the (Bragg) lattice plane spacing. Depending on the position of an atom relative to the Bragg planes, the local intensity of the standing wavefield is different and may be measured by techniques such as x-ray photoelectron spectroscopy, Auger electron spectroscopy, or x-ray fluor-

escence spectroscopy (see Sec. 3.1.2). Thus, the position of the absorbing atoms can be deduced, as will be described in the following. The description is mainly based on the explanations contained in Refs. 28, 29, 160. In general, x-ray standing wavefield absorption experiments require synchrotron radiation in order to reduce the data accumulation time to the necessary minimum.²⁸ Especially if, as in the present work, the XSW experiments are performed in an scanning-energy mode, the use of synchrotron radiation is inevitable since the energy of the x-ray beam has to be tunable. The creation and the properties of synchrotron radiation are described in Refs. 28, 161–163.

3.1.1 Dynamical theory of x-ray diffraction

Reviews of the dynamical theory of x-ray diffraction are found in Refs. 160, 164, 165, and references therein. Here, the fundamental aspects are described. The dynamical theory takes into account all wave interactions within a crystal. Hence, multiple-scattering effects are considered explicitly in contrast to the kinematical theory which is often used as a good first approximation for x-ray diffraction. However, the results predicted by the kinematical approximation are grossly incorrect for highly ordered crystals, i.e., “perfect” single crystals.^{160,164}

The occurrence of diffraction spots is determined by *Bragg’s law*¹⁶⁶ which is either expressed in its vector form (Laue equation) as:²⁸

$$\mathbf{K}_H = \mathbf{K}_0 + \mathbf{H}_{hkl}, \quad (3.1)$$

or directly as Bragg’s equation:²⁸

$$n \lambda = 2 d_{hkl} \sin \theta_B. \quad (3.2)$$

In these equations, \mathbf{K}_H and \mathbf{K}_0 are the propagation vectors of the reflected and the incident wave, respectively, \mathbf{H}_{hkl} is the scattering or diffraction vector,^{a)} n is the order of diffraction, d_{hkl} is the lattice plane spacing of the family $\{hkl\}$ of lattice planes, and θ_B is the Bragg angle with respect to the lattice planes. The diffraction vector \mathbf{H}_{hkl} is related to the reciprocal lattice vector \mathbf{G}_{hkl} via:²⁸

$$\mathbf{H}_{hkl} = \mathbf{G}_{hkl} (2\pi)^{-1}. \quad (3.3)$$

The magnitude of the propagation vectors \mathbf{K}_i is given by the inverse wavelength λ :^{28, b)}

$$|\mathbf{K}_i| = \lambda^{-1}. \quad (3.4)$$

Based on Eq. (3.2), the Bragg energy E_B can be calculated as:

$$E_B = \frac{h c}{\lambda} = n \cdot \frac{h c}{2 d_{hkl} \sin \theta_B}. \quad (3.5)$$

According to the kinematical theory, a Bragg reflection is infinitely sharp. In the framework of the dynamical theory, however, the actual, finite width of the Bragg reflection is described cor-

^{a)}The term “diffraction vector” for \mathbf{H}_{hkl} will be utilized in the course of the present work, in agreement with the notation employed in Ref. 28. We note, however, that the term “scattering vector” generally is more common.

^{b)}Note that in the present work two definitions of a wavevector, \mathbf{K}_i and \mathbf{k}_i , are employed. The two wavevectors differ in their magnitudes by a factor of 2π . As opposed to Eq. (3.4), which holds for \mathbf{K}_i , the magnitude of \mathbf{k}_i is given by $k_i = |\mathbf{k}_i| = 2\pi/\lambda$ (see also Sec. 3.2.1). Here, we have adopted the definition of \mathbf{K}_i and $|\mathbf{K}_i|$, respectively, from Ref. 28 (which is quite conventional in the field of crystallography).

rectly. The width of the Bragg reflection is not infinitesimal because the index of refraction for the incident and the Bragg-reflected beams differs from the average index of refraction in the crystal (see also Sec. 3.1.2).¹⁶⁰ Within the width of the Bragg reflection, an x-ray interference field, the x-ray standing wave, is generated via the superposition of two coherently coupled electromagnetic waves.^{28,160} Assuming that they are planar and linearly polarized, and that their electric-field vectors are parallel, i.e., for σ polarization,²⁹ these incident and Bragg-reflected electromagnetic waves are characterized by their complex amplitudes, ε_0 and ε_H , respectively:²⁸

$$\varepsilon_0 = E_0 \exp [2\pi i (\nu_0 t - \mathbf{K}_0 \cdot \mathbf{r})], \quad (3.6)$$

and

$$\varepsilon_H = E_H \exp [2\pi i (\nu_H t - \mathbf{K}_H \cdot \mathbf{r})]. \quad (3.7)$$

In these equations, E_0 and E_H are the complex electric-field amplitudes of the incident and Bragg-reflected waves, respectively, ν_i is the frequency of the radiation, and \mathbf{r} is a position vector. Further assuming that $\nu_H = \nu_0 = \nu$ (with the straightforward consequence that $|\mathbf{K}_H| = |\mathbf{K}_0|$), and that ε_H and ε_0 are coherent, the complex electric-field amplitudes E_i are related via:²⁸

$$E_H = \sqrt{R} E_0 \exp (i \nu). \quad (3.8)$$

In Eq. (3.8), $\nu = \nu(E, \theta_{sc})$ defines the phase relationship of the two complex amplitudes which depends on the photon energy and the scattering angle. The reflectivity R , i.e., the reflected fraction I_H of the incident intensity I_0 , is also a function of photon energy and scattering angle, $R = R(E, \theta_{sc})$, and its value is simply given by:^{28,29}

$$R = \frac{I_H}{I_0} = \frac{|E_H|^2}{|E_0|^2}. \quad (3.9)$$

The phase ν can be expressed as:²⁸

$$\nu = \begin{cases} \zeta & \text{for } \text{Re}(E_H/E_0) > 0, \\ \zeta + \pi & \text{for } \text{Re}(E_H/E_0) < 0, \end{cases} \quad (3.10)$$

where the complex argument ζ of the ratio of the electric-field amplitudes is given by:²⁸

$$\zeta = \arctan \left[\frac{\text{Im} \left(\frac{E_H}{E_0} \right)}{\text{Re} \left(\frac{E_H}{E_0} \right)} \right] = \arg \left(\frac{E_H}{E_0} \right). \quad (3.11)$$

The total wavefield which is generated by the superposition of the incident and the Bragg-reflected wave now is:²⁸

$$\begin{aligned} \varepsilon &= \varepsilon_0 + \varepsilon_H \\ &= E_0 \exp [2\pi i (\nu t - \mathbf{K}_0 \cdot \mathbf{r})] + \sqrt{R} E_0 \exp (i \nu) \exp [2\pi i (\nu t - \mathbf{K}_H \cdot \mathbf{r})]. \end{aligned} \quad (3.12)$$

With some further mathematical conversions²⁸ and also considering Eq. (3.1), the normalized intensity $I(\mathbf{r})/I_0$ of the wavefield at the position \mathbf{r} becomes:^{28,29,160}

$$\begin{aligned} \frac{I(\mathbf{r})}{I_0} &= \frac{\varepsilon \varepsilon^*}{|E_0|^2} = \left| 1 + \sqrt{R} \exp [i(\nu - 2\pi \mathbf{H}_{hkl} \cdot \mathbf{r})] \right|^2 \\ &= 1 + R + 2 \sqrt{R} \cos (\nu - 2\pi \mathbf{H}_{hkl} \cdot \mathbf{r}). \end{aligned} \quad (3.13)$$

The calculation of R and ν as well as the implications of the above equation are discussed in the following section.

3.1.2 Intensity of the x-ray standing wavefield and determination of perpendicular positions

The intensity of the standing wavefield as given by Eq. (3.13) modulates in the direction of \mathbf{H}_{hkl} , that is, normal to the lattice planes. Figure 3.1 illustrates the formation of the standing wavefield and its characteristics. The lattice plane spacing $d_{hkl} = |\mathbf{H}_{hkl}|^{-1} = \frac{1}{2} \lambda$ defines the period of the standing wavefield.²⁸ The position of the minima and maxima, or the nodes and antinodes, of the standing wave is determined by the phase ν . In the experiment when the scattering angle or, equivalently, the photon energy is scanned through the Bragg condition, ν changes its value by π according to Eq. (3.10). Thus, the nodes and antinodes exchange their positions over the range where $R > 0$. The effect of ν on the position of the standing wavefield with respect to the Bragg planes is discussed in detail in Ref. 167, for example. Usually, at the onset of the reflectivity range where x-ray the standing wavefield exists, i.e., for photon energies slightly lower than the Bragg energy E_B , the nodes are found at the position of the Bragg planes and shift to a position centrally arranged between the Bragg planes for photon energies slightly higher than E_B .^{28,29,160}

This means that, for a given position relative to the Bragg planes, the intensity of the standing wavefield can be changed in the experiment. If the intensity $I(\mathbf{r})/I_0$ of the standing wavefield is monitored as a function of E or θ_{sc} , the position \mathbf{r} , which corresponds to that of an atomic absorber, may be deduced. This will be elucidated in the following.

In principle, XSW experiments can be performed either by scanning the photon energy through the Bragg condition with the scattering angle being fixed, or by changing the scattering angle for a fixed photon energy.^{28,29} In the present work, the former has been done. Thus, the following equations and parameters will be given in terms of their energy dependence. In expansion of equations (3.8) and (3.9), the ratio of the complex electric-field amplitudes, E_H/E_0 , is given by:^{28,29,160}

$$\left(\frac{E_H}{E_0} \right)^2 = R \exp (i 2 \nu) = |b| \left(\eta \pm (\eta^2 - 1)^{\frac{1}{2}} \right)^2 \frac{F_H}{F_{\bar{H}}}, \quad (3.14)$$

or, with the convention that $\sqrt{|b|}$ denotes the principal square root of $|b|$ and thus has a positive sign:²⁹

$$\frac{E_H}{E_0} = \sqrt{R} \exp (i \nu) = -\sqrt{|b|} \left(\eta \pm (\eta^2 - 1)^{\frac{1}{2}} \right) \sqrt{\frac{F_H}{F_{\bar{H}}}}. \quad (3.15)$$

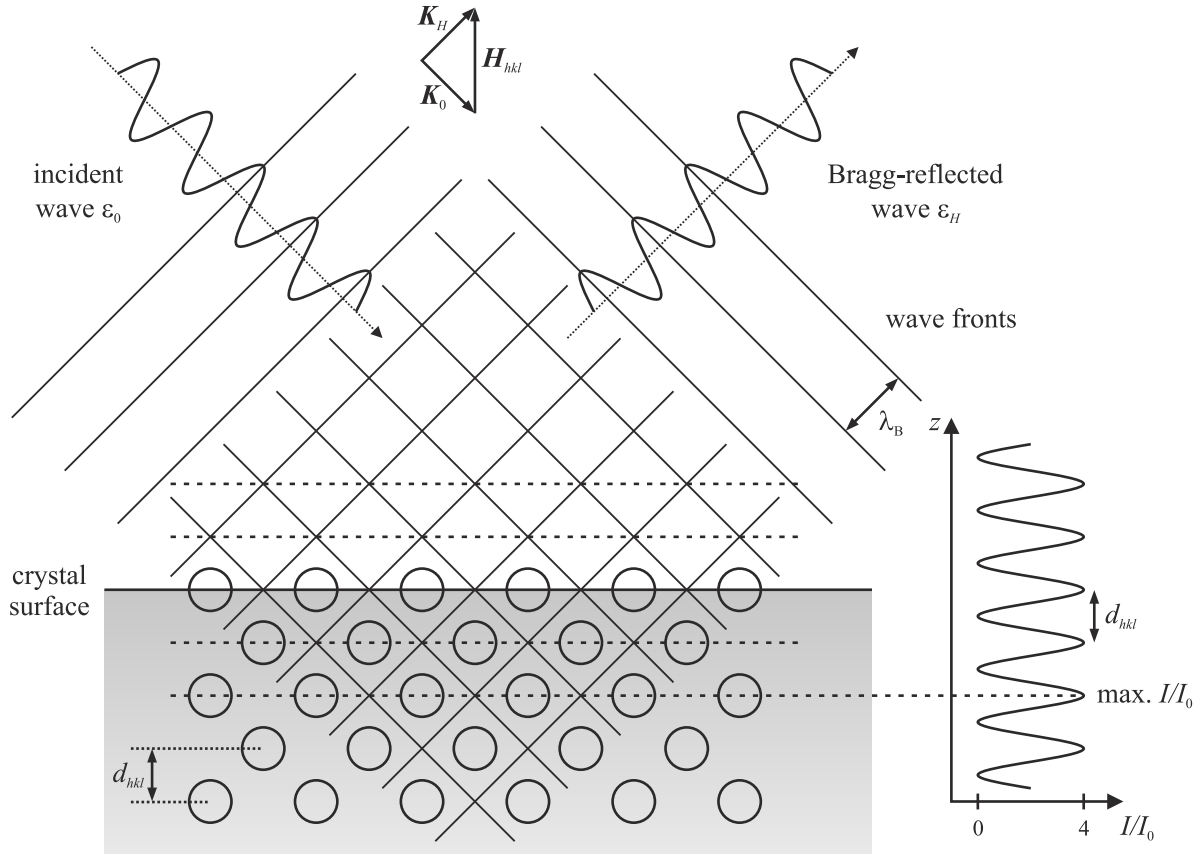


FIG. 3.1. Principle of the formation of an x-ray standing wavefield which is created by superposition of the incident and Bragg-reflected waves ε_0 and ε_H inside the crystal and above the surface, depicted for a first-order Bragg reflection. The intensity maxima of the standing wavefield (dashed lines) coincide with the position of the lattice planes parallel to the surface (black circles represent the atoms in the crystal) which corresponds to the phase $\nu = 0$. The periodicity of the wavefield intensity modulation, $I(z)/I_0$, is determined by the lattice plane spacing d_{hkl} . The Bragg condition $\mathbf{K}_H = \mathbf{K}_0 + \mathbf{H}_{hkl}$ is shown as an inset. Own representation based on Fig. 4 in Ref. 28 (p. 213).

In conjunction with Eqs. (3.10) and (3.11), the above equation allows to determine ν if R is known. The reflectivity R , which is a real quantity, calculates as:¹⁶⁰

$$R = \frac{|E_H|^2}{|E_0|^2} = |b| \left| \eta \pm (\eta^2 - 1)^{\frac{1}{2}} \right|^2, \quad (3.16)$$

with the complex parameter η being a measure of how far the scattering conditions are from the midpoint of the reflectivity curve. F_H and $F_{\bar{H}}$ are the structure factors for the reflections defined by \mathbf{H}_{hkl} and $-\mathbf{H}_{hkl}$, respectively.²⁹ Their explicit calculation, together with the calculation of the corresponding Debye-Waller factors, is treated in Appendix B. For centrosymmetric crystals, such as *fcc* crystals, the structure factors F_H and $F_{\bar{H}}$ are equal if the origin of the Bravais lattice is taken at a center of symmetry.¹⁶⁰ Therefore, the last factor on the right-hand side of Eq. (3.14) is unity and drops out. Because $F_H = F_{\bar{H}}$ is a good approximation in general,¹⁶⁰ i.e., also for non-centrosymmetric crystals, this term has been omitted in the derivation of Eq. (3.16).^{c)} The

^{c)}The approximation of F_H and $F_{\bar{H}}$ being equal has been employed as a general rule in the course of the present work, with the consequence that $(F_H F_{\bar{H}})^{\frac{1}{2}} = F_H$ [see Eq. (3.17) below, for example].

parameter b describes the asymmetry of the Bragg reflection and is the ratio of the direction cosines of the incident and emergent beams (see Sec. 3.1.3 for details). Whether the + or the – sign applies to the expression in brackets in equations (3.14) to (3.16) depends on which branch of the dispersion surfaces is excited and thus on the photon energy.¹⁶⁰ Also, η depends on the deviation of the photon energy from the Bragg energy, $\Delta E = E - E_B$:²⁹

$$\eta = \frac{-2(\Delta E/E) \sin^2 \theta_B + \Gamma F_0}{|P| \Gamma (F_H F_{\bar{H}})^{\frac{1}{2}}}. \quad (3.17)$$

The polarization factor P is unity for σ polarization and normal incidence (see also below), and has values of $\cos(2\theta_B)$ for π polarization and a more general angle of incidence.^{d), e)} F_0 is the structure factor for the (000) reflection, and Γ , which is the constant of proportionality between the Fourier coefficients of the charge density, i.e., the electron density within the crystal, and the dielectric constant, is given by:^{28, 29, 160}

$$\Gamma = \frac{r_e \lambda^2}{\pi V_{uc}} = \left(\frac{e^2}{4\pi \epsilon_0 m_e c^2} \right) \frac{\lambda^2}{\pi V_{uc}}, \quad (3.18)$$

with $r_e = (e^2/4\pi \epsilon_0 m_e c^2)$ being the classical electron radius and V_{uc} being the volume of the crystal unit cell. Here, e denotes the elementary charge, ϵ_0 the vacuum permittivity or electric constant, and m_e the electron mass.

For non-absorbing crystals, where the structure factors F_0 and F_H are real, total reflectivity occurs in the range of η from -1 to $+1$, where $R = 1$.^{28, 29, 160} Note that, due to an index of refraction effect, the center of the reflectivity curve, which is defined by $\eta = 0$, is found at $2(\Delta E/E) \sin^2 \theta_B = \Gamma F_0$ and thus is displaced from the Bragg energy E_B .^{28, 160} For absorbing crystals, the structure factors F_0 and F_H are complex numbers and the reflectivity curve is lowered. In addition, R as a function of E or θ_{sc} becomes asymmetric.^{28, 29, 160} The reflectivity curve is called *Darwin curve* or *Darwin-Prins curve* for the scenarios without or with absorption, respectively.^{29, 160} Exemplary curves are shown in Fig. 3.2(a).

As has already been pointed out above, the x-ray standing wavefield evolves in the range where the reflectivity is non-zero. Based on the explanations in Sec. 3.1.1, the position of an absorbing atom relative to the Bragg planes is accessible if the intensity of the standing wavefield at its particular position is monitored while the photon energy is scanned through the Bragg condition.

^{d)}For σ polarization, the electric-field vectors \mathbf{E}_i of the incident and emergent waves are collinear and normal to \mathbf{H} , i.e., they are perpendicular to the scattering plane defined by \mathbf{K}_0 and \mathbf{K}_H . For π polarization, both electric-field vectors lie in the scattering plane, i.e., in the plane of \mathbf{K}_0 and \mathbf{K}_H .^{28, 160, 168}

^{e)}Note that there is a slight deviation from the above-made assumption of σ polarization in our experiments. Synchrotron radiation is linearly polarized, horizontally in the plane of the storage ring, and elliptically above and below.^{28, 169} Hence, for the experimental setups used in the present work (see Figs. 4.2 and 4.3 in Sec. 4.1.2, pages 45 and 46, respectively), the requirements for σ polarization are only fulfilled in the case of perfect normal incidence of the x-ray beam on the respective Bragg planes of the sample, that is, for $\theta_B = 90^\circ$. Due to experimental reasons, such as the detection of the Bragg-reflected intensity and the position of the electron analyzer relative to the incident beam (in the plane of the synchrotron storage ring), the actual Bragg angle θ_B is about 88° and π polarization is present, in fact, since the electric-field vectors of the incident and emergent waves lie in the scattering plane (see also Fig. 3.1). The absolute value of the corresponding polarization factor, $|P|$, amounts to ≈ 0.9976 and is sufficiently close to unit to justify the assumption of σ polarization also to apply here. Thus, the effect is neglected.

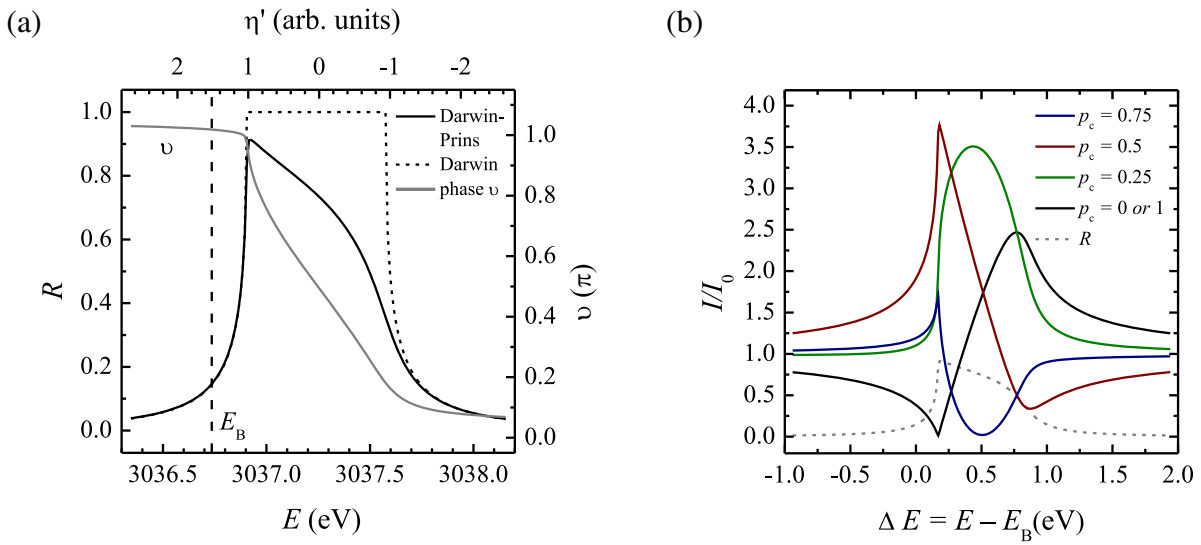


FIG. 3.2. (a) Shape of the Bragg reflection from a perfect crystal without absorption (Darwin curve, black solid line) and with absorption (Darwin-Prins curve, black dashed line). The reflectivity R is given on both an energy scale as well as an $\eta' = \text{Re}(\eta)$ scale. The phase ν (gray solid line) varies by π over the reflectivity range. The curves are simulated with the XSWAVES routine for a perfect Ag(100) crystal, employing the (200) Bragg reflection with $d_{200} = 2.043 \text{ \AA}$ at a Bragg angle θ_B of 88° . The Bragg energy ($E_B = 3036.74 \text{ eV}$) is indicated by a black dashed line. (b) XSW profiles for selected values of the coherent fraction p_c , i.e., for different perpendicular positions relative to the lattice planes. The coherent fraction f_c is unity in all cases. In addition, the corresponding Darwin-Prins curve R is depicted as a gray dashed line. Note that instrumental broadening is not considered here. Own representation based on Fig. 30 in Ref. 160 (p. 706) and on Fig. 5 in Ref. 28 (p. 214).

For this purpose, it is convenient to rewrite Eq. (3.13) with the help of the fact that the scalar product $\mathbf{H}_{hkl} \cdot \mathbf{r}$ can be written as:^{28,29}

$$\mathbf{H}_{hkl} \cdot \mathbf{r} = \frac{z_{hkl}}{d_{hkl}}, \quad (3.19)$$

with the z axis being parallel to \mathbf{H}_{hkl} and z_{hkl} as the perpendicular position relative to the Bragg planes, i.e., modulo d_{hkl} . With this, Eq. (3.13) turns into:^{28,29}

$$\frac{I(z_{hkl})}{I_0} = 1 + R + 2 \sqrt{R} \cos \left(\nu - 2\pi \frac{z_{hkl}}{d_{hkl}} \right). \quad (3.20)$$

Figure 3.2(b) shows exemplary curves which reproduce the normalized intensity of the x-ray standing wavefield at different value of z_{hkl} as a function of E . The perpendicular position z_{hkl} may, thus, be determined from an experimentally conducted XSW profile due to its unique shape, as will be described in the following subsections. Note that the x-ray standing wavefield not only evolves within the crystal but also outside the crystal. Hence, atoms which are adsorbed on the crystal surface are immersed in the standing wavefield, too,²⁹ allowing structural investigations of atoms and molecules on surfaces with XSW.

Coherent position and coherent fraction

So far, the above equation neglects the fact that the atoms of interest can adopt different positions. This is accounted for by the two parameters coherent position p_c and coherent fraction f_c .^{28,29} In many cases, the latter may be understood as a measure for the structural order of the atoms relative to the Bragg planes. It can have values between 0 and 1. The former represents the (weighted) average position modulo d_{hkl} .

The atomic positions z_{hkl} may differ due to vibrational or static disorder, or to several different discrete sites.^{28,29} The distribution of positions can be represented by a distribution of z_{hkl} values, with a probability of a given value being given by $f(z_{hkl}) \cdot dz_{hkl}$ within a range dz_{hkl} about the value z_{hkl} .²⁹ Now, Eq. (3.20) is replaced by:²⁹

$$\frac{I(z_{hkl})}{I_0} = 1 + R + 2 \sqrt{R} \int_0^{d_{hkl}} f(z_{hkl}) \cos\left(\nu - 2\pi \frac{z_{hkl}}{d_{hkl}}\right) dz_{hkl}, \quad (3.21)$$

which can be expressed in the form of:²⁹

$$\frac{I(z_{hkl})}{I_0} = 1 + R + 2 \sqrt{R} f_c \cos(\nu - 2\pi p_c), \quad (3.22)$$

with the help of the coherent position p_c and the coherent fraction f_c . These two parameters are the phase and the amplitude of one Fourier component of the distribution function $f(z_{hkl})$.²⁹ Further details, also on their exploitation in so-called x-ray standing waves imaging, are found in Refs. 170–174. Often, p_c and f_c are graphically represented in form of an *Argand diagram*, where f_c is the length of a vector in the complex plane and $2\pi p_c$ is the phase angle relative to the positive x axis.^{29,170} Such Argand diagrams are helpful in the interpretation of XSW results when contributions from different positions z_{hkl} of one element have to be discerned.

Equation (3.22) allows the structural clarification of adsorption structures via the parameters coherent position p_c and coherent fraction f_c when fitted to experimental data. Thus, the normalized intensity of the x-ray standing wavefield, $I(z_{hkl})/I_0$, at the position of the atoms of interest must be known. It can be measured indirectly by several different techniques, namely, x-ray photoelectron spectroscopy, x-ray fluorescence spectroscopy or Auger electron spectroscopy.²⁸

Monitoring the intensity of the x-ray standing wavefield

The above-mentioned techniques rely on the photoexcitation of an electron from a core hole of the respective atom to an unbound state (see also Sec. 3.2.3 for details). In principle, the number of photoexcitation processes is directly proportional to the intensity of the x-ray standing wavefield at the location of the emitting atoms. Thus, the measured integral intensity of the electron or the fluorescence emission signal depends on both the atomic positions as well as the phase of the standing wavefield.²⁸ There may be cases, however, where the emission process is not exclusively initialized by the standing wavefield but also by secondary electrons or re-absorption of fluorescence photons. This is particularly true for the emission of Auger electrons and x-ray fluorescence photons, especially if the corresponding energy is low compared to that of the x-ray beam.^{28,41,159,175} In photoemission, however, the proportionality between the intensity of the x-ray

standing wavefield and the angle-resolved, i.e., differential, photoelectron yield $dY/d\Omega$ remains valid in most cases.^{28,176}

$$\frac{I(z_{hkl})}{I_0} \propto \frac{dY}{d\Omega}. \quad (3.23)$$

All techniques yield element-specific signals. In addition, when employing x-ray photoelectron spectroscopy, XSW may be *chemically* sensitive in the sense that different species of one element in nonequivalent chemical environments can be distinguished due to their chemical shifts.²⁸ It requires that the corresponding peaks can be discerned in the photoemission spectrum. In particular, the deconvolution of photoemission spectra into distinct contributions of chemically nonequivalent atoms of one element is used in the present work for clarifying the intramolecular structure of an adsorbed molecule. A discussion of the photoemission process in the framework of the dipole approximation, as well as the consideration of indispensable quadrupole contributions, is found in Sec. 3.1.4.

Normal incidence x-ray standing wavefield absorption (NIXSW)

For the investigation of (molecules on) metal substrates, the XSW experiment has to be performed under (near-)normal incidence of the x-ray beam with respect to the Bragg planes, i.e., for Bragg angles θ_B close to 90° . The reason behind the requirement for (near-)normal incidence is the lower degree of perfection of metal single crystals, as compared to semiconductor crystals, for example.^{28,29} The width of reflectivity curve depends on the Bragg angle θ_B and is proportional to $\tan(\theta_B)$.¹⁷⁷ Hence, for $\theta_B \rightarrow \pi/2$ it approaches ∞ .^{28,29} A more complete derivation shows that for $\theta_B \approx \pi/2$ the width of the reflectivity curve becomes very large¹⁵⁷ and is on the order of several hundred milli-electronvolts.²⁹ For a description of the XSW technique and a modification of the common dynamical theory of diffraction with emphasis on normal incidence see Refs. 178 and 179, for example.

The lower quality of metal substrates is caused by their higher crystal mosaicity. For $\theta_B \approx \pi/2$, however, the Bragg condition, given by Eq. (3.2), is essentially unaffected by small angular deviations because the gradient with respect to θ_s is infinitesimal.¹⁵⁷ Thus, by setting the Bragg angle close to 90° , the desired insensitivity of the XSW technique to the substrate quality is achieved. This was exploited for the XSW experiments in the present work.

3.1.3 Asymmetric Bragg reflections

The lattice planes, which fulfill the Bragg condition in an XSW experiment, are not necessarily parallel to the crystal surface. If the lattice planes are parallel to the surface, one speaks of a *symmetric* Bragg reflection, while the case where the lattice planes and the surface enclose an angle $\varphi_{\text{asym}} \neq 0$ is called *asymmetric* Bragg case. For the Bragg case, the incident and the reflected beams run through the same surface as opposed to the Laue case, where the beams run through different faces of the sample. Note that only the Bragg case is relevant for (NI)XSW experiments. In general, φ_{asym} influences the shape of the reflectivity curve. The asymmetry of the reflection enters the calculation of R via the parameter b , as has already been mentioned in Sec. 3.1.2 [see Eq. (3.16), for example].^{180–183} For the symmetric Bragg case (where $\varphi_{\text{asym}} = 0^\circ$), $b = -1$ applies, while for the symmetric Laue case (where $\varphi_{\text{asym}} = 90^\circ$), $b = 1$ pertains.^{160,184} In the context of the present work, b had to be considered for the experiments on the Ag(100) surface (see Sec. C.4 in the appendix) where XSW profiles were conducted with respect not only to the (200) lattice

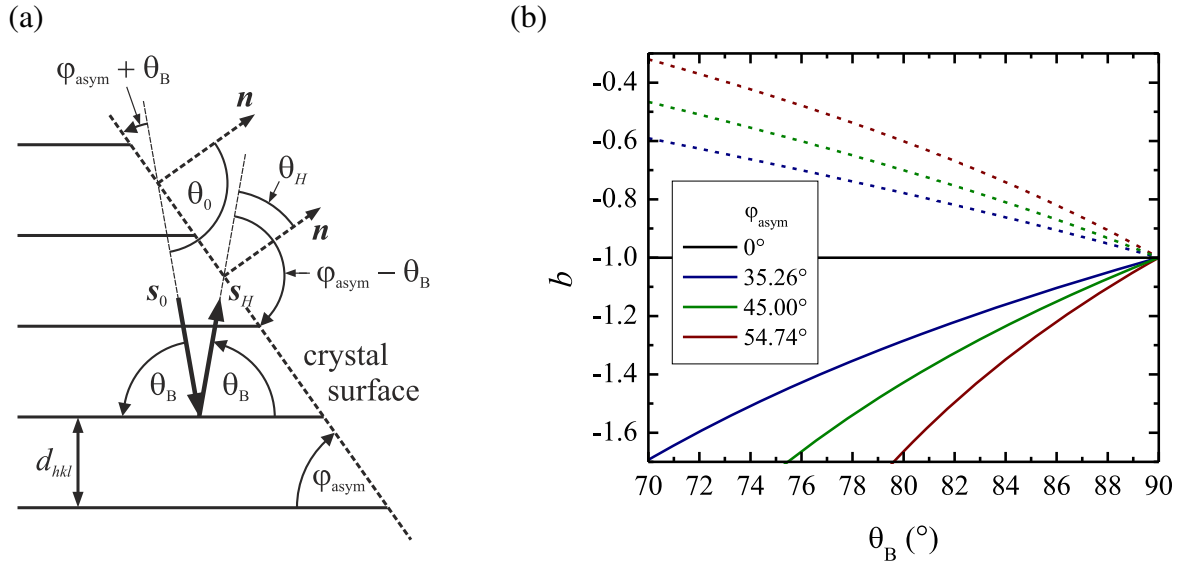


FIG. 3.3. Asymmetric Bragg reflection and resulting values of the asymmetry parameter b . (a) Illustration of an asymmetric Bragg reflection where the surface (black dashed line) makes an angle $\varphi_{\text{asym}} = -54.74^\circ$ with the lattice planes (black solid lines). The surface normal \mathbf{n} and the unit vectors in the incident and diffracted beam directions, \mathbf{s}_0 and \mathbf{s}_H , are indicated. θ_B denotes the Bragg angle, and θ_0 and θ_H are the enclosed angles of \mathbf{s}_0 and \mathbf{s}_H with \mathbf{n} . Own representation based on Figs. 14.17 and 14.18 in Ref. 164 (pp. 348–349). (b) Exemplary curves for the parameter b as a function of Bragg angle θ_B . The depicted values of φ_{asym} correspond to the symmetric Bragg case, and to the angles between the lattice planes (110) and (111), (110) and (100), as well as (111) and (100), respectively. Solid lines hold for $\varphi_{\text{asym}} > 0$, and dashed lines for $\varphi_{\text{asym}} < 0$.

planes, which are parallel to the crystal surface, but also with respect to the (111) Bragg planes, which are not.

The parameter b is defined as:¹⁶⁰

$$b = \frac{\gamma_0}{\gamma_H} = \frac{\mathbf{n} \cdot \mathbf{s}_0}{\mathbf{n} \cdot \mathbf{s}_H} = \frac{\cos \theta_0}{\cos \theta_H}. \quad (3.24)$$

Here, \mathbf{n} denotes the surface normal, and \mathbf{s}_0 and \mathbf{s}_H are the unit vectors in the incident and diffracted beam directions with θ_0 and θ_H being the corresponding angles with respect to \mathbf{n} . Hence, b as the ratio of the direction cosines γ_0 and γ_H of the incident and Bragg-reflected beams with respect to the incident surface describes the asymmetry of the reflection. For the Bragg case, b can be expressed as a function of φ_{asym} simply as:¹⁸¹

$$b = \frac{\sin(\varphi_{\text{asym}} + \theta_B)}{\sin(\varphi_{\text{asym}} - \theta_B)}. \quad (3.25)$$

This follows from geometrical considerations, as is illustrated in Fig. 3.3(a). In addition, the variation of b with θ_B is shown in Fig. 3.3(b). For $\theta_B = \pi/2$, however, $b = -1$ independent of φ_{asym} . Note that, by definition, φ_{asym} is the *acute* angle enclosed by the Bragg-reflecting lattice planes and the crystal surface, and is positive if the reflected beam is concentrated.¹⁸¹ The cross-sectional area

is reduced for the beam which forms the smaller angle with the crystal surface.^{164,180} At the same time, the angular width of that beam is greater by \sqrt{b} .^{164,182,183}

3.1.4 Dipole approximation of the photoemission process and its limitations

Usually, the photoemission process is treated in the dipole approximation. If, however, the wavelength of the x-radiation is on the same order as the spatial expansion of the atomic orbitals, this approximation ceases to be valid, and the theory describing the photoexcitation process needs to be amended. This section explains how experimental XSW profiles may be correctly interpreted considering also nondipolar contributions. Profound descriptions of the underlying theory are found in Refs. 168, 176, 185–188, for example. In the non-relativistic limit, the differential photoionization cross section $d\sigma/d\Omega$ and hence also the differential photoelectron yield $dY/d\Omega$ are proportional to the magnitude squared of the matrix element M_{fi} :^{159,176,187,188}

$$d\sigma/d\Omega \propto dY/d\Omega \propto |M_{fi}|^2 = |\langle f | \exp(i \mathbf{k}_0 \cdot \mathbf{r}) \mathbf{e}_0 \hat{\mathbf{p}} | i \rangle|^2, \quad (3.26)$$

which describes the photoexcitation of an electron from an initial bound state $|i\rangle$ to a final continuum state $|f\rangle$. Here, \mathbf{k}_0 denotes the wavevector of the incident photon (with magnitude $|\mathbf{k}_0| = 2\pi/\lambda$), \mathbf{r} the electron position vector, \mathbf{e}_0 the polarization unit vector of the electric field, and $\hat{\mathbf{p}} = -i\hbar\nabla$ the momentum operator. The exponential in Eq. (3.26) may be expanded in a Taylor series:^{176,187,188}

$$\exp(i \mathbf{k}_0 \cdot \mathbf{r}) = 1 + i \mathbf{k}_0 \cdot \mathbf{r} - \frac{1}{2} (\mathbf{k}_0 \cdot \mathbf{r})^2 - \dots \quad (3.27)$$

For $\mathbf{k}_0 \cdot \mathbf{r} \ll 1$, all terms but the first one on the right-hand side of Eq. (3.27) are omitted, resulting in $\exp(i \mathbf{k}_0 \cdot \mathbf{r}) \approx 1$. This is the so-called (electric) dipole approximation, which holds for low photon energies and requires that spatial variation of the electromagnetic wavefield over the initial state wavefunction is negligible.¹⁸⁸ Now the differential photoionization cross section may be written as:^{176,188}

$$d\sigma/d\Omega = \frac{\sigma}{4\pi} \left[1 + \beta P_2(\cos \theta_p) \right] = \frac{\sigma}{4\pi} \left[1 + \frac{\beta}{2} (3 \cos^2 \theta_p - 1) \right], \quad (3.28)$$

where σ is the photoionization cross section, $P_2(\cos \theta_p) = (3 \cos^2 \theta_p - 1)/2$ is a second-order Legendre polynomial, and θ_p is the angle between the photoelectron detection direction and the polarization vector \mathbf{e}_0 [see Fig. 3.4(a)]. The dipolar asymmetry parameter β varies from -1 to $+2$ depending on the symmetry of the initial state.^{176,188} For an initial s state, for example, $\beta = 2$ and thus $d\sigma/d\Omega \propto \cos^2 \theta_p$. The angular dependence is hence symmetric about \mathbf{e}_0 ,¹⁸⁸ as depicted in Fig. 3.4(b). Note that, since the dipole selection rule $\Delta l = \pm 1$ applies,¹⁸⁹ only a p wave is allowed as the outgoing state with the orbital angular momentum quantum number $l = 1$ in this case.¹⁸⁸

Deviations from the dipole approximation, however, have been shown to occur even for moderate photon energies below 3 keV.^{190–194} Thus, nondipolar contributions to the photoemission process have to be considered. In a first-order approximation to the expansion in Eq. (3.27), the first two terms are now taken into account, giving $\exp(i \mathbf{k}_0 \cdot \mathbf{r}) \approx 1 + i \mathbf{k}_0 \cdot \mathbf{r}$. Thereby, in addi-

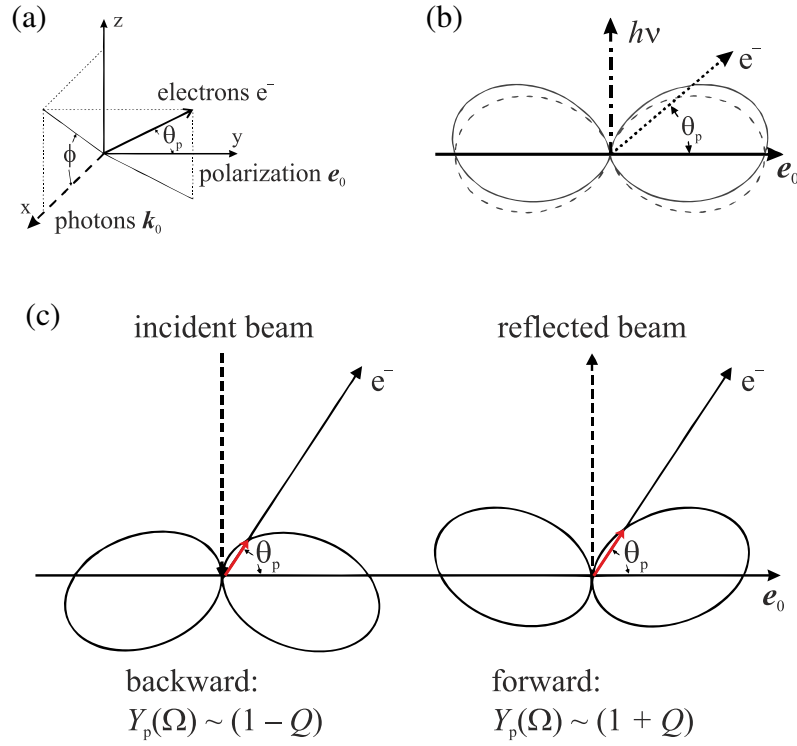


FIG. 3.4. Influence of the nondipolar contributions on the angular distribution of photoemission from an initial s state ($\beta = 2$, $\delta = 0$). (a) Definition of the vectors and angles used in the text for an arbitrary photoelectron emission direction. (b) Angular distribution of photoemission considering nondipolar effects (solid line, $\gamma = 1$) compared with the dipole case (dashed line). (c) Schematic representation of the forward/backward asymmetry in photoemission for an XSW experiment. The observed photoelectron yield $Y_p(\Omega)$ (illustrated by the length of the red arrow) depends on the asymmetry parameter Q . Adapted from Ref. 190.

tion to the electric dipole transition, electric quadrupole and magnetic dipole transitions are now accounted for.^{185,187,188} Hence, Eq. (3.28) may be amended as:^{176,188}

$$\begin{aligned} d\sigma/d\Omega &= \frac{\sigma}{4\pi} \left[1 + \beta P_2(\cos \theta_p) + (\delta + \gamma \cos^2 \theta_p) \sin \theta_p \cos \phi \right] \\ &= \frac{\sigma}{4\pi} \left[1 + \frac{\beta}{2} (3 \cos^2 \theta_p - 1) + (\delta + \gamma \cos^2 \theta_p) \sin \theta_p \cos \phi \right], \end{aligned} \quad (3.29)$$

where ϕ is the angle between the direction of photon propagation (given by \mathbf{k}_0) and the projection of the photoelectron wavevector onto the plane perpendicular to \mathbf{e}_0 [see Fig. 3.4(a)].¹⁸⁸ For photoelectron detection in the plane defined by \mathbf{e}_0 and \mathbf{k}_0 , as was indeed the case in our XSW experiments (see Figs. 4.2 and 4.3 in Sec. 4.1.2, pages 45 and 46, of the present work, respectively, for schematic representations of the experimental setups), the term $\cos \phi$ is therefore +1 or -1 for photoelectron detection in forward or backward direction, respectively.^{f)} The two additional asymmetry parameters δ and γ are associated with the nondipolar terms. γ expresses the major correction corresponding to the dipole–electric quadrupole interference, while δ represents the magnetic–electric dipole term, which can only be present if core-relaxation occurs.¹⁸⁵ The pa-

^{f)}Note that the forward direction is the direction defined by the wavevector of the Bragg-reflected beam here [see also Fig. 3.4(c)].^{176,190} Hence, $\mathbf{k}_0 \equiv 2\pi \mathbf{K}_H$ applies in the context of the XSW experiments within the present work.

parameters β , γ and δ vary for different elements, subshells and photon energies and are tabulated in Refs. 195–198, for example.

The nondipolar contributions lead to a forward/backward asymmetry in the photoemission process which is usually accounted for by the parameter Q :¹⁷⁶

$$Q = \frac{(\delta + \gamma \cos^2 \theta_p) \sin \theta_p \cos \phi}{1 + \beta P_2(\cos \theta_p)}. \quad (3.30)$$

As a consequence of the forward/backward asymmetry, the proportionality between the intensity of the x-ray standing wavefield and the differential photoelectron yield, as given by Eq. (3.23), ceases to be valid in the XSW experiment. Looking at Fig. 3.4(c), one sees that the photoelectron emission in the forward direction, which is caused by the Bragg-reflected beam, exceeds that in the backward direction caused by the incident beam. Thus, Eq. (3.22) has to be modified in order to ensure a correct description of the XSW profiles. This is done with the help of the parameters S_R and $S_I = |S_I| \exp(i\psi)$,¹⁸⁷ which can be calculated from Q and the phase difference Δ between the dipole and the quadrupole matrix elements ϕ_d and ϕ_q , respectively:¹⁷⁶

$$S_R = \frac{1 + Q}{1 - Q} = \frac{1 + \beta P_2(\cos \theta_p) + (\delta + \gamma \cos^2 \theta_p) \sin \theta_p \cos \phi}{1 + \beta P_2(\cos \theta_p) - (\delta + \gamma \cos^2 \theta_p) \sin \theta_p \cos \phi}, \quad (3.31)$$

$$|S_I| = \frac{(1 + \tan^2 \psi)^{\frac{1}{2}}}{1 - Q}, \quad (3.32)$$

$$\tan \psi = Q \tan \Delta, \quad (3.33)$$

and

$$\Delta = \phi_q - \phi_d. \quad (3.34)$$

Note that for an initial s state, where $\beta = 2$ and $\delta = 0$,^{185,189} Eqs. (3.30) and (3.34) simplify to:^{188,190}

$$Q = \frac{\gamma \sin \theta_p \cos \phi}{3}. \quad (3.35)$$

and

$$\Delta = \delta_d - \delta_p, \quad (3.36)$$

where δ_d and δ_p are the partial phase shifts of the final quadrupole-excited d and dipole-excited p states of the emitted electron. Values for δ_d and δ_p are tabulated in Ref. 199, for example, while general values for $\Delta = \phi_q - \phi_d$ are not as readily accessible.¹⁷⁶

Having the parameters S_R , $|S_I|$, and ψ at hand, Eq. (3.22) may be written as:¹⁸⁸

$$\frac{I(z_{hkl})}{I_0} = 1 + S_R R + 2 |S_I| \sqrt{R} f_c \cos(\nu - 2\pi p_c + \psi). \quad (3.37)$$

The above equation can be computed and fitted to experimental XSW profiles, yielding the structural parameters f_c and p_c as a result. In the context of the present work, the evaluation routine XSWAVES was developed for this purpose which is based on the theory described above. The corresponding source code and the features of XSWAVES are presented in Appendix A.

Besides structural characterizations, Eq. (3.37) allows to determine experimentally the forward/backward asymmetry parameter Q for adsorbate species if they form an incoherent layer with $f_c = 0$.^{g)} Incoherence may be present either in monolayer films with respect to lattice planes which are not parallel to the surface or in multilayer films. Experimental values for Q are compiled in Ref. 190, for example. Note, however, that Q depends via Eqs. (3.30) or (3.35) on the actual experimental geometry which makes the values, which may be derived from different experiments, comparable only by the parameter γ . In several cases, the experimental values for Q deviate significantly from those which are predicted by theory, i.e., up to a factor of two.¹⁹⁰ Therefore, only theoretically derived values of Q were used in the present work, although, in the strict sense, they only hold for single atoms and not for atoms *in* a molecule *on* a surface. Additional effects might be present here, such as charge redistribution and photoelectron scattering, which may alter the angular dependence of the photoelectron yield. The impact of the choice of Q on the fitting results of f_c and p_c obtained for our experimental data will be discussed in Sec. 4.3.3 (see also Appendix E for graphical representations of the effect). In brief, mainly the results for f_c were affected (maximal to a factor of 3) while the results for p_c typically remain unaltered within 15 %.

3.2 Additional experimental methods

In this section, the additional experimental techniques which were used in the present work are introduced in brief. The results of these techniques concerning both the lateral geometric and the electronic structure of the adsorbate help to understand the relevant details of the interfacial bonding mechanism.

3.2.1 Low energy electron diffraction

The low energy electron diffraction (LEED) method is one of the most common techniques for determining structural order and symmetry elements at surfaces. This technique yields structural parameters of the surface with high precision, that is, on the sub-ångström scale. Furthermore, LEED experiments provide information about the surface morphology and the presence of defects, such as steps or domain boundaries. Profound descriptions of the LEED method are given in Refs. 62, 157, 200–205, for example. Only basic aspects of LEED are highlighted here. LEED exploits the wave character of electrons which was first proven in an experiment by Davisson and Germer in 1927.²⁰⁶ According to the de Broglie relation,²⁰⁷ the electron wavelength λ is given by:^{157, 202}

$$\lambda = \frac{h}{m_e |\mathbf{v}|} = \frac{h}{\sqrt{2 m_e E_{\text{kin}}}}. \quad (3.38)$$

In Eq. (3.38), m_e is the electron mass, \mathbf{v} is the electron velocity and E_{kin} is the kinetic energy. Typically, electrons with kinetic energies between 10 eV and 500 eV are used. Hence, their wavelength is in the range of 0.5 Å to 4 Å which is of the order of interatomic distances. Therefore,

^{g)}Note that, in principle, also the nondipolar parameter Δ , i.e., the phase difference, can be obtained experimentally because $Q \propto \cos \Delta$ according to Nelson *et al.*¹⁷⁶

LEED is well suited for structural analysis on the atomic or molecular scale. In addition, due to the strong interaction of electrons with matter, LEED is a very surface-sensitive technique with a typical information depth of about 1 nm or, in other words, of about two or three atomic layers.¹⁵⁷

In a LEED experiment, electrons are backscattered elastically from a surface and may interfere constructively or destructively, resulting in a diffraction pattern with maxima and minima of intensity. The diffraction pattern can be experimentally recorded in different ways, as will be discussed below. It is theoretically predicted employing geometrical considerations and the kinematic approximation of diffraction which assumes the presence of identical scattering units over the entire surface and the absence of multiple scattering.^{157,200,202} The surface, as an arrangement of lattice points which is periodic in two dimensions, is considered as an ensemble of parallel rows of scatterers with directions $[h'k']$ and mutual distances $d_{h'k'}$. Then, the interference maxima are observed at an angle φ with respect to the surface normal on the basis of the condition:²⁰²

$$n \lambda = d_{h'k'} (\sin \varphi - \sin \varphi_0), \quad (3.39)$$

where n is the order of diffraction, φ_0 is the angle of incidence and h', k' are the Miller indices. Often, n is included in the Miller indices, giving the so-called Laue indices $h = n h', k = n k'$.^{h), i)} The LEED pattern of a given surface can be geometrically predicted with the aid of the so-called *Ewald sphere* construction which is depicted in Fig. 3.5. The incident electron wavevector \mathbf{k}_0 is drawn such that it terminates at the origin of the reciprocal lattice. A sphere of radius $|\mathbf{k}_0| = k_0 = 2\pi/\lambda$ is constructed about the beginning of vector \mathbf{k}_0 . Considering the conservation of energy and the conservation of momentum for those components which are parallel to the surface, the Bragg condition for electron diffraction is expressed as:^{157,200,202}

$$\mathbf{G}_{hk} = \mathbf{k}_{H,\parallel} - \mathbf{k}_{0,\parallel}. \quad (3.40)$$

In Eq. (3.40), \mathbf{G}_{hk} is a reciprocal lattice vector, and $\mathbf{k}_{0,\parallel}$ and $\mathbf{k}_{H,\parallel}$ are the parallel components of the incident and the emergent wavevectors, respectively. As opposed to x-ray diffraction from a bulk crystal,^{164,208,209} the perpendicular component of \mathbf{k}_0 , $\mathbf{k}_{0,\perp}$, is not subject to a selection rule in the electron diffraction process, and the perpendicular component of the scattering vector $\mathbf{k} = \mathbf{k}_H - \mathbf{k}_0$, \mathbf{k}_\perp , may therefore have an arbitrary value for an ideal periodic surface. Hence, the reciprocal lattice is composed of one-dimensional, infinite rods instead of lattice points.¹⁵⁷ Where the Ewald sphere intersects the reciprocal lattice rods, intensity maxima are observed in the diffraction pattern (see Fig. 3.5).

From the diffraction pattern, the size and the relative orientation of the unit cell, i.e. the crystal lattice, can be deduced. Also, from the systematic extinction of diffraction spots, the presence of certain symmetry elements in the unit cell can be concluded.^{157,210,211} However, the filling of the unit cell, i.e. the crystallographic basis, is not available through a simple LEED experiment. It can in principle be obtained by so-called LEED- $I(V)$ measurements where the intensity of the diffraction spots is monitored as a function of the electron energy. In this case, the scattering process has to be treated in the framework of the dynamical theory of diffraction where multiple-scattering processes are considered.^{157,200,202}

^{h)}The Miller and Laue indices for the third dimension are denoted l' and $l = n l'$, respectively.

ⁱ⁾The differentiation of Miller and Laue indices is not strictly obeyed in the literature. For reasons of simplicity, in the present work Laue indices are used also in those cases where Miller indices would be required by definition, i.e., for the notation of crystal planes in a Bravais lattice. In that case, however, the order of diffraction, n , equals one, and therefore Miller and Laue indices are identical anyhow. This has already been utilized in Sec. 3.1.1 without explicit mentioning.

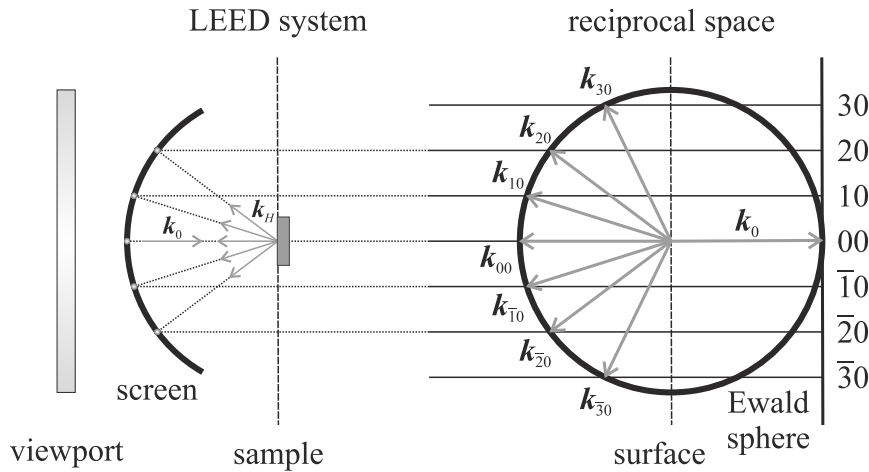


FIG. 3.5. Ewald sphere construction in reciprocal space (right) and schematic representation of the formation of the diffraction pattern in a conventional LEED system (left). The incident and emergent electron wavevectors, k_0 and k_H , respectively, are represented by gray arrows while the Ewald sphere is given as a black circle. Diffraction maxima are observed where the lattice rods (black lines) intersect the Ewald sphere. The positions of the sample and the phosphor-coated screen are indicated. Own representation based on Figs. 3.5.3 and 3.6.1 in Ref. 200 (p. 130–131).

In a conventional LEED system, the diffraction pattern is imaged on a green phosphor-coated screen. The screen curvature and that of the Ewald sphere correspond to each other and, in principle, a distortion-free diffraction pattern is observed. Typically, the electron current onto the sample is on the order of $1 \mu\text{A}$. In particular, organic adsorbates may be decomposed by the electron bombardment. The electron current onto the sample can be reduced down to the nanoampere regime if the scattered electrons are multiplied with a channel electron multiplier before they hit the phosphor-coated screen.²¹² This is employed in micro-channel plate low energy electron diffraction (MCP-LEED) for the investigation of structures which are sensitive to charging effects, electron-stimulated decomposition or desorption. Since the micro-channel plate and thus also the phosphor-coated screen are planar in an MCP-LEED, the detected diffraction pattern is distorted and needs to be equalized for proper geometric analysis with a trigonometric correction function.^{213,214}

Regarding the electron current onto the sample, the same magnitude as in MCP-LEED can be obtained with high resolution spot profile analysis low energy electron diffraction (SPA-LEED).^{215,216} In this technique, however, the scattered electrons are guided into a fixed single electron channel-tron detector by means of an electrostatic deflection unit whose deflection plates are arranged as sets of octopoles. Thereby, the diffraction pattern is recorded in a scanning mode with high lateral resolution, and also the spot profiles may be analyzed. For SPA-LEED, due to the fixed small angle between the incident and the emergent electron wavevectors, k_0 and k_H , the radius of the Ewald sphere is larger by a factor of nearly two in comparison to conventional LEED.²¹⁵

Profiles of diffraction spots contain information about the surface morphology. Different scenarios have to be discerned depending on the scattering condition S which describes the phase difference of electrons scattered from terraces of different height. For example, for the (00) spot (where the parallel component of the scattering vector k , $k_{\parallel} = k_{H,\parallel} - k_{0,\parallel}$, is zero) the scattering condition S is given by:²¹⁵

$$S = \frac{2d_z \cos \varphi_0}{\lambda}, \quad (3.41)$$

where d_z denotes the height difference of a monoatomic step.

Independent of S , a diffraction spot consists of a sharp central spike which is due to the long-range order of the substrate and a diffuse part. The width $\Delta k_{\parallel, \text{diff}} = |\Delta \mathbf{k}_{\parallel}|$ of the diffuse part of the spot profile, i.e., the “diameter” or “size” in k space, depends on the surface morphology and may vary with the scattering condition S . For *in-phase* conditions $S = n + \delta S$ where $\delta S \ll 1$, i.e., for a diffraction condition close to a Bragg condition, $\Delta k_{\parallel, \text{diff}}$ is determined by the correlation length ξ of the surface height function and thus is a measure of the large-scale roughness of the surface.²¹⁵ For *out-of-phase* conditions $S = n + 1/2$, $\Delta k_{\parallel, \text{diff}}$ is inversely proportional to the average terrace width or the average “island size”, i.e., the mean diameter of the periodic structures, $\bar{\Gamma}$:^{202, 215}

$$\Delta k_{\parallel, \text{diff}} = \begin{cases} \frac{2\pi}{\xi} & \text{if } S = n + \delta S \text{ (in-phase condition),} \\ \frac{2\pi}{\bar{\Gamma}} & \text{if } S = n + 1/2 \text{ (out-of-phase condition).} \end{cases} \quad (3.42)$$

In the simplest approximations, the normalized shape of the diffuse part of the profile, $I_{\text{diff}}(\mathbf{k}_{\parallel})$, can either be described by a Lorentzian function for one-dimensional problems:²¹⁵

$$I_{\text{diff}}(\mathbf{k}_{\parallel}) = \frac{\omega}{2} \left(\omega^2 + |\mathbf{k}_{\parallel}|^2 \right)^{-1}, \quad (3.43)$$

or by a Lorentzian function with exponent $3/2$ for two-dimensional islands:²¹⁵

$$I_{\text{diff}}(\mathbf{k}_{\parallel}) = \frac{\omega}{2} \left(\omega^2 + |\mathbf{k}_{\parallel}|^2 \right)^{-\frac{3}{2}}. \quad (3.44)$$

In Eqs. (3.43) and (3.44), $\mathbf{k}_{\parallel} = \mathbf{k}_{H, \parallel} - \mathbf{k}_{0, \parallel}$ is the parallel component of the scattering vector \mathbf{k} . $\omega = 2/\bar{\Gamma}$ is determined by the mean diameter of the periodic structures (see above) and corresponds the half width at half maximum (HWHM) of the diffuse part of the diffraction spot in the case of a Lorentzian profile [see Eq. (3.43)].

For metal substrates, the broadening of the diffraction spots due to bulk or surface defects, such as small angle mosaics/grain boundaries, point defects, steps or domain boundaries, is greater than the spot broadening due to the instrumental response function.²¹⁵ In that case, $\Delta k_{\parallel, \text{diff}}$ is difficult to quantify because the diffuse part of the experimental spot profile is overlapped by the broadened central spike. Therefore, $\Delta k_{\parallel, \text{diff}}$ can be only approximated by the full width at half maximum (FWHM) of the (hk) diffraction spot profile, $\Delta k_{hk} = |\Delta \mathbf{k}_{hk}|$. In principle, the transfer width T_w of the SPA-LEED instrument can be calculated from Δk_{hk} :²¹⁵

$$T_w = a_0 \frac{k_{01}}{\Delta k_{hk}}, \quad (3.45)$$

with $k_{01} = |\mathbf{k}_{01}|$ being the distance between two neighboring fundamental diffraction spots and a_0 being the atomic row distance at the surface.^{j)} For the reasons given above, the effective transfer

^{j)}Note that the atomic row distance a_0 is equal to the interatomic distances at the surface only in those cases where the surface unit cell is rectangular or quadratic. In all other cases, a_0 has to be deduced from the unit cell parameters by geometric considerations.²⁰² The atomic row distance is generally given by $a_0 = a \sin \alpha$, with $\alpha = 120^\circ$ for a hexagonal surface, for instance. Here, $a = |\mathbf{a}_1| = |\mathbf{a}_2|$ denotes the surface lattice constant and α the angle which is enclosed by the unit cell vectors \mathbf{a}_i .

width $T_{w,\text{eff}}$ can be considered a reliable measure for the spatial coherence of the surface^{202,217,218} and thus also for the large-scale surface roughness or the average terrace width, respectively:^{k)}

$$T_{w,\text{eff}} = a_0 \frac{k_{01}}{\Delta k_{hk}} \approx \begin{cases} \xi & \text{if } S = n + \delta S \text{ (in-phase condition),} \\ \bar{\Gamma} & \text{if } S = n + 1/2 \text{ (out-of-phase condition).} \end{cases} \quad (3.46)$$

Usually, the FWHM of the specular (00) diffraction spot of the bare surface is employed if the spatial coherence of the substrate surface is to be quantified. The spatial coherence of an adsorbate layer can be characterized using the FWHM of an overlayer diffraction spot. For further details concerning the analysis of diffraction spot profiles, the reader is referred to Ref. 215 and references therein.

3.2.2 Scanning tunneling microscopy

Scanning tunneling microscopy (STM) is a versatile tool for the investigation of surface structures in real space.^{62,157,200,201,219,220} As opposed to the other experimental techniques which are introduced in this chapter, it yields information on the surface properties only on a local scale and thus is a non-averaging technique. STM has been invented in the early 1980s and employs the quantum tunneling effect.^{221–224} Electron tunneling may occur if two conducting materials are brought sufficiently close together since the electron wavefunctions close to the Fermi level E_F leak out of their confining potential wells and hence overlap for small distances which are in the ångström or nanometer regime typically. If the Fermi levels E_F of the two materials differ, i.e., if $E_{F,1} \neq E_{F,2}$, an electron current will occur across the vacuum gap from one material to the other. For example, $E_{F,1} \neq E_{F,2}$ applies in the case of different work functions Φ of the two materials, that is, for $\Phi_1 \neq \Phi_2$, provided that a common vacuum level is present. If, however, the two materials are electrically connected and thus act as electrodes, the Fermi levels equilibrate, such that there is a unique Fermi level E_F for both metals. By applying a bias voltage U_{bias} between the two electrodes, the alignment of the Fermi levels is revoked which results in a tunneling current I_t between the electrodes. This is schematically depicted in Fig. 3.6. I_t decays exponentially with the distance s between the electrodes:^{157,200,219,220}

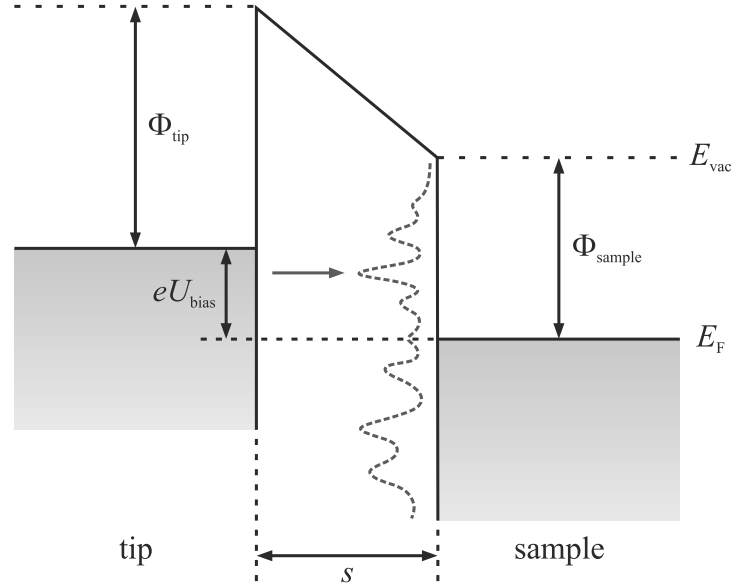
$$I_t \propto U_{\text{bias}} \exp \left[-2 \hbar^{-1} (2 m_e \Phi_{\text{eff}})^{\frac{1}{2}} s \right], \quad (3.47)$$

where m_e is the electron mass, Φ_{eff} denotes the effective local work function (and thus the local potential barrier height) and the parameter $\kappa = \hbar^{-1} (2 m_e \Phi_{\text{eff}})^{\frac{1}{2}}$ is the exponential inverse decay length.

In an STM experiment, a metal electrode in form of an atomically sharp tip is laterally scanned over the surface of the sample of interest which acts as the second electrode. By convention, the applied bias voltage denotes the potential of the sample. For instance, positive values of U_{bias} cause a tunneling of electrons from occupied tip states into unoccupied sample states. In principle, two modes of operation have to be discerned, namely, the constant current and the constant height mode. In the constant current mode, the tunneling current is maintained during the scan of the tip across the surface. A constant value of I_t is achieved by means of a feedback loop which changes the tip-sample distance accordingly. The vertical displacement of the tip, $\Delta z(\mathbf{r})$, is monitored as a function of its lateral position vector $\mathbf{r} = \mathbf{r}(x, y)$. In the constant height mode of operation, the vertical tip position is kept unmodified while $I_t(\mathbf{r})$ is measured. Depending on the tip condi-

^{k)}Considering Eqs. (3.42) and (3.45), Eq. (3.46) requires that $k_{01} = 2\pi/a_0$. This applies by definition.

FIG. 3.6. Energy level diagram for an STM tunneling junction: Two electrodes, tip and sample, are separated by a vacuum gap s . Due to the applied (positive) bias voltage U_{bias} , electrons tunnel from the tip into empty sample states (gray arrow). The dashed gray line represents the sample LDOS. Φ_{tip} and Φ_{sample} are the electrode work functions, and E_{vac} and E_{F} are the vacuum and the Fermi level, respectively. Own representation based on Fig. 1.76 in Ref. 220 (p. 143).



tions, a lateral resolution on the ångström scale as well as chemical and, for molecular adsorbates, intramolecular contrast can be achieved with STM.^{225–233}

Although the constant current mode is often called topography mode, STM does not image atoms, i.e., the geometric structure of the sample surface, but the surface local density of states (LDOS) at the Fermi level convoluted with that of the tip apex atom. In the Tersoff–Hamann theory, which holds in the limit of low temperatures and small bias voltages, the tip state is approximated by an s wave.²²⁵ Thus, the tip properties are simplified to a large extent. In this approximation the tunneling current is proportional to the surface LDOS $n_{\text{surface}}(\mathbf{r}, E_{\text{F}})$ at the Fermi level:^{157,219,220,225}

$$I_{\text{t}} \propto n_{\text{surface}}(\mathbf{r}, E_{\text{F}}). \quad (3.48)$$

Taking into account the actual electronic states of a real tip and finite bias voltages,^{226,227} Eq. (3.48) turns into:^{157,219,220,226,227}

$$I_{\text{t}} \propto \int_{E=0}^{e U_{\text{bias}}} n_{\text{tip}}(\mathbf{r}, \pm e U_{\text{bias}} \pm E) \cdot n_{\text{surface}}(\mathbf{r}, E) \cdot T(E, e U_{\text{bias}}) dE, \quad (3.49)$$

with $T(E, e U_{\text{bias}})$ as the energy- and bias-dependent transmission coefficient of the tunneling junction. Assuming that $dn_{\text{tip}}/dU_{\text{bias}} \approx 0$, it can be concluded from Eq. (3.49) that structure in the derivative $dI_{\text{t}}(U_{\text{bias}})/dU_{\text{bias}}$ as a function of U_{bias} can be attributed to features in the surface LDOS $n_{\text{surface}}(\mathbf{r}, E)$.^{219,220} Such $dI_{\text{t}}(U_{\text{bias}})/dU_{\text{bias}}$ curves are measured in scanning tunneling spectroscopy (STS), yielding the local electronic structure in the range of a few electronvolts around the Fermi level.

3.2.3 X-ray photoelectron spectroscopy

The fundamental principles of x-ray photoelectron spectroscopy (XPS) are briefly summarized here. Details can be found in Refs. 62, 157, 200–202, 234–238, for example. The XPS technique allows the investigation of the chemical state of atoms in a sample, as well as the quantification of the exact composition of the sample. In principle, solid, liquid and gaseous samples can be

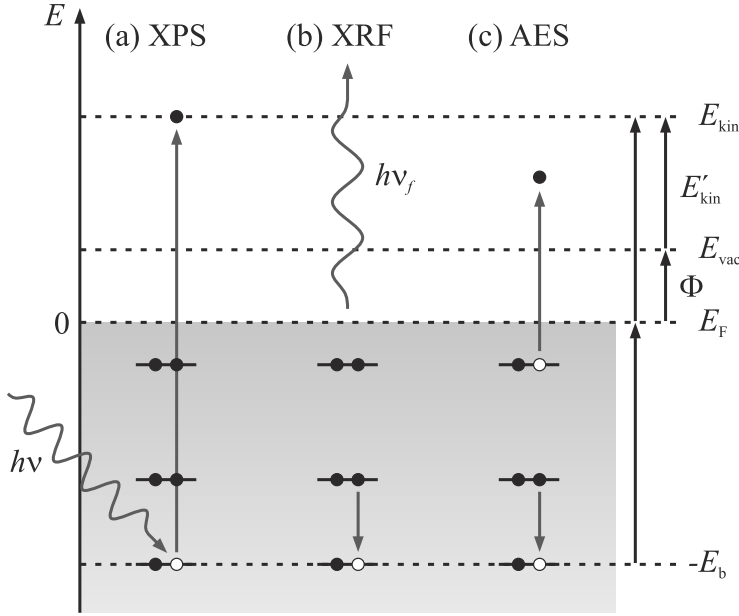


FIG. 3.7. Principle of x-ray photoemission and successive effects: (a) X-ray photoelectron spectroscopy, XPS, (b) x-ray fluorescence spectroscopy, XRF, and (c) Auger electron spectroscopy, AES. A photon (gray wave) excites an electron (\bullet) to the continuum and creates a core hole (\circ). E_{kin} denotes the kinetic energy of the emitted electron (with respect to the Fermi level), E_{vac} the vacuum level, E_{F} the Fermi energy, E_{b} the binding energy, $h\nu$ the photon energy, and Φ the work function of the sample. $E'_{\text{kin}} = E_{\text{kin}} - \Phi$ is the kinetic energy with respect to E_{vac} . See text for further explanations.

investigated with XPS.^{237,239,240} Only solid state samples are examined in the context of the present work. XPS is based on the photoelectric effect^{241,242} which describes the excitation of an electron from a bound state to the continuum upon illumination with light: An electron is emitted from a core level of an atom within the sample by a photon of the energy $h\nu$ which typically is in the range of about 100 eV to 15 keV. The kinetic energy E_{kin} of the photoelectron, which is referenced against the Fermi level E_{F} for solid substrates by convention, is given by:^{157,202,235}

$$E_{\text{kin}} = h\nu - E_{\text{b}}, \quad (3.50)$$

or, with $E'_{\text{kin}} = E_{\text{kin}} - \Phi$ as the kinetic energy being referenced against the vacuum level E_{vac} .^{157,202,235}

$$E'_{\text{kin}} = h\nu - E_{\text{b}} - \Phi. \quad (3.51)$$

In the above equations, E_{b} is the binding energy of the electron (relative to E_{F}) and Φ the work function of the sample, i.e., the energy difference between E_{vac} and E_{F} .^{84,202} The schematics of the photoemission process are depicted in Fig. 3.7(a). In an XPS experiment, E_{kin} is measured.²⁰² This allows to calculate E_{b} according to Eq. (3.50). Since binding energies are unique for the distinct energy levels of the atoms, XPS is chemically sensitive.

According to *Koopmans' theorem*, the binding energy E'_{b} (with respect to the vacuum level, that is, $E'_{\text{b}} = E_{\text{b}} + \Phi$ in the present context; see also Fig. 3.7) is equal to the negative orbital energy of the emitted electron.²⁴³ This approximation, however, does neither consider relativistic and correlation effects in the initial state nor relaxation effects in the final state because it employs a single-electron picture. Yet, these effects have to be taken into account for many-body systems. Relaxation effects denote the intra- and interatomic reorganization of the electronic structure after creation of a core hole. The relaxation improves the screening of the created core hole and thus leads to a lower binding energy. This is often referred to as polarization effect for the interatomic relaxation. Besides, as part of the intra-atomic relaxation, further electron excitations may occur which lead to corresponding satellite lines at higher binding energies in the XP spectrum. They are called shake-up or shake-off satellites, depending on whether the multiple excitations occur into higher-lying bound states or into free continuum states. Also, for molecular adsorbates the

filling of (intrinsically) empty levels becomes possible during the photoemission process. This manifests in shake-down satellite lines at lower binding energy (due to an enhanced screening of the core hole) which can be interpreted as a measure for the strength of the substrate-adsorbate interaction.^{244–246}

With XPS, it is possible to experimentally differentiate between atoms of one element in non-equivalent chemical states and/or environments due to their chemical shift. This shift often is a combination of initial and final state effects, e.g., the oxidation state of the atom and screening effects of the surroundings. The resolution of chemical shifts in XPS is essential for the experimental quantification of submolecular geometric differences within of large adsorbed molecules (which will also be referred to as molecular distortions later in this work) with the XSW technique, as it was done in the present work.

By tuning the photon energy or the detection angle the information depth of XPS can be varied. The escape depth of the photoelectrons from the solid sample is typically in the range of a few to about one hundred ångströms, as can be seen from the universal curve.^{247–249} This makes XPS a very surface-sensitive technique. The escape depth d_e depends on the emission angle θ of the photoelectron relative to the surface normal and on its inelastic mean free path λ_{IMFP} in the solid:^{202, 250}

$$d_e(E_{\text{kin},Z,j}, \theta) = \lambda_{\text{IMFP}}(E_{\text{kin},Z,j}) \cos \theta. \quad (3.52)$$

In turn, $\lambda_{\text{IMFP}}(E_{\text{kin},Z,j})$ differs for different elements and compounds, and is a function of the kinetic energy of the respective photoelectron. Experimentally and theoretically determined values for λ_{IMFP} are tabulated.^{251–259}

For quantitative analysis of XP spectra the integrated intensity of an XPS peak has to be determined. Given a small entrance aperture of the electron spectrometer and a uniform illumination of the sample, the photoelectron yield $Y_{Z,j}$ on photoemission from orbital j of element Z in a homogenous sample calculates as follows:^{202, 237, 250, 260}

$$Y_{Z,j} = \sigma_{Z,j}(E_{\text{kin},Z,j}) D(E_{\text{kin},Z,j}) L_{Z,j}(\gamma) J_0 N_Z \lambda_{\text{IMFP}}(E_{\text{kin},Z,j}) \cos \theta \cdot G(E_{\text{kin},Z,j}). \quad (3.53)$$

In Eq. (3.53), $\sigma_{Z,j}(E_{\text{kin},Z,j})$ is the photoionization cross section, $D(E_{\text{kin},Z,j})$ the detection efficiency of the electron spectrometer, $L_{Z,j}(\gamma)$ the angular asymmetry of the emitted intensity with respect to the angle γ between the direction of incidence and of detection,¹⁾ J_0 the flux of primary photons on the sample surface, N_Z the density of atoms, θ the angle of detection with respect to the surface normal and $G(E_{\text{kin},Z,j})$ the transmission of the electron analyzer. Note that $D(E_{\text{kin},Z,j})$, being a function of the kinetic energy intrinsically,²⁶² is constant if the electron analyzer is operated at a constant pass energy, as is usually the case.²⁰²

In cases when the substrate surface of element A is covered with a thin overlayer of element B with thickness $d_{\text{I,B}}$, the photoelectron yield $Y_{A,j}$ from the substrate is attenuated according to:^{202, 235}

$$Y_{A,j} = Y_{A,j}^0 \exp\left(-\frac{d_{\text{I,B}}}{\lambda_{\text{IMFP}}(E_{\text{kin},A,j}) \cos \theta}\right). \quad (3.54)$$

¹⁾Note that the angular asymmetry parameter $L_{Z,j}(\gamma)$ also accounts for the polarization of the x-ray photons.^{202, 250, 261}

Here, $Y_{A,j}^0$ is the expected intensity^{m)} in agreement with Eq. (3.53). In turn, the photoelectron yield $Y_{B,j'}$ of the overlayer signal is given by:^{202,235}

$$Y_{B,j'} = Y_{B,j'}^0 \left[1 - \exp\left(-\frac{d_{l,B}}{\lambda_{\text{IMFP}}(E_{\text{kin},B,j'}) \cos \theta}\right) \right], \quad (3.55)$$

where $Y_{B,j'}^0$ denotes the maximum intensity of a thick overlayer according to Eq. (3.53). Equations (3.54) and (3.55) can be used to determine the overlayer thickness d_l if $Y_{Z,j}$ and $Y_{Z,j}^0$ are known from the experiment. If the surface is only covered to a fraction ϑ_B with a submonolayer of element B, Eq. (3.54) changes to:^{202,235}

$$Y_{A,j} = Y_{A,j}^0 \left[1 - \vartheta_B + \vartheta_B \exp\left(-\frac{d_{l,B}}{\lambda_{\text{IMFP}}(E_{\text{kin},A,j}) \cos \theta}\right) \right]. \quad (3.56)$$

In the course of the present work, the above equations will be used in order to determine surface coverages of PTCDA (see Sec. 4.3.2). Note, however, that intensity variations in XP spectra cannot only occur due to the presence of an adsorbate on the surface but also due to diffraction effects. This is employed in photoelectron diffraction (PhD) where the azimuthal angle ϕ is varied in addition to the polar angle θ and the photon energy.^{157,263} The PhD technique is used to determine local adsorption structures on surfaces and thus is complementary to XSW (see Sec. 3.1). While XSW determines vertical adsorption heights with respect to (virtual) Bragg planes, the PhD technique allows to determine the exact structure, that is, atomic positions, at the interface.

As has already been depicted in Figs. 3.7(b) and (c), in addition to the above-described emission of a photoelectron, the core hole of the ionized atom can be filled by an electron from a level with lower binding energy. On the one hand, this can yield a photon of the energy $h\nu_f < h\nu_i$ which is detected in x-ray fluorescence spectroscopy (XRF). On the other hand, the energy which is produced by the filling of the core hole can be transferred to a second electron in an electronic level with lower binding energy which is then excited to the continuum. These so-called Auger electrons are detected in Auger electron spectroscopy (AES). In principle, both techniques as well as XPS are suited as detection methods for XSW (see Sec. 3.1).

3.2.4 Ultraviolet photoelectron spectroscopy

Ultraviolet photoelectron spectroscopy (UPS) allows the detailed investigation of the electronic structure of occupied valence states in atoms and molecules. The physical principles of UPS are identical to those in XPS.^{62,157,200–202,234,236} They have already been illustrated in Sec. 3.2.3.

Solid and gaseous samples may be investigated with UPS. Compared to XPS, considerably lower photon energies, i.e., energies between about 10 eV and 100 eV, are employed. In a typical lab source experiment, He discharge lamps which can produce photons with energies of 21.22 eV (He I radiation) and 40.81 eV (He II radiation) are used.^{202,234} Due to the low photon energies, the photoionization cross sections are larger compared to XPS. Considering the inherent, small line width of He radiation,²⁰² the valence band structure of the sample can be examined in more detail even for low concentrations of the substance of interest.

Owing to the low kinetic energies of the photoemitted electrons, UPS is a very surface-sensitive technique and hence suitable for the investigation of adsorbate layers on surfaces. Substrate UP sig-

^{m)}In the context of this work, the term “intensity (of a photoemission signal)” is used as a synonym for the photoelectron yield $Y_{Z,j}$ and thus denotes the peak area integrated over E_{kin} , although, in the literal sense, the term “intensity” refers to the count rate, i.e., the number of detected photoelectrons per second at a small interval of E_{kin} .

nals may exhibit shifts due to the interaction with the adsorbate, and additional UP peaks may occur which originate from occupied atomic/molecular orbitals of the adsorbate or substrate–adsorbate hybrid states, for example. Depending on the nature of the adsorbate and also on the nature of the substrate–adsorbate interaction, these additional peaks may be broad and exhibit widths ΔE of up to several hundred milli-electronvolts due to the small lifetime Δt of the ionic state of the adsorbate.²⁰² This follows from *Heisenberg’s uncertainty principle* which states that ΔE is inversely proportional to Δt .²⁶⁴ The lifetime of the adsorbate valence hole which is produced by the photoionization process is limited, that is to say, small, because it can be filled with an electron from the underlying (metal) substrate.

The work function Φ of the sample is available through an UPS experiment from the width of the spectrum, $\Delta E_{\text{kin}} = E_{\text{kin}}^{\text{max}} - E_{\text{kin}}^{\text{min}}$, via.²⁰²

$$E_{\text{kin}}^{\text{max}} - E_{\text{kin}}^{\text{min}} = h\nu - \Phi, \quad (3.57)$$

where $E_{\text{kin}}^{\text{max}}$ is the maximum kinetic energy (at the Fermi level) and $E_{\text{kin}}^{\text{min}}$ the minimum value (at the cut-off) of the respective UP spectrum.²⁰² For adsorbate-covered samples, possible changes in the work function as a function of surface coverage, $\Delta\Phi(\theta_Z)$, can be determined with the help of Eq. (3.57). $\Delta\Phi$ provides information about charge redistribution and charge transfer at and across the interface, respectively, as a consequence of the present adsorbate–substrate interactions. If, for a given sample, $E_{\text{b},Z,j}$, Φ and $\Delta\Phi$ are known from the experiment, the ionization potential $I_{\text{p},Z,j}$ of a specific electron in orbital j of element Z calculates as follows:²⁰²

$$I_{\text{p},Z,j} = E_{\text{b},Z,j} + \Phi + \Delta\Phi. \quad (3.58)$$

The hereby determined values of $I_{\text{p},Z,j}$ for the adsorbate on the surface can be directly compared to those of the respective atom or molecule in the bulk material, in the gas phase or on different surfaces because work function effects cancel out.

By varying the polar or azimuthal angle of emission, θ or ϕ , respectively, or the photon energy $h\nu$ in the UPS experiment, information about the dispersion of electronic bands, their identification with respect to their origin, i.e., their assignment to a specific orbitalⁿ⁾ or state, and the orientation of the adsorbate molecules relative to the substrate can be deduced.^{123,265–270} These applications are employed in angle-resolved ultraviolet photoelectron spectroscopy (ARUPS).^{157,200,202,271,272} The orientation of molecular adsorbates with respect to the surface may be derived²⁷³ since selection rules do apply to the photoemission process.²⁰²

ⁿ⁾For organic molecules on surfaces, the deconvolution of UP spectra into individual orbital contributions from their spatial distribution is often referred to as orbital tomography.

4

Experimental

All experiments in the present work were done under ultrahigh vacuum (UHV) conditions.¹⁵⁷ In this chapter, the utilized setups for the different types of experiments are described (see Sec. 4.1). Besides, the general procedure for sample preparation as well as for acquisition and treatment of experimental data are introduced in Secs. 4.2 and 4.3, respectively.

4.1 Experimental setups

Several UHV setups were used for the experimental investigations in the present work. The chambers which were used for LEED and XSW experiments are described in detail below. A detailed description of the UHV chamber in which the STM measurements were performed is given in Ref. 274. In brief, the STM setup is equipped with a variable temperature STM (VT-STM) of type UHV 300/SPM 1000 from RHK Technology (Troy, MI, USA) with operation temperatures from 20 K to 570 K, a single plate MCP-LEED instrument of type BDL800IR-MCP from OCI Vacuum Microengineering (London, Ontario, Canada), and a quadrupole mass spectrometer (QMS) of type PrismaPlus QMG 220 M2 (1–200 u) from Pfeiffer Vacuum (Asslar, Germany). The base pressure of the STM setup is 2×10^{-10} mbar, typically.

The UPS investigations were performed in cooperation with Manuel Marks from the group of Professor Dr. Ulrich Höfer at Philipps-Universität Marburg (Marburg, Germany). The respective experimental setup is described in detail in Ref. 275. Among others, the UPS setup is equipped with a He discharge lamp of type UPS/1 from Vacuum Generators (St Leonards-on-Sea, UK), an x-ray source with Al/Mg anode of type XR50 from SPECS Surface Nano Analysis (Berlin, Germany), a hemispherical electron analyzer of type HSA 150 from VSW Atomtech (Witney, UK), and a 4-grid rear-view LEED optics of type SPECTALEED from Omicron NanoTechnology (Taufkirchen, Germany). Typically, the base pressure of the UPS setup is below 1×10^{-10} mbar.

4.1.1 SPA-LEED setup

The SPA-LEED experiment were performed in the UHV setup depicted in Fig. 4.1 with a typical base pressure of 2×10^{-10} mbar. The UHV chamber is equipped with a SPA-LEED instrument from Omicron NanoTechnology, a water-cooled quartz crystal microbalance (QCM) from CABURN-MDC (Glynde, UK) in combination with a remote oscillator of type 782-900-010 from INFICON (East Syracuse, NY, USA) and a thickness/rate monitor of type STM-100/MF from Sycon Instruments (East Syracuse, NY, USA), and an xyz sample manipulator with one rotation from Vacuum Generators. The sample is mounted on a homemade sample stage which allows cooling to 85 K with liquid N₂ and heating to more than 1250 K with a W filament and additional electron bombardment. The sample temperature is measured with a K-type thermocouple

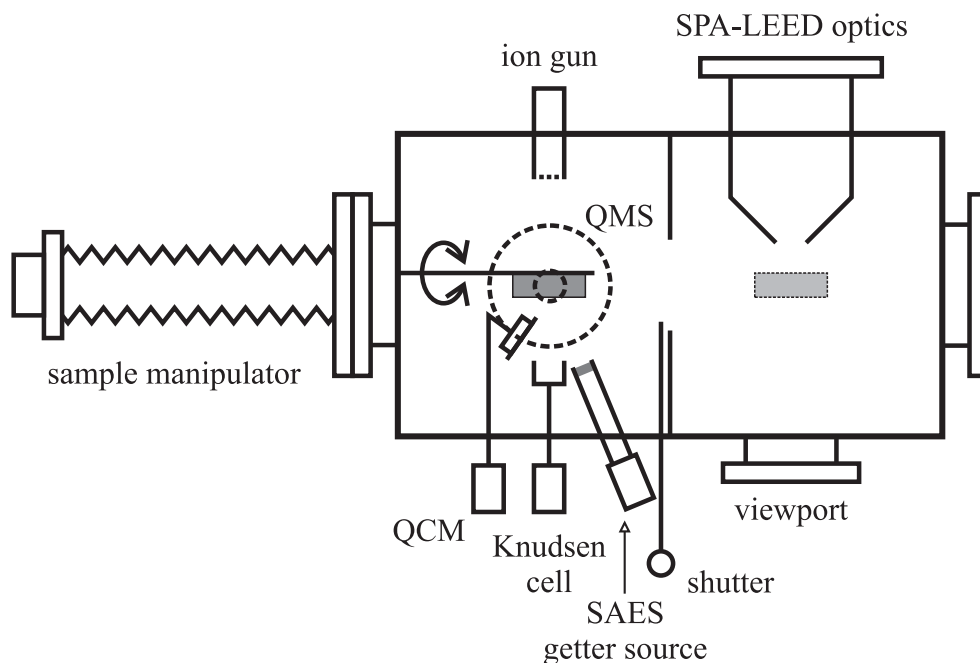


FIG. 4.1. Cross-sectional top view of the SPA-LEED setup. The main components are indicated. See text for further details.

(chromel–alumel) attached to the side of the crystal. The annealing process of the sample is controlled with a proportional-integral-derivative (PID) controller of type EUROTHERM 2408 from Invensys Eurotherm (Worthing, UK). An ion source with internal gas inlet of type IQE 11/35 from SPECS Surface Nano Analysis is provided for sample preparation. Temporarily, a QMS of type QMG 420 (1–2048 u) from BALZERS (Balzers, Liechtenstein) was available.

The UHV chamber is lined with a μ -metal sheet in order to shield the interior of the chamber from external magnetic fields. In the preparation part of the chamber, homemade evaporation sources (so-called Knudsen cells) are mounted, as illustrated in Fig. 4.1. The SPA-LEED part of the UHV chamber can be separated from the preparation part with a stainless-steel shutter. In order to achieve higher count rates of the diffracted electron beams at the channeltron detector of type KBL 428 from Dr. Sjuts Optotechnik (Göttingen, Germany), the original pinhole aperture (with a diameter of $100\ \mu\text{m}$) was replaced by an aperture with larger diameter ($300\ \mu\text{m}$) of type AZ313P from Plano (Wetzlar, Germany).

4.1.2 XSW setups I and II

Two different UHV setups were used for the XSW experiments.²⁷⁶ They were both located at the beamline ID32 of the European Synchrotron Radiation Facility (ESRF) in Grenoble, France.²⁷⁷ XSW setup I had been in operation already since 1995 while more powerful (in terms of the metrological capabilities such as the higher surface sensitivity; see also below) XSW setup II had been available to external users only since 2010, that is, in the second half of the present work. Both setups differ in their experimental geometry, as will be described in the following. The experimental geometry is relevant for the evaluation of the XPS and XSW data, as has been outlined in Chapter 3. In particular, XSW setup II avoids contributions from nondipolar effects in photoemission. Note that the ESRF closed the beamline ID32 at the end of 2011 in the course of their Upgrade Programme for financial reasons.²⁷⁸

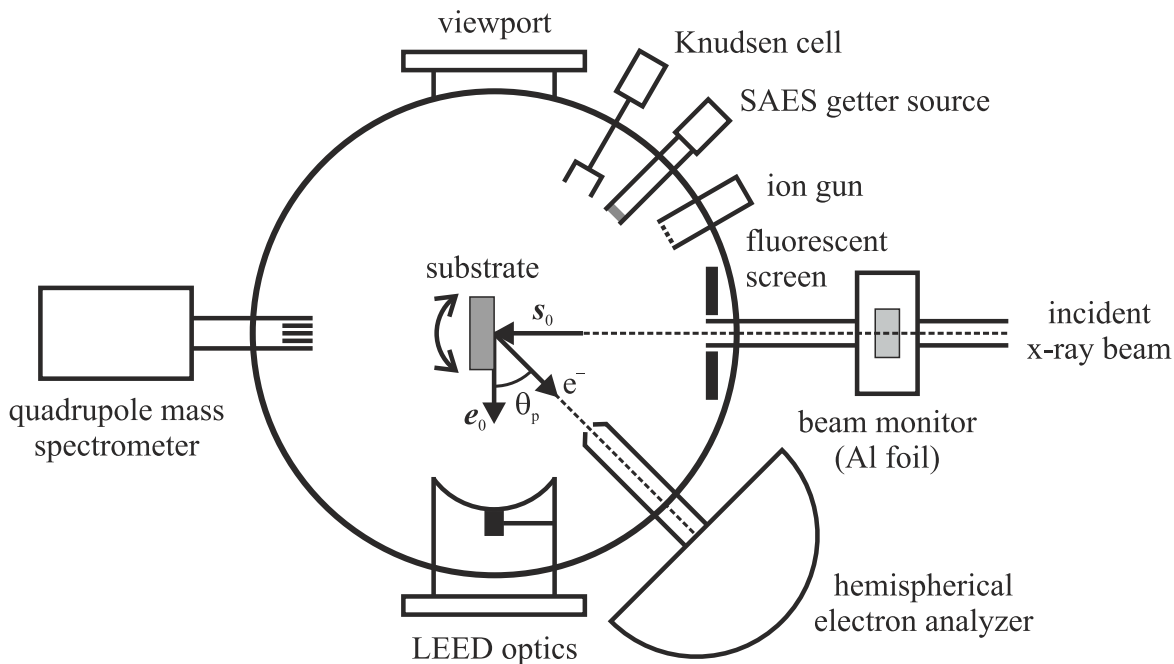


FIG. 4.2. Cross-sectional top view of XSW setup I, located at beamline ID32 of the ERSF (Grenoble, France). The main components are labeled. Besides, the direction vector s_0 of the incident x-ray beam, its polarization vector e_0 , the direction of photoelectron detection, e^- , and the enclosed angle θ_p are indicated. See text for further details.

A schematic representation of XSW setup I is given in Fig. 4.2. This setup consists of a single UHV chamber equipped with a PHI hemispherical electron analyzer of 150 mm radius and a 16-channels detector system from Physical Electronics (Chanhassen, MN, USA), an Omniax xyz sample manipulator with two rotations together with a XL25 sample holder from Vacuum Generators, and a rear-view LEED-Optics from Omicron NanoTechnology. The sample can be heated up to about 1070 K by a resistive heater element made of pyrolytic graphite (PG) encapsulated in pyrolytic boron nitride (PBN), and cooled down to 30 K with a copper braid connected to a liquid He cryostat. The sample temperature is measured with a K-type thermocouple (chromel–alumel) attached to the sample holder next to the crystal. An ion gun from Perkin-Elmer Physical Electronics (Eden Prairie, MN, USA) in combination with a gas line is available for sample preparation, as well as a QMS for residual gas analysis (RGA). In addition, evaporation sources can be mounted as depicted in Fig. 4.2. Typically, the base pressure of XSW setup I was 7×10^{-10} mbar or below. Note that the angle θ_p between the direction of photoelectron detection, which is given by the analyzer position at an angle of 45° with respect to the incident x-ray beam in the plane of the synchrotron storage ring, and the polarization vector of the x-ray beam is 45° in this setup (see Fig. 4.2).

In XSW setup II, in contrast, the photoelectrons are detected at an angle of 90° with respect to the incident beam in the plane of the synchrotron storage ring, yielding $\theta_p = 0^\circ$ (see Fig. 4.3). This setup consists of two individual UHV chambers for sample preparation and analysis, respectively, which are separated by a gate valve. Besides, samples may be exchanged via an additional load-lock chamber and stored under UHV conditions in a sample parking device from VG Scienta (St Leonards-on-Sea, East Sussex, UK). The samples are mounted on transferable flag-style sample holders and can be heated up to 1220 K by resistive heating with a W filament at the manipulator stages. The sample temperature in both chambers is measured with a K-type thermocouple (chromel–alumel) attached to the manipulator stages close to the crystal. The samples can be

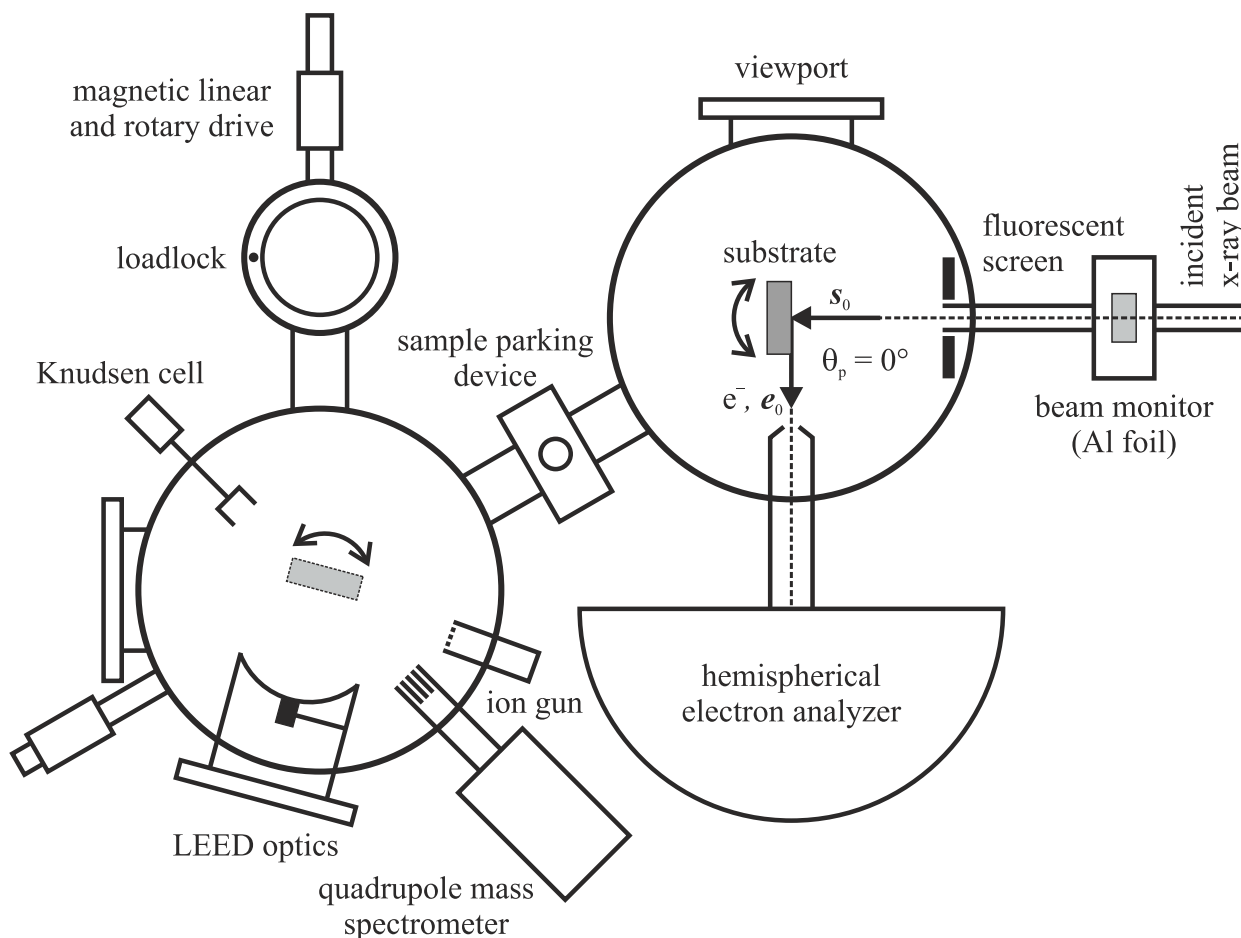


FIG. 4.3. Cross-sectional top view of XSW setup II, located at beamline ID32 of the ERSF (Grenoble, France). The main components are labeled. Besides, the direction vector s_0 of the incident x-ray beam, its polarization vector e_0 , and the direction of photoelectron detection, e^- , with an enclosed angle $\theta_p = 0$ are indicated. See text for further details.

transferred from one chamber to the next with magnetic linear and rotary drives, also from VG Scienta. The analysis chamber is equipped with an Omniax xyz sample manipulator with two rotations from Vacuum Generators and a PHOIBOS 225 hemispherical electron analyzer from SPECS Surface Nano Analysis. The hemispherical electron analyzer has a radius of 225 mm and is equipped with a two-dimensional delayline detector.²⁷⁹ The resolving power in energy amounts to $\Delta E/E = 10^{-6}$.^{276,279} The preparation chamber provides an Omniax xyz sample manipulator with one rotation from VG Scienta, as well as an ion source with internal gas inlet of type IQE 11/35 for sample preparation and a rear-view LEED optics, both from SPECS Surface Nano Analysis. In addition, a QMS of type PrismaPlus QMG 220 M3 (1–300 u) from Pfeiffer Vacuum and home-made evaporation sources (so-called Knudsen cells) were mounted to the chamber (see Fig. 4.3). The base pressures of the preparation chamber and the analysis chamber in XSW setup II were 8×10^{-10} mbar and 4×10^{-10} mbar, respectively.

In both setups, the intensity of the reflected x-ray beam is monitored by the photoelectron current generated on a (fluorescent) screen at a small angle close to the incident x-ray beam. The intensity of the primary x-ray beam is monitored by the photoelectron current generated on an Al foil in the beam path. Due to the more grazing angle of detection for the photoelectrons and the higher sensitivity of the electron analyzer in XSW setup II in comparison to setup I, data with a

larger signal-to-noise ratio and an improved energy resolution could be recorded in less time in XSW setup II. As a result, more detailed XP spectra and smoother XSW profiles were obtained. Unfortunately, this setup was not available prior to 2010, that is, for the XSW experiments on the Ag(110) surface, in particular.

4.2 Sample preparation

All sample crystal were bought from MaTeck (Jülich, Germany). The hat-shaped samples were about 2 mm in height, and 8 mm and 10 mm in diameter at the top and at the bottom, respectively, and were of single-crystalline quality with a miscut below 0.1° against the specified surface orientation. The sample crystal surfaces were prepared by repeated cycles of sputtering and annealing. The structural order and the cleanliness of the prepared surfaces were checked by means of LEED and XPS, if the latter was available. Typical preparation parameters were sputtering with Ar^+ ions of 500 eV to 1500 eV kinetic energy for 15–60 min at an Ar partial pressure of 1×10^{-5} mbar under normal incidence, resulting in an ion current of 4–20 $\mu\text{A}/\text{cm}^2$ on the sample, and subsequent annealing at high temperatures for 15–90 min. Typical heating and cooling rates during the annealing process were 1 K s^{-1} and below.

PTCDA was bought from Sigma-Aldrich (Steinheim, Germany) with 97 % purity and further purified by repeated cycles of gradient sublimation in high vacuum, until dark red to violet colored, needle-shaped crystals were obtained. Mass spectra of the purified material did not show any contamination. PTCDA was deposited onto the sample surface via physical vapor deposition (PVD), in particular via organic molecular beam epitaxy (OMBE), by evaporation from a homemade Knudsen cell. Each evaporation source was thoroughly calibrated prior to the preparation by checking the evolution and the changes in LEED patterns of the surface structures of PTCDA. In addition, the calibration was confirmed using temperature programmed desorption (TPD) spectroscopy by monitoring a fragment of the PTCDA molecule ($m/z = 124 \text{ u}$) for the STM and XSW experiments (setup II). Where available, the deposition process was monitored by means of a QCM or a mass spectrometer. The deposition rate was in the range of about $0.8\text{--}3.2 \text{ \AA min}^{-1}$ typically.

In the present work, the surface coverage is given in monolayers (ML) where 1 ML corresponds to the number of molecules in a single, close-packed, ordered layer on the respective surface. For the QCM measurements, a layer thickness of 3.2 \AA (see also Table 2.1 in Sec. 2.2.1, page 12, of the present work) was taken to be equivalent to a full monolayer of PTCDA molecules on the surface, yielding an effective deposition rate of $0.25\text{--}1.0 \text{ ML/min}$.^{a)} The amount of deposited PTCDA was controlled via the deposition temperature and, in particular, via the deposition time. Usually, the pressure in the UHV chamber stayed well in the 10^{-10} mbar regime during the deposition process. The surface coverage was also validated with LEED, as well as with XPS and STM, if available. When PTCDA coverages on different surfaces were compared, the respective surface densities of the molecules were taken into account. In some cases, the PTCDA layers were treated with mild post-annealing in order to improve the structural order at the surface. In other cases, PTCDA could be obtained by thermal desorption of multilayers. The long-range order of the prepared PTCDA films was always proven by the observed bright and sharp LEED patterns. Also, the absolute coverage as well as the stoichiometric ratio C : O present at the surface were checked by means of XPS, if available (see Sec. 4.3.2, among others).

^{a)}Note that the (potentially) different packing densities of the various PTCDA superstructures were neglected in this approach. Judging from the packing densities of the PTCDA molecules on the Ag(111),⁹⁸ Ag(100),¹²⁰ and Ag(110) surfaces,⁹⁸ which range from 8.38×10^{-3} to 7.07×10^{-3} molecules per square ångströms, this effect is on the order of 15 % or below and thus small, i.e., within the typical accuracy of the QCM measurements.

The deposition of K was done from a homemade evaporation source with a commercially available K metal dispenser of type K/NF/2.2/12 FT 10+10 from SAES Getters (Milano, Italy). The K metal dispenser is filled with K_2CrO_4 which is reduced by a Zr–Al alloy (Zr 84 %, Al 16 %) upon heating.^{20,280,281} The K evaporation source was thoroughly calibrated using LEED, in particular, as well as QMS and XPS (see also Secs. D.3.1 and D.3.2 in the appendix of the present work). The calibration of the K evaporation source made use of the fact that K atoms, if deposited on the *clean* Ag(110) surface, form different ordered superstructures as a function of coverage: a (1×2) superstructure is formed for $0.04 \text{ ML} < \theta_{\text{K}} \leq 0.19 \text{ ML}$ while a (1×3) superstructure forms in the case of lower and higher coverages.²⁸² Note that a coverage of $\theta_{\text{K}} = 1 \text{ ML}$ corresponds to one K atoms per Ag surface atom [at the Ag(110) surface] here.

The amount of deposited K was controlled via the deposition temperature and the deposition time. The temperature of the K metal dispenser cannot be measured directly but is available from the electric current applied to the dispenser material.²⁸⁰ Prior to the first utilization, the K metal dispenser was outgassed by applying a current of 10 A, corresponding to a evaporation source temperature of above 1100 K,²⁸⁰ for a few seconds. It was found that after first heating of the K metal dispenser, which starts the reduction reaction,²⁸⁰ an electric current of 3 A ($T \approx 700 \text{ K}$) had to be applied permanently, that is, during off-times, in order to prevent a rise in pressure upon next heating. For lower currents, the K metal dispenser adsorbs residual gases, or the already formed K even reacts with them, apparently. If kept constantly at $T \geq 700 \text{ K}$, the base pressure of the UHV chamber remained uninfluenced and an increase in pressure was not observed during the deposition process. For the deposition of K in the SPA-LEED setup, a current of 4.8 A was applied to the K metal dispenser (during on-times), corresponding to a temperature of about 900 K. The increase in electric current by 1.8 A resulted in an increased K evaporation rate by a factor of 2.3, as observed with QMS.²⁸³ The dispenser was held at the evaporation temperature for 1 min prior to the deposition process in order to guarantee a constant deposition rate of 0.13(1) K atoms per Ag surface atom [at the Ag(110) surface] and minute, judging from the observed LEED patterns in conjunction with the XPS results (see Secs. D.3.1 and D.3.2). Following the identical protocol ($I = 5.5 \text{ A}$ in this case), the deposition of K in XSW setup I was performed at a rate of 0.28(1) K atoms per Ag surface atom and minute. Again, the long-range order of the prepared, binary K + PTCDA films was proven by the observed bright and sharp LEED patterns while the absolute coverage as well as the stoichiometric ratios present at the surface were checked by means of XPS.

Unless otherwise stated, the crystal was kept at room temperature during sputtering and PTCDA or K deposition. Inevitable deviations from the general procedure for sample preparation are given in the chapters covering the experimental results.

4.3 Experimental data acquisition and treatment

This section describes those parts of the experimental data acquisition and treatment which are common to all data presented in this work. For purposes of structuring the present work, also the treatment of the STM and UPS data is described here, although respective data are only available for one of the systems within the scope of this work.

4.3.1 LEED data

The present work contains data from conventional LEED, MCP-LEED, and SPA-LEED experiments. The MCP-LEED patterns have been corrected for intrinsic distortion with the help of the program MCPdeskew written by Dr. Julian Ikonov from Rheinische Friedrich-Wilhelms-

Universität Bonn (Bonn, Germany). Sometimes, especially for electron energies below 30 eV, also LEED patterns from SPA-LEED experiments suffered from distortions caused by limitations of the SPA-LEED optics.^{213,284} Although correction algorithms and deskewing tools are available,^{213,284–286} distortion corrections have been waived for the two-dimensional SPA-LEED images because these corrections are very precarious. One-dimensional SPA-LEED scans, in contrast, have been corrected for possible distortions (see below). In general, the room-temperature lattice constants of the substrates and, in some cases, also of the adsorbate structures have been used for calibration. The surface lattice constants of the substrates were deduced from the respective bulk lattice constants a_{bulk} by geometrical considerations (for example, see Tables B.1 to B.3, pages 291–293, in Sec. B.1 in the appendix of the present work for the explicit a_{bulk} values.)^{287–289} The surface lattice constants of the adsorbate structures are stated in the corresponding sections on the experimental results. Temperature effects have been neglected since thermal expansion amounts to only 0.4 % of the surface lattice constant, that is, maximal 0.02 Å in the case of Ag(110), for example, for the coinage metal substrates in the employed temperature ranges of the present work (about 100 K to 300 K)²⁹⁰ which is within the accuracy of the LEED measurements. A slightly larger value of about 1 % applies to the in-plane linear thermal expansion of the herringbone arrangement of PTCDA.²⁹¹ In general, for a non-commensurate superstructure, the thermal expansion of the overlayer does not necessarily follow that of the substrate.

From the LEED patterns, the reciprocal lattice parameters may be derived which then yield the lattice parameters in real space. The surface basis vectors in real and reciprocal space, \mathbf{a} and \mathbf{a}^* , respectively, obey the relation:^{200–202}

$$\mathbf{a}_i \cdot \mathbf{a}_j^* = 2\pi \cdot \delta_{ij} = \begin{cases} 0 & \text{if } i \neq j, \\ 1 & \text{if } i = j, \end{cases} \quad (4.1)$$

where δ_{ij} is *Kronecker's delta* and $i, j = 1, 2$ refer to the two lattice vectors at the surface. The magnitudes of the respective vectors in real and reciprocal space, $a_i = |\mathbf{a}_i|$ and $a_i^* = |\mathbf{a}_i^*|$, respectively, are related via:^{201,202}

$$a_i^* = \frac{1}{a_i \sin \alpha}, \quad (4.2)$$

with α being the enclosed angle between \mathbf{a}_1 and \mathbf{a}_2 . The angle between the basis vectors in reciprocal space calculates as $\alpha^* = \pi - \alpha$, simply.²⁰² In the context of the present work, the parameters \mathbf{a}_i , \mathbf{a}_i^* , a_i , a_i^* , α , and α^* always refer to the substrate while the parameters for the adsorbate structure are denoted as \mathbf{b}_i , \mathbf{b}_i^* , b_i , b_i^* , β , and β^* , respectively. The substrate and adsorbate lattices \mathbf{a} and \mathbf{b} may be related by a superstructure matrix \mathfrak{M} :^{62,200–202}

$$\begin{pmatrix} \mathbf{b}_1 \\ \mathbf{b}_2 \end{pmatrix} = \mathfrak{M} \cdot \begin{pmatrix} \mathbf{a}_1 \\ \mathbf{a}_2 \end{pmatrix}. \quad (4.3)$$

Accordingly, the above equation holds for the corresponding reciprocal space vectors employing the inverse transposed matrix $\mathfrak{M}^* = \widetilde{\mathfrak{M}}^{-1}$.^{62,201,202} Thus, the real space lattice parameters can be obtained from the reciprocal space lattice parameters which for their part may be deduced from the LEED pattern. The vectors \mathbf{b}_i^* and matrices \mathfrak{M} presented in this work follow the conventions established by Barlow and Raval in Ref. 3.

In general, the two-dimensional LEED patterns have been used to derive angles and directions. Lengths were taken from corresponding one-dimensional LEED scans since this allows a much more precise determination. For this purpose, the x scale of the original one-dimensional SPA-

LEED data was calibrated employing the position of nearby diffraction spots which originate from known structures of the substrate or, to a lesser extent, of the adsorbate. If the SPA-LEED line scans did not contain diffraction spots suitable for calibration, additional line scans containing appropriate spots were taken with the same electron energy at small angles with respect to the original ones. Note that the distortions of SPA-LEED patterns are usually not uniform. The spot profiles in the one-dimensional LEED scans were fitted with the computer program Origin,²⁹² employing a linear background, typically, and either a Lorentzian function:

$$y = \frac{2A}{\pi} \frac{w}{4(x - x_c)^2 + w^2} + y_0, \quad (4.4)$$

or a so-called pseudo-Voigt function, which is a linear combination of Lorentzian and Gaussian functions:

$$y = A \left[m \cdot \frac{2}{\pi} \frac{w}{4(x - x_c)^2 + w^2} + (1 - m) \cdot \frac{\sqrt{4 \ln 2}}{\sqrt{\pi} w} \exp\left(-\frac{4 \ln 2}{w^2}(x - x_c)^2\right) \right] + y_0. \quad (4.5)$$

In the above equations, the x and y axes refer to the (positive or negative) magnitude of the scattering vector, $k_{\parallel} = \pm |\mathbf{k}_{\parallel}|$, and the measured intensity $I(\mathbf{k}_{\parallel})$ of diffracted electrons, respectively. x_c denotes the center of the spot profile, A the amplitude, and m the Gaussian-to-Lorentzian ratio with values between 0 and 1, where $m = 1$ is a pure Lorentzian function. w is the width of the spot profile, and corresponds to the FWHM of the pure Lorentzian and Gaussian functions. y_0 is a (small) vertical offset which, in some cases, had to be considered in addition to the “intrinsic”, pre-defined background in order to achieve a good agreement of the fitting result with the experimental data. It was verified that using both Lorentzian and pseudo-Voigt functions gave the same results regarding the center of the spot. The widths Δk_{\parallel} of the spot profiles, however, were generally taken from the fitting results employing the pure Lorentzian function only. They were used to determine the effective transfer width $T_{w,\text{eff}}$ and thereby the spatial coherence of the prepared surfaces [see Sec. 3.2.1, in particular Eq. (3.46)], for example. The Gaussian contribution to the spot profile, which is represented by the second term in square brackets on the right-hand side of Eq. 4.5, may be caused by instrumental broadening or limited long-range order, for instance.

The analysis of the two-dimensional LEED patterns was performed with simulations using the computer program GLE.²⁹³ In addition, the obtained results were verified with the help of the programs Spot-Plotter²⁹⁴ and LEEDpat.²⁹⁵ Note that the SPA-LEED patterns in the present work are shown on a logarithmic scale.

4.3.2 XPS data

All XPS experiments were performed in different beamtimes at the undulator beamline ID32 of the European Synchrotron Radiation Facility (ESRF) at Grenoble, France, in conjunction with the XSW experiments (see Sec. 4.3.3 for details on the individual beamtimes). In limited cases, also Auger spectra were recorded. They have received the same treatment as the XP spectra. Thus, the Auger spectra will not be mentioned explicitly in the description of all individual steps in the treatment of the electron spectroscopy data. In order to avoid any influence of the XSW effect on the XP spectra, the spectra of the substrate and adsorbate signals, which were used for surface characterization and development of fitting models (see below), were taken at photon energies of 10 eV to 15 eV below the respective Bragg energies (“off-Bragg” photon energies), i.e., at photon energies from about 2.6 keV to 4.3 keV depending on the substrate and the Bragg reflection (hkl)

which were employed in the corresponding XSW experiments. Typically, pass energies in the range from 10 eV to 100 eV were used, depending on the experimental setup and the XPS signals under investigation. Note in this context that the experimentally observed Bragg energies might deviate from the calculated Bragg energies E_B by up to ± 6 eV. We attribute this to small differences in the bulk lattice constant a_{bulk} of the substrate crystals from those reported in the literature (see Refs. 288, 289 or Table 4.6, for example, for the explicit values). In the case of the (220) reflection of the Ag(110) substrate, for example, a lattice constant, which is larger by $\Delta a_{\text{bulk}} = 0.005 \text{ \AA}$ only, causes the Bragg energy to change by as much as $\Delta E_B = -5.25 \text{ eV}$. The size of the effect in a_{bulk} is well within the accuracy of the XSW experiment and thus negligible.

PTCDA multilayer spectra were conducted with the same photon energies as the (sub-)monolayer spectra on the same surface in order to have the same influence of the so-called recoil effect.^{296–300} Due to the conservation of momentum during the photoemission process, parts of the kinetic energy are imparted to the emitting atom. This effect becomes significant under the excitation of core level spectra with photons in the energy regime of several kilo-electronvolts.^{299,300} Then, the photoelectron spectra show a remarkable shift (up to a few hundred milli-electronvolts^{296,299}) towards higher binding energies and line broadening as compared to the case of excitation by softer x-rays.³⁰⁰ Therefore, peak shifts obtained by the comparison of spectra with different PTCDA coverages, taken at the same photon energy, rather than absolute peak positions are discussed in the course of the present work. Note, however, that (potential) recoil effects do *not* affect the validity of our XSW results because XSW solely considers the photoelectron yields $Y_{Z,j}$, i.e., the integral intensities of the XPS signals or, in the case of a differential analysis (see below), their individual components. The integral intensities are not influenced by the recoil effect.

Data processing

The XPS data were analyzed employing the computer program CasaXPS.³⁰¹ The energy scales of the XP spectra were calibrated using the position of the Ag3*d* signal or the Au4*d* signal as a reference, respectively.^{162,302} A background of linear or Shirley³⁰³ type was subtracted from the individual XP spectra. The substrate Auger and XP spectra were numerically integrated, while for the adsorbate signals, sophisticated fitting models were employed (see below).^{304,305} The relevant spectra will be presented later in this work, that is, in the individual sections covering the XPS results in the respective chapters on the experimental data. The integral intensities, i.e., the photoelectron yields $Y_{Z,j}$, were generally normalized to the intensity of the incident beam, I_0 . The errors of the integral intensities were computed by means of the Monte Carlo-based procedure embedded in CasaXPS.^{67,301,306} In brief, this procedure creates 400 synthetic spectra, where pseudorandom noise from Monte Carlo simulation techniques is introduced, on the basis of one experimental spectrum. These synthetic spectra are then evaluated using the original background and, if applicable, the original peak parameters. From the scattering of the results, the errors of the integral intensities are deduced. Thus, the errors derived from this Monte Carlo-based procedure give information about both the quality of the experimental XPS data as well as the consistency of the fitting model with the spectrum. These statistical errors were also propagated to the XSW curves. In addition, our fitting models were validated by the fact that these gave the highest coherent fractions f_c in comparison with alternative models.

The C1*s* and O1*s* XP spectra of PTCDA on the different coinage metal surfaces and also the K2*p* XP spectra were fitted with several components. This allowed to differentially analyze the chemically nonequivalent species of one element within the molecule. For the main lines, a linear combination of a Gaussian and a Lorentzian profile was used. Typically, Lorentzian contributions of up to 20 % gave the best agreement with the experimental data. The corresponding satellite

peaks were always fitted with pure Gaussian functions. This type of fitting is well established in the literature (see Ref. 307, for example) and was very successful. That is, the fitting gave sufficiently good agreement with the experimental data in all cases and very reasonable results in both the deconvolution of the XP spectra into the individual components and the evaluation of the XSW data. Concerning the peak areas of the individual components, all fitting models meet the expected stoichiometry of the PTCDA molecule, namely, $C_{\text{peryl}} : C_{\text{funct}} = 20 : 4$ and $O_{\text{carb}} : O_{\text{anhyd}} = 4 : 2$. The details of the so-obtained XPS fitting models will be reported in the following chapters. The respective fitting models were employed in the XSW data analysis (see Sec. 4.3.3).

Coverage calibration

Applying the equations already introduced in Sec. 3.2.3, XPS data were also used to quantify the PTCDA coverages θ_{PTCDA} on the different surfaces for those experiments performed at beamline ID32. Several different methods were chosen:

- The attenuation of substrate XPS signals was evaluated using Eqs. (3.54) and (3.56), assuming a layer-by-layer (Frank-van der Merwe) growth mode⁶² for reasons of simplicity.
- Applying Eq. (3.55), also the increase in intensity of the adsorbate C1s XPS signal was taken to derive the thickness of PTCDA (sub-)monolayers on Ag(100) and Ag(110) where multilayer data were available as a reference.
- For the experiments on Ag substrates, the ratios of the C and Ag atom densities at the surface, $N_{\text{C}}/N_{\text{Ag}}$, were determined from the photoelectron yield ratios of the C1s and Ag3d XPS signals, $Y_{\text{C1s}}/Y_{\text{Ag3d}}$, and compared to the ratios which were found for exactly 1 ML PTCDA on Ag(111) in earlier experiments.³⁰⁸ On the Ag(111) surface, a full monolayer can be prepared simply by thermal desorption of PTCDA multilayers.¹¹³

In Eqs. (3.54), (3.55) and (3.56), the thickness of a single PTCDA monolayer was considered to be identical to the spacing of the (102) planes in the bulk phase, namely, $d_{102} = 3.22 \text{ \AA}$ for the α modification (see Table 2.1).^{105–107, b)} Note that Eqs. (3.54) and (3.55) apply in the presence of PTCDA multilayers, while Eq. (3.56) applies in the presence of PTCDA submonolayers because it explicitly considers a fractional coverage of PTCDA on the substrate surface.

The inelastic mean free paths $\lambda_{\text{IMFP}}(E_{\text{kin},Z,j})$ of the respective photoelectrons within the PTCDA overlayers were calculated according to Ref. 254, modeling the adsorbate overlayers as pristine layers of C atoms [see Table 4.1; the respective values for $\lambda_{\text{IMFP}}(E_{\text{kin},Z,j})$ within the substrate crystals are summarized in Table 4.2].^{c)} The so-obtained values compare well with those calculated for various organic compounds.²⁵⁷ The *nominal* angles of detection with respect to the surface normal,

^{b)}Judging from the determined adsorption heights (also within the present work; see Sec 7.1, for example), which are below 3 Å in some cases, this may imply a strong extrapolation or simplification for PTCDA (sub-)monolayers at least on the more reactive coinage metal surfaces. The different two-dimensional packing densities of the PTCDA molecules, however, in the monolayers on the respective coinage metal surfaces, in particular on the Ag surfaces, were considered explicitly.

^{c)}In the determination of relevant parameters such as the inelastic mean free paths $\lambda_{\text{IMFP}}(E_{\text{kin},Z,j})$, the photoionization cross sections $\sigma_{Z,j}(E_{\text{kin},Z,j})$ (see below), or the nondipolar correction terms β , γ , δ , and Δ (see Sec. 4.3.3), we have assumed that the underlying tabulated parameters are given as a function of the kinetic energy E_{kin} , where the Fermi level E_{F} is used as reference, and not as a function of E'_{kin} , which is referenced against the vacuum level E_{vac} . Hence, the sample work function Φ was neglected for the calculation of the kinetic energies of the respective photoelectrons [see also Eqs. (3.50) and (3.51)]: $E_{\text{kin}} = h\nu - E_{\text{b}}$. Note that the work functions Φ of the individual samples amount to about 5 eV, typically, and thus are very small compared to the employed photon energies. Thus, neglecting Φ is justified in any case.

θ ,^{d)} are 45° in XSW setup I and 90° in XSW setup II (see also Figs. 4.2 and 4.3). Note that the incident angle of the x-ray beam on the sample was nearly 90°. Although the total acceptance angle of the PHOIBOS 225 analyzer in XSW setup II is $\pm 6^\circ$, this angular range cannot be used in full since photoelectrons can only be detected at angles ranging from 0° to 90° with respect to the surface normal, of course. Because the sample was turned towards the analyzer by 2° and thereby slightly off normal incidence of the x-ray beam (resulting in a Bragg angle of 88°, see Sec. 4.3.3), the *effective* angle of detection θ amounts to 86°, as follows from geometric considerations and also assuming a constant acceptance over the full angular range. In those cases where XSW setup I was used, the slight rotation ($\pm 2^\circ$) of the sample away from normal incidence was neglected since the rotation direction was not consistent throughout all experiments. Thus, an effective angle of detection of 45° was assumed. The resulting errors of about $\pm 3.5\%$ in the coverage determination, however, are well within the typical accuracy of XPS intensity measurements.^{202,309}

Method (a) was used to determine the absolute coverages of PTCDA multilayers on Ag(100) and Ag(110). The results obtained from methods (a) and (b) for (sub-)monolayer coverages, however, were to some extent either not compatible with the observations in monitoring the deposition process with QMS or not plausible for the observed LEED patterns. This is especially true for the experiments on Ag(110) in XSW setup I where the employed photon energies were higher, the angle of detection was smaller and the background signal from inelastically scattered photoelectrons was higher. As a result, the obtained values for the photoelectron yield $Y_{Z,j}$ were smaller and the signal-to-noise was lower, giving rise to larger uncertainties in the quantification of θ_{PTCDA} . Thus, for all (sub-)monolayer experiments which were performed in XSW setup I, method (c) was employed. Due to the different experimental geometries, (c) could not be utilized for the experiments performed in XSW setup II, where appropriate reference data for PTCDA multilayers was missing. Here, the PTCDA coverages were determined by monitoring the integral ion current for a fragment of the PTCDA molecule ($m/z = 124$ u) during the deposition from a thoroughly calibrated evaporation source with the mass spectrometer (QMS). Table 4.3 reports the *final* values for θ_{PTCDA} which were obtained by both XPS, via (a) the attenuation of the substrate Ag3d_{5/2} or Au4d signals or (c) the photoelectron yield ratios $Y_{\text{C}1s}/Y_{\text{Ag}3d}$, and QMS, respectively. Values for $\theta_{\text{PTCDA}}^{\text{XPS}}$ given in square brackets are not compatible with the observed LEED patterns and/or the QMS results, and therefore are considered as outliers. The θ_{PTCDA} results obtained from the QMS monitoring have been found to be more reliable here. Note that for PTCDA/Cu₃Au(111) a change in the C1s and O1s XPS signal shapes was observed with increasing x-ray irradiation time, as will be reported in detail in Chapter 6. Therefore, footnote *b* of Table 4.3 contrasts θ_{PTCDA} values for this system obtained for different spots on the sample which were either “fresh”, i.e. they had not been irradiated with x-rays before, or which had been exposed to the x-ray beam for a few hours already. However, a change in PTCDA coverage as a function of irradiation time may be excluded within the accuracy of the XPS measurements.

^{d)}The term “nominal angle of detection” refers to the situation of perfect normal incidence of the x-ray beam on the sample surface. In our experiments, the sample was tilted slightly off normal incidence due to experimental reasons, in fact (see also below).

TABLE 4.1. Inelastic mean free paths $\lambda_{\text{IMFP}}(E_{\text{kin},Z,j})$ within the PTCDA overlayers on the respective substrate surfaces of the photoelectrons of interest in the present work. The adsorbate layer was modeled as a pristine layer of C atoms. All values were calculated utilizing an empirical expression (named TPP-2²⁵⁴) and tabulated parameters from Ref. 254. The kinetic energies $E_{\text{kin},Z,j} \approx h\nu - E_b$ of the photoelectrons result from the employed photon energies $E = h\nu$, which typically were 10–15 eV below the Bragg energy for the reflection (hkl) in use, and the corresponding binding energies E_b of the XPS levels.^{162,302} For those XPS signals, where spin-orbit coupling/splitting is present,³¹⁰ i.e., for $l \geq 1$, the averaged values for E_b and $\lambda_{\text{IMFP}}(E_{\text{kin},Z,j})$ were obtained by averaging the corresponding values for the spectroscopic levels with different total angular momentum quantum number j , weighted with the respective degeneracies. Note that for the XPS investigations of PTCDA on the Ag(110) surface two slightly different photon energies were used (n.d. = not determined).

(hkl)	E (eV)	Cu ₃ Au(111)		Ag(100)		Ag(110)	
		(111)	(111)	(111)	(200)	(220)	(220)
		2858.0	2615.0	3024.0	4276.0	4280.0	
	E_b (eV) ^a	λ_{IMFP} (Å) ^b	λ_{IMFP} (Å) ^b	λ_{IMFP} (Å) ^b	λ_{IMFP} (Å) ^b	λ_{IMFP} (Å) ^b	λ_{IMFP} (Å) ^b
C1s	285.0 ^c	57.24	52.77	60.25	82.31	82.38	
O1s	531.0	52.72	48.19	55.77	78.06	78.13	
K1s	3608.4	n.d.	n.d.	n.d.	n.d.	19.84	
K2p _{1/2}	297.3	n.d.	n.d.	n.d.	n.d.	82.17	
K2p _{3/2}	294.3	n.d.	n.d.	n.d.	n.d.	82.22	
K2p average	295.2	n.d.	n.d.	n.d.	n.d.	82.20	
Cu2p _{1/2}	952.3	44.82	n.d.	n.d.	n.d.	n.d.	
Cu2p _{3/2}	932.7	45.19	n.d.	n.d.	n.d.	n.d.	
Cu2p average	939.2	45.07	n.d.	n.d.	n.d.	n.d.	
Ag3d _{3/2}	374.0	n.d.	51.12	58.64	80.78	80.85	
Ag3d _{5/2}	368.3	n.d.	51.23	58.74	80.88	80.95	
Ag3d average	370.6	n.d.	51.19	58.70	80.84	80.91	
Au3d _{3/2}	2291.0	17.50	n.d.	n.d.	n.d.	n.d.	
Au3d _{5/2}	2206.0	19.40	n.d.	n.d.	n.d.	n.d.	
Au3d average	2240.0	18.64	n.d.	n.d.	n.d.	n.d.	
Au4d _{3/2}	353.2	55.99	n.d.	n.d.	n.d.	n.d.	
Au4d _{5/2}	335.1	56.32	n.d.	n.d.	n.d.	n.d.	
Au4d average	342.3	56.19	n.d.	n.d.	n.d.	n.d.	
CuL ₃ M ₄₅ M ₄₅	918.6 ^d	25.16	n.d.	n.d.	n.d.	n.d.	
AgM ₅ N ₄₅ N ₄₅	351.6 ^d	n.d.	n.d.	12.48	n.d.	12.48	

^aTaken from Refs. 162, 302.

^bCalculated utilizing an empirical expression (named TPP-2²⁵⁴) and tabulated parameters from Ref. 254. For the Cu₃Au(111) substrate, the individual parameters for Cu and Au were weighted in accordance with the stoichiometric ratio of Cu : Au = 3 : 1 and then averaged.

^cThe values for E_b given here are representative for the respective electronic levels. In general, the precise values depend on the chemical environment.³¹¹ Two examples are values of 284.5 eV and 284.9 eV for the C1s levels in graphite³¹² and benzene,³¹³ respectively.

^dThe (apparent) binding energy E_b of Auger lines depends on the photon energy $E = h\nu$ because the kinetic energy of Auger electrons is only determined by the electronic levels which are involved in the Auger process [see Sec. 3.2.3, Eq. (3.50)]. Thus, the respective values E_{kin} of the kinetic energies, referenced against the Fermi level, are given here for the Auger lines.^{302,314}

TABLE 4.2. Same as Table 4.1 but for the inelastic mean free paths $\lambda_{\text{IMFP}}(E_{\text{kin},Z,j})$ within the respective substrates of the photoelectrons of interest in the present work (n.d. = not determined).

(hkl)	E (eV)	Cu ₃ Au(111)	Ag(100)		Ag(110)	
		(111)	(111)	(200)	(220)	
		2858.0	2615.0	3024.0	4276.0	4280.0
	E_b (eV) ^a	λ_{IMFP} (Å) ^b	λ_{IMFP} (Å) ^b	λ_{IMFP} (Å) ^b	λ_{IMFP} (Å) ^b	λ_{IMFP} (Å) ^b
K1s	3608.4	n.d.	n.d.	n.d.	n.d.	10.71
K2p _{1/2}	297.3	n.d.	n.d.	n.d.	n.d.	41.44
K2p _{3/2}	294.3	n.d.	n.d.	n.d.	n.d.	41.47
K2p average	295.2	n.d.	n.d.	n.d.	n.d.	41.46
Cu2p _{1/2}	952.3	25.02	n.d.	n.d.	n.d.	n.d.
Cu2p _{3/2}	932.7	25.22	n.d.	n.d.	n.d.	n.d.
Cu2p average	939.2	25.15	n.d.	n.d.	n.d.	n.d.
Ag3d _{3/2}	374.0	n.d.	26.18	29.88	40.76	40.79
Ag3d _{5/2}	368.3	n.d.	26.23	29.93	40.81	40.84
Ag3d average	370.6	n.d.	26.21	29.91	40.79	40.82
Au3d _{3/2}	2291.0	10.45	n.d.	n.d.	n.d.	n.d.
Au3d _{5/2}	2206.0	11.47	n.d.	n.d.	n.d.	n.d.
Au3d average	2240.0	11.06	n.d.	n.d.	n.d.	n.d.
Au4d _{3/2}	353.2	30.93	n.d.	n.d.	n.d.	n.d.
Au4d _{5/2}	335.1	31.10	n.d.	n.d.	n.d.	n.d.
Au4d average	342.3	31.03	n.d.	n.d.	n.d.	n.d.
CuL ₃ M ₄₅ M ₄₅	918.6 ^c	14.56	n.d.	n.d.	n.d.	n.d.
AgM ₅ N ₄₅ N ₄₅	351.6 ^c	n.d.	n.d.	7.10	n.d.	7.10

^aTaken from Refs. 162, 302.

^bCalculated utilizing an empirical expression (named TPP-2⁵⁴) and tabulated parameters from Ref. 254. For the Cu₃Au(111) substrate, the individual parameters for Cu and Au were weighted in accordance with the stoichiometric ratio of Cu : Au = 3 : 1 and then averaged.

^cThe (apparent) binding energy E_b of Auger lines depends on the photon energy $E = h\nu$ because the kinetic energy of Auger electrons is only determined by the electronic levels which are involved in the Auger process [see Sec. 3.2.3, Eq. (3.50)]. Thus, the respective values E_{kin} of the kinetic energies, referenced against the Fermi level, are given here for the Auger lines.^{302,314}

TABLE 4.3. PTCDA coverages θ_{PTCDA} of the systems under investigation in the present work. The coverages were determined using either XPS or mass spectrometry (QMS). See text for details on the coverage determination. Values for $\theta_{\text{PTCDA}}^{\text{XPS}}$ given in square brackets are not compatible with the observed LEED patterns and/or the QMS results, and therefore are considered as outliers. $N_{\text{C}}/N_{\text{O}}$ denotes the carbon-to-oxygen ratio in the prepared PTCDA layers (n.a. = not available).

system	preparation no.	$\theta_{\text{PTCDA}}^{\text{XPS}}$ (ML)	$\theta_{\text{PTCDA}}^{\text{QMS}}$ (ML)	$N_{\text{C}}/N_{\text{O}}$
PTCDA/Ag(100)	Apr'08-1	28.94(94)	n.a.	4.03(16)
PTCDA/Ag(110)	Apr'08-1	35.36(71)	n.a.	4.37(18)
PTCDA/Ag(110)	Feb'09-1	1.15(4)	n.a.	5.50(38)
PTCDA/Ag(110)	Feb'09-2a	0.91(4)	n.a.	5.10(43)
K + PTCDA/Ag(110)	Feb'09-2b	[0.60(4)] ^a	n.a.	4.68(51)
PTCDA/Ag(100)	Feb'11-1	[0.46(3)]	0.78(10)	5.40(30)
PTCDA/Ag(100)	Feb'11-2	[0.04(4)]	0.22(3)	4.85(36)
Cu ₃ Au(111)	Feb'11-1	0.00	0.00	n.a.
PTCDA/Cu ₃ Au(111)	Feb'11-2	[0.65(3)] ^b	0.76(10)	6.18(24) ^c

^aThe PTCDA coverage in this preparation is in fact assumed to be identical to that of preparation no. Feb'09-2a since prep. Feb'09-2b results from prep. Feb'09-2a by additional deposition of K atoms and subsequent (mild) annealing.

^bDetermined via attenuation of the Au4*d* substrate signal after exposition of the sample spot to the x-ray beam for about two hours. Besides, the attenuation of the Au3*d*_{5/2} and Cu2*p*_{3/2} signals by the PTCDA overlayer was measured on both fresh and exposed spots. Identical values (within the errors) were obtained for the individual XPS levels on the fresh and exposed spots, namely, values of 0.80(1) ML and 0.78(4) ML for Au3*d*_{5/2}, and 0.69(3) ML on both spots for Cu2*p*_{3/2}, respectively. Therefore, irradiation-induced desorption (possibly accompanied with preceding decomposition) may be excluded.

^cValid for an exposed spot. On a fresh spot, the atom ratio $N_{\text{C}}/N_{\text{O}}$ was determined as 7.34(45).

Method (c) is based on Eq. (3.53) which allows to calculate the photoelectron yield $Y_{Z,j}$. When calculating the photoelectron yield ratio $Y_{\text{C}1s}/Y_{\text{Ag}3d}$, most parameters from Eq. (3.53) drop out:^{e)}

$$\begin{aligned} \frac{Y_{\text{C}1s}}{Y_{\text{Ag}3d}} &= \frac{\sigma_{\text{C}1s}(E_{\text{kin,C}1s})D(E_{\text{kin,C}1s})L_{\text{C}1s}(\gamma)J_0N_{\text{C}}\lambda_{\text{IMFP}}(E_{\text{kin,C}1s})\cos\theta \cdot G(E_{\text{kin,C}1s})}{\sigma_{\text{Ag}3d}(E_{\text{kin,Ag}3d})D(E_{\text{kin,Ag}3d})L_{\text{Ag}3d}(\gamma)J_0N_{\text{Ag}}\lambda_{\text{IMFP}}(E_{\text{kin,Ag}3d})\cos\theta \cdot G(E_{\text{kin,Ag}3d})} \\ &\propto \frac{\sigma_{\text{C}1s}(E_{\text{kin,C}1s})}{\sigma_{\text{Ag}3d}(E_{\text{kin,Ag}3d})} \cdot \frac{\lambda_{\text{IMFP}}(E_{\text{kin,C}1s})}{\lambda_{\text{IMFP}}(E_{\text{kin,Ag}3d})} \cdot \frac{N_{\text{C}}}{N_{\text{Ag}}}. \end{aligned} \quad (4.6)$$

This is due to the following assumptions and conditions:

- (1) Because the pass energy of the electron analyzer is kept constant throughout the experiments, the detection efficiency $D(E_{\text{kin,Z},j})$ is also constant and cancels out.²⁰²
- (2) The ratio of the angular asymmetries of the emitted intensity, $L_{Z,j}(\gamma)$, from the C1*s* and Ag3*d* levels remains constant since the the angle γ between the direction of incidence and of detection is fixed by the experimental geometry.

^{e)}Note that Eq. (3.53) holds for the photoelectron yield $Y_{Z,j}$ on photoemission from orbital j of element Z in a *homogeneous* sample. In the present case, however, we consider the photoemission data from a layered sample, namely, PTCDA on Ag(*hkl*). Therefore, the presence of the parameter $\lambda_{\text{IMFP}}(E_{\text{kin,C}1s})$, which takes into account the re-absorption (that is, damping) of photoelectrons emitted from the C1*s* level by the PTCDA layer itself, may be called into question at first glance. However, the effect of re-absorption has to be included here because the angle of detection is $\theta \gtrsim 45^\circ$ (see above). Thus, indeed, the C1*s* photoelectrons have to pass the PTCDA layer to some extent.

- (3) The flux of primary photons on the sample surface, J_0 , cancels because the photoelectron yields are generally normalized to the intensity of the incident beam, I_0 .
- (4) The angle of detection with respect to the surface, θ , was identical for the measurements of both XPS signals. Thus, the cosini cancel out.
- (5) The transmission of the electron analyzer, $G(E_{\text{kin},Z,j})$, is assumed to be approximately equal for the photoelectrons emitted from the levels of interest here, namely, $\text{C}1s$ and $\text{Ag}3d$. Their binding energies and hence also the kinetic energies of the emitted photoelectrons differ by less than 100 eV, which is small compared to the absolute kinetic energies in the range from approximately 2300 eV for the experiments on $\text{Ag}(111)$ to approximately 3950 eV for those on $\text{Ag}(110)$.^{162,302} Thus, the difference in $\lambda_{\text{IMFP}}(E_{\text{kin},Z,j})$ is expected to be marginal, too (see also Table 4.1).

Because $Y_{\text{C}1s}/Y_{\text{Ag}3d}$ is known from the experiment, Eq. (4.6) yields the ratio of the atom densities, $N_{\text{C}}/N_{\text{Ag}}$, present at the surface, and thereby gives the PTCDA coverage in monolayers, when referenced against the respective ratio for 1.00 ML PTCDA/ $\text{Ag}(111)$ (see Table 4.3).³⁰⁸ Note that the different densities of the PTCDA molecules in the respective monolayer structures on the different surfaces were taken into account. They amount to 8.38×10^{-3} , 7.49×10^{-3} , and 7.07×10^{-3} molecules per square ångströms for PTCDA on $\text{Ag}(111)$,⁹⁸ $\text{Ag}(100)$,¹²⁰ and $\text{Ag}(110)$,⁹⁸ respectively. However, the actual structure at the interface, i.e., the metal surface being (partially) covered by an ultrathin PTCDA layer, and hence the attenuation of the $\text{Ag}3d$ signal due to the adsorbate overlayer was neglected. The photoionization cross sections $\sigma_{Z,j}(E_{\text{kin},Z,j})$ needed in Eq. (4.6) were obtained by linear interpolation of the tabulated values in Ref. 197, which, in turn, have been calculated for free atoms. The derived values are compiled in Table 4.4.

Carbon-to-oxygen ratio

By analogy with Eq. (4.6), also the carbon-to-oxygen ratios $N_{\text{C}}/N_{\text{O}}$ in the prepared PTCDA layers were determined. The results are presented in Table 4.3. For the multilayer films, the stoichiometric ratio expected for PTCDA of $N_{\text{C}}/N_{\text{O}} = 24 : 6 = 4$ is found with good approximation. For small coverages, in contrast, values significantly greater than the stoichiometric ratio (by about 20 % to 50 %, see Table 4.3) are found. However, decomposition of the PTCDA molecules on the surface, as is postulated for PTCDA on $\text{Cu}(100)$,^{117,315,316} can be ruled out on the basis of other experimental data, such as UPS,⁵⁹ STM,^{98,120} and LEED results.^{98,120} Besides, contamination of the sample surfaces with C residues prior to the deposition can be excluded, as XP spectra for the freshly prepared, clean surfaces showed. Also, the evaporated material, which was thoroughly purified in advance of the experiments (see also Sec. 4.2), did not contain any contamination, as follows from two observations. On the one hand, the carbon-to-oxygen ratios of the multilayer films, which were generally prepared under identical conditions, show only small deviations (below 10 %) from the stoichiometric value. On the other hand, inspections of the evaporated material in the gas phase with the mass spectrometer did neither indicate any contamination nor decomposition of the molecules.

Therefore, at least two other aspects may play a role here. Firstly, the cross sections for the C and O atoms within the PTCDA molecules in the (sub-)monolayers might be (differentially) altered by the presence of the metal surface and/or coadsorbates. For example, this is indicated by the stoichiometric ratios $N_{\text{C}}/N_{\text{O}}$ for PTCDA on $\text{Ag}(110)$ with and without K coadsorption in preparation nos. Feb'09-2b and Feb'09-2a, respectively. The former preparation was obtained from the latter by additional deposition of K atoms and subsequent annealing at elevated temperatures below 470 K, where thermal desorption is not expected. Thus, the $N_{\text{C}}/N_{\text{O}}$ values should be identical

TABLE 4.4. Photoionization cross sections $\sigma_{Z,j}(E_{\text{kin},Z,j})$ for the spectroscopic levels of interest in the present work (in kilobarns; $1 \text{ kb} = 10^{-21} \text{ cm}^2$). All values were obtained by linear interpolation of the tabulated values in Refs. 197, 198. The kinetic energies $E_{\text{kin},Z,j} \approx h\nu - E_b$ of the photoelectrons result from the employed photon energies $E = h\nu$, which typically were 10–15 eV below the Bragg energy for the reflection (hkl) in use, and the corresponding binding energies E_b of the XPS levels.^{162,302} For those XPS signals, where spin-orbit coupling/splitting is present,³¹⁰ i.e., for $l \geq 1$, the averaged values for E_b and $\sigma_{Z,j}(E_{\text{kin},Z,j})$ were obtained by averaging the corresponding values for the spectroscopic levels with different total angular momentum quantum number j , weighted with the respective degeneracies. Note that for the XPS investigations of PTCDA on the Ag(110) surface two slightly different photon energies were used (n.d. = not determined, n.a. = not available/applicable).

(hkl)	E (eV)	Cu ₃ Au(111)	Ag(100)		Ag(110)	
		(111)	(111)	(200)	(220)	
	E_b (eV) ^a	σ (kb) ^b	σ (kb) ^b	σ (kb) ^b	σ (kb) ^b	σ (kb) ^b
C1s	285.0 ^c	2.182	2.742	1.799	0.543	0.541
O1s	531.0	6.459	7.669	5.632	1.905	1.898
K1s	3608.4	n.d.	n.d.	n.d.	n.d.	43.589
K2p _{1/2}	297.3	n.d.	n.d.	n.d.	n.d.	0.593
K2p _{3/2}	294.3	n.d.	n.d.	n.d.	n.d.	1.136
K2p average	295.2	n.d.	n.d.	n.d.	n.d.	0.955
Cu2p _{1/2}	952.3	18.104	n.d.	n.d.	n.d.	n.d.
Cu2p _{3/2}	932.7	34.154	n.d.	n.d.	n.d.	n.d.
Cu2p average	939.2	28.804	n.d.	n.d.	n.d.	n.d.
Ag3d _{3/2}	374.0	n.d.	18.361	12.254	3.312	3.295
Ag3d _{5/2}	368.3	n.d.	26.366	17.508	4.675	4.651
Ag3d average	370.6	n.d.	23.164	15.406	4.129	4.109
Au3d _{3/2}	2291.0	n.a.	n.a.	n.a.	n.a.	n.a.
Au3d _{5/2}	2206.0	n.a.	n.a.	n.a.	n.a.	n.a.
Au3d average	2240.0	n.a.	n.a.	n.a.	n.a.	n.a.
Au4d _{3/2}	353.2	32.077	n.d.	n.d.	n.d.	n.d.
Au4d _{5/2}	335.1	44.966	n.d.	n.d.	n.d.	n.d.
Au4d average	342.3	39.810	n.d.	n.d.	n.d.	n.d.

^aTaken from Refs. 162, 302.

^bObtained by linear interpolation of the tabulated values in Refs. 197, 198.

^cThe values for E_b given here are representative for the respective electronic levels. In general, the precise values depend on the chemical environment.³¹¹ Two examples are values of 284.5 eV and 284.9 eV for the C1s levels in graphite³¹² and benzene,³¹³ respectively.

in both preparations. However, we observe that the ratio N_C/N_O is reduced by about 0.4 (–8 %) by the presence of K atoms on the Ag(110) surface. Secondly, the choice of the background in the respective XP spectra might cause systematic errors if background contributions from inelastically scattered photoelectrons are partitioned off incompletely or if contributions from the XPS signal of interest are falsely cut off. This applies in particular to PTCDA/Cu₃Au(111), preparation no. Feb'11-2, where the (relatively weak) O1s XPS signal with $E_b = 531.0$ eV is located at the onset of the nearby, much stronger Au4p_{3/2} signal at 546.3 eV.¹⁶² Hence, the deduced integral intensities for O1s might systematically be too small. However, an incorrect choice of the background in the XP spectra can hardly lead to a systematic overestimate in N_C/N_O by 20 % and more as observed here (see Table 4.3).

Recently, also photoelectron diffraction (PhD) effects have been discussed for the deviation of atomic ratios observed with XPS from the intrinsic stoichiometry of the adsorbed molecule.³¹⁷ Diller *et al.* have observed a variation in the photoelectron yield ratio of the chemically different N atoms in tetraphenylporphyrin on Cu(111) by up to a factor of 2.5, depending on the film thickness and, in the case of monolayer, on the angle of detection. They have attributed this finding to contributions of diffracted photoelectrons to the N1s XPS signal.³¹⁷ We can exclude PhD effects to play a role here for the following reasons. Firstly, we have found a systematic deviation of the N_C/N_O ratio, being larger than the stoichiometric value. Since photoelectron diffraction effects vary as a function of the kinetic energy E_{kin} of the photoelectrons and thus as a function of the photon energy, a systematic deviation $N_C/N_O > 4$ for PTCDA (sub-)monolayers on *all* coinage metal surfaces under investigation is not plausible. Secondly, PhD effects are only significant for $E_{kin} \leq 500$ eV.^{157,263} In our experiments, however, the kinetic energies of the C1s and O1s photoelectrons were well above 2 keV.

If different cross section σ were used,³¹⁸ the same effect of the N_C/N_O values being larger than the expected value of 4 was present. In particular, we obtained identical values (within ± 7 %) for the ratios N_C/N_O in comparison to those reported in Table 4.3 utilizing cross sections which were derived from the parameters given in Ref. 318. Hence, we conclude that the systematic deviations of N_C/N_O from the expected value for PTCDA (sub-)monolayers are *not* due to (potential) errors in the theoretically derived σ values. Note that, assuming that the above-stated scenario of altered σ values at the metal surface is indeed correct, the well-established, so-called sum rule in XPS is violated.^{202,319–323} In brief, the sum rule says that the integral intensity of a given XPS signal is independent of its shape or, in other words, that the sum of the integral intensities of all components (such as adiabatic peak, shake-ups, and shake-offs) contributing to the XPS signal is constant (because σ is constant).³²⁴ Our finding, however, may indicate that the cross section σ and thus the integral intensity, i.e., the photoelectron yield $Y_{Z,j}$, of a given XPS signal in fact depends on the chemical environment of the respective atom and thus on the bonding situation of the individual PTCDA molecules on the surface, in particular. This, in turn, would disqualify XPS as a *quantitative* technique in surface science.^{f)} Hence, further systematic XPS studies are required here for clarification.

4.3.3 XSW data

All normal incidence x-ray standing waves (NIXSW) experiments were performed at the undulator beamline ID32 of the European Synchrotron Radiation Facility (ESRF) at Grenoble, France,

^{f)}Indeed, strong variations of the integral peak intensities (up to 40 %) have already been observed for the first-row transition metals and the rare earth metals depending on their chemical state.³²⁵ These variations have been attributed to multi-electron processes.³²⁵

TABLE 4.5. Beamtimes and systems under investigation in the framework of the present work. All XSW experiments were performed at the beamline ID32 of the ERSF (Grenoble, France) in two different setups. The results obtained from the earlier two beamtimes are not reliable due to technical and experimental complications and hence not reported in the present work (n.r. = not reliable/reported).

beamtime	date	XSW setup	objectives/systems	results
SI-1451	Nov. 2006	I	PTCDA/Ag(100) PTCDA/Ag(110)	Ref. 327
SI-1645	Apr. 2008	I	PTCDA/Ag(100) PTCDA/Ag(110)	n.r.
SI-1829	Feb. 2009	I	PTCDA/Ag(110) K + PTCDA/Ag(110)	this work
SI-2186	Feb. 2011	II	PTCDA/Ag(100) PTCDA/Cu ₃ Au(111)	this work

in a joint research project of the group of Professor Dr. Moritz Sokolowski from Rheinische Friedrich-Wilhelms-Universität Bonn (Bonn, Germany) in collaboration with the group of Professor Dr. Frank Stefan Tautz from Forschungszentrum Jülich (Jülich, Germany). Namely, the data were conducted by the author, Christoph Heinrich Schmitz, Benjamin Fiedler, Maria Buchholz and Professor Dr. Moritz Sokolowski from Rheinische Friedrich-Wilhelms-Universität Bonn (Bonn, Germany), together with Giuseppe Mercurio, Martin Willenbockel, Adam Lassise, Dr. Serguei Soubatch, and Professor Dr. Frank Stefan Tautz from Forschungszentrum Jülich (Jülich, Germany). An independent analysis of the data concerning PTCDA on the Ag(110) surface, as a pristine overlayer and also with K atoms being coadsorbed, is found in Ref. 326. The XSW data, and also the corresponding XPS data (see Sec. 4.3.2), were collected in different beamtimes which are listed in Table 4.5. Due to technical and experimental complications,³²⁷ the results from the earlier two beamtimes in November 2006 and April 2008 are considered to not be reliable and thus will not be reported in the present work. Only the XPS data for PTCDA multilayers on Ag(100) and on Ag(110) from the beamtime in April 2008 will be presented in Sec. C.3.3 in the appendix of the present work.

For the XSW experiments, the photon energy was scanned successively in steps of 0.10–0.15 eV in an interval of about 4–6 eV around the Bragg energies of the reflections (hkl) of the respective substrates (see Table 4.6, for example). Note that those (hkl) Bragg reflections, where the Miller indices h, k, l are *not* all odd or all even,²⁰⁹ e.g., the (100) and (110) reflections, are systematically extinct for the Ag substrates due to the *fcc* bulk structure.²⁰ For PTCDA/Ag(100), also the (111) reflection, which is not parallel to the substrate surface, was employed for the determination of the PTCDA adsorption site (see Sec. C.4). The Bragg energies E_B , which were calculated from the respective lattice plane spacings d_{hkl} and the Bragg angle of $\theta_B = 88^\circ$ utilizing Eq. (3.5), are also given in Tables 4.6 and 4.7. The d_{hkl} values were determined from the lattice constants a_{bulk} of the Cu₃Au²⁸⁸ and Ag substrates,²⁸⁹ which both form cubic lattices.^{20, 164, 328} Owing to the necessity to measure the intensity of the Bragg-reflected x-ray beam (see also Figs. 4.2 and 4.3), XSW experiments could not be realized with perfect normal incidence of the x-ray beam, but the samples had to be turned slightly off the ideal normal-incidence position. The effective Bragg angle was $\approx 88^\circ$. Thus, the calculated E_B values amount to minimal 2629.89 eV for the (111) reflection of Ag and maximal 4294.59 eV for the (220) reflection of Ag for the XSW experiments

(see Tables 4.6 and 4.7). Note that the exact E_B value is not relevant for the XSW data analysis. The photon flux was estimated at about 40 photons per molecule and second.^{54,55}

The XSW data were collected by monitoring the intensities of various adsorbate and substrate signals by AES and/or XPS. The respective signals for the individual systems are given in Tables 4.6 and 4.7. Typical recording times for an XSW experiment were 30–120 min for the adsorbate signals and 15–60 min for the substrate signals. Usually, 25 to 50 data points per XSW photoelectron yield curve were recorded. We employed the same pass energies as in the XPS studies, i.e., pass energies in the range from 10 eV to 100 eV depending on the experimental setup and the XPS signals under investigation (see also Sec. 4.3.2). The explicit values will be given in the respective chapters on the experimental data. To exclude beam damage, the shape of the adsorbate XPS signals was carefully observed as a function of beam exposure. Besides, as a precaution, a new position of the x-ray beam on the sample was chosen after every other XSW scan at the latest. Where changes in XP spectra were observed after longer irradiation times, as was the case for K + PTCDA/Ag(110) after about 30–40 min (see also Sec. D.2 in the appendix of the present work), for instance, the time per spot did not exceed 30 min. As an alternative, in the case of PTCDA/Cu₃Au(111), a full data set for one XSW photoelectron yield curve was collected in a scanning mode on several different spots on the sample which had not been exposed to the x-ray beam before (see Chapter 6 for details).

The intensity of the reflected x-ray beam, I_0 , was monitored by the photoelectron current generated on a screen at a small angle close to the incident x-ray beam. Prior to the data collection, the position of the x-ray beam on the clean sample was optimized in order to give the narrowest reflectivity curve, which typically had a half width of 0.93 eV for the (111) reflection of the Cu₃Au(111) substrate crystal, and a half width of 0.97 eV for the (111) reflection, 0.74 eV for the (200) reflection, and 0.81 eV for the (220) reflection of the Ag substrate crystals, respectively.^{g)} The intensity I_0 of the primary x-ray beam was monitored by the photoelectric current generated on an Al foil in the beam path (see also Sec. 4.1.2). All experimental XSW data, i.e., the integral intensities (that is, the photoelectron yields $Y_{Z,j}$) of the XPS signals under investigation as well as the intensity I of the reflected x-ray beam, were normalized to I_0 prior to the data analysis/fitting (see below for details).

The general treatment of the photoelectron data has already been described in Sec. 4.3.2. For the adsorbate signals, sophisticated XPS fitting models were employed in the XSW data analysis. Based on the XPS studies of Schöll *et al.*³⁰⁷ on PTCDA/Ag(111) in the multilayer regime and also on our multilayer XPS data for both PTCDA/Ag(100) and PTCDA/Ag(110), we developed respective fitting models for our XPS data on PTCDA (sub-)monolayers (see also Sec. 4.3.2). They fulfilled the following requirements: (1) Concerning the peak areas of the individual components, the expected stoichiometry of the PTCDA molecule, namely, $C_{\text{peryl}} : C_{\text{funct}} = 20 : 4$ and $O_{\text{carb}} : O_{\text{anhyd}} = 4 : 2$, were met for photon energies off the Bragg energy E_B (10–15 eV below, typically), and (2), employing these XPS fitting models, higher coherent fractions f_c were

^{g)}The theoretically predicted half widths of the reflectivity curves for perfect crystals amount to 0.69 eV for the (111) reflection of the Cu₃Au(111) substrate crystal (+35 % observed in the experiment), and a half width of 0.86 eV for the (111) reflection (+13 % observed in the experiment), 0.64 eV for the (200) reflection (+16 % observed in the experiment), and 0.35 eV for the (220) reflection (+131 % observed in the experiment) of the Ag substrate crystals, respectively. Data evaluation with XSWAVES³²⁹ (see below and Appendix A) as well as theoretical simulations have shown that, in all cases, the broadening of the reflectivity curves observed in the experiment mainly originates from the finite width in energy of the incident x-ray beam. Broadening due to imperfections in the substrate crystals is of minor importance here. This is concluded from the fact that the Gaussian functions, which account for these imperfections and which were fitted to the experimental data in the analysis as part of a convolution (see Sec. A.3 in the appendix of the present work), had a FWHM of only around 0.15 eV, typically.

obtained in the XSW data analysis than with alternative models. The relative integral intensities $Y_{C1s}(C_{\text{peryl}}) : Y_{C1s}(C_{\text{funct}})$ and $Y_{O1s}(O_{\text{carb}}) : Y_{O1s}(O_{\text{anhyd}})$ were allowed to vary throughout the XSW scan, while the full width at half maximum (FWHM) and the relative positions of the peaks were constrained. The so-obtained XSW photoelectron yield curves were fitted with the homemade data evaluation routine XSWAVES, version 2.5,³²⁹ which is based on the theory presented in Sec. 3.1. The details behind this routine will be presented in Appendix A. In addition, the same XSW data for PTCDA on the different Ag surfaces was evaluated by Giuseppe Mercurio and Martin Willenbockel, respectively, from Forschungszentrum Jülich (Jülich, Germany) with the independent XSW program Torricelli by Mercurio.^{326,330} Identical results (within the errors) were obtained, ensuring the absence of systematic and/or numerical errors by the evaluation routines. Typically, more than one XSW photoelectron yield curve was collected per signal of interest. The results for the coherent fractions f_c and the coherent positions p_c given in the course of the present work were then obtained by averaging the individual fitting results. The errors in f_c and p_c were derived as the standard deviation of the individual fitting results, while the errors in the vertical adsorption heights d were propagated from the errors in p_c .

Due to the high photon energies employed in the XSW experiments, nondipolar correction terms had to be considered in the fitting process (see Sec. 3.1.4 for details). Often, the nondipolar corrections are expressed in terms of the parameters Q , S_R , $|S_I|$, and ψ , which are given in Tables 4.6 and 4.7. These parameters were calculated on the basis of Eqs. (3.30) to (3.36) from tabulated values for β , γ , δ ,^{197,198} and Δ ¹⁹⁹ for the relevant photon energies, XPS levels and experimental geometries in the present work. They are also listed in Tables 4.6 and 4.7. In particular, the parameters β , γ , δ , and $\Delta = \delta_d - \delta_p$ were generally derived from theoretical values of the free atoms,^{197–199} in the case of β , γ , δ via linear interpolation of the tabulated values. For those XPS signals, where spin-orbit coupling/splitting is present,³¹⁰ i.e., for $l \geq 1$, the values β , γ , δ , and Δ for the spectroscopic levels with different total angular momentum quantum number j were weighted with the corresponding degeneracies and then averaged in order to give the respective values independent of j . Note that, for the photoemission from an initial s state, β and δ amount to 2 and 0, respectively.^{188,190} For the emission from an initial p or d state, Δ values are not available and thus were set to 0 in the framework of the present work. In principle, however, Δ values for subshells with $l \geq 1$ may be obtained from an XSW experiment.¹⁷⁶ Note further that for the measurements on PTCDA/Cu₃Au(111) and PTCDA/Ag(100) the nondipolar parameter Q equals 0 due to the specific experimental geometry (XSW setup II, $\theta_p = 0^\circ$), making $S_R = 1$, $|S_I| = 1$, and $\psi = 0$, respectively. For the Auger signals Δ and Q were set to 0 because nondipolar effects generally do not apply.^{159,331} Possible photo-/Auger-electron stimulated or secondary-radiation stimulated contributions to the Auger signals were neglected.^{28,41,159,175} Within the present work, Auger signals have been recorded for the Cu₃Au(111), Ag(100), and Ag(110) substrates. Neglecting the potential additional contributions to the Auger signals was justified by the finding that both XPS and Auger signals yielded similar results in XSW.

In principle, the Q values can be determined experimentally from the XSW photoelectron yield curves of incoherent films (see also Sec. 3.1.4). This has been waived here for two reasons. On the one hand, our experimental attempts to determine Q on PTCDA multilayer films on Ag(100) and Ag(110) in beamtime SI-1645 suffered from technical problems, yielding XSW curves which did not converge to a constant background for photon energies some electronvolts off E_B , as expected from theory, and whose maxima were offset in energy from the maxima of the corresponding reflectivity curves (not shown). Analyzing these curves nonetheless yielded Q values which were smaller than the theoretically determined values by 35–50 % and thus considered not to be reliable. On the other hand, experimentally determined values from the literature show a large spread.¹⁹⁰

TABLE 4.6. Nondipolar parameters for the evaluation of the XSW photoelectron yield curves of the adsorbate XPS levels for the different photon energies used in this work. In addition, the bulk lattice constants a_{bulk} (valid at room temperature, RT), the employed reflections (hkl), the corresponding lattice plane spacings d_{hkl} (also at RT), the Bragg energies E_B (calculated for $\theta_B = 88^\circ$), as well as the angles θ_p and ϕ (determined by the experimental geometry) are given. Note that for $\theta_p = 0^\circ$ (XSW setup II, in contrast to $\theta_p = 45^\circ$ in XSW setup I), $Q, \psi = 1$ and $S_R, |S_I| = 1$ applies necessarily (n.a. = not available/applicable).

	Cu ₃ Au		Ag									
	3.75 ^a		(111)		(200)		(220)					
a_{bulk} (Å)	3.75 ^a		(111)		(200)		(220)					
(hkl)	(111)		(111)		(200)		(220)					
d_{hkl} (Å)	2.165		2.359		2.043		1.444					
E_B (eV)	2865.04		2629.89		3036.74		4294.59					
θ_p (°)	0		0		0		45					
ϕ (°)	0		0		0		0					
XPS level	C1s	O1s	C1s	O1s	C1s	O1s	C1s	O1s	K1s	K2p _{1/2}	K2p _{3/2}	K2p
β^c	2.000	2.000	2.000	2.000	2.000	2.000	2.000	2.000	2.000	0.783	0.795	0.791
γ^c	1.119	1.041	1.062	0.978	1.160	1.087	1.422	1.349	0.283	0.922	0.926	0.925
δ^c	0.000	0.000	0.000	0.000	0.000	0.000	0.000	0.000	0.000	0.128	0.128	0.128
δ_p^d	0.779	0.984	0.799	1.010	0.766	0.967	0.693	0.872	-0.082	n.a.	n.a.	n.a.
δ_d^d	0.577	0.702	0.588	0.714	0.570	0.693	0.527	0.644	-1.202	n.a.	n.a.	n.a.
Δ	-0.202	-0.282	-0.211	-0.296	-0.197	-0.273	-0.166	-0.227	-1.119	0.000 ^e	0.000 ^e	0.000
Q	0.000	0.000	0.000	0.000	0.000	0.000	0.335	0.318	0.067	0.348	0.349	0.348
S_R	1.000	1.000	1.000	1.000	1.000	1.000	2.008	1.932	1.143	2.068	2.070	2.070
$ S_I $	1.000	1.000	1.000	1.000	1.000	1.000	1.506	1.470	1.082	1.534	1.535	1.535
ψ	0.000	0.000	0.000	0.000	0.000	0.000	-0.056	-0.073	-0.137	0.000	0.000	0.000

^aTaken from Ref. 288.

^bTaken from Ref. 289.

^cObtained by linear interpolation of the tabulated values in Ref. 197.

^dTaken from Ref. 199.

^e Δ values for subshells with $l \geq 1$ are not available and thus were set to 0.

TABLE 4.7. Same as Table 4.6 but for the nondipolar parameters for the evaluation of the XSW photoelectron yield curves of the substrate XPS levels for the different photon energies used in this work. For the sake of completeness, also the Auger signals $\text{Cu}L_3M_{45}M_{45}$ and $\text{Ag}M_5N_{45}N_{45}$, denoted as $\text{Cu}LMM$ and $\text{Ag}MNN$, respectively, are contained in the table, although nondipolar corrections do not apply here (n.a. = not available/applicable).¹⁵⁹

	Cu ₃ Au			Ag									
a_{bulk} (Å)	3.75 ^a			4.0853 ^b									
(hkl)	(111)			(111)			(200)			(220)			
d_{hkl} (Å)	2.165			2.359			2.043			1.444			
E_B (eV)	2865.04			2629.89			3036.74			4294.59			
θ_p (°)	0			0			0			45			
ϕ (°)	0			0			0			0			
signal	Au3d _{5/2}	CuLMM	Ag3d _{3/2}	Ag3d _{5/2}	Ag3d	Ag3d _{3/2}	Ag3d _{5/2}	Ag3d	AgMNN	Ag3d _{3/2}	Ag3d _{5/2}	Ag3d	AgMNN
β^c	n.a.	n.a.	1.136	1.109	1.120	1.090	1.063	1.074	n.a.	0.956	0.930	0.940	n.a.
γ^c	n.a.	n.a.	0.625	0.627	0.626	0.721	0.720	0.720	n.a.	0.956	0.948	0.951	n.a.
δ^c	n.a.	n.a.	0.093	0.096	0.094	0.106	0.110	0.108	n.a.	0.147	0.153	0.151	n.a.
Δ^d	0.000	0.000	0.000	0.000	0.000	0.000	0.000	0.000	0.000	0.000	0.000	0.000	0.000
Q	0.000	0.000	0.000	0.000	0.000	0.000	0.000	0.000	0.000	0.357	0.360	0.359	0.000
S_R	1.000	1.000	1.000	1.000	1.000	1.000	1.000	1.000	1.000	2.109	2.125	2.119	1.000
$ S_I $	1.000	1.000	1.000	1.000	1.000	1.000	1.000	1.000	1.000	1.555	1.562	1.559	1.000
ψ	0.000	0.000	0.000	0.000	0.000	0.000	0.000	0.000	0.000	0.000	0.000	0.000	0.000

^aTaken from Ref. 288.

^bTaken from Ref. 289.

^cObtained by linear interpolation of the tabulated values in Refs. 197, 198.

^d Δ values for subshells with $l \geq 1$ are not available and thus were set to 0.

For example, $Q_{\text{C}1s}$ was found to be 0.31(3) for PTCDA/Ag(111),³³² while for SnPc/Ag(111) it was determined as 0.24(2) and hence being almost 25 % smaller,⁴⁵ employing the (111) substrate reflection in both cases. Apparently, except for the geometric dependence, the Q values are *not* an intrinsic property of the XPS level of the respective atom, but they are also influenced by the chemical environment (within the molecule), as well as the presence and the nature of the surface, and possible bond formations at the interface.³³² Note, however, that the choice of Q has only a second-order effect within a few percent on the experimentally determined adsorption heights d (see below and Appendix E for the impact on the obtained fitting results for f_c and p_c).

One further reason behind the difference in experimentally and theoretically derived Q values may also be photoelectron diffraction effects, causing photoelectrons from the adsorbate, which were originally emitted in the direction towards the surface (incident beam direction), to be scattered towards the electron analyzer (back-reflected beam direction) by the surface atoms. This would lead to a decrease in the forward/backward asymmetry and thus smaller values of Q . The influence of the choice of Q on the fitting results has been tested for C1s and O1s in those cases, where $Q \neq 0$, namely, PTCDA/Ag(110) and K + PTCDA/Ag(110) (see Tables 4.6 and 4.7), over a wide range of Q values. Mainly the results for f_c were affected (maximal to a factor of 3) while the results for p_c typically remain unaltered within 15 % (see also Fig. E.1, page 366, in Appendix E of the present work), making the presented values for p_c and also the conclusions drawn thereof meaningful.

4.3.4 STM data

The STM experiments on PTCDA/Cu₃Au(111) were performed together with Dr. Julian Ikonov from Rheinische Friedrich-Wilhelms-Universität Bonn (Bonn, Germany). All STM images presented in this work were conducted in constant current mode at room temperature (RT). Mechanically cut Pt/Ir wires (Pt 90 %, Ir 10 %) from Advent Research Materials (Oxford, UK) were used as STM tips. Given bias voltages U_{bias} refer to the sample. All STM images were thoroughly processed with the computer program SPIP³³³ by (global, local or line-wise) plane correction and by careful smoothening via Median filtering, except for those images with atomic or molecular steps. Here, plane correction was waived. The STM images were corrected for thermal drift and calibrated with SPIP³³³ [in the fast Fourier transforms (FFTs) of the respective images] to the more reliable lattice parameters of the bare surface known from the literature and the PTCDA surface structures known from LEED, respectively. The latter were known from SPA-LEED measurements. Only for large-scale STM images with dimensions above 50 nm × 50 nm, the calibration was omitted.

4.3.5 UPS data

The UPS measurements on PTCDA/Ag(100) were performed by Manuel Marks in the group of Professor Dr. Ulrich Höfer at Philipps-Universität Marburg (Marburg, Germany) within a joint research project on the electronic structure at the metal/organic interface. An independent analysis of the data is found in Ref. 275. UP spectra were taken for the clean Ag(100) surface as well as for PTCDA layers with different coverages up to 3.5 ML, eventually. The latter were prepared by subsequent deposition in five steps at a rate of 0.14 ML min⁻¹ with the sample being held at 290 K. The PTCDA coverage was determined with XPS by the attenuation of the photoelectron yield from the Ag3d substrate signal, as described in Sec. 3.2.3 [see Eq. (3.54)], after the last

preparation step.²⁷⁵ A constant deposition rate for every single (and identical) deposition step is assumed.

The UP spectra were conducted at normal emission using (non-monochromatized) He I radiation with an energy of 21.22 eV.³³⁴ The sample temperature was kept constant at 290 K during the UPS measurements, as well. All UP spectra presented in this work are referenced against the Fermi energy E_F of the prepared samples. The position of E_F was determined by a fit to the experimental data for the clean surface plotted as a function of E_{kin} of the detected photoelectrons and was also applied to the PTCDA-covered surface. Note that, due to the metrological realization of the experiment, E_{kin} of the photoelectrons emitted from the Fermi level is identical for all samples and is thus unaffected by the PTCDA coverage.²⁰² The fitting of the Fermi edge was performed in Origin²⁹² with a (scaled) Fermi-Dirac distribution function³³⁵ of type:^{h)}

$$y = \frac{A_1 - A_2}{1 + \exp\left(\frac{x - x_0}{B}\right)} + A_2, \quad (4.7)$$

where the photoelectron intensity $I(E_{\text{kin}})$ is represented by y , the kinetic energy E_{kin} by x , and the thermal energy $k_B T$ by the parameter B . x_0 denotes the point of inflection of the fitting curve and hence corresponds to E_{kin} acquired by those photoelectrons which are emitted from E_F . A_1 and A_2 are the initial and final values of $I(E_{\text{kin}})$, respectively.

The work functions Φ of the samples were determined from the width ΔE_{kin} of the UP spectra, applying Eq. (3.57) (see Sec. 3.2.4). $\Delta E_{\text{kin}} = E_{\text{kin}}^{\text{max}} - E_{\text{kin}}^{\text{min}}$ is given by the difference in the kinetic energy of the electrons from the Fermi level (with $E_{\text{kin}}^{\text{max}}$) and those at the cut-off (with $E_{\text{kin}}^{\text{min}}$). The latter was determined by the intersection of a linear fit to the cut-off region with the baseline of the respective spectra (see also Sec. C.3.2, in particular Fig. C.3, page 304, in Appendix C of the present work). In order to clearly separate the cut-off region of the respective UP spectra from the onset of the kinetic-energy scale, i.e., from $\Delta E_{\text{kin}} = 0$ eV, the sample was placed at negative bias of -1 V with respect to the analyzer.²⁰²

In determining $E_{\text{kin}}^{\text{min}}$, the point of inflection at the low kinetic-energy side of the secondary-electron peak should be considered in the strict sense.²⁰² This approach was also tested on the available UP spectra, but it yielded Φ values with a comparably large scattering (see also below) for the clean Ag(100) surface because identifying the respective point of inflection often was ambiguous. Hence, we relied on the above-stated procedure of extrapolating the low kinetic-energy side of the secondary-electron peak to the background level. This procedure yielded a smaller scattering in the results for the work functions Φ of the clean Ag(100) surface (± 0.11 eV, as opposed to ± 0.22 eV in the case where the point of inflection was considered), indicating indeed a higher robustness of the method. Admittedly, this method gives rise to a (small) systematic deviation in the determination of Φ . The deviation to those results for Φ , which were obtained if the point of inflection was considered, was found to be $-0.21(15)$ eV on average. Because we focus on work function shifts as a function of PTCDA coverage, $\Delta\Phi(\theta_{\text{PTCDA}})$, rather than on the absolute values of $\Phi(\theta_{\text{PTCDA}})$ in the course of this work, this systematic deviation can be neglected here. Spectral features in the UPS data were fitted with pseudo-Voigt functions, as given in Eq. (4.5), where x and y refer to the binding energy E_b (with respect to E_F) and the corresponding photoelectron intensity $I(E_{\text{kin}})$.

^{h)}This standardly provided, sigmoidal function is (falsely) termed ‘‘Boltzmann’’ in Origin.

5

PTCDA on Cu(111)

As has already been pointed out in Sec. 2.2.2, PTCDA exhibits a *boat*-like adsorption configuration on the Cu(111) surface,⁴³ where the C backbone of the molecule is closer to the surface than the O atoms. It is therefore tempting to conclude that the interaction of the perylene core with the substrate is the predominant bonding channel. In contrast, the O_{carb} atoms are closest to the surface in the case of PTCDA on Ag(111),^{32,55} indicating perceptible $O_{\text{carb}}-\text{Ag}$ interactions. Now the question arises why similar $O_{\text{carb}}-\text{Cu}$ interactions are apparently not present on the Cu(111) surface although Cu is the more reactive metal.²⁰ Indications may be found in the lateral structure of the PTCDA molecules in the monolayer regime on Cu(111). Indeed, STM investigations are available (see Sec. 5.1), but we have performed additional SPA-LEED experiments in order to obtain the lattice parameters with higher precision.^{a)} The reasoning is twofold: On the one hand, the structure models presented in Ref. 115 may be verified. This would constitute a solid basis on which the surface bonding mechanism may be discussed. On the other hand, the so-obtained lattice parameters and structural models of the metal/organic interface will be available for comparison with those for PTCDA on the $\text{Cu}_3\text{Au}(111)$ surface in the next chapter.

5.1 Review of the literature

The adsorption configuration of PTCDA on Cu(111) is known from XSW experiments,⁴³ and the electronic structure of the valence states is known from UPS investigations.⁶⁰ Both have already been presented in Sec. 2.2.2. Hence, we focus on the lateral structure, the growth mode, and the energetics of the adsorption process here. The former have been derived from STM experiments,¹¹⁵ while the latter have been deduced from TPD investigations.^{337,338} PTCDA exhibits a Stranski-Krastanov growth mode⁶² on the Cu(111) surface, forming at least 3 closed layers and additional nanocrystals for higher coverages.³³⁸ The desorption of the multilayers, which takes place at temperatures below ≈ 550 K, can be clearly discerned from that of the second layer, for which the desorption peak reaches its maximum at a higher temperature of 573 K, in the TPD spectra.³³⁸ However, desorption of the monolayer is not observed,³³⁸ indicating strong chemisorptive bonding of the PTCDA molecules to the Cu(111) surface. The activation energies $E_{\text{a,des}}$ for desorption, which are often understood to be identical to the adsorption energies, amount to 2.35(20) eV for the second layer and 2.20(20) eV for the multilayers, respectively.³³⁸

On the basis of STM measurements, Wagner *et al.* have presented structural models for PTCDA on Cu(111) in the (sub-)monolayer regime¹¹⁵ which are shown in Fig. 5.1. Two structures were found which have similar lattice parameters but differ in their orientations with respect to the close-packed substrate directions.¹¹⁵ The respective lattice parameters are given in Table 5.1 while the

^{a)}Preliminary SPA-LEED investigations on PTCDA/Cu(111) have already been reported in Ref. 336.

TABLE 5.1. Structural results for PTCDA in the first and second layer on the Cu(111) surface by Wagner *et al.* (Ref. 115). The lattice constants b_i , the enclosed angle β , and the area of the unit cell, A_{uc} , are given based on both STM experiments and corresponding structural models for three individual structures.¹¹⁵

Layer Phase/structure	1st				2nd
	‘1’		‘2’		herringbone
	STM	model	STM	model	STM
b_1 (Å) ^a	13.6(7)	12.8	13.6(7)	13.4	13.4(7)
b_2 (Å) ^a	21.6(11)	22.1	21.6(11)	22.0	20.3(10)
β (°) ^a	90(5)	90	92(5)	92	90(5)
A_{uc} (Å ²)	294(21)	282.9	294(24)	294.6	272(20)

^aTaken from Ref. 115.

superstructure matrices are given as insets in Fig. 5.1. In both structures, the PTCDA molecules arrange in a *herringbone*-like motif with an enclosed angle of 90° between the long molecular axes.¹¹⁵ Hence, the structural motifs may be referred to as *T-shape* and *L-shape*, respectively. Both structures are present in parallel on the surface. One of the structures, denoted as ‘1’ in Ref. 115, is commensurate while structure ‘2’ is commensurate only to higher order.¹¹⁵ Note that in structure ‘1’ the PTCDA molecules have been proposed (but not been experimentally verified) to adsorb with their center in an on-top site, while the O atoms do not have unique adsorption site but occupy different positions, roughly being either in threefold hollow sites, in bridge sites, or near on-top sites (see Fig. 5.1). This will be of importance in the discussion of the general surface bonding mechanism for PTCDA later in this work (see Chapter 7). In the second layer, a herringbone arrangement of the molecules is present, too.

Remarkably, *all* experimental values for the respective lattice constants are larger, up to a maximum of 11 %, than those found for bulk PTCDA (see also Table 2.1). Furthermore, the resulting packing densities for the PTCDA molecules on Cu(111) in the monolayer regime, i.e., 7.07×10^{-3} and 6.79×10^{-3} molecules per square ångströms for the structures ‘1’ and ‘2’, respectively, are identical to or even lower than that found for PTCDA/Ag(110), where it amounts to 7.07×10^{-3} molecules per square ångströms.⁹⁸ In contrast to PTCDA/Cu(111), the intrinsically favored herringbone arrangement of the molecules is abandoned on the Ag(110) surface in favor of a *brick-wall* arrangement,⁹⁸ implying even stronger metal/molecule interactions. Therefore, the smallest packing density would be expected to be present on the Ag(110) surface. However, the structure models in Fig. 5.1 exhibit noticeable empty spaces between some of the molecules, whereas at other positions in the unit cell of structure ‘1’ a strong overlap of the vdW radii of the atoms in two neighboring molecules occurs [see the molecule in the center of the unit cell in Fig. 5.1(a), for example]. This might call structure model ‘1’ into question, at least. Besides, according to the structural models, structure ‘1’ exhibits the larger packing density (by 4 %) than structure ‘2’. This is exceptional for a commensurate superstructure (‘1’) in comparison to an incommensurate one (‘2’). We note, however, that this effect may be an artifact of structural modeling because the parameters b_1 and b_2 determined with STM are in fact identical (see Table 5.1). Hence, the experimentally determined lattice parameters and, as a consequence, also the proposed

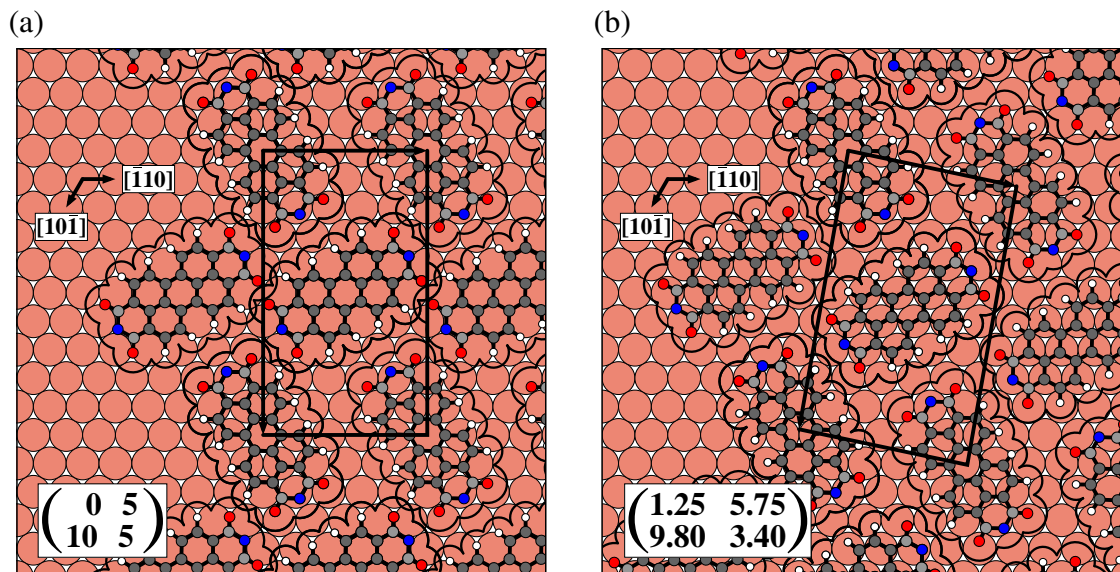


FIG. 5.1. Structural models of PTCDA on the Cu(111) surface which are present in the (sub-)monolayer regime, as proposed by Wagner *et al.* (Ref. 115): (a) Structure ‘1’ and (b) structure ‘2’.¹¹⁵ The PTCDA molecules are shown as ball-and-stick models, including a two-dimensional projection of the molecular vdW surface. Solid black lines indicate the respective unit cells. The substrate directions are also indicated. The superstructure matrices¹¹⁵ are given as insets.

structure models by Wagner *et al.* for PTCDA on Cu(111) might exhibit systematic errors, and therefore need to be verified.

5.2 Experimental procedure

In order to prepare long-range ordered Cu(111) surfaces of adequate quality, rigorous conditions were found to be necessary. The sample was held at 800 K during sputtering^{339,340} with Ar⁺ ions of 600 eV kinetic energy for 20 min. The Ar partial pressure was 1×10^{-5} mbar, and the ion current on the sample typically was $14 \mu\text{A}/\text{cm}^2$. After sputtering, the sample was annealed at 1250 K for 5 min and then slowly cooled to room temperature (RT) at a rate of 0.5 K s^{-1} . This treatment resulted in surfaces with effective transfer widths of about 240 Å for out-of-phase conditions ($E = 105.9 \text{ eV}$) and about 275 Å for in-phase conditions ($E = 77.8 \text{ eV}$), respectively, as determined with SPA-LEED from the width of the (00) reflection. PTCDA was deposited at a rate of 0.25 ML min^{-1} with the sample being held at room temperature. The deposition rate was deduced from a thorough calibration of the evaporation source by carefully monitoring the attenuation of the {10} substrate spots by PTCDA overlayers of different thicknesses in the submonolayer regime, in advance to the experimental series. The absolute coverages of the individual preparations were then controlled by means of the deposition time. The uncertainties in the absolute coverages amount to approximately 10%. In those cases, where annealing of the prepared PTCDA layers was performed, the heating and cooling rates were 1 K s^{-1} , typically. Unless otherwise stated, all SPA-LEED measurements were performed at 100 K. Note that, apart from the expected changes, such as reduced spot intensities and small shifts of the spot positions caused by thermal expansion of the prepared sample, identical LEED patterns were observed also for measurements at room temperature. Since the intensity of the adsorbate-related diffraction spots was low, i.e., about a factor of 10^2 smaller

than that of the (00) spot for a coverage of 1 ML PTCDA, relatively high electron beam intensities were used during the LEED experiments in order to achieve decent integral spot intensities. The electric current generated on the sample by the incident electron beam usually amounted to 10–20 nA. Since a strong decrease in the intensities of the adsorbate spots was observed after a few hours of irradiation, especially for multilayers, a fresh spot on the sample was chosen after two hours at the latest. The sensitivity of the prepared PTCDA layers to the electron bombardment indicates the occurrence of electron-stimulated processes, such as disordering or decomposition of the molecules on the surface, or desorption.

5.3 Results

PTCDA structures on the Cu(111) surface have been investigated for surface coverages ranging from 0.25 ML to 6 ML. Figure 5.2(a) shows a typical LEED pattern for 1 ML PTCDA/Cu(111). Although the relative intensities of the adsorbate-induced LEED spots are low compared to those of the substrate spots, high-order diffraction spots (up to k_{\parallel} values of $\approx 2 \text{ \AA}^{-1}$) of the adsorbate structure can be identified. This proves the long-range order of the PTCDA superstructure(s). However, the spot patterns which are observed around the first- and second-order substrate spots are very similar to that around the specular reflection [(00) spot], indicating the presence of multiple scattering effects. Thus, the spots which are observed for $k_{\parallel} > 2 \text{ \AA}^{-1}$ are mostly caused by multiple scattering. This finding strongly points to the fact that the structure of the PTCDA overlayer is *not* commensurate with the Cu(111) substrate. For a commensurate overlayer structure, the diffraction spots caused by single and multiple scattering effects superimpose which leads to enhanced intensities of the adsorbate spots, especially in higher orders. Furthermore, the surface atoms become part of the periodic scattering unit for a commensurate and thus well-defined registry between the adsorbate and the substrate.²¹⁶ Since the heavier substrate atoms, which now contribute to the scattering from the adsorbate layer, exhibit larger atomic scattering factors,³⁴¹ the intensity of the adsorbate spots should be further enhanced. This may also be ruled out here.

The region around the (00) spot is shown as a close-up in Fig. 5.2(b). Sharp spots are observed, indicating long-range order in the adsorbate layer. Almost all spots in the LEED pattern can be explained by a single PTCDA phase, depicted in dark red. In addition, a set of six diffraction spots around the specular reflection is observed which are identified as the first-order spots of a reconstruction of the PTCDA-covered Cu(111) surface [see Fig. 5.3(a) for a high-resolution LEED pattern, as well as Figs. 5.3(b) and 5.5 for corresponding LEED spot profiles along the $[11\bar{2}]$ direction]. Note that these spots are *not* present on the clean Cu(111) surface. Upon (mild) annealing at 470 K for 5 min, weak spots of a second PTCDA phase (green) appear [see Fig. 5.2(c)]. The two individual phases and the surface reconstruction will be described in detail below. By subsequent deposition of additional PTCDA molecules, giving a total coverage of 3 ML PTCDA, additional weak spots develop, in particular for k_{\parallel} values of 0.3–0.6 \AA^{-1} [see Fig. 5.2(d)]. Some of them can be assigned to the two already present phases of PTCDA. Those which are not explained by these two PTCDA phases could *not* be modeled by surface structures with unit cells which either accommodate one or two flat-lying PTCDA molecules without unreasonably large intermolecular distances or massive overlap of the vdW radii, respectively. These spots are marked with black crosses. Because they have very low intensities, the corresponding, so far unknown structures must be considered minority species which are not of further interest in the context of the present

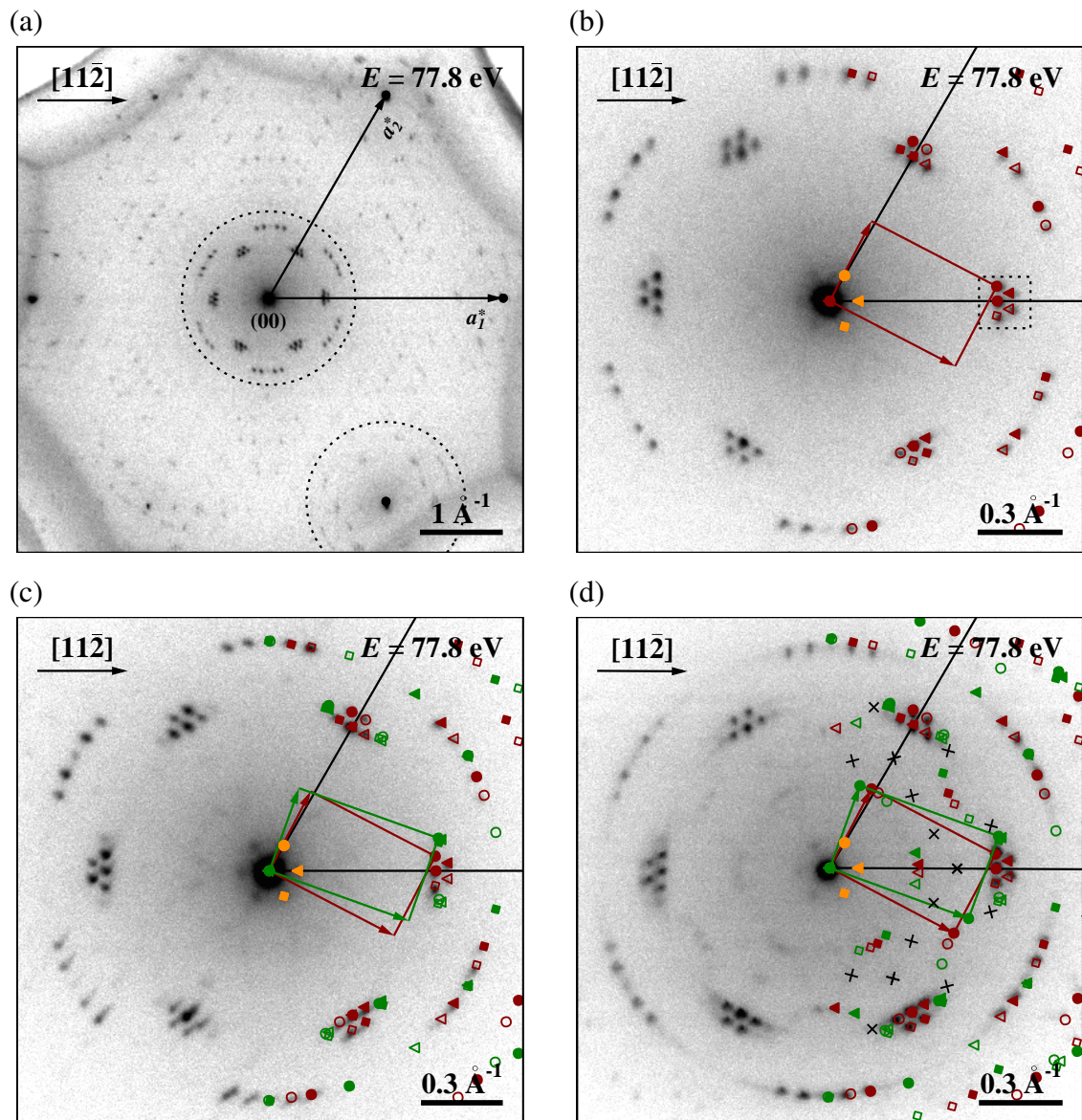


FIG. 5.2. LEED patterns of PTCDA on the Cu(111) surface. (a) 1 ML PTCDA/Cu(111), (b) close-up of the region around the specular reflection [dashed circle around the (00) spot in (a)] for 1 ML PTCDA/Cu(111), (c) 1 ML PTCDA/Cu(111) after annealing at 470 K for 5 min, and (d) 3 ML PTCDA/Cu(111), prepared from (c) by additional deposition of PTCDA molecules. On the right-hand sides of the LEED patterns, corresponding simulations are superimposed. Different colors refer to different phases present at the surface while different symbol shapes indicate different domains of one particular phase: α phase spots are shown in dark red, β phase spots in green, and surface reconstruction spots in orange. Substrate directions, substrate spots, and reciprocal substrate vectors are depicted in black. Black crosses mark positions in k space where (weak) diffracted intensity is observed in addition to those spots which are explained by the simulations. Dashed circles in (a) highlight very similar spot patterns around the (00) and the first-order (i.e., the {10} and {11}) substrate spots, respectively. The framed region in (b) is shown as a close-up in Fig. 5.3(c). All measurements were performed at an electron energy of 77.8 eV and a sample temperature of 100 K.

work.^{342, b)} Besides, very weak and indistinct intensity in the vicinity of the (00) spot (at k_{\parallel} values of about $0.2\text{--}0.3 \text{ \AA}^{-1}$) may be detected in Figs. 5.2(b) and (c). However, further analysis was not possible since these features are at the detection limit of the SPA-LEED instrument. Also, they were not observed in all of the accomplished preparations. In sum, besides the surface reconstruction, two different PTCDA phases were observed. In principle, these phases exist from the (sub-)monolayer to the multilayer regime of PTCDA on the Cu(111) surface. This finding indicates again that the PTCDA overlayers are *not* commensurate (see also above).

5.3.1 Ordered PTCDA structures

First, we turn to the analysis and the description of the two individual, ordered PTCDA structures which give the diffraction spots marked in dark red and green in Fig. 5.2. As judged from the relative spot intensities, the former originate from the main PTCDA phase (α) while the second phase is a minority phase (β).

Structural clarification

The most prominent feature in the LEED patterns in Fig. 5.2 is the double-triangle arrangement of diffraction spots [see the framed region in Fig. 5.2(b), for example]. Figure 5.3(c) shows a high-resolution LEED image of this double-triangle motif for 1 ML PTCDA/Cu(111). This motif is quite characteristic for herringbone (HB) phases of PTCDA on the Ag(111)^{98, 113} and Au(111)^{114, 116} surfaces. In contrast to those two coinage metal (111) surfaces, however, where two neighboring triangle composed of six diffraction spots are observed, the $\{11\}$ and $\{20\}$ spots^{c)} behind this motif form a *corner-connected* double-triangle on Cu(111). Nonetheless, the presence of a HB phase also on the Cu(111) surface may be presumed. For that reason, the observed PTCDA phase will be referred to as main HB phase or α phase in the following (see also below). Also for the minority phase, a herringbone arrangement of the molecules is expected because the corresponding LEED pattern is qualitatively similar to that of the main HB phase α [see the respective unit cells and the positions of the $\{10\}$ spots in Fig. 5.2(d), for example]. Figure 5.3(d) shows typical spot profiles for the $\{11\}$ spots of the α phase, recorded along the $[\bar{1}10]$ direction. A fit of several Lorentzian functions to the spot profiles reveals that all $\{11\}$ spots, which form the baseline of the double-triangle motif in Fig. 5.3(c), have the same full width at half maximum (FWHM) within $\pm 5\%$. Therefore, the central spot most probably results from a perfect superposition of two individual $\{11\}$ spots, resulting in the observed, corner-connected double-triangle arrangement of the α phase (that is, the main HB phase) $\{11\}$ and $\{20\}$ spots.

We will now describe the structural clarification for PTCDA/Cu(111) and the resulting structural models in more detail. Corresponding simulations of the LEED patterns have already been presented in Fig. 5.2 above. We focus on the (sub-)monolayer regime first [see Figs. 5.2(a)–(c)]. The simulations for both PTCDA phases, namely, the α and β phase, are in very good agreement with the experimental observations. Noticeably, all $\{h0\}$ and $\{0k\}$ spots for which h or k is odd are systematically extinct in the monolayer regime [see Figs. 5.2(b) and (c)]. From

^{b)}Conclusive real-space models of these structures are not available. One may also speculate that (some of) the additional spots originate from adsorbate structures formed by (or at least including) decomposed PTCDA molecules or from facets. The presence of facets can in principle be evidenced in a SPA-LEED experiment by varying the kinetic energy of the incident electrons.²¹⁵ Unfortunately, such measurements are not available here.

^{c)}The curly brackets (braces) denote families $\{hk\}$ of symmetry-equivalent spots. In the course of the present work, a sixfold symmetry has been assumed for the coinage metal (111) surfaces, although the real symmetry is only threefold due to the ABC stacking of the atomic layers in the bulk of *fcc* crystals.^{20, 343}

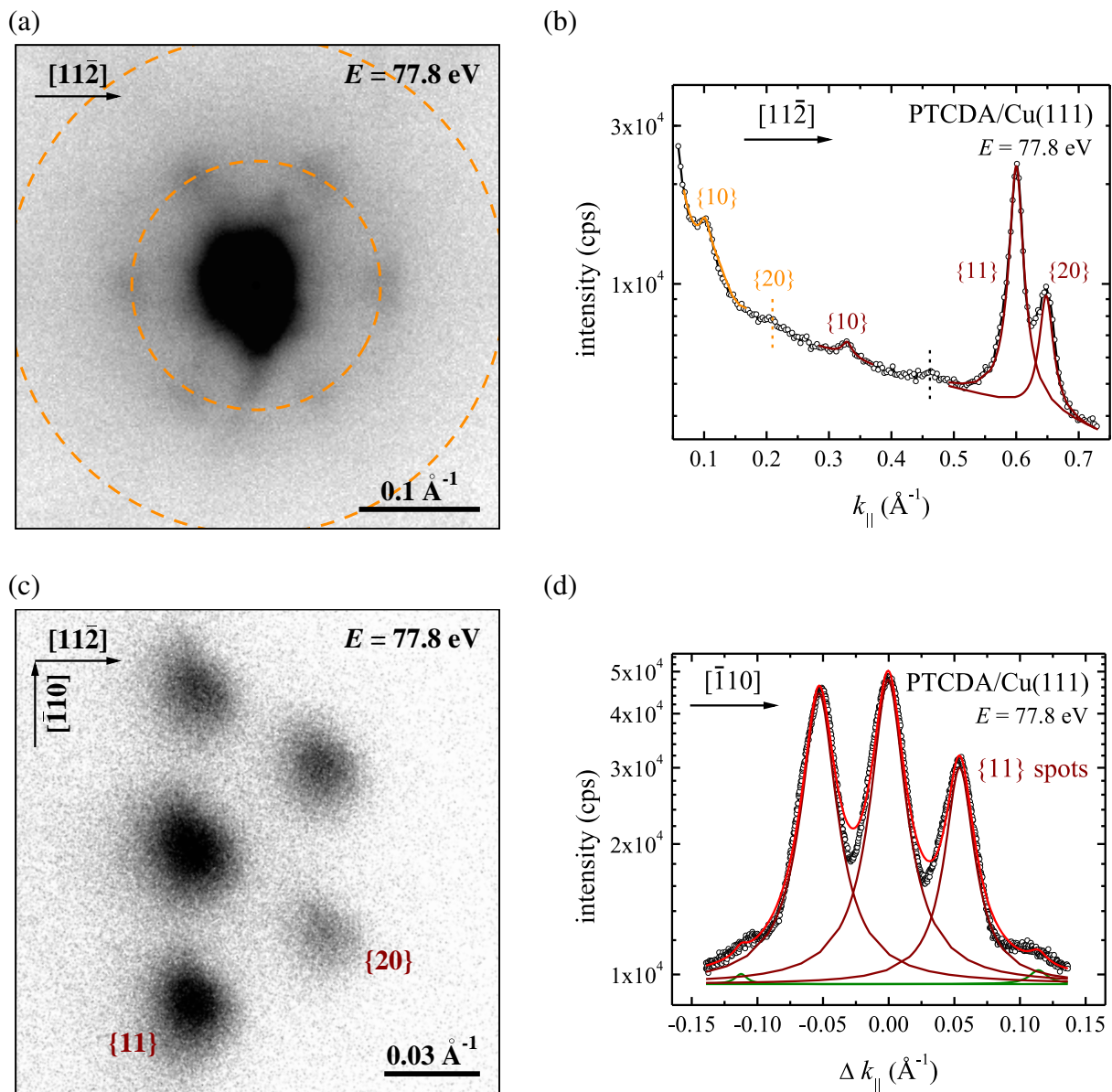


FIG. 5.3. High-resolution one-dimensional LEED scans and two-dimensional LEED patterns of PTCDA/Cu(111). (a) Two-dimensional LEED pattern of the (00) spot and the first-order reconstruction spots for 1 ML PTCDA/Cu(111), prepared by thermal desorption of multilayers. Dashed orange circles mark the (expected) radial positions of the long-range reconstruction spots. (b) LEED spot profiles along the $[11\bar{2}]$ direction for 1 ML PTCDA/Cu(111) after annealing at 470 K for 5 min [see Fig. 5.2(c) for the corresponding two-dimensional LEED pattern]. Profiles of the surface reconstruction spots (orange) and the α phase spots (dark red) have been fitted with Lorentzian line shapes. The black dashed line marks a spot profile which could not be indexed. Further LEED spot profiles along the $[11\bar{2}]$ direction, including also the specular reflection, are shown in Fig. 5.5. (c) Two-dimensional LEED pattern of the double-triangle motif in the LEED pattern of 1 ML PTCDA/Cu(111) [see also Fig. 5.2(b)]. (d) LEED spot profiles of those spots which form the base line of the double-triangle motif in (c), i.e., the $\{11\}$ spots of the α phase (dark red), recorded along the $[\bar{1}10]$ direction. Again, the profiles have been fitted with Lorentzian line shapes. In addition, weak spot profiles originating from the β phase (green) can be identified. The sum of all components is represented by a red line ($E = 77.8$ eV, $T_{\text{sample}} = 100$ K).

TABLE 5.2. Structural results for PTCDA on the Cu(111) surface, obtained from SPA-LEED experiments, and proposed model parameters. The lattice constants b_i , the enclosed angle β , and the area of the unit cell, A_{uc} , are given. ϕ denotes the enclosed angle between the surface lattice vectors \mathbf{a}_1 and \mathbf{b}_1 , ϱ is the angle of inclination of the long molecular axis with respect to \mathbf{b}_1 (values in square brackets refer to the second molecule within the unit cell), and τ is the herringbone angle, i.e., the enclosed (acute) angle between the long molecular axes of the two symmetry-nonequivalent molecules in the unit cell. In addition, the two-dimensional space groups and the superstructure matrices \mathfrak{M} are given (HB = herringbone, n.a. = not applicable).

	α phase (HB)	β phase (HB)	surface reconstruction
b_1 (Å)	12.4(2)	11.8(2)	2.56
b_2 (Å)	19.5(3)	19.9(5)	68.8(13)
β (°)	90.0(9)	90.0(13)	120
A_{uc} (Å ²)	242(6)	234(6)	152(3)
ϕ (°)	2.5(7)	10.3(10)	0
ϱ (°)	40.0 [140.0]	41.5 [138.5]	n.a.
τ (°)	80.0	83.0	n.a.
Two-dim. space group ^a	$p2gg$	$p2gg$	$p1$
\mathfrak{M}	$\begin{pmatrix} 4.98(9) & 0.25(7) \\ 4.06(11) & 8.79(15) \end{pmatrix}$	$\begin{pmatrix} 5.01(8) & 0.95(9) \\ 3.03(15) & 8.82(20) \end{pmatrix}$	$\begin{pmatrix} 1.00 & 0.00 \\ 0.00 & 26.92(52) \end{pmatrix}$

^aOnly the atomic positions within the adsorbate layers are considered for the determination of the two-dimensional space groups whereas the substrate surface atoms are neglected. The symmetry of the respective interface structures in their entireties, i.e., including the substrate atoms, reduces to space group $p1$ for both HB phases.

this observation, the presence of glide planes in both adsorbate structures can unambiguously be concluded.^{157,210} The derived structural parameters which are summarized in Table 5.2 are well compatible with the above-made conclusion of herringbone structures being formed by the PTCDA molecules on the Cu(111) surface. In particular, the lattice parameters of the α phase (that is, of the main HB phase), $b_1 = 12.4(2)$ Å, $b_2 = 19.5(3)$ Å, and $\beta = 90.0(9)^\circ$, are identical to those of the β modification of bulk PTCDA within the errors [see Table 2.1]. The lattice parameters of the β phase (that is, of the minor HB phase), $b_1 = 11.8(2)$ Å, $b_2 = 19.9(5)$ Å, and $\beta = 90.0(13)^\circ$, agree with those of the α modification. The corresponding superstructure matrices \mathfrak{M} are $(4.98(9) \ 0.25(7) \mid 4.06(11) \ 8.79(15))$ and $(5.01(8) \ 0.95(9) \mid 3.03(15) \ 8.82(20))$ with respect to the unreconstructed Cu(111) surface. In both superstructure matrices, one column has integer numbers (within the error margins) as matrix entries only. Thus, both structures exhibit *point-on-line* (p-o-l) commensurability with the (unreconstructed) Cu(111) surface.³⁴⁴ Note that this finding for the two PTCDA phases, which are present in (sub-)monolayer regime on Cu(111), also holds with respect to the *reconstructed* surface (see also Sec. 5.3.2 below) since the direction of the compression of the surface layer induced by the reconstruction is parallel to the respective grid lines, to which p-o-l commensurability is observed. Thus, the relevant integer matrix entries (in the first column in each case) remain unaffected by the compression of the surface layer, that is, they are identical with respect to both the reconstructed and the unreconstructed Cu(111) surface. The corresponding superstructure matrices with respect to the reconstructed Cu(111) surface will be given explicitly in Sec. 5.3.2 below. For the β phase, real commensurability (which is identified by *all* matrix entries being integers^{157,344}) might even be possible within the error margins.

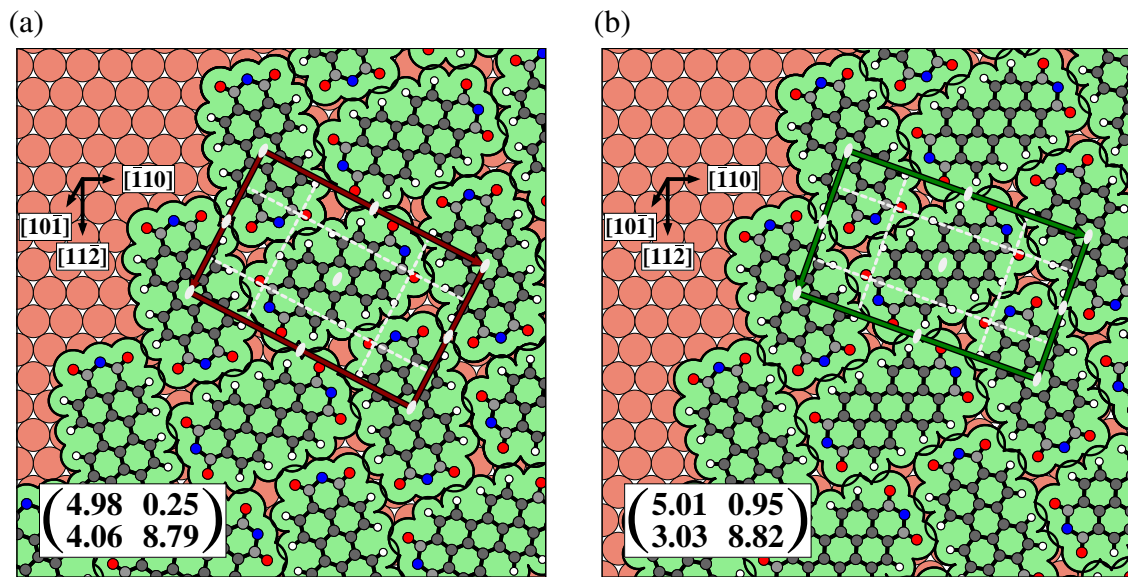


FIG. 5.4. Structural models of the PTCDA phases on the Cu(111) surface which are present in the (sub-)monolayer as well as in the multilayer regime, as deduced from SPA-LEED experiments: (a) α /main HB phase and (b) β /minor HB phase. The PTCDA molecules are shown as ball-and-stick models, including a two-dimensional projection of the molecular vdW surface. The adsorption sites have been chosen arbitrarily. The Cu(111) surface is shown in its ideal, unreconstructed state. Solid lines indicate the respective unit cells, i.e., dark red for the α phase and green for the β phase. The substrate directions are also indicated. The superstructure matrices are given as insets. Symmetry operations are shown in light gray.

Conclusive models for the PTCDA structures are depicted in Fig. 5.4. In both structures, the flat-lying PTCDA molecules are densely packed and arranged in a herringbone motif.^{105–107} In accordance with the findings from LEED, glide planes are present in the unit cells, resulting in the two-dimensional space group $p2gg$ in both cases. Due to the molecular arrangement on the surface, $C_{\text{funct}}-\text{O}\cdots\text{H}-C_{\text{peryl}}$ hydrogen bonds may form.^{4,111} In addition, the HB arrangement is favored by the quadrupole moment of the PTCDA molecules.⁴ The β phase bears similarities to structure ‘2’ proposed by Wagner *et al.* [see also Fig. 5.1(b)]:¹¹⁵ The superstructure matrix for structure ‘2’ may also be expressed as $(5.75 \ 1.25 \mid 3.40 \ 9.80)$.³ The orientations of the unit cell vectors of structure ‘2’ then agree with those of the β phase within $\pm 1.6^\circ$ for b_1 and are parallel for b_2 (within $\pm 0.2^\circ$). The discrepancies in the length of the unit cell vectors may be due to an improper correction of the STM images for thermal drift, and/or they may be an artifact of the structural modeling. Note, however, that no indications of the structure ‘1’ proposed by Wagner *et al.*¹¹⁵ are found. The authors of Ref. 115 present STM images of 0.4 ML PTCDA/Cu(111) where the ratio of the two structures is approximately 1 : 1 (Fig. 2 in that publication). Judging from the observed LEED patterns, we find only the α phase to be present in the submonolayer regime, i.e., for coverages of 0.25 ML.^{d)} Yet, a commensurate phase was never observed.

The average domain size for the α phase was deduced from fits of Lorentzian line shapes to the $\{11\}$ spot profiles along the $[11\bar{2}]$ direction, as shown in Fig. 5.3(b).^{e)} It amounts to about

^{d)}It can not be fully excluded that spots originating from the (potentially also existing) β phase were overlooked in this SPA-LEED experiment due to their weakness. If the β phase had actually been present, the respective domains would have been small in their lateral dimensions and small in number. Note that the sample was not post-annealed in this experiment.

^{e)}Note that the $[11\bar{2}]$ direction coincides with that of the α_1^* substrate vector.

315 Å for 1 ML PTCDA/Cu(111) after mild annealing [see Fig. 5.2(c)], proving again the long-range order of the prepared films. Before annealing, the average domain size is lower by $\approx 15\%$. Furthermore, the effective transfer width, as calculated from the FWHM of the (00) spot, is 290 Å after mild annealing (to be compared to 265 Å prior to the annealing step). Therefore, two aspects can be concluded here: (a) The effective transfer width has increased by about 5% in comparison to the clean Cu(111) surface (see also Sec. 5.2). Thus, the adsorption of PTCDA on the Cu(111) surface (including subsequent mild annealing) does not only lead to an (improved) ordering within the adsorbate layer but also, to a smaller degree, at the Cu(111) surface itself. (b) The size of the PTCDA domains is not necessarily limited by the coherence of the surface which is found to be about 8% smaller. Apparently, the PTCDA domains can overgrow domain boundaries at the substrate surface to some extent.

We now proceed with the structures for PTCDA coverages above 1 ML. Figure 5.2(d) has already shown a typical LEED pattern for 3 ML PTCDA/Cu(111). In addition, Fig. 5.5 presents spot profiles for PTCDA overlayers of different thickness which were recorded along the $[11\bar{2}]$ direction. Most prominent, except for the specular reflection, are the {11} and {20} spot profiles of the α phase. They do not shift as a function of coverage. Two scenarios are possible here. On the one hand, only a single wetting layer of PTCDA molecules is present at the interface while the additional molecules form nanocrystals,³³⁸ which are not visible in LEED. On the other hand, the higher layers adapt the structure of the first PTCDA layer such that there is no mismatch between the layers. The latter scenario is much more likely due to several reasons. Firstly, the intensities of the prominent spot profiles increase with PTCDA coverage. Note at this point that the one-dimensional LEED scans in Fig. 5.5 are normalized to their maximum intensities. Secondly, the (relative) intensity of the specular reflection decreases. Thirdly, for a coverage of 3 ML, also a {10} spot is observed, which is hardly detectable in the monolayer regime, in full agreement with the findings from the two-dimensional LEED patterns in Fig. 5.2. Thus, the extinction rules do not apply, and glide planes are no longer present in the unit cell.

This last observation may be understood as follows. The proposed space group $p2gg$ of the PTCDA unit cell only pertains if the Cu atoms at the surface are neglected. If they are taken into account, all symmetry operations are lost and the space group is $p1$. However, the LEED patterns for 1 ML PTCDA/Cu(111) are nicely modeled under the assumption of $p2gg$ space-group symmetry. Apparently, the scattering from the PTCDA layer remains unaffected by the presence of the Cu atoms underneath. We speculate that the much smaller periodicity of the Cu atoms as single scatterers in comparison to the larger PTCDA molecules is indeed too small in order to be “felt” by the electrons scattered at the PTCDA layer. In the presence of multilayers, however, the periodicity of scatterers in both layers is identical. As a result, lower-lying layers may no longer be neglected in the determination of potential symmetry operations within the unit cell. Since the unit cells in adjacent PTCDA layers are most likely shifted with respect to each other, as is the case for PTCDA in the bulk phases,^{107,110} all symmetry operations disappear, making $p1$ the valid space group. In conclusion, our LEED data indicate that PTCDA exhibits either a true layer-by-layer (Frank-van der Merwe) growth or a layer-plus-islands (Stranski-Krastanov) growth with two or more complete layers. The latter had already been proven by TPD investigations.³³⁸

Closer inspection of the spot profiles in Fig. 5.5 reveals an additional aspect. For the one-dimensional LEED scan of 6 ML PTCDA/Cu(111), the intensity ratio of {11} and {20} spot profiles is inverted in comparison to the spot profiles for lower coverages (see Fig. 5.5, top). Two explanations are plausible: Either multiple scattering effects play a role here which alter the structure factor and thereby the intensities of the spots.¹¹³ Or the azimuthal orientation with respect to the substrate surface changes by a few degrees for coverages above 3 ML, with the result that rather the {20} than

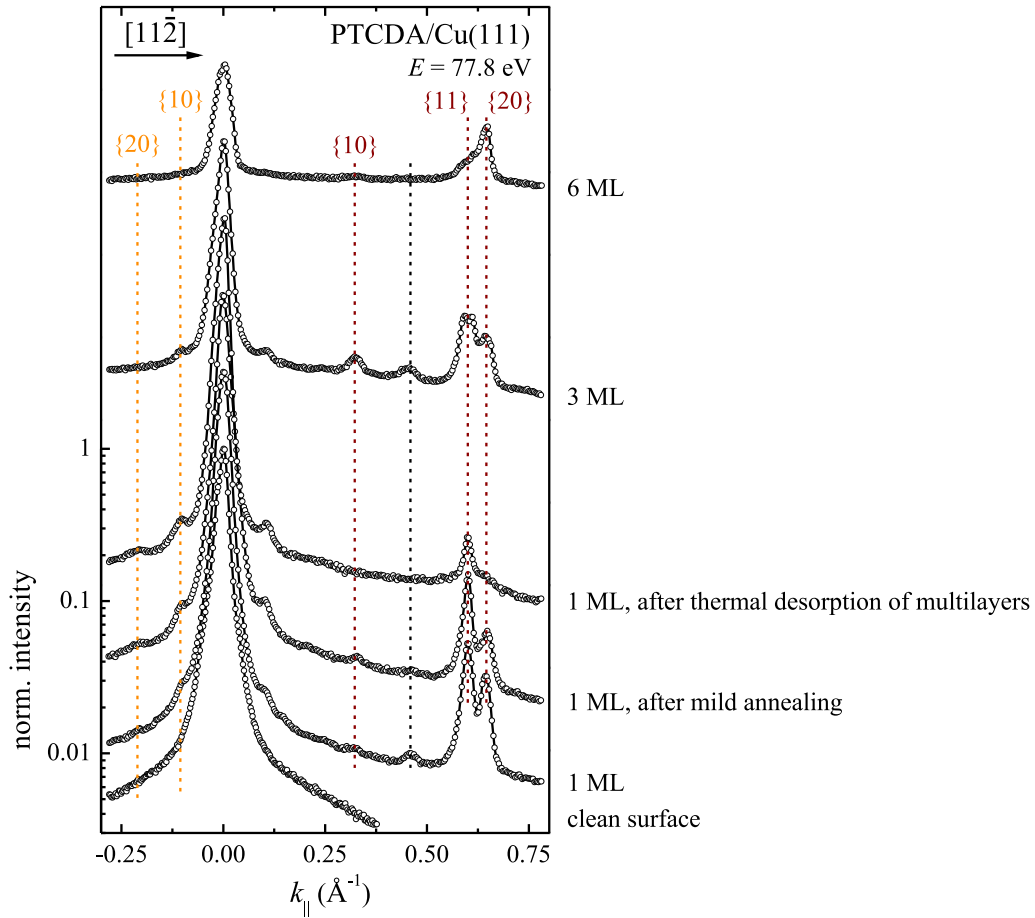


FIG. 5.5. LEED spot profiles of PTCDA on the Cu(111) surface at different stages of the sample preparation. All one-dimensional LEED scans have been recorded along the $[11\bar{2}]$ direction, i.e., along the direction of the \mathbf{a}_1^* vector, and normalized to their maximum intensities ($E = 77.8$ eV, $T_{\text{sample}} = 100$ K). The spot profiles are indexed and color-coded in accordance with the simulations already presented in Fig. 5.2, i.e., α -phase spot profiles in dark red and surface-reconstruction spot profiles in orange. Spot profiles which could not be indexed are marked in black. Note that the splitting of the $\{11\}$ spot in the case of 3 ML PTCDA/Cu(111) (second profile from the top) is an experimental artifact which is absent for all other adsorbate spots, and which is most probably caused by inhomogeneities of the electromagnetic field.

the $\{11\}$ spots are detected in the $[11\bar{2}]$ direction, as opposed to the situation for lower coverages.^{f)} Considering also the LEED patterns for PTCDA multilayers on the PTCDA/Cu₃Au(111) surface (see Sec.6.6.1), the former explanation is true. By annealing at 575 K for a few seconds, where higher layers of PTCDA are desorbed,³³⁸ a PTCDA monolayer with the usual intensity ratio of the diffraction spots can be recovered. Yet, the long-range order of the PTCDA structure is reduced in comparison to before, as judged from the intensity and the width of the spot profiles. Among others, this may be caused by the rather rapid cooling with a rate of about 3.5 K s^{-1} to low temperatures (100 K). According to the observed LEED pattern (not shown), solely the α phase, that is, the main HB phase of PTCDA, is present as a monolayer phase on the Cu(111) surface while, again, no indications for a commensurate PTCDA phase¹¹⁵ are found.

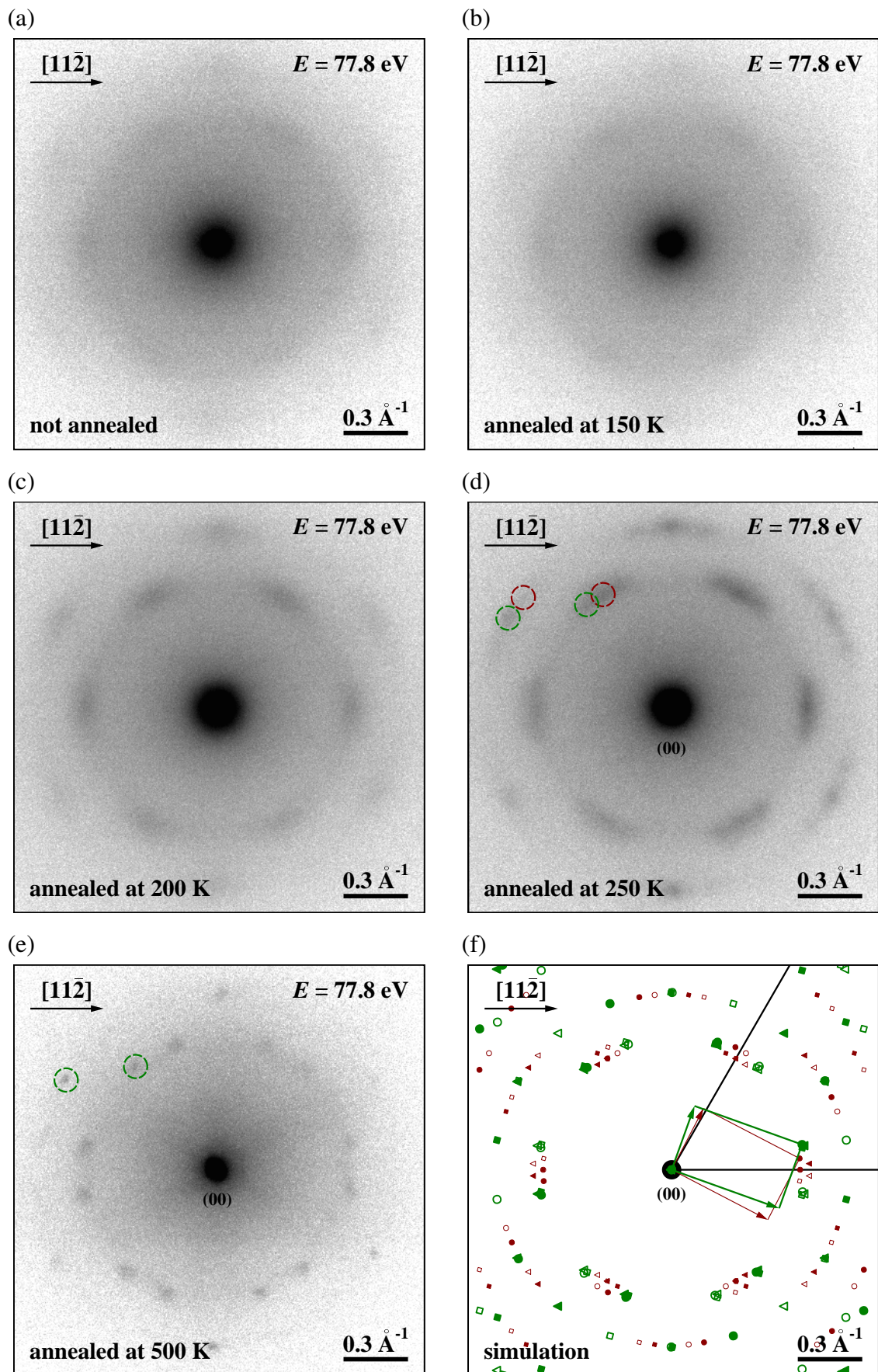
^{f)}Unfortunately, a two-dimensional LEED pattern of this preparation with 6 ML PTCDA/Cu(111) is not available.

Deposition at low sample temperature

Since a PTCDA structure comparable to structure ‘1’ by Wagner *et al.*¹¹⁵ could not be prepared by deposition with the sample being at room temperature, also the effect of deposition at lower sample temperature was investigated. Figure 5.6(a) shows the observed LEED pattern after the deposition of an equivalent of 1 ML PTCDA onto the Cu(111) surface at a sample temperature of 100 K. No sharp spots are detected, and only very weak and diffuse intensity may be discerned at positions in k space where spots are expected for the two HB phases [see Fig. 5.6(f)]. Upon stepwise annealing to higher temperatures for 5 min each, the diffuse intensity transforms to slightly more distinct spots, as shown in Figs. 5.6(b)–(d). Interestingly, the intensities of the spots from the *minor* HB phase β is *higher* than those of the *main* HB phase α at all stages of the preparation. Thus, the α phase seems to evolve only to a very small extent and with marginal long-range order. Remarkably, the signal-to-background ratio of the (00) spot intensity is still on the order of 1×10^3 for the PTCDA-covered Cu(111) surface, being only slightly smaller than that of the clean surface (by a factor of 3 to 5). From this finding, we conclude that a significant amount of the deposited PTCDA molecules is not in direct contact with the Cu(111) surface but located in higher layers and/or nanocrystals (which are not visible in LEED).³³⁸ Apparently, due to the Ehrlich-Schwoebel barrier,^{345–347} diffusion of these PTCDA molecules across step edges of the adsorbate layer(s) towards the bare (that is, still-uncovered) Cu(111) surface is kinetically hindered at these temperatures ($T \leq 250$ K), inhibiting the formation of larger two-dimensional PTCDA islands. This conclusion is based on the picture of a “hit-and-stick” mechanism of the PTCDA adsorption process at low temperatures.^{348–350} After annealing to 500 K for 5 min, only the β phase remains. The intensities of the corresponding LEED spots, however, are as weak as for the preparations at room temperature (see also Fig. 5.2). Hence, the absolute surface coverage of this phase is still low, even in the absence of the α phase.

Note that all LEED patterns in Fig. 5.6 are shown on an identical scale. Therefore, the width and the intensity of the LEED spots, as well as the background intensity are directly comparable. It is apparent that the width of the (00) spot increases by annealing at 200 K and 250 K, respectively, while it is strongly reduced after annealing at 500 K. At the same time, the background intensity around this spot increases at first and eventually decreases again. This may be interpreted as follows: When deposited onto the cold Cu(111) surface, the PTCDA molecules are essentially immobilized and, due to the low temperature of 100 K, they can hardly overcome the activation energy for surface diffusion. Therefore, a static disorder is present at the surface which causes a constant background intensity.²⁰⁰ Upon stepwise annealing, molecular diffusion is activated but only to an extent which is *not* sufficient for the formation of *large*, long-range ordered islands. However, the statistical distribution of the molecular islands on the surface now results in an increased background around the specular reflection and a broadening due to the decreased coherence at the surface.²⁰⁰ Further annealing leads to an increased order of the (still small) β phase islands, enhancing the coherence at the surface again. From the sharpening of the (00) spot it can be concluded that the other molecules, which have been deposited initially [the nominal coverage

FIG. 5.6 (following page). Temperature dependence of the structure formation for PTCDA on the Cu(111) surface: SPA-LEED patterns of 1 ML PTCDA/Cu(111) (a) after deposition at 100 K and (b–e) after annealing at elevated temperatures for 5 min. All measurements were performed with 77.8 eV electron energy at a sample temperature of 100 K. Note that the grayscale is identical for all images. (f) Simulation of the LEED patterns for the two previously observed structures, namely, the α phase (dark red) and the β phase (green). Corresponding regions in (d) and (e), where diffracted electron intensity is expected for these phases, are marked with dashed circles.



amounted to 1 ML PTCDA/Cu(111)], are no longer statistically distributed across the Cu(111) surface. Since no α phase islands have formed and since the annealing temperatures are too low for thermal desorption,³³⁸ we speculate that the additional PTCDA molecules, which are not incorporated in islands of the β phase, aggregate in three-dimensional nanocrystals³³⁸ which the LEED technique is not sensitive to. In any case, a new, so-far unknown phase is not formed. Note, however, that, in contrast to the findings for the experiments at room temperature, no reconstruction spots around the specular reflection are observed.^{g)}

5.3.2 Surface reconstruction

As outlined above, six additional spots are observed in the vicinity of the specular reflection for the PTCDA-covered PTCDA surface [see Fig. 5.3(a) for a high-resolution LEED pattern, as well as Figs. 5.3(b) and 5.5 for corresponding LEED spot profiles along the $[11\bar{2}]$ direction]. In principle, several scenarios may lead to the presence of such “satellite” spots:²¹⁵ (1) multiple scattering, (2) a vicinal surface, (3) faceting, or (4) reconstruction of the surface. The first scenario does not explain the observed spots, as has been thoroughly tested by simulating the respective LEED patterns of multiple scattering including the scattering vectors of the first-order (i.e., the $\{10\}$ and $\{11\}$) substrate spots. The scenarios (2) and (3) can be ruled out by the fact that (weak) second-order spots are observed in the one-dimensional LEED scans of Fig. 5.5. Therefore, the satellite spots may be unambiguously attributed to the presence of a surface reconstruction. This conclusion is further supported by the fact that the satellite spots are absent for the clean surface, dismissing the scenario of a vicinal surface. Furthermore, PTCDA-induced faceting of the Cu(111) surface may be ruled out on the basis of experimental findings for PTCDA adsorption on another coinage metal (111) surface. While the adsorption of PTCDA has been shown to allow the formation of facets on *vicinal* Ag(111) surfaces,³⁵¹ no faceting occurs on the true Ag(111) surface.^{98,113} Facets of structures formed by the adsorbate molecules themselves, i.e., facets of PTCDA nanocrystals, are expected only for coverages of several ten monolayers.¹¹³ In the present case, the PTCDA coverage amount to 1 ML, and the Cu surface is of (111) orientation where the packing of surface atoms is most dense. Thus, considering the surface atoms alone, no energetic gain may be expected from a potential formation of less densely packed facets.

It can be concluded that a reconstruction of the Cu(111) surface is induced by the PTCDA adsorption. The size of the reconstruction domains of about 300 Å, as derived from the width of the first-order spot profiles [see Fig. 5.3(b)], is comparable to the average domain size of the PTCDA α phase (about 315 Å, see above), further corroborating this conclusion. The observed LEED pattern is explained by a reconstruction with superstructure matrix $\mathfrak{M} = (1\ 0\ | 0\ 26.9(5)) \approx (1\ 0\ | 0\ 27)$ (see also Table 5.2). Note that for the first-order substrate spots the satellites could not be clearly resolved. Only shoulders on the respective spot profiles were observed which may be interpreted as reconstruction spots of low intensity (not shown).

The reconstruction may be modeled by assuming a uniaxial contraction of the surface unit cell by 3.70% along the $[\bar{1}10]$ direction. As depicted in the real-space model in Fig. 5.7, 28 Cu atoms instead of the intrinsic (bulk) number of 27 are now present in the surface layer. This model is inspired by the $(\sqrt{3} \times 22)$ reconstruction which is present on the Au(111) surface already in the *clean* state, and which is also explained by a uniaxial contraction of the surface unit cell along the $[\bar{1}10]$ direction.^{352–354} In the case of Au(111), however, the corresponding LEED spots are

^{g)}In the corresponding one-dimensional LEED scans, the reconstruction spots (if present) are at the detection limit of the SPA-LEED instrument. Only small shoulders on the (00) spot profiles are observed which may be interpreted as reconstruction spots of very low intensity.

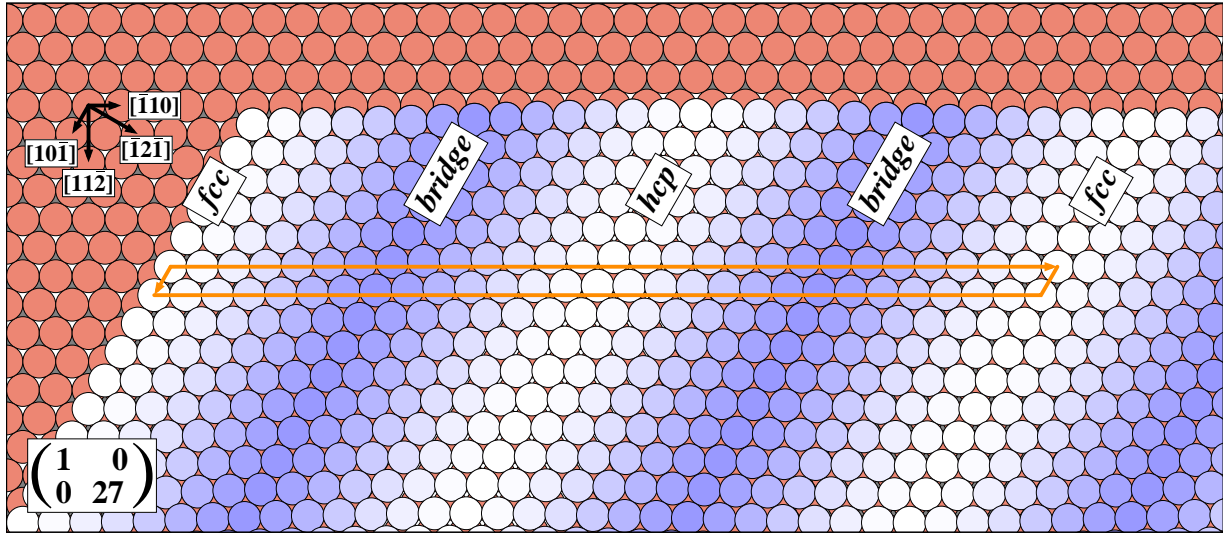


FIG. 5.7. Model of the surface reconstruction present for PTCDA adsorption on Cu(111). PTCDA molecules are omitted for clarity. The substrate atoms in the surface layer are depicted in white and different shades of blue. The intenseness of the blue color represents the lateral deviation of a given surface atom from a preferred threefold hollow site, being either of *fcc* (white) or *hcp* nature (dark gray). At the passage from one type to the other, also bridge sites are occupied. The unit cell is indicated by solid orange lines. The respective superstructure matrix is given as an inset. The substrate directions are also indicated.

not observed along the $[11\bar{2}]$ direction but at an angle of 30° with respect to that direction. In order to account for these differences in the observed LEED patterns of the reconstructed (clean) Au(111) and (PTCDA-covered) Cu(111) surfaces, the model in Fig. 5.7 includes a shear along the $[\bar{1}10]$ direction in addition to the uniaxial contraction, thereby achieving agreement with the experimental observations.^{h)}

The two effects described above, namely, the *uniform* contraction accompanied by the shear, would only lead to a new surface unit cell with vectors $s_1 = a_1$, $s_2 = \frac{27}{28} a_2 = 0.9643 a_2$ for the Cu(111) surface reconstruction, which does not explain the observed periodicity of $27 \cdot a_2$ along $[\bar{1}10]$. Therefore, in analogy to the Au(111) reconstruction,^{352–354} also a lateral displacement of the Cu atoms in the surface layer has to be considered. Figure 5.7 shows a plausible scenario where the Cu atoms at the surface are offset along the $[11\bar{2}]$ direction up to a maximum value of 0.85 \AA . This allows most of the Cu atoms in the compressed surface layer to adopt bulk-termination sites, i.e., threefold hollow sites corresponding to either face-centered cubic (*fcc* hollow sites, depicted in white in Fig. 5.7) or hexagonal close-packed (*hcp* hollow sites, depicted in dark gray) stacking. At the passage from one type of threefold hollow sites to the other, bridge sites may be adopted. These regions are sometimes referred to as *discommensuration lines*³⁵⁷ or *soliton walls*³⁵⁸ although

^{h)}Note that, in principle, the observed LEED pattern of the Cu(111) surface reconstruction can also be simulated by a superstructure of type $\mathfrak{M} \approx (1 \ 0 \mid 13.5 \ 27)$. This implies a uniaxial contraction along the $[\bar{1}2\bar{1}]$ direction which indeed forms an angle of 30° with the $[\bar{1}10]$ direction. Therefore, the above-proposed shear along $[\bar{1}10]$ would not be needed to build a real-space model (see also below). Nonetheless, a conclusive model for this alternative superstructure could not be found. Furthermore, this alternative superstructure is *not* in commensurate registry with the subsurface layers of the Cu(111) crystal. Although a few examples have indeed been reported,^{355,356} incommensurate surface reconstructions are very unusual. In general, a commensurate registry is present because then largest possible number of surface atoms is located in their preferred sites. These preferred sites are given by the energy potential which, in turn, is determined by the bulk structure. In the present case of the Cu(111) surface, *fcc* threefold hollow sites are preferred due the ABC layer stacking in *fcc* crystals. On these grounds, the alternative superstructure with $\mathfrak{M} \approx (1 \ 0 \mid 13.5 \ 27)$ is dismissed in the course of the present work.

the soliton model, implying a well-defined transition between two commensurate and uncontracted regions,³⁵⁸ has been shown to be oversimplified.³⁵⁴ For the Au(111) reconstruction, also a vertical displacement of the surface atoms of up to $\pm 0.20(5)$ Å has been reported.^{353,354,357} This cannot be excluded for the PTCDA-covered Cu(111) surface but XSW experiments have not given any indication.⁴³ Furthermore, we speculate that, if present, a potential vertical displacement of the Cu atoms is smaller than that of the Au(111) atoms. The former may be more compressible than the latter (see also Table 2.3) since they do not experience the so-called lanthanide contraction.¹⁴⁶ Hence, the steric demand and consequently the need for a vertical evasion may be reduced for the Cu surface atoms. This is indeed the case, as has been revealed by DFT calculations.³⁵⁹

It is known that organic adsorbates can in principle modify an intrinsic surface reconstruction^{360–362} and can also induce a reconstruction on an ideal surface.^{118,363} In the latter case, Ni(110) and Cu(110) surfaces were used as substrates. To the best of our knowledge, however, a reconstruction of a densely packed *fcc* (111) surface induced by the adsorption of organic molecules has not been reported so far. Now the questions arises whether the reconstruction of the Cu(111) surface results from the fact that one of the PTCDA phases is commensurate to the reconstructed surface.ⁱ⁾ In order to clarify this point the corresponding superstructure matrices with respect to the new basis (s_1, s_2) were determined. While, for the α phase, the formation of the surface reconstruction does not lead to a commensurate registry [The superstructure matrix $\mathfrak{M}_{\text{rec}}$ with respect to the reconstructed Cu(111) surface is $(4.98(9) \ 0.26(7) \ | \ 4.06(11) \ 9.12(16))$ for the α phase of PTCDA^{j)}], the β phase is commensurate to the surface reconstruction within the error margins [superstructure matrix $\mathfrak{M}_{\text{rec}} = (5.01(8) \ 0.98(10) \ | \ 3.03(15) \ 9.15(21))$]. Note, however, that a commensurate registry cannot be excluded for the unreconstructed surface, either (see Table 5.2). Judging from the higher intensities of the reconstruction spots in comparison to those of the β phase, a possibly commensurate β phase is not the driving force for the surface reconstruction. Besides, the reconstruction is hardly observed when only the β phase is present on the surface [see Fig. 5.6(e)]. Therefore, the reconstruction most probably results from electronic effects alone.

5.4 Concluding Discussion

Two PTCDA phases have been found to form on the Cu(111) surface for both coverages below and above 1 ML. Both phases bear strong similarities with the two PTCDA polymorphs which are known for the bulk material, and exhibit p-o-l commensurability. In a generous and wide interpretation, the PTCDA structure which represents the minority phase in the present study might be identified as structure ‘2’ described by Wagner *et al.*¹¹⁵ A PTCDA phase, however, which is identical or, at least, similar to the commensurate structure ‘1’ reported by Wagner *et al.*¹¹⁵ was

ⁱ⁾Note again that the p-o-l commensurability of the two phases α and β with respect to the unreconstructed Cu(111) surface is not lifted by the surface reconstructing. This is due to the fact that the direction of the induced compression of the surface layer is in fact along the respective grid lines, to which p-o-l commensurability is observed. (see also Sec. 5.3.1 above).

^{j)}Note that, starting from a different domain of the PTCDA α phase with $\mathfrak{M} = (4.98(8) \ 4.73(8) \ | \ 4.06(13) \ -4.73(11))$ with respect to the *unreconstructed* Cu(111) surface, $\mathfrak{M}_{\text{rec}} = (4.98(8) \ 4.91(9) \ | \ 4.06(13) \ -4.91(12))$ is obtained with respect to the *reconstructed* surface. This domain is commensurate to the reconstructed substrate within the error margins. However, assuming the real superstructure matrix for a truly commensurate registry to be $\mathfrak{M} = (5.00 \ 4.82 \ | \ 4.00 \ -4.83)$ with respect to the unreconstructed Cu(111) surface and $\mathfrak{M}_{\text{rec}} = (5.00 \ 5.00 \ | \ 4.00 \ -5.00)$ with respect to the reconstructed surface, respectively, the observed LEED patterns of the α phase are not described correctly by the corresponding simulations (not shown). For example, the linear baseline of the double-triangle motif in the two-dimensional LEED patterns [see also Fig. 5.3(c)] is not reproduced.

not found. On the contrary, the α phase, that is, the main HB phase, from this work has not been present in the STM studies of submonolayer PTCDA/Cu(111) by Wagner *et al.*¹¹⁵ We now turn to the discussion of these discrepancies in the experimental findings.

Thermodynamic versus kinetic stabilization

The most apparent difference in the experimental procedures between the two studies is the deposition rate. While Wagner *et al.* employed deposition rates of 1–2 ML min⁻¹,¹¹⁵ the PTCDA molecules were deposited at a rate of 0.25 ML min⁻¹ in the present work. Apparently, lower growth rates favor the formation of the α phase, in particular. Thus, we conclude that the α phase is the thermodynamically stable phase while all other structures are kinetically stabilized. This conclusion is further supported by the findings that (1) the α phase can only be transformed to a marginal extent into the β phase, that is, the minor HB phase, upon annealing of the sample, and that (2) even in those cases where the β phase is exclusively present at the surface only small and/or poorly ordered PTCDA islands are formed.

The β phase can be prepared selectively by PTCDA deposition onto the cold Cu(111) surface and subsequent annealing. Clearly, the activation energy for the phase transition towards the α phase is too high to be overcome even at temperatures of 500 K, in agreement with earlier findings by Wagner *et al.* from STM investigations that mild post-annealing does not substantially alter the topography at the PTCDA/Cu(111) interface.¹¹⁵ However, these temperatures are sufficient to activate the formation (if not already present) or the further growth of nanocrystals at the cost of small, poorly ordered islands of the α phase which might have been present before. Employing the picture of *Ostwald ripening*,^{347,364} the island size for the α phase apparently needs to exceed a critical value in order to be stable against annealing at these elevated temperatures in those cases where PTCDA nanocrystals (or nucleation centers for their formation, respectively) are already present at the surface. This proves again that the α phase is *not* kinetically, *but* thermodynamically stabilized.^{k)} In this herringbone phase the molecules are able to form intermolecular hydrogen bonds ($C_{\text{funct}} - O \cdots H - C_{\text{peryl}}$). In addition, the molecular arrangement is favored by quadrupole interactions. Both effects contribute to the energetic stabilization of this phase. For the two structures proposed by Wagner *et al.*,¹¹⁵ however, where the packing density of the molecules on the surface is substantially lower (by 15–20 % in comparison to the structures presented in this work and in comparison to the bulk structures, as well; see also Tables 2.1, 5.1, and 5.2), these potential ways of energetic stabilization may be ruled out. At the same time, a strong impact on those structures by the presence of the Cu(111) surface may not be anticipated since the preferred herringbone motif is still present. Again, this supports the conclusion of solely kinetic stabilization to be relevant for the formation of these metastable structures found by Wagner *et al.*¹¹⁵

Reconstruction of the PTCDA-covered surface

As opposed to Au(111),³⁵² for example, the clean Cu(111) surface does not show a reconstruction. According to DFT calculations, this can be explained by the rather small tensile stress of the Cu(111) surface and the high energetic cost for the Cu atoms to adopt non-threefold hollow sites at the surface.^{359,365} Upon PTCDA adsorption, however, the Cu(111) surface also exhibits a reconstruction. As already pointed out above, this is not caused by geometric effects. Thus, electronic effects must play a role in the reconstruction of the PTCDA-covered Cu(111) surface.

^{k)}Note, however, that forming the reconstruction of the PTCDA-covered Cu(111) surface may constitute a significant energetic barrier for the formation of the ordered PTCDA superstructure phases.

For PTCDA in the monolayer regime on Cu(111), UPS experiments have shown a strong charge transfer from the metal to the molecule upon adsorption.^{60,1)} Very likely, this charge transfer leads to a decreased electron density at the metal surface, thus reducing the attractive forces between neighboring, now “partially positive” Cu atoms. As a consequence, the surface force constant is smaller, making it energetically less unfavorable for the Cu surface atoms, which are now less tightly bound, to adopt non-ideal sites. The small tensile stress which is intrinsic to the surface may now be sufficient to induce the before-hindered reconstruction.^{365,366} In conclusion, there is a delicate balance between the tendency towards reconstruction on the one hand and the prevalent interatomic forces at the Cu(111) surface at the other hand. The electronic “perturbation” caused by PTCDA adsorption (through the accompanied charge transfer) obviously is sufficient to shift this balance from one side to the other, that is, towards the reconstruction of the Cu(111) surface.

Surface Bonding/Chemisorption

A strong influence of the Cu(111) surface on the arrangement of PTCDA molecules may *not* be deduced from the observed lateral structures. At the same time, however, the adsorption height of the molecule above the surface,⁴³ which is below the sum of the vdW radii of the involved atoms, shows that the surface bonding is of chemisorptive nature (see also Sec. 2.2.2). Consequently, the PTCDA molecules in the monolayer cannot be desorbed as intact molecules upon annealing, as shown in the present study and also earlier by TPD experiments.³³⁸ Besides, the most substantial changes in the electronic structure of the molecular valence states are observed for PTCDA adsorbed on the Cu(111) surface in comparison to Au(111) and Ag(111),⁶⁰ implying stronger surface bonding. In particular, the lowering of the LUMO below the Fermi level is ascribed to a significant charge redistribution upon adsorption, i.e., to negative charging of the adsorbed molecules.^{59,60} This certainly leads to Coulomb interactions at the metal/organic interface, explaining the chemisorptive nature of the (rather delocalized) bonding.

However, as has been mentioned in Sec. 2.2.2 already, the adsorption height of PTCDA on Cu(111) actually is larger than that on Ag(111) if the size of the substrate surface atoms is considered—as should be the case in order to render this relation meaningful (see Fig. 7.6 in Sec. 7.3, page 193, of the present work for a graphical representation of the correlation between the observed adsorption heights d_{vdW} , which have been corrected for the different vdW radii of the substrate atoms, and the work functions Φ of the clean substrates). Having this in mind, the surface bonding may be regarded as being weaker on the Cu(111) surface. Indeed, we do not find a commensurate registry between the PTCDA overlayer and the surface atoms, in contrast to the situation on Ag(111).^{98,113} This is consistent with the adsorption configuration of the PTCDA molecules:⁴³ Local $\text{O}_{\text{carb}}-\text{Cu}$ bonds cannot be formed due to structural reasons, and the O atoms are thus further away from the surface than the perylene core of the molecule. Here, the structural reasons are that (a) a well-defined, i.e., commensurate, registry between the O atoms in PTCDA and the Cu atoms in the substrate surface is missing (see above) and (b) the O atoms do (generally) not reside in surface sites which preferentially allow for the formation of such local $\text{O}_{\text{carb}}-\text{Cu}$ bonds (potentially on-top of the Cu atoms). Most of the O atoms in PTCDA do not have Cu atoms as potential binding partners in their periphery, simply.^{m)} Also, the difference in the lattice constants of

¹⁾Unfortunately, information on the explicit structure of the PTCDA layers in these experiments are not available.⁶⁰

^{m)}Note that this argument also holds for the two (sub-)monolayer structures proposed by Wagner *et al.*¹¹⁵ for PTCDA/Cu(111), although one of them indeed is commensurate (see also Fig. 5.1). Therefore, the XSW results by Gerlach *et al.* may be discussed regardless of the actual lateral structures of the PTCDA monolayers present in those experiments (which have not been specified).⁴³

the (111) surfaces of Cu and Ag [2.556 Å for Cu(111)²⁸⁷ and 2.889 Å for Ag(111),²⁸⁹ respectively] may play a role here. The relevance of local interactions will be discussed in detail in Chapter 7.

From the above conclusions, it becomes clear that the electronic structure of the molecular valence states alone does not have direct implications for (1) the bonding distance of the PTCDA molecules (which can be related to the strength of the chemisorptive surface bond^{56,57}), (2) the lateral structure of the PTCDA overlayer, and/or (3) the adsorption configuration of the molecules in this system. Interestingly, the experimental observations in the UP spectra are nicely reproduced by DFT calculations even if an artificial, commensurate PTCDA structure is assumed.¹⁵³ This shows that the electronic structure of PTCDA/Cu(111) is essentially independent of the actual geometric structure at the interface. In the present case, only the observed surface reconstruction is interpreted as to originate from electronic effects, in turn.

6

PTCDA on Cu₃Au(111)

The structural clarification of PTCDA on the Cu₃Au(111) surface is a further, consecutive step in our investigation of the detailed bonding mechanism(s) for PTCDA adsorption on the coinage metal surfaces. From the reported lateral and vertical structures of PTCDA on Au(111),^{54, 114, 116} Ag(111),^{55, 98} and Cu(111) surfaces^{43, 115} (see also Chapters 2 and 5), a general trend concerning the surface bonding may be deduced, as has already been mentioned in Sec. 2.2.2 and will be discussed in more detail in Chapter 7. Using the *ordered*, binary alloy Cu₃Au as the substrate material provides the possibility to study the predictive power of the chemically intuitive picture that the metal/molecule interactions increase and, at the same time, the adsorption heights decrease with the reactivity of the metal. Because now two types of metal atoms with different reactivity are present, namely, Cu and Au atoms, it may be anticipated that the overall reactivity of the surface follows from a Vegard-like behavior^{328, 367, 368} of the properties for the involved elements, yielding an adsorption configuration of the PTCDA molecules which is then a “compromise” between those on Au(111)⁵⁴ and Cu(111).⁴³

However, it cannot be excluded *a priori* that the surface bonding, and thus also the lateral and vertical structures, is not (solely) determined by the average composition and thus by the average reactivity of the substrate but rather by individual effects. Due to the higher fraction of Cu atoms in the substrate in combination with their higher reactivity, it appears almost as likely that the chemical interactions between the PTCDA molecules and the Cu atoms in the surface will be the dominant ones. To a certain extent, the Au atoms would be regarded as “spectators” in the surface bonding mechanism, contributing only by dispersive interactions and/or steric hindrance. Under these circumstances, the surface bonding gains a more localized character, due to specific interactions of the adsorbed PTCDA molecules with selected surface atoms, that is, here the Cu atoms. In this picture of more localized interactions across the metal/organic interface, a modification of the Cu₃Au(111) surface, via reconstruction or phase separation/segregation of the two elements, for example, may even be anticipated. In order to clarify the above-raised issues, the structure of the clean as well as the PTCDA-covered Cu₃Au(111) surface have been investigated with various experimental techniques within the present work.

6.1 Review of the literature

In the copper-gold system, the two elements exhibit complete miscibility over the full stoichiometric range Cu_xAu_{1-x} where $0 \leq x \leq 1$.³⁶⁹ In addition, three *ordered* binary alloys with well-defined stoichiometries are formed, namely, Cu₃Au, CuAu, and CuAu₃.³⁶⁹ At elevated temperatures, however, these stoichiometric phases undergo a phase transition into disordered phases. In the case of Cu₃Au, the first-order phase transition³⁷⁰ from the ordered to the disordered phase is observed at a critical temperature of $T_c = 663$ K.^{369, 371-375} Above T_c the Cu₃Au alloy forms an *fcc* structure (A1

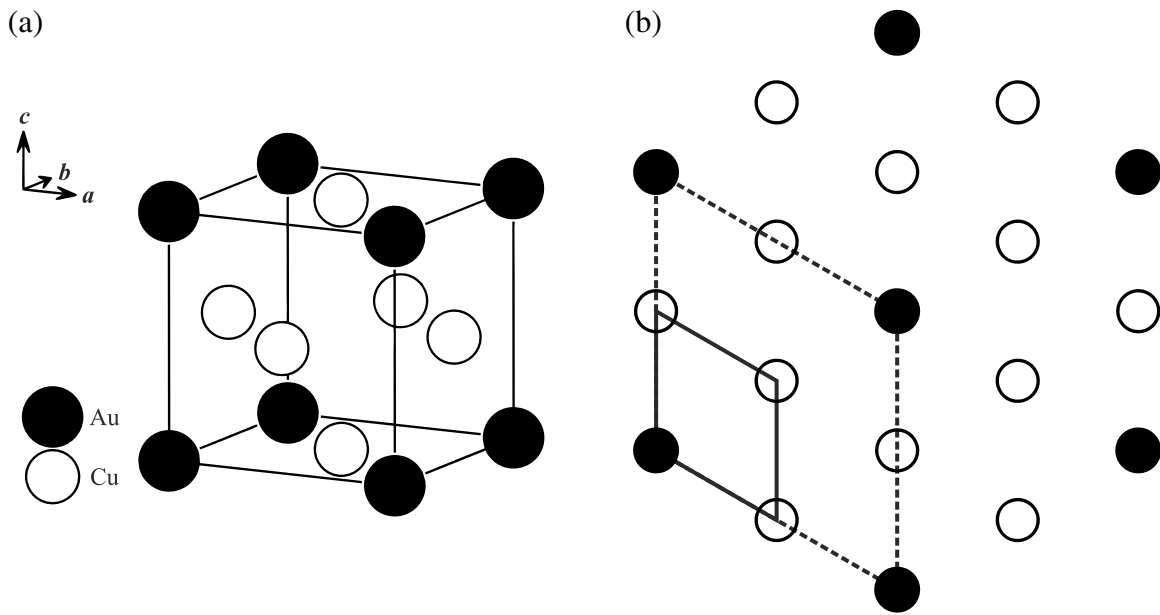


FIG. 6.1. Bulk structure and (111) surface of the ordered, binary alloy Cu_3Au . (a) Primitive cubic unit cell of Cu_3Au in the ordered bulk phase (L_{12} phase).^{369,375} The bulk lattice constant amounts to $a = 3.75 \text{ \AA}$.^{288,388} Au atoms are shown in black and Cu atoms in white. The lattice vectors a, b, c are indicated. (b) Schematic representation of the ideal $\text{Cu}_3\text{Au}(111)$ surface. The surface unit cell of the ordered phase is indicated by black dashed lines while the surface unit cell of the disordered phase is indicated by black solid lines. Note that the structure of disordered Cu_3Au can be described as being of *fcc* type. As a consequence, the ordered (111) surface of Cu_3Au is then referred to as a $p(2 \times 2)$ reconstruction of the disordered (111) surface.³⁸⁹

phase³⁶⁹) where all lattice positions are statistically occupied by Cu and Au atoms, respectively. Thus, while short-range order persists, long-range order vanishes in the disordered phase.³⁷⁵ Below T_c , i.e., in the ordered phase (L_{12} phase³⁶⁹), a primitive cubic structure is adopted where the Au atoms occupy the corner positions and the Cu atoms occupy all face-center positions of a cube, as shown in Fig. 6.1(a). The ordering phenomena in the bulk phase of Cu_3Au have widely been investigated, see Refs. 374, 376–381, for example. Investigations of the electronic structure have been reported in Refs. 382–387, for instance.

Also the structure and the properties of the canonical (111),^{390–400} (100),^{372,373,401–415} and (110) surfaces^{416–418} of Cu_3Au have been strongly investigated with various methods.⁴¹⁹ All canonical surfaces are terminated by surface layers which contain both Cu and Au atoms,⁴²⁰ although for the (100) and (110) surfaces a bulk-like termination with only Cu atoms would principally be possible, too [see also Fig. 6.1(a)]. However, for both surfaces a termination with lattice planes of CuAu composition is found.⁴²⁰ This is explained by the lower surface energy of the pure Au(*hkl*) surfaces in comparison to the respective pure Cu(*hkl*) surfaces (by about 25–35 % according to theoretical calculations; see Refs. 421, 422).^{418,423,424} The ideal, well-ordered $\text{Cu}_3\text{Au}(111)$ surface is depicted in Fig. 6.1(b) and is of stoichiometric composition ($\text{Cu}_{0.75}\text{Au}_{0.25}$, as is the case for *all* lattice planes).⁴²⁰ Based on the *fcc*-type description of the Cu_3Au bulk structure in the disordered $A1$ phase, the ordered (111) surface is often described as a $p(2 \times 2)$ reconstruction of the disordered (111) surface [see the unit cell marked by black dashed lines in Fig. 6.1(b)].³⁸⁹ Crystal truncation rod (CTR) measurements have shown that the L_{12} phase exhibits the ordered structure of Cu_3Au up to the topmost (111) surface layer.³⁹⁷ However, an inward relaxation is observed, i.e., the in-

terlayer spacing between the first and the second layer is reduced by 2.3%.³⁹⁷ Besides, both Au and Cu sites are occupied only by 70% in the surface layer.³⁹⁷ In contrast, an AES experiment (on a different crystal) showed the surface of Cu₃Au(111) to be enriched in Au, i.e., a stoichiometry of Cu_{0.61}Au_{0.39} with an uncertainty of $\pm 6\%$ for the topmost surface layer.^{420,425} This finding has further been confirmed by reflection electron microscopy (REM) experiments,³⁹² theoretical work employing DFT,^{426–428} and additional AES investigations on (111)-oriented Cu-Au alloy films of various compositions.⁴²⁹ The Au-enrichment is restricted to the topmost layer, and the Au concentration may range from 50% to 75%.^{426–429} An Au-enrichment of the surface layers is also known for the Cu₃Au(110) surface.^{416–418} DFT calculations predict, however, that the adsorption of O atoms on the Cu₃Au(111) surface leads to the segregation of Cu towards the topmost layer.^{426,428} In contrast, an “Au-enrichment” at the (clean) Cu₃Au(111) surface can also be achieved by dealloying through selective, anodic dissolution of the Cu atoms.^{399,400,430} The so-obtained Au-rich (or even Cu-free, pure Au) layers are no longer epitaxial to the underlying substrate but exhibit a larger in-plane lattice constant which is close to that of pure Au(111).⁴⁰⁰

To the best of our knowledge, little is known about the adsorption of *large* molecules on Cu₃Au surfaces. So far, only photoemission spectra of metal carbonyl clusters on polycrystalline Cu₃Au,⁴³¹ as well as STM images of isolated pentacene molecules on Cu₃Au(100)⁴³² and thiol self-assembled monolayers (SAMs) on Cu₃Au(111)⁴³⁰ have been reported. Yet, the adsorption of *small* molecules or atoms, namely, oxygen, nitrogen, and sulfur,^{433–439} has been investigated in more detail, revealing quite noticeable differences for the different surface orientations. For example, oxygen readily adsorbs on the Cu₃Au(110) surface at room temperature,^{436,440} as is also the case for Cu(110).^{441–445} N₂ molecules do not adsorb on the (110) surface of either the alloy⁴⁴⁶ or pure Cu.^{447,448} However, nitrogen-covered (110) surfaces of both Cu₃Au and Cu may be obtained by means of the ion implantation technique and subsequent annealing.^{446–448} The same holds for the Cu₃Au(100)⁴³⁴ and Cu(100) surfaces,^{447,448} as well. In contrast to the (110) surface, however, O₂ molecules do not adsorb on Cu₃Au(100)⁴³⁴ or on Au(100) while they indeed adsorb on the Cu(100) surface.^{449–451} Oxygen-covered Cu₃Au(100) may only be obtained via the ion implantation technique and subsequent annealing,⁴³⁴ in analogy to the nitrogen-covered (100) and (110) surfaces of Cu₃Au. Thus, it has been concluded that the Cu₃Au(110) surface behaves rather like the pure Cu(110) surface while the (100) and (111) Cu₃Au surfaces behave like the pure Au(100) and pure Au(111) surfaces, respectively.^{434,452} This surprising finding disagrees with chemical intuition that Cu₃Au(111), which exhibits the highest nominal ratio of Cu atoms at the surface, is expected to act Cu(111)-like. Thus, it challenges the above-made hypothesis of prevailing interactions between the PTCDA molecules and Cu atoms at the surface.

Bearing in mind that the Cu₃Au(111) surface may also behave like the pure Au(111) surface concerning the adsorption of large organic molecules, the lateral structure of PTCDA on Au(111) is briefly reviewed at this point. The adsorption configuration and the electronic structure have already been reviewed in Sec. 2.2.2. In the monolayer regime, PTCDA forms two herringbone (HB) phases and, to a minor extent, a so-called square (S) phase on the Au(111) surface.^{114,116,453} The respective lattice parameters are summarized in Table 6.1. One of the HB phases (A) is preferentially present in preparations with high deposition rates¹¹⁶ and/or at room temperature.¹¹⁴ Because the presence of phase A is strongly reduced upon preparation at elevated sample temperatures (450 K), this phase is interpreted as being kinetically stabilized, and hence it is also referred to as *non-equilibrium* phase.¹¹⁴ The other HB phase (B) exists with two different azimuthal orientations, resulting in a point-on-line (p-o-l) registry with respect to the native reconstruction of the Au(111) surface for each of the two azimuths.¹¹⁴ The so-called S phase has almost exclusively been ob-

TABLE 6.1. Reported structural parameters for PTCDA on the Au(111) surface, obtained from LEED, SPA-LEED, and STM experiments.^{114,116,453} Three individual phases have been found, namely, two herringbone phases (A, B) and one so-called square phase (S). Note that two azimuthal orientations which are not symmetry-equivalent exist for the phases B and S, respectively. The lattice constants b_i , the enclosed angle β , and the area of the unit cell, A_{uc} , are given. ϕ denotes the enclosed angle between the surface lattice vectors \mathbf{a}_1 and \mathbf{b}_1 , and τ is the herringbone angle, i.e., the enclosed (acute) angle between the long molecular axes of the two symmetry-nonequivalent molecules in the unit cell (n.a. = not available).

Phase	A (Ref. 114)	B ₁ , B ₂ (Ref. 114)	S ₁ , S ₂ (Ref. 116)
b_1 (Å)	12.3(1)	12.1(1)	16.1(8)
b_2 (Å)	19.2(2)	19.2(2)	16.5(8)
β (°)	90.0(3)	90.0(3)	91(2)
A_{uc} (Å ²)	236(3)	232(3)	266(21)
ϕ (°) ^a	22.5(3)	9.5(5), 7.0(5)	4(2), 33(2)
τ (°) ^b	n.a.	83	83

^aDeduced from the angles δ given in Refs. 114, 116, which describe the angle between \mathbf{b}_1 and the $[\bar{1}\bar{1}2]$ direction of the Au substrate, by geometrical considerations.

^bTaken from Ref. 453.

served in STM images^{114,116,453, a)} and exhibits a nearly quadratic unit cell with an $\approx 10\%$ smaller molecular packing density^{116,453} in comparison to the two HB phases (see also Table 6.1). Again, islands with two symmetry-nonequivalent azimuthal orientations are found.¹¹⁶ The formation of the S phase is more favored by elevated sample temperatures during PTCDA deposition, and its surface fraction may also be increased by post-annealing of the prepared PTCDA films.⁴⁵³

6.2 Experimental procedure

Two individual Cu₃Au(111) crystals were used for the experiments reported here. One crystal was used for the SPA-LEED investigations, and a second one for the STM experiments. This second crystal which was slightly smaller in height, as required by technical/experimental limitations in the STM chamber, was also employed in the XPS and XSW investigations. Both Cu₃Au(111) crystals were new and had not been prepared before. Due to the order-disorder transition of Cu₃Au upon annealing above 663 K (see Sec. 6.1), a customized surface preparation protocol had to be established. This protocol was in principle followed for both crystals in all experimental setups in use (within the technical capabilities), resulting in well-ordered surface structures. In all cases, the long-range order of the prepared, clean Cu₃Au(111) surfaces, which exhibited the typical $p(2 \times 2)$ reconstruction that is indicative of the ordered alloy, as well as that of the prepared PTCDA layers were proven by the bright and sharp LEED patterns.

^{a)}To the best of our knowledge, the only exception to the S phase being only observed in STM images are the XSW measurements of Henze *et al.*⁵⁴ In their work, the authors have determined the adsorption height of the C atoms of PTCDA/Au(111) in the S phase.⁵⁴ The obtained result has been concluded also to be representative for PTCDA/Au(111) in the two HB phases.⁵⁴

SPA-LEED experiments

During the first preparation cycle of the crystal employed in the SPA-LEED experiments, the $\text{Cu}_3\text{Au}(111)$ crystal was sputtered with Ar^+ ions of 1050 eV kinetic energy for 30 min at an Ar partial pressure of 5×10^{-5} mbar under normal incidence, resulting in an ion current of $4.5 \mu\text{A}/\text{cm}^2$ on the sample. Subsequently, the crystal was annealed at 1000 K for 15 min and then cooled to 623 K at a rate of 1 K s^{-1} . This sample temperature, which is 40 K below the critical temperature T_c for the transition to the disordered phase, was kept constant for another 15 h in order to allow the sample to restore the ordered bulk structure ($L1_2$ phase) again.³⁸¹ Eventually, the sample was cooled to room temperature with 0.1 K s^{-1} . Besides the $p(2 \times 2)$ reconstruction spots, additional sharp spots were present in the LEED pattern (not shown) which were attributed to the segregation of impurities from the bulk of the Cu_3Au crystals to the surface forming an ordered structure. In order to remove these impurities from the $\text{Cu}_3\text{Au}(111)$ surface, only one additional, shorter preparation cycle with annealing at significantly lower temperatures was necessary. In this and all further preparation cycles, the sample was sputtered with Ar^+ ions of 875–1050 eV kinetic energy for 15–30 min ($p_{\text{Ar}} = 5 \times 10^{-5}$ mbar, $I_{\text{sample}} = 4.5 \mu\text{A}/\text{cm}^2$) and annealed at 623 K for 1 h. Typical heating and cooling rates during the annealing process were $1\text{--}2 \text{ K s}^{-1}$ and $0.5\text{--}1.0 \text{ K s}^{-1}$, respectively.

For the SPA-LEED experiments, PTCDA was deposited with the sample temperature being between 300 K and 350 K, or at low temperatures (85–200 K). The latter procedure resulted in disordered films which did not show a LEED pattern. The PTCDA coverages were controlled via the deposition times and temperatures, and the deposition rates typically amounted to 0.2–0.5 ML/min, as revealed by QCM monitoring of the deposition process. The uncertainties in the absolute coverages are estimated to be approximately $\pm 10\%$. In those cases where post-annealing of the prepared PTCDA layers was performed typical heating and cooling rates were 1 K s^{-1} , respectively. Unless otherwise stated, all SPA-LEED measurements were performed at 85 K. Note that, apart from the expected changes, such as reduced spot intensities and small shifts of the spot positions caused by thermal expansion of the prepared sample, identical LEED patterns were observed also for measurements at room temperature. Since the intensity of the adsorbate-related diffraction spots was low, i.e., a factor of 10^2 or more smaller than that of the (00) spot for a coverage of 1 ML PTCDA, relatively high electron beam intensities were used during the LEED experiments in order to achieve decent integral spot intensities. The electric current generated on the sample by the incident electron beam usually amounted to 5–20 nA. In contrast to the findings for PTCDA/Cu(111) (see Sec. 5.2), beam damage to the prepared films was only observed for PTCDA multilayers ($\theta_{\text{PTCDA}} \geq 6 \text{ ML}$).

STM experiments

The second $\text{Cu}_3\text{Au}(111)$ crystal, which was employed in the STM experiments (and later also in the XPS and XSW experiments), was initially sputtered with Ar^+ ions of 1000 eV kinetic energy for 60 min ($p_{\text{Ar}} = 1 \times 10^{-5}$ mbar, $I_{\text{sample}} = 4 \mu\text{A}/\text{cm}^2$) under 45° incidence with respect to the surface normal, and then annealed at 975 K for 20 min. Again, additional sharp spots were observed in the resulting LEED pattern. In order to remove the surface impurities, which had segregated from the bulk, and to restore the ordered $L1_2$ phase of the $\text{Cu}_3\text{Au}(111)$ crystal, two additional preparation cycles with 30 min to 60 min sputtering with Ar^+ ions of 800 eV kinetic energy ($p_{\text{Ar}} = 1 \times 10^{-5}$ mbar, $I_{\text{sample}} = 2 \mu\text{A}/\text{cm}^2$) and 2 h to 4.5 h annealing at 623 K were necessary. Further preparations, giving optimal surface order, were performed as follows: sputtering with Ar^+ ions of 1050 eV kinetic energy for 30 min with $p_{\text{Ar}} = 1 \times 10^{-5}$ mbar and $I_{\text{sample}} = 2 \mu\text{A}/\text{cm}^2$ under

45° incidence with respect to the surface normal, and subsequent, stepwise annealing at 633 K, 623 K, and 610 K for 60 min each.³⁸¹ PTCDA was typically deposited at rates of 0.6–2.6 ML min⁻¹ with the sample being at room temperature, yielding PTCDA coverages of in the range of about 0.6 ML to 4.5 ML. The absolute coverages were determined from large-scale STM images with uncertainties of approximately ±10%. In some cases, post-annealing of the PTCDA layers was performed. Typical heating and cooling rates were 0.3 K s⁻¹ in all annealing steps for both the clean and the PTCDA-covered Cu₃Au(111) surface. All STM experiments were performed in constant current mode at room temperature. Typical tunneling parameters were bias voltages U_{bias} from -1 V to 1 V and tunneling currents I_t around 15 pA for the investigation of the PTCDA overlayers.

XPS and XSW experiments

The XPS and XSW experiments were performed in XSW setup II on the same Cu₃Au(111) crystal as the STM experiments before. Judging from the observed LEED patterns, repeated cycles of sputtering and annealing *below* the order-disorder transition temperature were sufficient in order to restore the long-range ordered structure at the sample surface, which had been present already in the earlier STM experiments. Annealing at higher temperatures was found not to be necessary. The preparation conditions were as follows: sputtering with Ar⁺ ions of 850 eV kinetic energy for 15 min with $p_{\text{Ar}} = 1.5 \times 10^{-5}$ mbar and $I_{\text{sample}} = 12 \mu\text{A}/\text{cm}^2$ under 30° incidence with respect to the surface normal, and subsequent annealing at 648 K for 60 min.³⁸¹ The heating and cooling rates during the annealing process were $\leq 1 \text{ K s}^{-1}$ and $\leq 0.5 \text{ K s}^{-1}$, respectively. PTCDA was deposited on the room-temperature sample at a rate of 0.3 ML/min. According to the integral ion current monitored by QMS during the deposition process (PTCDA fragment at $m/z = 124$ u), a coverage of 0.76(10) ML PTCDA/Cu₃Au(111) was obtained (see also Sec. 4.3.2). Post-annealing of the prepared PTCDA submonolayer was waived in this case.

All XPS and XSW data were conducted at room temperature. For determining the vertical positions of the atoms of interest, the (111) Bragg reflection of the Cu₃Au(111) substrate crystal (for which the respective lattice planes are parallel to the surface) was employed in the XSW measurements under near-normal incidence of the x-ray beam (with $d_{111} = 2.165 \text{ \AA}$, $\theta_{\text{B}} = 88^\circ$, and $E_{\text{B}} = 2865.04 \text{ eV}$). XP and Auger spectra of the substrate signals, namely, Au3d_{5/2}, Cu2p_{1/2}, Cu2p_{3/2}, and CuL₃M₄₅M₄₅, were acquired with a pass energy of 30 eV while the C1s and O1s spectra of the adsorbed PTCDA molecules were conducted with a pass energy of 100 eV ($E = 2858.0 \text{ eV}$ in each case). For the XSW experiments, pass energies of 50 eV (Au3d_{5/2}) and 100 eV (CuL₃M₄₅M₄₅, C1s, and O1s) were employed, respectively. Several XSW data sets were acquired for both the clean as well as the PTCDA-covered sample: three Au3d_{5/2} and three CuL₃M₄₅M₄₅ data sets for the clean surface (preparation no. Feb'11-1; see Table 4.3 in Sec. 4.3.2, page 56, of the present work), and two Au3d_{5/2} and three CuL₃M₄₅M₄₅ data sets for the PTCDA-covered surface (preparation no. Feb'11-2), respectively. Because the C1s and O1s XP spectra exhibited changes in both the peak shapes and the peak positions as a function of x-ray beam exposure, two C1s and two O1s XSW data sets were conducted in a *scanning* mode where the individual data points of one XSW photoelectron yield curve were collected on different, fresh spots on the sample (i.e., two data points per spot; see also Sec. 6.6.3). In addition, five C1s and four O1s XSW photoelectron yield curves were acquired in the usual, non-scanning mode.

6.3 Results for the clean $\text{Cu}_3\text{Au}(111)$ surface

The $\text{Cu}_3\text{Au}(111)$ surface was characterized in the clean state due to the ambiguous results concerning the surface composition. Yet, not only the surface stoichiometry was determined but also the $\text{Cu}_3\text{Au}(111)$ surface structure was further clarified by several, complementary experimental techniques. These aspects will be of importance for the understanding of the adsorption properties of PTCDA on this surface, in particular regarding the interface structure and the nature of the surface bonding, as will be reported in Secs. 6.5 and 6.6.

6.3.1 Lateral structure

Figure 6.2(a) shows a typical LEED pattern of the ordered $\text{Cu}_3\text{Au}(111)$ surface. Diffracted intensity which originates from the $p(2 \times 2)$ reconstruction of the surface can clearly be identified as sharp spots, proving the expected order of the binary alloy to be present at the surface.³⁸⁹ However, the intensity of the reconstruction spots is unexpectedly low in comparison to that of the (fundamental) substrate spots. Besides, it varies strongly with the kinetic energy of the electron beam, as the corresponding one-dimensional LEED scans show [see Fig. 6.2(b)]. This may indicate an incomplete or perturbed order of the surface and thus a more complex surface structure than the one depicted in Fig. 6.1(b) and also in Fig. 6.4(a) below for the ideal surface. The reason for the low intensity of the $p(2 \times 2)$ reconstruction spots observed in LEED will be addressed in detail below in conjunction with the STM results. Yet, the formation of either pure Cu or pure Au domains at the surface can be ruled out here. Such domains would result in additional spots with different k_{\parallel} values [up to $\pm 9\%$ judging from the lattice constants of the pure (111) surfaces] along the $[1\bar{1}2]$ direction which are not observed. Note at this point that the intense background around the first-order fundamental substrate spots in Figs. 6.2(a) and (b) for $E = 50.4$ eV was only observed at this particular electron energy and absent for all other electron energies. Due to the observed asymmetry of the respective shoulders we assume that the intense background may be an experimental artifact and originates rather from drastic and sudden changes in the detection efficiency of the SPA-LEED instrument for high k_{\parallel} values at low electron energies than from structural properties of the surface.

Order of the $\text{Cu}_3\text{Au}(111)$ surface

The coherence of the prepared surfaces is exceptionally good, as the width of the observed spot profiles reveal. At an electron energy of $E = 72.3$ eV, which nominally corresponds to an in-phase condition for the (00) spot ($S = 3.0$), the effective transfer width $T_{w,\text{eff}}$ amounts to about 655 \AA on average [see Table 6.2 and also Fig. 6.2(d)]. Furthermore, a transfer width of as much as 1050 \AA was found at an energy of 32.1 eV (also nominally in-phase, $S = 2.0$). For nominal out-of-phase conditions, $T_{w,\text{eff}}$ amounts to 790 \AA at 50.2 eV ($S = 2.5$) and to 410 \AA at 98.4 eV ($S = 3.5$). Thus, $T_{w,\text{eff}}$ decreases with increasing E (see also Table 6.2). The observed trend for $T_{w,\text{eff}}$ as a function of E is well explained by the presence of bulk defects in the $\text{Cu}_3\text{Au}(111)$ substrate crystal, in particular, the mosaicity inherent to the sample. Small angle mosaics, i.e., misorientation of the crystallites within the bulk crystal, lead to a spot-profile broadening which is proportional to the magnitude of the vertical scattering vector k_{\perp} .²¹⁵ In the present case of $\text{Cu}_3\text{Au}(111)$, the width of the (00) spot, to which $T_{w,\text{eff}}^{(00)}$ is inversely proportional [see also Eq. (3.46)], indeed scales linearly with $|k_{\perp}|$ and quadratically with $E \propto |k_{\perp}|^2$ in good approximation, as curve fittings to the data have revealed (not shown).

TABLE 6.2. Averaged effective transfer widths $T_{w,\text{eff}}$ deduced from LEED spot profiles of the clean Cu₃Au(111) surface for different electron energies. $T_{w,\text{eff}}$ values are given for the specular reflection [(00)] as well as for the first-order spots of both the $p(2 \times 2)$ reconstruction (only present in the ordered $L1_2$ phase) and the substrate, i.e., the fundamental spots (present in the disordered $A1$ phase, too, originating from the average fcc structure; see also Fig. 6.1). $S_{(00)}$ denotes the scattering condition for the (00) spot where integer values refer to in-phase conditions and half-integer values refer to out-of-phase conditions. Note that different scattering conditions $S_{(hk)}$ apply for the first-order spots. The stated, averaged values of $T_{w,\text{eff}}$ are subject to a mean error of about 25 Å (n.a. = not available).

E (eV)	$S_{(00)}$	$T_{w,\text{eff}}$ (Å)		
		(00)	$p(2 \times 2)$	substrate
32.1	2.0	1050	200	n.a.
50.2	2.5	790	190 ^a	160
72.3	3.0	655	150	115 ^b
98.4	3.5	410	280 ^c	150

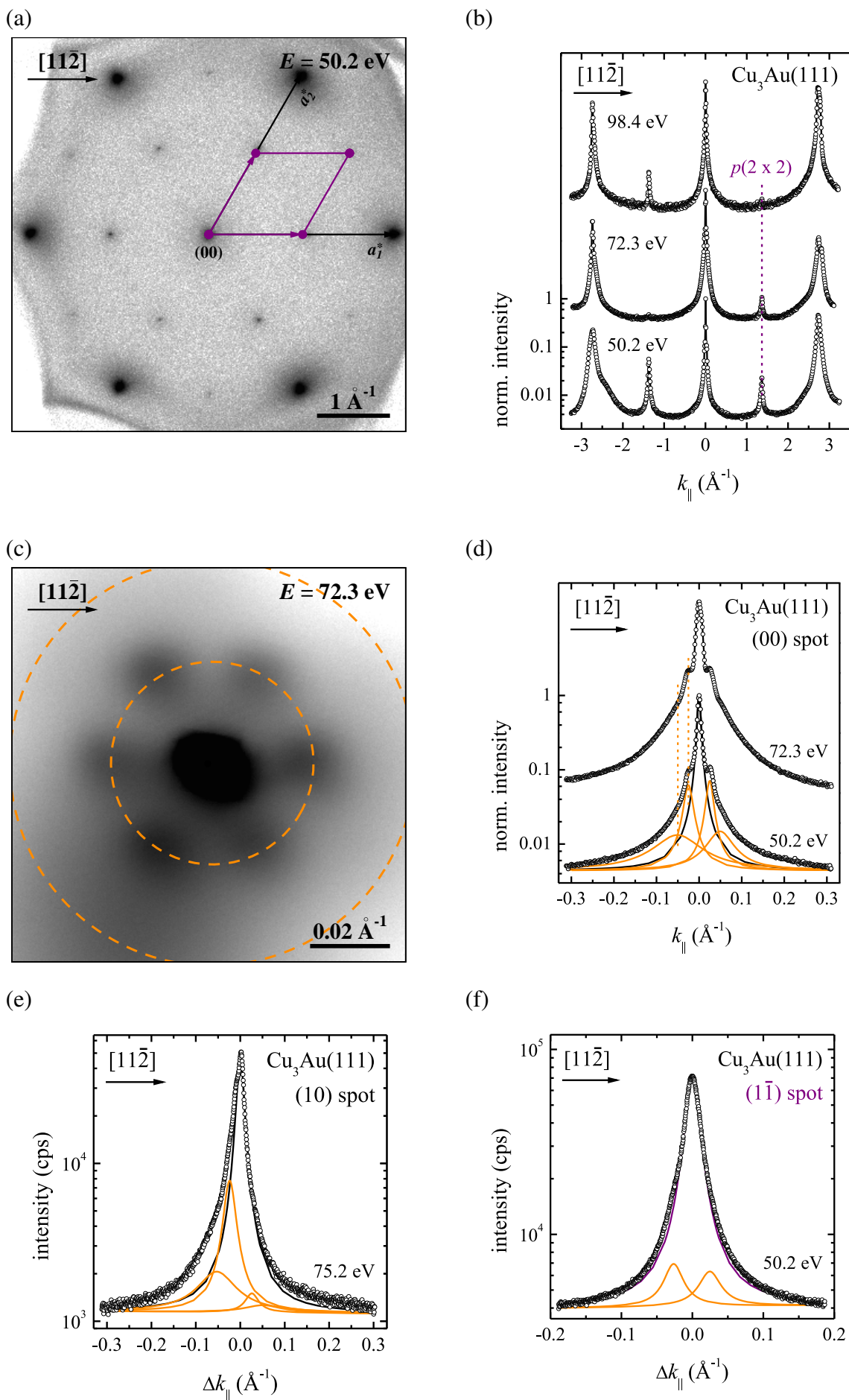
^aA single maximum value of $T_{w,\text{eff}} = 280$ Å was obtained under optimized conditions (such as focusing of the electron beam, positioning of the sample) at this electron energy.

^bA single maximum value of $T_{w,\text{eff}} = 335$ Å was obtained under optimized conditions (such as focusing of the electron beam, positioning of the sample) at a slightly higher electron energy of 75.2 eV.

^cA single maximum value of $T_{w,\text{eff}} = 315$ Å was obtained under optimized conditions (such as focusing of the electron beam, positioning of the sample) at this electron energy.

From the widths of the first-order spots^{b)} of both the substrate [i.e., the first-order fundamental spots which are present in the disordered $A1$ phase of Cu₃Au(111), too, originating from the average fcc structure] and the $p(2 \times 2)$ reconstruction^{c)} significantly smaller average values of $T_{w,\text{eff}}$ are deduced. For example, $T_{w,\text{eff}}$ is found to be 115–160 Å for the substrate, and 150–280 Å for the $p(2 \times 2)$ reconstruction, respectively (see Table 6.2), in the above-noted energy range. Note that the electron energies which were employed here do not correspond to explicit in-phase or

FIG. 6.2 (following page). One-dimensional LEED scans and two-dimensional LEED patterns of the clean Cu₃Au(111) surface. The individual electron energies are specified in the respective figures. (a) Two-dimensional LEED pattern of the ordered Cu₃Au(111) surface. The reciprocal lattice vectors \mathbf{a}_i^* of the (disordered) substrate are indicated in black while the unit cell of the $p(2 \times 2)$ reconstruction is indicated in purple. (b) One-dimensional LEED scans along the $[11\bar{2}]$ direction through the specular reflection at various electron energies. Note that the shoulder on the (10) substrate spot profile at $E = 72.3$ eV is an experimental artifact which is absent at all other substrate spots and electron energies and which is most probably caused by inhomogeneities of the electromagnetic field. (c) Close-up of the LEED pattern in (a) around the (00) spot. Dashed orange circles mark the (expected) radial positions of the long-range reconstruction spots. (d) Close-up of the one-dimensional LEED scans in (b) for two different energies. In addition, spot profiles of the (e) (10) substrate spot at $E = 75.2$ eV and the (f) $(1\bar{1})$ spot originating from the $p(2 \times 2)$ reconstruction at $E = 50.2$ eV are shown. Lorentzian line shapes have been fitted to the spot profiles in (d)–(f). Note that the intense background around the first-order fundamental substrate spots in (a) and (b) for $E = 50.4$ eV was only observed at this particular electron energy and absent for all other electron energies. All measurements were performed at 85 K, except for the spot profile measurement at 98.4 eV in (b) ($T = 345$ K) and those in (e) and (f) ($T = 325$ K).



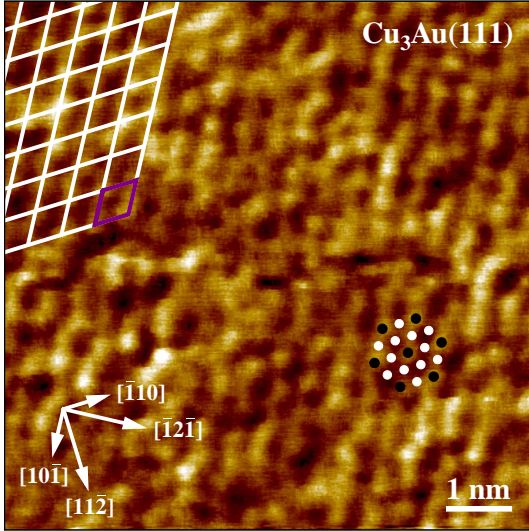


FIG. 6.3. STM image of the clean and ordered $\text{Cu}_3\text{Au}(111)$ surface. Au atoms appear as bright protrusions. The ideal $\text{Cu}_3\text{Au}(111)$ surface is modeled by black (Au) and white circles (Cu). In addition, grid lines of the $p(2 \times 2)$ reconstruction are superimposed in the upper left corner of the image and the respective unit cell is marked in purple. The substrate directions are indicated. The STM image has thoroughly been corrected for thermal drift ($8 \text{ nm} \times 8 \text{ nm}$, $U_{\text{bias}} = -177 \text{ mV}$, $I_t = -137 \text{ pA}$).

out-of-phase conditions for these spots, in contrast to the (00) spot. Note further that under specific experimental conditions, which were optimized for measuring the respective spots (regarding the focusing of the incident electron beam, the angle of incidence and the sample position) at the stated electron energies, larger $T_{w, \text{eff}}$ values around 300 \AA were found for both the substrate and the $p(2 \times 2)$ reconstruction (see the footnotes of Table 6.2). In particular, if only the minimal values are considered (which are thought to be the most reliable measure for the surface quality), the domain sizes are comparably small for metal surfaces, and long-range order is hence limited.

Also, we emphasize that the minimal transfer width which is deduced from the fundamental spots is smaller than that obtained from the $p(2 \times 2)$ reconstruction spots at all employed electron energies (see Table 6.2), thus being independent of the actual scattering conditions $S_{(hk)}$ (which are different for the two families $\{hk\}$ of reflections). This fact is surprising because antiphase domain boundaries²⁰² between the ordered $L1_2$ -phase domains within the substrate-crystal bulk, which represent domain boundaries also for the $p(2 \times 2)$ reconstruction at the $\text{Cu}_3\text{Au}(111)$ surface, should cause the inversed effect, i.e., a broadening of the $p(2 \times 2)$ reconstruction spots in comparison to the fundamental spots. However, the potential impact of these defects on the $p(2 \times 2)$ spot profiles is outweighed here, apparently. An increase in $\Delta k_{hk} = \pm |\Delta \mathbf{k}_{hk}|$ with $k_{\parallel} = k_{hk} = |\mathbf{k}_{hk}|$, as observed here, can generally be explained by missing long-range order. Thus, we could conclude from our LEED results that the surface layer of $\text{Cu}_3\text{Au}(111)$ may resemble a liquid crystal-like or paracrystalline phase.^{85, d)}

The non-perfect order of the $\text{Cu}_3\text{Au}(111)$ surface is also evidenced by STM. Although the overall surface morphology is very smooth and terraces with a width of up to 1000 \AA have been found (not shown), structural deviations from the expected, ideal surface are observed upon closer in-

^{b)}That is, spots of type $\{10\}$ and $\{11\}$, respectively, for a hexagonal substrate.

^{c)}Note that the first-order spots of the $p(2 \times 2)$ reconstruction can also be regarded as spots of type $\{\frac{1}{2}0\}$ and $\{\frac{1}{2}\frac{1}{2}\}$, respectively, with respect to the fundamental substrate spots.

^{d)}The finding that the minimal transfer width which is deduced from the fundamental spots is smaller than that obtained from the $p(2 \times 2)$ reconstruction spots may in general also be ascribed (in parts) to two additional effects. On the one hand, satellite spots which arise from a long-range reconstruction of the surface (see below) have not been clearly resolved and thus may have not been fully separated from the intrinsic substrate spot profile. Hence, the obtained FWHM values of the respective spot profiles systematically are too large by mistake. On the other hand, technical limitations of the SPA-LEED instrument (optics), in particular regarding spatial resolution and sensitivity, for greater values of k_{\parallel} may result in a broadening of the spots. However, these two effects are expected to be of minor importance here because, for instance, the observed trend holds independent of the electron energy (see Table 6.2).

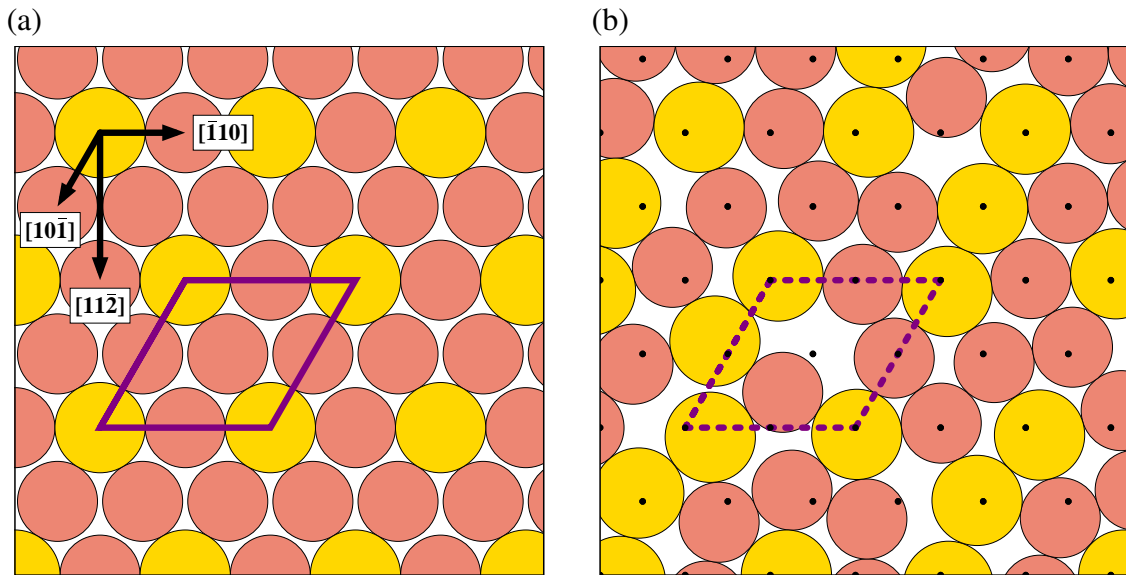


FIG. 6.4. Schematic models of (a) the ideal and (b) the real $\text{Cu}_3\text{Au}(111)$ surface. Cu and Au atoms are depicted in respective colors. The unit cell of the $p(2 \times 2)$ reconstruction is shown in purple. Black dots in (b) mark the atom positions as determined from the bulk structure [and as assumed in (a)]. The substrate directions are indicated. Note that the atoms are depicted at 97.5 % of their metallic radius r_m reported in the literature¹⁴² only (see Table 2.3 in Sec. 2.2.2, page 16, of the present work for the explicit values) in order to avoid overlap of the spheres.

spection. In particular, Au atoms adopt non- $p(2 \times 2)$ or inter-lattice sites, as will be described in detail in the following. Note, however, that this type of disorder does *not* lead to a broadening of the $p(2 \times 2)$ reconstruction spots but *only* to a reduced integral intensity, as has indeed been observed with LEED [see Fig. 6.2(b), for example]. Figure 6.3 shows an STM image of the clean and ordered $\text{Cu}_3\text{Au}(111)$ surface with atomic resolution. In this image, the bright protrusions are identified as the Au atoms. This interpretation is supported by the fact that the average distance between the bright protrusions even in the unprocessed image, *prior to* drift correction, agrees within 1 % with the expected distance of 5.30 Å between two Au atoms^{288,388} as next-nearest neighbors at the perfectly ordered $\text{Cu}_3\text{Au}(111)$ surface [see also Fig. 6.1(b)].^{369,375,389} Furthermore, DFT calculations have shown that, depending on the bias voltage, the Au atoms at the $\text{Cu}_3\text{Au}(100)$ surface are observed primarily or even selectively.⁴¹⁵ The Cu atoms could not be imaged in the present case.

In principle, the Au atoms at the $\text{Cu}_3\text{Au}(111)$ surface form a hexagonal lattice, as indicated by the white grid lines and the purple unit cell in Fig. 6.3. However, the STM image reveals that a noticeable number of Au atoms at the surface do not occupy ideal lattice positions, i.e., positions at the (111) surface which are determined by the bulk structure of ordered Cu_3Au . The ideal structure of a perfectly ordered $\text{Cu}_3\text{Au}(111)$ surface is schematically depicted again in Fig. 6.4(a). Instead, two aspects can be learned from the STM image in Fig. 6.3: (1) Many Au atoms are displaced from the ideal, bulk-determined lattice positions, and (2) additional Au atoms are present at the clean $\text{Cu}_3\text{Au}(111)$ surface which adopt positions close to former Cu sites. This situation is schematically depicted in Fig. 6.4(b). We emphasize again that the statistical displacement of the surface atoms from the ideal lattice sites, which, in turn, are determined by the bulk structure of the $\text{Cu}_3\text{Au}(111)$ crystal, causes a reduced integral intensity of the respective LEED spots [see also Figs. 6.2(a) and (b)] but does not lead to a spot-profile broadening. However, our STM images do not support

the above conclusion of a paracrystalline phase at the $\text{Cu}_3\text{Au}(111)$ surface, as our LEED results indicate, because the bulk-determined structure is maintained at the surface (apart from statistically distributed displacements of surface atoms).

The above findings (1) and (2) can only be explained such that former Cu sites at the $\text{Cu}_3\text{Au}(111)$ surface are either empty or occupied with Au atoms, partially replacing the Cu atoms. However, there must be a net decrease in the total number of atoms being present at the surface, because (a) Au atoms are larger than Cu atoms (by about 13 % considering the metallic radii r_m ; see also Table 2.3), and (b) the observed displacements of the surface Au atoms are only possible if the surface layer is less densely packed than in the ideal case. This points to the fact that the stoichiometry of the $\text{Cu}_3\text{Au}(111)$ surface is different from (namely, smaller than) the ideal ratio of $N_{\text{Cu}}/N_{\text{Au}} = 3 : 1$. Hence, the question arises whether the Cu atoms which are replaced by Au atoms (mostly) either occupy former Au lattice sites or diffuse into the bulk crystal, leading to a substantially reduced Cu fraction at the surface or, looking at it the other way round, to an Au-enrichment.^{425,429} Judging from the the STM image, the Cu atoms indeed diffuse into the bulk and are largely replaced by Au atoms. This is concluded from the facts that the $\text{Cu}_3\text{Au}(111)$ surface appears rather homogeneous in the STM images and only a few and small “holes”, which indicate missing surface atoms (see black areas in Fig. 6.3), are observed while additional Au atoms can be identified, too. This situation has already been considered in Fig. 6.4(b) where, on average, about 0.7 Cu atoms have been replaced by 0.4 Au atoms per unit cell, thereby decreasing the packing density of the surface atoms by about 5 % (in absolute terms). Furthermore, it can be stated that neither the formation of two-dimensional, pure Au or pure Cu domains nor the segregation of surface atoms to three-dimensional nanocrystals, may it be selective or not, were observed with STM, in agreement with our results from LEED. Yet, the issue of where the replaced Cu atoms go cannot be completely solved by the so-far presented results, but it will be addressed further in Sec. 6.3.2.

Long-range reconstruction of the $\text{Cu}_3\text{Au}(111)$ surface

We now turn to a further result of the LEED investigations above. As shown exemplarily in Fig. 6.2(c), six additional satellite spots are observed around the specular reflection. These satellites are also observed as distinct spot profiles in respective one-dimensional LEED scans along the $[11\bar{2}]$ direction [see Fig. 6.2(d)]. Note that the positions of the satellite spots in reciprocal space do not change as a function of electron energy.^{e)} In addition, second-order spots can be identified as shoulders, and they may be fitted with Lorentzian profiles. Such shoulders at identical values of Δk_{\parallel} are found at the spot profiles of the fundamental substrate spots, as well, and also (weakly) at the $p(2 \times 2)$ reconstruction spot profiles due to multiple scattering effects [see Figs. 6.2(e) and (f), for instance]. Hence, the satellite spots may unambiguously be assigned to a second, *long-range* surface reconstruction, which is present in addition to the $p(2 \times 2)$ reconstruction. The pure Au(111) surface also exhibits a $(\sqrt{3} \times 22)$ reconstruction which leads to additional satellite spots.^{114,352} In contrast to the situation on the Au(111) surface where the satellite spots are observed at an angle of 30° with respect to the $[11\bar{2}]$ direction, the satellite spots are found along $[11\bar{2}]$ on $\text{Cu}_3\text{Au}(111)$. A similar pattern of satellite spots with identical orientation has also been observed for the Cu(111) surface in the presence of PTCDA [see Sec. 5.3.2, in particular Fig. 5.3(a)]. On the $\text{Cu}_3\text{Au}(111)$ surface, however, the corresponding superstructure is intrinsic to the surface, that is to say, it is also present on the *clean* surface. Thus, the situation here is neither purely Au-like nor purely Cu-like. Besides, the periodic unit is much larger than on those two surfaces. While the periodicities

^{e)}We did neither observe a pronounced energy dependence of the satellite-spot intensities in the employed electron-energy interval from about 30 eV to 100 eV.

amount to about 63 \AA^{352} and $69(1) \text{ \AA}$ (see also Table 5.2) for the reconstruction of the $\text{Au}(111)$ and $\text{Cu}(111)$ surfaces, respectively, a periodicity of $291(10) \text{ \AA}$ is realized on the $\text{Cu}_3\text{Au}(111)$ surface.

The long-range reconstruction of the $\text{Cu}_3\text{Au}(111)$ surface may be described by the superstructure matrix $\mathfrak{M} = (1 \ 0 \ | \ 0 \ 110(4))$ (see also Table 6.6). Since the LEED pattern of the reconstruction is, at least qualitatively, similar to that of the reconstruction of the PTCDA-covered $\text{Cu}(111)$ surface, it is evident to assume that the underlying structural motif is also similar. Therefore, we speculate that the reconstruction arises from an uniaxial contraction of the surface unit cell together with a shear along the $[\bar{1}10]$ direction, as is the case for PTCDA/ $\text{Cu}(111)$ (see also Sec. 5.3.2). Furthermore, a lateral displacement, and maybe also a vertical one, of the surface atoms has to be considered, similar to the cases of the reconstructed (clean) $\text{Au}(111)$ and (PTCDA-covered) $\text{Cu}(111)$ surfaces, because the above-mentioned contraction and shear alone do *not* result in a periodicity which is substantially different from the original surface lattice constant.

Note that, in principle, the observed LEED spots can also be explained as originating simply from the Moiré effect between the unreconstructed subsurface layers and the reconstructed (i.e., compressed and sheared) surface layer through multiple scattering effects, as has been demonstrated only recently by Meissner *et al.*⁴⁵⁴ In this case, additional lateral and/or vertical displacements of the surface atoms are not required in order to explain the experimentally observed LEED pattern. However, we assume these displacements to be present in the case of the $\text{Cu}_3\text{Au}(111)$ surface for two reasons: Firstly, the bulk lattice constant of Cu_3Au and thus also the surface lattice constant of the ideal $\text{Cu}_3\text{Au}(111)$ surface is smaller by 2.5 % than that expected from Vegard's law^{328,367,368} considering the lattice constants of the pure metals [$a_{\text{bulk}}(\text{Cu}) = 3.6149 \text{ \AA}^{287}$ and $a_{\text{bulk}}(\text{Au}) = 4.0782 \text{ \AA}^{455}$ respectively] and/or the metallic radii r_m of the composing elements (see Table 2.3 in Sec. 2.2.2, page 16, of the present work for the explicit values). Therefore, the $\text{Cu}_3\text{Au}(111)$ surface may be understood as being already compressed in the ideal state. Secondly, the surface atoms are substantially displaced from the bulk-determined lattice sites according to our STM results. Both effects strongly favor the above-mentioned additional displacements of the atoms, in particular in the vertical direction, also to be present at the reconstructed $\text{Cu}_3\text{Au}(111)$ surface due to a potential overlap of the atomic spheres. Since the periodicity of the reconstruction is so large ($110 \cdot \mathbf{a}_2$ along $[\bar{1}10]$), and since two chemical elements in various lattice sites are involved, a conclusive structural model will necessarily be very complex and of speculative nature. Thus, the development of an exact structural model for the $\text{Cu}_3\text{Au}(111)$ surface has been waived here. However, the general structural motifs in the long-range surface reconstruction may be the same as for PTCDA/ $\text{Cu}(111)$ (see also Fig. 5.7).

The observed average domain size of the surface reconstruction ranges from 325 \AA to 590 \AA , as revealed by the width of Lorentzian fits to the corresponding first-order LEED spot profiles at electron energies of 50.2 eV and 72.3 eV , respectively [applying Eqs. (3.42) and (3.46), respectively]. Due to the large periodicity of the reconstruction, this corresponds to a length of one or two unit cells only. Interestingly, the deduced domain sizes are substantially larger than the $T_{w,\text{eff}}$ values which were found for the first-order spots of the substrate and the $p(2 \times 2)$ reconstruction (see above). Thus, it can be concluded that long-range surface reconstruction is to a certain extent insensitive to structural defects, such as the occupation of non-ideal lattice sites by some of the Au surface atoms, due to its large periodicity. Note that this long-range periodicity could not be observed in the STM images. Also, STM did not yield any indications for the presence of discommensuration lines³⁵⁷ or soliton walls³⁵⁸ on the $\text{Cu}_3\text{Au}(111)$ surface, in contrast to the findings for the $\text{Au}(111)$ reconstruction.^{352–354} This is possibly because the changes in the electronic structure at the surface, which result from the surface reconstruction and thereby from the altered arrange-

ment of the surface atoms, are too small, and/or they modulate on a lateral scale which is too large in order to discern these variations from the background level.

6.3.2 Surface composition

An issue raised by the structural investigations (see previous section) is the chemical composition Cu_xAu_{1-x} of the Cu₃Au(111) surface where $0 \leq x \leq 1$. In order to tackle this question, XPS experiments were performed on the clean surface ($E = 2858.0$ eV). In particular, the photoelectron yield ratios $Y_{\text{Cu},j}/Y_{\text{Au},j'}$ of different Cu and Au XP and Auger signals, namely, Cu2p_{3/2}, CuL₃M₄₅M₄₅, and Au3d_{5/2}, were determined for various angles of emission θ [see also Eqs. (3.53) and (4.6)]. The effective angle θ was chosen as 28°, 48°, 68°, and 86°, respectively. Thereby, the escape depth d_e of the photo- and Auger electrons was varied from about 10 Å to 1 Å if the λ_{IMFP} values for Au3d_{5/2} photoelectrons in Cu₃Au are considered (see Table 4.2). In any case, the XPS experiments are rather surface sensitive. For the CuL₃M₄₅M₄₅ Auger electrons, the escape depth is comparable because the respective λ_{IMFP} value is larger by only about 25%. In the case of the Cu2p_{3/2} XPS signal, however, the measurements are less surface sensitive, i.e., d_e is larger, since λ_{IMFP} is larger by about 120%.

Exemplary XP and Auger spectra of the above-noted signals acquired with a photon energy of $E = 2858.0$ eV for $\theta = 86^\circ$ are shown in Fig. 6.6. While for Cu2p_{3/2} and Au3d_{5/2} XP spectra with good signal-to-noise ratios could be obtained, the statistics of the CuL₃M₄₅M₄₅ Auger spectrum only allows to clearly identify one peak at an apparent binding energy of about 1939.5 eV. Additional signals which are expected at apparent binding energies of about 1937 eV, 1942 eV, and 1944 eV³⁰² may not be clearly discerned. Note, however, that with decreasing θ the absolute intensities increased according to Eq. (3.53), with the consequence that the signal-to-noise ratio was improved and that the additional peaks were well resolved. This allowed for the unambiguous identification of the before-mentioned signals also in the Auger spectrum of Fig. 6.6(b).

By numerical integration of the respective XP and Auger spectra, the photoelectron yield ratios $Y_{\text{Cu}2p_{3/2}}/Y_{\text{Au}3d_{5/2}}$ and $Y_{\text{Cu}L_3M_{45}M_{45}}/Y_{\text{Au}3d_{5/2}}$ were determined, respectively. Because the cross section $\sigma_{\text{Au}3d_{5/2}}$ is not available in the literature unfortunately (see also Table 4.4), a normalization of the $Y_{\text{Cu},j}/Y_{\text{Au},j'}$ ratios was required. Figure 6.5 shows the normalized results where the ratios obtained for the largest escape depth were normalized to 3. This value is expected from the stoichiometric ratio $N_{\text{Cu}}/N_{\text{Au}} = 3 : 1$ in Cu₃Au. Essentially, the stoichiometric ratio $N_{\text{Cu}}/N_{\text{Au}}$ remains unchanged for photoelectron escape depths of $d_e \geq 2d_{111}$ (considering the λ_{IMFP} values for Au3d_{5/2} photoelectrons in Cu₃Au; see Table 4.2), that is, for subsurface layers n with $n \leq -2$.^{f)} Only in the topmost layer, the $Y_{\text{Cu},j}/Y_{\text{Au},j'}$ ratio is reduced. Depending to the Cu signal, surface stoichiometries of Cu_{0.61(2)}Au_{0.39(2)} and Cu_{0.71(3)}Au_{0.29(3)} are obtained for the Cu2p_{3/2} and CuL₃M₄₅M₄₅ signals, respectively. The former result is perfectly identical to previous experimental studies employing AES,⁴²⁵ and it is also supported by DFT calculations.⁴²⁶⁻⁴²⁹ The discrepancy between the results for the two Cu signals may be ascribed to the fact that Auger transitions can also be stimulated by secondary radiation and also electrons.²⁸ If such contributions are indeed present, they may vary with θ and thereby distort the result for $Y_{\text{Cu}L_3M_{45}M_{45}}/Y_{\text{Au}3d_{5/2}}$. Hence, $Y_{\text{Cu}2p_{3/2}}/Y_{\text{Au}3d_{5/2}}$ is considered the more reliable measure for the stoichiometric ratio Cu_xAu_{1-x}.

^{f)}Note that the data points in Fig. 6.5 give the $Y_{\text{Cu},j}/Y_{\text{Au},j'}$ ratio as an integral over the escape depth d_e where $d_e = 0$ is the surface. Therefore, the data points are to be understood as an weighted average over d_e to which the stoichiometric ratios $N_{\text{Cu}}/N_{\text{Au}}$ in all layers within d_e contribute. Yet, the contribution by the outmost layers decreases with increasing values of d_e . Because $Y_{\text{Cu},j}/Y_{\text{Au},j'} \approx 3 : 1$ for $d_e \geq 2d_{111}$ already, we conclude that only in the topmost layer $N_{\text{Cu}}/N_{\text{Au}} < 3 : 1$. Hence, the calculation of the explicit ratio $N_{\text{Cu}}/N_{\text{Au}}$ for every subsurface layer is waived here.

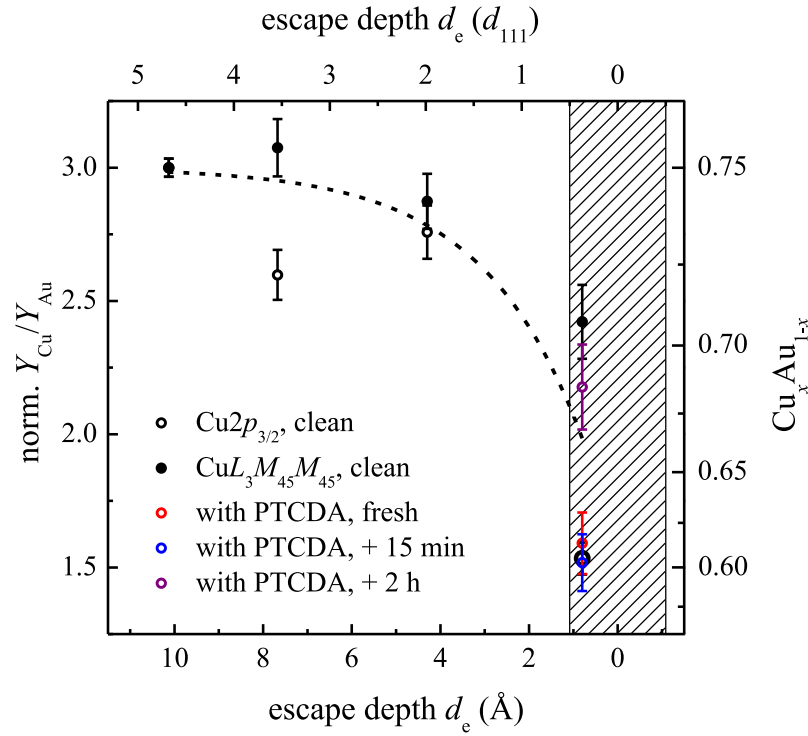


FIG. 6.5. Experimental depth profile of the $\text{Cu}_3\text{Au}(111)$ substrate. The normalized photoelectron yield ratios $Y_{\text{Cu}2p_{3/2}}/Y_{\text{Au}3d_{5/2}}$ and $Y_{\text{Cu}L_3M_{45}M_{45}}/Y_{\text{Au}3d_{5/2}}$ and the stoichiometric ratios $\text{Cu}_x\text{Au}_{1-x}$ are shown as open and filled circles against the escape depth d_e . The latter is given on both an ångström scale and a d_{111} scale where d_{111} denotes the spacing of the (111) lattice planes and thus the thickness of the atomic layers. The range of the topmost layer is marked by the hatched area. The black dashed line is a guide to the eye. The $Y_{\text{Cu}2p_{3/2}}/Y_{\text{Au}3d_{5/2}}$ results for the PTCDA-covered $\text{Cu}_3\text{Au}(111)$ surface are shown in different colors for different times of x-ray beam exposure, as indicated in the inset.

Concluding so far, three scenarios are compatible with the ratio $N_{\text{Cu}}/N_{\text{Au}}$ at the $\text{Cu}_3\text{Au}(111)$ surface as deduced from XPS: The surface layer is either (a) depleted in Cu atoms, (b) enriched in Au atoms, or (c) a combination of both. Considering also the STM results, where neither a formation of Au adatoms, islands or clusters nor a roughening of the surface was observed, the scenario of sheer Au enrichment, while the number of Cu atoms at the surface is constant [scenario (b)], may be ruled out. Therefore, a surface depletion in Cu atoms must occur. Assuming that the number of Au atoms in the surface layer is constant [scenario (a)], the experimental finding of $N_{\text{Cu}}/N_{\text{Au}} \propto Y_{\text{Cu}2p_{3/2}}/Y_{\text{Au}3d_{5/2}} = 1.53(6) : 1$ implies that about every second Cu atom is missing at the $\text{Cu}_3\text{Au}(111)$ surface as compared to the ideal surface, where $N_{\text{Cu}}/N_{\text{Au}} = 3 : 1$. However, this is inconsistent with our above result from STM that the surface is nearly as densely packed as expected in the ideal case [see also Figs. 6.3 and 6.4(b)]. Since STM has revealed additional Au atoms to be present at the $\text{Cu}_3\text{Au}(111)$ surface, which adopt non-intrinsic lattice sites or inter-lattice sites, scenario (c) applies. In an extreme case, where the fraction of the surface area covered by Cu and Au atoms is assumed to be constant (that is, $\sum_i \pi r_{m,i}^2 = \text{const}$), a stoichiometric ratio of $N_{\text{Cu}}/N_{\text{Au}} = 2.34(5) : 1.52(5)$ is expected, considering both the observed $Y_{\text{Cu}2p_{3/2}}/Y_{\text{Au}3d_{5/2}}$ ratio and the metallic radii r_m of Cu and Au (see Table 2.3). In other words, 0.66(5) Cu atoms at the $\text{Cu}_3\text{Au}(111)$ surface are replaced by 0.52(5) Au atoms per unit cell on average in this scenario. This is indeed close to our observation from STM where, on average, about 0.7 Cu atoms had been

replaced by 0.4 Au atoms per unit cell [which corresponds to about -5% (in absolute terms) in the packing density of the surface atoms; see also Fig. 6.4(b)]. Note again that the deviation in the ratio $N_{\text{Cu}}/N_{\text{Au}}$ from the bulk value at the Cu₃Au(111) surface does neither lead to a segregation of one or both of the chemical elements into pure domains nor affect the surface lattice constant (see Sec. 6.3.1).

In conclusion, the stoichiometry of the clean Cu₃Au(111) surface amounts to Cu_{0.61(2)}Au_{0.39(2)} according to XPS, deviating from the stoichiometry of Cu_{0.75}Au_{0.25} expected for the ideal surface. We note that this finding applies irrespective of the potential presence of vacancies at the Cu₃Au(111) surface. Vacancies have indeed been concluded to be present (to a small extent) at the clean Cu₃Au(111) surface on the basis of our STM data (see Sec. 6.3.1 above).

6.3.3 Vertical structure

Although deviations on the lateral lattice constants have been excluded experimentally, it is not *a priori* clear that the Cu₃Au(111) surface does not exhibit a relaxation. In order to tackle the issue whether an altering of the vertical structure is present, XSW experiments were performed. In particular, the CuL₃M₄₅M₄₅ Auger and the Au3d_{5/2} XPS signals have been employed as parameters for the vertical structure of the two elements in the ordered, binary alloy.^{g)} Due to the experimental geometry in XSW setup II with an effective angle of detection θ of 86° , the escape depth of the photo- and Auger electrons is limited to about 1 \AA (see also Table 4.2). Thus, the XSW experiments were only sensitive to the topmost surface layer. Figure 6.7 displays exemplary XSW photoelectron yield curves for both elements including respective fitting curves. The individual XSW profiles are almost identical, indicating very similar structural parameters. The averaged fitting results to the XSW profiles are compiled in Table 6.3 below. Indeed, the results are very similar for both signals. Yet, before the explicit fitting results are reported, we comment on the degree of agreement between the fitting curves and the experimental data points.

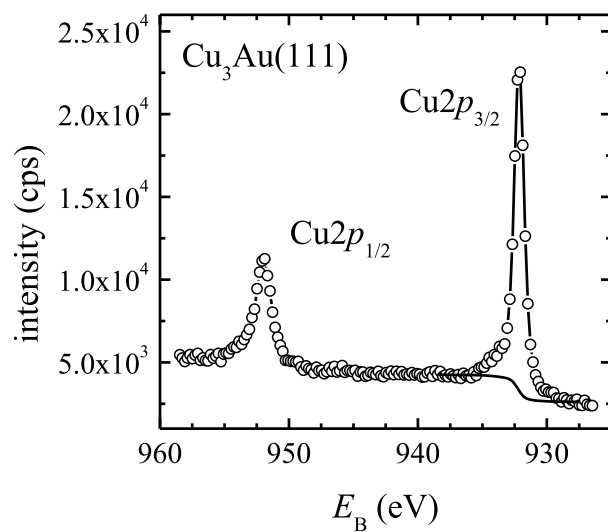
Quality of the fitting

Looking at the fitting curves for the photoelectron yield curves of Cu and Au in Fig. 6.7, one sees that the agreement with the experimental data may be in need of improvement. We consider the underlying aspects in detail at this point because they are of general importance for the evaluation of *all* XSW data on Cu₃Au(111) and PTCDA/Cu₃Au(111) presented in this work (see also Secs. 6.5.3 and 6.6.3 below).

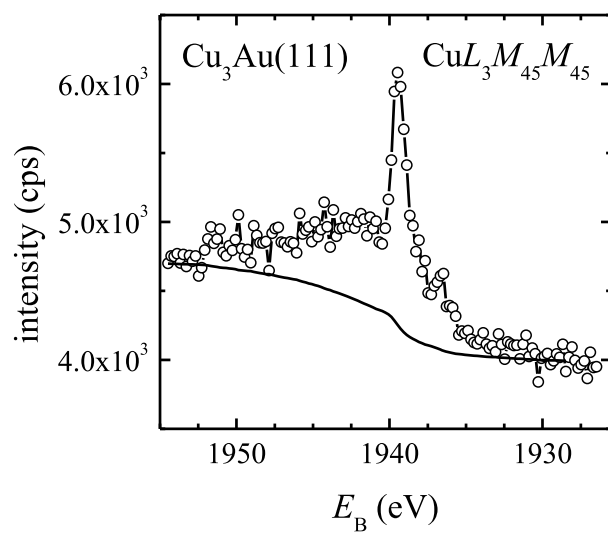
^{g)}In principle, photo-/Auger-electron stimulated or secondary-radiation stimulated processes may contribute to Auger signals.^{28,41,159,175} However, we found that the experimental results for both the CuL₃M₄₅M₄₅ Auger and the Au3d_{5/2} XPS signal agree very well, i.e., $f_c(\text{CuL}_3\text{M}_{45}\text{M}_{45}) = f_c(\text{Au}3d_{5/2})$ and $p_c(\text{CuL}_3\text{M}_{45}\text{M}_{45}) \approx p_c(\text{Au}3d_{5/2})$ (see below). If additional processes contributed to the Auger signal here, this finding could only be reasoned by a (nearly perfect) cancellation of different effects, for example, the presence of additional, stimulated Auger processes in combination with a different degree of order and/or a different vertical height of the Cu atoms as compared to the Au atoms. This appears very unlikely. For this reason, potential additional contributions to Auger signal were excluded to play a role here, and we thus consider our XSW results for the CuL₃M₄₅M₄₅ Auger signal as trustworthy, indeed.

FIG. 6.6 (following page). XP and Auger spectra of the substrate levels for the clean Cu₃Au(111) surface. (a) Cu2p_{1/2} and Cu2p_{3/2}, (b) CuL₃M₄₅M₄₅, and (c) Au3d_{5/2}. All XP spectra were acquired with a photon energy of $E = 2858.0 \text{ eV}$ at an effective angle of 86° of the photoelectron analyzer with respect to the surface normal. The employed backgrounds of Shirley type are shown as black lines.

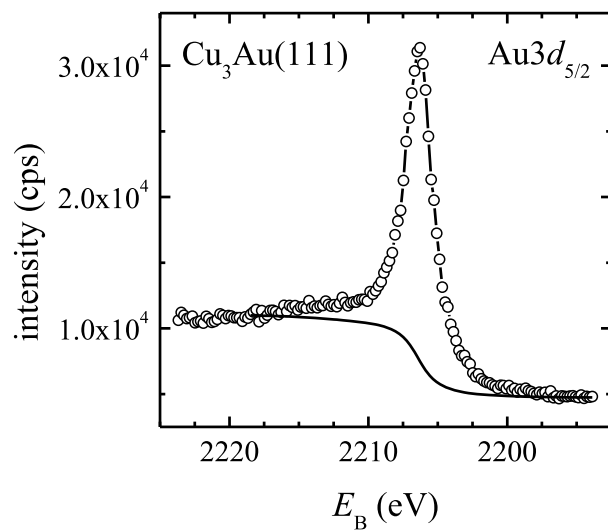
(a)



(b)



(c)



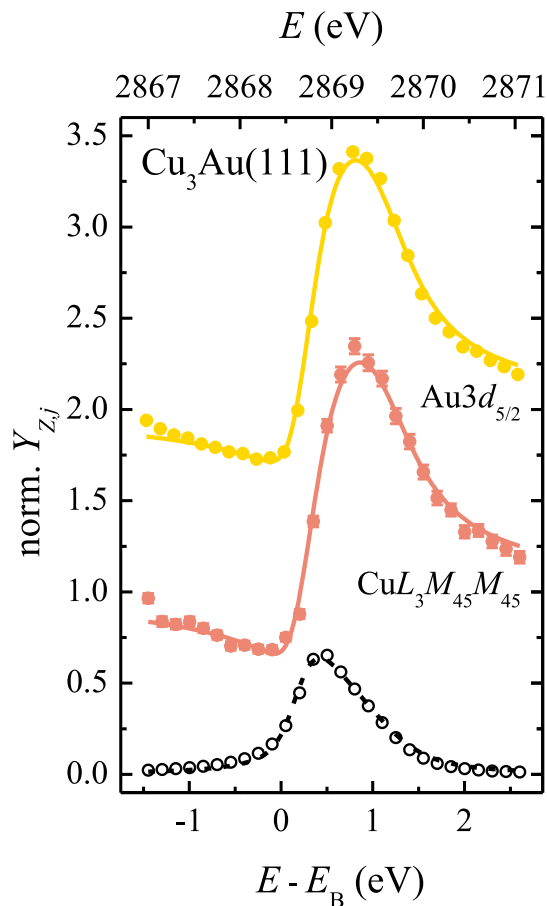


FIG. 6.7. Typical XSW photoelectron yield curves of Cu and Au at the clean $\text{Cu}_3\text{Au}(111)$ surface. The $\text{Cu}L_3M_{45}M_{45}$ and $\text{Au}3d_{5/2}$ signals were employed in the respective XSW experiments. Experimental data points are shown as filled circles while respective fits to the data are shown as solid lines. The curves have been vertically offset for clarity. Error bars are so small that they are almost hidden by the data points. In addition, the measured reflectivity of the substrate employing the (111) lattice planes (open circles) and the corresponding fit (dashed line) are shown. Error bars have been omitted for clarity here. Note that only the topmost surface layer has been probed in these experiments.

As a first observation from Fig. 6.7, we notice that for both XSW photoelectron yield curves the maximum is not quite correctly described by the fitting curve but systematically underestimated within a few percent.^{h)} In general terms, we have found deviations of the fitting curves from the experimental data for $E - E_B$ values in the region of about 0.0 eV to 0.5 eV for all XSW data on clean $\text{Cu}_3\text{Au}(111)$ and PTCDA/ $\text{Cu}_3\text{Au}(111)$ (see also Figs. 6.11, 6.28, and 6.29 below). This can be traced back to a non-adequate fitting of the reflectivity curves $R(E)$ in all cases. In Fig. 6.7, for example, the underestimation of the XSW data by the corresponding fitting curves coincides with the underestimation of the $R(E)$ curves by their fitting curves (see Fig. 6.8 for a representation on an enlarged scale). At the same time, the tails of the reflectivity curve are not correctly described, either. This may be due to two reasons: Either the stoichiometry in the bulk of the $\text{Cu}_3\text{Au}(111)$ substrate crystal deviates from the nominal value of $N_{\text{Cu}}/N_{\text{Au}} = 3 : 1$ or the long-range order in the bulk crystal is limited, that is, the bulk crystal suffers from alloy inhomogeneities (which cause local deviations from the ideal lattice plane spacing) and exhibits a rather paracrystalline character. Our LEED results point to a paracrystalline character of the lateral order of the $\text{Cu}_3\text{Au}(111)$ surface, indeed.

Both scenarios alter the shape of the reflectivity or Darwin-Prins curve. According to Eqs. (3.16) and (3.17), the actual shape of the $R(E)$ curve is largely determined by the structure factors F_0 and

^{h)}See Appendix F of the present work for a validation of controversial approximations in the computational algorithm behind the data evaluation routine XSWAVES,³²⁹ which (incorrectly) employs convolutions instead of cross-correlations in order to account for broadening effects. In brief, these approximations do not affect the line of argument here.

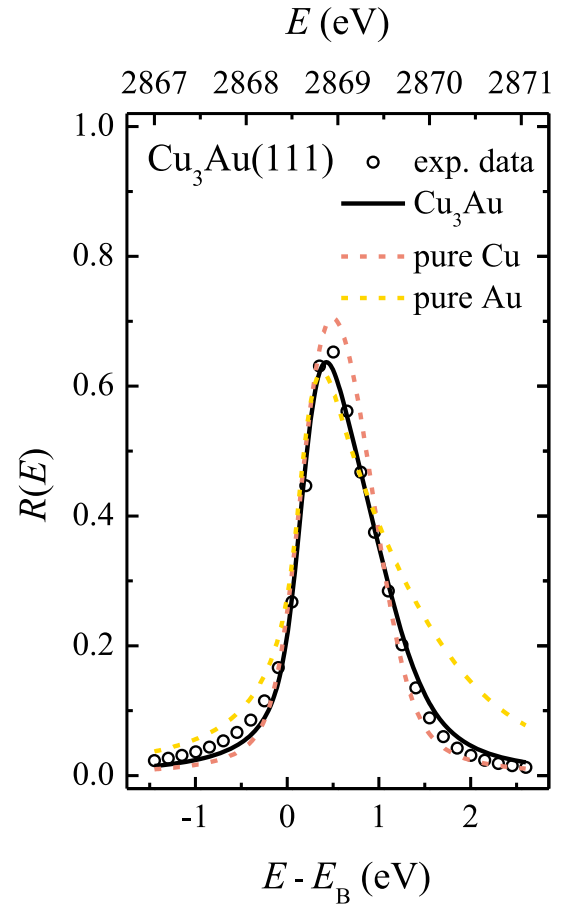


FIG. 6.8. Typical Darwin-Prins curve $R(E)$ of the (clean) $\text{Cu}_3\text{Au}(111)$ substrate crystal (black open circles; error bars have been omitted for clarity). The reflectivity of the substrate was measured employing the (111) lattice planes. The corresponding fit is shown as a black solid line. In addition, two fitting curves are shown as dashed lines in respective colors where the substrate was modeled as being composed of either Cu or Au atoms only. Note that the $R(E)$ data shown here are the same as in Fig. 6.7.

F_H . They, in turn, depend on the chemical elements, the quantities, and the exact positions of the atoms in the bulk unit cell (see Appendix B of the present work). In the present case of the (111) Bragg reflection of Cu_3Au , the shape of the reflectivity curve with its comparably sharp maximum resembles that of pure Au⁵⁴ rather than that of pure Cu⁴³ because the atomic scattering factor $f_Z = (f_0 + \Delta f' + i\Delta f'')$ _Z of Au is much larger than that of Cu (see Table B.1 in Sec. B.1, page 291, of the present work). In particular, the imaginary parts $\Delta f''$ of the dispersion correction, which account for absorption effects and strongly influence the curve shape, are larger by a factor of 10 for Au than for Cu, resulting in a pronounced asymmetric shape of the Darwin-Prins curve. Figure 6.8 demonstrates the impact of the F_0 and F_H values on the shape of $R(E)$: the experimental data from Fig. 6.7 have been fitted under the assumption that the substrate crystal is composed of either Cu or Au atoms exclusively (in an ideal *fcc* lattice), adapting the structure factors accordingly and leaving all other parameters constant. In the case of Cu atoms only, the overall shape of the experimental Darwin-Prins curve is much better reproduced than in the case of Au atoms only, although the maximum of $R(E)$ is now overestimated. Hence, it is indeed tempting to conclude at this point that the actual stoichiometry of the employed $\text{Cu}_3\text{Au}(111)$ substrate crystal deviates from the nominal ratio in favor of an increased Cu fraction or, looking at it the other way round, a decreased Au fraction.

We can exclude, however, that the bulk stoichiometry of the substrate crystal (substantially) deviates from the nominal $N_{\text{Cu}}/N_{\text{Au}}$ ratio because the expected Bragg energy $E_B = 2865.04$ eV is reproduced within 3.5 eV. This means, that the (average) lattice constant of the employed crystal agrees with that of Cu_3Au within 0.005 \AA , strongly indicating the correct $N_{\text{Cu}}/N_{\text{Au}}$ ratio to be

present in the bulk. Therefore, we conclude that alloy inhomogeneities, i.e., local disorder, leads to the observed deviations between theory and experiment, ruling out the above scenario of an altered bulk stoichiometry. Yet, XSW on non-perfectly ordered crystals requires a new theory because the theory behind our evaluation presented in Sec. 3.1 assumes perfect crystals. Tolkiehn *et al.* have recently suggested a kinematical approach which accounts for the mosaicity of the substrate crystal, for example.⁴⁵⁶ Note, however, that there are no indications for limited long-range order in Cu₃Au crystals in the literature.³⁷⁵

In principle, the above-described discrepancies between experimental XSW data and the corresponding fitting curves can be overcome by fitting the parameters (i.e., width and center) of the Gaussian function, which accounts for instrumental broadening (the fitting curve is a convolution of the theoretically predicted curve with a Gaussian function), together with the coherent fraction f_c and the coherent position p_c to the actual experimental data with the evaluation routine XSWAVES (by default, the parameters of the Gaussian function have been obtained by fitting the Darwin-Prins curve and then transferred to the XSW profile fit; see also Appendix A). In doing so, the obtained fitting curves agree very well with the experimental data (not shown). However, the impact on the fitting results themselves is rather small on average: $\Delta f_c = +0.07(6)$, $\Delta p_c = +0.01(2)$, and $\Delta d = +0.03(4)$ Å [averaged over *all* XSW data on both clean Cu₃Au(111) and PTCDA/Cu₃Au(111)].ⁱ⁾

Obviously, the improvements are essentially cosmetic in nature, in particular concerning the obtained vertical heights and hence also the adsorption configurations. Furthermore, this non-standard evaluation procedure yields a different Gaussian function for every XSW data fit, also in the case of differential analysis where different components of *one* individual XPS signal from *one* XSW experiment are analyzed. However, if the Gaussian function is understood as also mimicking the order within the Cu₃Au(111) substrate crystal, it is physically unreasonable to have different parameters of the Gaussian function for one and the same data set. Therefore, we have refrained from the relying on the results from this non-standard procedure for XSW data evaluation in the framework of this study. We have ensured, however, that both the standard and the non-standard evaluation procedures yield (qualitatively) perfectly identical results concerning the adsorption configurations of PTCDA on the Cu₃Au(111) surface, rendering our results meaningful and reliable. Hence, our conclusions on the relevant bonding channels drawn from the structural data are not challenged by the (small) discrepancies between the experimentally obtained XSW data and the corresponding theoretical fitting curves which are based on the assumption of a perfectly ordered Cu₃Au(111) substrate crystal.

As a second observation from Fig. 6.7, it is apparent that the very first value of both $Y_{Z,j}(E)$ curves, that is, the data point at minimal photon energy E_{\min} , is systematically too large as compared to both the data points for larger E and the fitting curve. In fact, this applies to *all* XSW profiles presented in this work. We ascribe this to a systematic error in the normalization of the data to the intensity I_0 of the incident beam. I_0 (as well as the drain current I from the sample) was always measured prior to the XPS or Auger data at the respective energy. For the first data point, we observed I_0 being smaller systematically than for the subsequent data points. Apparently, there was a malfunction (potentially a time delay) in the automatized experimental procedure monitoring I_0 which caused this effect at the start of every measurement. However, exemplary evaluations of data sets for which the first data point had been removed have proven that this systematic error is negligible ($|\Delta f_c| \leq 0.01$, $|\Delta p_c| \ll 0.01$, and $|\Delta d| < 0.01$ Å).

ⁱ⁾The largest deviations in the f_c values were obtained for the individual C1s components of PTCDA/Cu₃Au(111) in the initial and the final state, amounting to $\Delta f_c = +0.15(2)$ and $\Delta f_c = +0.09(3)$, respectively (see also Secs. 6.6.3 and 6.6.4).

TABLE 6.3. Averaged vertical shifts for the Cu and Au atoms at the clean Cu₃Au(111) surface as obtained from XSW experiments. The CuL₃M₄₅M₄₅ and Au3d_{5/2} signals were employed in the respective XSW experiments. The parameters f_c and p_c denote the coherent fraction and position, respectively, while $d = p_c d_{hkl}$ is the vertical adsorption height. d_{hkl} is the lattice plane spacing of the employed (111) Bragg reflection of the Cu₃Au substrate crystal. Note that only the topmost surface layer has been probed in the XSW experiments.

	clean Cu ₃ Au(111)		
	f_c	p_c	d (Å)
CuL ₃ M ₄₅ M ₄₅	0.82(5)	0.13(1)	0.28(1)
Au3d _{5/2}	0.81(7)	0.15(1)	0.33(2)

Fitting results

We now turn to the explicit fitting results (see Table 6.3). Two aspects are noticeable here. Firstly, the coherent fractions f_c are by about 20 % lower than the expected value of $f_c = 1$ for a perfectly ordered structure, and also lower than for Ag substrates, for example, by up to 10 % (see Sec. C.3.4 on page 316 et seqq. in the appendix of the present work). Therefore, a significant vertical disorder might be concluded at this point. In a rough estimation employing a simple scenario of only two distinct values of d being equally adopted by the surface atoms, a vertical displacement between ± 0.16 Å to ± 0.22 Å would be required in order to result in the above-mentioned reductions in f_c . Such an amplitude of a potential surface buckling is comparable to that of the pure Au(111) surface for which values of $\pm 0.15(4)$ Å to $\pm 0.20(5)$ Å have been reported.^{353,354,357} We speculate that this surface buckling may be caused by the long-range reconstruction of the Cu₃Au(111) surface which was observed in LEED. Note, however, that the STM measurements have not given indication of a surface buckling. Thus, it cannot be excluded that other aspects may also play a role here. Photoelectron diffraction effects^{157,263} as well as contributions to the Auger process by electron and/or secondary-radiation stimulation^{28,175} might be present. Nondipolar contributions to the photoemission process (which generally do not apply to Auger signals^{159,331}) may be excluded in the present case due to the experimental geometry. Note at this point that our f_c values for the Cu₃Au(111) substrate crystal agree within 0.02 with those of Tolkien *et al.* obtained for a Cu₃Au(100) substrate, employing the (200) Bragg reflection.⁴⁵⁶

The second, more than noticeable aspect of the XSW results is the finding that the Cu and Au surface atoms exhibit an outward relaxation of +13(1) % and +15(1) % of the lattice plane spacing, respectively. This is equivalent to a vertical displacement of as much as +0.28(1) Å and +0.33(2) Å. So far, only an inward relaxation of the topmost layer of Cu₃Au(111) by -2.3 % has been reported on the basis of x-ray diffraction data.³⁹⁷ For the sample employed in that particular study, however, an *equivalent* depletion of both Cu and Au atoms at the surface was found,³⁹⁷ maintaining the ideal surface stoichiometry, in contrast to our results of an Au-enriched surface layer. The pure Au(111) surface also exhibits an outward relaxation of +3.3 %.⁴⁵⁷

6.4 Concluding Discussion, part I: the clean Cu₃Au(111) surface

We now turn to the discussion of the experimental results for the clean Cu₃Au(111) surface. Besides the already-known $p(2 \times 2)$ surface reconstruction of the ordered alloy,³⁸⁹ several new aspects have been observed:

- (a) The Cu fraction at the Cu₃Au(111) surface is reduced while the Au fraction is increased, resulting in a surface stoichiometry of Cu_{0.61(2)}Au_{0.39(2)}. The altering of the ratio $N_{\text{Cu}}/N_{\text{Au}}$ is limited to the topmost layer.
- (b) The Cu₃Au(111) surface exhibits only a limited long-range order. Au atoms are found to also occupy non-ideal lattice sites in terms of the $p(2 \times 2)$ surface reconstruction, i.e., nominal Cu sites and/or inter-lattice sites. The LEED results point to a paracrystalline structure of the Cu₃Au(111) surface.
- (c) A long-range reconstruction of the Cu₃Au(111) surface with a periodicity of 291(10) Å is present, which is equivalent to the length of 110(4) surface unit cells (of the disordered alloy).
- (d) A buckling of the Cu₃Au(111) surface layer is deduced from the comparably small coherent fractions f_c of Cu and Au and, in addition, from the (slightly) different vertical shifts [$\Delta d = d(\text{Au}) - d(\text{Cu}) = +0.05(2)$ Å].
- (e) The topmost layer of the Cu₃Au(111) surface is relaxed in outward direction by about 15 %.

The observed surface depletion in Cu atoms and enrichment in Au atoms (**ad a**) is in contradiction to an earlier CTR measurement.³⁹⁷ An Au-enrichment, however, has also been observed for the two outmost layers of the Cu₃Au(110) surface.^{416,458} By low energy ion scattering, Au fractions of 0.45(2) and 0.20(4) were found for the first and second layer while values of 0.50 and 0.00 are expected for the ideal surface.^{416,458} Furthermore, our result for the (111) surface is in quantitative agreement with various other experimental observations using different techniques,^{392,425,429} and is also supported by theoretical work^{416–418} (see also Sec. 6.1 for further details on the reported results). In the case of the Cu₃Au(110) surface, the segregation of Au into the surface region has been explained by the lower surface energy of the pure Au(110) surface in comparison to the pure Cu(110) surface [1700 mJ/m² versus 2237 mJ/m² according to Ref. 421; see also Refs. 422–424 for further tabulated values of metal surface energies].⁴¹⁸ Therefore, it is concluded that the driving force for the observed Cu depletion and Au enrichment of the Cu₃Au(111) surface is the reduced surface energy.⁴²⁶

Surface order

As a consequence of the Cu depletion and the partial replacement by Au atoms, former Cu sites in the Cu₃Au(111) surface layer and maybe even inter-lattice sites are occupied by Au atoms. Besides, due to the larger size of the Au atoms, most surface atoms are substantially displaced from the ideal, bulk-terminated lattice sites [see Fig. 6.4(b) for a schematic representation of the “real” Cu₃Au(111) surface] which reduces the long-range order at the surface (**ad b**). This is consistent with the observations from LEED that the $p(2 \times 2)$ reconstruction spots are less intense than the fundamental substrate spots, which are fundamental in the sense that they could also originate from the disordered A1 phase. Since the ideal order of the Cu₃Au is only present in subsurface layers, the corresponding LEED (sub-)pattern is attenuated by the less ordered surface layer. The order is

expected to be nearly ideal already in the second layer for two reasons, firstly, because the observed composition of the second layer is essentially identical to the bulk composition, and, secondly, because x-ray diffraction measurements have proven a “nearly perfect” order (see Ref. 375 and also references therein) for Cu_3Au crystals in the ordered $L1_2$ phase, i.e., at sample temperatures below $T_c = 663$ K.

Our LEED results have revealed, however, that the widths of the first-order LEED spot profiles which originate from the ordered $L1_2$ phase, i.e., from the $p(2 \times 2)$ reconstruction, are systematically smaller than those of the fundamental substrate spots. In more general terms, we have observed that the spot-profile widths increase with k_{\parallel} , thus indicating limited long-range order and a paracrystalline character of the $\text{Cu}_3\text{Au}(111)$ surface. If the surface layer is indeed paracrystalline, two possibly underlying scenarios need to be considered. Either the $\text{Cu}_3\text{Au}(111)$ substrate crystal is paracrystalline in nature also within the bulk or only the very surface layer exhibits paracrystallinity, being “structurally decoupled” from the well-ordered bulk of the substrate crystal. At first sight, the first scenario of a paracrystalline bulk crystal appears more likely as the valid explanation for a paracrystalline surface layer here because the atomic positions at the surface are usually determined by the bulk structure. However, as already stated above, there are no indications from the literature for a decreased long-range order in Cu_3Au crystals under the experimental conditions employed here.^{j)} In our XSW experiments, we have observed the (111) Bragg reflection of the $\text{Cu}_3\text{Au}(111)$ crystal, evidencing a substantial degree of order within the substrate at least with respect to the fundamental fcc lattice.^{k)} Besides, the stoichiometry of the bulk crystal corresponds indeed to the nominal value of $N_{\text{Cu}}/N_{\text{Au}} = 3 : 1$, as expected for an ideal $\text{Cu}_3\text{Au}(111)$ substrate crystal. This is deduced from the the experimentally observed value of E_B which agrees well with the theoretically expected Bragg energy. Thus, the lattice constant of the substrate crystal, which in turn depends on the relative fractions of Cu and Au atoms in the bulk material,^{328,367,368} is in fact the nominal one of Cu_3Au (on average, disregarding potential local alloy inhomogeneities), thereby ruling out a non-stoichiometric substrate crystal. Therefore, we conclude that, very likely, the $\text{Cu}_3\text{Au}(111)$ substrate as a bulk material does *not* suffer from a considerably limited long-range order.

Hence, only the second scenario of a single paracrystalline surface layer remains as a potential explanation for our findings from LEED. This scenario is indeed compatible with the substantial outward relaxation of the surface layer (**ad e**) and also with the comparably small f_c values (**ad d**). It employs the picture of a “structurally decoupled” or “floating” surface layer where the vertical order is reduced due to local, attractive or repulsive interactions between atoms in the surface layer and those in the first subsurface layer. However, this scenario is not supported by our STM results. According to our atomically resolved STM images, the Cu and Au atoms at the $\text{Cu}_3\text{Au}(111)$ surface are essentially arranged according to the bulk-determined lattice sites (although displaced, admittedly). Therefore, this issue of the actual degree of crystallinity of the $\text{Cu}_3\text{Au}(111)$ surface cannot be unambiguously resolved on the basis of the available data and further investigations are needed.^{l)} We state, however, that our results concerning both the lateral structure and the adsorp-

^{j)}After an initial annealing step above the critical temperature $T_c = 663$ K, which yielded the disordered A1 phase, our $\text{Cu}_3\text{Au}(111)$ substrate crystals were further annealed at $T < T_c$ in order to restore the equilibrium condition, i.e., the ordered $L1_2$ phase. Yet, we note at this point that the annealing times of the $\text{Cu}_3\text{Au}(111)$ substrate crystals at $T < T_c$ were shorter by a factor of about 10 in comparison to some of the earlier x-ray diffraction studies where the long-range order in the bulk crystal was determined (see Refs. 371, 459, for example).

^{k)}The (111) Bragg reflection is a fundamental reflection because the value of the corresponding structure factor F_H is invariant to possible exchanges between Cu and Au atoms in their positions (see also Sec. B.1).

^{l)}Note that two different $\text{Cu}_3\text{Au}(111)$ crystals were used for our experiments, namely, one for the SPA-LEED investigations and a second one for the STM, XPS, and XSW measurements. Yet, because both crystals were cut from the

tion configurations of PTCDA on the Cu₃Au(111) surface (see Sec. 6.6) are *not* questioned by this ambiguities because we only found incommensurate superstructures [in agreement with both PTCDA/Au(111) and PTCDA/Cu(111)] and no indications for relevant local interactions (of type O–M, i.e., local bonds between O atoms within the PTCDA molecule and metal surface atoms M = Cu, Au) across the interface.

Long-range surface reconstruction

The observed long-range reconstruction may be also caused by the reduced Cu fraction at the Cu₃Au(111) surface (**ad c**). The clean Au(111) surface exhibits a reconstruction³⁵² while the clean Cu(111) surface does not (see also Secs. 5.3.2 and 5.4). Apparently, the “Au-rich” Cu₃Au(111) surface bears more similarities with the pure Au(111) surface than with the Cu(111) surface, although the Au fraction at the surface is below 50 %, still making the Au atoms the minority species. We conclude that the Au atoms determine the properties of the Cu₃Au(111) surface nonetheless, thus allowing for the surface reconstruction.

The reconstruction of *fcc* (111) surfaces has lately been theoretically described in terms of the Frenkel-Kontorova model.³⁶⁶ In essence, the tendency towards a reconstruction depends on the delicate balance of physical properties of the surface. The determining factors are the surface energy γ and the surface stress τ on the one hand, and the surface force constants μ between neighboring surface atoms, describing the strength of interatomic bonds in the surface layer, and the average potential energy W , i.e., the average amplitude of the corrugated potential of the second layer, which describes the interaction of surface atoms with the substrate, on the other hand via:^{365,366}

$$P = \frac{A \left(\gamma - 4 \frac{\tau}{3} \right)}{\frac{2}{\pi} \sqrt{2\mu W a^2}}. \quad (6.1)$$

The above equation holds for the reconstruction of (111) surfaces of the pure *fcc* metals.³⁶⁵ P is the so-called misfit parameter,⁴⁶⁰ a is twice the distance from the *fcc* hollow site to the nearest *hcp* hollow site on the (111) surface, and A is the surface area per atom.³⁶⁵ In Eq. (6.1), dominance of the one of the two parameters γ and τ over the other two parameters μ and W leads to a reconstruction of the surface: for $P > 1$ the reconstruction is expansive and for $P < -1$ the reconstruction is compressive, while for $|P| < 1$ a reconstruction is not present.^{359,365,366} In the case of pure Cu(111), the intrinsic surface stress is rather small, and thus does not result in a surface reconstruction.^{359,365} For pure Au(111), in contrast, the surface stress is moderately large while the surface force constant and the average potential energy are smaller than for Cu(111),^{359,365} in full agreement with chemical intuition. The increase in the relative Au fraction at the Cu₃Au(111) surface presumably increases the surface stress, and reduces the surface energy as well as the surface force constants. This may be explained by the greater “nobility” of Au in comparison to Cu. According to the Frenkel-Kontorova model, a surface reconstruction becomes more likely now. A surface reconstruction is indeed observed in the experiment.

In analogy to Au(111), the long-range reconstruction of the Cu₃Au(111) surface is expected to be of compressive nature.^{352,365} The (uniaxial) compression of the surface will most likely lead to

same crystal rod and the surfaces were treated following essentially the same protocol (see also Sec. 6.2), we argue at this point that both crystals exhibited the same structural properties and thus were of the same quality. Therefore, the non-agreeing results from LEED on the one hand and from further techniques, also from earlier studies,³⁷⁵ on the other hand cannot be attributed to the crystal quality here.

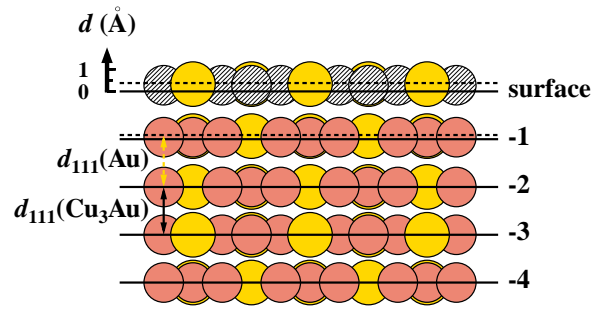


FIG. 6.9. Schematic representation of the outward relaxation of the clean $\text{Cu}_3\text{Au}(111)$ surface. The $\text{Cu}_3\text{Au}(111)$ substrate is shown in a side view along the $[11\bar{2}]$ direction. The cut through the crystal is made along the $[\bar{1}10]$ direction at the position of a densely packed row of alternating Cu and Au atoms. See Fig. 6.17 for an illustration of the crystallographic directions, for example. The (111) lattice planes of Cu_3Au and pure Au are indicated by solid and dashed lines with spacings $d_{111}(Z)$, respectively. Cu atoms in the surface layer are drawn as hashed circles in order to indicate depletion. Note that the atoms are depicted at 70 % of their metallic radii r_m for reasons of clarity.¹⁴²

a lateral and/or vertical evasion of the surface atoms. In particular, this applies to the Au atoms for which a lower compressibility is expected due to their already small metallic radius r_m (in comparison to their lighter homologues Cu and Ag) as a consequence of the so-called lanthanide contraction.¹⁴⁶ A vertical evasion, that is, a (varying) vertical displacement of the surface atoms, will express itself in a surface buckling. Indeed, indications for a buckled $\text{Cu}_3\text{Au}(111)$ surface have been obtained from the comparably low f_c values in the XSW experiments and the different vertical shifts of Cu and Au surface atoms (**ad d**). Lateral evasion, however, may only be possible to a limited extent because the $\text{Cu}_3\text{Au}(111)$ surface can be regarded as being compressed already to the ideal state. Considering the lattice constant of the pure metals [$a_{\text{bulk}}(\text{Cu}) = 3.6149 \text{ \AA}$ ²⁸⁷ and $a_{\text{bulk}}(\text{Au}) = 4.0782 \text{ \AA}$,⁴⁵⁵ respectively] and/or the metallic radii r_m of the composing elements (see Table 2.3 in Sec. 2.2.2, page 16, of the present work for the explicit values), the bulk lattice constant of Cu_3Au and thus also the surface lattice constant of the ideal $\text{Cu}_3\text{Au}(111)$ surface would in fact be expected to be larger by 2.5 % assuming Vegard behavior.^{328,367,368} Despite the altered surface composition with a higher fraction of (larger) Au atoms, however, the surface layer is still epitaxial with the substrate and the surface lattice constant is conserved.^{m)} Therefore, we conclude that the limited ability for lateral evasion of the surface atoms is the reason for the very large periodicity of the $\text{Cu}_3\text{Au}(111)$ surface reconstruction, being almost five times larger than that of the pure Au(111) surface.³⁵²

Surface relaxation

Finally, we will discuss the relaxation of the topmost $\text{Cu}_3\text{Au}(111)$ layer (**ad e**). Our XSW experiments revealed a substantial *outward* relaxation (of about $+0.3 \text{ \AA}$) of the Au-enriched surface layer of $\text{Cu}_3\text{Au}(111)$.ⁿ⁾ For a $\text{Cu}_3\text{Au}(111)$ surface with ideal stoichiometric ratio an *inward* relaxation by -2.3% had been found by Stierle *et al.* before,³⁹⁷ in quantitative agreement with theoretical

^{m)}An ideal, i.e., maximal, quantity of atoms at the surface as determined by the number of lattice sites (given by the crystal bulk structure) is assumed here. The real number of surface atoms may be lower as a consequence of the surface depletion in Cu atoms and the solely partial replacement by Au atoms [see also Fig. 6.4(b)].

ⁿ⁾According to x-ray scattering measurements, the clean Au(111) surface exhibits an expansion of the layer spacing between the two topmost surface layers of 3.3(4) %.⁴⁵⁷ Theoretical calculations, however, have predicted a contraction of about 3 %.⁴²²

results.⁴²⁶ However, with an increasing Au fraction being present at the surface, the relaxation is expected to point outward⁴²⁶ simply because of the larger metallic radius r_m of Au in comparison to Cu.¹⁴² Figure 6.9 shows a schematic representation of the outward relaxation, as determined by our XSW experiments. The observed relaxation of about +15 % is modeled such that, in fact, the two topmost layer are relaxed outward. In particular, the layer spacing between the surface layer and the second layer (i.e., the first subsurface layer; labeled “-1” in Fig. 6.9) is no longer that of the Cu₃Au (111) lattice planes, $d_{111}(\text{Cu}_3\text{Au}) = 2.165 \text{ \AA}$,³⁸⁸ but that of the (111) lattice planes in pure Au, $d_{111}(\text{Au}) = 2.355 \text{ \AA}$ ⁴⁵⁵ (which is considered as a reasonable upper limit for the layer spacing here). Both types of lattice planes are depicted as solid and dashed lines in Fig. 6.9, respectively. The difference between the two amounts to $\Delta d_{111} = d_{111}(\text{Au}) - d_{111}(\text{Cu}_3\text{Au}) = 0.19 \text{ \AA}$. In addition, Cu and Au atoms within the second layer are relaxed by +47 % and 74 % of Δd_{111} (i.e., by +0.09 Å and +0.14 Å), respectively, in order to match the experimentally observed d values for Cu and Au atoms at the surface.^{o)} All other layers are kept in place at the ideal positions as defined by the Cu₃Au (111) lattice planes. Indeed, more sophisticated models may be constructed than simply relaxing the two outmost layers only, which in turn has necessitated a distinct transition from the ideal lattice plane spacing in Cu₃Au to that in pure Au. In principle, also deeper-lying subsurface layers can exhibit relaxations.^{p)} For instance, a smoother crossover from one spacing to the other following an exponential function according to:

$$\Delta d(z) = d_{\text{surface}} \exp(-\kappa |z|) \quad (6.2)$$

may be plausible where $z = 0, -1, -2, \dots$ denotes the (sub-)surface layers, $\Delta d(z)$ the outward relaxation of layer z , $d_{\text{surface}} = d$ the experimentally determined relaxation of the surface layer, i.e., the adsorption height, and κ the exponential inverse decay length. For reasons of simplicity and due to the fact that no further structural information on the subsurface layers are available from our experiments, which allowed to estimate κ , such a more complex model has been waived here.

The experimentally determined outward relaxation of the Cu₃Au(111) surface is in qualitative and, to a certain extent, even (semi-)quantitative agreement with theoretical predictions on DFT-GGA level by Moreira *et al.*⁴²⁶ For the most stable structure of the ones under investigation, a surface composition of Cu_{0.50}Au_{0.50} was found while the composition of all subsurface layers exhibited the ideal ratio of $N_{\text{Cu}}/N_{\text{Au}} = 3 : 1$. In their calculations, Moreira *et al.* found an outward movement for the two Au atoms in the surface layer with values of +0.10 Å and +0.21 Å with respect to the Cu surface atoms, yielding a vertical displacement of about ±0.05 Å between the Au atoms.⁴²⁶ Yet, the relaxation of the Cu atoms themselves is marginal (+0.03 Å in comparison to the ideal case; yielding an overall vertical displacement of about ±0.10 Å considering all surface atoms).⁴²⁶ We find a relaxation which is larger by a factor of two on average. Also, the (potential) surface buckling is present in both our experimental and the reported theoretical results. Again, the experimentally observed surface buckling which was proposed here on the basis of the both the obtained f_c values and the long-range surface reconstruction is larger by a factor about 3 to 4 if only the vertical positions of the Au atoms are considered, and agrees with the theoretical predictions within a factor of 2, as mentioned before, if the differences in the vertical positions of *all* surface atoms are taken into account, regardless of their chemical nature. Our results show that both Cu and Au atoms exhibit vertical displacements, i.e., outward relaxations and buckling, of similar size [$\Delta d = d(\text{Au}) - d(\text{Cu}) = +0.05(2) \text{ \AA}$]. We conclude that the surface *as a whole* relaxes and

^{o)}Note that both the surface layer and the first subsurface layer are buckled in this scenario.

^{p)}Furthermore, potential alloy inhomogeneities may cause local variations in the lattice plane spacing, i.e., $d_{111}(\text{Cu}_3\text{Au}) \neq \text{const.}$

buckles. Discrepancies between our experimental findings and the theoretical predictions may be due to the fact that the DFT calculations do not include the long-range surface reconstruction. This reconstruction leads to only a small surface buckling on a local scale, i.e., between neighboring surface atoms (also of different chemical nature).

The Au atoms are considered as being the driving force behind these effects (see below) while the Cu atoms follow the displacements due to attractive interatomic forces in the surface layer, which outweigh the interlayer attractive forces. In contrast, a selective outward relaxation of only the Au atoms [$+0.12(1)$ Å with respect to the Cu surface atoms] has been proven experimentally for the $\text{Cu}_3\text{Au}(100)$ surface by means of ion scattering.^{410,411} As compared to $\text{Cu}_3\text{Au}(111)$, the buckling of the $\text{Cu}_3\text{Au}(100)$ surface, which originates from the different vertical heights of Cu and Au atoms, is larger by a more than a factor of 2. For the present case of $\text{Cu}_3\text{Au}(111)$, the denser packing of the surface atoms (+15 % if comparing the ideally ordered surfaces) apparently favors the surface relaxation as a “rigid” layer i.e., without a substantial buckling between Cu and Au atoms on a *local* scale. The discrepancies between the experimental and the theoretical results are attributed to the fact that Moreira *et al.* employed structure models for $\text{Cu}_3\text{Au}(111)$ with only 4 surface atoms in their DFT calculations,⁴²⁶ corresponding to the number of atoms within the unit cell of the $p(2 \times 2)$ reconstruction, whereas the long-range surface reconstruction expands over more than one hundred surface atoms. We speculate that calculations on a larger surface ‘unit cell’ may lead to a better agreement between experimental and theoretical results concerning both the surface relaxation and the long-range reconstruction.

It has been noted already in the context of the LEED results (see Sec. 6.3.1) that a lateral mismatch between the surface layer and subsurface layers does not exist, in spite of the altered surface composition (the presence of the long-range surface reconstruction is neglected at this point due to its huge lattice constant and the thus very small in-plane lattice mismatch). That is, the surface lattice constant is not affected by the altered surface composition. Presumably, the reason is as follows: the total number of atoms at the surface is reduced since Cu atoms segregate into the bulk crystal at a given rate while the segregation rate of Au atoms towards the surface is smaller. This results in a surface layer which is less densely packed than the ideal $\text{Cu}_3\text{Au}(111)$ surface. In turn, a larger surface lattice constant would be expected for $\text{Cu}_3\text{Au}(111)$ assuming a constant quantity of surface atoms (and also neglecting that the actual sites of the surface atoms are usually bulk-determined; see also above). Yet, the lower surface atom density diminishes the (otherwise inevitable) surface stress. Therefore, the energetic cost of a lattice mismatch between the topmost atomic layer and the subsurface layers is not overcome. Due to the larger size of the Au atoms in comparison to Cu (13 % in r_m , see Table 2.3), however, steric hindrance or, in other words, Pauli repulsion occurs between the first and the second surface layer if the Au atoms also occupy former Cu sites or inter-lattice sites at the surface (as indicated by STM) which then leads to the observed outward relaxation. In addition, the interlayer bonding may be weakened between the surface layer and the second layer due to partial absence of the more reactive Cu atoms within the topmost layer and its thus more Au-like character. In terms of the *trans influence* (also termed structural *trans* effect),^{17,20,461,462} a stronger bonding and thus a reduced spacing between the second and third layer, that is, an inward relaxation of the second layer, is expected due to an enhanced electron density at the subsurface metal atoms available for interlayer bonding.^{422,463} The concept of the *trans* influence originates from coordination chemistry and states that a weaker and thus longer bond of a ligand to a metal center strengthens and thus shortens the bond to the ligand in *trans* position.^{56,57,461} Concerning the three topmost $\text{Cu}_3\text{Au}(111)$ surface layers, such an effect is not covered by our simple model. At this point, further investigations which potentially clarify this issue, for example, LEED- $I(V)$, surface x-ray diffraction, or ion scattering measurements, are

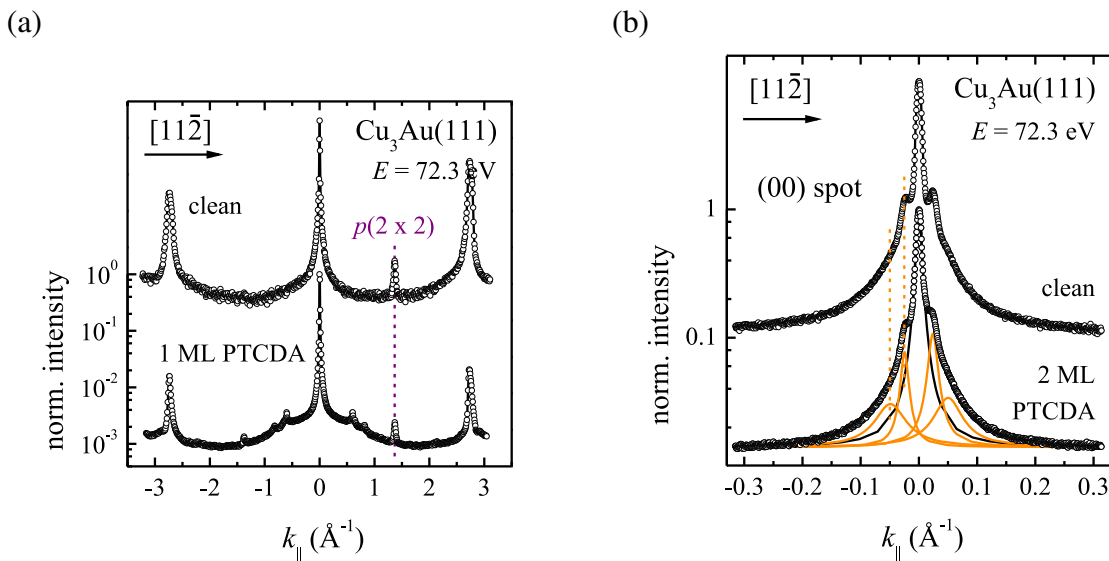


FIG. 6.10. One-dimensional LEED scans of the PTCDA-covered $\text{Cu}_3\text{Au}(111)$ surface in comparison to those of the clean surface at an electron energy of 72.3 eV. (a) One-dimensional LEED scans along the $[11\bar{2}]$ direction through the specular reflection for the clean surface (top, $T = 350$ K) and for 1 ML PTCDA/ $\text{Cu}_3\text{Au}(111)$ (bottom, $T = 85$ K). The $p(2 \times 2)$ reconstruction spots are indicated in purple. Spots with k_{\parallel} values from 0.5 \AA^{-1} to 1.0 \AA^{-1} originate from the PTCDA superstructure. The PTCDA overlayer was prepared by thermal desorption of multilayers (annealing at 575 K for 5 min). (b) Profiles of the (00) spot for the clean (top) and the PTCDA-covered surface (bottom) at 85 K. The PTCDA coverage was 2 ML in the latter case, and the PTCDA/ $\text{Cu}_3\text{Au}(111)$ sample had been annealed at 500 K for 5 min prior to the measurements. Lorentzian line shapes have been fitted to the spot profiles. Components from the substrate and the long-range reconstruction are shown in black and orange, respectively.

needed. We speculate that an outward relaxation also of the second layer may be due to the weak, but still present bonding to the first, buckled layer. The second layer may follow the buckling of the topmost layer. As a consequence, the bonding to the third layer is disturbed and thus also weakened.

6.5 Results for the PTCDA-covered $\text{Cu}_3\text{Au}(111)$ surface

We have also investigated the influence of PTCDA adsorption on the properties of the $\text{Cu}_3\text{Au}(111)$ surface. The results concerning the metal surface are presented here. The results on the PTCDA layers themselves will be reported in the following section. A collective discussion of the experimental results for PTCDA on $\text{Cu}_3\text{Au}(111)$ is found in Sec. 6.7.

6.5.1 Lateral structure

Figure 6.10(a) shows representative one-dimensional LEED scans of the clean as well as the PTCDA-covered $\text{Cu}_3\text{Au}(111)$ surface. The PTCDA coverage amounted to 1 ML in the displayed case where the overlayer was prepared by thermal desorption of PTCDA multilayers [by means of annealing at 575 K for 5 min; see Fig. 6.19 below for a TPD spectrum of PTCDA/ $\text{Cu}_3\text{Au}(111)$]. Spots originating from the PTCDA superstructure may already be discerned at k_{\parallel} values of 0.5–

1.0 \AA^{-1} . The PTCDA superstructure(s) will be reported in Sec. 6.6.1. Here, we focus on the spot profiles of the first-order spots of the substrate at $k_{\parallel} = 2.74 \text{ \AA}^{-1}$ and the $p(2 \times 2)$ reconstruction at $k_{\parallel} = 1.37 \text{ \AA}^{-1}$ [marked in purple in Fig. 6.10(a)], respectively. The spot profiles of the specular reflection from both the clean and the PTCDA-covered surface are not compared here due to contributions from the PTCDA overlayer in the latter case. The intensity of the first-order substrate spots is attenuated by about one order of magnitude by the PTCDA monolayer.⁹⁾ The $p(2 \times 2)$ spots are also attenuated but to a smaller degree. That is to say, the integral intensity of the $p(2 \times 2)$ spots increases by a factor of 3 to 5 relative to that of the first-order substrate spots. This indicates a higher degree of order at the $\text{Cu}_3\text{Au}(111)$ surface with more and/or larger $p(2 \times 2)$ reconstruction domains in the presence of PTCDA. Indeed, the first order $p(2 \times 2)$ spots exhibit a smaller width for the PTCDA-covered surface. The average domain size increases from about 150 \AA to 250 \AA , as the widths of the respective spot profiles at an electron energy of 72.3 eV reveal, for example.

At the same time, also the profiles of the first-order (fundamental) substrate spots become more narrow, yielding domain sizes of about 165 \AA (+50 % in comparison to the clean surface).¹⁾ As is the case for the clean surface, no indications for a lateral segregation of one of the two chemical elements into pure domains at the surface are found. Hence, the interactions across the metal/organic interface result in an enhanced order and stabilize the ideal structure of the ordered alloy surface. This is also reflected in the average width of the (00) spot and thus in the overall coherence of the $\text{Cu}_3\text{Au}(111)$ surface which increases to 845 \AA (+30 %).

As Fig. 6.10(b) shows, the presence of the PTCDA molecules does not lead to an altering, i.e., a change in the lattice constant, or a lifting of the long-range surface reconstruction, which in principle may be possible.^{360–362} Seemingly, the metal/molecule interaction is rather moderate. Still, the satellite spots can be clearly discerned from the intrinsic (00) spot profile, and even second-order satellite spots may be identified by fitting Lorentzian line shapes to the experimental data. Only the width of the satellite spots [to which $T_{w,\text{eff}}$ is inversely proportional; see also Eq. (3.46)] is increased compared to the clean $\text{Cu}_3\text{Au}(111)$ surface even after thermal annealing at temperatures of 500 K to 575 K for a few minutes, yielding average domain sizes of about 465 \AA at electron energies of 72.3 eV (–20 % in comparison to the clean surface) for coverages above 1 ML and about 550 \AA at electron energies of 32.1 eV (–30 % in comparison to the clean surface) for monolayer coverages. Apparently, the interaction of the surface atoms with the PTCDA molecules slightly lowers the tendency for the $\text{Cu}_3\text{Au}(111)$ surface to reconstruct. Furthermore, the enhanced overall order of the PTCDA-covered $\text{Cu}_3\text{Au}(111)$ surface (see above and also the following chapter on the surface composition) may restrict the long-range reconstruction to a certain extent. Alternatively, *local* interactions between the PTCDA molecules and the surface atoms may lead to a subtle rearrangement of the latter, thereby lowering the average size of the long-range surface reconstruction domains.

6.5.2 Surface composition

Now the question arises what the reasons for the enhanced order and the lower degree of long-range reconstruction at the PTCDA-covered $\text{Cu}_3\text{Au}(111)$ surface may be. One obvious parameter

⁹⁾Note that the sample temperatures for the two one-dimensional LEED scans which are displayed in Fig. 6.10(a) were different. Yet, the attenuation of the fundamental substrate spots is of comparable size, i.e., identical within a factor of only about 1.5, also in LEED patterns where the sample temperatures were identical. Thus, thermal effects on the (relative) spot intensities are small and may be neglected here.

¹⁾The fact that the determined average domain size of the $p(2 \times 2)$ reconstruction is larger than that of the (fundamental *fcc*-like) substrate also for the PTCDA-covered surface is again attributed the paracrystallinity of the substrate surface (see Sec. 6.3.1 for the results on the clean surface).

to be altered upon PTCDA adsorption could be the surface composition. Therefore, this was investigated by means of photoemission spectroscopy (see also Sec. 6.3.2). XP spectra of the Cu_{2p_{3/2}} and Au_{3d_{5/2}} signals were conducted on a preparation with a coverage of about 0.8 ML PTCDA/Cu₃Au(111) for different times of x-ray beam exposure at a photon energy of 2858.0 eV and at an effective angle θ of 86°. The results regarding the normalized photoelectron yield ratio $Y_{\text{Cu}2p_{3/2}}/Y_{\text{Au}3d_{5/2}}$ are shown in Fig. 6.5. Note that for the determination of the normalized photoelectron yield ratio $Y_{\text{Cu}2p_{3/2}}/Y_{\text{Au}3d_{5/2}}$, in accordance with Eq. (3.56), the attenuation of the individual photoemission signals by the PTCDA overlayer was taken into account.

On a fresh spot, i.e., on a spot which has previously not been exposed to the x-ray beam, the surface composition agrees nicely with that of the clean Cu₃Au(111) surface, being Cu_{0.61(3)}Au_{0.39(3)}.^{s)} The same is true after the first 15 min of beam exposure. Over a period of 2 h, which approximately corresponds to the time span of two full XSW profile measurements, however, the surface composition changes towards the expected stoichiometry of $N_{\text{Cu}}/N_{\text{Au}} = 3 : 1$ for the ideal surface, being Cu_{0.69(4)}Au_{0.31(4)} eventually. Considering the same two scenarios as for the clean surface (see Sec. 6.3.2), the following two extreme cases can be evaluated. Assuming that the number of Au atoms in the surface layer is constant and corresponds to that in the ideal state, the experimental finding of $N_{\text{Cu}}/N_{\text{Au}} \propto Y_{\text{Cu}2p_{3/2}}/Y_{\text{Au}3d_{5/2}} = 2.18(16) : 1$ implies that about every fourth Cu atom is missing at the Cu₃Au(111) surface as compared to the ideal surface, where $N_{\text{Cu}}/N_{\text{Au}} = 3 : 1$. In the second case, where the fraction of the surface area covered by Cu and Au atoms is assumed to be constant (that is, $\sum_i \pi r_{m,i}^2 = \text{const}$), a stoichiometric ratio of $N_{\text{Cu}}/N_{\text{Au}} = 2.70(11) : 1.24(11)$ is expected, considering both the observed $Y_{\text{Cu}2p_{3/2}}/Y_{\text{Au}3d_{5/2}}$ ratio and the metallic radii r_m of Cu and Au (see Table 2.3). In other words, 0.30(11) Cu atoms at the Cu₃Au(111) surface are replaced by 0.24(11) Au atoms per unit cell on average in this scenario. Regardless of the valid scenario, the Cu fraction at the surface obviously increases by intense x-ray illumination in the presence of PTCDA on the surface. Yet, the reaction kinetics of this process are slow. This may be explained by (1) the sample temperature of about 300 K being too low for substantial diffusion of the involved atoms, as well as by the fact (2) that numerous atoms have to diffuse from the Cu₃Au(111) crystal bulk towards the metal/organic interface, i.e., distances on a scale of at least several ten nanometers, in order to achieve the observed change in the surface composition.

Nonetheless, the influence of PTCDA adsorption on the surface composition is evident. The now larger surface fraction of Cu atoms results in the observed, enhanced degree of order at the Cu₃Au(111) surface. Because the surface composition is close to that of the Cu₃Au bulk, adopting the ideal, bulk-like structure also in the topmost layer is favored while deviations from the ideal structure are energetically more costly. Two reasons are conceivable for the Cu diffusion towards the surface layer. Firstly, the Cu segregation may be caused by electronic effects, i.e., by an altered charge balance at the surface due to the presence of the organic (acceptor) molecules. Secondly, local interactions between the surface Cu atoms and the PTCDA molecules seem plausible. For example, O—Cu and N—Cu interactions have been shown to induce a reconstruction and Cu segregation at the Cu₃Au(110) surface.^{436,440,446} But before we turn to the properties of the adsorbed PTCDA molecules and thus to the surface bonding, also the vertical structure of the PTCDA-covered Cu₃Au(111) surface will be clarified.

6.5.3 Vertical structure

It has been shown in Sec. 6.3.3 that the clean Cu₃Au(111) surface exhibits an outward relaxation. This has been explained by the Cu depletion in the topmost layer. Bearing in mind that the Cu

^{s)}Note that one data set of both Cu_{2p_{3/2}} and Au_{3d_{5/2}} XP spectra was recorded within 2 min.

FIG. 6.11. Typical XSW photoelectron yield curves of Cu and Au at the PTCDA-covered $\text{Cu}_3\text{Au}(111)$ surface. The $\text{Cu}L_3M_{45}M_{45}$ and $\text{Au}3d_{5/2}$ signals were employed in the respective XSW experiments. Experimental data points are shown as filled circles while respective fits to the data are shown as solid lines. The curves have been vertically offset for clarity. In the case of $\text{Au}3d_{5/2}$, error bars are so small that they are almost hidden by the data points. In addition, the measured reflectivity of the substrate employing the (111) lattice planes (open circles) and the corresponding fit (dashed line) are shown. Error bars have been omitted for clarity here. Note that only the topmost surface layer has been probed in these experiments. Both XSW curves were acquired successively on the same (but previously exposed) spot on the sample.

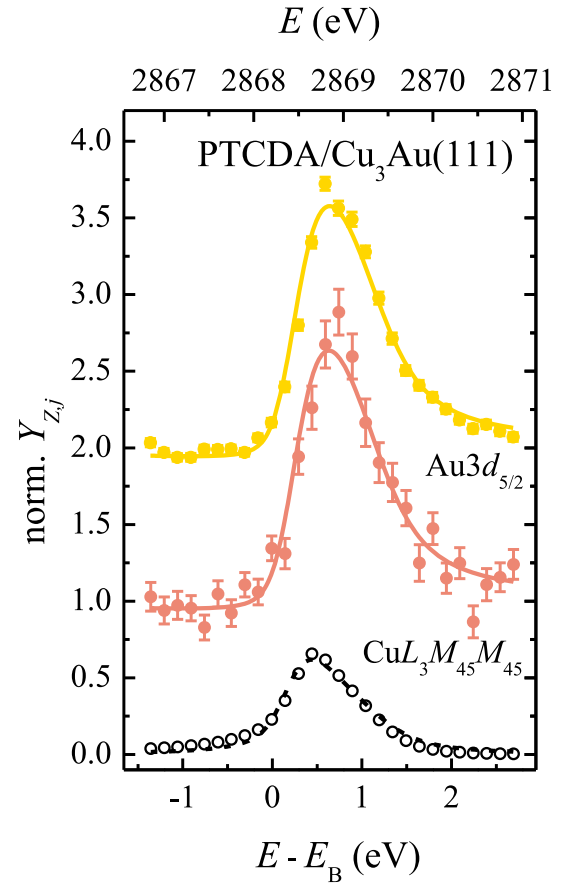


TABLE 6.4. Averaged vertical shifts for the Cu and Au atoms at the PTCDA-covered $\text{Cu}_3\text{Au}(111)$ surface as obtained from XSW experiments for both acquisitions # 1 and # 2. In addition, the results for the clean surface are given. The $\text{Cu}L_3M_{45}M_{45}$ and $\text{Au}3d_{5/2}$ signals were employed in the respective XSW experiments. The parameters f_c and p_c are the coherent fraction and position, respectively, while $d = p_c d_{hkl}$ is the vertical height. d_{hkl} is the lattice plane spacing of the employed (111) Bragg reflection of the Cu_3Au substrate crystal. $\Delta d = d_{\text{PTCDA}} - d_{\text{clean}}$ denotes the relaxation of the surface layer upon PTCDA adsorption. Note that only the topmost surface layer has been probed in the XSW experiments.

	clean $\text{Cu}_3\text{Au}(111)$			PTCDA/ $\text{Cu}_3\text{Au}(111)$			
	f_c	p_c	d (Å)	f_c	p_c	d (Å)	Δd (Å)
$\text{Cu}L_3M_{45}M_{45}$	0.82(5)	0.13(1)	0.28(1)	0.92(8)	0.25(1)	0.55(1)	+0.27(2)
$\text{Au}3d_{5/2}$	0.81(7)	0.15(1)	0.33(2)	0.81(2)	0.27(4)	0.58(8)	+0.25(8)

fraction at the surface increases upon PTCDA adsorption, it seems evident that the relaxation decreases for the PTCDA-covered surface. Indeed, the observed XSW profiles of the substrate CuL₃M₄₅M₄₅ and Au3d_{5/2} signals, as displayed in Fig. 6.11, have changed in shape and show a larger variation in the photoelectron yield as a function of the photon energy now than those of the clean surface (see also Fig. 6.7). Note that the XSW profiles for both types of atoms have changed in a similar manner. Therefore, the altering in the vertical positions is concluded to be very similar for both the Cu and the Au atoms. This reflects in the deduced structural parameters f_c and p_c which are summarized in Table 6.4.¹⁾ In contrast to our above assumption, however, the surface relaxes *further outward* upon PTCDA adsorption, namely, by almost +0.3 Å or, in other words, +12 % of the lattice plane spacing. Obviously, the (attractive) interaction of the surface atoms with the PTCDA molecules weakens the interlayer bonding between the outmost surface layers such that the layer spacing is expanded.

Note again at this point that collecting a complete data set of XSW photoelectron yield curves for both Cu and Au atoms (which was acquired on *one* identical spot on the sample) lasted about 2 h. Therefore, the XSW experiments probed the sample surface in the Cu-enriched state where the surface segregation of Cu atoms either was in progress or had even saturated [see also Sec. 6.5.2 and Fig. 6.5 in Sec. 6.3.2, page 101, for the evolution of the Cu₃Au(111) surface stoichiometry over time of x-ray exposure]. Indeed, the results of the individual XSW experiments show a dependency on the chronological order [acquisition # i , where $i = 1$ (i.e., acquisition # 1) refers to the first XSW measurement on a previously unexposed spot] as Table 6.5 reveals. For the CuL₃M₄₅M₄₅ signal, p_c changed only marginally by -0.01 upon variation of the chronological order, i.e., from first to second experiment or, equivalently, after about 1 h of x-ray beam exposure. The f_c result, however, decreased by 0.13 when the CuL₃M₄₅M₄₅ signal was collected lastly, being almost identical to that of the Au3d_{5/2} signal eventually. Unfortunately, XSW photoelectron yield curves of the Au3d_{5/2} signal on a fresh, that is, on a previously unexposed spot are not available. Note, however, that the p_c result for the Au3d_{5/2} signal showed a relatively large variation of 0.05 between the two exposed spots where XSW data was collected (acquisition # 2); the result in f_c , in contrast, essentially remained unaffected (within 0.02). Despite the discrepancies in the fitting results for both f_c (in the case of CuL₃M₄₅M₄₅) and p_c (in the case of Au3d_{5/2}), we relied on the averaged values as stated in Table 6.4 in the course of the present work in order to improve the experimental statistics (only one data set was available for the CuL₃M₄₅M₄₅ signal in acquisition # 2, and two data sets were available for the CuL₃M₄₅M₄₅ signal in acquisition # 1 and for the Au3d_{5/2} signal in acquisition # 2, respectively) and/or because the deviations were within the experimental accuracy of XSW.¹⁾

Judging from the (averaged) f_c values for the Au3d_{5/2} signal (see Table 6.4 above), which are identical for both the clean and the PTCDA-covered surface, the surface buckling which is (proposed to be) present at the clean Cu₃Au(111) surface is maintained also for the PTCDA-covered surface. The f_c values for the CuL₃M₄₅M₄₅ Auger signal, however, have increased by about 10 %. In principle, there are two possible ways of interpretation here. Either the Cu atoms do not follow the vertical displacements of the Au atoms as likely any more as at the clean surface. The presence of the PTCDA molecules leads to a more defined vertical position of the Cu atoms which we explain by the interaction with the “rigid and planar” PTCDA layer. Or the f_c value has increased simply due to non-structural effects, such as altered and/or additional contributions to the Auger

¹⁾Note that the fitting curves obtained here are subject to the same (small) imperfections as those obtained for the XSW data of the surface atoms at the clean Cu₃Au(111) surface (see Sec. 6.3.3). Again, these imperfections do not challenge the stated fitting results.

¹⁾Note that such discrepancies in the XSW results for different times of x-ray beam exposure, that is, for different acquisitions # i , were not observed for the clean Cu₃Au(111) surface [$|\Delta f_c| \leq 0.03(3)$, $|\Delta p_c| \leq 0.01(1)$, and $|\Delta d| \leq 0.02(1)$ Å].

TABLE 6.5. XSW results for the Cu and Au atoms at the PTCDA-covered Cu₃Au(111) surface for different times of x-ray beam exposure. The CuL₃M₄₅M₄₅ and Au3d_{5/2} signals were employed in the respective XSW experiments. Data sets for both substrate signals have been acquired on the same, previously unexposed spot on the sample with alternating chronological order (# 1 and # 2, respectively). The results of two individual data sets were averaged for the CuL₃M₄₅M₄₅ signal in the case of acquisition # 1 and for the Au3d_{5/2} signal in the case of acquisition # 2. Only one XSW data set was available for the CuL₃M₄₅M₄₅ signal in the case of acquisition # 2 while the Au3d_{5/2} signal was not recorded on a fresh spot, i.e., for acquisition # 1. The parameters f_c and p_c are the coherent fraction and position, respectively, while $d = p_c d_{hkl}$ is the vertical height. d_{hkl} is the lattice plane spacing of the employed (111) Bragg reflection of the Cu₃Au substrate crystal. $\Delta d = d_2 - d_1$ denotes the change in the vertical height with increasing x-ray beam exposure, i.e., the difference between the d values of acquisitions # 2 and # 1 in one spot (n.d. = not determined, n.a. = not available/applicable).

	PTCDA/Cu ₃ Au(111)						
	# 1			# 2			Δd (Å)
	f_c	p_c	d (Å)	f_c	p_c	d (Å)	
CuL ₃ M ₄₅ M ₄₅	0.96(1)	0.26(1)	0.56(1)	0.83(7)	0.25(1)	0.53(2)	-0.03(2)
Au3d _{5/2}	n.d.	n.d.	n.d.	0.81(2)	0.27(4)	0.58(8)	n.a.

process by stimulation through electrons and/or secondary radiation.^{28,175} This issue cannot be definitely resolved at this point. However, the structural results for the PTCDA molecules themselves, in particular the observed high coherent fractions for the C and O atoms in PTCDA (see Table 6.8), apparently favor the former interpretation over the latter, i.e., the picture of a more defined vertical position of the Cu atoms. Yet, the observed trend in the f_c results of the individual CuL₃M₄₅M₄₅ XSW measurements with increasing duration of x-ray beam exposure (see above) is contradictory to this conclusion, and indicates that this difference has to be interpreted by altered and/or additional contributions to the Auger process.

6.6 Results for PTCDA on the Cu₃Au(111) surface

Finally, the results on the structural and electronic properties of PTCDA on the Cu₃Au(111) surface will be presented in this section. The geometric structure of the adsorbate was investigated with various methods, namely, with LEED and STM (see Sec. 6.6.1), as well as with XSW (see Secs. 6.6.3 and 6.6.4). In addition, the electronic structure of the core levels was investigated by means of XPS (see Sec. 6.6.2). This set of complementary experimental techniques has been employed in order to unravel the presumably very complex situation at the PTCDA/Cu₃Au(111) interface regarding the surface bonding of the adsorbed molecules.

6.6.1 Lateral structure and growth

PTCDA forms long-range ordered structures on the Cu₃Au(111) surface. The lattice parameters of these structures were derived by LEED measurements while STM investigations yielded the molecular arrangement within the unit cells, among others. For purposes of structuring the obtained results, we firstly focus on the structures in the monolayer regime. The structures in the

multilayers regime and the consequences of thermal treatment of the prepared PTCDA layers will be address subsequently.

Monolayer structures

Exemplary LEED patterns of nominal 1 ML PTCDA/Cu₃Au(111), which were obtained for differently treated preparations, are displayed in Fig. 6.13. The left part of this figure shows experimental data for a monolayer of PTCDA which was obtained by annealing of about 5 ML PTCDA at 575 K for 2 min, that is, by thermal desorption of multilayers (see also below). The right part of this figure, in contrast, shows data which was obtained for a preparation where nominally 1 ML PTCDA was grown on the Cu₃Au(111) at a sample temperature of 350 K and a deposition rate of 0.4 ML min⁻¹. Common to both preparations is the presence of sharp superstructure spots (marked in dark red) which exhibit the double-triangle motif that is well-known from herringbone (HB) phases of PTCDA on surfaces [see Figs. 6.13(c) and (d), in particular, for this detail].^{98,114} For the preparation route, however, where the PTCDA monolayer was grown as such, additional, much weaker spots are present in the diffraction pattern. These additional spots have to be distinguished due to their different origins. First of all, spots which were at the detection limit of the SPA-LEED instrument in the experiments shown in Figs. 6.13(a) and (c) are more prominent in Figs. 6.13(b) and (d) (also marked in dark red; see $|k_{\parallel}|$ values in the range of about 0.30 Å to 0.55 Å, in particular). Yet, these spots also originate from the *same* HB phase as the above-mentioned sharp and relatively intense superstructure spots. This phase will be referred to as α phase (or main HB phase) in the following (dark red in Fig. 6.13). Obviously, an extinction rule, which may be softened to some extent (see also below), applies due to the presence of glide planes within the unit cell of the α phase.^{157,210} The presence of this symmetry element in the unit cell of the α phase was also proven by STM data. The results of the STM investigations regarding the molecular arrangement on the surface will be reported below.

In addition to the spots of the α phase, two further phases may be identified from the LEED patterns. They are depicted in green and blue in the simulations in Fig. 6.13. The diffraction spots of both phases also exhibit the double-triangle motif, but they are of lower intensity than the spots of the α phase. Therefore, these PTCDA phases will be referred to as β and γ phase, respectively. Both minor HB phases have similar lattice constants as the α phase, as judged from the respective k_{\parallel} values of the observed diffraction spots. However, the angular orientation of the corresponding unit cells differs for the three phases. Before this will be analyzed in more detail, we briefly focus on a further observation in the LEED patterns of Fig. 6.13. Additional weak spots are observed in the vicinity of the intense spots of the α phase. They are exemplarily marked by orange arrows in Figs. 6.13(c) and (d). Presumably, these spots are due to multiple scattering effects. As shown in Figs. 6.13(e) and (f), and also as respective close-ups in Figs. 6.12(a) and (b), assuming the presence of long-range reconstruction spots also around the α -phase spots is very consistent with the experimental observations. Thus, this finding further corroborates the conclusions drawn in Sec. 6.5.1 that the long-range reconstruction of the Cu₃Au(111) surface remains essentially unaffected by PTCDA adsorption.

From the respective two-dimensional LEED patterns (see Fig. 6.13, for example) and one-dimensional LEED scans (not shown), the lattice parameters of the three HB phases were determined. The obtained values are compiled in Table 6.6. Remarkably, the lattice parameters b_1 , b_2 , and β are identical within the error margins for all three HB phases. All phases exhibit rectangular unit cells within the error margins. The only substantial difference between these phases is the angle ϕ which describes the orientation of the corresponding unit cells with respect to the close-packed substrate direction. Apparently, the metal/molecule interaction is rather moderate since the

lattice constants are not influenced by the relative orientation of the unit cells and the substrate. This is also expressed in the incommensurate registry between the superstructure unit cells and the substrate surface. In all cases, the lattice parameters are similar to those of two bulk polymorphs of PTCDA (see also Table 2.1). Only the areas of the unit cells are about 3–5 % smaller here. Still, however, the unit cells accommodate two PTCDA molecules in flat-lying geometries, as is expected for an herringbone arrangement and as was revealed by respective STM images (see Fig. 6.16 below, for example).

Before the STM results will be looked at in more detail, we firstly compare the lattice parameters for PTCDA on $\text{Cu}_3\text{Au}(111)$, which were obtained from SPA-LEED, with those for PTCDA on $\text{Au}(111)$ ^{114,116} (see Table 6.1) and $\text{Cu}(111)$ (see Table 5.2 in Chapter 5 of the present work). Strikingly, the lattice parameters b_1 , b_2 , and ϕ of the α phase and the β phase of PTCDA/ $\text{Cu}_3\text{Au}(111)$ are almost identical to those found by Kilian *et al.*¹¹⁴ for PTCDA/ $\text{Au}(111)$, i.e., to those of phase B (within 0.1 Å and 0.2°) and phase A (within 0.4 Å and 3.5°), respectively. Note that, in all cases, the angle β enclosed by the surface unit cell vectors amounts to 90° within the error margins. Also, the relative intensities of the two diffraction sub-patterns and thus the relative surface fractions, which are covered by one or the other HB phase, are comparable [see Fig. 4(d) and (e) in Ref. 114, for example]. Therefore, we conclude at this point that the (111) surface of Cu_3Au essentially behaves like a pure $\text{Au}(111)$ surface regarding the adsorption properties, as has already been stated in Sec. 6.1. In accordance with Ref. 114, we identify the α phase as the thermodynamically stable, *equilibrium* phase (B) and the β phase as a *non-equilibrium* phase (A). Thus, the β phase may be thermodynamically (slightly) less favorable and kinetically stabilized. Indeed, we find that the presence of the β phase can be reduced or even prevented by three conditions, namely, low coverages, low deposition rates, and post-annealing at low heating and cooling rates ($\leq 1 \text{ K s}^{-1}$). These conditions allow for an enhanced surface diffusion of the molecules and an enhanced ordering, enabling the system thereby to reach the thermodynamic equilibrium.^{v)}

The γ phase, however, is similar to the α phase which is formed by PTCDA on the $\text{Cu}(111)$ surface (see Table 5.2). The lattice constants agree within 0.5 Å, and the angular orientations of the unit cells are identical ($\Delta\phi = 0.2^\circ$).^{w)} Therefore, the HB phases on the $\text{Cu}_3\text{Au}(111)$ surface may also be termed as “Au-analogues” (α and β phase) or “Cu-analogue” (γ phase), respectively. However, we emphasize again that the similarities in the surface structures of PTCDA on $\text{Cu}_3\text{Au}(111)$ to those on the pure Au and Cu surfaces does not mean that (nearly) pure domains of one of the two elements, Au or Cu, are present at the surface. This had been excluded on the basis of the SPA-LEED results presented in Sec. 6.5.1 where no indications for lateral segregation upon PTCDA adsorption were found. Therefore, the following scenario for the presence of both Au-analogous and Cu-analogous HB phases on $\text{Cu}_3\text{Au}(111)$ seems plausible. This scenario employs the argument that the structure of a given PTCDA domain is determined by its initial nucleation site, which may be a step site, a kink site, a defect site, or a terrace site, for instance. *Local* variations in the geometric structure at either of these sites, which in turn are facilitated by the (initial) Cu depletion of the surface, may favor one of the three phases over the others at the starting point of the nucleation. A potential transition to the equilibrium phase for larger domain sizes is kinetically hindered, apparently. From the fact that the spots of all HB phases are of comparable width we conclude that the average domain sizes are similar (see below for details on the average domain size). Hence, the structure of

^{v)}Note at this point that sample temperatures in the range from 300 K to 350 K during the preparation of the PTCDA films were tested. Within this temperature interval no clear dependency of the surface fraction of β phase on the sample temperature during growth could be made out. Higher T_{sample} values were not tested here, e.g., 450 K as in Ref. 114.

^{w)}Discrepancies in the lattice constants may also be due to small systematic errors in the calibration of the SPA-LEED instrument.¹¹⁴

TABLE 6.6. Structural results for PTCDA on the Cu₃Au(111) surface, as obtained from (SPA-)LEED and STM experiments, and proposed model parameters. The lattice constants b_i , the enclosed angle β , and the area of the unit cell, A_{uc} , are given. ϕ denotes the enclosed angle between the surface lattice vectors \mathbf{a}_1 and \mathbf{b}_1 , ϱ is the angle of inclination of the long molecular axis with respect to \mathbf{b}_1 (values in square brackets refer to the second molecule within the unit cell), and τ is the herringbone angle, i.e., the enclosed (acute) angle between the long molecular axes of the two symmetry-nonequivalent molecules in the unit cell. In addition, the two-dimensional space groups and the superstructure matrices \mathfrak{M} are given (HB = herringbone, S = square, n.a. = not applicable).

	α phase (HB)	β phase (HB)	γ phase (HB)	δ phase (S)	surface reconstruction
b_1 (Å)	12.1(1)	11.9(2)	12.0(2)	16.2(2)	2.65
b_2 (Å)	19.1(1)	19.0(3)	19.0(2)	16.2(2)	291(10)
β (°)	90.0(8)	90.5(9)	90.1(7)	90.0(10)	120
A_{uc} (Å ²)	231(2)	227(5)	228(4)	264(4)	667(23)
ϕ (°)	9.3(4)	26.0(4)	2.3(3)	8.0(7)	0
ϱ (°)	43(5) [137(5)]	43(5) [137(5)] ^a	43(5) [137(5)] ^a	60(3) [145(3)]	n.a.
τ (°)	86(7)	86(7) ^a	86(7) ^a	85(4)	n.a.
Two-dim. space group ^{b,c}	$p2gg$	$p211 [p2gg]$	$p211 [p2gg]$	$p211$	$p1^d$
\mathfrak{M}	$\begin{pmatrix} 4.92(2) & 0.85(3) \\ 2.93(9) & 8.21(6) \end{pmatrix}$	$\begin{pmatrix} 5.18(6) & 2.28(5) \\ 0.50(13) & 7.40(14) \end{pmatrix}$	$\begin{pmatrix} 4.62(7) & 0.21(3) \\ 3.84(9) & 8.28(8) \end{pmatrix}$	$\begin{pmatrix} 6.56(8) & 0.98(9) \\ 2.65(9) & 7.00(7) \end{pmatrix}$	$\begin{pmatrix} 1.00 & 0.00 \\ 0.00 & 110(4) \end{pmatrix}$

^aThe angles ϱ (and τ , respectively), which are given for the two minor HB phases β and γ here, are assumed to be the same as those found for the α phase. This assumption is justified by the almost identical lattice parameters for all HB phases. The explicit ϱ values for the β and the γ phase could not be determined from the STM experiments because the intrinsic error margins regarding angular measurements in STM did not always allow for an unambiguous assignment of the respective (smaller) HB domains to one of the (minor) HB phases.

^bOnly the atomic positions within the adsorbate layers are considered for the determination of the two-dimensional space groups whereas the substrate surface atoms are neglected. The symmetry of the respective interface structures in their entireties, i.e., including the substrate atoms, reduces to space group $p1$ for all PTCDA phases.

^cStatements in square brackets hold under the assumption of truly rectangular units cells. Indeed, an enclosed angle β of 90° was found for the unit cells of the minor HB phases β and γ within the error margins.

^dA real-space model of the surface reconstruction which is qualitatively similar to that for the reconstruction of the PTCDA-covered Cu(111) surface (see Sec. 5.3.2), including lateral and vertical displacements of surface atoms off the direction of uniaxial compression, is assumed here.

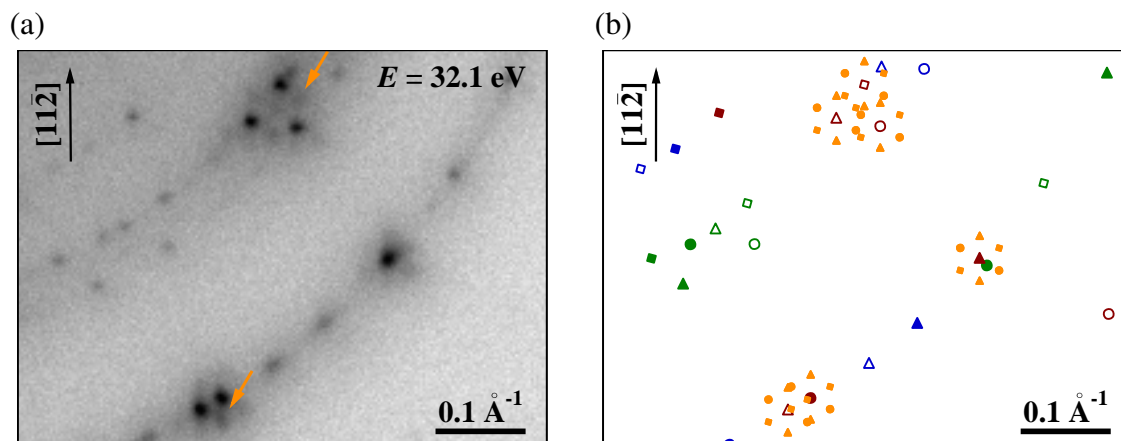
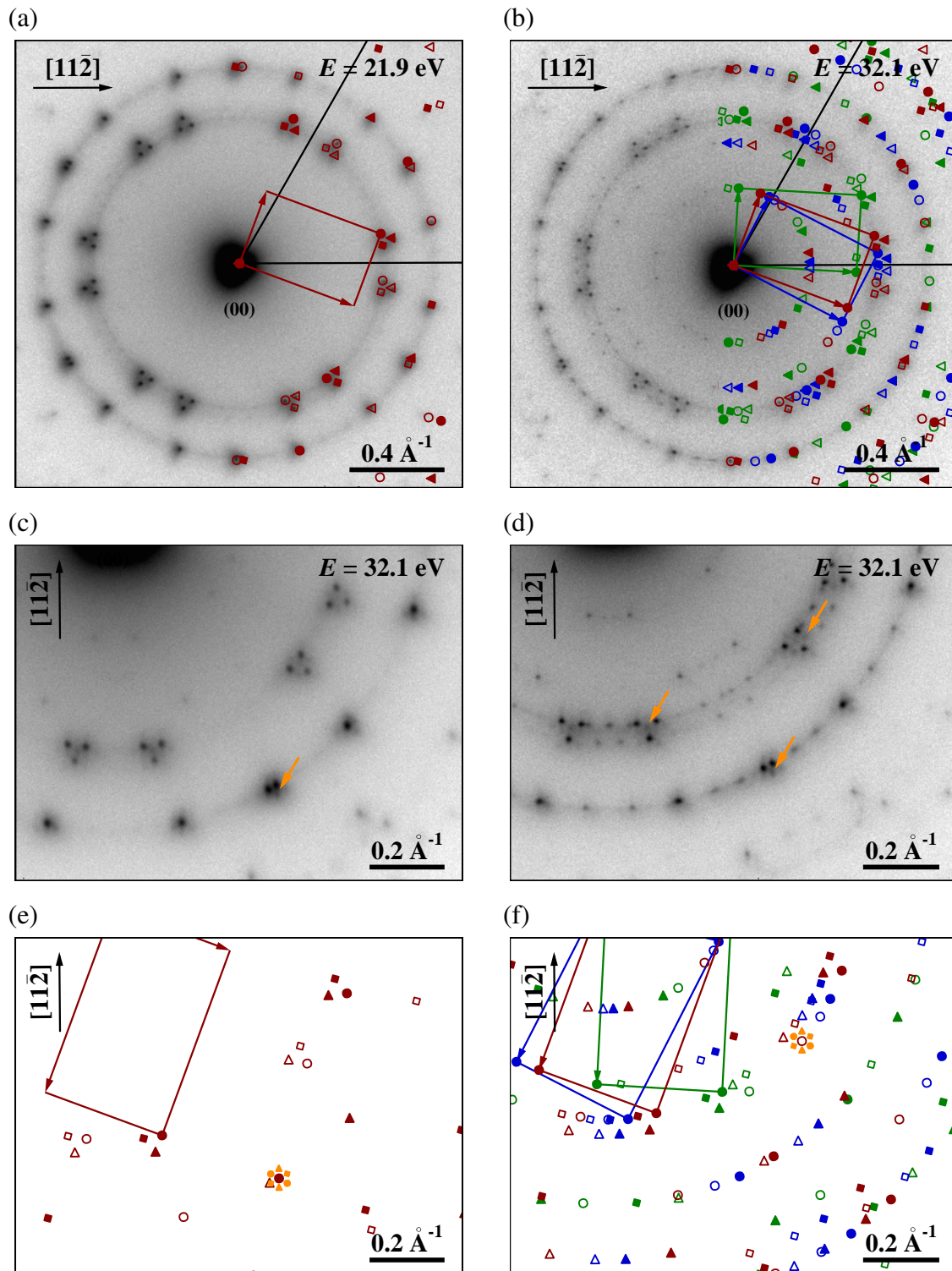


FIG. 6.12. Close-up of the LEED pattern in Fig. 6.13(d). (a) LEED pattern of nominal 1 ML PTCDA/ $\text{Cu}_3\text{Au}(111)$, as grown at $T_{\text{sample}} = 350$ K, recorded with $E = 32.1$ eV at $T = 85$ K. The region around the two orange arrows in the right half of Fig. 6.13(d) is shown. The respective original image has been enlarged by a factor of 2. (b) Corresponding simulation of the LEED pattern in (a). Spots of the three PTCDA HB phases α , β , and γ are indicated in dark red, green, and blue, respectively. Orange arrows in (a) mark exemplary positions where additional weak intensity is observed around the most intense adsorbate spots. The additional spots are explained by multiple scattering effects and originate from the long-range surface reconstruction of $\text{Cu}_3\text{Au}(111)$ as schematically depicted in orange in (b).

the domains is largely independent of the explicit, local surface structure underneath, supporting the above-raised idea of moderate (or even weak) metal/molecule interactions. We conclude that intermolecular interactions, i.e., hydrogen bond-like and quadrupole interactions,^{4,111} determine the structure formation.

Indeed, the size of the PTCDA domains is not limited by the degree of order of the $\text{Cu}_3\text{Au}(111)$ surface. For the substrate, average domain sizes of 250 \AA and 165 \AA were deduced from the width of the $\{10\}$ and $\{11\}$ $p(2 \times 2)$ reconstruction spots and substrate spots of the PTCDA-covered $\text{Cu}_3\text{Au}(111)$ surface at an electron energy of 72.3 eV (see Sec. 6.5.1), respectively. At lower energies of 32.1 eV, the former value was found to be 200 \AA on average for the clean $\text{Cu}_3\text{Au}(111)$ surface (see also Sec. 6.3.1). For the α phase, larger average domain sizes ranging from 380 \AA to 530 \AA are deduced from the second- and first-order superstructure spot widths. We note, however, that these values refer to preparations where the PTCDA monolayers were grown as such. Mono-

FIG. 6.13 (following page). LEED patterns of PTCDA monolayers on the $\text{Cu}_3\text{Au}(111)$ surface. (a) LEED pattern of 1 ML PTCDA/ $\text{Cu}_3\text{Au}(111)$, prepared by thermal desorption of multilayers ($T = 575$ K for 2 min). (b) LEED pattern of nominal 1 ML PTCDA/ $\text{Cu}_3\text{Au}(111)$, as grown at $T_{\text{sample}} = 350$ K. (c) Close-up of the left lower quadrant in (a). (d) Close-up of the left lower quadrant in (b). (e) Simulation of the LEED pattern in (c). (f) Simulation of the LEED pattern in (d). Orange arrows in (c) and (d) mark exemplary positions where additional weak intensity is observed. The observed LEED patterns in (a)–(d) are fully explained by the presence of three HB phases on the surface, namely, the α phase (dark red), β phase (green), and γ phase (blue). The additional intensity in (c) and (d) may be explained by multiple scattering: Around the most intense adsorbate spots, the long-range reconstruction spots (orange) are observed, as well, as is indicated exemplarily in (e) and (f) for two spots of the α phase. The respective electron energies are indicated within the figures. All measurements were performed at 85 K.



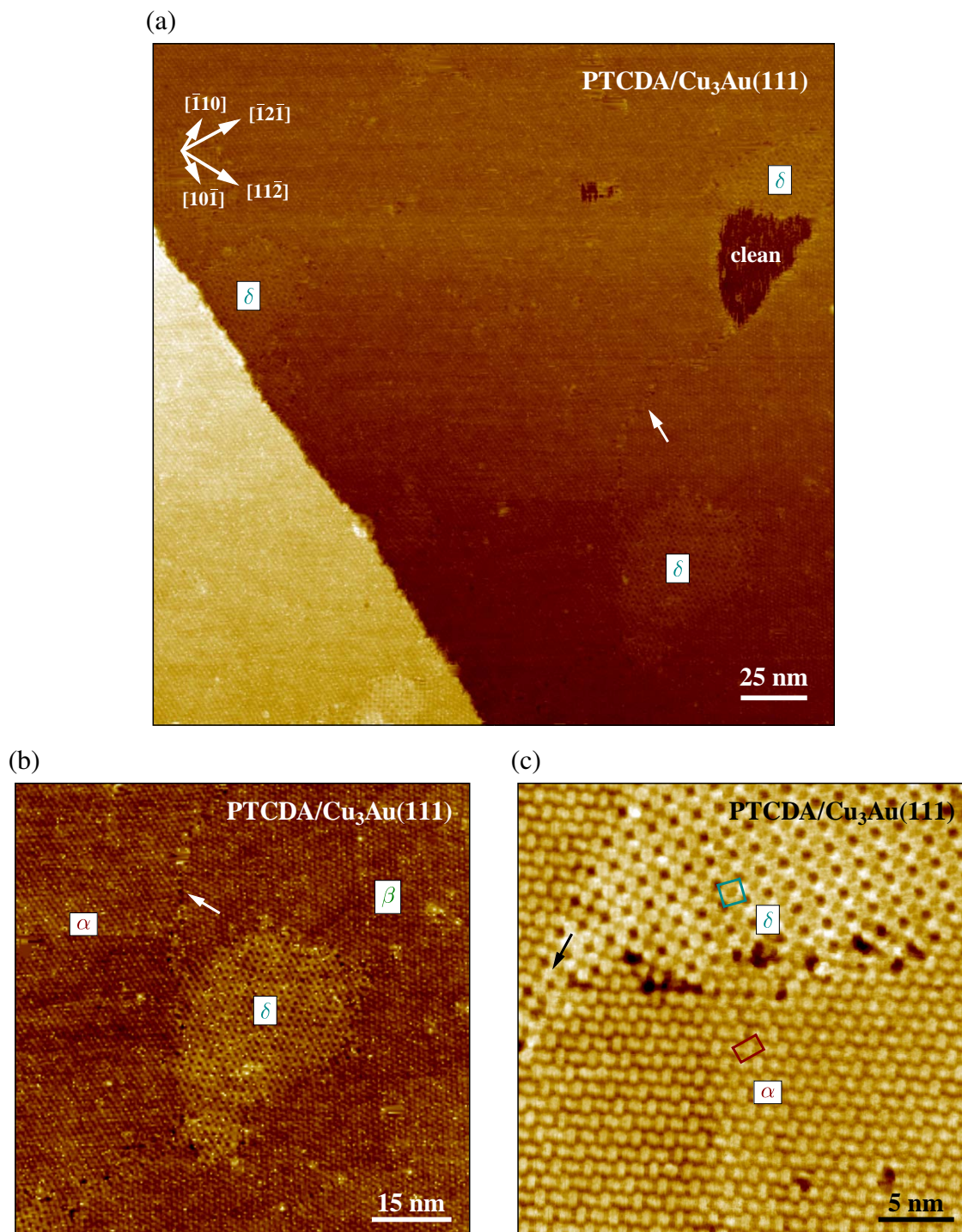


FIG. 6.14. STM images of PTCDA (sub-)monolayers on the $\text{Cu}_3\text{Au}(111)$ surface. (a) Large-scale STM image of almost 1 ML PTCDA/ $\text{Cu}_3\text{Au}(111)$ after mild annealing at 393 K for 5 min ($171 \text{ nm} \times 171 \text{ nm}$, $U_{\text{bias}} = -810 \text{ mV}$, $I_t = -15.5 \text{ pA}$). (b) Close-up of the right lower part of the image in (a) ($85.6 \text{ nm} \times 85.6 \text{ nm}$). (c) STM image of the domain boundaries between different PTCDA phases. This image was obtained on a different preparation with 0.6 ML PTCDA/ $\text{Cu}_3\text{Au}(111)$ without post-annealing ($30 \text{ nm} \times 30 \text{ nm}$, $U_{\text{bias}} = 353 \text{ mV}$, $I_t = 15.1 \text{ pA}$). Domain boundaries are exemplarily marked by arrows. Domains of the particular herringbone phases are denoted as α and β , respectively. Also, three larger domains of the (quadratic) δ phase are exemplarily marked. In addition, the unit cells of the α and the δ phase are indicated in dark red and dark cyan, respectively, in (c).

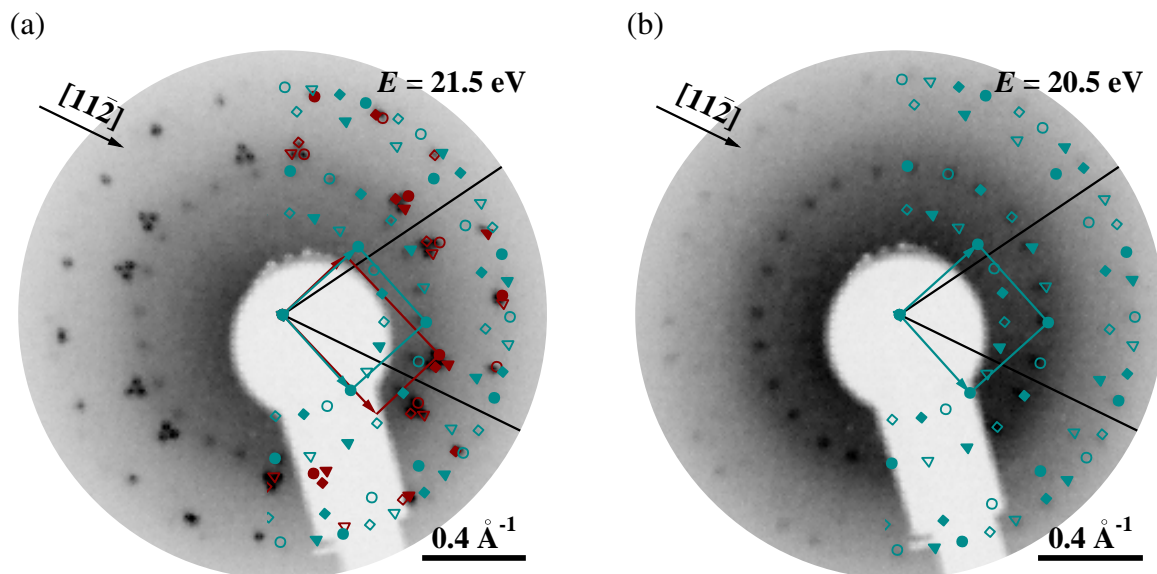


FIG. 6.15. LEED patterns of PTCDA layers on the $\text{Cu}_3\text{Au}(111)$ surface after thermal annealing. These images were obtained for PTCDA layers in the STM setup with an MCP-LEED after thermal desorption of multilayers. (a) LEED pattern of PTCDA/ $\text{Cu}_3\text{Au}(111)$ after annealing at 573 K for 5 min ($E = 21.5$ eV). (b) LEED pattern of PTCDA/ $\text{Cu}_3\text{Au}(111)$ after annealing at 525 K for 5 min ($E = 20.5$ eV). The heating and cooling rates amounted to 1 K s^{-1} in (a) and 0.3 K s^{-1} in (b). On the right-hand side of the LEED patterns, simulations are superimposed. α -phase spots are shown in dark red and δ phase spots in dark cyan. Black lines indicate the (fundamental) reciprocal lattice vectors \mathbf{a}_i^* of the substrate.

layers which were obtained by thermal desorption of multilayers exhibited smaller domain sizes (by about 10 % on average, see also below for the corresponding STM results) and thus less sharp diffraction spots. This can be also seen from a careful comparison of the two-dimensional LEED patterns presented in Fig. 6.13. Nonetheless, the PTCDA overlayer may apparently overgrow domain boundaries which are present within the $\text{Cu}_3\text{Au}(111)$ surface layer. The high degree of order and the large lateral extension of the PTCDA domains was confirmed by STM images, as shown in Fig. 6.14(a). The PTCDA domain in the center of the image, for example, extends almost across the entire lower terrace (within the field of view). The lateral dimension amounts to about 1500 \AA and more. A small part of the surface (about 3 %) is not covered by PTCDA islands. In this region, no adequate STM image with good resolution could be obtained. Instead, only stripes and hardly any protrusions were observed here. This holds for the STM experiments on all PTCDA preparations in the submonolayer regime. We attribute this to the high mobility of the PTCDA molecules on the surface at room temperature.^{x)} This hints at the weak interaction between the molecules and the substrate again.

All above-introduced HB phases of PTCDA on $\text{Cu}_3\text{Au}(111)$ were identified in the STM images, too. Also for the minor HB phases β and γ , islands with lateral extensions of several hundred ångströms were observed. The left lower corner of Fig. 6.14(a), displays an example of one domain of the β phase. The α phase, however, was the majority phase, as had already been indicated by the LEED results. The general appearance regarding the intermolecular contrast and the lattice constants, for instance, of the three HB phases in the STM images was identical and independent of the applied bias voltage. In the large-scale images, only a faint stripe pattern was made out in

^{x)}STM images of PTCDA/ $\text{Cu}_3\text{Au}(111)$, in particular for the submonolayer regime, at low temperatures are not available unfortunately.

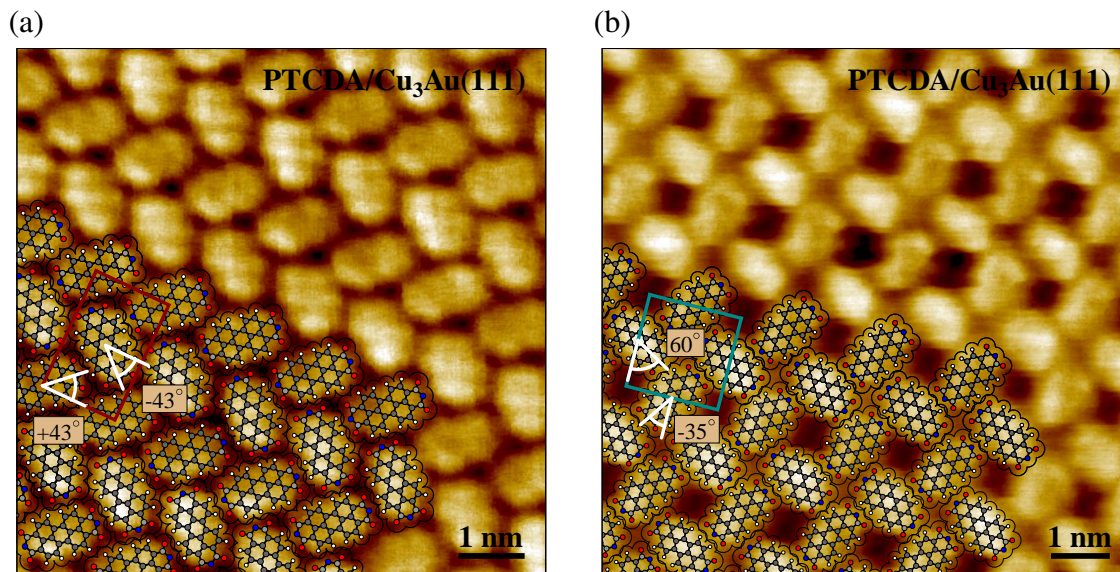


FIG. 6.16. STM images of PTCDA molecules on the $\text{Cu}_3\text{Au}(111)$ surface, revealing the molecular arrangement within the unit cell. These images were acquired on a 0.6 ML PTCDA/ $\text{Cu}_3\text{Au}(111)$ film. (a) α phase ($7.99 \text{ nm} \times 7.99 \text{ nm}$, $U_{\text{bias}} = 540 \text{ mV}$, $I_t = 13.4 \text{ pA}$). (b) δ phase ($9 \text{ nm} \times 9 \text{ nm}$, $U_{\text{bias}} = -224 \text{ mV}$, $I_t = -13.4 \text{ pA}$). The unit cells of the α and the δ phase are indicated in dark red and dark cyan, respectively. The PTCDA molecules are overlaid as ball-and-stick models, including a two-dimensional projection of the molecular vdW surface, in order to determine the angles ϱ (white) which describe the angle of inclination of the long molecular axis with respect to \mathbf{b}_1 .

the HB domains [see Fig. 6.14(b), for example]. Therefore, these phases could only be discerned by their (relative) angular orientation. This could not always be achieved without ambiguities because the differences in the respective angles ϕ are small regarding the angular accuracy of an STM measurement (see also Table 6.6), and because the symmetry of the substrate surface gives rise to six rotational and mirror domains per HB phase, that is, to a total number of 18 HB domains.

Furthermore, a so-far unknown PTCDA phase can be identified in the STM images of Fig. 6.14 which may be clearly discerned from the HB phases. This phase will be called δ phase or square (S) phase, due to its quadratic unit cell, in the following. This phase is also a minority phase, and has not been observed in our SPA-LEED investigations (on another crystal in a different experimental setup). Presumably, the surface fraction of the δ phase in the SPA-LEED experiments was too low and/or the average domain size was too small such that the corresponding LEED pattern was below the detection limit of the SPA-LEED instrument and thus overlooked. In the STM setup, however, it was possible to obtain LEED patterns of this phase (see Fig. 6.15). They allowed to accurately determine the corresponding lattice parameters (see Table 6.6). The obtained values of $b_1, b_2 = 16.2(2) \text{ \AA}$ and $\beta = 90(1)^\circ$ are in perfect agreement with the reported results by Mannsfeld *et al.* (see Table 6.1),¹¹⁶ who has observed a square phase of PTCDA in STM also on the pure Au(111) surface. Only the angle ϕ is larger by 4° in the present case of $\text{Cu}_3\text{Au}(111)$.^{y)} Note that a square phase has also been reported to exist for PTCDA on the Cu(111) surface.³⁴² STM images, such as the one shown in Fig. 6.16(b), reveal the arrangement of the PTCDA molecules in the δ phase on $\text{Cu}_3\text{Au}(111)$. The angles ϱ which describe the angle of inclination of the long molecular axis with respect to \mathbf{b}_1 could be determined with an accuracy of $\pm 3^\circ$. The two flat-lying molecules

^{y)}The lattice parameters which were determined by STM agree with the LEED results within $\pm 0.3 \text{ \AA}$ and $\pm 2^\circ$, respectively.

within the unit cell are not perfectly perpendicular to each other, and they do not exhibit an angle of $\varrho = \pm 45^\circ$. Both conditions are necessary for a square symmetry of the unit cell. Instead, the two-dimensional space group $p211$ applies here.²⁾ As a consequence of ϱ being unequal to $\pm 45^\circ$, the PTCDA molecules are arranged in a L-shape motif (instead of a T-shape motif). Quadrupole interactions and also hydrogen bond-like interactions are thus still plausible. Yet, the intermolecular interactions can be assumed to be reduced in comparison to those in the HB phases because the quadratic δ phase exhibits substantial empty space between the molecules [at the corners of the unit cell in Fig. 6.16(b)]. Indeed, the δ phase is less densely packed by about 15 % in comparison to the HB phases. In turn, the interactions across the metal/molecule interface may be enhanced due to a more defined registry between the adsorbate layer and the surface. A p-o-l commensurability is found for the δ phase, in contrast to the HB phases. Figure 6.17(d) displays a structural model of the δ phase.

The molecular arrangement within the unit cell of the α phase is shown exemplarily in the STM image of Fig. 6.16(a). As mentioned above, two flat-lying molecules are nicely accommodated in the unit cell, and form the above-proposed herringbone motif. Moreover, both molecules enclose the same angle $|\varrho| = 43(5)^\circ$ with the superstructure unit cell vector \mathbf{b}_1 . Therefore, glide planes exist in this structure, and the resulting two-dimensional space group is $p2gg$.^{aa)} Since the lattice parameters of the phases β and γ are practically identical to those of the α phase (see Table 6.6), the relative orientations of the molecules in the unit cells are also the same, presumably. In essence, space group $p2gg$ is expected to pertain for them, too. Structural models for the HB phases of PTCDA on Cu₃Au(111) are depicted in Fig. 6.17(a)–(c). Because of the valid space group $p2gg$, extinction rules apply to the LEED patterns.^{157,210} Indeed, the diffraction spots $\{h0\}$ and $\{0k\}$ for which h or k is odd are systematically extinct in the monolayer regime [see Figs. 6.13(a) and (c)].^{bb)} In cases, where the monolayer structures were grown as such with relatively high deposition rates, and where post-annealing was waived, however, the respective spots could be faintly observed [see Figs. 6.13(b) and (d)]. Evidently, the molecular arrangement was not as perfect then, with the consequence of partially lifting the extinction rule.

δ phase at domain boundaries

We now turn to the δ phase once again. As can be seen from Fig. 6.14, the δ phase exists at step edges and at domain boundaries between HB domains. This is in analogy to the findings for PTCDA on Au(111).^{116,453,464} Detached islands of the δ phase were only observed in the submonolayer regime, i.e., for PTCDA coverages below 0.1 ML (not shown). Figure 6.14(c), in particular, shows that the δ phase can exist in stripes with a width of essentially one unit cell only (see the black arrow).⁴⁶⁴ This becomes more apparent in Fig. 6.18(a) where four domains of the α phase are visible. They are separated from each other by thin strips of the δ phase which form an “X”. At the crossing point, in the center of the image, some defects and/or disorder are present. In the left middle part of the image, unit cells of both phases are superimposed to the experimental data. Remarkably, a comparison of the relative positions of those unit cells, which belong to the

²⁾Only the atomic positions within the adsorbate layers are considered for the determination of the two-dimensional space group whereas the substrate surface atoms are neglected. The symmetry of the respective interface structure in their entirety, i.e., including the substrate atoms, reduces to space group $p1$.

^{aa)}Footnote z) on page 128 of this chapter applies here, too.

^{bb)}Very faint $\{10\}$ spots may be identified in Fig. 6.13(c), nonetheless. This is because the presence of the surface atoms underneath the PTCDA molecules, which are not in a defined registry with the overlayer structure, reduces the symmetry of the unit cell to space group $p1$, thereby softening the extinction rule to some extent. See below and also Sec. 5.3.1 where the validity of the extinction rules has been elucidated for the case of PTCDA/Cu(111).

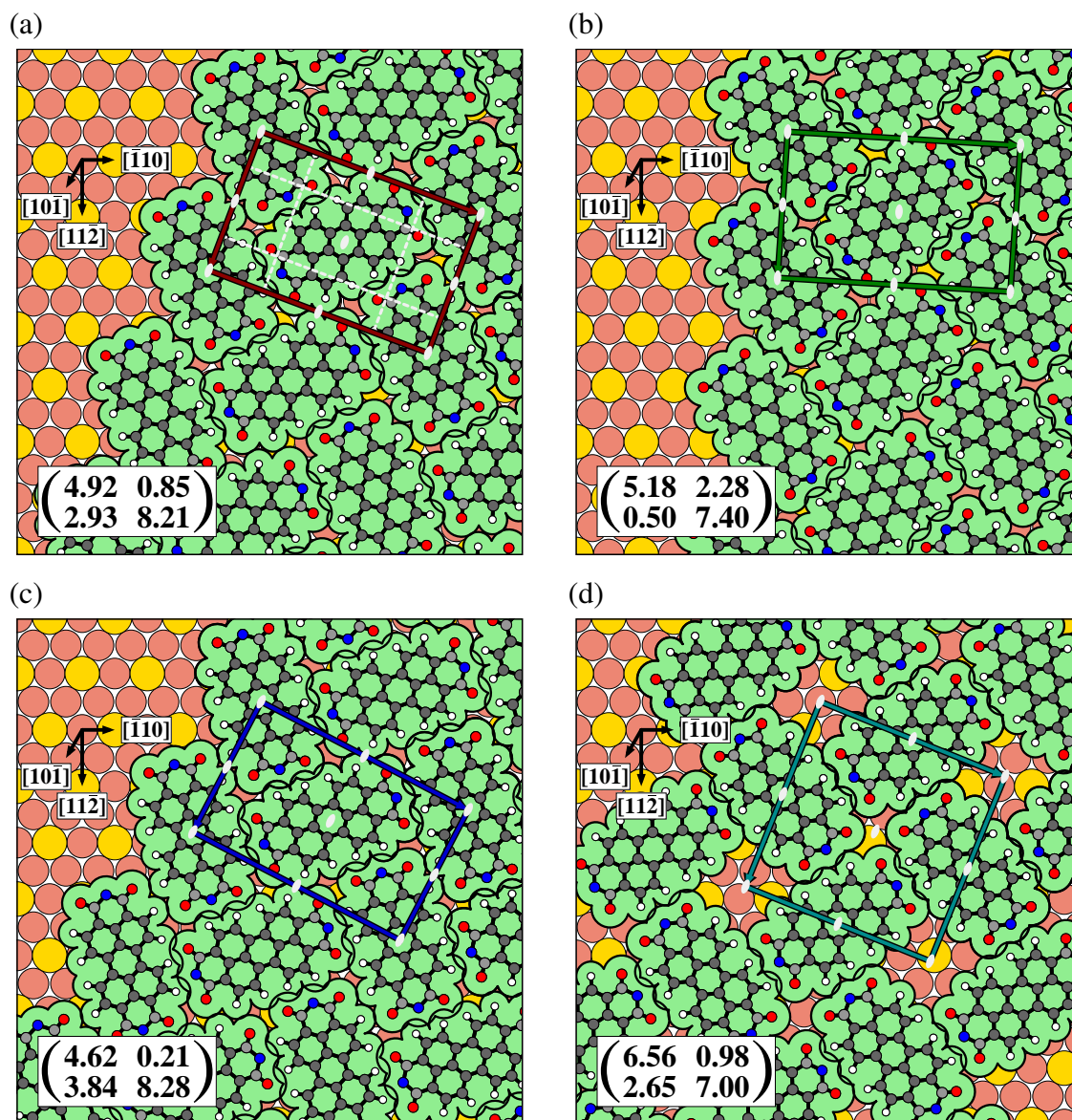


FIG. 6.17. Structural models of the PTCDA phases on the $\text{Cu}_3\text{Au}(111)$ surface which are present in the (sub-)monolayer as well as in the multilayer regime, as deduced from LEED and STM experiments: (a) α phase, (b) β phase, (c) γ phase, and (d) δ phase. The PTCDA molecules are shown as ball-and-stick models, including a two-dimensional projection of the molecular vdW surface. The adsorption sites have been chosen arbitrarily. Solid lines indicate the respective unit cells, i.e., dark red for the α phase, green for the β phase, blue for the γ phase, and dark cyan for the δ phase. The substrate directions are also indicated. The superstructure matrices are given as insets. Symmetry operations are shown in light gray. Note that for reasons of simplicity the $\text{Cu}_3\text{Au}(111)$ surface is shown in its ideal, ordered state. Note further that the atoms are depicted at 97.5 % of their metallic radius r_m reported in the literature¹⁴² only (see Table 2.3 in Sec. 2.2.2, page 16, of the present work for the explicit values) in order to avoid overlap of the spheres.

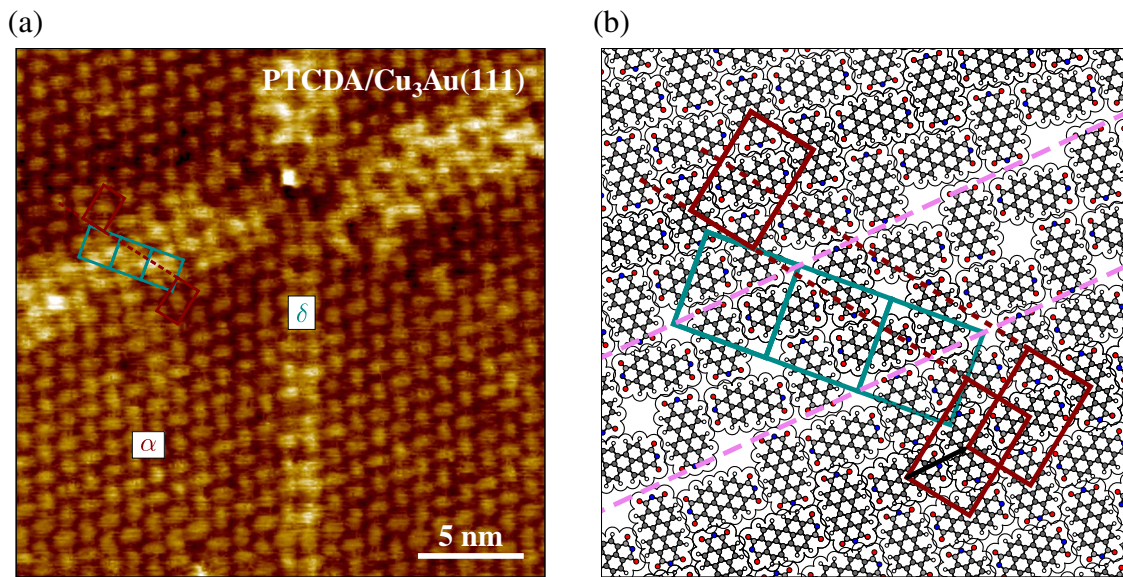
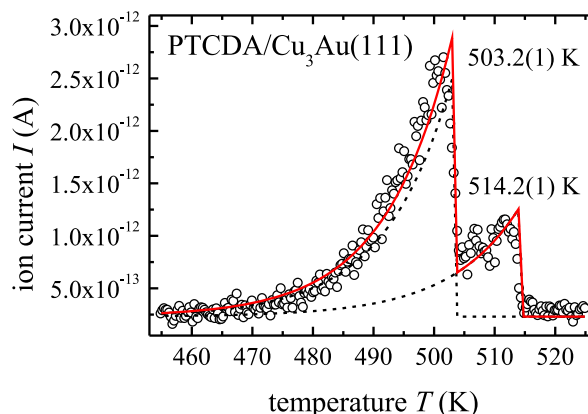


FIG. 6.18. STM image and corresponding structural model of the δ phase of PTCDA on the Cu₃Au(111) surface at domain boundaries. (a) STM image of four α phase domains which are separated by stripes of the δ phase (25 nm \times 25 nm, $U_{\text{bias}} = -405$ mV, $I_t = -13.8$ pA). This image was acquired on a PTCDA monolayer which had been obtained by thermal desorption of multilayers (annealed at 573 K for 5 min). The unit cells of the α and the δ phase are indicated in dark red and dark cyan, respectively. (b) Corresponding structural model of the left middle part of the STM image in (a). The PTCDA molecules are shown as ball-and-stick models, including a two-dimensional projection of the molecular vdW surface. Violet dashed lines indicate domain boundaries between the α phase (top and bottom) and the δ phase (middle). Surface atoms have been omitted for clarity.

α phase on both sides of the δ phase stripe, shows that the embedded δ phase allows to connect both α -phase domains without a mismatch of the lattice rows (indicated by the dark red dashed line). Now the questions arises, of course, why the embedded δ phase is stable and does not transform into the α phase, thereby eliminating the domain boundary.

A closer inspection of the STM image in Fig. 6.18(a) unravels this puzzle. It is indeed true that the lattice rows of the α phase are continued across the embedded δ phase. Yet, the orientation of the PTCDA molecules on the respective lattice rows is different. This is also depicted schematically in Fig. 6.18(b). In comparison to the representation in Fig. 6.18(a) a second unit cell is drawn for the lower domain of the α phase. This second unit cell is shifted by one-half of the unit cell vectors \mathbf{b}_1 and \mathbf{b}_2 with respect to the first one. The shift is represented by a black arrow and is equivalent to half a lattice row along the direction of \mathbf{b}_2 , which is parallel to the long edge of the unit cell. Regarding the molecular basis, that is, the orientation of the PTCDA molecules within the unit cell, only the second unit cell is identical to that in the upper domain of the α phase. In the hypothetical case where the δ phase is not present at the domain boundary the mismatch between the two domains of the α phase and therefore the energetic cost would be maximal. Instead, two domain boundaries (violet dashed lines) are realized. Yet, the energetic cost is expected to be much lower here since the crossover from the α phase and vice versa is very smooth and seamless, as the “leaking” of the δ phase unit cell across the domain boundaries illustrates. Obviously, the energetic cost is lower than the activation energy for the healing of the domain boundary in the hypothetical case which would require a lateral (stepwise) movement of one of the (large) α -phase domains.

FIG. 6.19. Thermal desorption spectrum of PTCDA multilayers on the $\text{Cu}_3\text{Au}(111)$ surface. A PTCDA fragment with $m/z = 124$ u was monitored. The heating rate amounted to 0.3 K s^{-1} and the initial coverage was 4.1 ML PTCDA/ $\text{Cu}_3\text{Au}(111)$. The experimental data (open circles) was fitted with two desorption peaks (black dashed lines; the red line corresponds to the sum of the two components) assuming zeroth-order kinetics.^{62,201}



Yet, we emphasize at this point that the δ phase is not only present in narrow stripes between domains of the HB phases of PTCDA/ $\text{Cu}_3\text{Au}(111)$ but also in (individual) well-extended domains (see Fig. 6.14 above, for example). Furthermore, the δ phase can be prepared with an increased surface fraction starting from both PTCDA multilayers and PTCDA (sub-)monolayers on $\text{Cu}_3\text{Au}(111)$ through (mild or rather rigorous) thermal treatment, as will also be reported in the following.

Thermal effects on the PTCDA structures

In some of the PTCDA monolayer preparations presented above, the possibility to thermally desorb multilayers had been exploited. Figure 6.19 shows an exemplary TPD spectrum of 4.1 ML PTCDA/ $\text{Cu}_3\text{Au}(111)$ for a PTCDA fragment with $m/z = 124$ u. The heating rate was chosen as 0.3 K s^{-1} due to technical requirements. Clearly, two peaks can be discerned. The peak at lower T values, i.e., at about 500 K, is assigned to the desorption of PTCDA from—maybe “bulk-like”—multilayers while the peak at about 510 K originates from the desorption of PTCDA molecules from the second layer. This peak assignment is justified by the finding that after annealing at $T \geq 525 \text{ K}$ PTCDA molecules were still present on the $\text{Cu}_3\text{Au}(111)$ surface, as was revealed by LEED and STM.

From a fit to the experimental data in Fig. 6.19,^{cc)} assuming zeroth-order desorption kinetics,^{62,201} the position of the desorption rate maxima were determined as 503.2(1) K and 514.2(1) K. This is similar to the case of PTCDA on pure $\text{Au}(111)$. Fenter *et al.* reported that the desorption from a multilayer film occurs at about 513 K, and that the PTCDA bilayer is stable from 513 K to 523 K while the PTCDA monolayer is stable for $T < 673 \text{ K}$.⁴⁶⁵ We also find a temperature difference of about 10 K for PTCDA desorption from the multilayer and the second layer to occur on $\text{Cu}_3\text{Au}(111)$. Although our temperature measurement has a large error bar of approximately 25 K—the thermocouple could neither be attached firmly to the sample crystal, nor was the temperature measurement reproducible with adequate accuracy—the general trend in the desorption behavior of PTCDA from the $\text{Cu}_3\text{Au}(111)$ surface is in less agreement with that from the pure $\text{Cu}(111)$ surface. Starting from an about 6 ML thick PTCDA layer on $\text{Cu}(111)$ (at a heating rate of 1.0 K s^{-1}), the maxima in the desorption rates are found at about 550 K and 573 K, respectively.³³⁸ Hence, our TPD results are consistent with the structural results—most of the PTCDA structures on $\text{Cu}_3\text{Au}(111)$ being Au-analogous—and thus also with the above conclusion that the $\text{Cu}_3\text{Au}(111)$ surface behaves Au-like.

^{cc)}The fitting was done with the computer program Origin,²⁹² employing a routine written by Mathias Müller from Rheinische Friedrich-Wilhelms-Universität Bonn (Bonn, Germany).

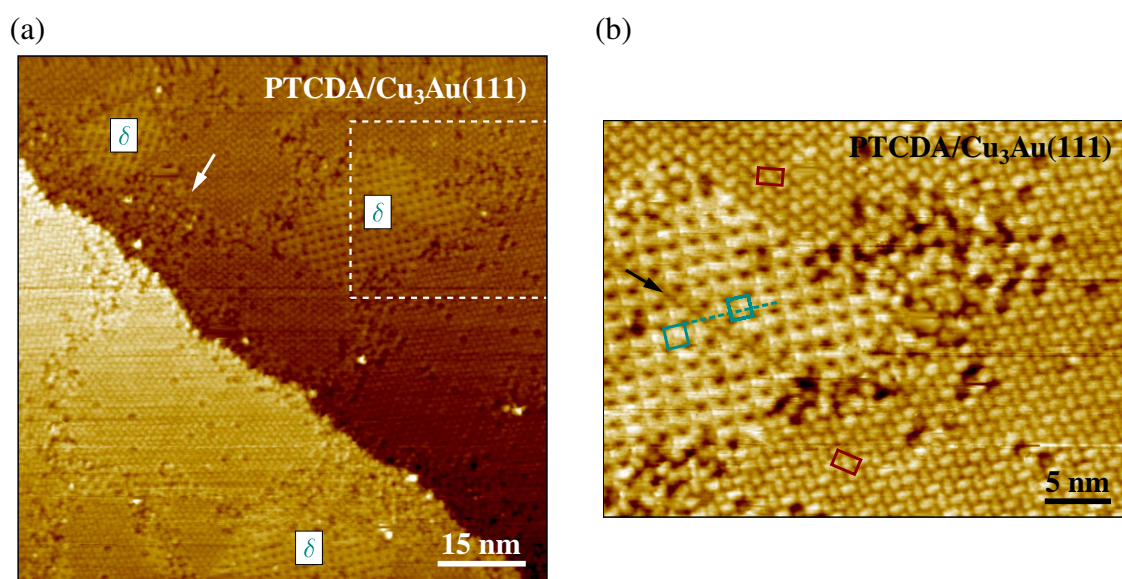


FIG. 6.20. STM image of a PTCDA overlayer on the $\text{Cu}_3\text{Au}(111)$ surface after thermal annealing. (a) Nominal 1 ML PTCDA/ $\text{Cu}_3\text{Au}(111)$ obtained by thermal desorption of multilayers (annealed at 525 K for 5 min; $90 \text{ nm} \times 90 \text{ nm}$, $U_{\text{bias}} = 1000 \text{ mV}$, $I_t = 13.4 \text{ pA}$). Domains of the δ phase are marked. The white arrow points at a disordered region. (b) Close-up of the framed region in (a) ($40 \text{ nm} \times 30 \text{ nm}$, $U_{\text{bias}} = 1000 \text{ mV}$, $I_t = 13.8 \text{ pA}$). The black arrow marks a domain boundary between two δ -phase domains. The unit cells of the α and the δ phase are indicated in dark red and dark cyan, respectively.

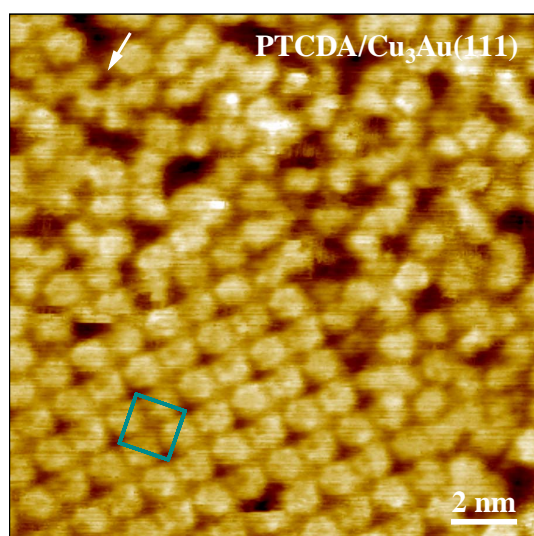


FIG. 6.21. Close-up STM image of a PTCDA overlayer on the $\text{Cu}_3\text{Au}(111)$ surface after thermal annealing ($16 \text{ nm} \times 16 \text{ nm}$, $U_{\text{bias}} = 840 \text{ mV}$, $I_t = 28 \text{ pA}$), showing a δ -phase domain and disordered PTCDA molecules. The initial coverage prior to annealing was 4.1 ML PTCDA/ $\text{Cu}_3\text{Au}(111)$. PTCDA multilayers were desorbed by annealing at 525 K for 5 min. The unit cell of the δ phase is indicated in dark cyan. The white arrow marks points at an “PTCDA oligomer”.

In accordance with the SPA-LEED results (see above), we observed ordered PTCDA monolayers on the Cu₃Au(111) surface after thermal desorption of multilayers also with STM. Yet, these monolayers exhibited smaller domain sizes and a lower degree of long-range order in comparison to those PTCDA monolayers which were grown as such. An exemplary large-scale STM image is shown in Fig. 6.20(a). The size of the HB phase domains is reduced to only a few hundred ångströms here whereas, for the as-grown layers, domain sizes of more than a thousand ångströms could readily be observed. Also, more point defects, that is, missing molecules, are present within the domains here compared to the as-grown layers (see also Fig. 6.14). Furthermore, a substantial fraction of the surface is covered with PTCDA molecules in a disordered state. These disordered areas are found at step edges [see the white arrow in Fig. 6.20(a), for example] as well as at domain boundaries within the PTCDA layer. Figure 6.20(b) displays a close-up of the latter case. Most of the observed protrusions in the disordered area still resemble the general appearance of the PTCDA molecules within the ordered islands. Therefore, we assume that (mainly) intact PTCDA molecules are present in the disordered phase. However, we also observed protrusions (see the white arrow in Fig. 6.21 for an example) which do not match the typical STM appearance of PTCDA molecules on the Cu₃Au(111) surface. Apparently, also a partial “oligomerization” of—maybe decomposed—PTCDA molecules may occur upon the annealing process (525 K for 5 min).

Regarding the surface fractions of the different phases, the following trends were observed: Upon post-annealing of the PTCDA layers the surface fraction of the δ phase and also of the disordered phase increased. This has also been found to be the case for PTCDA on pure Au(111) in earlier STM investigations by Chizhov *et al.*⁴⁵³ Thus, our findings are in agreement with the earlier conclusion of the Cu₃Au(111) surface behaving like a pure Au(111) surface with regard to the PTCDA adsorption properties. In the preparation which is exemplarily depicted in Fig. 6.20(a) the surface fraction of the δ phase and the disordered phase amounted to one third in each case [see Fig. 6.15(a) on page 126 of the present work for the corresponding LEED pattern]. The rest of the Cu₃Au(111) surface was covered with the HB phases. In another preparation, the PTCDA (mono-)layer was transformed into the disordered phase by as much as 90 %, with no HB phases and only 10 % δ phase being left. A corresponding LEED patterns is shown in Fig. 6.15(b). The LEED spots from the δ phase are broad, indicating small domain sizes. Furthermore, an intense background signal is observed which is most likely caused by the disordered phase. The differences between the two preparations of partial and complete transformation to the disordered phase consisted in the maximal annealing temperatures as well as in the heating and cooling rates of the sample during the post-annealing process. Remarkably, for the almost complete transformation to the disordered phase, lower maximum temperatures ($T = 525$ K for 5 min versus $T = 573$ K for 5 min) and lower heating and cooling rates (0.3 K s⁻¹ versus 1 K s⁻¹) were employed. In the SPA-LEED investigations, the δ phase was not observed at all although, typically, the post-annealing parameters were essentially identical to those in the case of the partial transformation in the STM setup ($T = 575$ K for 2 min and rates of 1 K s⁻¹). Apparently, milder post-annealing conditions, i.e., annealing at lower temperatures (but still above the desorption temperature of the second layer at about 510 K) and lower rates, enhance the transformation of the PTCDA layer towards the disordered phase. This effect may also be related to the sample quality^{dd)} and needs to be further validated.

^{dd)}Note again that two different Cu₃Au(111) crystals were used for the SPA-LEED and STM experiments. These two crystals, however, were prepared following the same protocol (within the technical capabilities; see also Sec. 6.2).

Multilayer structures

We have also investigated the growth mode and the structures of PTCDA in the multilayer regime on Cu₃Au(111). Figure 6.22 shows typical LEED patterns for 6.3 ML PTCDA/Cu₃Au(111) and 3.7 ML PTCDA/Cu₃Au(111), respectively. The observed LEED patterns resemble those which were obtained for PTCDA monolayers (see Fig. 6.13). Spots of the three already known HB phases are present up to higher order. Indeed, the same lattice parameters are found for both the monolayer and the multilayer regime (see also Table 6.6). This is surprising because the almost complete attenuation of the substrate spots indicates that the Cu₃Au(111) surface is covered with more than one complete adsorbate layer (the corresponding one-dimensional LEED data is not shown). Therefore, two scenarios may be considered here. Either PTCDA exhibits Stranski-Krastanov growth⁶² with more than one wetting layer. Or a layer-by-layer (Frank-van der Merwe) growth mode⁶² is present. The layer-by-layer growth scenario may be ruled out here since, as stated above, the lattice constants are the same for the mono- and multilayer regime. Because the determined lattice parameters (in the monolayer regime) are smaller than those in the bulk polymorphs of PTCDA—the unit cell areas on the Cu₃Au(111) surface are smaller by 3–5 %, for example (see above)—an increase of the lattice constants with layer thickness would be expected in order to reduce lateral stress. This is not the case here. Hence, Stranski-Krastanov growth⁶² seems to be the plausible scenario.

The presence of high-order superstructure spots shows the long-range order of the PTCDA wetting layers. Indeed, a value for the average domain size of 385 Å is derived from the second-order superstructure spot widths of the α phase which is effectively identical to that in the monolayer regime (380 Å, see also above). Two further observations can be made from the LEED patterns in Fig. 6.22. Firstly, the {10} spots are visible which is essentially not the case in the LEED pattern of the PTCDA monolayer of Fig. 6.13(a). Therefore the extinction rules and the two-dimensional space group $p2gg$ no longer apply. The reasoning is the same as that which has already been employed in Sec. 5.3.1 for PTCDA multilayers on Cu(111). If not only the topmost PTCDA layer is considered but also lower-lying PTCDA layers, which presumably are shifted with respect to each other, all symmetry operations within the unit cell are lost and the space group is $p1$. The same holds for PTCDA in the monolayer regime, in principle, where the substrate atoms have to be considered. We speculate that the much smaller periodicity of the surface atoms as single scatterers in comparison to the larger PTCDA molecules is indeed too small in order to be “felt” by the electrons scattered at the PTCDA layer. Therefore, the scattering from the PTCDA monolayer remains unaffected by the presence of the Au and Cu atoms underneath, making $p2gg$ the valid space group. Considering the LEED pattern in Fig. 6.13(a) and (c), this holds in good approximation. Secondly, for the higher coverage of 6.3 ML PTCDA/Cu₃Au(111), the intensity ratio of those spots which form the characteristic double-triangle motif for the HB phases is altered in comparison to the monolayer. The {20} spots at the “top” of the triangles are the most intense ones while, in the monolayer regime, they were of identical or even lower intensity as compared to the {11} spots on the base line of the double-triangle motif. This has also been observed for PTCDA multilayers on Cu(111) (see Sec. 5.3.1). A plausible reason is the presence of multiple-scattering effects which alter the structure factor and thereby the intensities of the individual spots.^{113, ee)}

In order to confirm the above-proposed Stranski-Krastanov growth mode,⁶² STM investigations were performed on a PTCDA multilayer film on the Cu₃Au(111) surface with a nominal coverage of 4.8 ML, which had also been post-annealed at 393 K for 15 min before. Figure 6.23 displays

^{ee)}Interestingly, the reversed effect concerning the spot intensity ratio within the double-triangle motif has been observed for PTCDA/Ag(111) where the PTCDA superstructure is commensurate,¹¹³ as opposed to PTCDA/Cu₃Au(111) and PTCDA/Cu(111).

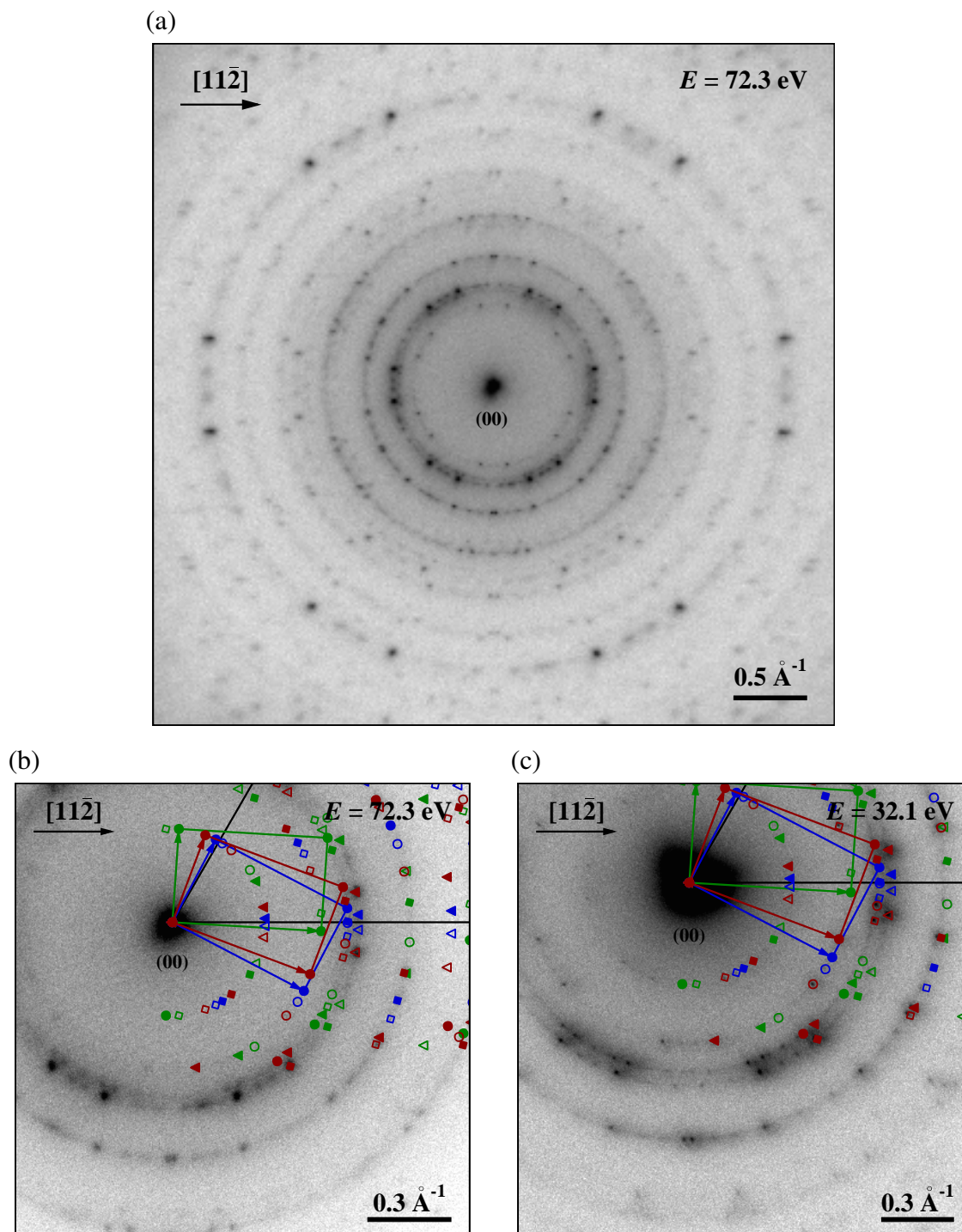


FIG. 6.22. LEED patterns of PTCDA multilayers on the $\text{Cu}_3\text{Au}(111)$ surface. (a) Two-dimensional LEED pattern of 6.3 ML PTCDA/ $\text{Cu}_3\text{Au}(111)$ after annealing at 500 K for 5 min ($E = 72.3 \text{ eV}$). (b) Close-up of the left lower part of the LEED pattern in (a). (c) LEED pattern of 3.7 ML PTCDA/ $\text{Cu}_3\text{Au}(111)$ without post-annealing ($E = 32.1 \text{ eV}$). Corresponding simulations are overlaid on the upper right-hand side of the LEED patterns in (b) and (c). The three already-known HB phases, namely, the α phase (dark red), the β phase (green), and the γ phase (blue), which were observed in the monolayer regime, are also present in the multilayer regime. Black lines indicate the (fundamental) reciprocal lattice vectors \mathbf{a}_i^* of the substrate. Note the different intensity ratios of the superstructure spots which form the typical double-triangle motif. All measurements were performed at 85 K.

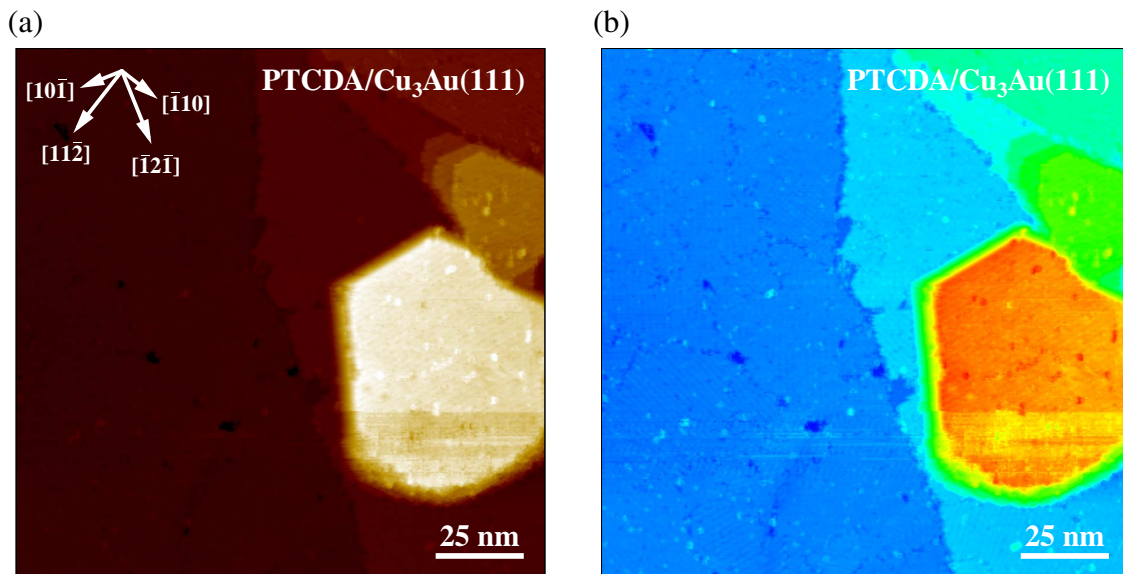


FIG. 6.23. STM image of PTCDA multilayers on the $\text{Cu}_3\text{Au}(111)$ surface. The nominal PTCDA coverage amounted to 4.8 ML PTCDA/ $\text{Cu}_3\text{Au}(111)$. The PTCDA layer had been post-annealed at 393 K for 15 min prior to the STM measurements ($150 \text{ nm} \times 150 \text{ nm}$, $U_{\text{bias}} = 1700 \text{ mV}$, $I_t = 15.3 \text{ pA}$). (a) STM image in typical brown colors. At the left-hand side of the image, a PTCDA nanocrystallite of eight layers height is observed. Above, three PTCDA layers have grown on top of each other. (b) Same image as in (a) but on a color scale (red–high, blue–low) in order to enhance the contrast in the lower terraces of the image.

an exemplary large-scale STM image of that preparation on two different color scales. The typical brown scale in Fig. 6.23(a) allows to identify a PTCDA cluster, which will also be called “nanocrystallite” for reasons given below, at the right-hand side of the image. The lateral dimensions are above $50 \text{ nm} \times 50 \text{ nm}$. The edges of this nanocrystallite are well-defined and steep. The nearly hexagonal shape of the cluster resembles that of crystalline PTCDA clusters which were observed with STM on other noble metal surfaces, as well.⁴⁶⁶ The (apparent) height of the nanocrystallite is found to be about 21 \AA . This corresponds to 8 PTCDA layers because the apparent height of a single PTCDA layer was determined as $2.60(2) \text{ \AA}$ (from the well-resolved step edges of the topmost PTCDA layers of smaller PTCDA clusters and single-layer islands, respectively) under the employed tunneling parameters ($U_{\text{bias}} = 1700 \text{ mV}$, $I_t = 15.3 \text{ pA}$). In the topmost layer of the nanocrystallite, the typical stripe-like appearance of the HB phases can faintly be made out.^{ff)} Thus, the term nanocrystallite is justified for this PTCDA cluster because it is reasonable to assume that not only the topmost but all PTCDA layers within the cluster are well-ordered and exhibit an herringbone arrangement of the PTCDA molecules. Above the nanocrystallite in Fig. 6.23 three layers of PTCDA can be identified which have grown on top of each other and which also exhibit the typical herringbone arrangement of the PTCDA molecules. Three-dimensional PTCDA islands as those described above, with a height of several layers, were observed to cover about 25 % of the surface area.

The main interest in this STM experiment, however, focused on the region between the three-dimensional islands. Figure 6.23(b) displays the same image, which has been described in the previous paragraph, with a color scale which enhances the contrast in the lower terraces. The entire $\text{Cu}_3\text{Au}(111)$ surface is covered with a continuous layer of PTCDA islands which are of several hundred ångströms in diameter. These islands form a wetting layer, proving the Stranski-

^{ff)}Unfortunately, a close-up STM image of that region is not available.

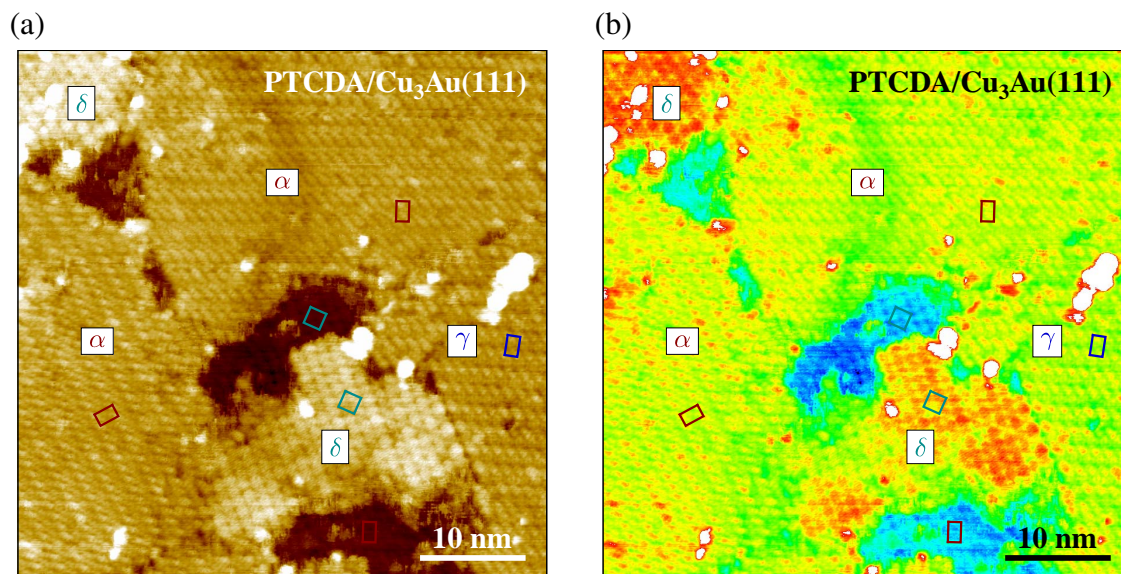


FIG. 6.24. STM image of the wetting layers in PTCDA multilayers on the $\text{Cu}_3\text{Au}(111)$ surface. The nominal PTCDA coverage amounted to 4.8 ML PTCDA/ $\text{Cu}_3\text{Au}(111)$. The PTCDA layer had been post-annealed at 393 K for 15 min prior to the STM measurements ($50.1 \text{ nm} \times 50.1 \text{ nm}$, $U_{\text{bias}} = 790 \text{ mV}$, $I_t = 20.3 \text{ pA}$). (a) STM image in typical brown colors. The domains of different PTCDA superstructures are labeled as α , γ , and δ , respectively. The assignment of the two HB phases was possible due to their angular orientation with respect to each other as well as with respect to the δ phase. Unit cells of the α , the γ , and the δ phase are indicated in dark red, blue, and dark cyan, respectively. (b) Same image as in (a) but on a color scale (red–high, blue–low) in order to enhance the contrast in the lower PTCDA layer.

Krastanov growth mode to exist indeed on this surface. A close-up of the wetting layer is shown in Fig. 6.24, again with two different color scales. In agreement with the LEED results, the HB phases, namely, the α and the γ phase in this particular case, are present in the wetting layer [see Fig. 6.24(a)]. Also, small islands of the δ phase are observed. In addition, bright protrusions are spread over the entire wetting layer. Most probably, these are (disordered) PTCDA clusters of very small size. The wetting layer, however, is not fully closed but it exhibits holes with diameters of several ten ångströms. Closer inspection of the lower terraces, i.e., the region within the holes, reveals that there is another PTCDA layer underneath the top layer instead of the clean $\text{Cu}_3\text{Au}(111)$ surface [see Fig. 6.24(b)]. Therefore, our conclusion, which was made on the basis of the LEED data, is correct, and at least two wetting layers are present in the multilayer regime of PTCDA/ $\text{Cu}_3\text{Au}(111)$. In the lower PTCDA layer, the unit cells of the δ phase as well as of the α phase can be identified. Apparently, the different PTCDA domains and PTCDA phases, in particular, can overgrow each other rather easily. Thus, the interlayer interaction must be moderate because, in terms of potential energy, a well-defined vertical stacking of the PTCDA layers is obviously not exceptionally favored here. Since there is no defined registry between the adjacent PTCDA layers, apparently, a determination of the adsorption sites in the topmost PTCDA layer in Fig. 6.24 with respect to the layer below was waived.

6.6.2 Electronic structure of the core levels in PTCDA

The results of structural investigations in the previous section have revealed that the $\text{Cu}_3\text{Au}(111)$ surface behaves essentially Au-like with regard to the structures which are formed by PTCDA

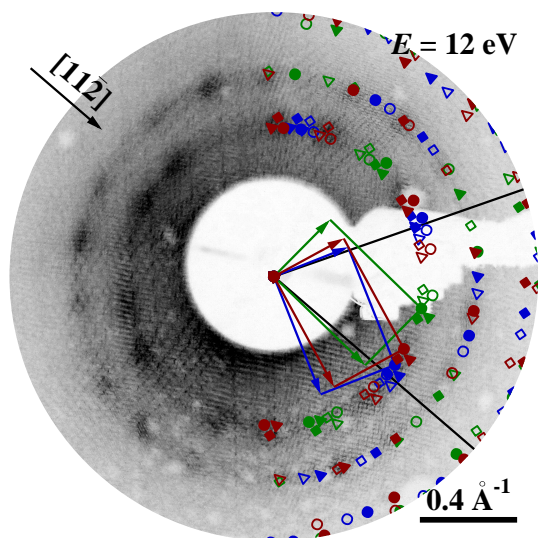


FIG. 6.25. LEED pattern of the PTCDA submonolayer on the $\text{Cu}_3\text{Au}(111)$ surface which was employed in the XPS and XSW experiments ($E = 12$ eV, taken at the ESRF prior to the XPS and XSW experiments). The overall quality of the LEED pattern is inadequate due to technical limitations. Nonetheless, the spots of the PTCDA HB phases can in principle be identified. On the right-hand side of the LEED pattern, a simulation is superimposed. α -phase spots are shown in dark red, β -phase spots in green, and γ -phase spots in blue, respectively. Black lines indicate the (fundamental) reciprocal lattice vectors \mathbf{a}_i^* of the substrate.

on the surface. Hence, it may be concluded that the metal/molecule interaction is similar to the case of PTCDA on pure $\text{Au}(111)$ where the molecules are physisorbed.⁵⁴ In order to make further progress in either validating or falsifying this conclusion, we performed core level spectroscopy on a PTCDA submonolayer on the $\text{Cu}_3\text{Au}(111)$ surface. Furthermore, a detailed understanding of the core level structure, which includes the development of educated fitting models in order to identify the individual components contributing to the signal, will allow for a “chemically resolved” analysis of the adsorption configuration in the next section (see also Sec. 3.1.1).

The XPS experiments (as were the XSW experiments, too) were done on a of 0.76(10) ML PTCDA/ $\text{Cu}_3\text{Au}(111)$ layer (see Sec. 6.2). Figure 6.25 displays a LEED patterns of the prepared PTCDA submonolayer. Although the overall quality of the LEED pattern is inadequate due to technical limitations, the observed LEED pattern is principally very similar to those reported in Sec. 6.6.1. The spots originating from the α phase may not be clearly resolved but the can be identified from the most intense features in Fig. 6.25. The presence of the minor HB phases β and γ as minority species may also be concluded. Only the spots of the δ phase are not observed, which means that its surface fraction is small (or zero). Since the prepared (sub-)monolayer structures were the same in all experimental setups—apart from those preparations obtained by post-annealing in the STM setup—the photoemission results obtained here, as well as the XSW results, may be directly correlated with the findings from the structural investigations above. Since the lattice parameters of the PTCDA HB phases are essentially identical (see Sec. 6.6.1) and therefore the chemical environment of the molecules in the different phases presumably is very similar, we do neither expect substantially different XPS signals for the three HB phases nor to be able to differentiate them. Hence, we will take the obtained XP spectra to be representative for the main HB phase α and the two minor HB phases β and γ .

Evolution of spectral features with x-ray beam exposure

Figure 6.26 shows XP spectra for both the $\text{C}1s$ and the $\text{O}1s$ level in PTCDA on the $\text{Cu}_3\text{Au}(111)$ surface. All XP spectra were acquired with a photon energy of $E = 2858.0$ eV (“off-Bragg” photon energy) at an effective angle of 86° of the photoelectron analyzer with respect to the surface normal. For both signals, two well-separated peaks can be discerned. In the case of $\text{C}1s$, there is an intense peak at a binding energy of about 284 eV and a second, less intense peak at $E_b \approx 288$ eV. In the case of $\text{O}1s$, the two peaks are observed at binding energies of about 531 eV and

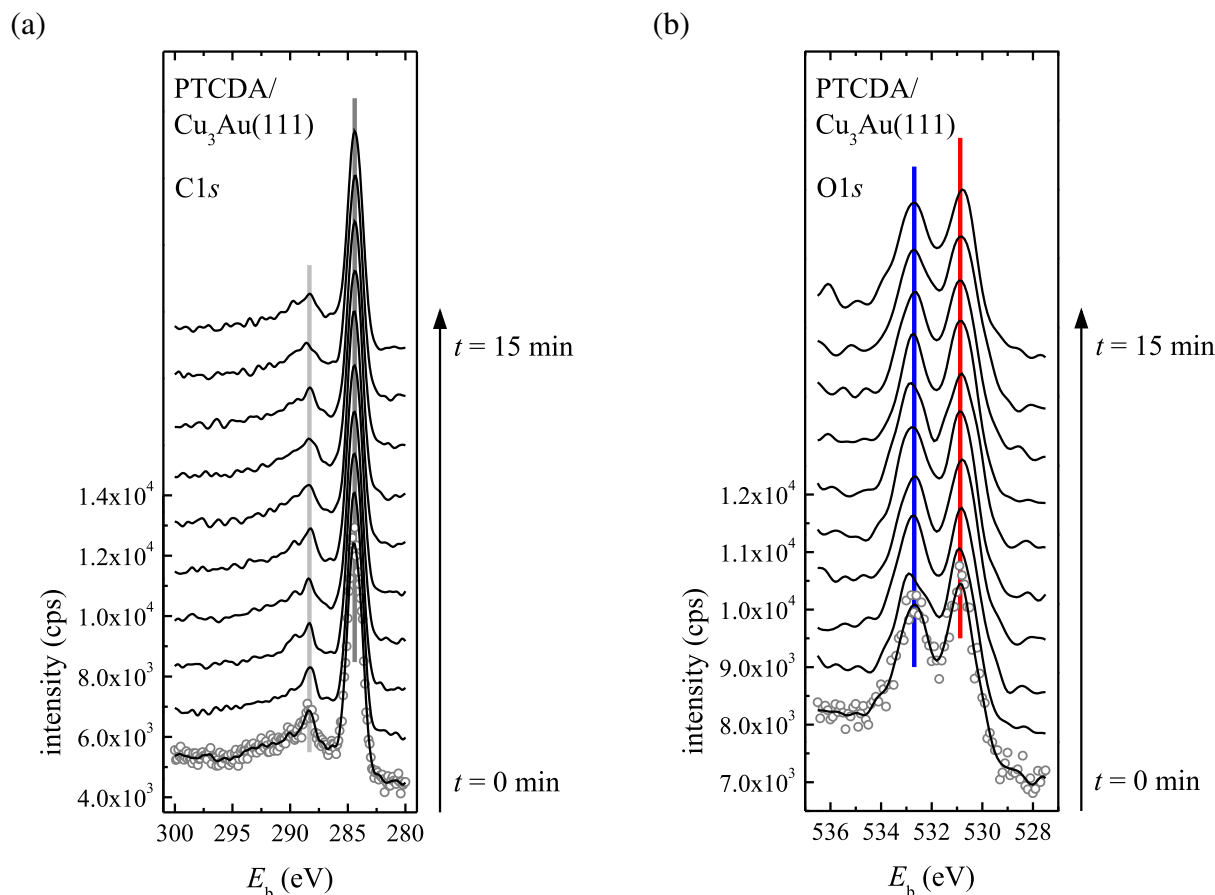


FIG. 6.26. XP spectra of the (a) $\text{C}1s$ and (b) $\text{O}1s$ levels of PTCDA on the $\text{Cu}_3\text{Au}(111)$ surface as a function of x-ray beam exposure, that is, as a function of time t . The PTCDA coverage amounted to $0.76(10)$ ML. All XP spectra were acquired with a photon energy of $E = 2858.0$ eV at an effective angle of 86° of the photoelectron analyzer with respect to the surface normal. The spectra have been carefully smoothed. In addition, the original data are shown exemplarily for the XP spectra at $t = 0$ min as gray open circles. Peak positions are marked by vertical solid lines.

533 eV, respectively. The exact assignment of these peaks to chemically nonequivalent atoms will be reported below. Firstly, we focus on another aspect. Each XP spectrum in Fig. 6.26 was conducted within 90 s. For each of the two XPS levels, ten spectra were acquired in sequence in order to monitor the spectral shape as a function of the exposition time t to the x-ray beam. Indeed, the spectral shape changed with t for both XPS levels within the chosen time interval of 15 min. Note that after about 40 min the spectral shapes did not change any further. Yet, the most pronounced changes occurred during the first minutes of x-ray beam exposure. While the peak positions remained essentially constant, the line shapes altered. In particular, the observed peaks broadened and spectral intensity was redistributed. This is most pronounced for the peak at $E_b \approx 288$ eV in the $\text{C}1s$ spectrum of Fig. 6.26. While the initially sharp peak has broadened and lost intensity, the intensity between the two $\text{C}1s$ peaks has increased during the employed period of time. Similarly, the two peaks in the $\text{O}1s$ spectra have assimilated in intensity to a certain extent with increasing t . At the same time, the spectral intensity between the two peaks has increased.

These effects may be indicative of an increased, that is, more chemisorptive, metal/molecule interaction after illumination with x-ray photons. Indeed, elaborate XPS investigations on

NTCDA^{307,467} and PTCDA mono- and multilayers^{307,468} on the Ag(111) surface have revealed that re-distributions of spectral intensity upon adsorption prove both charge transfer across the interface⁴⁶⁸ and metal/molecule interaction of (weak to strong) chemisorptive nature.^{307,467,468} In particular, such re-distributions of spectral intensity become manifest in (considerable) shifts of peak positions towards lower E_b and enhanced, more continuous satellite contributions.^{307,467,468} In the present case of PTCDA/Cu₃Au(111), a broadening of the peaks was indeed observed. Furthermore, peak shifts towards lower E_b by about 0.1 eV to 0.2 eV will be revealed by our sophisticated XPS fitting models (see below). We hence conclude at this point that an (enhanced) electron transfer from the Cu₃Au(111) substrate to the adsorbed PTCDA molecules occurs upon x-ray beam exposure.^{gg)} As a consequence, the surface bonding of PTCDA cannot be considered to be solely physisorptive any more after exposure to x-ray photons for several minutes.

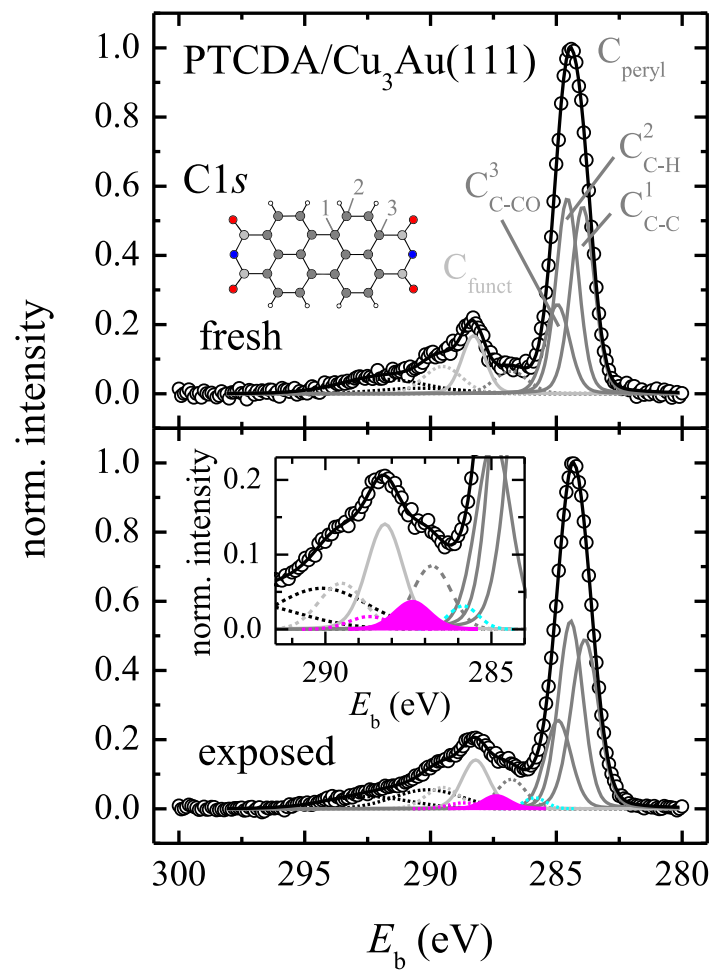
In principle, the above conclusion may be challenged by several aspects which could also lead to changes in the XP spectra with (illumination) time. However, these aspects can be ruled out to apply here. Firstly, small and weakly bound molecules from the residual gas may have been adsorbed on the surface or on the PTCDA layer which were then desorbed during the XPS measurement. This has been observed for PTCDA/Ag(111) at low temperatures.⁵⁵ This can be excluded here for two reasons. On the one hand, the base pressure in the analysis chamber of XSW setup II, where the XPS experiments were performed, was 4×10^{-10} mbar and thus too low for substantial adsorption of impurity molecules. On the other hand, typical molecules from the residual gas, such as CO or H₂O, are not stable even on the more reactive Cu(111) surface at temperatures above ≈ 200 K.^{469,470} Thus, residual gases are not expected to readily adsorb on the Cu₃Au(111) surface at room temperature, either. Secondly, the PTCDA molecules may have decomposed upon x-ray excitation. We expect that potential molecular fragments, in particular those fragments which contain O atoms, e.g., CO or CO₂, desorbed from the Cu₃Au(111) surface. This would have resulted in a lower overall surface coverage, and maybe in an increased N_C/N_O ratio on the surface, too.

Neither of the two scenarios was observed here (see Sec. 4.3.2, Table 4.3, in particular, for details). To the contrary, the surface coverage, as determined from the attenuation of substrate

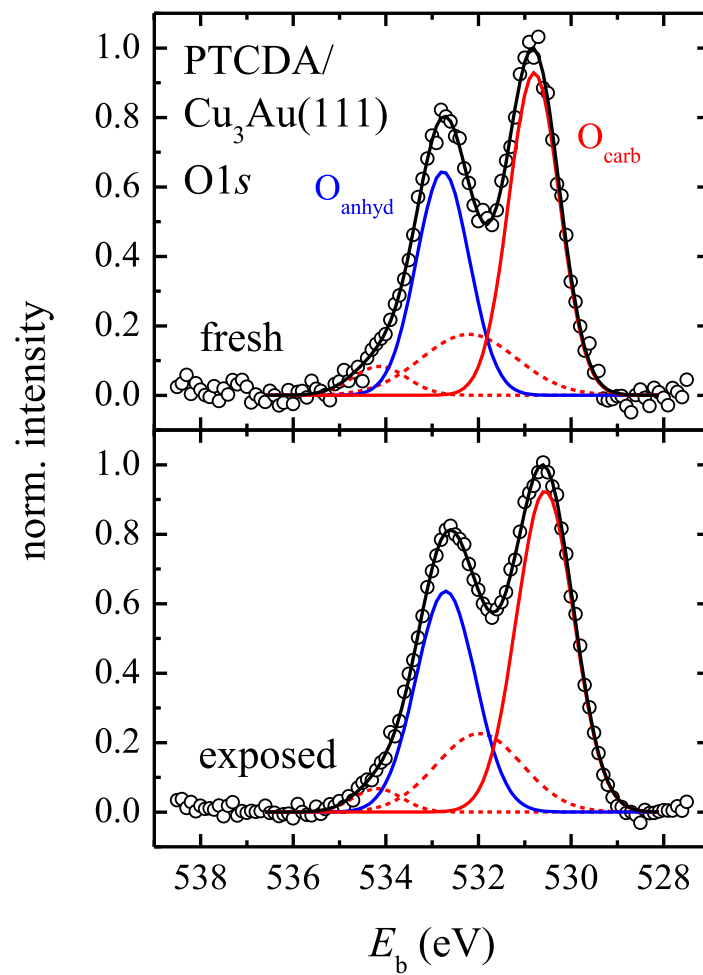
^{gg)}PTCDA is an electron acceptor molecule due to its high electron affinity of about 4.1 eV (determined for PTCDA in condensed films).¹⁰²

FIG. 6.27 (following page). Normalized XP spectra of the (a) C1s and (b) O1s levels of PTCDA on the Cu₃Au(111) surface with corresponding fitting models for short (fresh) and long times of x-ray beam exposure (exposed). The PTCDA coverage amounted to 0.76(10) ML. All XP spectra were acquired with a photon energy of $E = 2858.0$ eV at an effective angle of 86° of the photoelectron analyzer with respect to the surface normal. They were corrected with a linear or Shirley background function. Contributions from the carbon atoms within the perylene core and within the functional groups are shown in dark gray (C_{C-C}, C_{C-H}, and C_{C-CO}) and light gray (C_{funct}), respectively, while the contributions from the chemically nonequivalent oxygen atoms are shown in red (O_{carb}) and blue (O_{anhyd}). The main photoemission peaks are drawn as full lines, the (corresponding) satellite peaks as dashed lines, in respective colors. Unassigned satellite peaks are depicted in black. In addition, the resulting sum of all components is shown as a black line. In the C1s XP spectrum of PTCDA/Cu₃Au(111) on the exposed spot, three additional components are present, namely, C_{peryl, sat}^{*} (cyan, dashed line), C_{funct}^{*} (magenta, full line), and C_{funct, sat}^{*} (magenta, dashed line). For the sake of better visibility, the C_{funct}^{*} peak area is colored in magenta, too. The inset in (a), bottom, shows a blowup of the respective binding-energy region of the C1s XP spectrum on the exposed spot. A ball-and-stick model of the PTCDA molecule is shown as an inset in (a), top. Note that for the evaluation of the XSW data all C atoms of the perylene core were combined to give the C_{peryl} signal.

(a)



(b)



XPS signals, was constant, and the N_C/N_O ratio even decreased with x-ray beam exposure. The latter finding is explained by altered cross sections of the C1s and the O1s level of intact PTCDA due to an altered bonding situation, as has been discussed in more detail in Sec. 4.3.2 already. Thirdly, the presence of PTCDA molecules in the second layer, which either desorbed or diffused into the first layer under the x-ray beam, is excluded here because molecules in the second layer have not been present in the STM experiments on PTCDA (sub-)monolayers, either. Therefore, we conclude that the bonding situation of the PTCDA molecules on the surface indeed changes as a function of x-ray beam exposure—potentially from a “precursor” or *initial* state to a *final* state.^{hh)} Presumably, this correlates with the re-increasing Cu fraction at the surface upon x-ray beam exposure (see Sec. 6.5.2 above). Note that the term “precursor” commonly refers (solely) to a molecular adsorption state,^{62,201,471} but in the context of the present work it includes also the diffusion of substrate atoms (see also Sec. 6.5 above for the respective experimental findings).

In order to analyze the spectral features in more detail, the C1s and the O1s XP spectra have been recorded with improved statistics (see Fig. 6.27). The XP spectra for long times of x-ray beam exposure (termed *exposed* in Fig. 6.27) were acquired with an acquisition time of about 50 min per spectrum. The O1s spectrum was acquired on a spot which had previously been illuminated for about 60 min already. Thus, the evolution of the spectral features with x-ray beam exposure had finished. The C1s spectrum was acquired in a nominally “fresh” spot which had only been exposed to the beam for a few minutes before. Since the most pronounced changes in the spectral features are known to occur during these first minutes of x-ray beam exposure (see above), the C1s spectrum in Fig. 6.27(a), bottom, was regarded as being fully representative for an exposed spot. Although the evolution of the spectral features with x-ray beam exposure had not completely finished and (small) contributions from the non-exposed, fresh state were certainly present in this XP spectrum, too, these contributions were considered to be marginal. This assumption was validated by the facts that (a) the spectral shape of the C1s XP spectrum had remained unaltered since after about half of the total acquisition time already, and that (b) the C1s fitting model, which was then developed on the basis of this XP spectrum, showed very good agreement with the individual XP spectra of the XSW data sets (see also below).

The XP spectra for short times of x-ray beam exposure (termed *fresh* in Fig. 6.27) were obtained by acquiring spectra for each XPS signal, namely, C1s and the O1s, within about 5 min on two individual spots which had previously not been illuminated. Then, these spectra were added up in order to improve the signal-to-noise ratio. The so-obtained XP spectra are contrasted in Fig. 6.27. As already noted in the context of the XP spectra in Fig. 6.26, the individual C1s and O1s peaks are broader [by +0.15(4) eV or +12(3) % on average, judging from the fitting results for the widths w (full width at half maximum, FWHM) of the individual main components; see also Table 6.7 below], and spectral intensity has accumulated between the respective peaks in the spectra from the exposed spot (bottom row in Fig. 6.27) in comparison to the XP spectra from the fresh spots (top row). Furthermore, small shifts of the peak positions of about 0.1 eV towards lower binding energies may be perceived.

These qualitative observations were quantified with the help of sophisticated fitting models. The fitting parameters of the individual models are summarized in Table 6.7. Fitting the C1s main components from the perylene core, namely, C_{C–C}, C_{C–H}, and C_{C–CO} (see below), as well as from the functional groups, C_{funct} and C_{funct}^{*} (where observed; see also below), with pseudo-Voigt functions, i.e., a linear combination of Lorentzian and Gaussian functions,³⁰⁶ with 15 % Lorentzian contribution and all other components (including the O1s main components, O_{carb} and O_{anhyd}; see

^{hh)}We emphasize that the terms “initial state” and “final state” refer to different bonding situations (states)—possibly also with different adsorption configurations—here.

TABLE 6.7. XPS fitting parameters for the C1s and O1s levels of PTCDA on the Cu₃Au(111) surface. E_b denotes the binding energy, w the full width at half maximum (FWHM) of the peak, and A the relative peak area. The respective values are given for all components observed in the XP spectra on a fresh and/or on an exposed spot. The corresponding XP spectra are shown in Fig. 6.27 and were acquired on a 0.76(10) ML PTCDA/Cu₃Au(111) film. The C1s main components, namely, C_{C–C}, C_{C–H}, C_{C–CO}, C_{funct}, and C_{funct}^{*} (where observed), were fitted with pseudo-Voigt functions with 15 % Lorentzian contribution while all other components were fitted with pure Gaussian functions. In addition, the binding energies which were observed in a condensed PTCDA film on Ag(111) are given as a reference (taken from Ref. 307). $\Delta E_b = E_{b, \text{exposed}} - E_{b, \text{fresh}}$ is the shift in binding energy between an exposed and a fresh spot. $\Delta E_{b, i} = E_{b, i} - E_{b, \text{condensed}}$ denotes the changes in E_b for the fresh and the exposed spot in the submonolayer regime with respect to the multilayer regime, i.e., with respect to the condensed PTCDA film (n.o. = not observed, n.a. = not applicable).

	fresh			exposed			ΔE_b (eV)	condensed PTCDA film ^a		
	E_b (eV)	w (eV)	A (%)	E_b (eV)	w (eV)	A (%)		E_b (eV)	$\Delta E_{b, \text{fresh}}$ (eV)	$\Delta E_{b, \text{exposed}}$ (eV)
C _{C–C}	283.95	1.10	28.03	283.86	1.28	26.77	–0.09	284.52	–0.57	–0.66
C _{C–H}	284.56	1.05	28.03	284.43	1.16	26.77	–0.13	285.03	–0.47	–0.60
C _{C–CO}	284.96	1.15	14.02	284.93	1.23	13.39	–0.03	285.11	–0.15	–0.18
C _{peryl, sat}	286.81	1.59	4.55	286.79	1.35	4.57	–0.02	287.00	–0.19	–0.21
C _{funct}	288.29	1.11	8.76	288.21	1.28	7.67	–0.08	288.57	–0.28	–0.36
C _{funct, sat}	289.52	1.77	6.18	289.51	1.58	3.88	–0.01	290.01	–0.49	–0.50
C _{sat 1}	290.38	3.98	2.78	290.10	3.23	7.05	–0.28	n.o.	n.a.	n.a.
C _{sat 2}	291.90	4.15	7.65	292.50	3.99	5.56	0.60	n.o.	n.a.	n.a.
C _{peryl, sat} [*]	n.o.	n.o.	n.o.	285.85	1.06	1.33	n.a.	n.o.	n.a.	n.a.
C _{funct} [*]	n.o.	n.o.	n.o.	287.38	1.27	2.03	n.a.	n.o.	n.a.	n.a.
C _{funct, sat} [*]	n.o.	n.o.	n.o.	288.68	1.44	0.98	n.a.	n.o.	n.a.	n.a.
O _{carb}	530.80	1.29	45.95	530.56	1.46	46.74	–0.24	531.65	–0.85	–1.09
O _{carb, sat 1}	532.21	2.42	16.28	531.98	2.18	17.05	–0.23	533.97	–1.76	–1.99
O _{anhyd}	532.77	1.35	33.33	532.71	1.52	33.33	–0.06	533.41	–0.64	–0.70
O _{carb, sat 2}	534.13	1.39	4.44	534.18	1.23	2.88	0.05	535.35	–1.22	–1.17
O _{anhyd, sat}	n.o.	n.o.	n.o.	n.o.	n.o.	n.o.	n.a.	537.72	n.a.	n.a.

^aBinding energies for a condensed film of PTCDA molecules on the Ag(111) surface, with a coverage well above 10 ML, as reported in Ref. 307. Here, these E_b values serve as a reference for the energetic positions of the respective XPS levels in the bulk phase and also in the multilayer regime on Cu₃Au(111). Potential work function effects are neglected.

below) with pure Gaussian functions gave the best agreement with the experimental data. The widths and the centers of the individual pseudo-Voigt profiles were subject to the fitting while the ratios of the integral intensities were constrained to the respective stoichiometric values of the PTCDA molecule, namely, $C_{\text{peryl}} : C_{\text{funct}} = 20 : 4$ and $O_{\text{carb}} : O_{\text{anhyd}} = 4 : 2$ (see also Sec. 4.3.2). The peak assignment agrees with XPS results reported by Schöll *et al.* in Ref. 307 for PTCDA multilayers on Ag(111) and also with our XPS results for PTCDA multi- and (sub-)monolayers on the Ag(100) and Ag(110) surfaces (see Sec. C.3.3 in the appendix of the present work).

XP spectra on fresh spots

We first focus on the data from the fresh spots, that is, on the C1s data, in particular [see Fig. 6.27(a), top row]. The intense peak in the XP spectrum originates from the C atoms in the perylene core of PTCDA. At least, three species of chemically nonequivalent C atoms have to be discerned here, namely, those which are only bound to other C atoms in the perylene core ($C_{\text{C-C}}$), those which carry the H atoms ($C_{\text{C-H}}$), and those which are bound to C atoms in the functional groups ($C_{\text{C-CO}}$). The intensity ratio of these peaks was constrained to match the stoichiometric ratio of $C_{\text{C-C}} : C_{\text{C-H}} : C_{\text{C-CO}} = 8 : 8 : 1$ which is present in PTCDA. Note that for the evaluation of the XSW data all C atoms of the perylene core are combined to give the C_{peryl} signal. The second peak in the C1s spectrum mainly originates from the C atoms within the functional groups (C_{funct}). In order to maintain the stoichiometric ratio of $C_{\text{peryl}} : C_{\text{funct}} = 20 : 4 = 5 : 1$ in PTCDA, however, satellite peaks had to be introduced, namely, one for the C atoms in the perylene core ($C_{\text{peryl, sat}}$) and one for the functional C atom ($C_{\text{funct, sat}}$). Furthermore, two additional satellite peaks ($C_{\text{sat 1}}$ and $C_{\text{sat 2}}$) are present in the spectrum which cannot unambiguously assigned to one of the C species [see Fig. 6.27(a), top row, and also Table 6.7]. The peak assignment for the main components can be rationalized as follows: A higher electron density at the electron-emitting atom as well as a higher polarizability of the chemical surroundings lead to lower values of E_b . This is because the effective nuclear charge is lower (initial-state effect) and the created core hole is more effectively screened (final-state effect). In the case of PTCDA, the C atoms within the perylene core fulfill these requirements, for example, due to the extended, delocalized π system of electron. The C_{funct} are depleted in electron density due to the neighboring, more electronegative O atoms.^{20, 146}

In the (sub-)monolayer regime of PTCDA on the Cu₃Au(111) surface, all C1s components are shifted towards lower E_b in comparison to the PTCDA multilayer or the bulk phase (see Table 6.7). The binding energies which were reported for a condensed (multilayer) PTCDA film on Ag(111) by Schöll *et al.*³⁰⁷ [see also Zou *et al.*⁵⁹ for additional multilayer XPS data on PTCDA/Ag(111)] serve as a reference here because XPS data for PTCDA multilayers on Cu₃Au(111) are not available. Regarding the C_{peryl} signal as a whole for reasons of simplicity (see Table 6.7 for the shifts of the individual components), the peak position is shifted by about -0.6 eV, i.e., towards lower E_b , in comparison to the condensed PTCDA film where it is found at 285.0 eV.^{59, 307} This value is comparable to the shift of about -0.5 eV for 1 ML PTCDA/Au(111).⁵⁹ By analogy, it may be concluded that PTCDA is (initially) physisorbed also on the Cu₃Au(111) surface, and that the observed shift is caused by the better screening of the core hole in the final state by the image charge in the substrate as compared to the less effective delocalization or polarization effects of the PTCDA neighbors in the multilayer case.⁵⁹ In contrast, the shift of the C_{funct} peak in comparison to the multilayer case is smaller [about -0.3 eV; $E_{b, \text{condensed}}(C_{\text{funct}}) \approx 288.6$ eV for PTCDA multilayers on Ag(111)^{59, 307}]. Hence, there is a *differential* shift of the individual C1s components, as opposed to a *rigid* shift which would be expected on the basis of pure physisorption. For 1 ML PTCDA/Au(111),^{59, 307} where a physisorptive character of the surface bonding has been concluded,^{54, 59, 60, 153} the shifts of both the C_{funct} peak and the C_{peryl} peak amount to about -0.5 eV and thus are identical, indeed.

The two peaks in the O1s XP spectrum of Fig. 6.27)(b), top, can essentially be attributed to the O_{carb} and O_{anhyd} components. The peak at lower E_b corresponds to the O_{carb} atoms due to the higher electron density and the better screening at the place of the emitters in comparison to the O_{anhyd} atoms. The enhanced stabilization of the initial and the final state for the O_{carb} atoms can be understood by the presence of the C=O double bonds and can be visualized with the help of molecular resonance structures which may place a negative charge on the O_{carb} atoms. As in the case of the C1s signal, satellite peaks are present. The fitting model agrees with the stoichiometric ratio of O_{carb} : O_{anhyd} = 4 : 2 = 2 : 1 if the respective satellite peaks are included. Note at this point that a satellite peak of the O_{anhyd} component was expected at $E_b \approx 537$ eV (see also Sec. C.3.3 in the appendix of the present work for XPS reference data of PTCDA on Ag surfaces).³⁰⁷ This satellite peak is not observed here. Presumably, it is of comparably low intensity and thus overlooked due to the onset of the nearby, much stronger Au4p_{3/2} signal at 546.3 eV [This peak has been cut off in the depicted XP spectra of Fig. 6.27)(b)].¹⁶² Again, the peaks shift *differentially* towards lower E_b with respect to the multilayer. The shift of the O_{carb} component is 0.2 eV larger than that of the O_{anhyd} component (−0.85 eV versus −0.64 eV). In contrast, a rigid shift of about −0.8 eV is observed for PTCDA on pure Au(111).⁵⁹ Hence, we may conclude that, at least to a small extent, PTCDA interacts differently—and presumably more strongly or, more precisely, less weakly—with the Cu₃Au(111) surface than with the pure Au(111) surface. Apparently, the metal/molecule interaction has a stronger impact on the O_{carb} atoms. This conclusion is also supported by the fact that the energetic splitting between O_{carb} and the corresponding satellite O_{carb, sat 1} is decreased by 0.9 eV in comparison to the multilayer case. For the multilayer, this splitting in E_b of 2.3 eV was essentially identical to the optical HOMO–LUMO gap of 2.2 eV or the transport gap of about 2.5 eV in condensed PTCDA.⁴⁷² Note that also the splitting of the C_{funct} main and satellite components is reduced by 0.2 eV in comparison to the multilayer (see Table 6.7).

After all, we summarize that the absolute values of the peak shifts towards lower binding energies of the C1s and O1s levels in PTCDA on the Cu₃Au(111) surface are similar to those observed on the pure Au(111) surface. However, a differential shift is observed in the present case of Cu₃Au(111) [see Fig. 7.8 in Sec. 7.4, page 202, of the present work for a graphical representation of the peak shifts ΔE_b observed in XPS for PTCDA (sub-)monolayers on various coinage metal surfaces, including Cu₃Au(111) and Au(111)]. Therefore, we conclude that two aspects have to be considered here. On the one hand, the presence of the metal substrate causes screening effects which lead to lower binding energies for all XPS levels. On the other hand, a (partial and thus small) electron transfer may occur from the metal to the molecule, resulting in an enhanced electron density and thereby also in lower binding energies for the core level electrons in PTCDA. The latter aspect of electron transfer does not influence all core levels to the same extent, giving rise to a differential shift of the core level signals. This mainly affects the O_{carb} and C_{funct} atoms, and will be elucidated in Sec. 7.4 in more detail. Roughly speaking, a partial electron transfer leads to a partial filling of the PTCDA LUMO and thus to an electronic restructuring which allows for the accumulation of valence electrons preferentially at the O_{carb} and C_{funct} atoms.

XP spectra on exposed spots

We now turn to the C1s and O1s XP spectra on the exposed spots (see Fig. 6.27, bottom). In principle, similar fitting models apply here. In comparison to the fresh spots, the main peaks have larger width (by 12.5 % on average, see also Table 6.7). Furthermore, all components have shifted further towards lower binding energies. This is most likely due to enhanced screening effects by

the substrate as well as due to a (larger) metal-to-molecule charge transfer, and may thus indicate a smaller adsorption height.

The main C1s components exhibit a nearly rigid shift of about -0.1 eV with respect to the fresh spot. In the case of the O1s components, the O_{anhyd} peak has not shifted substantially (-0.06 eV). The O_{carb} peak, however, has shifted by -0.24 eV. As has been the case for PTCDA in the fresh state already, the largest shift of all main components is observed for O_{carb}. This agrees with the above conclusion of an enhanced charge transfer from the metal to the molecule causing an increased electron density on the PTCDA molecules that is, on the O_{carb} atoms, in particular. Most remarkably, however, three additional components appear in the C1s XP spectrum in Fig. 6.27(a), bottom row, namely, one further satellite for the C atoms in the perylene core (C_{peryl, sat}^{*}, depicted in cyan) and two new components which are attributed to the C atoms within the functional groups of PTCDA in a chemically different bonding state (C_{funct}^{*} and C_{funct, sat}^{*}, depicted in magenta).ⁱⁱ⁾ Portioning the intensities of the additional components to the C atoms in the perylene core and in the functional groups, respectively, accompanied with small adjustments to the relative intensities of all other components ensured that the stoichiometric ratio of C_{peryl} : C_{funct} = 20 : 4 = 5 : 1, which is present in PTCDA, was still fulfilled by the fitting model.

The “new” C_{funct}^{*} peak is observed at $E_b = 287.38$ eV which is 0.83 eV below the binding energy of the “original” C_{funct} component and 1.19 eV below the corresponding E_b value of C_{funct} for PTCDA in the multilayer regime. Thus, the C_{funct}^{*} is considerably shifted towards lower E_b . Following the above argumentation, this indicates an substantially enhanced metal-to-molecule charge transfer after x-ray illumination of PTCDA on the Cu₃Au(111) surface. We suggest that the new components C_{peryl, sat}^{*}, C_{funct}^{*} and C_{funct, sat}^{*} are representative of PTCDA molecules in a *final*, more strongly bound state while the other components resemble those in the fresh, *initial* state (more weakly bound “*precursor*”).^{ij)} Apparently, the transition from the initial to the final state is stimulated by x-ray photons. We anticipate that the adsorption configurations of PTCDA on the Cu₃Au(111) surface in the two bonding states differ due to an altered interaction. This was investigated in detail employing XSW.

It will be demonstrated in Sec. 6.6.4 below that those XPS data (and also the XSW data) which were recorded on the exposed spots do *not* represent the XP spectra (and XSW photoelectron yield curves, neither) of the *pure* final state of PTCDA/Cu₃Au(111). These data in fact represent a linear combination of the respective XP spectra (and XSW curves) of both the initial and the final state. Thus, fitting models with a larger number of components (i.e., about twice the number of components present in the XP spectra on the fresh spots) should have been employed here. Due to their complexity, however, plausible and self-consistent fitting models including so many components—which also allowed to differentially analyze the C1s and O1s XSW data on the exposed spot in a conclusive manner [see also footnote ii) on page 146 of this chapter]—could not be developed on the basis of the available XPS data. Hence, the analysis and discussion of the XPS and XSW data of PTCDA/Cu₃Au(111) on exposed spots, which are presented in this work, are based on XPS fitting models with “effective” components. Yet, this does not affect the

ⁱⁱ⁾We note that the C1s XP spectrum on an exposed spot in Fig. 6.27(a), bottom, could also be fitted to the same degree of agreement with different fitting models which either employed only those components, which had already been present in the C1s XP spectrum on a fresh spot in Fig. 6.27(a), top, or which employed a smaller number of additional components. These alternative fitting models, however, did not agree with *all* XP spectra belonging to one individual C1s XSW data set on an exposed spot. Only the above-discussed model, which allowed differential fitting of the two sets of new components (C_{peryl, sat}^{*} and C_{funct}^{*} plus C_{funct, sat}^{*}, respectively), showed good agreement for the entire C1s XSW data set.

^{ij)}Note at this point that also the C_{peryl, sat}^{*} component is shifted by -0.94 eV with respect to the “original” C_{peryl, sat} component and by -1.15 eV with respect to the corresponding C_{peryl, sat} component in the condensed PTCDA film.

validity of our experimental data or the conclusions drawn thereof at any point because they are consistent with the general trends observed for PTCDA on (other) coinage metal surfaces (see also the following sections and Chapter 7, in particular Secs. 7.3 to 7.6).

6.6.3 XSW photoelectron yield curves

Due to the changes in the C1s and O1s XP spectra with x-ray exposure time (see Sec. 6.6.2), the XSW experiments had to be performed in two different modes. The XSW data sets on the exposed spots were acquired in the usual way where all data points of one XSW photoelectron yield profile were collected in *one* spot on the sample. Typically, one C1s and one O1s data set were acquired consecutively on the same spot with alternating chronological order. The acquisition time for one single XSW data set was about 75 min and hence about twice as long as the period of time for which changes in C1s and O1s XP spectra were observed. Thus, potential effects by altering adsorption configurations, which may be associated with the transition from the initial to the final state in XPS, are only present at the beginning of the XSW measurement on a previously unexposed spot. Furthermore, these XSW experiments probed the sample surface in the Cu-enriched state where the surface segregation of Cu atoms either was in progress or had even saturated (see also Sec. 6.5.2).

Experimentally more challenging, however, was the investigation of the PTCDA adsorption configuration in the initial state because the most pronounced changes in the XP spectra occurred during the first few minutes of x-ray beam exposure (see also Fig. 6.26). Therefore, the time per spot was limited if the initial state was to be probed selectively. If the XSW data had been acquired in the usual way, that is, with all data point being collected in one spot, the acquisition time per data point and thus per XP spectrum would have been reduced to several seconds only. This was not sufficient for acquiring XP spectra with adequate signal-to-noise ratio and good resolution which allowed for differential analysis of the individual contributions to the XPS signal later on. Hence, we performed the XSW measurements for the initial state in a *scanning mode*: We measured only two data points of one XSW photoelectron yield curve on one spot on the Cu₃Au(111) surface which had previously not been exposed to the x-ray beam and then measured the next two data points for two different photon energies on another, previously unexposed spot. The so-obtained data, i.e., reflectivity and XP spectra, were combined in order to give a complete XSW photoelectron yield curve which could then be fitted. For one data set, 14 spots distributed over the Cu₃Au(111) surface were considered. The acquisition time per data point amounted to 3.5 min, approximately, and thus was on a the same time scale as the XP spectra in Fig. 6.27, top, which were used for developing XPS fitting models and which did not yet show indications for substantial contributions from the final state.

For the differential analysis of the XSW data, the XPS fitting models from Sec. 6.6.2 were employed. Here, differential analysis means that the adsorption heights d of the individual components in the XP spectra, namely, C_{peryl}, C_{funct}, C_{sat}, O_{carb}, and O_{anhyd}, were determined by separately fitting theoretical XSW photoelectron yield curves to the respective experimental XSW profiles. For this purpose, all XP spectra of one XSW data set were fitted with the corresponding fitting model (see Table 6.7). For the evaluation of the C1s XSW data, the relative intensities of all C atoms of the perylene core, i.e., C_{C-C}, C_{C-H}, and C_{C-CO}, were constrained, and their integral intensities were then combined to give the C_{peryl} signal. All satellite components which were specifically assigned to one of the main components, namely, C_{peryl, sat}, C_{funct, sat}, O_{carb, sat 1}, and O_{carb, sat 2}, were constrained in their intensities relative to the corresponding main components, as given by the fitting models in Fig. 6.26, too. The relative intensities C_{peryl} : C_{funct} and O_{carb} : O_{anhyd} as well as the relative satellite intensities of the unassigned satellite peaks (C_{sat 1} and C_{sat 2}) were

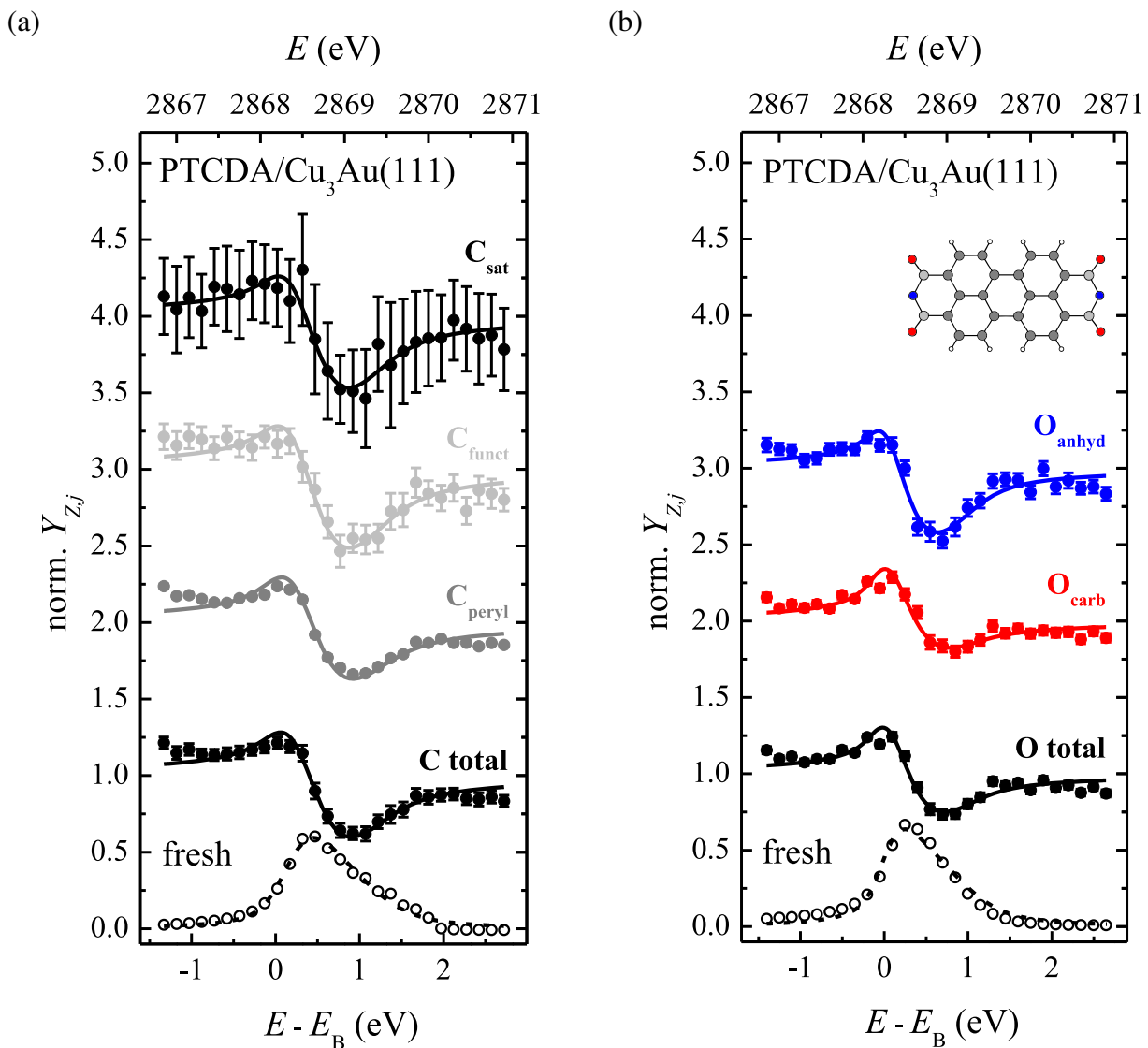


FIG. 6.28. Typical XSW photoelectron yield curves of carbon and oxygen in PTCDA on the $\text{Cu}_3\text{Au}(111)$ surface on a *fresh* spot. The (a) $\text{C}1s$ and the (b) $\text{O}1s$ signals were employed in the respective XSW experiments. The XP fitting models allowed for a differential analysis of the XSW data regarding the individual components: (a) C_{pery} (dark gray), C_{func} (light gray), and C_{sat} (black) for the $\text{C}1s$ signal, and (b) O_{carb} (red) and O_{anhyd} (blue) for the $\text{O}1s$ signal. In addition, the summed data of the individual $\text{C}1s$ and $\text{O}1s$ components are shown in black. Experimental data points are shown as filled circles while respective fits to the data are shown as solid lines. The curves have been vertically offset for clarity. In some cases, error bars are so small that they are almost hidden by the data points. In addition, the measured reflectivity of the substrate employing the (111) lattice planes (open circles) and the corresponding fit (dashed line) are shown. Error bars have been omitted for clarity here. A color-coded ball-and-stick model of the PTCDA molecule is shown as an inset in (b).

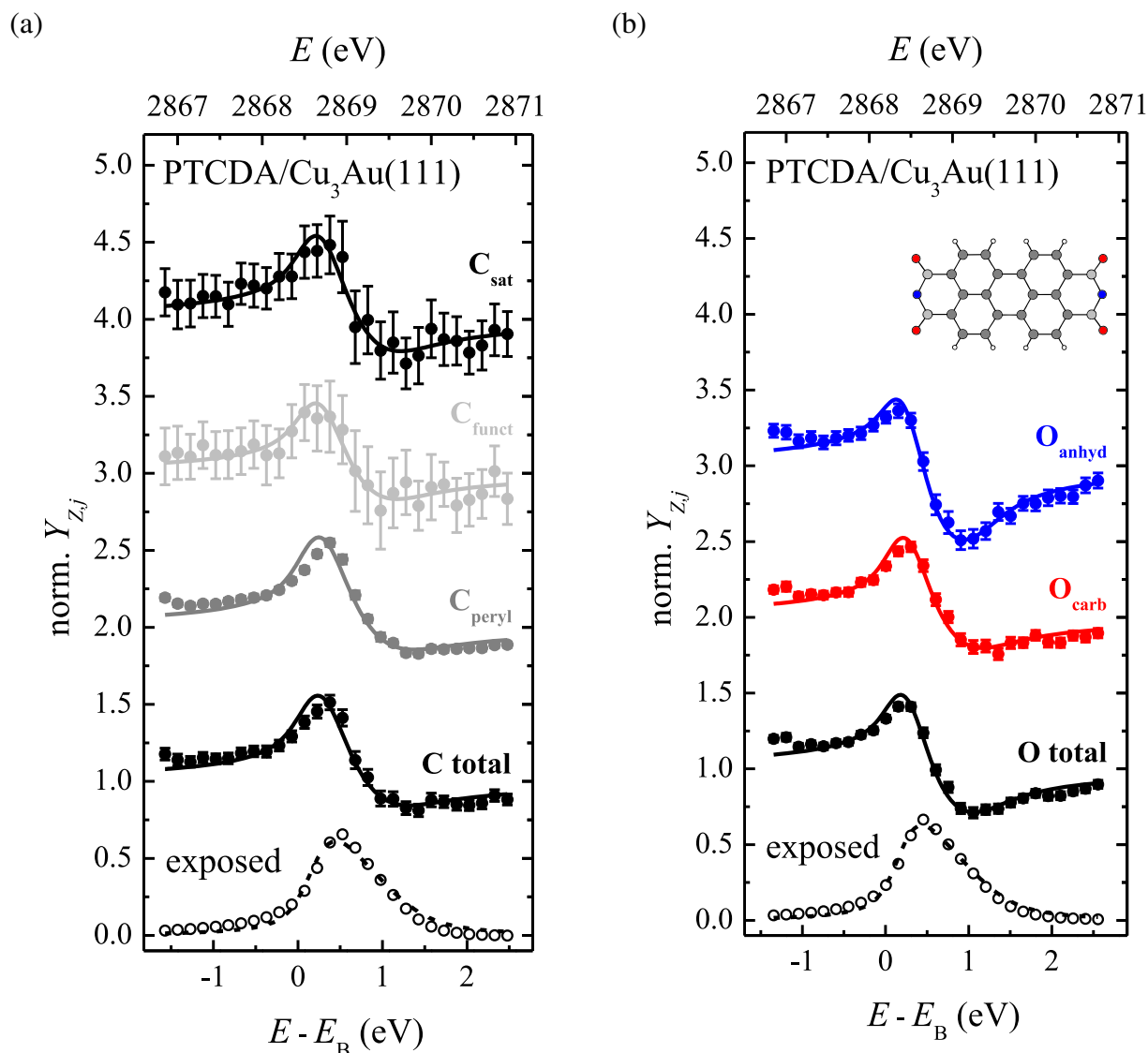


FIG. 6.29. Same as Fig. 6.28 but for an exposed spot: Typical XSW photoelectron yield curves of carbon and oxygen in PTCDA on the $\text{Cu}_3\text{Au}(111)$ surface on an *exposed* spot. The (a) $\text{C}1s$ and the (b) $\text{O}1s$ signals were employed in the respective XSW experiments. The XP fitting models allowed for a differential analysis of the XSW data regarding the individual components: (a) C_{panyl} (dark gray), C_{func} (light gray), and C_{sat} (black) for the $\text{C}1s$ signal, and (b) O_{carb} (red) and O_{anhyd} (blue) for the $\text{O}1s$ signal. In addition, the summed data of the individual $\text{C}1s$ and $\text{O}1s$ components are shown in black. Experimental data points are shown as filled circles while respective fits to the data are shown as solid lines. The curves have been vertically offset for clarity. In some cases, error bars are so small that they are almost hidden by the data points. In addition, the measured reflectivity of the substrate employing the (111) lattice planes (open circles) and the corresponding fit (dashed line) are shown. Error bars have been omitted for clarity here. A color-coded ball-and-stick model of the PTCDA molecule is shown as an inset in (b).

allowed to vary throughout the XSW scan, while the full widths at half maximum (FWHM) and the positions of the peaks relative to each other were fixed.^{kk)} Note that in the case of the C1s data on the exposed spots also the relative intensities of the new $C_{\text{peryl, sat}}^*$ and C_{funct}^* components were allowed to vary while the intensity of the $C_{\text{funct, sat}}^*$ satellite component was constrained relative to that of corresponding C_{funct}^* main component with the same ratio that had been present in the XP spectrum in Fig. 6.26(a), top.

Exemplary XSW photoelectrons yield curves for measurements on fresh as well as on exposed spots are shown in Figs. 6.28 and 6.29, respectively. The scanning-mode XSW experiments on fresh spots yielded both smooth reflectivity curves and pronounced photoelectron yield profiles as Fig. 6.28 demonstrates. The XSW profiles for all components of interest here exhibited similar shapes. This hints at the fact that the PTCDA molecules in the fresh/initial state do not show a considerable distortion upon adsorption on the Cu₃Au(111) surface. Indeed, this hypothesis is confirmed by fitting theoretical XSW profiles to the experimental data. The obtained fitting parameters are given in Table 6.8. All components have coherent fractions f_c above 0.5. This indicates a high degree of vertical order, considering that PTCDA is a large organic molecule which may be subject to intramolecular distortions upon adsorption on the Cu₃Au(111) surface [for comparison, see the f_c values for PTCDA on the Ag(100) and Ag(110) surfaces reported in Sec. C.3.4 in the appendix of the present work which are in the range of 0.50–0.77 and 0.24–0.43, respectively], and also considering that, at least to a certain extent, all three HB phases of PTCDA are present. Apparently, the adsorption configurations are very similar in the three HB phases. This conclusion is in accordance with the findings from LEED and XPS that the respective lattice parameters are nearly identical (see Sec. 6.6.1), and that the metal/molecule interactions are rather moderate (see Sec. 6.6.2), not giving rise to a substantially different adsorption configuration for PTCDA in one of the three HB phases compared to the others. Note that this reasoning concerning the adsorption configurations in the different PTCDA phases not only applies to the situation on fresh spots but also to that on exposed spots, in principle.

On the contrary, the standard-mode XSW experiments on exposed spots yielded photoelectron yield curves with distinct differences regarding the line shapes (see Fig. 6.29). On the one hand, the XSW curves for the C1s components with their pronounced maximum at $E - E_B$ values of about 0.5 eV exhibit a different shape than those for the O1s components. Here, the most pronounced feature is a minimum at $E - E_B \approx 1.0$ eV. The different line shapes may indicate a vertical distortion of the PTCDA molecules upon adsorption on the Cu₃Au(111) surface *after* appropriate time of illumination with the x-ray beam. On the other hand, the XSW curves for the C1s components with their maximum, in particular, have changed substantially for the exposed spots as compared to the fresh spots where a minimum was observed, too ($E - E_B \approx 0.5$ eV; see Fig. 6.28). This finding hints at an altered adsorption height after x-ray beam exposure. Considering also the new components in the C1s XP spectra on exposed spots at lower E_b values as compared to the “original” components (see also Sec. 6.6.2), we expect a smaller adsorption height of the C backbone in PTCDA in the exposed state than in the fresh state.

Before the actual results derived from the XSW photoelectron yield curves will be presented (see Sec. 6.6.4 below), we comment on the degree of agreement between the fitting curves and the experimental data again. As has been outlined in Sec. 6.3.3 already, systematic discrepancies between the fitting curves and the experimental data are present for the XSW data PTCDA/Cu₃Au(111). Two aspects can be observed in Figs. 6.28 and 6.29. Firstly, the obtained fitting curves do not correctly explain the first few and the last few data points of one XSW curve, i.e., the

^{kk)}The absolute peak positions E_b were allowed to vary slightly ($\Delta E_b \leq 0.1$ eV) in order to account for statistical deviations and inaccuracies in the (nominal) photon energy.

data points at $E - E_B \leq -1$ eV and $E - E_B \geq 2$ eV.^{ll)} Secondly, the data points in the $E - E_B$ range of about 0.0 eV to 0.5 eV are systematically overestimated by the fitting curves. Obviously, both aspects can be traced back to the fitting of the corresponding reflectivity curves $R(E)$ (see also Fig. 6.8 in Sec. 6.3.3, page 105, of the present work). The discrepancies in the fits to the XSW curves coincide with those in the fits to the $R(E)$ curves. As also mentioned in Sec. 6.3.3, these discrepancies between experimental XSW data and the corresponding fitting curves can in principle be overcome by adapting the evaluation procedure in XSWAVES. Exemplary tests confirmed that the so-obtained fitting curves agree very well with the experimental data (not shown). However, the impact on the fitting results for PTCDA/Cu₃Au(111) concerning the coherent f_c and the coherent position p_c is rather small on average: $\Delta f_c = +0.08(6)$, $\Delta p_c = +0.01(2)$, and $\Delta d = +0.02(4)$ Å [averaged over *all* XSW data on PTCDA/Cu₃Au(111)].^{mmm)} In particular, the results for the adsorption heights and thus also for the adsorption configurations are essentially unaffected by the fitting quality here, ensuring the validity of the determined adsorption configurations which will be presented in the following section. Hence, a refined analysis of the entire XSW data set on PTCDA/Cu₃Au(111) by a modified evaluation procedure was not necessary.

6.6.4 Adsorption configurations

We now turn to the explicit adsorption configurations of PTCDA on the Cu₃Au(111) surface. As already indicated by the substantially different shapes of the XSW profiles obtained on fresh and exposed spots (see Figs. 6.28 and 6.29), at least two different adsorption configurations are present depending on the time of x-ray beam exposure. They will also be referred to as *initial state* and *final state* adsorption configurations in the following. The adsorption configuration in the initial state was determined in scanning-mode XSW experiments on fresh spots (see also Sec. 6.6.3). As will be elucidated in detail further below, the final state is not present as a pure phase on the Cu₃Au(111) surface. Only the *effective* adsorption configuration of a *mixed state* could be experimentally determined with XSW on exposed spots. The experimental result for the mixed state is considered to be a combination of the two adsorption configurations in the initial and the final state, and, thus, it does *not* represent an adsorption configuration of PTCDA which is actually present at the Cu₃Au(111) surface. The adsorption configuration in the final state was then obtained from an “extrapolation” of the experimental results for the initial and the mixed state.

Initial state

We found the PTCDA molecules at an averaged adsorption height d of 3.18(1) Å in the initial state, as deduced from the C_{peryl} component (see Table 6.8). The stated adsorption height has *not* been referenced against the ideal surface which, in turn, would be defined by the position of the (111) Bragg planes but against the relaxed surface (see also Sec. 6.5.3). In particular, we took the averaged vertical position of the Au atoms, which was determined at 0.58(8) Å with respect to the ideal position, as a reference here because the surface has been shown to behave rather Au-like with regards to the adsorption behavior of PTCDA. Also, the averaged vertical position of the Cu atoms of 0.55(1) Å or the (stoichiometric) average of the two values could have been employed as a reference instead. Thus, the choice of the surface reference may cause systematic but *small*

^{ll)}In addition, the $Y_{Z,j}(E)$ value of the very first data point is too large due to a systematic error in the normalization of the data to the intensity I_0 of the incident beam (see also Sec. 6.3.3).

^{mmm)}The largest deviations in the f_c values were obtained for the individual C1s components of PTCDA/Cu₃Au(111) in the initial and the final state, amounting to $\Delta f_c = +0.15(2)$ and $\Delta f_c = +0.09(3)$, respectively [see also footnote i) on page 106 of this chapter].

TABLE 6.8. Summary of the final XSW results for the adsorption configuration of PTCDA on the Cu₃Au(111) surface. Results are given for fresh spots (which correspond to the initial state), for exposed spots (which correspond to the mixed state), and for the final state (as an extrapolated state). The C1s and O1s levels were measured, respectively. The parameters f_c and p_c are the coherent fractions and positions, respectively, which were obtained from the fits to the photoelectron yield curves. The d values denote the averaged vertical adsorption height of the specific atoms. Here, d is calculated at $d = [n + p_c - p_c(\text{Au}3d_{5/2})]d_{hkl}$ with $n = 1$ and $p_c(\text{Au}3d_{5/2}) = 0.27(4)$ (see also Table 6.4). d_{hkl} is the lattice plane spacing of the employed (111) Bragg reflection of the Cu₃Au substrate crystal. $\Delta d = d_i - d_{\text{fresh/initial}}$ denotes the changes in the averaged vertical adsorption heights for the exposed-spot/mixed-state or final-state data i with respect to the fresh-spot/initial-state data. For the specification of the atoms, see Figs. 6.28(b) and 6.29(b), for example. The values for C total and O total were obtained by performing the fitting of the XSW photoelectron yield curves to the sum of the integral intensities of all components contributing to the respective XPS signal.

	PTCDA/Cu ₃ Au(111)										
	fresh/initial			exposed/mixed				final ^a			
	f_c	p_c	d (Å)	f_c	p_c	d (Å)	Δd (Å)	f_c	p_c	d (Å)	Δd (Å)
C total	0.60(11)	0.74(1)	3.18(1)	0.47(7)	0.68(2)	3.07(5)	-0.11(5)	0.42(13)	0.63(2)	2.95(5)	-0.23(5)
C _{peryl}	0.58(10)	0.73(1)	3.18(1)	0.46(7)	0.68(2)	3.05(5)	-0.13(5)	0.43(13)	0.63(2)	2.94(5)	-0.24(5)
C _{funct}	0.72(8)	0.75(1)	3.21(2)	0.54(11)	0.70(2)	3.11(4)	-0.10(5)	0.46(14)	0.65(2)	3.00(4)	-0.21(5)
C _{sat}	0.64(14)	0.73(2)	3.17(5)	0.42(5)	0.69(3)	3.07(6)	-0.10(8)	0.31(14)	0.63(4)	2.95(8)	-0.22(9)
O total	0.60(9)	0.77(2)	3.25(4)	0.60(3)	0.73(2)	3.16(5)	-0.09(6)	0.62(9)	0.70(3)	3.10(6)	-0.15(8)
O _{carb}	0.54(9)	0.76(2)	3.24(4)	0.53(4)	0.72(2)	3.14(5)	-0.10(6)	0.54(10)	0.69(3)	3.07(6)	-0.17(8)
O _{anhyd}	0.73(7)	0.78(2)	3.27(4)	0.75(2)	0.74(3)	3.19(6)	-0.08(6)	0.79(8)	0.72(3)	3.14(7)	-0.13(8)

^aCalculated from the XSW results for PTCDA/Cu₃Au(111) on the fresh and exposed spots under the assumption that the contribution of the final state to the latter results amounts to 60 %.

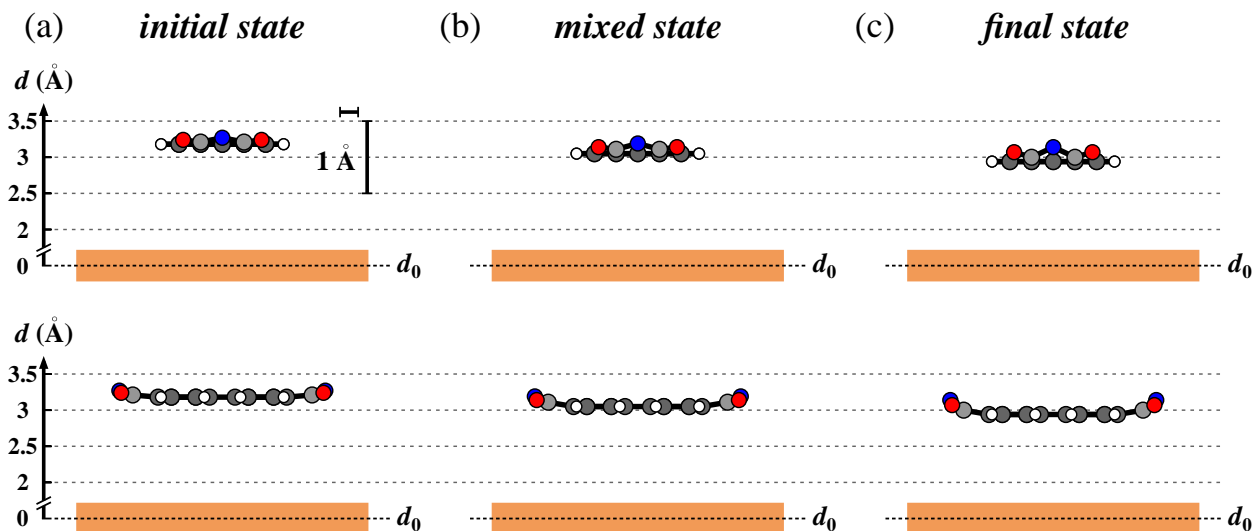


FIG. 6.30. Adsorption configurations of PTCDA on the $\text{Cu}_3\text{Au}(111)$ surface at different times of x-ray beam exposure, that is, (a) in the initial state (determined on fresh spots), (b) in the mixed state (determined on exposed spots), and (c) in the final state. The adsorption configuration in the final state was calculated from the XSW results for PTCDA/ $\text{Cu}_3\text{Au}(111)$ on the fresh and exposed spots under the assumption that the contribution of the final state to the latter results amounts to about 60%. The top row shows side views along the long molecular axis while the bottom row shows side views along the short molecular axis. H atoms are shown in white, C_{func} and C_{peryl} atoms in light gray and dark gray, and O_{carb} and O_{anhyd} atoms in red and blue, respectively. The surface is depicted as a colored region. d denotes the vertical adsorption height; the vertical scale is enlarged by a factor of 4 and referenced against the (averaged) position of the relaxed surface (dashed line, d_0), i.e., against the (averaged) vertical height of the Au atoms in the topmost layer of the PTCDA-covered $\text{Cu}_3\text{Au}(111)$ surface.

differences in the stated d values. However, this does not affect the validity of our experimental data or the conclusions drawn thereof at any point. Recalling the vdW radii of the involved elements from Table 2.3, the sums of the vdW radii amount to 3.41 \AA and 3.31 \AA for Au plus C and Au plus O, respectively. Since the vdW radius of Cu is smaller by 0.26 \AA in comparison to that of Au, these values amount to 3.15 \AA and 3.05 \AA for Cu plus C and Cu plus O, respectively. The sum of the covalent radii are around 2 \AA in all cases. Because the $\text{Cu}_3\text{Au}(111)$ surface is rather Au-like, although the Au atoms are the minority species at the surface, and because the Au atoms are larger, giving rise to steric hindrance and larger Pauli repulsion potentially, we will compare the determined adsorption heights to the sum of the vdW radii considering solely the Au atoms in the following. Doing so, we find that the obtained adsorption height of the perylene core in PTCDA on $\text{Cu}_3\text{Au}(111)$ is 7% smaller than expected for pure vdW interactions [to be compared to 4% for PTCDA/ $\text{Au}(111)$],⁵⁴ for example].

The XSW results reveal a distortion of $0.09(4) \text{ \AA}$ of the intrinsically planar PTCDA molecules upon adsorption (already) in the initial state (see Table 6.8). The determined adsorption configuration is illustrated in Fig. 6.30(a). The atoms within the functional groups of PTCDA are found at slightly higher adsorption heights and thus have bent away from the surface with respect to the perylene core. This is in particular true for the O atoms. The averaged adsorption height of $3.25(4) \text{ \AA}$ deduced from the O total signal is almost identical to the sum of the vdW radii for Au and O (-2%). In the broadest sense, the adsorption configuration on $\text{Cu}_3\text{Au}(111)$ resembles that

TABLE 6.9. XSW results for the adsorption configuration of PTCDA on the Cu₃Au(111) surface for subsequent acquisition of individual data points on *fresh* spots. The C1s and O1s levels were measured, respectively. Two data points of an individual XSW data set for the fresh/initial state were subsequently acquired on the same, previously unexposed—that is, initially fresh—spot on the sample. These data points acquired at different photon energies from different spots were combined in order to give a complete XSW data set, i.e., a complete XSW photoelectron yield profile. Averaged results are given for the subsequent acquisitions # 1 and # 2. For each XPS signal and acquisition # *i*, the results of two individual XSW data sets were averaged. The parameters f_c and p_c are the coherent fractions and positions, respectively, which were obtained from the fits to the photoelectron yield curves. The d values denote the averaged vertical adsorption height of the specific atoms. Here, d is calculated at $d = [n + p_c - p_c(\text{Au}3d_{5/2})] d_{hkl}$ with $n = 1$ and $p_c(\text{Au}3d_{5/2}) = 0.27(4)$ (see also Table 6.4). d_{hkl} is the lattice plane spacing of the employed (111) Bragg reflection of the Cu₃Au substrate crystal. $\Delta d = d_2 - d_1$ denotes the change in the vertical adsorption height with increasing x-ray beam exposure, i.e., the difference between the d values of acquisitions # 2 and # 1. For the specification of the atoms, see Figs. 6.28(b) and 6.29(b), for example. The values for C total and O total were obtained by performing the fitting of the XSW photoelectron yield curves to the sum of the integral intensities of all components contributing to the respective XPS signal.

PTCDA/Cu ₃ Au(111) (<i>fresh</i>)							
	# 1			# 2			
	f_c	p_c	d (Å)	f_c	p_c	d (Å)	Δd (Å)
C total	0.63(12)	0.74(1)	3.20(1)	0.58(9)	0.73(1)	3.17(1)	−0.03(2)
C _{peryl}	0.60(11)	0.74(1)	3.19(1)	0.56(9)	0.73(1)	3.17(1)	−0.02(2)
C _{funct}	0.73(10)	0.75(1)	3.21(3)	0.70(6)	0.75(1)	3.21(3)	0.00(4)
C _{sat}	0.70(15)	0.75(2)	3.20(1)	0.60(10)	0.71(4)	3.13(9)	−0.07(9)
O total	0.61(8)	0.77(2)	3.26(5)	0.60(10)	0.77(2)	3.25(4)	−0.01(6)
O _{carb}	0.55(10)	0.76(2)	3.24(5)	0.54(10)	0.76(1)	3.24(3)	0.00(6)
O _{anhyd}	0.74(4)	0.78(2)	3.28(4)	0.72(12)	0.77(2)	3.26(4)	−0.02(6)

of PTCDA on the Cu(111) surface where a *boat*-like adsorption configuration has been found with XSW, too.⁴³

In order to confirm that the above-stated results truly represent the adsorption configuration of PTCDA in the fresh state and do not already suffer from a partial transition to the final state, we re-analyzed the experimental data such that we only considered every other data point of the respective XSW profile. Remember that two data points of an individual XSW data set for the fresh/initial state were subsequently acquired in the same, previously unexposed—that is, initially fresh—spot on the sample. By doing so, we split one complete XSW data set into two new data sets each of which a theoretical XSW photoelectron yield curve was fitted to. The so-obtained data sets represented the exclusive combination of only acquisitions # 1 and # 2 per spot on the sample, respectively. Of course, the newly obtained data sets only had only half the number of data points and twice the step size in photon energy compared to the original, full data sets. The respective fitting results are contrasted in Table 6.9. Obviously, the results for all main components, namely, C_{peryl}, C_{funct}, O_{carb}, and O_{anhyd}, regarding the coherent position p_c are identical within the error margins for acquisitions # 1 and # 2. The determined lowering in adsorption height of maximal 0.02 Å is at the accuracy limit of the XSW technique. In principle, also the f_c values agree within the error margins for both acquisitions although a small tendency towards lower values may be

TABLE 6.10. Same as Table 6.9 but for exposed spots: XSW results for the adsorption configuration of PTCDA on the Cu₃Au(111) surface at different times of x-ray beam exposure on *exposed* spots. The C1s and O1s levels were measured, respectively. Data sets for both XPS signals have been acquired on the same spot on the sample with alternating chronological order. Note that the respective spots on the sample had usually not been exposed to the x-ray beam prior to acquisitions # 1. Due to the long acquisition times of about 1 h per XSW data set, however, mainly the mixed state was probed in these experiments. Averaged results are given for the subsequent acquisitions # 1 and # 2. For each XPS signal and acquisition # *i*, the results of two individual XSW data sets were averaged, except for the O1s signal in the case of acquisition # 1 where only one data set was available. The values for C total, C_{peryl} total, C_{funct} total, and O total were obtained by performing the fitting of the XSW photoelectron yield curves to the sum of the integral intensities of all (corresponding) components contributing to the respective XPS signal (n.d. = not determined, n.a. = not available/applicable).

PTCDA/Cu ₃ Au(111) (<i>exposed</i>)							
	# 1			# 2			
	f_c	p_c	d (Å)	f_c	p_c	d (Å)	Δd (Å)
C total	0.53(5)	0.70(2)	3.11(5)	0.41(2)	0.67(1)	3.04(2)	-0.07(6)
C _{peryl} total	0.53(5)	0.70(3)	3.09(6)	0.39(1)	0.66(1)	3.02(1)	-0.07(6)
C _{funct} total	0.63(11)	0.71(2)	3.13(4)	0.44(1)	0.69(2)	3.09(4)	-0.04(6)
C _{funct}	n.d.	n.d.	n.d.	0.41(5)	0.72(1)	3.14(3)	n.a.
C _{funct} *	n.d.	n.d.	n.d.	0.49(8)	0.67(3)	3.03(6)	n.a.
C _{sat}	0.40(6)	0.71(3)	3.12(6)	0.44(6)	0.67(2)	3.03(4)	-0.09(8)
O total	0.64(1)	0.76(1)	3.23(1)	0.58(2)	0.72(2)	3.14(4)	-0.09(4)
O _{carb}	0.57(1)	0.75(1)	3.21(1)	0.50(3)	0.70(2)	3.11(3)	-0.10(4)
O _{anhyd}	0.77(2)	0.77(1)	3.26(1)	0.75(2)	0.73(2)	3.17(4)	-0.09(5)

anticipated (-4 % on average). In conclusion, however, the chosen approach of scanning mode XSW indeed allowed to selectively probe the adsorption configuration of PTCDA on Cu₃Au(111) in the initial state.

Mixed and final state

The XSW measurement which were performed in the usual way yielded the *effective* adsorption configuration of PTCDA/Cu₃Au(111) in an exposed spot, i.e., the adsorption configuration of the mixed state. The results are summarized in Table 6.8 and illustrated in Fig. 6.30(b). In comparison to the fresh/initial state, the f_c values have decreased by about 25 % on average for the C1s components. Yet, f_c has essentially not changed for the O1s components. Furthermore, the adsorption heights of *all* atoms in PTCDA have decreased by about 0.1 Å. In particular, the perylene core (C_{peryl}) has been depressed by 0.13(5) Å. Now, the adsorption height has decreased to 89 % of the summed vdW radii of Au and C. Because the decrease in d is larger by 0.05 Å for the C_{peryl} atoms than for the O_{anhyd} atoms, which are furthest away from the surface, the overall distortion of the molecule increases to 0.14(7) Å (+55 %). Our XSW results may be interpreted such that upon x-ray beam exposure the surface bonding of PTCDA on the Cu₃Au(111) surface slightly intensifies and gains a (weak) chemisorptive character.

For the above analysis, the new signals $C_{\text{peryl, sat}}^*$ and C_{funct}^* (including $C_{\text{funct, sat}}^*$) had been added to the original C_{peryl} and C_{funct} signals. Two problems were encountered when these signals were analyzed separately. Firstly, the relative intensity of the $C_{\text{peryl, sat}}^*$ signal was so small that no meaningful XSW profiles could be derived from the fits to the individual XP spectra. Secondly, both signals evolved, that is, increased with time, during the first acquisition of a data set on a given spot which had not been exposed before. This is in accordance with the finding from XPS that the changes in the spectral shapes occurred within about 40 min which corresponds to about half the acquisition time of one individual XSW data set. Thus, the acquisitions # 1 on each spot actually gave XSW profiles which were a *time-dependent* combination of the initial and the final state. Hence, we selectively re-analyzed the acquisitions # 2 per spot where the ratio between the initial-state and the final-state contributions was *constant* due to the large exposure time (see also below). Thereby, we could overcome the second problem, and meaningful XSW photoelectron yield curves were obtained also for the C_{funct}^* component to which theoretical curves were fitted (not shown). The so-obtained fitting results are presented in Table 6.10 and contrasted to the fitting results for acquisition # 1. Indeed, the d results for acquisition # 2 are lower by 0.04–0.10 Å for the atoms of interest here in comparison to acquisition # 1. This is because the results for acquisition # 1 include (larger) contributions from the fresh (initial) state. Furthermore, the f_c values for C_{peryl} , C_{funct} , and O_{carb} are higher for acquisition # 1. This finding is also due to the different ratio between the initial-state and the final-state contributions for the two acquisitions per spot. The final-state contribution is of course higher in the case of acquisition # 2, i.e., for larger times of x-ray beam exposure.

Regarding the C_{funct} and C_{funct}^* signals, non-identical results were obtained (see Table 6.10). Namely, a vertical splitting of 0.11(7) Å was found, with the C_{funct}^* being closer to the surface at $d = 3.03(6)$ Å. This value corresponds to 89 % of the expected vdW distance of Au and C. Apparently, even in the exposed state—*after* the transition from the initial to the final state has occurred and *finished* judging from the respective XP spectra—molecules with two different adsorption configurations are present at the Cu₃Au(111) surface, justifying our above differentiation between the exposed/mixed state and the final state. These two adsorption configurations in the mixed state reflect in the C_{funct} and C_{funct}^* signals in XPS and also in XSW for the less and more chemisorptively bound states, respectively. Apart from $C_{\text{peryl, sat}}^*$, the other components of the two individual adsorption configurations could not be discerned in our XPS data. If we assume, however, that the adsorption configuration of the PTCDA molecules is qualitatively identical in all bonding states, i.e., boat-like, the perylene core for the more strongly bound molecules is expected at $d(C_{\text{peryl}}) \approx 2.95$ Å, thus being at about 87 % of the expected vdW distance. This percentage is comparable to the value of 84 % which has been found for PTCDA/Cu(111) (see also Sec. 2.2.2).⁴³

The above statements and conclusions are based on not more than two individual XSW measurements per XPS signal and acquisition # i , and they are hence not highly reliably. In order to validate and enhance the above conclusions, a second approach was chosen to identify the adsorption configuration in the final state. Here, the term “final state” solely refers to the bonding state which causes the C_{funct}^* signal in XPS and in XSW, and thus has to be discerned from the exposed state. This terminology will be retained in the following.

For the purpose of clarifying the adsorption configuration of PTCDA in the final state, the typical contribution of the final state to the observed total photoelectron yield and thus also to the experimental XSW data for an exposed spot had to be quantified. The typical contribution was estimated as being about 60(5) %. Broadly speaking, we have subtracted the fresh-spot XP spectrum from the exposed-spot XPS data in order to obtain this value. The exact procedure was as follows: The C1s XP spectrum on an exposed spot, as shown in Fig. 6.27(a), bottom, was fitted

with the particular fitting model which had specifically been developed for the C1s XP spectrum on a fresh spot from Fig. 6.27(a), top. In order to achieve good agreement of this fitting model also with the experimental data on the exposed spot, three additional components had to be introduced (the fitting result is not shown here; see Table 6.7 for details on the fitting model). In the broadest sense, these additional components may be understood as to virtually represent, among others, the $C_{\text{peryl, sat}}^*$, C_{funct}^* , and $C_{\text{funct, sat}}^*$ components of the C1s signal of the *final* state, which are shown in Fig. 6.27(a), bottom, whereas the components from the model for the fresh spots represent the *initial* state. The fraction of the newly introduced final-state components was 60(5) % of the total intensity of the spectrum in Fig. 6.27(a), bottom.^{nm)} Note that the so-obtained XPS fitting model for the C1s level was not employed in the evaluation of the XSW data because the three additional components do not have a physical or chemical meaning. Therefore, a differential analysis of the XSW data would not have been possible. Note further that XPS fitting models with more physical/chemical meaning and thus higher complexity, such as a linear combination of *all* initial-state and final-state components (the latter are not available here), could not be employed in the XSW data evaluation because the fits to the respective XSW photoelectron yield curves (as well as to the underlying XP spectra) did not converge.

The same procedure for the O1s spectrum in Fig. 6.27(b), bottom, employing two additional components, yielded a smaller value of about 43(4) % for the final state contribution (fitting result not shown). Because the differences in the C1s XP spectra at different times of x-ray beam exposure were more pronounced and the obtained value was larger for the C1s level in comparison to the O1s level, the respective C1s value of 60 % was taken as the more realistic value for the eventual surface fraction of PTCDA molecules in the final state.^{oo)}

Considering the final-state contribution of the 60 %, the adsorption configuration of the final state was calculated from the XSW results for the fresh/initial and the exposed/mixed state. Here, we considered the XSW results for the exposed/mixed state which had been obtained as an average by analyzing *all* XSW data sets on exposed spots, i.e., both acquisitions # 1 and # 2. These results had already been presented in Table 6.8 above. We considered all data sets, that is, five C1s and four O1s data sets in total, although at least three of them, i.e., acquisitions # 1, exclusively probed the initial state at the very beginning of the XSW scans (see above).^{pp)} However, the higher statistical validity of this group including all experiments was assumed to prevail the systematic inaccuracy, that is to say, the interference with undesired contributions, of some of the included data sets. This assumption will be justified by the results which are to be reported.

For determining the adsorption configuration in the final state, the results vectors for the respective components on the exposed spots and on the fresh spots were subtracted (in proportion to their contribution) in an Argand-diagram representation of the data. Note that the superposition of the

^{nm)}If solely the determined integral intensities of the actual $C_{\text{peryl, sat}}^*$, C_{funct}^* , and $C_{\text{funct, sat}}^*$ components of the C1s signal as depicted in Fig. 6.27(a), bottom, had been taken as a measure of the final-state contribution to the XP spectrum, a value of only about 4 % ($= [Y_{\text{C1s}}(C_{\text{peryl, sat}}^*) + Y_{\text{C1s}}(C_{\text{funct, sat}}^*) + Y_{\text{C1s}}(C_{\text{peryl, sat}}^*)] / Y_{\text{C1s, total}}$) would have been obtained (see also Table 6.7). Note again that the components of the PTCDA/Cu₃Au(111) XP spectrum on the exposed spot, as discussed in Sec. 6.6.2, represent “effective” components only.

^{oo)}If the value of 43 % had been used in the XSW analysis of the final state (see below), the p_c results would have been lower by 0.05 to 0.10 for the C components, and lower by about 0.03 for the O components. In particular, this corresponded to adsorption heights of 2.83(5) Å and 2.88(5) Å for the C components C_{peryl} and C_{funct} and adsorption heights of 3.02(6) Å and 3.10(7) Å for the O components O_{carb} and O_{anhyd} , respectively. The f_c results would have altered by ± 0.05 at the most.

^{pp)}One C1s and one O1s data set were taken in parallel on a previously unexposed spot. Because the time scales of these measurements were twice as long as the duration of the other, non-parallel C1s and O1s XSW measurements, they could neither be unambiguously assigned to acquisition # 1 nor to acquisition # 2. However, they rather represent acquisition # 2 than acquisition # 1 due to their long acquisition time of about 2.5 h.

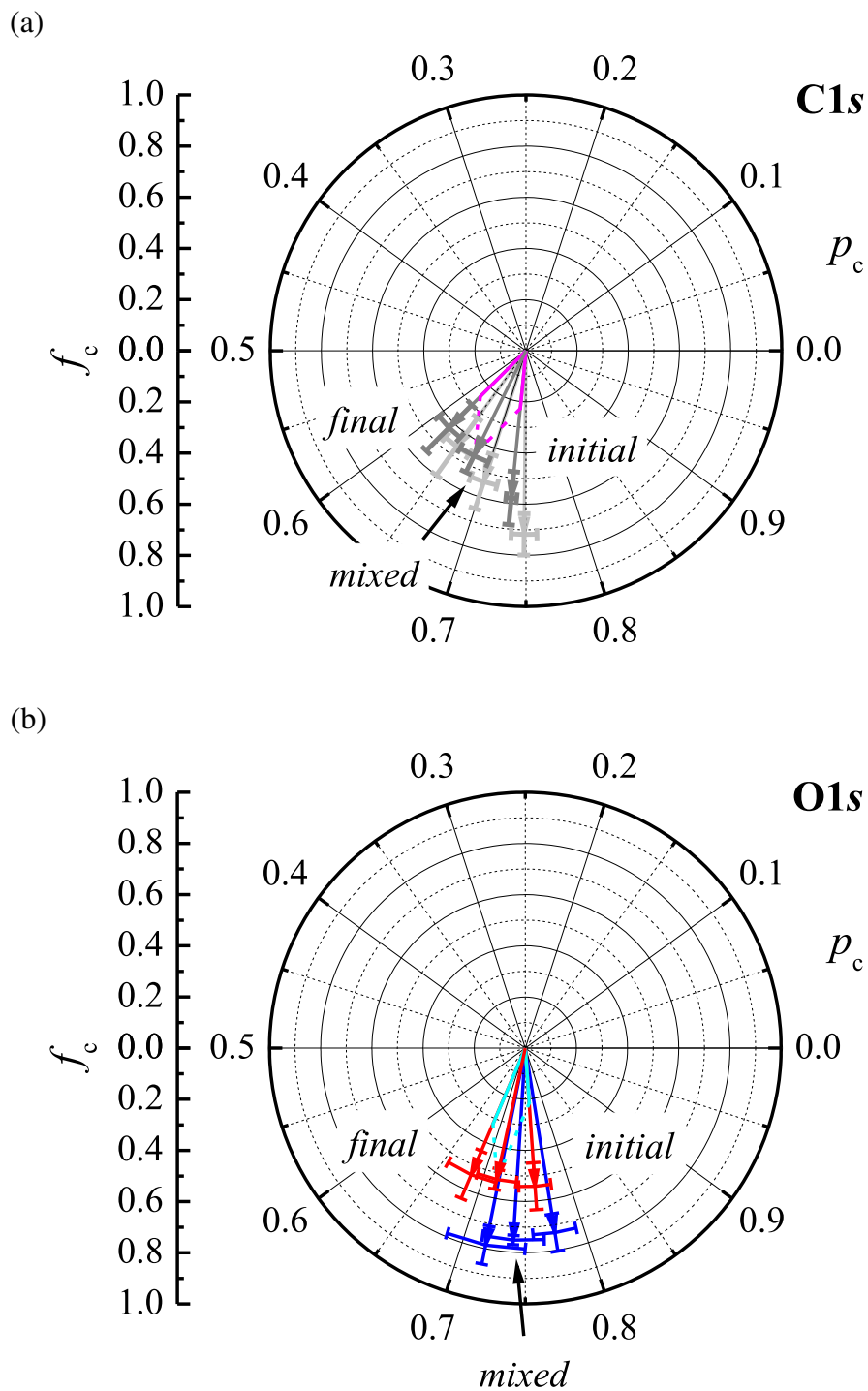


FIG. 6.31. Schematic representation of the XSW results for PTCDA on the $\text{Cu}_3\text{Au}(111)$ surface in an Argand diagram. (a) The vectors for the C_{peryl} (dark gray) and C_{funct} (light gray) signals, and (b) the vectors for the O_{carb} (red) and O_{anhyd} signals (blue) are depicted for the three different states or experimental stages, namely, fresh/initial, exposed/mixed, and final. The former two are experimental results while the vectors for the final state have been calculated thereof, assuming a final state contribution to the exposed state of 60%. Exemplarily, the backwards construction of the C_{peryl} and O_{carb} vectors in the exposed/mixed state from those in the fresh/initial and the final state are shown in magenta and cyan, respectively. This demonstrates the correctness of the vectors calculated for the final state.

XSW photoelectron yield curves of two species (here: two different adsorption heights of “chemically equivalent” atoms) results in an Argand vector in this representation which corresponds to the weighted sum of the individual Argand vectors of these species.^{29, 170} This was employed here.

The determination of the final-state results vector according to this procedure is exemplary shown in Fig. 6.31 for the C_{peryl} and O_{carb} signals, respectively, assuming a final-state contribution to the exposed state of 60 % as deduced from the C1s XP spectrum. In addition, the results for all components are compiled in Table 6.8. Noticeably, the result for C_{funct} in the final state agrees nicely within the error margins with the result that had been obtained for C_{funct}^{*} in acquisition # 2 of the exposed state (see above). This finding of identical C_{funct}^(*) results cross-validates both approaches for the determination of the adsorption configuration in the final state and renders the obtained values meaningful. Note that for reasons of simplicity the asterisk (*) has been dropped in the terminology of the final state components of both C and O atoms in this second approach (i.e., in Table 6.8 above).

The adsorption configuration of PTCDA on Cu₃Au(111) in the final state is illustrated in Fig. 6.30(c). Again, the PTCDA molecule exhibits a boat-like configuration but it sits closer to the surface than in the initial state. The C atoms in PTCDA, namely, C_{peryl} and C_{funct}, have decreased further, i.e., by more than 0.2 Å in comparison to the initial state. Thus, the C—Au vertical distance for the C_{peryl} atoms is reduced to 86 % of the expected vdW distance, in perfect agreement with the above result based on the approach where acquisitions # 1 and # 2 on the exposed spots were contrasted and a value of 87 % has been estimated. Since the O atoms have only decreased by about 0.15 Å in comparison to the initial state, the molecular distortion has increased to 0.20(8) Å in the final state. That is, the absolute (overall) vertical distortion is twice as large in the final state compared to the initial state and the O atoms reside at about 94 % of the expected vdW distance. Interestingly, the f_c values for the O atoms are essentially identical in all three states, that is, in the fresh/initial, the exposed/mixed, and the final state. For the C atoms in the final state, the f_c values are lower by about 10 % even in comparison to the results for the exposed spot which, in turn, are a combination of the initial- and the final-state results. Thus, this finding is counter-intuitive at this point. In Sec. 6.7 below, we will relate this to a certain level of “vertical disorder” of the PTCDA molecules in the final state.

6.7 Concluding Discussion, part II: PTCDA on Cu₃Au(111)

We now turn to the discussion of all the experimental data which were obtained for the properties of both the PTCDA-covered Cu₃Au(111) surface and the adsorbed PTCDA molecules. For purposes of structuring the discussion and as a reminder, the main results are briefly stated here again:

- (a) The degree of order of the Cu₃Au(111) surface has increased by several ten percents upon PTCDA adsorption, judging from the widths of the observed LEED spot profiles. The long-range surface reconstruction is neither lifted nor altered by the presence of PTCDA. As is the case for the clean Cu₃Au(111) surface, too, pure Cu and/or pure Au domains are not formed at the surface.
- (b) The surface fraction of Cu atoms increases again by x-ray beam exposure and reaches a final value of Cu_{0.69(4)}Au_{0.31(4)} (within the monitored period of time of about 2 h), which is close to the ideal surface stoichiometry of Cu_{0.75}Au_{0.25}.

- (c) The PTCDA-covered surface of Cu₃Au(111) has (further) relaxed outward by almost 0.6 Å with respect to the ideal, bulk-determined position. Judging from the f_c values, in particular, of the Au atoms, a buckling of the surface can still be anticipated.
- (d) Three herringbone (HB, namely, α , β , and γ) phases and one quadratic (S or δ) phase have been found. Apart from the γ phase, which resembles the structure of the α phase of PTCDA on pure Cu(111), these PTCDA phases are essentially analogous to those on pure Au(111). None of the PTCDA phases on Cu₃Au(111) exhibits a commensurate registry with the surface. Only the δ phase is p-o-l commensurate (within the error margins) to the substrate surface.
- (e) The XP spectra of PTCDA on the Cu₃Au(111) surface changed with increasing x-ray beam exposure. The observed peaks shifted (further) towards lower binding energies—also with respect to the multilayer positions—and exhibited line broadening. The peak shifting was found to be differential.
- (f) The adsorption heights of PTCDA on Cu₃Au(111) decreased with x-ray beam exposure while the boat-like distortion of the molecule enhanced, with the C atoms in PTCDA being closer to the surface than the O atoms. Two distinct adsorption configurations were identified: Upon illumination with the x-ray beam, about 60 % of the PTCDA molecules on the Cu₃Au(111) surface transitioned from the initial to the final state, exhibiting larger vertical distortions (by a factor of about 2 or about +0.1 Å) and smaller adsorption heights [about –8 % judging from the $d(\text{C}_{\text{peryl}})$ values].

In brief, the final results can be anticipated as follows (see below for a detailed discussion): the initial-state adsorption configuration of PTCDA exists on the Cu-depleted, “Au-rich” Cu₃Au(111) surface. Upon x-ray beam exposure, the adsorption configuration transforms in parts to that of the final state, accompanied by a re-enrichment of the surface in Cu atoms. At the same time, the lateral order of the surface layer is enhanced. Apparently, these variations in both the surface composition and the bonding situation (as implied by the different adsorption configurations) are mutually dependent to a large extent. Yet, we note at this point that, judging from the observed LEED patterns, neither the re-enrichment of the Cu₃Au(111) surface in Cu atoms nor the transition of the PTCDA adsorption configuration from the initial to the final state led to a change in the *lateral* structure at the metal/organic interface. Hence, the discussion concerning the lateral structures of the PTCDA overlayers on Cu₃Au(111) applies to both the initial and the final state. The same holds for our discussion regarding the surface relaxation, as deduced from structural arguments concerning the determined adsorption heights in both states.

As will also be elucidated below, we propose that the transition from the Cu-depleted to the “Cu-rich” (PTCDA-covered) Cu₃Au(111) surface cannot only be initialized by the x-ray beam but also by thermal treatment and/or an electron beam. Thus, the following discussion concerning the lateral structure and the degree of order of the PTCDA-covered Cu₃Au(111) surface primarily applies to the final state because the argument of a surface re-enrichment in Cu is employed here. Regarding the electronic core-level structure of PTCDA and the adsorption configurations in the initial and the final state, the discussions will of course be distinguished for these two states as a result of the extensive experimental data.

Surface order and re-enrichment in Cu

The enhanced long-range surface order observed with SPA-LEED proves that less defects are present at the PTCDA-covered Cu₃Au(111) surface, and it thus indicates a higher degree of order

in comparison to the clean surface (**ad a**). The clean surface is depleted in Cu atoms, as has been shown with XPS (see Sec. 6.3.2), and the corresponding STM images indicate that also non-ideal sites at the surface, i.e., former Cu sites, are occupied by Au atoms (see Sec. 6.3.1). In sum, Cu atoms at the clean Cu₃Au(111) surface are largely replaced by Au atoms. Besides, all surface atoms are substantially displaced from their ideal lattice sites due to steric reasons. These two effects were interpreted as being the reason for the limited long-range order of the surface observed in LEED and STM. In turn, we conclude that an enhanced order at the Cu₃Au(111) surface indicates the re-segregation of Cu atoms to the surface layer and thus the re-replacing of Au by Cu atoms to some extent. A re-enrichment of the surface in Cu has indeed been observed with XPS (**ad b**). However, this segregation process was initialized by exposure to the x-ray beam and exhibited slow kinetics. Within the first 15 min of beam exposure, the surface composition remained constant within the error margins (with a Cu fraction of about 60 %). The re-increased Cu fraction of 69(4) % was only observed after 2 h. The slow kinetics are attributed to the fact that the diffusion coefficients in the solid are very small (about 5×10^{-13} cm²/s for Au atoms in Cu₃Au at elevated temperatures of 823 K,⁴⁷³ for example) and that the experiments were performed at room temperature. Despite the low diffusion coefficients, the segregation can apparently be triggered by x-ray photons. We speculate that the segregation is truly initialized either by photoelectrons or secondary electrons, which occur during the photoemission process upon illumination with x-ray photons, or by thermal activation, and that it is *not* initialized by the x-ray photons themselves. One argument supporting this hypothesis is the fact that the re-segregation of Cu atoms to the surface upon PTCDA adsorption, which was concluded from the enhanced order at the PTCDA-covered Cu₃Au(111) surface, was also observed in the SPA-LEED measurements apparently where no x-ray beam but only an electron beam was present. Furthermore, most of the PTCDA-covered Cu₃Au(111) surface monolayer preparations were obtained by thermal desorption of multilayers at 575 K. Especially the so-prepared surfaces exhibited the enhanced long-range order [$\approx +20$ % in comparison to the surfaces which had *not* been post-annealed, judging from the widths of the respective (00) LEED spot profiles]. We note, however, that post-annealing has not been performed for the PTCDA/Cu₃Au(111) preparation which was employed in the XPS and XSW measurements.

The re-segregation of Cu towards the surface (**ad b**) indicates a stabilization of the (near-)ideal Cu₃Au(111) surface over the Cu-depleted surface in the case of PTCDA adsorption. The depletion of the clean Cu₃Au(111) surface in Cu atoms was explained by the thereby lowered surface energy (see Sec. 6.4). Apparently, the presence of the PTCDA overlayer reduces or overcomes the higher surface energy of the (near-)ideal and “Cu-enriched” Cu₃Au(111) surface. Two scenarios seem plausible here. On the one hand, the PTCDA molecules could interact more strongly with the Cu atoms (on a local scale) than with the more noble Au atoms.²⁰ This scenario employs a bonding mechanism with *localized* Cu–PTCDA interactions as a relevant bonding channel. Note that such local interactions are expected to result in vertical distortions of the molecular backbone. In particular, O–Cu interactions may be expected in this scenario due to the higher stability of O–Cu bonds in comparison to C–Cu bonds.²⁰ For instance, the bond dissociation energies for the CuO and CuCH₃ molecules in the gas phase at 298 K amount to 288(12) kJ mol⁻¹ and 55(4) kJ mol⁻¹, respectively.^{290,474} Yet, the determined boat-like adsorption configurations of PTCDA with the O atoms being furthest away from the Cu₃Au(111) surface do not support this explanatory approach (**ad f**). Thus, we favor another explanation of the re-segregation of Cu towards the surface layer. We propose a (partial) charge transfer from the metal to the PTCDA molecules as electron acceptors.^{102,475} Here, a more *delocalized* picture of the surface bonding is employed where the electron density at the surface is altered by the different surface stoichiometry as compared to the clean surface. Such a metal-to-molecule charge transfer is indicated by the observed (differential) peak

shifts towards lower binding energies in XPS, especially in the final (exposed) state (**ad e**) (see below for a more detailed discussion of the XPS results). The charge transfer leads to an accumulation of negative net charge above the surface which, in turn, creates a positive image charge in the topmost surface layer(s). A positive image charge will be better stabilized by a higher fraction of the more reactive Cu atoms at the surface. The more noble Au atoms are not as easily oxidized as Cu atoms [see also footnote b) in Chapter 1, page 3, of the present work].²⁰ Thus, a positive image charge in an “Au-enriched”, i.e., Cu-depleted, Cu₃Au(111) surface is energetically less favorable. Hence, an increasing metal-to-molecule charge transfer facilitates a re-enrichment of the surface layer in Cu atoms and vice versa. In this scenario, both effects go hand in hand in a synergistic manner. Indeed, the re-segregation of Cu towards the surface and the formation of the final state in XPS, which is interpreted as the proof for the metal-to-molecule charge transfer, occur on a similar time scale of about one or two hours, strongly supporting this second explanatory approach for the almost complete re-development of the ideal Cu₃Au(111) surface upon PTCDA adsorption.

Within the time span of our experiments, we did not observe a Cu-enrichment of the Cu₃Au(111) surface in the literal sense, that is, a surface fraction of Cu atoms exceeding the ideal value of 75 %. DFT calculations have indeed suggested a pure Cu termination of the Cu₃Au(111) sample for high coverages of adsorbed oxygen.⁴²⁸ This is explained with the larger oxygen affinity of Cu atoms in comparison to Au atoms.⁴²⁸ For the (110) and (100) surfaces of Cu₃Au, a pure Cu-termination of the O- and N-covered surfaces has been proven with impact collision ion scattering spectroscopy with neutral particle detection (NICISS), in particular.^{434,436,440,446} Again, the formation of O—Cu or N—Cu bonds, respectively, is thought to be the driving force.⁴³⁶ The existence of such local O—Cu bonds also in the present case of PTCDA/Cu₃Au(111) has already been ruled out (see above). Furthermore, the metal/molecule interaction is presumed to be rather moderate because the long-range surface reconstruction of the Cu₃Au(111) surface, which is known from the clean surface, persists (**ad a**). In contrast, the adsorption of perylene and FePc monolayers have been shown to alter the intrinsic reconstruction of the clean Au(111) surface.³⁶² This is caused by re-distributions of electronic charge, i.e., charge transfer across the interface, upon adsorption of the molecules on the surface which induces surface stress.^{362,476} This surface stress is relieved by altering the surface reconstruction.^{362,476} For PTCDA on Au(111), where the molecules are physisorbed,⁵⁹ a small change in the surface reconstruction is only observed after post-annealing of the PTCDA monolayer.¹¹⁴ SPA-LEED showed that the periodicity of the reconstruction then increased by 7(3)%.¹¹⁴ In the present case, a change in the periodicity of 291(10) Å was not observed at all upon PTCDA adsorption and subsequent post-annealing. Therefore, we conclude that the metal/molecule interaction is rather moderate in the case of PTCDA/Cu₃Au(111) (in particular in the initial state, considering also the determined adsorption heights). We cannot exclude, however, that small changes have been overlooked due to the huge periodicity of the reconstruction and also due to the fact that only the first-order reconstruction spots could be clearly discerned in LEED while higher-order spots were only identified as weak shoulders on the substrate spot profiles.

Surface relaxation

We now turn to the discussion of the relaxation of the Cu₃Au(111) surface (**ad c**). The PTCDA-covered surface has further relaxed outward by about 0.25 Å in comparison to the clean Cu₃Au(111) surface, that is, by almost 0.6 Å with respect to the ideal, bulk-determined position. This outward relaxation has experimentally been verified for the Cu₃Au(111) surface in the final state but is proposed to be already present in the initial state, too, as will be reasoned further below. The averaged outward relaxations of the Cu and Au atoms differ by only 0.03(8) Å. This differ-

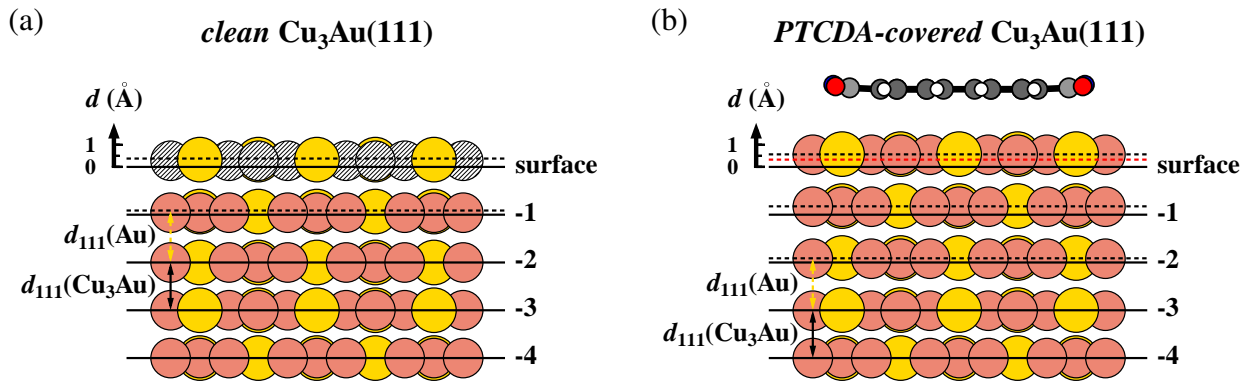


FIG. 6.32. Schematic representation of the outward relaxation of (a) the clean and (b) the PTCDA-covered Cu₃Au(111) surface. The Cu₃Au(111) substrate is shown in a side view along the $[11\bar{2}]$ direction. The cut through the crystal is made along the $[\bar{1}10]$ direction at the position of a densely packed row of alternating Cu and Au atoms. See Fig. 6.17 for an illustration of the crystallographic directions, for example. The (111) lattice planes of Cu₃Au and pure Au are indicated by solid and dashed lines with spacings $d_{111}(Z)$, respectively. The red dashed line in (b) marks the position of the Cu₃Au(111) surface layer without PTCDA. Cu atoms in the surface layer in (a) are drawn as hashed circles in order to indicate depletion. In (b), an ideal Cu₃Au(111) is assumed while the experimentally determined surface stoichiometry amounts to Cu_{0.69(4)}Au_{0.31(4)}. The PTCDA model (shown as a ball-and-stick model) is depicted in the final-state adsorption configuration (see Sec. 6.6.4) and, for reasons of better illustration, perfectly aligned with the $[\bar{1}10]$ direction (in contrast to the situation in the experimentally determined PTCDA structures from LEED and STM and in the corresponding structural models, respectively; see also Fig. 6.17). Note that the substrate atoms are depicted at only 70 % of their metallic radii r_m for reasons of clarity.¹⁴² The atoms within the PTCDA molecule are depicted at only 25 % of their vdW radii r_{vdW} .¹⁴¹

ence is not significant with regards to the error margins. Hence, a substantial surface buckling on a short length scale, i.e., for neighboring Cu and Au atoms, does apparently not occur, as opposed to the proposed surface buckling due to the long-range reconstruction. Similar to the relaxation of the clean Cu₃Au(111) surface, the relaxation of the PTCDA-covered surface can be modeled by assuming the (111) lattice plane spacing of pure Au, $d_{111}(\text{Au}) = 2.355 \text{ \AA}$,⁴⁵⁵ instead of the (111) lattice plane spacing of Cu₃Au, $d_{111}(\text{Cu}_3\text{Au}) = 2.165 \text{ \AA}$,³⁸⁸ to apply to the *three* outmost layers (see Fig. 6.32). The difference between the two lattice plane spacings amounts to $\Delta d_{111} = d_{111}(\text{Au}) - d_{111}(\text{Cu}_3\text{Au}) = 0.19 \text{ \AA}$ which is exactly one third of the observed outward relaxation of $0.55(1) \text{ \AA}$ and $0.58(8) \text{ \AA}$ of the Cu and Au atoms, respectively, in the topmost surface layer. All deeper-lying layers, that is, surface- n layers with $n \geq 3$ in Fig. 6.32, have been kept in place at the ideal positions as defined by the Cu₃Au (111) lattice planes. As has already been mentioned in the discussion of the relaxation of the clean Cu₃Au(111) surface (see Sec. 5.4), more sophisticated models may be constructed than simply relaxing the three outmost layers solely. For reasons of simplicity and due to the fact that no further structural information on the subsurface layers are available from our experiments, however, the development of a more complex model has been waived here.

As a consequence, we solely focus on the vertical positions of the atoms in the topmost surface layer here. Their further outward movement in comparison to the clean Cu₃Au(111) surface is remarkable. First of all, usual surface relaxations range from -10% to $+3\%$ of the ideal layer spacing approximately (see Ref. 422 for tabulated theoretical values and see the references therein for the experimental values). For instance, the clean Au(111) surface exhibits an expansion of the

layer spacing between the two topmost surface layers of 3.3(4) % according to x-ray scattering measurements (theoretical calculations have predicted a contraction of about 3 %, ⁴²² however).⁴⁵⁷ In the case of Cu₃Au(111), however, already the clean surface exhibited an outward relaxation of about 15 % (see Sec. 6.3.3) which is much larger than any so-far reported value to the best of our knowledge. This relaxation has been attributed to the Cu depletion of the surface layer which may diminish the interlayer interaction. Therefore, a reduced outward relaxation of the PTCDA-covered surface had been expected because it is re-enriched in Cu again, potentially re-enforcing the interlayer interactions.

It has already been concluded above that Cu atoms segregate to the surface in order to stabilize the positive image charge which originates from the (partial) charge transfer to the adsorbed PTCDA molecules. In turn, the Cu₃Au(111) surface layers may be (partially) depleted in electrons due to the metal-to-molecule charge transfer. Because less electrons may now be available for the interlayer bonding at the metal surface, the bonding between the outmost surface layers in Cu₃Au(111) surface may be reduced in strength, and the topmost surface layer relaxes further outward despite its increased Cu fraction. Hence, we conclude that the surface re-enrichment in Cu facilitates the charge transfer across the metal/molecule interface at the cost of the interlayer bonding at the Cu₃Au(111) surface.

Note at this point that the reported outward relaxation of the PTCDA-covered Cu₃Au(111) surface was observed in the final (exposed) state. Yet, the surface in the fresh state presumably exhibits a very similar or even identical relaxation. This is implied by the determined p_c values for the C and O components in PTCDA on the Cu₃Au(111) surface in the initial state. These p_c values can only be translated to chemically reasonable adsorption heights under the assumption that the outward relaxation is *instantly* present upon PTCDA adsorption. The nearly identical p_c values for the Cu atoms at the PTCDA-covered Cu₃Au(111) surface which were determined on fresh (i.e., previously unexposed) and on exposed spots further corroborate this conjecture. In the hypothetical case of an ideal, non-relaxed Cu₃Au(111) surface, adsorption heights of 3.75(1) Å [$d = (n + p_c) d_{hkl}$ with $n = 1$] or 1.59(1) Å ($n = 0$) are obtained for C_{peryl} in the initial state, for example. The former value is larger than the sum of the vdW radii of Au and C by 10 %, and the latter value is smaller than the respective sum of the covalent radii by 24 %, rendering both values chemically meaningless. Thus, we can conclude the initial (fresh) PTCDA-covered Cu₃Au(111) surface also to be relaxed outward.

PTCDA structures and surface bonding

The Cu₃Au(111) surface has been shown to behave rather Au-like with regards to the adsorption properties of PTCDA. This conclusion is supported by the TPD results as well as by the structural results from LEED and STM. The observed lateral structures of PTCDA on Cu₃Au(111) resemble those found for PTCDA on the pure Au(111) surface both qualitatively and quantitatively to a great extent (**ad d**) (see Sec. 6.6.1). Only the γ phase can be regarded as being Cu-analogous. This is counter-intuitive to the finding from XPS that 60–70 % of the surface atoms are Cu atoms and that the Au atoms are the minority species. Nonetheless, the Au atoms seem to govern the lateral structure formation. We attribute this to the larger size of the Au atoms in comparison to Cu (19 % larger vdW radius; see also Table 2.3) which prevent substantial Cu–PTCDA interactions due to steric hindrance/Pauli repulsion. Roughly speaking, the potential binding partners, Cu and PTCDA (or an individual atom of the ensemble of atoms within the PTCDA molecule), do not get close enough to each other simply in order to create a chemical bond, indicating moderate interfacial interactions again. Hence, the formed lateral structures must be largely determined by intermolecular interactions. More precisely, quadrupole interactions between the molecules as

well as hydrogen bond-like interactions between the partially negatively charged O atoms within the functional groups and the partially positively charged H atoms at the perylene core lead to the observed herringbone arrangement of the flat-lying PTCDA molecules which is also known from the bulk polymorphs.^{104, 107}

Hence, the metal/molecule interactions may be regarded as being rather moderate. Apparently, they do not outweigh the above-mentioned, intermolecular interactions. The substrate influence on the PTCDA structures mainly reflects in two findings. One finding is the defined orientation of the PTCDA unit cell with respect to the substrate directions which is described by the angle ϕ . All ϕ values which were observed for PTCDA/Cu₃Au(111) are essentially present for PTCDA on Au(111) and Cu(111), too ($\Delta\phi \leq 3.5^\circ$). The other finding is the denser packing of the PTCDA molecules on the Cu₃Au(111) surface than in the bulk phases by up to 5%. A plausible factor favoring the denser molecular packing is again a partial charge transfer to the molecules. The additional charge will preferentially accumulate at the electronegative O atoms in PTCDA, thereby increasing the quadrupole moment of the molecule and the tendency for the formation of hydrogen bonds. At first sight, this argument of charge transfer being responsible for the higher packing density conflicts with the finding that PTCDA on Cu(111) is less densely packed by about 6% than in the γ phase on Cu₃Au(111), which is considered as Cu-analogous, although the Cu(111) surface is thought to be more reactive and the metal-to-molecule charge transfer presumably is more pronounced (see also Sec. 2.2.2).⁶⁰ We speculate that the slightly larger lattice constants for PTCDA on Cu(111) may be due to the fact the increased lattice constants allow for a p-o-l commensurability on Cu(111) which is not the case on Cu₃Au(111).

Finally, we point out that the PTCDA structures on Cu₃Au(111) admittedly are very similar to those on the pure Au(111) and Cu(111) surface, but that the PTCDA molecules do *not* modify the surface in the sense that (nearly) pure patches of either Au or Cu atoms are formed at the Cu₃Au(111) surface. For instance, the enhanced order regarding the $p(2 \times 2)$ reconstruction of the Cu₃Au(111) surface upon PTCDA adsorption, as observed with SPA-LEED, contradicts the scenario of lateral segregation of (one of) the two metals. Instead, we assume that the analogies between the PTCDA structures on the pure surfaces, in particular on Au(111), and the Cu₃Au(111) alloy surface originate from *local* variations of the surface stoichiometry. The exact surface structure and composition at the nucleation site of a PTCDA domain, that is, at the initial stage of the island growth, may determine the structure of the entire domain, regardless of whether the local surface structure may be slightly different in other sites underneath the PTCDA island. The structure of the Cu₃Au(111) surface may vary locally to a small extent because the surface is still depleted in Cu atoms to a minor degree and the ideal surface composition is not fully restored upon the adsorption of PTCDA. Therefore, potential nucleation sites, such as step edges, kinks, or defects, may exhibit local Cu-enrichment or depletion which then selectively favors one PTCDA structure over the others at this site. This initial structure is then maintained during the island growth, in full agreement with our finding that large islands of all three HB phases are observed in LEED and STM for as-grown PTCDA/Cu₃Au(111) monolayers (see Sec. 6.6.1).

Metal-to-molecule charge transfer

We have employed the scenario of charge transfer from the metal to the molecule in the reasoning several times, for example, as being the driving force behind the Cu segregation to the surface layer and as an explanatory approach for the outward relaxation of the PTCDA-covered Cu₃Au(111) surface. However, we have not yet firmly justified the charge-transfer scenario. In particular, the conclusion of a gold-like Cu₃Au(111) surface concerning the adsorption properties implies that the surface bonding of the PTCDA molecules is purely physisorptive in nature. An essentially

physisorptive bonding has been concluded for PTCDA on Au(111) on the basis of XPS⁵⁹ and UPS data.⁶⁰ Yet, Duhm *et al.* have pointed out already that the comparably small decrease in the Au(111) work function of 0.40 eV induced by a monolayer of PTCDA, which is about a factor of two smaller than expected from the push-back effect (in the range of 1 eV for this surface^{477,478}), may indicate a small metal-to-molecule charge transfer and thus (very) weak chemisorption.⁶⁰

Unfortunately, UPS data for PTCDA/Cu₃Au(111), in particular, for the monolayer regime, is not available. Our XP spectra, however, point along the same lines (**ad e**) (see Sec. 6.6.2; the respective XP spectra are shown in Fig. 6.27 on page 140 of this chapter). Although the observed shifts for the individual C1s and O1s components towards lower binding energies in comparison to the multilayer may be explained by screening effects due to presence of the metal surface, this does not explain all shifts as a *collective*. We have found a *differential* shifting for the individual components which proves a—presumably weak—chemical interaction between the PTCDA molecules and the surface (see Table 6.7 on page 143 of this chapter for the explicit ΔE_b values). Pure physisorption would give rise to the same shift for all components, that is, to a rigid shift.

Charge transfer in the initial state

Regarding the initial state, the C_{peryl} and O_{carb} components experience the largest shifts in binding energy [$\Delta E_b(\text{C}_{\text{peryl}}) \approx -0.6$ eV and $\Delta E_b(\text{O}_{\text{carb}}) = -0.85$ eV; see also Tables 6.7 and 7.6]. These are those atoms which mainly contribute to the PTCDA LUMO (see Fig. 7.5 in Sec. 7.2, page 188, of the present work for a graphical representation). A (partial) filling of the PTCDA LUMO by electrons from the metal upon adsorption on the Cu₃Au(111) surface would lead to an enhanced electron density at the C_{peryl} and O_{carb} atoms, in particular, and thus to a reduced final state energy of the respective core levels upon photoemission. Hence, the XPS results indeed suggest a partial filling of the PTCDA LUMO, i.e., a small metal-to-molecule charge transfer. The above elucidations indicate that the PTCDA initial state on Cu₃Au(111), that is, the state when the surface is still depleted in Cu (termed fresh), is not solely physisorbed, but that there are weak chemisorptive aspects about the surface bonding. Yet, the bonding is still regarded as being essentially physisorptive because the differential effects in the peak shifting are small (about 0.1 eV to 0.4 eV for the O1s and C1s main components, respectively; see also Table 6.7).

Charge transfer in the final state

In the final (exposed) state, which occurs in a time-wise correlation with the re-enrichment of the surface layer in Cu atoms, all components shift further towards lower E_a , in agreement with the determined smaller adsorption height (**ad f**) (see also below). Again, the shifting is differential. On the one hand, the O_{carb} component exhibits the largest additional shift [$\Delta E_{b,\text{add}}(\text{O}_{\text{carb}}) = -0.24$ eV; see also Table 6.7]. This matches the above conclusion regarding the peak shifts for the initial state and indicates an *enhanced* charge transfer. Neglecting potential inhomogeneous line broadening due to the only partial transition from the initial to the final state, an enhanced metal/molecule interaction may also be deduced from the fact that all XP main components have broadened in comparison to the initial state by 7–17%. Due to closer proximity of the metal surface and due to the hence faster and more effective metal-to-molecule electron transfer upon photoexcitation, the life time of the photoexcited state is reduced with the result of a larger peak width.

The strongest evidence, however, for the metal-to-molecule charge transfer in the final (exposed) state is the presence of the C_{funct}^{*} component in the corresponding C1s XP spectrum. This component is interpreted as the photoemission signal of the C atoms within the functional groups of PTCDA in the final state. This peak exhibits a substantial shift in binding energy E_b of almost -1.2 eV in comparison to the corresponding peak (i.e., C_{funct}) in the multilayer spectrum (see also Table 6.7). Although the contribution of the C_{funct} valence orbitals to the PTCDA LUMO is com-

parably small, an enhanced valence electron density at these atoms supports the charge-transfer picture and thus the picture of a (partial) filling of the LUMO nonetheless. The reason is as follows. Upon filling of the LUMO, the C_{funct}=O_{carb} bond is weakened because the PTCDA LUMO is antibonding with respect to this bond. As a consequence, the double-bond character of the C_{funct}—O_{carb} bond is reduced. This, in turn, decreases the electron withdrawal from the C_{funct} by the more electronegative O_{carb} atoms due to the lower orbital overlap and the thereby “broken” orbital conjugation. Hence, the C_{funct} atoms gain valence electron density in comparison to the situation where the C_{funct}=O_{carb} double bond is intact, and the corresponding XPS peak shifts to lower E_b .

The lowering of the nominal bond order explains why the C_{funct}^{*} atoms show the largest of all the binding energy shifts (see also Chapter 7 for a general discussion including similar findings for PTCDA on Ag surfaces). The same trend has been observed for PTCDA on the (100) and (110) surfaces of Ag (see Sec. C.3.3 in the appendix of the present work). Besides, the PTCDA molecules show a substantial distortion on these surfaces (see Sec. C.3.4). Among others, one reason for the molecular distortion is the increased flexibility of the intramolecular bonds upon filling of the LUMO. Indeed, the overall distortion of the PTCDA molecule on the Cu₃Au(111) surface in the final state has also increased compared to the initial state (**ad f**) (see also below). Hence, the XPS and XSW results concerning the surface bonding mechanism are in qualitative agreement. We conclude so far that the bonding of the PTCDA molecule to the Cu₃Au(111) surface has gained a more chemisorptive character in the final state.

Furthermore, we emphasize again that there is, to a certain extent, a time-wise correlation between the Cu segregation towards the surface layer and the occurrence of the C_{funct}^{*} peak in XPS. The Cu segregation was observed after about 2 h of x-ray beam exposure, eventually, and the evolution of the C_{funct}^{*} within about 40 min. Unfortunately, the surface stoichiometry at $t = 40$ min is not known. We speculate, however, that the Cu segregation has already progressed substantially at this point in time, and that the actual stoichiometry is close to the final value of Cu_{0.69(4)}Au_{0.31(4)}. Therefore, we conclude that the segregation of the reactive Cu atoms towards the surface enhances the metal-to-molecule charge transfer, for example, due to a now lower work function of the substrate. As a result, the electrostatic interactions across the interface, that is, the (chemical) interactions between the partially negatively charged PTCDA molecules and the partially positively charged atoms within the Cu₃Au(111) surface layer(s), are enhanced and the adsorption height of the PTCDA molecules decreases. In a Newns-Anderson picture of the bonding mechanism (see Sec. 2.1.2), the decreased adsorption height in turn results in a stronger charge transfer again and thus also in a further increased driving force for the Cu atoms to segregate to the surface (see above). Thus, these three processes of (1) Cu (re-)segregation, (2) charge transfer, and (3) smaller adsorption height are considered to be self-reinforcing, i.e., *synergistic*, at this point. A detailed discussion of this (universal) phenomenon in terms of the Newns-Anderson model, i.e., the correlation between the molecular adsorption height, the charge transfer, and the work function of the (clean) sample, will be given in Sec. 7.3 and, to a small extent, also further below.

Adsorption configurations of PTCDA and relevant bonding channels

The adsorption configurations of PTCDA on Cu₃Au(111) in the initial and in the final state, respectively, allow to identify the relevant bonding channels. The determined adsorption heights d for the individual atoms within the PTCDA molecule in the initial and in the final state on Cu₃Au(111) are compiled in Table 6.11 and also compared to the respective known values for PTCDA on Au(111) and Cu(111). Figure 6.33 shows schematic representations of the adsorption configurations in these four cases.

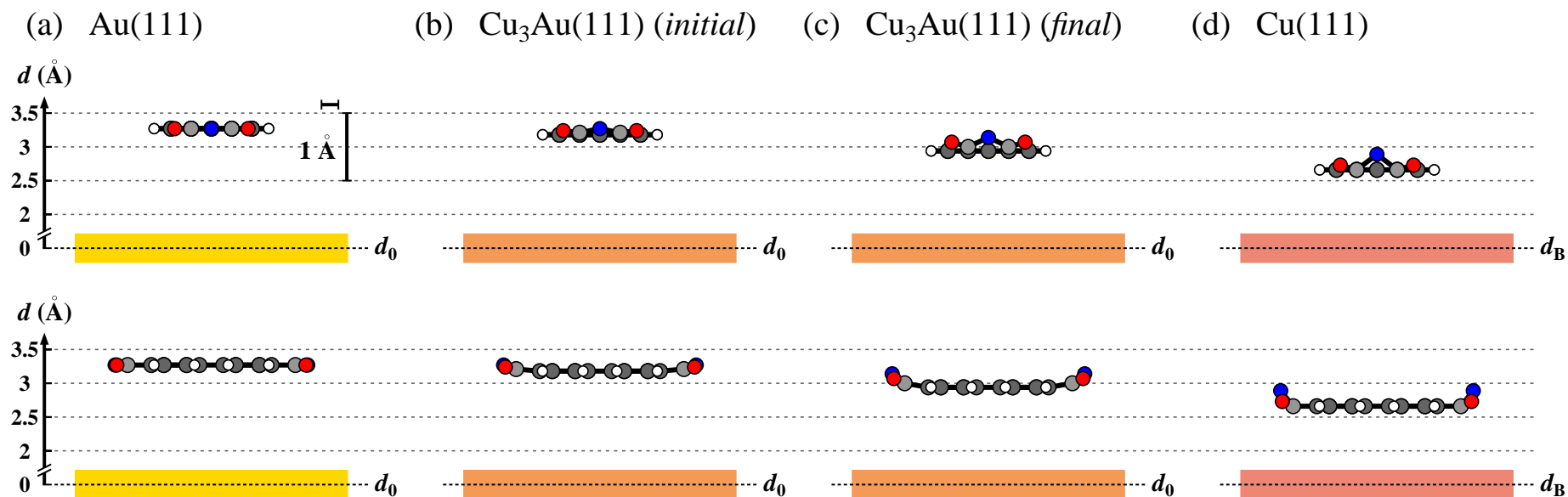


FIG. 6.33. Adsorption configurations of PTCDA on the (111) surfaces of (a) Au,⁵⁴ (b, c) Cu₃Au, and (d) Cu.⁴³ For PTCDA/Cu₃Au(111), the adsorption configurations (b) in the initial and (c) in the final state are depicted. The top row shows side views along the long molecular axis while the bottom row shows side views along the short molecular axis. H atoms are shown in white, C_{funct} and C_{peryl} atoms in light gray and dark gray, and O_{carb} and O_{anhyd} atoms in red and blue, respectively. The individual surfaces are depicted as colored regions. d denotes the vertical adsorption height; the vertical scale is enlarged by a factor of 4 and referenced against the Bragg plane (dashed line, d_B) or the (averaged) position of the relaxed surface (dashed line, d_0), respectively. Note that for PTCDA/Au(111) the O atoms are depicted at the same adsorption height as C_{funct} and C_{peryl} although their positions are not known for experimental reasons.⁵⁴ Note further that C_{funct} and C_{peryl} atoms could not be distinguished experimentally for PTCDA on Au(111) and Cu(111).^{43,54}

TABLE 6.11. Values for averaged vertical distances d of the carbon and oxygen atoms for PTCDA adsorbed on the Cu₃Au(111) surface in comparison to PTCDA adsorbed on the Au(111)⁵⁴ and Cu(111)⁴³ surfaces. $\Delta d = d_{\max} - d_{\min}$ is the absolute (overall) vertical distortion of the (intrinsically planar) PTCDA molecule, $\Delta d(\text{C}) = d(\text{C}_{\text{funct}}) - d(\text{C}_{\text{peryl}})$ is the vertical displacement of the C atoms, and $\Delta d(\text{O}) = d(\text{O}_{\text{anhyd}}) - d(\text{O}_{\text{carb}})$ is the vertical displacement of the O atoms, respectively. Note that for the determination of Δd only the main components have been taken into account while the C_{sat} component was disregarded due to its non-unambiguous character. For PTCDA/Au(111) the O positions were not measured for experimental reasons, and a differentiation of the C_{peryl} and C_{funct} atoms was not made.⁵⁴ In the case of PTCDA on Cu(111), C_{peryl} and C_{funct} were concluded to exhibit the same d values within the experimental resolution (n.d. = not determined).⁴³

	PTCDA			
	Au(111) (Ref. 54)	Cu ₃ Au(111) (<i>initial</i>) (this work)	Cu ₃ Au(111) (<i>final</i>) ^a (this work)	Cu(111) (Ref. 43)
$d(\text{C total})$ (Å)	3.27(2)	3.18(1)	2.95(5)	2.66(2)
$d(\text{C}_{\text{peryl}})$ (Å)	n.d.	3.18(1)	2.94(5)	n.d.
$d(\text{C}_{\text{funct}})$ (Å)	n.d.	3.21(2)	3.00(4)	n.d.
$d(\text{C}_{\text{sat}})$ (Å)	n.d.	3.17(5)	2.95(8)	n.d.
$d(\text{O total})$ (Å)	n.d.	3.25(4)	3.10(6)	2.81(3)
$d(\text{O}_{\text{carb}})$ (Å)	n.d.	3.24(4)	3.07(6)	2.73(6)
$d(\text{O}_{\text{anhyd}})$ (Å)	n.d.	3.27(4)	3.14(7)	2.89(6)
Δd (Å)	n.d.	0.09(4)	0.20(8)	0.23(6)
$\Delta d(\text{C})$ (Å)	n.d.	0.03(3)	0.06(6)	n.d.
$\Delta d(\text{O})$ (Å)	n.d.	0.03(6)	0.07(9)	0.16(8)

^aCalculated from the XSW results for PTCDA/Cu₃Au(111) on the fresh and exposed spots under the assumption that the contribution of the final state to the latter results amounts to 60 %.

In both the initial- and the final-state adsorption configuration, the PTCDA molecules exhibit a boat-like distortion, with the O atoms in PTCDA being further away from the surface than the C atoms (**ad f**). The determined adsorption configurations are in (qualitative) agreement with that of PTCDA on the Cu(111) surface.^{43, 99} While the overall distortion of the molecules is rather small in the initial state [$\Delta d = 0.09(4)$ Å], it more than doubles upon transition to the final state [$\Delta d = 0.20(8)$ Å]. Thus, it is close to the value of $\Delta d = 0.23(6)$ Å which has been determined for PTCDA/Cu(111) by Gerlach *et al.*⁴³

Besides, the d values for the C_{peryl} atoms, which are closest to the Cu₃Au(111) surface in both states, decreases from 93 % of the expected vdW distance in the initial state to 86 % in the final state. Only the Au atoms at the Cu₃Au(111) surface were considered here; the Cu atoms are smaller than the Au atoms and thus are not regarded as being the limiting factor for the (minimal) adsorption height, in contrast to the larger Au atoms (due to steric hindrance/Pauli repulsion; see

⁹⁹Note at this point that for PTCDA/Au(111) the O positions were not determined for experimental reasons.⁵⁴ Since the bonding of PTCDA to the Au(111) surface is considered as being physisorptive essentially,^{59, 60} and because the C backbone of PTCDA resides at an adsorption height of as much as 96 % of the expected vdW distance between the involved Au and C atoms,⁵⁴ the molecular distortion is expected to be marginal. Indeed, if the O atoms resided at the same d value as the C backbone [3.27(2) Å] this value would agree with the sum of the vdW radii of Au and O within 1 %, as is plausible for purely physisorptive interaction.

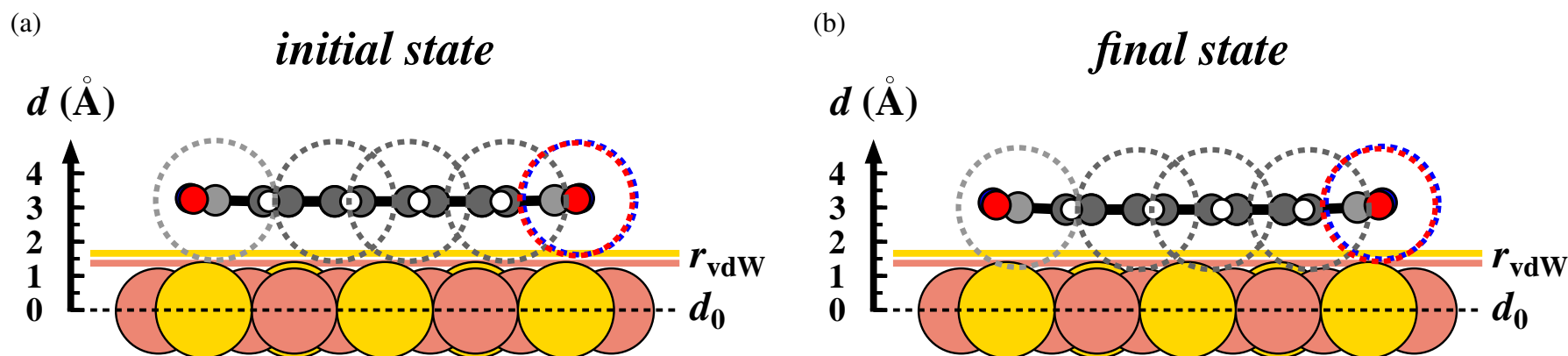


FIG. 6.34. Schematic representation of the PTCDA adsorption configurations (a) in the initial state and (b) in the final state on the $\text{Cu}_3\text{Au}(111)$ surface, including the vdW radii of the individual atoms. Atoms are depicted as filled circles. The $\text{Cu}_3\text{Au}(111)$ substrate is shown in a side view along the $[11\bar{2}]$ direction. The cut through the crystal is made along the $[\bar{1}10]$ direction at the position of a densely packed row of alternating Cu and Au atoms. See Fig. 6.17 for an illustration of the crystallographic directions, for example. H atoms are shown in white, C_{func} and C_{peryl} atoms in light gray and dark gray, and O_{carb} and O_{anhyd} atoms in red and blue, respectively. Van der Waals radii r_{vdW} are indicated by dashed circles in respective colors.¹⁴¹ The adsorption sites of the PTCDA molecules, including the azimuthal orientations, have been chosen arbitrarily (the PTCDA superstructures are incommensurate to the substrate surface). d_0 denotes the position of the relaxed PTCDA-covered $\text{Cu}_3\text{Au}(111)$ surface as judged from the (averaged) vertical shift of the Au atoms (black dashed line; see also Table 6.4). Solid lines in copper and gold indicate the vdW surfaces of $\text{Cu}_3\text{Au}(111)$ based on the vdW radii and the determined (averaged) vertical positions of the Cu and Au atoms, respectively.¹⁴¹ Note that the substrate atoms are depicted at 97.5 % of their metallic radius r_m reported in the literature¹⁴² only (see Table 2.3 in Sec. 2.2.2, page 16, of the present work for the explicit values) in order to avoid overlap of the spheres. The atoms within the PTCDA molecules (as filled circles) are depicted at 25 % of their vdW radii r_{vdW} (as given by the dashed circles) for reasons of clarity.¹⁴¹

also Sec. 6.6.4). A graphical illustration of the here-discussed, relative distances with respect to the sum of the vdW radii is given in Fig. 6.34 (respective values for PTCDA on various coinage metal surfaces are compiled in Table 7.2 in Sec. 7.1, page 186, of the present work). At the same time, the averaged adsorption height of the O atoms, taken to be equal to $d(\text{O total})$, only reduces from 98 % to 94 % of the sum of the vdW radii of Au and O. Hence, the relative adsorption height, that is, the determined adsorption heights with respect to the sums of the corresponding vdW radii of the involved atoms, of the O atoms in the final state is still larger than the relative adsorption height of the C_{peryl} atoms in the initial state.

Several conclusions for the bonding of PTCDA to the Cu₃Au(111) surface can be drawn from these findings:

- (1) In the initial state, the surface bonding is less purely physisorptive in character than in the case of PTCDA/Au(111), as is revealed by the relative adsorption heights (96 % versus 93 % of the sum of the vdW radii of Au and C, respectively). This is ascribed to the presence of Cu atoms in the surface layer. Yet, we still consider this bonding situation as being essentially physisorptive in nature, for example, due to comparably small differential shifts in XPS, and due to the still comparably large adsorption heights.
- (2) The PTCDA molecule mainly interacts via the perylene core with the Cu₃Au(111) surface as the adsorption configurations imply.
- (3) This bonding channel is the prevailing “chemical” bonding channel in both adsorption states. Of course, vdW interactions will still play the major role in the surface bonding here. This is concluded from the results for the bonding mechanism of PTCDA on the (more reactive) Ag surfaces where the dispersion effects constitute minimal 70 % to the total adsorption energy (see Sec. 7.6).
- (4) The relative contribution of the bonding channel located on the perylene core to the overall surface bonding is larger in the final state than in the initial state. Therefore, a (more) chemisorptive character of the surface bonding has evolved.
- (5) In conjunction with the XPS results (differential peak shifts towards lower E_b ; see above) and also having a Newns-Anderson-like picture of the bonding mechanism in mind, we propose a metal-to-molecule charge transfer which enhances with decreasing adsorption height. Thus, there is an electrostatic interaction between the (partially) negatively charged PTCDA molecules and the corresponding image charges within the metal surface. In accordance with the determined adsorption configurations, we may assume the (partial) negative charges to be located on the C_{peryl} atoms, in particular, which contribute strongest to the LUMO, that is, to the acceptor state, of the free PTCDA molecule (see Fig. 7.5).
- (6) The O atoms in PTCDA do not interact directly with the Cu₃Au(111) surface, in contrast to atomic O which, according to DFT predictions, even induces a complete segregation of Cu, that is, an exclusive accumulation of Cu, at the topmost surface layer.^{427,428} The bending of the O atoms away from the surface (with respect to the C backbone) contradicts the potential formation of local O—Cu (and also of O—Au) bonds.
- (7) Although the O atoms do not interact directly with the surface, their adsorption heights are lower in the final state than in the initial state. This can be explained such that, on the one hand, the O atoms follow the downward movement of the C backbone in PTCDA upon transition to the final state. On the other hand, their downward movement is smaller than that of the C atoms, thereby enhancing the distortion of the molecule, because they suffer from

Pauli repulsion due to decreased d values which is not compensated for by attractive chemical interactions as in the case of the C_{peryl} atoms.

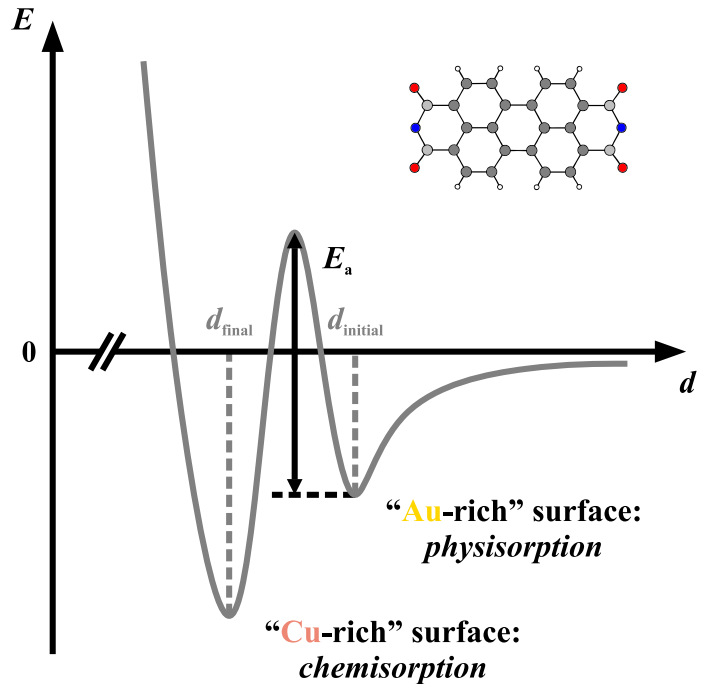
- (8) Nonetheless, the O atoms and the functional groups as a whole, respectively, may be assumed to facilitate the metal-to-molecule charge transfer by enhancing the electron acceptor strength of the PTCDA molecule in comparison to perylene, for example ($E_A = 4.1$ eV for PTCDA¹⁰² in a condensed film versus $E_A = 2.5$ eV for perylene⁴⁷⁹), due to their electron-withdrawing effect.³⁰

It has already been stated that the adsorption configurations of PTCDA on Cu₃Au(111) and on pure Cu(111) are very similar, in particular, in the final state. This is not only true concerning the overall distortion of the PTCDA molecule upon adsorption [$\Delta d = 0.20(8)$ Å versus $\Delta d = 0.23(6)$ Å, see above], but also concerning the relative adsorption heights. The absolute d values for the C and O atoms in Table 6.11 may differ by about 0.3 Å for PTCDA in the final state on Cu₃Au(111) and for PTCDA on Cu(111), but the different sizes of the (larger) Au and (smaller) Cu atoms ($\Delta r_{\text{vdW}} = -0.26$ Å, see Table 2.3) have to be considered, too. Assuming that only the vdW radius of the Au atoms and not that of the Cu atoms determines the “contact distance” for physisorbed PTCDA molecules on the Cu₃Au(111) surface, as has been done throughout this chapter, the difference in r_{vdW} for Au and Cu has to be taken into account in order to make the respective d values in Table 6.11 directly comparable. Because the differences in d for both systems and in r_{vdW} for the two elements, Au and Cu, are of almost identical magnitude, subtracting Δr_{vdW} out yields an agreement of the so-processed d values for PTCDA/Cu₃Au(111) (final state) and PTCDA/Cu(111) within 0.08 Å in the worst case, that is, for the O_{carb} atoms. In the case of the C_{peryl} atoms, the processed d values are indeed identical within the error margins or, more precisely, within 0.02 Å. This can also be seen from the relative adsorption heights (of the perylene core or the C backbone, respectively) which are nearly identical, i.e., 86 % of the expected vdW distance for PTCDA/Cu₃Au(111) and 84 % for PTCDA/Cu(111) [see also Fig. 6.34(b) and Table 7.2].⁴³ In conclusion, the bonding situation in the final state for PTCDA on the Cu₃Au(111) surface can be regarded as being Cu(111)-analogous. The bonding situation in the initial state, however, is rather Au(111)-analogous by tendency [relative adsorption heights of 93 % on Cu₃Au(111) versus 96 % on Au(111); see also conclusion 1 of the above list].

Figure 6.35 schematically depicts the bonding situation, i.e., the potential energy curve, for PTCDA on Cu₃Au(111) on the basis of our experimental results. In the initial state, that is, for a larger d value, the PTCDA molecules are essentially physisorbed. The surface layer is depleted in Cu atoms and thus “Au-rich” in comparison to the ideal Cu₃Au(111) surface. The molecules are in a “precursor state”,⁴⁷¹ and the metal-to-molecule charge transfer—which we postulate as the prevalent “chemical” bonding channel—has either not yet established or has only occurred to a minor degree. Upon excitation, the molecules overcome the potential barrier, i.e., the activation energy E_a , to the final state with smaller d . This transition can surely be initialized by an intense x-ray beam, as our experiments have proven. We speculate, however, that also thermal activation and an electron beam may be able to trigger the transition (see above). In the final state, the PTCDA molecules are chemisorbed. The surface is re-enriched in Cu atoms,^{††)} and a (partial) charge transfer from the metal to the molecules occurs. The charge transfer gives rise to an attractive electrostatic interaction between the two. Thus, (delocalized) chemical bonds are formed, justifying the above appraisal of a chemisorptive character of the surface bonding of PTCDA on Cu₃Au(111).

^{††)}The re-segregation of Cu atoms towards the surface layer contributes to the potential barrier between the initial and the final state, of course.

FIG. 6.35. Schematic representation of the potential energy E as a function of the adsorption height d for PTCDA, in particular, for the C_{peryl} atoms, on the Cu₃Au(111) surface (not to scale). Realized values for $d(\text{C}_{\text{peryl}})$ in the initial and the final state are marked by dashed lines. E_a denotes the activation energy for the transition from the initial, physisorbed state (“precursor”) to the final, chemisorbed state. Note that this potential barrier also includes the diffusion (i.e., the re-segregation) of Cu atoms towards the surface layer. A ball-and-stick model of the PTCDA molecule is shown as an inset.



Hammer-Nørskov model

In a gross simplification, the bonding situation turns from Au-like in the initial state to Cu-like in the final state. This may also be understood in the framework of the Hammer-Nørskov model which correlates the strength of a chemisorptive bond for an adsorbate on a transition metal surface with both the center of the d -band, ϵ_d , and the coupling matrix element V_{ad} , i.e., the overlap, between the metal d -band states and an adsorbate orbital (see also Sec. 2.1.4).^{15,82,93,94} In particular, we will consider the frontier orbitals, namely, the HOMO and the LUMO of PTCDA, as the relevant adsorbate orbitals here. As will be elucidated in the following, an energy gain is only to be expected from the interaction of the PTCDA LUMO with the d states in Cu₃Au(111).

Considering a filled adsorbate level, i.e., the PTCDA HOMO in the present case, Eq. (2.2)—which is reproduced here for reasons of clarity (see Sec. 2.1.4, page 10, of the present work for details)—describes the total hybridization energy $E_{d\text{-hyb}}$ as the sum of the (potential) energy gain due to the filling of hybrid states (first term on the right-hand side) and the energy cost due to Pauli repulsion (via V_{ad} ; second term on the right-hand side) within the framework of the Hammer-Nørskov model:^{15,94,95}

$$E_{d\text{-hyb}} = -2(1 - f_d) \frac{V_{ad}^2}{|\epsilon_d - \epsilon_a|} + 2(1 + f_d) \alpha V_{ad}^2. \quad (6.3)$$

Although the ϵ_d value is about 0.9 eV higher for Cu than for Au,⁸² the higher ϵ_d of a “Cu-rich” Cu₃Au(111) surface in comparison to a “Au-rich” surface^{ss)} does *not* lead to an energy gain here

^{ss)}It is known from theory that (surface) alloying or the presence of metal overlayers, where a monolayer of one metal is deposited on top of another metal, can lead to a shift in ϵ_d of the bulk material.^{82,96,480} As a rule of thumb, the deposition of lower Z elements onto higher Z elements for the late transition metals shifts ϵ_d upward in energy and thus leads to a stronger bonding across the metal/organic interface.^{82,96} For example, model calculations at DFT-LDA level and DFT-GGA level for CO adsorption on the Cu₃Pt(111) surface have been reported by Ruban *et al.*⁹⁶ and Mavrikakis *et al.*,⁴⁸¹ respectively. The adsorption energy E_{ads} was calculated for both CO adsorption on top of an Cu atom and on top of an Pt atom at the Cu₃Pt(111) surface. E_{ads} for CO on Cu:Cu₃Pt(111) is approximately 0.1 eV lower (in absolute terms) than that on the pure Cu(111) surface (≈ -0.5 eV versus ≈ -0.6 eV).⁴⁸¹ E_{ads} for CO on

because for coinage metals the d states are completely filled, i.e., $f_d = 1$. Therefore, the first term on the right-hand side of the above equation drops out, and only the second term accounting for the Pauli repulsion remains, resulting in an overall energy cost ($E_{d\text{-hyb}} > 0$). Since V_{ad} is by a factor of 3.35 larger for Au than for Cu,^{82,96} stronger Pauli repulsion and thus a larger adsorption height is expected for PTCDA on an Au-like initial-state than on a Cu-like final-state Cu₃Au(111) surface, validating our above statement.

If an empty (or not completely filled) adsorbate level is considered, such as the PTCDA LUMO, Eq. (2.3) as a more general expression applies (reproduced here from Sec. 2.1.4, page 10):^{15,96}

$$E_{d\text{-hyb}} = -C(f_a, f_d) \frac{V_{ad}^2}{|\epsilon_d - \epsilon_a|} + \alpha V_{ad}^2. \quad (6.4)$$

The first term on the right-hand side does not drop out here because $f_a < 1$. Thus, there is also a negative contribution to the total hybridization energy $E_{d\text{-hyb}}$ which leads to an *attractive* interaction between the adsorbate and the metal surface. If we assume the metal d states to participate in the surface bonding of PTCDA on Cu₃Au(111), as the Hammer-Nørskov model implies, a stronger bonding and hence also a decreased adsorption height is expected from the PTCDA LUMO/metal d -states interaction for a more Cu-like final-state Cu₃Au(111) surface (due to the higher-lying center of the d -band), in good agreement with our experimental findings concerning the adsorption heights $d(C_{\text{peryl}})$ in the initial and the final state, respectively. The crossover from the more Au-like to the more Cu-like surface originates from the re-segregation of Cu atoms towards the initially Cu-depleted Cu₃Au(111) surface. In conclusion, the Hammer-Nørskov model allows to explain the bonding situation of PTCDA on Cu₃Au(111) via the d -band interaction in a qualitative manner.

Newns-Anderson model and metal-state contributions to the surface bonding

The same holds for the Newns-Anderson model.^{11,81} In the context of the metal-to-molecule charge transfer discussed above, we have already stressed the correlation between the re-segregation of the more reactive Cu atoms (in comparison to Au atoms) on the one hand and the smaller adsorption heights, being indicative of an enhanced charge transfer, on the other hand. On the basis of these findings, and as is necessary for successfully applying the Newns-Anderson model to both the initial and the final state of PTCDA/Cu₃Au(111), we have already proposed a lowering of the work function Φ of Cu₃Au(111) upon transition from the initial to the final state as a consequence of the increased Cu fraction at the surface (see also Sec. 7.3). At this point of the discussion, we primarily focus on the metal states which may be involved in the surface bonding of PTCDA on Cu₃Au(111).

The Newns-Anderson model considers the contribution from both the metal sp states and the metal d states to the surface bonding. The Hammer-Nørskov model, in contrast, emphasizes the contribution of the metal d states. Hence, we conclude at this point that *a priori* metal sp states as well as metal d states may participate in the surface bonding. Yet, the Newns-Anderson scenario of *weak* chemisorption (as opposed to *strong* chemisorption, see Sec. 2.1.2) and thus sp -band interaction appears more plausible here because the determined adsorption heights are still ≥ 0.9 Å above the sum of the covalent radii of the involved elements. Furthermore, in accordance with the Hoffmann model (see Sec. 2.1.3), an interaction of the low-lying d -band of Cu₃Au(111), which is found more at about 2 eV to 4.5 eV below the Fermi level E_F [to be also compared to the theoretical ϵ_d values for the pure elements, $\epsilon_d(\text{Cu}) = -2.67$ eV and $\epsilon_d(\text{Au}) = -3.56$ eV,^{82,96} respectively],³⁹⁵

Pt:Cu₃Pt(111), however, is approximately 1.0 eV higher (in absolute terms) than on Cu:Cu₃Pt(111).⁴⁸¹ Also, it is approximately 0.1 eV higher (in absolute terms) than for CO adsorption on the pure Pt(111) surface (≈ -1.5 eV versus ≈ -1.4 eV).⁴⁸¹ The adsorption energy of CO on Cu/Pt(111) amounts to ≈ -1.0 eV.⁴⁸¹

with the much higher-lying PTCDA LUMO, for example, is energetically not favored very much. Therefore, a predominant interaction of the PTCDA frontier orbitals with the metal *sp* states is concluded here. UPS measurement as well as theoretical investigations are desirable in order to further clarify this point.

Note that two Shockley-like surface states at -1.0 eV and -0.4 eV (with respect to E_F) have been proven to exist for the clean Cu₃Au(111) surface with ARUPS.^{395,482} The state at -0.4 eV is also observed at the pure Cu(111) surface.³⁹⁵ It has been shown by means of 2PPE—taking the examples of PTCDA/Ag(111) and NTCDA/Ag(111)^{135,275}—that a Shockley state may substantially shift (about 450 meV to 650 meV upwards in energy, that is, above E_F in the referred cases) upon adsorption of organic molecules. The pure Au(111) surface exhibits a surface state, too, as has been shown by ARUPS.^{483,484} Upon PTCDA adsorption (physisorption), however, the Au(111) surface state was observed to shift only marginally upwards in energy by about 40 meV, which was at the detection limit of the respective STS experiment.¹²⁵ Since the shift of the Shockley-like surface state is strongly dependent on the distance of the adsorbate molecules from the metal surface (as well as on their surface density),¹³⁵ it can be regarded as a measure for the adsorption height, and thus also for the character and the strength of the metal/molecule interaction. Hence, we expect shifts of the surface states for PTCDA adsorption on Cu₃Au(111) and also on Cu(111), as well. Furthermore, we speculate that the shift will be more pronounced for PTCDA in the final state on the Cu₃Au(111) surface than in the initial state, where the adsorption heights are larger. As an outlook, it would be more than interesting to compare the respective shifts of the surface states in order to further validate our conclusions about the analogies in the bonding situations of PTCDA on the Cu₃Au(111) alloy surface with those on the pure coinage metal surfaces.

Transition from the initial to the final state

We now return to the discussion on the transition from the initial to the final state for PTCDA/Cu₃Au(111) once gain. Remarkably, not *all* PTCDA molecules on the surface transition into the final state within the time span of our experiments (about 2 h). This has been concluded from the XP spectra because contributions from the initial state may still be identified. They amount to 40 % in the case of the C1s XP spectrum. An incomplete transition from the initial to the final state is also indicated by the fact that the coherent fractions f_c which were determined for the C atoms in the exposed spots are about 20–25 % smaller than those for the fresh spots. This may be because the results for the exposed spots represent a mixture of the adsorption configurations in the initial and in the final state, respectively. Admittedly, we did not observe significantly altered f_c values for the O atoms in the exposed spots, in contradiction to the expectations for a mixture of two different adsorption configurations; yet, the decrease in d is about 35 % smaller for the O atoms than for the C atoms when comparing the final and the initial state. The (smaller) lowering of the f_c values from the fresh spots to the exposed spots may have been overlooked for the O atoms due to the comparably large uncertainties in f_c of about 0.1, in particular, for the fresh spots. However, the presence of the additional components in the C1s XP spectrum and the XSW data for the exposed spots strongly support the conclusion of an incomplete transition to the final state. We can only speculate on the origin of this incomplete transition here. Maybe, local effects, such as the individual adsorption site of a PTCDA molecule—the PTCDA overlay is not in commensurate registry with the substrate surface—, favor the one bonding state over the other site-dependently, for example due to potential π interactions between C_{peryl}=C_{peryl} double bonds and a surface atom M, or due to the potential formation of local C_{peryl}–M or C_{funct}–M bonds, where M is either a Au atom or, more likely, a Cu atom. Local π interactions have been shown to exist for PTCDA on the Ag(100) and Ag(110) surfaces (see Sec. 7.6). In those adsorption sites

where such interaction cannot occur due to geometric reasons, that is, due to the (relative) positions of the potential binding partners at the interface, the adsorbed PTCDA molecule will remain in the “precursor” state.

The same argumentation may apply to the finding that the f_c values for the C atoms in the final state are again smaller by about 10 % in comparison to the already-decreased f_c values for the exposed spots, and even about 30 % smaller than in the initial state. The occurrence of local π interactions or the formation of local C—M bonds (with M = Cu, Au) are more likely in the final state than in the initial state because of the closer proximity of the binding partners. If such interactions occurred *locally* at the metal/organic interface, the individual PTCDA molecule would be distorted more strongly which then would result in smaller f_c values. Considering the perylene core of PTCDA, i.e., the C_{peryl} atoms, an increase of $\Delta d \approx \pm 0.25 \text{ \AA}$ in their vertical displacement relative to the average $d(\text{C}_{\text{peryl}})$ value is estimated from the reduction in the f_c values when comparing the initial with the final state (see also Table 6.8). This rough estimation employs a simple scenario of only two distinct values of d being equally adopted by the C_{peryl} atoms. Although the absolute Δd value appears too large in comparison to the determined—and thus averaged—overall distortion of the PTCDA molecule, the reasoning of selective and local C—M interactions agrees by tendency with the finding of reduced f_c values in the final state. Again, a potential reduction of the f_c values for the O atoms may have been overlooked (see above). However, $f_c(\text{O})$ may not depend on the bonding state as strongly as $f_c(\text{C})$ because O—M interactions apparently do not occur in any of the two cases, judging from the respective adsorption configurations.

An alternative explanatory approach concerning the reduced f_c values in the final state involves the rigidity of the PTCDA overlayer in conjunction with the postulated buckling of the Cu₃Au(111) surface (**ad c**) which may still be present also upon PTCDA adsorption. One could imagine that the PTCDA layer in the initial state is *rigid* in the sense that it does not follow the (long-range) buckling of the surface due to the rather weak surface bonding. Thus, the corresponding f_c values are comparably high. The PTCDA layer in the final state, however, may follow the surface buckling due to the enhanced surface bonding, with the consequence of lower f_c values due to the decreased vertical order. Hence, the PTCDA layer has to be envisaged as being *buckled*, too, in this scenario due to a “template effect” by the buckled Cu₃Au(111) surface. The similar vertical displacements of $\Delta d \approx \pm 0.25 \text{ \AA}$ for the C_{peryl} atoms (see above) and $\pm 0.16 \text{ \AA}$ to $\pm 0.22 \text{ \AA}$ for the surface atoms (at the clean surface; see Sec. 6.3.3) support this reasoning. However, the f_c values for the O atoms—as opposed to those of the C atoms—are not reduced in the final state, contradicting this explanatory approach (contrary to the scenario above) because the vertical positions of the O atoms in PTCDA should essentially be determined by those of the C backbone and thus also follow the surface buckling. At this point, we cannot ultimately clarify this issue. Yet, the first explanatory approach of selective and local C—M interactions appears more consistent with the experimental findings, such as the re-segregation of Cu atoms towards the Cu₃Au(111) surface layer upon PTCDA adsorption and the incomplete transition from the initial to the final state. Besides, a stronger distortion of the C backbone in PTCDA upon an increased chemisorptive character of the surface bonding in the final state for PTCDA on the Cu₃Au(111) surface agrees well with chemical intuition.

7

Overview on the experimental results and general discussion

In this chapter, we will discuss the observed spectroscopic features and the determined adsorption configurations for PTCDA on the different coinage metal surfaces at large. Special emphasis will be put on the identification of relevant bonding channels for the surface bonding in the individual cases, as well as on the interplay of the respective bonding channels. We will present a general bonding mechanism of broad validity for PTCDA on the coinage metal surfaces, involving all plausible bonding channels, and discuss the requirements for the potential bonding channels to be present in the surface bonding at the individual surfaces.

This chapter is organized as follows: Sec. 7.1 gives an overview over the experimental results for PTCDA in the (sub-)monolayer regime on coinage metal surfaces. The theoretical methods behind our DFT calculations are outlined in Sec. 7.2. The respective DFT results are presented and discussed throughout this chapter in appropriate positions. The discussion of the individual bonding channels relevant to the surface bonding of PTCDA is partitioned into several sections. The surface bonding via the perylene core is treated in Sec. 7.3, while the bonding via the functional groups is treated in Sec. 7.5. In the context of the surface bonding via the perylene core, the relevance of metal-to-molecule charge transfer is emphasized, and the actual occurrence of this charge transfer (to a varying extent, depending on the substrate surface) is evidenced in Sec. 7.4. The interplay of the individual bonding channels is examined in Sec. 7.6. Section 7.7 discusses how this interplay can be experimentally probed and manipulated. This chapter finishes with the final general conclusions concerning the bonding mechanism for PTCDA adsorption on coinage metal surfaces in Sec. 7.8 and an outlook in Sec. 7.9.

7.1 PTCDA on coinage metal surfaces: a review of the lateral structures and adsorption configurations

We will only deal with (sub-)monolayer properties of PTCDA on coinage metal surfaces in the following. Multilayer properties will not be addressed. Concerning the (111) surfaces of Cu, Au and Cu₃Au, the lateral structures and adsorption configurations have been widely presented in Chapters 5 and 6 of the present work. An additional review of the experimental results reported in the literature for PTCDA monolayers on Cu(111), Au(111) and also on Ag(111) has been given in Sec. 2.2.2. At this point, we will mainly focus on PTCDA on the (100) and (110) surfaces of Ag, in conjunction with PTCDA on Ag(111), for reasons of consistency in the later presentation of the arguments. Our results on the adsorption configurations of PTCDA on Ag(100) and Ag(110), also upon coadsorption of K atoms in the latter case, have largely been published in Refs. 66, 67,

and 68 already. Therefore, the explicit description and discussion of our results on these system in dedicated chapters has been waived here. For reasons of completeness, however, our experimental data are compiled and presented in brief in Appendix C for PTCDA/Ag(100) and PTCDA/Ag(110), and in Appendix D for K + PTCDA/Ag(110).

Lateral structures and adsorption sites

The aim of the present work is to unveil the relevant bonding channels for surface bonding of PTCDA on coinage metal surfaces. For this purpose, as will be shown in detail below, the adsorption sites of PTCDA on the individual coinage metal surfaces have to be considered in order to identify potential *local* interactions. Of course, the adsorption sites are determined by the lateral arrangement of the molecules on the respective surface. On Au(111),^{114,116} Cu₃Au(111) (see Sec. 6.5.1), and Cu(111) (see Sec. 5.3.1), incommensurate superstructures have been found. Therefore, there is no defined registry between the surface atoms and the adsorbed molecules. Hence, potential local interactions with surface atoms are not possible in an identical manner for all PTCDA molecules. Note, however, that Wagner *et al.* have indeed proposed a commensurate structure for PTCDA/Cu(111), in contrast to our findings.¹¹⁵ In that proposed structure [see Fig. 5.1(a), structure ‘1’, in Sec. 5.1, page 69, of the present work for an illustration] the molecules adsorb with their centers in on-top positions. Due to the specific azimuthal orientations of the molecules, equivalent adsorption sites are found neither for the C atoms nor for the O atoms in PTCDA. Thus, the above statement of non-equivalent local interactions, if present, remains valid.

On the low-index Ag surfaces, that is, on Ag(111) [in the ordered room temperature (RT) phase],⁹⁸ Ag(100),¹²⁰ and Ag(110),⁹⁸ however, PTCDA forms commensurate superstructures as depicted in Figs. 7.1(a–c). On Ag(111), both molecules of the unit cell adsorb in bridge positions, but at different angles with respect to the close-packed $\langle 110 \rangle$ substrate directions.¹²⁴ One molecule (A) is (nearly) aligned with the substrate, i.e., within 2°, with the O_{carb} atoms being on-top and the O_{anhyd} as well as the C_{funct} atoms being in bridge sites. The second molecule (B) is rotated by 17° versus $\langle 110 \rangle$ and has all atoms within its functional groups roughly in bridge positions [see Fig. 7.1(a)]. Note that molecules A and B could not be distinguished in the XPS and XSW experiments. Thus, average values, for example, concerning the adsorption heights d , are considered in the following. For PTCDA/Ag(100), the adsorption site has been determined in the framework of the present work (see Sec. C.4 in the appendix of the present work). We have found that the center of the molecule is located on-top of a Ag surface atom. Furthermore, both O_{carb} and O_{anhyd} atoms reside above a Ag atom, while the C_{funct} atoms sit close to bridge sites [see Fig. 7.1(b)]. On Ag(110), the molecule adsorbs with its center on a bridge position above a groove.⁴⁸⁵ As a consequence, the O_{carb} and O_{anhyd} atoms sit close to on-top positions, while the C_{funct} atoms occupy off-short-bridge positions, i.e., positions close to short-bridge positions [see Fig. 7.1(c)]. Hence, we make the remarkable observation here that the O atoms in PTCDA occupy positions (close to) on top of Ag surface atoms in most cases.

Upon coadsorption of K atoms in addition to PTCDA on the Ag(110) surface and thermal treatment (see Appendix D of the present work and also Refs. 68, 326), the metal/organic interface undergoes a substantial rearrangement. The K atoms are incorporated in the Ag surface, and a (1 × 3) surface reconstruction is induced.²⁸² This reconstruction, however, only extends over one or two periodic units in the [001] direction (see Fig. 7.2 for a structural model). Then, a step edge occurs and the (1 × 3) surface reconstruction re-starts on the next terrace. We will refer to this K-modified Ag(110) surface as K:Ag(110) in the following. Consequently, we will prefer to use the term “PTCDA/K:Ag(110)” rather than “K + PTCDA/Ag(110)” for the system described in the following where K and PTCDA have been coadsorbed on the Ag(110) surface and subsequent

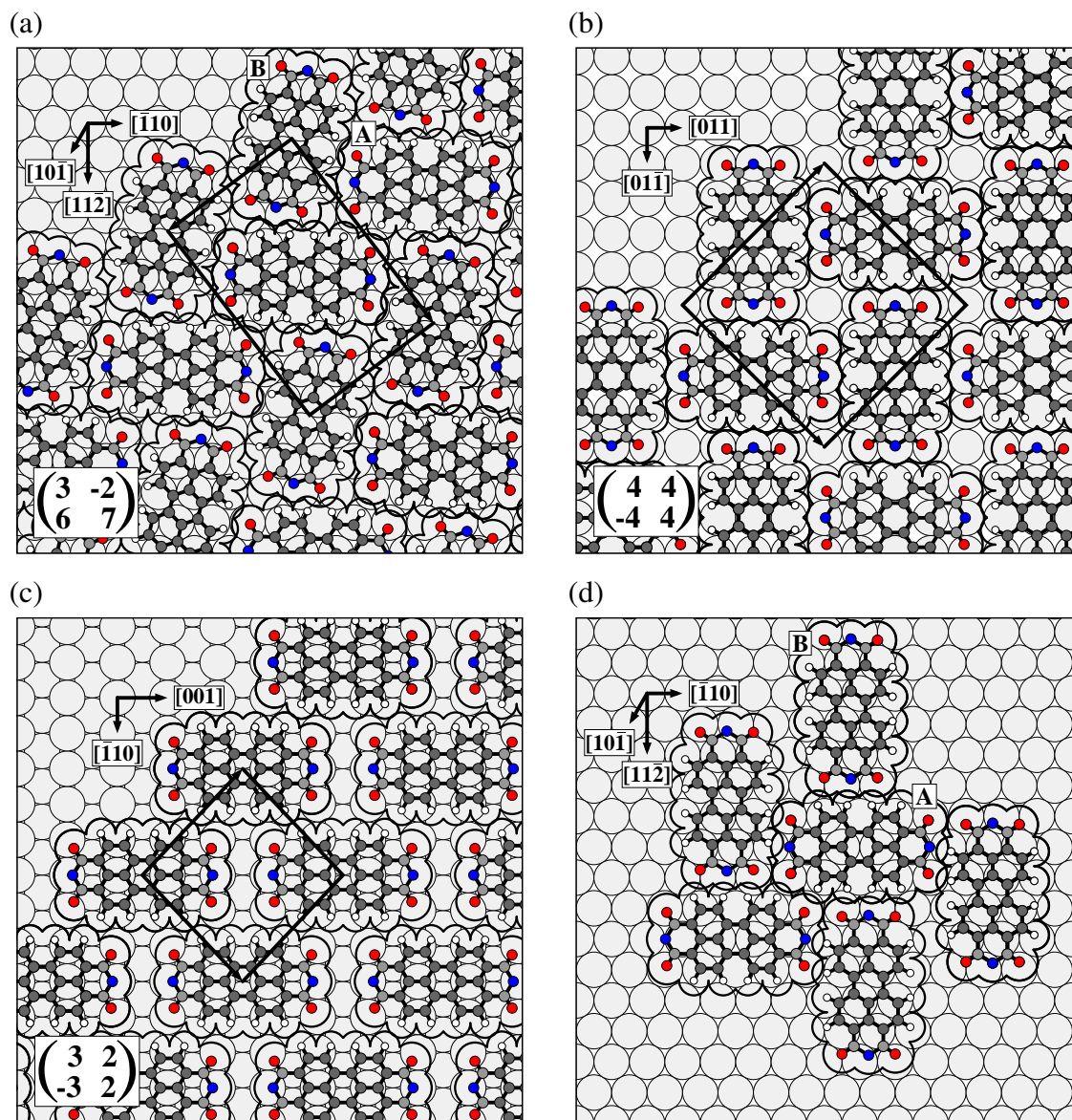


FIG. 7.1. Structural models for PTCDA in the monolayer regime on the (a) (111),⁹⁸ (b) (100),¹²⁰ and (c) (110) surfaces of Ag.⁹⁸ The molecules exhibit a herringbone arrangement on Ag(111), a T-shape arrangement on Ag(100), and a brick-wall arrangement on Ag(110). The PTCDA molecules are shown as ball-and-stick models, including a two-dimensional projection of the molecular vdW surface. Solid lines indicate the respective unit cells. The substrate directions are also indicated. The superstructure matrices are given as insets. Note that for (a) PTCDA/Ag(111) two non-equivalent adsorption sites are realized by the PTCDA molecules. Molecules A are aligned with the close-packed $\langle 110 \rangle$ substrate directions within 2° while molecules B are rotated by 17° with respect to the $\langle 110 \rangle$ substrate directions.¹²⁴ In addition, a potential, idealized arrangement of six PTCDA molecules in the LT phase on Ag(111) is shown in (d).¹⁴⁰

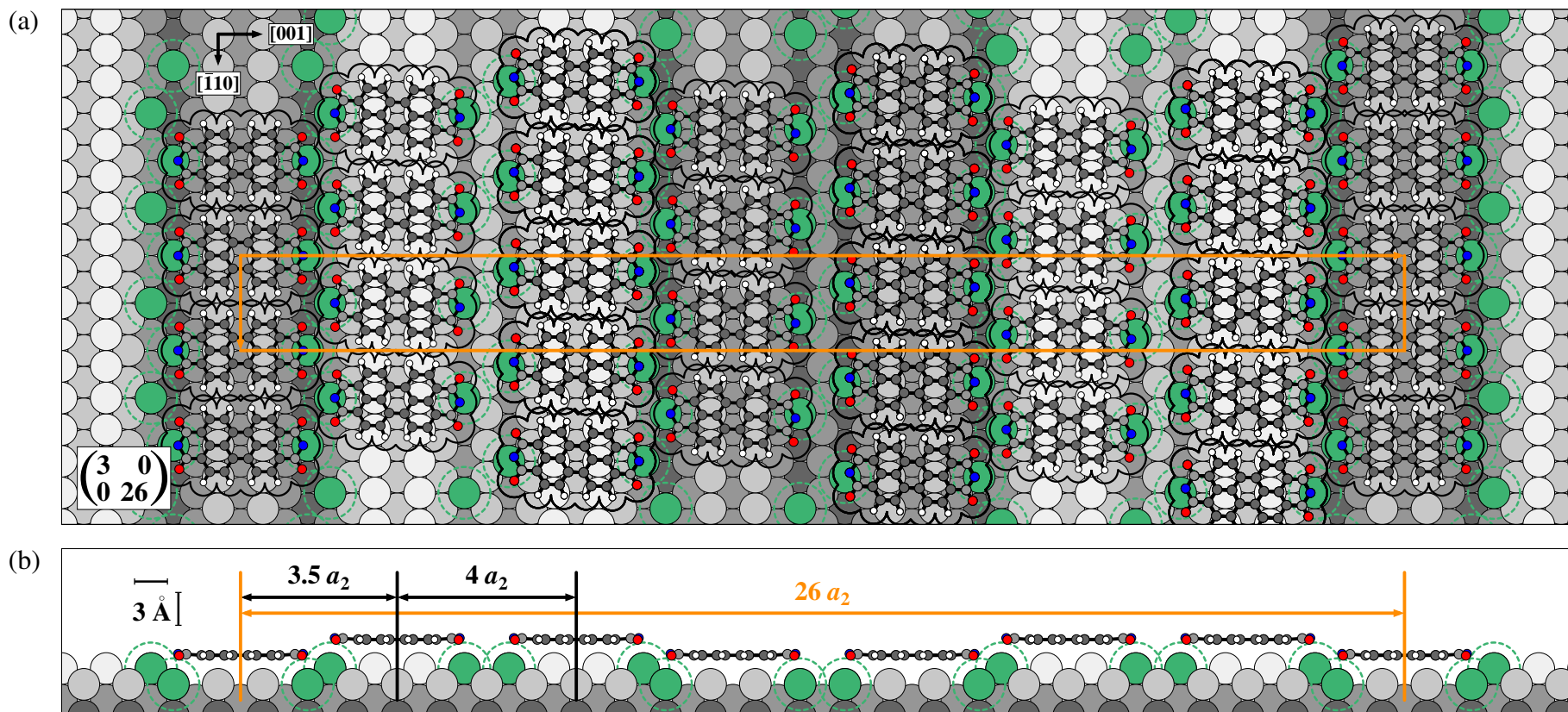
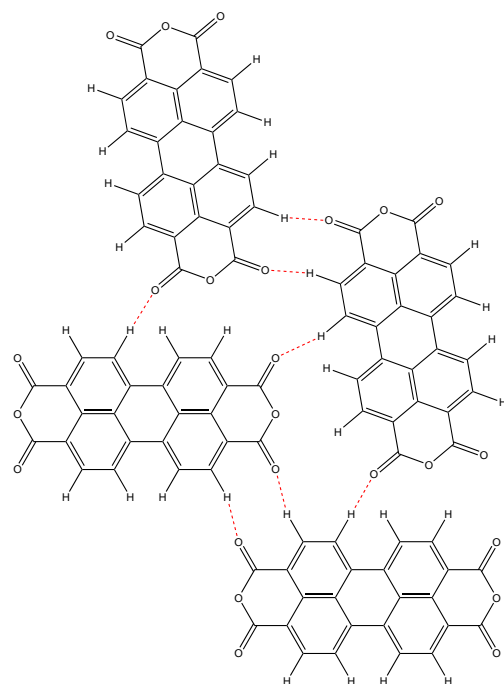


FIG. 7.2. Structural model for PTCDA in the monolayer regime on the K-modified Ag(110) surface for a K : PTCDA ratio of 2 : 1: (a) Top view and (b) side view along the $[\bar{1}10]$ direction. The PTCDA molecules are shown as ball-and-stick models, including a two-dimensional projection of the molecular vdW surface in (a). K atoms are depicted with the same metallic radius as the Ag atoms. The intrinsic metallic radius r_m of K atoms is indicated by green dashed circles (see Table 2.3 in Sec. 2.2.2, page 16, of the present work for the explicit values).¹⁴² Ag atoms are depicted in different shades of gray in order to indicate different layers. The topmost Ag layer is shown in light gray. The unit cell is indicated by solid orange lines. The substrate directions are also indicated, and the superstructure matrix is given as an inset in (a). The PTCDA molecules are rotated against the [001] direction by 2° , as deduced from SPA-LEED and STM data.⁶⁸ The positions of the K atoms along $[\bar{1}10]$ and of the PTCDA molecules relative to the substrate along $[\bar{1}10]$ are not known, but XPS data have suggested the largest influence of the K atoms on the O_{anhyd} atoms. Therefore, the molecules have been placed such that the O_{anhyd} atoms are on top of the K atoms. Lateral distances between the PTCDA molecules along [001] are given as multiples of the respective surface lattice constant of the Ag(110) substrate, $a_2 = 4.085 \text{ \AA}$,²⁸⁹ in (b). Adapted from Ref. 68.

FIG. 7.3. Hydrogen bonds between individual PTCDA molecules in the herringbone (HB) arrangement. The PTCDA molecules are represented by their valence bond structure while $C=O \cdots H-C$ hydrogen bonds are shown as red dashed lines. The angle between the long axes of the molecules is chosen as 80° in agreement with the HB structures of PTCDA in the bulk phases.^{108, 109}



annealing has been performed (see also Appendix D). If a stoichiometry of about 2 K atoms per PTCDA molecule is satisfied (within about 10%), a columnar or stripe-like motif is present for PTCDA/K:Ag(110). Columns of PTCDA molecules are formed along the $[\bar{1}10]$ direction. STM and XPS experiments have suggested that the O atoms within the PTCDA molecules, the O_{anhyd} atoms, in particular, are located closest to the K atoms. This has been considered in Fig. 7.2. Note that the exact positions of the K atoms along the $[\bar{1}10]$ direction as well as the positions of the PTCDA molecules relative to the substrate along this direction are not known with absolute certainty. SPA-LEED experiments have verified, however, that the K atoms and the PTCDA molecules are in registry with both the Ag substrate and each other, thus forming a commensurate superstructure. Taking account of the K : PTCDA ratio and also of the fact that the line widths in XPS are identical within 8% for PTCDA on the pure Ag(110) surface and on K:Ag(110), which strongly favors an identical positioning of all distinguishable atoms relative to the K atoms, the structural model in Fig. 7.2 with the K atoms underneath the O_{anhyd} of PTCDA indeed represents the most likely arrangement for the PTCDA/K:Ag(110) interface. It appears plausible that the PTCDA molecules adopt the same adsorption site on K:Ag(110) as on pure Ag(110) due to the strong surface bonding (the conclusion of strong surface bonding will be evidenced below). Only a small rotation of the molecules of 2° against the $[001]$ direction was deduced from the STM and SPA-LEED data (7° from ARUPS data).⁶⁸ Hence, the positioning of the individual atoms within the PTCDA molecule, especially those within the perylene core, relative to the surface atoms is assumed to be (nearly) identical for both PTCDA/Ag(110) and PTCDA/K:Ag(110).

Note that PTCDA can also be prepared in a disordered phase on the Ag(111) surface.¹⁴⁰ This will be of importance when discussing the relevance of intermolecular interactions for the surface bonding mechanism of PTCDA on coinage metal surfaces. The disordered phase, which is also referred to as LT phase, can be obtained for PTCDA deposition at sample temperatures below 150 K.¹⁴⁰ In this phase, the PTCDA molecules are arranged in dendritic clusters of irregular shape and size,¹⁴⁰ which consist of several ten molecules as may be seen from the STM images in Ref. 140. The molecules preferentially exhibit a tail-to-edge arrangement in this clusters¹⁴⁰ as is schematically depicted in Fig. 7.1(d) for a cluster of only six molecules. However, the azimuthal

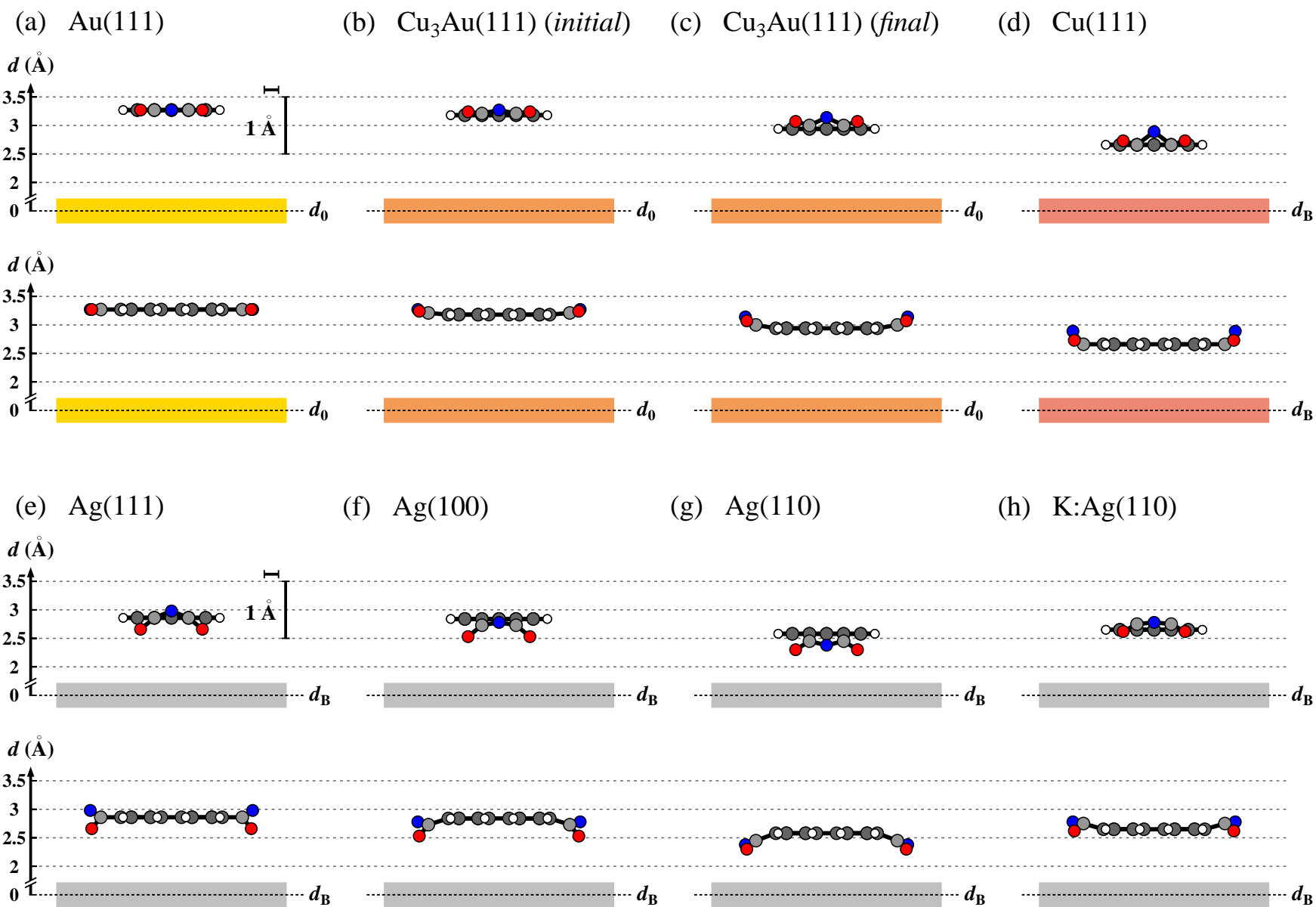
orientation of the molecules A and B is not restricted to the $[\bar{1}10]$ and $[11\bar{2}]$ substrate directions as Fig. 7.1(d) implies, but the molecules exhibit a variation in the azimuthal orientation of about $\pm 10^\circ$ against these directions. Therefore, the intermolecular interactions may be reduced due to the lower number of neighboring molecules, as well as due to the less ideal and thus less dense packing of the molecules.¹⁴⁰ Furthermore, the formation of $C=O\cdots H-C$ hydrogen bonds^{4,111} may be hindered because of a less preferential (relative) arrangement of the molecules. The ideal herringbone arrangement allows to form $C=O\cdots H-C$ hydrogen bonds since the axis of a $C=O$ bond of one PTCDA molecule is almost linearly aligned with the $H-C$ bond axis of the neighboring molecule as Fig. 7.3 shows. Due to (averaged) azimuthal orientations of the molecules and their lateral dimensions, we speculate, however, that most of the O_{carb} atoms in PTCDA may still adopt roughly on-top positions in the disordered phase of PTCDA/Ag(111) [see Fig. 7.1(d)], similar to the situation in the usual ordered RT phase (see above).

Adsorption configurations

Figure 7.4 contrasts the adsorption configurations of PTCDA on the individual coinage metal (hkl) surfaces which have been determined with XSW so far. The results for PTCDA/Au(111) have recently been reported by Henze *et al.*,⁵⁴ those for PTCDA/Cu(111) by Gerlach *et al.*,⁴³ and those for PTCDA/Ag(111) by Hauschild *et al.*^{32,55} Note that Fig. 7.4 only contains the adsorption configuration of PTCDA on Ag(111) in the ordered (RT) phase while the configuration in the disordered (LT) phase is depicted in Fig. 7.13 below. The adsorption configurations of PTCDA on $\text{Cu}_3\text{Au}(111)$ in both the initial and final state (see Sec. 6.6.4), of PTCDA on Ag(100) (see Sec. C.3.4 in the appendix of the present work), of PTCDA on Ag(110) (see Sec. C.3.4, too), and of PTCDA on K:Ag(110) (see Sec. D.3.3) have now been added to this series. In addition to the schematic representation of the experimental results concerning the adsorption configurations in Fig. 7.4, the determined adsorption heights d have also been compiled in Table 7.1.

Remarkably different adsorption configurations are found for PTCDA on the different coinage metal surfaces, namely, (nearly) planar, *boat-like*, *saddle-like*, and *arch-like* configurations (see Fig. 7.4). These different adsorption configurations can be categorized to a certain extent, that is, for the pure and binary Au and Cu surfaces on the one hand, and for the Ag surfaces on the other hand. For PTCDA/Au(111) the full adsorption configuration is not known due to experimental reasons, only the average adsorption height of the C atoms within the molecule (that is, the

FIG. 7.4 (following page). Adsorption configurations of PTCDA on various coinage metal surfaces, namely, of PTCDA on (a) Au(111),⁵⁴ (b) $\text{Cu}_3\text{Au}(111)$ in the initial state, (b) $\text{Cu}_3\text{Au}(111)$ in the final state, (d) Cu(111),⁴³ (e) Ag(111),⁵⁵ (f) Ag(100), (g) Ag(110), and (h) K:Ag(110). K:Ag(110) denotes the (110) surface of Ag which has been modified by a submonolayer of K atoms. The top rows show side views along the long molecular axis while the bottom rows show side views along the short molecular axis. H atoms are shown in white, C_{funct} and C_{peryl} atoms in light gray and dark gray, and O_{carb} and O_{anhyd} atoms in red and blue, respectively. The individual surfaces are depicted as colored regions. d denotes the vertical adsorption height; the vertical scale is enlarged by a factor of 4 and referenced against the Bragg plane (dashed line, d_B) or the (averaged) position of the relaxed surface (dashed line, d_0), respectively. Note that for PTCDA/Au(111) the O atoms are depicted at the same adsorption height as the C_{funct} and C_{peryl} atoms although their positions are not known for experimental reasons.⁵⁴ Note further that the C_{funct} and C_{peryl} atoms could not be distinguished experimentally for PTCDA on Au(111),⁵⁴ Cu(111),⁴³ and Ag(111).^{32,55} In the case of PTCDA on Cu(111), however, C_{peryl} and C_{funct} were concluded to exhibit the same d values within the experimental resolution.⁴³



average height of the perylene core essentially) was determined.⁵⁴ However, because of the comparably weak interaction of the molecules with the substrate judging from the adsorption height [a d value of 3.27(2) Å has been determined for the C atoms in PTCDA which is only 4 % smaller than the sum of the vdW radii¹⁴¹ of C and Au (see also Table 7.2)] and the incommensurate lateral structure of the molecules on the surface, which is presumably dominated by intermolecular interactions (see also Fig. 7.3), a (nearly) planar configuration is expected. Note that neither XPS nor UPS data have indicated a substantial chemical interaction of PTCDA with the Au(111) surface,^{59,60} supporting the above conclusion of a non-distorted adsorption configuration for PTCDA on Au(111).^{a)} With an increasing Cu fraction at the surface, that is, in the sequence Cu₃Au(111) in the initial state (“Au-rich”), Cu₃Au(111) in the final state (“Cu-rich”), and pure Cu(111), the adsorption height of the molecule [taken to be equal to $d(\text{C total})$, see Table 7.1] lowers by 19 %, indicating strongly enhanced chemical interactions. In the same sequence, the distortion of the PTCDA molecule increases to 0.23(6) Å, and a *boat*-like adsorption geometry is adopted where the O atoms are located further away from the substrate surface than the perylene core. Therefore, the determined adsorption configurations do not suggest the presence of local O–M interactions (with M = Cu, Au) as a relevant bonding channel here.

Concerning the low-index surfaces of silver, the following trends can be noticed: (1) The overall vertical adsorption height d of PTCDA, again taken to be equal to $d(\text{C total})$ (see Table 7.1), decreases by 0.30(1) Å in the sequence Ag(111), Ag(100), Ag(110). On all three Ag surfaces, the adsorption height is lower than expected for a pure vdW bonding (see also Table 7.2).¹⁴¹ (2) In contrast to the findings for PTCDA on the (pure or alloyed) Au and Cu surfaces, the O atoms, in particular the O_{carb} atoms, are located closer to the surface than the perylene core (see Fig. 7.4). The only exceptions are the O_{anhyd} atoms for PTCDA/Ag(111) [and also for PTCDA/K:Ag(110), see below]. Hence, the adsorption configuration changes from *saddle*-like to *arch*-like for the two more open Ag surfaces. (3) At the same time, the C backbone distortion, i.e., $|\Delta d(\text{C})| = |d(\text{C}_{\text{funct}}) - d(\text{C}_{\text{peryl}})|$, increases to 0.13(11) Å for PTCDA/Ag(110). Note at this point that the distortion of the C backbone for PTCDA/Ag(111), which has not been determined experimentally,^{32,55} is expected to be marginal. Due to the saddle-like adsorption configuration of the molecule, it is reasonable to assume that the C_{funct} atoms reside at an adsorption height close to $d(\text{O total})$ which, in turn, is identical to $d(\text{C total})$. (4) The difference in the adsorption heights of the distinguishable O atoms, i.e., $\Delta d(\text{O}) = d(\text{O}_{\text{anhyd}}) - d(\text{O}_{\text{carb}})$, decreases by 75 % in the above-stated sequence, i.e., it is reduced to 0.08(4) Å for PTCDA/Ag(110). These trends are also illustrated in Fig. 7.10 below. Finding (1) proves a chemisorptive interaction of the molecule with the substrate which is, judging from the well-established bond length–bond strength correlation,^{56,57} strongest for the most open (110) face, where the lowest adsorption height is found. Hence, the findings (2)–(4) indicate the presence of significant chemical interactions, in particular, between the O_{carb} and, to a smaller extent, the O_{anhyd} atoms and the Ag surface atoms.

Thus, we have already identified two potential bonding channels for PTCDA on coinage metal surfaces, apart from pervasive vdW interactions. We will sometimes refer to those bonding channels which are beyond the interactions of induced dipoles, i.e., beyond pure van der Waals interactions,¹⁴⁶ as *chemical* bonding channels in the following with the aim to circumscribe physisorptive and chemisorptive contributions to the surface bonding mechanism more clearly, and in order to point at the actual formation of chemical bonds, being covalent or electrostatic in nature, for ex-

^{a)}DFT calculations by Romaner *et al.* employing the PBE functional (and also including dispersion corrections) predict a saddle-like adsorption configuration with a total vertical distortion of only 0.04 Å.¹⁵³ More recent DFT results by Ruiz *et al.* (employing a different dispersion correction⁴⁸⁶) predict also a saddle-like adsorption configuration with a total vertical distortion of 0.07 Å.⁴⁸⁷

TABLE 7.1. Values for averaged vertical distances d of the carbon and oxygen atoms for PTCDA on different coinage metal (hkl) surfaces. LT means low temperature and denotes the metastable disordered phase of PTCDA on Ag(111) which can be prepared at $T < 150$ K.¹⁴⁰ $\Delta d = d_{\max} - d_{\min}$ is the absolute (overall) vertical distortion of the (intrinsically planar) PTCDA molecule, $\Delta d(\text{C}) = d(\text{C}_{\text{funct}}) - d(\text{C}_{\text{peryl}})$ is the vertical displacement of the C atoms, and $\Delta d(\text{O}) = d(\text{O}_{\text{anhyd}}) - d(\text{O}_{\text{carb}})$ is the vertical displacement of the O atoms, respectively. Note that for the determination of Δd only the main components have been taken into account while the C_{sat} component was disregarded due to its non-unambiguous character. For PTCDA/Au(111) the O positions were not measured for experimental reasons.⁵⁴ A differentiation of the C_{peryl} and C_{funct} atoms was not made for PTCDA/Au(111) and PTCDA/Ag(111).^{54,55} In the case of PTCDA on Cu(111), C_{peryl} and C_{funct} were concluded to exhibit the same d values within the experimental resolution (t.w. = this work, n.d. = not determined).⁴³

	PTCDA								
	Au(111) (Ref. 54)	Cu ₃ Au(111) (<i>init.</i>) (t.w.)	Cu ₃ Au(111) (<i>fin.</i>) (t.w.)	Cu(111) (Ref. 43)	Ag(111) (Ref. 55)	Ag(111), LT (Ref. 55)	Ag(100) (t.w.)	Ag(110) (t.w.)	K:Ag(110) (t.w.)
$d(\text{C total})$ (Å)	3.27(2)	3.18(1)	2.95(5)	2.66(2)	2.86(1)	2.81(2)	2.81(2)	2.56(1)	2.66(2)
$d(\text{C}_{\text{peryl}})$ (Å)	n.d.	3.18(1)	2.94(5)	n.d.	n.d.	n.d.	2.84(2)	2.58(1)	2.65(2)
$d(\text{C}_{\text{funct}})$ (Å)	n.d.	3.21(2)	3.00(4)	n.d.	n.d.	n.d.	2.73(1)	2.45(11)	2.75(3)
$d(\text{C}_{\text{sat}})$ (Å)	n.d.	3.17(5)	2.95(8)	n.d.	n.d.	n.d.	2.79(3)	2.55(1)	2.67(6)
$d(\text{O total})$ (Å)	n.d.	3.25(4)	3.10(6)	2.81(3)	2.86(2)	2.67(3)	2.64(2)	2.33(3)	2.67(8)
$d(\text{O}_{\text{carb}})$ (Å)	n.d.	3.24(4)	3.07(6)	2.73(6)	2.66(3)	2.50(4)	2.53(2)	2.30(4)	2.62(12)
$d(\text{O}_{\text{anhyd}})$ (Å)	n.d.	3.27(4)	3.14(7)	2.89(6)	2.98(8)	2.83(4)	2.78(2)	2.38(1)	2.78(10)
Δd (Å)	n.d.	0.09(4)	0.20(8)	0.23(6)	0.32(11)	0.33(8)	0.31(3)	0.28(4)	0.16(16)
$\Delta d(\text{C})$ (Å)	n.d.	0.03(3)	0.06(6)	n.d.	n.d.	n.d.	-0.11(2)	-0.13(11)	0.10(4)
$\Delta d(\text{O})$ (Å)	n.d.	0.03(6)	0.07(9)	0.16(8)	0.32(11)	0.33(8)	0.25(3)	0.08(4)	0.16(16)

TABLE 7.2. Relative values for averaged vertical distances d of the carbon and oxygen atoms for PTCDA on different coinage metal (hkl) surfaces. LT means low temperature and denotes the metastable disordered phase of PTCDA on Ag(111) which can be prepared at $T < 150$ K.¹⁴⁰ All values are given as a percentage of the sum of the vdW radii r_{vdW} (taken from Ref. 141) of neighboring atoms which may be involved in (local) surface bonding (see also Table 7.4). Specifically, potential C \cdots M and O \cdots M interactions between C and O atoms within the PTCDA molecule on the one hand and substrate metal atoms at the surface (with M = Cu, Ag, Au) on the other hand have been considered here (assuming a perfect on-top arrangement of C and O with respect to the metal surface atoms). Note that in the case of PTCDA/Cu₃Au(111) only the r_{vdW} value of Au, being larger than that of Cu by almost 20 % (see also Table 2.3) 141, has been considered. Note further that error margins below 0.5 %, which were obtained in some cases, have been rounded up to 1 % (t.w. = this work, n.a. = not available).

	PTCDA								
	Au(111) (Ref. 54)	Cu ₃ Au(111) (<i>init.</i>) (t.w.)	Cu ₃ Au(111) (<i>fin.</i>) (t.w.)	Cu(111) (Ref. 43)	Ag(111) (Ref. 55)	Ag(111), LT (Ref. 55)	Ag(100) (t.w.)	Ag(110) (t.w.)	K:Ag(110) (t.w.)
$d(\text{C total})$ (%)	96(1)	93(1)	87(1)	84(1)	82(1)	81(1)	81(1)	74(1)	77(1)
$d(\text{C}_{\text{peryl}})$ (%)	n.a.	93(1)	86(1)	n.a.	n.a.	n.a.	82(1)	74(1)	76(1)
$d(\text{C}_{\text{funct}})$ (%)	n.a.	94(1)	88(1)	n.a.	n.a.	n.a.	79(1)	71(3)	79(1)
$d(\text{C}_{\text{sat}})$ (%)	n.a.	93(1)	87(2)	n.a.	n.a.	n.a.	80(1)	73(1)	77(2)
$d(\text{O total})$ (%)	n.a.	98(1)	94(2)	92(1)	85(1)	79(1)	78(1)	69(1)	79(2) ^a
$d(\text{O}_{\text{carb}})$ (%)	n.a.	98(1)	93(2)	90(2)	79(1)	74(1)	75(1)	68(1)	78(4) ^b
$d(\text{O}_{\text{anhyd}})$ (%)	n.a.	99(1)	95(2)	95(2)	88(2)	84(1)	82(1)	71(1)	82(3) ^c

^aA value of 61(2) % is obtained for potential O \cdots K interactions under the assumption that K atoms are present in the Ag(110) surface layer underneath the O atoms. If the respective covalent radii were considered,¹⁴⁴ a value of 99(3) % would be obtained.

^bA value of 60(3) % is obtained for potential O_{carb} \cdots K interactions under the assumption that K atoms are present in the Ag(110) surface layer underneath the O_{carb} atoms. If the respective covalent radii were considered,¹⁴⁴ a value of 97(4) % would be obtained.

^cA value of 63(2) % is obtained for potential O_{anhyd} \cdots K interactions under the assumption that K atoms are present in the Ag(110) surface layer underneath the O_{anhyd} atoms.¹⁴⁴ If the respective covalent radii were considered,¹⁴⁴ a value of 103(4) % would be obtained.

ample. Note at this point that we do not classify intermolecular interactions such as hydrogen bond-like^{4,111} and/or quadrupole interactions,⁴ which are present between PTCDA molecules in the HB arrangement, as a chemical bonding channel here, either, since they are comparably weak in contrast to truly covalent or ionic interactions.^{85,146,b)} One of the potential *chemical* bonding channels is the interaction of the perylene core in PTCDA with the substrate. The chemical nature of this bonding channel, as well as implications for other relevant bonding channels, will be discussed in Secs. 7.3, 7.4 and 7.6. The second *chemical* bonding channel is the potential formation of O—M interactions (with M = Cu, Ag, Au). We will unveil this bonding channel on the anhydride groups further, for example, by looking at the bond lengths b between the involved atoms and also by looking at the chemical nature of the bonds in Sec. 7.5.

Eventually, we will discuss a potential interplay of bonding channels at the example of PTCDA/K:Ag(110). In contrast to the situation of PTCDA on the pure Ag(110) surface, where an arch-like configuration is present, a *saddle*-like adsorption configuration is adopted on the K-modified Ag(110) surface although the adsorption site is essentially identical. Nonetheless, interactions of the O atoms with the surface are obviously altered. Furthermore, the adsorption height of the perylene core increases by 0.07(2) Å. Apparently, the presence of K atoms within the surface layer significantly affects the bonding situation of PTCDA. We will shine light on the relevant effects for the bonding of PTCDA on K:Ag(110) in Sec. 7.7.

7.2 DFT calculations of PTCDA on Ag surfaces: theoretical methods

In addition to the experimental studies, density functional theory (DFT) calculations have been carried out for PTCDA on the low-index Ag surfaces. All calculations were performed by Dr. Werner Reckien and Professor Dr. Thomas Bredow from Rheinische Friedrich-Wilhelms-Universität Bonn (Bonn, Germany) in close collaboration with the author within a joint research project on surface bonding at the metal/organic interface. Several aspects have been investigated here. The DFT calculations yielded information on the electronic structure of the PTCDA molecule in the gas phase, which are needed as a reference in the discussion of the (potential) metal-to-molecule charge transfer. Also, they yielded information on the displacements of the individual Ag surface atoms upon PTCDA adsorption, which are not accessible by XSW. Furthermore, electron densities from DFT demonstrate the charge redistributions and the bond formations for PTCDA on the Ag surfaces. Eventually, these results can also be transferred, at least in a qualitative manner, to the adsorption situation for PTCDA on the other coinage metal surfaces discussed in the present work. The individual results will be discussed along with the experimental findings in the subsequent sections. In this section, only computational details are presented. Besides, the validity of the obtained results is evaluated.

^{b)}According to the International Union of Pure and Applied Chemistry (IUPAC), a chemical bond is defined as follows:⁸⁵

There is a chemical bond between two atoms or groups of atoms in the case that the forces acting between them are such as to lead to the formation of an aggregate with sufficient stability to make it convenient for the chemist to consider it as an independent ‘molecular species’.

The above definition justifies to consider neither the formation of hydrogen bonds nor quadrupole interactions between PTCDA molecules on the surface⁴ as *chemical* bonding channels.

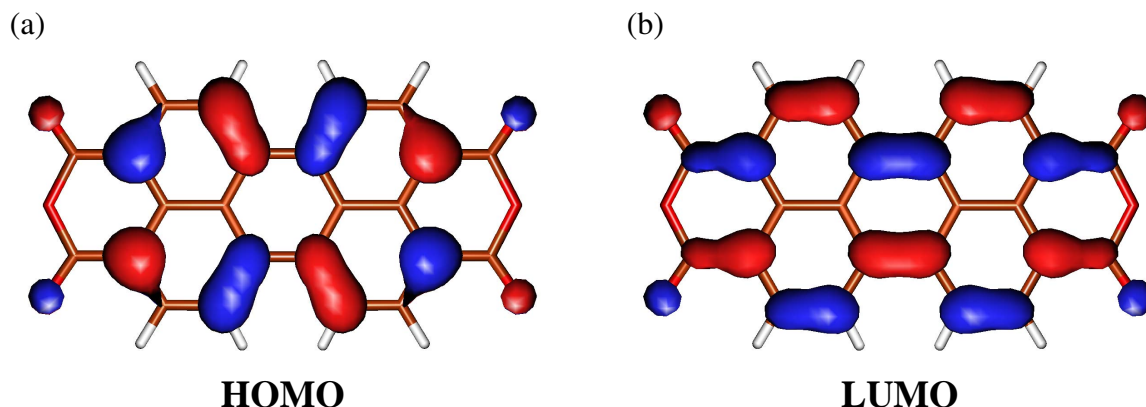


FIG. 7.5. Frontier orbitals, i.e., (a) highest occupied molecular orbital (HOMO) and (b) lowest unoccupied molecular orbital (LUMO), of the PTCDA molecule in the gas phase as obtained from hybrid DFT calculations. The isosurfaces of the probability densities for the respective MOs are shown with an isovalue of 0.35. Different colors of the orbital lobes indicate the sign of the wave function. The molecular backbone is depicted in brown (C atoms), red (O atoms), and white (H atoms), respectively.

Theoretical methods

The DFT calculations for the free PTCDA molecule were performed with the computer program Gaussian 03,⁴⁸⁸ employing the hybrid density-functional approximation KMLYP^{489,490} and segmented quadruple zeta valence basis sets QZVP, which are augmented by polarization functions.^{491,492} Isosurfaces of the probability densities for the molecular orbitals (MOs) were plotted using the computer program MOLDEN 5.0.⁴⁹³ The frontier orbitals of PTCDA in the gas phase, namely, the highest occupied molecular orbital (HOMO) and the lowest unoccupied molecular orbital (LUMO), are shown in Fig. 7.5.

In addition, DFT calculations of the periodic structures were performed, i.e., of PTCDA/Ag(111), PTCDA/Ag(100), and PTCDA/Ag(110) in the monolayer regime. The plane-wave code Vienna *Ab initio* Simulation Package^{494–496} (VASP) in combination with the projector-augmented wave (PAW) method,⁴⁹⁷ in order to account for the core electrons, was used. A cutoff energy of 400 eV for the plane-wave valence basis and a Monkhorst-Pack integration setup with a $3 \times 3 \times 1$ k -point mesh was chosen. These values had been obtained in preliminary convergence studies as an optimal compromise between accuracy and computational efficiency. The Perdew-Burke-Ernzerhof (PBE) functional⁴⁹⁸ was applied in combination with an empirical dispersion correction (termed D in the following).^{499–501} This approach has already been successfully tested for periodic systems whose interactions are dominated by dispersion forces.^{502,503} The dispersion-corrected DFT-D energy E_{DFT} was calculated by adding an empirical correction energy E_{disp} to the Kohn-Sham energy $E_{\text{KS-DFT}}$:

$$E_{\text{DFT}} = E_{\text{KS-DFT}} + E_{\text{disp}}. \quad (7.1)$$

Calculations with the original D3⁵⁰⁰ as well as with the improved D3(BJ) dispersion correction⁵⁰¹ were performed. However, only the PBE-D3(BJ) results will be presented here since these show a slightly better agreement with the experimental data. The silver surfaces were modeled by a super cell with matrix $\mathfrak{M} = \begin{pmatrix} 3 & -2 \\ 6 & 7 \end{pmatrix}$ for the Ag(111) surface, a super cell with $\mathfrak{M} = \begin{pmatrix} 4 & 4 \\ -4 & 4 \end{pmatrix}$ for the Ag(100) surface, and a super cell with $\mathfrak{M} = \begin{pmatrix} 3 & 2 \\ -3 & 2 \end{pmatrix}$ for the Ag(110) surface, respectively. The substrate slabs consisted of three Ag layers for Ag(111) and Ag(100), and seven layers

TABLE 7.3. Experimental and theoretical results for the adsorption geometry of PTCDA on the low-index Ag surfaces. Here, d_{exp} and d_{theo} values denote the averaged vertical adsorption heights of the specific atoms obtained from NIXSW experiments and DFT calculations, respectively (t.w. = this work, n.d. = not determined).

	PTCDA					
	Ag(111)		Ag(100)		Ag(110)	
	Ref. 55	t.w.	t.w.		t.w.	
	d_{exp} (Å)	d_{theo} (Å)	d_{exp} (Å)	d_{theo} (Å)	d_{exp} (Å)	d_{theo} (Å)
C total	2.86(1)	2.99	2.81(2)	2.78	2.56(1)	2.68
C _{peryl}	n.d.	3.00	2.84(2)	2.80	2.58(1)	2.71
C _{funct}	n.d.	2.94	2.73(1)	2.69	2.45(11)	2.53
O total	2.86(2)	2.86	2.64(2)	2.59	2.33(3)	2.40
O _{carb}	2.66(3)	2.80	2.53(2)	2.53	2.30(4)	2.38
O _{anhyd}	2.98(8)	2.98	2.78(2)	2.71	2.38(1)	2.46

for Ag(110). The Ag atoms in the bottom layers [one for the (111) as well as the (100) surface and two for the (110) surface, respectively] were fixed to their ideal bulk positions during the structural optimization process. PTCDA monolayers were obtained by the adsorption of two molecules for Ag(111) and Ag(100), and one molecule for Ag(110), respectively [see also Fig. 7.1(a–c)].

The net charge transfer from the Ag surfaces to the adsorbed PTCDA molecule was studied on the basis of a Bader analysis^{504,505} of the electron density $\rho(\mathbf{r})$. The electron densities $\rho(\mathbf{r})$ and the electron density difference $\Delta\rho(\mathbf{r})$ (see Fig. 7.12 below) which were obtained from the DFT calculations in VASP were analyzed with the computer program XCrySDen.⁵⁰⁶ Here, $\Delta\rho(\mathbf{r})$ is defined as $\rho(\mathbf{r})$ of the bonded system PTCDA/Ag(*hkl*) minus $\rho(\mathbf{r})$ of the free (but distorted) PTCDA molecule and minus $\rho(\mathbf{r})$ of the bare (but buckled; see Secs. 7.5, in particular, and 7.6) Ag(*hkl*) surface:

$$\Delta\rho(\mathbf{r}) = \rho_{\text{PTCDA/Ag}(hkl)}(\mathbf{r}) - \rho_{\text{PTCDA, distorted}}(\mathbf{r}) - \rho_{\text{Ag}(hkl), buckled}(\mathbf{r}). \quad (7.2)$$

Moreover, we calculated the adsorption energies E_{ads} for PTCDA on the low-index Ag surfaces. In analogy to above, E_{ads} is given as the energy $E = E_{\text{DFT}}$ of the bonded system PTCDA/Ag(*hkl*) minus E of the free (and undistorted) PTCDA molecule and minus E of the bare (and unbuckled) Ag(*hkl*) surface:

$$E_{\text{ads}} = E_{\text{PTCDA/Ag}(hkl)} - E_{\text{PTCDA, undistorted}} - E_{\text{Ag}(hkl), unbuckled}. \quad (7.3)$$

Validity of the theoretical results

The validity of the theoretical results is evaluated on the basis of the degree of agreement between the theoretically and experimentally determined adsorption configurations, respectively. Table 7.3 contrasts the respective d_{exp} and d_{theo} values. Indeed, the adsorption heights obtained from DFT match the experimental values within 5 % for all distinguishable atoms/groups.⁴⁸⁷ This renders the conclusions drawn from the DFT calculations meaningful. In the course of the present work, our

TABLE 7.4. Expected vdW and covalent distances of metal atoms at the substrate surface and C and O atoms in PTCDA. The expected distances are calculated as the sum of the individual vdW radii $r_{\text{vdW},i}$ and covalent radii $r_{\text{cov},i}$ of the respective atoms ($M = \text{Cu, Ag, Au, K}$). The corresponding r_{vdW} and r_{cov} values have been taken from Refs. 141 and 144, respectively (see also Table 2.3).

	sum of vdW radii, $\sum_i r_{\text{vdW},i}$ (Å)		sum of covalent radii, $\sum_i r_{\text{cov},i}$ (Å)	
	C···M	O···M	C—M	O—M
Cu	3.15	3.05	2.05	1.98
Ag	3.47	3.37	2.18	2.11
Au	3.41	3.31	2.09	2.02
K	4.50	4.40	2.76	2.69

DFT results will be interpreted in terms of both the structural implications of PTCDA adsorption for the individual Ag surfaces and the chemical nature of the interfacial interactions.

Note that Table 7.3 contains averaged d values for PTCDA/Ag(111). From the experimental point of view, the two non-equivalent molecules A and B which form the herringbone structure of PTCDA on the Ag(111) surface cannot be distinguished. In principle, they could exhibit different adsorption configurations. According to our DFT results, the fact that these two molecules A and B adopt different adsorption sites (see Sec. 7.1) does not affect the adsorption heights substantially. We found that the adsorption heights of the respective individual components, $d_{\text{theo},i}$, differ by maximal 0.05 Å between the two molecules. Therefore, averaging the $d_{\text{theo},i}$ values for both molecules, as done in Table 7.3, is indeed justified. In the case of PTCDA/Ag(100), the unit cell contains two molecules, too [see Fig. 7.1(b)]. Due to the symmetry of the substrate surface, however, the two translationally non-equivalent molecules exhibit identical adsorption sites. Hence, also identical adsorption configurations are expected. This conclusion was also verified by our DFT results.

7.3 Surface bonding via the perylene core: charge transfer and the Newns-Anderson model

The discussion of the individual, plausible bonding channels which are relevant in the surface bonding mechanism for PTCDA on coinage metal surfaces will be divided into several sections, each of which addresses one particular aspect of the bonding. Of course, the relevance of the potential bonding channels can substantially differ from one particular surface to the next such that one or the other bonding channel may be strongly altered, i.e., strongly enhanced or weakened, or even absent. Nonetheless, distinct trends may be discerned. We will start with the discussion of the surface bonding via the perylene core.

Correlation of adsorption heights and surface reactivity

As has been schematically depicted in Fig. 7.4 already, the adsorption height of the PTCDA molecule varies by about 0.7 Å across the coinage metal surfaces in the scope of the present work (see also Table 7.1). The molecular adsorption height $d(\text{PTCDA})$ is given by the d value for the C_{peryl} atoms here or, alternatively in those cases where this value has not been determined explicitly, by $d(\text{C total})$. Obviously, the nature of the surface determines the adsorption height of PTCDA. In agreement with chemical intuition, we ascribe the observed trend of decreasing adsorp-

TABLE 7.5. Reported work functions Φ of the clean coinage metal (hkl) surfaces^{63,389} and work function shifts $\Delta\Phi_{\text{PTCDA}}$ induced by the adsorption of PTCDA (sub-)monolayers.^{59,60} θ_{PTCDA} denotes the surface coverage of PTCDA in monolayers. Note that the reported Φ values of are subject to a considerable variation.^{59,60,63,389,507–518} In the worst case, i.e., for the clean Ag(111) surface, Φ values ranging from 4.45 eV to 4.90 eV have been determined ($\Delta\Phi = 0.45$ eV).^{59,60,508,512–515,517} On average, an error of ± 0.15 eV applies to the stated Φ values. The general trend regarding the (relative) Φ values, however, remains unaffected. In the framework of the present work, we solely refer to the experimental Φ values which have been compiled and reported in Ref. 63 (see also references therein; t.w. = this work, n.a. = not available).

	clean surface		PTCDA-covered surface		
	Φ (eV)	Ref(s).	θ_{PTCDA} (ML)	$\Delta\Phi_{\text{PTCDA}}$ (eV)	Ref.
Au(111)	5.31	63, 389	1.0	−0.40	60
Cu ₃ Au(111)	5.13	63, 389	n.a.	n.a.	n.a.
Cu(111)	4.94	507	1.0	−0.15	60
Ag(111)	4.74	508	1.0	0.10 [−0.15]	59 [60]
Ag(100)	4.64 ^a	510	0.7	0.13	t.w.
Ag(110)	4.52	510	n.a.	n.a.	n.a.
K:Ag(110)	n.a.	n.a.	n.a.	n.a.	n.a.
K (polycryst.)	2.30	519	n.a.	n.a.	n.a.

^aWe have determined a value of 4.40(2) eV, that is, a 0.24 eV smaller value than the value stated here, for the work function Φ of the clean Ag(100) surface in our UPS experiments. For reason of consistency, however, we still refer to the quoted value from Ref. 510 in the framework of the present work.

tion heights, namely, $d_{\text{Au}}(\text{PTCDA}) > d_{\text{Ag}}(\text{PTCDA}) > d_{\text{Cu}}(\text{PTCDA})$, to the increasing reactivity of the metal. Now the question arises how this reactivity may actually be described. In principle, the reactivity of chemical elements may be classified by their standard electrode potentials E° , for example [see footnote b) in Chapter 1, page 3, of the present work].²⁰ In doing so, we find that the reactivity of the employed elements increases in the sequence Au, Ag, and Cu, thus explaining the observed trend in $d(\text{PTCDA})$ qualitatively very well.

However, the above consideration exhibits two major restrictions. First of all, the determined $d(\text{PTCDA})$ values have to be correlated with the sizes of the involved binding partners in order to allow for a comparison among themselves. It has been pointed out in Sec. 7.1 already that, with respect to the sum of the vdW radii (see Table 7.4 for a compilation of the sum of the vdW radii and covalent radii relevant to this work), the relative adsorption height of PTCDA on Cu(111) is indeed larger than that on Ag(111) by 4% (see also Table 7.2), in apparent contradiction to chemical intuition. Due to the bond length-bond strength correlation,^{56,57} a stronger bonding and thus a smaller relative adsorption height for PTCDA on Cu(111) than on Ag(111) would have been expected. For the discussion to come in this section, for reasons of simplicity, we will use d_{vdW} values instead of d values, that is, values for the adsorption height which have been corrected for the different r_{vdW} according to:

$$d_{\text{vdW}}(i) = d(i) - r_{\text{vdW}}(j), \quad (7.4)$$

where i refers to the atoms of interest within the PTCDA molecule and j to the surface atoms. Secondly, also as a direct consequence of the above consideration, the standard electrode potentials

may not be an adequate measure for the reactivity of the substrate since these E° values refer to atoms in solution. In the present case, however, the substrate atoms form a solid surface. One obvious parameter to describe the (electronic) properties of a surface is the work function Φ and thus should be a more reliable measure of the substrate (surface) reactivity. Respective Φ values for the clean coinage metal surfaces, which are relevant to the present work, are compiled in Table 7.5. Remarkably, the work function decreases in the series Au, Cu, Ag, when comparing the Φ values of the respective (111) surfaces, in analogy to the d_{vdW} values for adsorbed PTCDA. This point will be elucidated in detail below.^{c)} Prior to this, we point out that the absolute values of Φ reported in the literature (see Refs. 59, 60, 63, 389, 507–518) are subject to a considerable variation. In the worst case, that is, for the clean Ag(111) surface, Φ values ranging from 4.45 eV to 4.90 eV have been determined (see Refs. 59, 60, 508, 512–515, 517), which corresponds to a variation of $\Delta\Phi = 0.45$ eV. On average, a variation of ± 0.15 eV applies to the reported Φ values. Yet, the general trend regarding the (relative) Φ values, which can be deduced from the representative values given in Table 7.5, remains unaffected by these variations. In the framework of the present work, we solely refer to the experimental Φ values which have been compiled and reported in Ref. 63 for reasons of consistency.

We now turn to the bond length-bond strength correlation^{56,57} in the case of PTCDA adsorption on coinage metal surfaces, that is, the correlation of d_{vdW} and Φ . Figure 7.6(a) shows the determined adsorption heights d_{vdW} , which have been corrected in accordance with Eq. (7.4), for C_{peryl} as a function of the work function Φ of the clean metal surfaces. The order of the data points runs as PTCDA/K:Ag(110) and PTCDA/Ag(110), PTCDA/Ag(100), PTCDA/Ag(111) (RT and LT phase), PTCDA/Cu(111), PTCDA/Cu₃Au(111) (initial and final state), and PTCDA/Au(111) from left to right. Note that this order is exactly reversed in comparison to that in Fig. 7.4. The corrected adsorption heights $d_{\text{vdW}}(C_{\text{peryl}})$ decrease with decreasing Φ and exhibit a linear dependency in very good approximation. The largest deviation from the linear correlation is observed for PTCDA/Cu₃Au(111) in the final state [see the data point at $\Phi = 5.13$ eV and $d_{\text{vdW}} = 1.28(5)$ Å in Fig. 7.6(a)]. We ascribe this finding to the fact that the surface composition of the Cu₃Au(111) has altered upon PTCDA adsorption in comparison to the clean surface (see Sec. 6.5.2). Most likely, the substrate work function is lowered by the increased surface fraction of Cu atoms, potentially towards that of pure Cu(111), and thereby the surface reactivity is enhanced, leading to a smaller $d_{\text{vdW}}(C_{\text{peryl}})$ value.

The linear correlation of $d_{\text{vdW}}(C_{\text{peryl}})$ and Φ is an experimental observation which so far cannot be explained in a quantitative manner. However, qualitative considerations in the framework of the Newns-Anderson model^{11,14,81} (see also Sec. 2.1.2) will be undertaken here. Note that such considerations have also been done earlier by Hauschild *et al.* for PTCDA on Au(111), Ag(111), and Cu(111) which we will recapitulate at this point.⁵⁵ Within the present work, however, the LT phase of PTCDA/Ag(111) is considered, too. Furthermore and more importantly, the data set by Hauschild *et al.* has been amended by five additional data point. Therefore, the argumentation is now put on a firmer foundation. The observed correlation shows that the bonding distance of the perylene core, given by $d_{\text{vdW}}(C_{\text{peryl}})$, to the substrate surface decreases for smaller values of Φ . The substrate surface is understood as being determined by its vdW surface and thus by its substrate electron density. The correlation of d_{vdW} and Φ originates from a metal-to-molecule charge transfer

^{c)}Note that a similar correlation has recently been reported also for NTCDA on Cu(100) and Ag(110) by Wießner *et al.*⁵²⁰ The Φ values of the clean surfaces amount to 4.59 eV and 4.52 eV^{507,510} while the corresponding d_{vdW} values for the O atoms have been calculated with DFT as 0.70 Å and 0.60 Å, respectively.⁵²⁰ ARUPS measurements have indeed revealed a stronger hybridization of the NTCDA LUMO with metal states on Ag(110).⁵²⁰

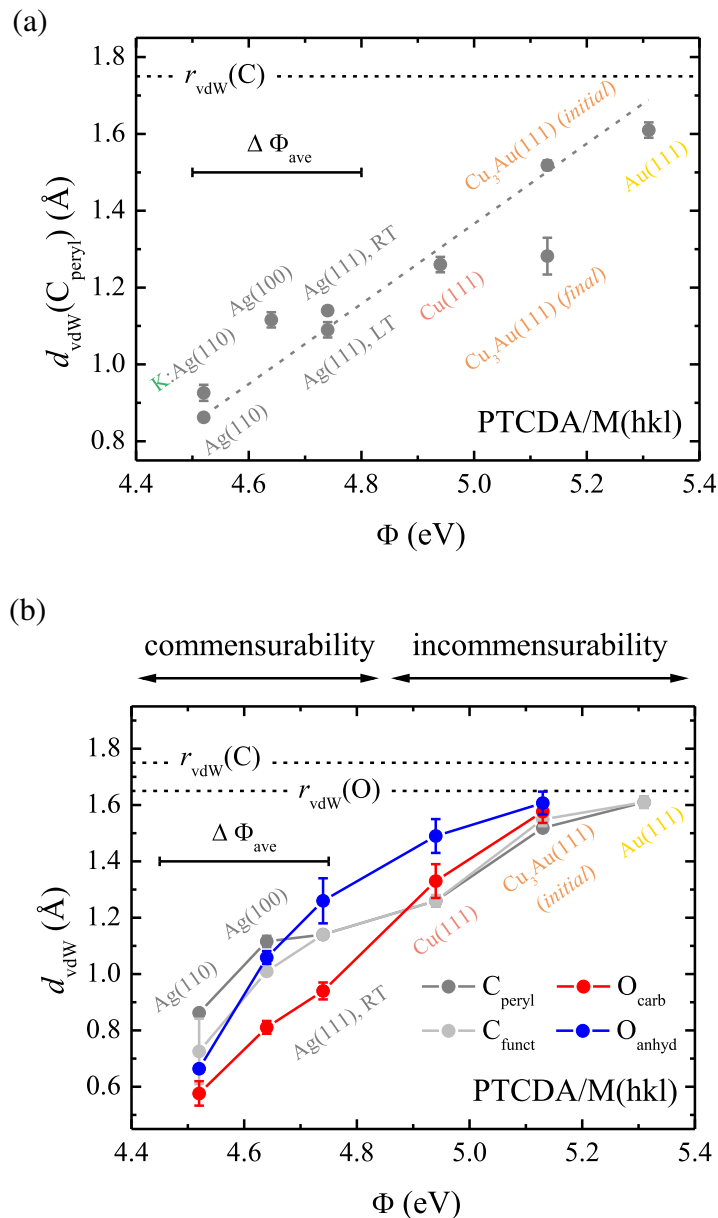


FIG. 7.6. Vertical bonding distances d_{vdW} of PTCDA on various coinage metal surfaces corrected for the different van der Waals radii r_{vdW} of the surface atoms j versus the work functions Φ of the respective clean coinage metal (hkl) surfaces, i.e., $d_{\text{vdW}}(i) = d(i) - r_{\text{vdW}}(j)$. The correction by r_{vdW} accounts for differences in the atomic sizes of the substrate surface atoms.¹⁴¹ Corresponding d ,^{43,54,55} r_{vdW} ,¹⁴¹ and Φ values⁶³ have been compiled in Tables 7.1, 2.3, and 7.5, respectively. (a) d_{vdW} versus Φ for the C_{peryl} atoms. In those cases where $d(\text{C}_{\text{peryl}})$ is not available, i.e., for PTCDA/Au(111),⁵⁴ PTCDA/Cu(111),⁴³ and PTCDA/Ag(111),⁵⁵ $d(\text{C}_{\text{peryl}})$ has been assumed to be identical to $d(\text{C total})$. The gray dashed line represents a linear fit to the data points. (b) d_{vdW} versus Φ for all differentiable components under the assumption that $d(\text{C}_{\text{peryl}}) \approx d(\text{C}_{\text{funct}}) \approx d(\text{C total})$ for PTCDA on Au(111),⁵⁴ Cu(111),⁴³ and Ag(111).⁵⁵ Dark gray: C_{peryl}, light gray: C_{funct}, red: O_{carb}, blue: O_{anhyd}. Lines are guides to the eye. The vdW radii of C and O are indicated by black dashed lines, representing the metal–molecule vdW contact distance. In some cases, error bars are so small that they are almost hidden by the data points. An error of $\Delta\Phi_{\text{ave}} = \pm 0.15$ eV applies to the Φ values on average (see also Table 7.5). Note that in (b), in contrast to (a), the respective data for PTCDA/Cu₃Au(111) in the final state, for PTCDA/Ag(111) in the disordered phase (LT),^{55,140} and for PTCDA/K:Ag(110) have been omitted for clarity. Adapted and expanded from Ref. 55.

which is postulated at this point.^{d)} This charge transfer has been evidenced from photoemission results (see Sec. 7.4 below) and leads to a (partial) filling of the PTCDA LUMO, which is the acceptor state in terms of the Newns-Anderson model. Due to the interaction with metal states, the LUMO is lowered in energy along the effective image potential (and also subject to broadening) for smaller distances from the surface, and becomes populated by metal electrons when it falls below the Fermi energy E_F . This scenario has been illustrated in Fig. 2.2(b) already. Since the energetic position of the LUMO for large d or d_{vdW} values, respectively, that is, for the free molecule, is given by the electron affinity $E_A = E_{\text{vac}} - E_{\text{LUMO}}$ and thus fixed, the variable parameter in the Newns-Anderson model is Φ . For smaller Φ values the occupation of the LUMO will occur earlier, roughly speaking, that is, at larger distances d of the molecule from the surface. This results in a stronger surface bonding which pulls the molecule closer to the surface, as expressed by the decrease in d_{vdW} .⁵⁵ Because the LUMO is mainly located on the perylene core of PTCDA [see Fig. 7.5(b)], this Newns-Anderson-like description of the PTCDA–coinage metal surface bonding addresses the bonding via the perylene core. The respective trends for the O and C_{funct} atoms, that is, $d_{\text{vdW}}(\text{O})$ and $d_{\text{vdW}}(\text{C}_{\text{funct}})$ versus Φ , will be elucidated separately in Sec. 7.5. Since the above description applies to PTCDA adsorption on *all* coinage metal surfaces where XSW data is available, the metal-to-molecule charge transfer is identified as an “universal” bonding channel whose relevance, however, varies for the different substrates, i.e., as a function of Φ .

The Newns-Anderson model has been used to describe, in particular, the interactions of the metal sp states with adsorbed molecules (see also Sec. 2.1.2).^{14,72} In principle, interactions with metal d states are also considered within the framework of this model.^{14,72} The Hoffmann model states that the energetic stabilization upon the hybridization of metal and molecular states is larger if the involved states have similar energies (see also Sec. 2.1.3).^{12,13} Thus, according to the Hoffmann model, an interaction of the PTCDA frontier orbitals with the low-lying d states of the metal substrate, which are located well more than 2 eV below the Fermi level,^{59,60,395} appears rather implausible, especially in the cases of Au and Ag substrates.^{e)} Therefore, one may conclude at this point that the perylene core–metal interaction mainly relies on the contribution from metal sp states. Our DFT calculations for PTCDA on low-index Ag surfaces, however, have verified by means of the projected density of states (PDOS, not shown) that, independent of the substrate face, Ag s , p , as well as d states contribute to the metal/molecule hybrid state(s) which is (are) formed upon this interaction. Therefore, a clear differentiation between interactions of PTCDA (frontier) orbitals with metal sp states and with metal d states and thus an explanation of the experimental findings solely within the framework of one individual model may not be possible here. We note that interactions with metal d states may presumably allow to explain apparent contradictions between the XSW results discussed here and reported UPS results which will be discussed in Sec. 7.4 below.⁵⁵ In particular, the more pronounced altering of the valence band structure for PTCDA/Cu(111) in comparison to PTCDA/Ag(111)^{59,60} is *not* accompanied with a smaller adsorption height $d_{\text{vdW}}(\text{C total})$. This will be explained by a non-increased or even less bonding character of the metal/molecule hybrid state(s) as a consequence of the increased contribution of metal d states in the case of PTCDA/Cu(111).

^{d)}Note again that PTCDA is an electron acceptor molecule due to its high electron affinity of about 4.1 eV (determined for PTCDA in condensed films).¹⁰²

^{e)}The theoretically obtained d -band centers ϵ_d of the pure elements are $\epsilon_d(\text{Au}) = -3.56$ eV, $\epsilon_d(\text{Ag}) = -4.30$ eV, and $\epsilon_d(\text{Cu}) = -2.67$ eV, respectively.^{82,96}

Determining parameters beyond the substrate work function

So far, we have only considered the work function of the clean substrate surface as the determining parameter for the adsorption height of the PTCDA molecule. Indeed, a remarkable correlation has been observed. However, this explanatory approach may be oversimplified for the presumably very complex bonding situation at the metal/organic interface. Hence, the influence of further parameters will be regarded here, as well. Among these are the lateral arrangement of the molecules on the surface and the size of the extended π system of the aromatic adsorbate molecule, for example. Concerning the lateral arrangement, we find that the actual molecular motif, that is, a herringbone, T-shape, or brick-wall arrangement of the PTCDA molecules on the surface, does *not* affect the correlation of $d_{\text{vdW}}(\text{C}_{\text{peryl}})$ and Φ such that substantial deviations from the linear relationship between the two may be discerned. This is also deduced from the finding that the adsorption heights $d_{\text{vdW}}(\text{C}_{\text{peryl}})$ for PTCDA on Ag(111) in the ordered (RT) and the disordered (LT) phase agree within only $0.05(2)$ Å.⁵⁵ The registry with the substrate, i.e., being commensurate or incommensurate to the substrate surface, does not lead to a modification of the correlation, either. This is apparent from the fact that *all* adsorption heights under discussion here [except for that on $\text{Cu}_3\text{Au}(111)$ in the final, Cu-rich state; see above] follow the linear trend in Fig. 7.6(a) although PTCDA forms commensurate superstructures on the Ag surfaces ($\Phi \lesssim 4.9$ eV) while incommensurate superstructures are present of the (pure or alloyed) Cu and Au surfaces. Along with the molecular arrangement, however, the intermolecular interactions are altered, especially in those cases where the structure deviates from the preferred HB arrangement (see Sec. 7.1). We conclude at this point that intermolecular interactions only have a minor impact on the ‘charge-transfer’ bonding channel (see also below) which presumably determines the adsorption height of the perylene core (and vice versa). We further conclude that the surface bonding via the perylene core is *delocalized* in the sense that there is not *one* defined interaction between one individual surface atom and one individual C atom in PTCDA common to *all* molecules on the surface, as would be the case between two binding partners in a covalent bond, for example.

Note, however, that the adsorption height of the perylene core in PTCDA *slightly* decreases in the (partial) absence of intermolecular interactions, in particular, of hydrogen bond-like interactions, as the example of PTCDA/Ag(111) in the disordered and the ordered phase shows [$\Delta d = -0.05(2)$ Å]. Yet, the adsorption configuration, that is, the intramolecular distortions are affected to a larger extent than the $d(\text{C}_{\text{peryl}})$ values by the intermolecular interactions. This will be elucidated in detail in Sec. 7.6.

The example of NTCDA on Ag(111) illustrates that the size of the extended π system affects the bonding via the aromatic core.^{41,42} The NTCDA molecule is similar to PTCDA but has a naphthalene core instead of perylene and thus a smaller π system (10 versus 20 C atoms in the aromatic core). Note that the electron affinity of NTCDA agrees with that of PTCDA within 0.1 eV ($E_{\text{A}} = 4.0$ eV for NTCDA⁵²¹ versus $E_{\text{A}} = 4.1$ eV for PTCDA¹⁰²). Hence, the acceptor strength of both molecules is essentially identical. An adsorption height of $3.00(2)$ Å has been determined by Stadler *et al.* with XSW for the C backbone of NTCDA while the O_{carb} and O_{anhyd} atoms are located at a heights of $2.75(3)$ Å and $3.00(2)$ Å above the surface Bragg plane, respectively.⁴² Thus, the adsorption height of the C backbone is $0.14(2)$ Å larger than for PTCDA/Ag(111).⁵⁵ Obviously, a smaller π system results in a larger adsorption height on the same surface (with the same Φ value, of course) even for (almost) identical values of E_{A} .

Note that the above trend apparently holds for unsubstituted (planar) aromatic hydrocarbons, too, where potential effects by the presence of functional groups (see below) can be excluded. For example, adsorption heights of $d = 3.47(16)$ Å and $d = 3.01(4)$ Å have been determined with

XSW for Pen⁵²² and Diindenoperylene⁵²³ (DIP) on the Ag(111) surface, respectively.^{f)} Here, the larger π system in DIP (32 versus 22 C atoms in the aromatic core of Pen) leads to a decrease in d of 0.46(16) Å. Yet, there are also examples which show the opposite trend: Pen and DIP on Cu(111) adsorb at d values of 2.34(2) Å³⁸ and 2.51(3) Å,⁵²³ respectively. Furthermore, a correlation of $d_{\text{vdW}}(\text{C})$ and Φ , similar to that for PTCDA on coinage metal surfaces, does not apply to DIP adsorption on the (111) surfaces of Cu, Ag, and Au.⁵²³ Thus, a description of surface bonding of large organic molecules on metal surfaces within the framework of the Newns-Anderson model may not be of general validity. Nonetheless, it applies well to the present case of PTCDA adsorption on coinage metal surfaces.

Role of the functional groups

Although we are discussing the surface bonding via the perylene core in this section, the role of the functional groups in the surface bonding mechanism needs to be considered here, too. This role is twofold: On the one hand, local interactions between atoms within the functional groups of PTCDA and the surface may evidently evolve, as the adsorption configurations of PTCDA on the Ag surfaces reveal. This will be discussed in Sec. 7.5. On the other hand, an indirect effect of the functional groups on the perylene core bonding may also be anticipated.¹²² We propose that the functional groups facilitate the metal-to-molecule charge transfer by enhancing the electron acceptor strength due to their electron-withdrawing effect.³⁰ This electron-withdrawing effect is caused by both the higher electronegativity χ of the O atoms in comparison to C atoms,^{g)} and the conjugation of the π bonds within the perylene core and the functional groups which allows for the mesomeric or resonance stabilization of potential positive charges on the molecule.³⁰ Indeed, the electron affinity E_A of the PTCDA molecule is larger than that of unsubstituted perylene ($E_A = 4.1$ eV for PTCDA¹⁰² in a condensed film versus $E_A = 2.5$ eV for perylene⁴⁷⁹).

The above conclusion also reflects in the adsorption heights which have been determined for other large aromatic molecules with XSW. For example, the adsorption height of the C atoms in pentacene (Pen) on Ag(111)⁵²² is $d = 3.47(16)$ Å and thus exactly agrees with the sum of the vdW radii of Ag and C atoms (see Table 7.4).¹⁴¹ Because both pentacene and perylene consist of five annulated aromatic, six-membered rings, we speculate that perylene exhibits a similar adsorption height, being several tenths of an ångström higher than that of the functionalized perylene molecule PTCDA on Ag(111), and that it hence less strongly bounds to the surface. This expectation is reasoned by the lower electron affinity and the thus smaller metal-to-molecule charge transfer, in line with the above conclusion. Our argumentation is further supported by the fact that perfluorinated pentacene (PFP) adsorbs at a height of $d = 3.16(6)$ Å (for both C and F atoms) on the Ag(111) surface and thus about 0.3 Å lower than native pentacene.³⁹ Apparently, the insertion of the electronegative F atoms^{h)} into the pentacene molecule increases the surface bonding strength due to their electron-withdrawing effect. In agreement with the above-described Newns-Anderson model, an enhanced metal-to-molecule charge transfer is anticipated which is caused by the almost 1.2 eV higher E_A value of PFP in comparison to Pen (the free molecules are compared here).⁴⁰ Hence, we conclude that functional atoms or groups, that is, anhydride groups in the case of PTCDA, can indeed participate in the surface bonding in an *indirect* manner even if no *direct* bonding channel is related to them.

^{f)}XSW data for native perylene on coinage metal surfaces is not available.

^{g)}Several different definitions of the electronegativity χ have been established.^{85,146} According to the formalism proposed by Allred and Rochow,⁵²⁴ for example, the χ values of C and O amount to 2.50 and 3.50.^{146,524}

^{h)}The electronegativity χ of F amounts to 4.10 according to the formalism proposed by Allred and Rochow, for example.^{146,524}

We need to admit, however, that the role of heteroatoms and functional groups within an organic molecule with regard to the surface bonding is not unique but may be influenced by other parameters, such as the chemical nature of the surface atoms. For Pen and PFP on the Cu(111) surface,³⁸ for example, a reversed effect for the adsorption heights has been found in comparison to the behavior on the Ag(111) surface.^{39,522} In particular, a 0.64(7) Å *larger* adsorption height has been found with XSW for the perfluorinated molecule PFP on Cu(111) than for native Pen³⁸ while the adsorption height is *smaller* by 0.31(17) Å on Ag(111).^{39,522} These findings for PFP/Cu(111) and Pen/Cu(111) are in contradiction to the so-far employed description of the bonding channel on the aromatic core (i.e., the pentacene core here and the perylene core in the case of PTCDA) in terms of the Newns-Anderson model: Due to high electronegativity of F^{146,524} and the thus higher electron affinity (in magnitude) of PFP as compared to Pen,⁴⁰ a smaller adsorption height is expected. A potential reason for this discrepancy may be intramolecular dipoles which are induced by the molecular distortion of PFP upon adsorption [the F atoms in PFP on Cu(111) are located 0.1 Å further away from the surface than the C atoms while the molecule remains planar on Ag(111)].^{38,39} Only recently, however, new XSW data regarding Pen/Ag(111) have been published by Duhm *et al.*,⁵²⁵ yielding substantially different results from those reported earlier by Hauschild *et al.*⁵²² According to these recent results, the adsorption height on the Ag(111) surface is also *smaller* for Pen than for PFP [by 0.04(8) Å to 0.18(8) Å depending on the Pen coverage],^{39,525} in agreement with the behavior on Cu(111). In this case, the role of heteroatoms and functional groups within an organic molecule with regard to the surface bonding apparently depends on *their* intrinsic chemical properties rather than on those of the surface (atoms).

7.4 Evidences for metal-to-molecule charge transfer from photoemission and DFT

In the previous section, we have already proposed a metal-to-molecule charge transfer as a relevant bonding channel for PTCDA on coinage metal surfaces. The occurrence of this charge transfer will now be evidenced in the discussion of our photoemission and DFT results in the context of previously reported results.

Adsorption-induced changes in the valence band structure

UP spectra of PTCDA (sub-)monolayers on the Au(111),⁶⁰ Ag(111),^{59,60,140} Ag(110),⁵⁹ and Cu(111) surfaces⁶⁰ have been reported. In addition, STS data are available for PTCDA on Au(111)^{125,126} and Ag(111).^{124,140} These data have been reviewed in Sec. 2.2.2 already. In essence, the UP spectra of PTCDA on the Ag and Cu surfaces indicate a hybridization of molecular states with metal states and chemisorptive bonding.^{59,60} In particular, a LUMO-derived peak (referred to as former LUMO or F-LUMO in the following) has been observed below the Fermi level at increasing binding energies in the sequence Ag(111) (ordered RT phase, $E_b = 0.3$ eV),⁵⁹ Ag(110)⁵⁹ ($E_b = 0.6$ eV) and Ag(111)¹⁴⁰ (disordered LT phase, $E_b = 0.6$ eV), and Cu(111)⁶⁰ ($E_b = 0.8$ eV). Besides, the HOMO-(F-)LUMO gap has been shown to reduce from 1.3 eV to 0.9 eV in the same series.^{59,60} Hence, the peak shifting is of differential kind. Note that for PTCDA/Au(111) an F-LUMO peak has not been observed.⁶⁰ The presence of the F-LUMO peak has been interpreted as a proof of the metal-to-molecule charge transfer which leads to a partial [on the Ag(111) surface in the ordered phase] or complete filling [in all other cases] of the (former) PTCDA LUMO.^{59,60}

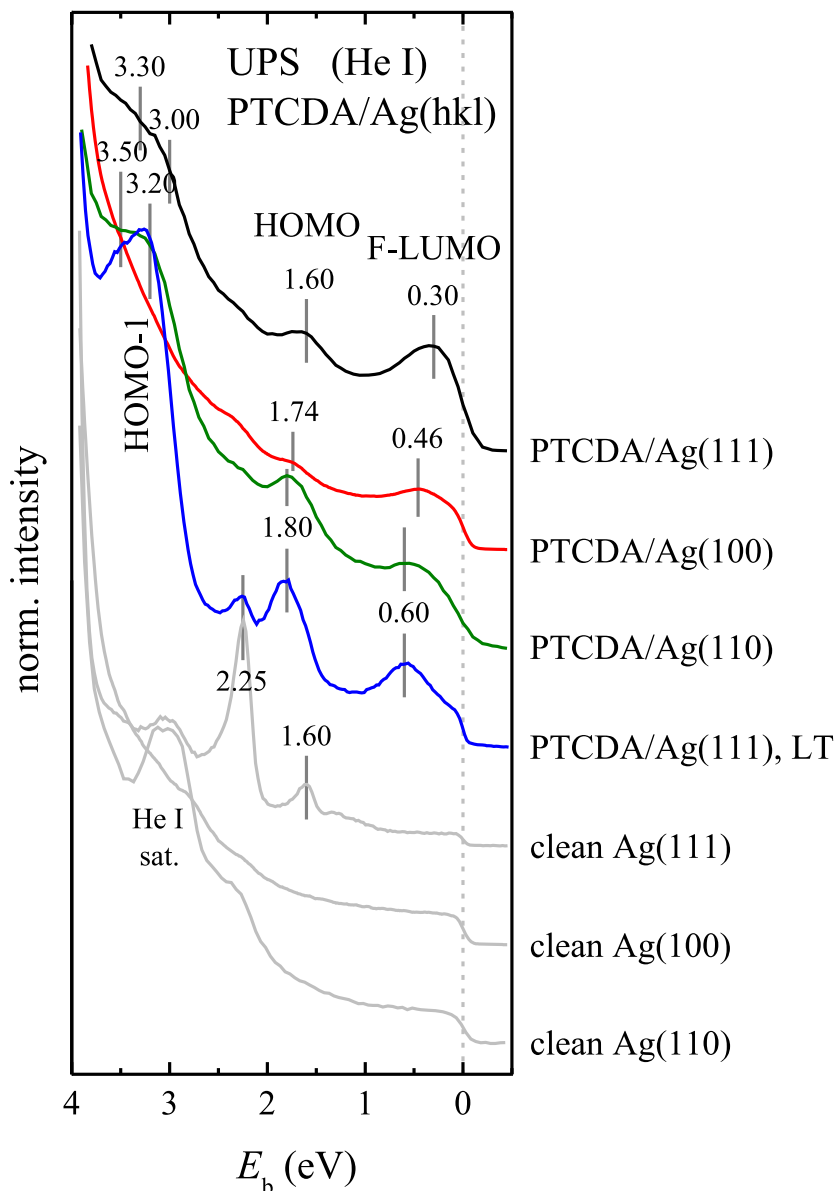


FIG. 7.7. UP spectra for PTCDA in the (sub-)monolayer regime on the low-index Ag surfaces. The UP spectra for PTCDA on the Ag(111) and Ag(110) surfaces, as well as for the clean Ag(110) surface, have been taken from Refs. 59 and 140. The UP spectrum for the clean Ag(111) surface was kindly provided by the authors of Ref. 140. All spectra have been acquired at an angle of 45° with respect to the surface normal employing He I radiation, except for those of PTCDA/Ag(100) and the clean Ag(100) surface where the detection angle was 0° (normal emission). The presented UPS data have been carefully smoothed. The PTCDA coverage amounted to 1 ML in the case of PTCDA/Ag(111) and PTCDA/Ag(110), and 0.7 ML in the case of PTCDA/Ag(100), respectively. Peak positions assigned to the maxima are marked by gray lines. Values from the literature have been expanded concerning the number of digits from the actually reported values because a similar accuracy as in our experiments is assumed. In the case of the clean Ag(111) surface, the origin of the spectral features at E_b values of 1.60 eV and 2.25 eV is not known.³³⁴ The peak at about 3.1 eV in the spectra of the clean Ag(111) and Ag(110) surfaces is a He I satellite feature of the very intense d -band peak which originates from the $\text{Ag}4d$ states.^{59,334} The position of the Fermi level is marked by a gray dashed line.

Within the framework of the present work, we have amended the available UPS data by the UP spectra for PTCDA/Ag(100) in the (sub-)monolayer regime. Figure 7.7 contrasts the our data with the UPS data of PTCDA on the other low-index Ag surfaces.^{59, 140} Indeed, a F-LUMO peak has been observed at $E_b = 0.46$ eV also for PTCDA/Ag(100). A detailed analysis has proven that this peak is located completely below the Fermi level (see Sec. C.3.2 in the appendix of the present work). Thus, the F-LUMO state is completely filled, in contrast to the partial filling in the case of PTCDA/Ag(111) [unless otherwise specified, we always refer to the ordered RT phase of PTCDA on Ag(111) in the following].⁵⁹ That is, the metal-to-molecule charge transfer is enhanced in comparison to the situation on the Ag(111) surface, in full agreement with the anticipated trend on the basis of the determined adsorption heights and the Newns-Anderson-like picture of the surface bonding described in Sec. 7.3.

The binding energy of the F-LUMO peak in the case of PTCDA/Ag(100) is smaller than that in the case of PTCDA/Ag(110) (see Fig. 7.7),⁶⁰ indicating a less pronounced hybridization with metal states. Again, this is in agreement with the above interpretation of the bonding mechanism (see Sec. 7.3). Also, the differential shifting of the peaks which originate mainly from the PTCDA valence states, that is, the reduction of the HOMO–(F-)LUMO gap which runs as 1.30 eV, 1.28 eV, and 1.20 eV in the series PTCDA/Ag(111),⁵⁹ PTCDA/Ag(100), and PTCDA/Ag(110),⁵⁹ further confirms the increasing degree of hybridization between molecular and metal states and the validity of the Newns-Anderson model which indeed predicts a decreasing HOMO–LUMO gap.⁸⁶

For PTCDA on Cu(111), the altering in the valence structure is even more pronounced than for PTCDA on the low-index Ag surfaces [$E_b^{\text{F-LUMO}} = 0.8$ eV and a HOMO–(F-)LUMO gap of 0.9 eV;⁶⁰ see also above]. However, we have pointed out in Sec. 7.3 that a lower degree of chemisorptive bonding for PTCDA/Cu(111) in comparison to the bonding of PTCDA on the low-index Ag surfaces is anticipated from the corresponding d_{vdW} values. We explain this apparent contradiction in the experimental findings with the different contributions of the metal states to the respective metal/molecule hybrid state, i.e., the (PTCDA) F-LUMO state. On the Ag surfaces, the metal s -band contributes to $\approx 10\%$ to the F-LUMO, as has been estimated from ARUPS measurements.¹²³ In the case of PTCDA on Cu(111), also metal d states may contribute to the F-LUMO state because their separation in energy from the LUMO of free PTCDA is smaller than for the d states of the Ag substrates.^{12, 13} The d states are located at binding energies above ≈ 2 eV for Cu(111)⁶⁰ and above ≈ 4 eV for the Ag surfaces.^{59, 60} Apparently, the hybridization of the PTCDA LUMO with metal d states (here: Cu3d states), in contrast to the hybridization with metal sp states (see Sec. 7.3), contributes only to a minor extent to the bonding distance of the PTCDA molecule,⁵⁵ and in that an increased d_{vdW} value is realized [$\Delta d_{\text{vdW}}(\text{C total}) = +0.12(2)$ Å for PTCDA on Cu(111) in comparison to Ag(111)]. Hence, we conclude that the admixture of d states, which is assumed to be present for PTCDA/Cu(111), does not lead to an increased bonding character (but maybe to a decreased bonding character) of the metal/molecule hybrid state, thereby explaining the larger d_{vdW} value on Cu(111) in comparison to Ag(111). Looking at it the other way round, we conclude again at this point that the bonding distance of PTCDA is largely determined by the admixture of metal sp states to the metal/molecule hybrid state, in accordance with the Newns-Anderson-like picture of the surface bonding elucidated in Sec. 7.3 above.

Quantification of the metal-to-molecule charge transfer

A complete filling of the F-LUMO state for PTCDA on Ag(100), Ag(110)⁵⁹ and Cu(111)⁶⁰ implies that the metal-to-molecule charge transfer Δq amounts to 2 electrons, and that the PTCDA molecules are thus twice negatively charged. Yet, by means of a Mulliken population analysis,⁵²⁶ DFT calculations have revealed a net charge of $-0.41 e$ per PTCDA molecule on Ag(110).¹⁵⁴ This

is indicative of substantial charge transfer to occur also *from* the molecule *to* the metal,^{97,154} e.g., via local interactions between C and O atoms in PTCDA and substrate surface atoms, as will be discussed in Secs. 7.5 and 7.6 below.

For PTCDA/Ag(111), where the F-LUMO is (only) partially filled,⁵⁹ net charges of $-0.35 e$ to $-0.47 e$ per molecule have been determined by DFT calculations [As for PTCDA/Ag(110), the latter value has been obtained by a Mulliken population analysis].^{97,153} Note that the reported value for PTCDA/Ag(110) is well within this range.¹⁵⁴ For PTCDA/Cu(111), an essentially identical Mulliken charge of $-0.50 e$ has been obtained¹⁵³ although the F-LUMO is fully below the Fermi level (see above) and thus expected to be fully occupied.¹⁵³ On the Au(111) surface, the net charge per PTCDA molecule is almost negligible ($-0.05 e$).¹⁵³

In order to clarify the trend in the net charges Δq as a function of the surface reactivity, we have performed a Bader analysis^{504,505} of the electron density $\rho(\mathbf{r})$ for PTCDA on the low-index Ag surfaces.ⁱ⁾ More open surfaces are considered to be more reactive due to the lower coordination number (CN) of the surface atoms and exhibit lower work functions.^{62,63,201} Note that *negative* values of Δq refer to a charge transfer, i.e., an *electron* transfer, from the metal to the molecule, that is, they refer to *negative* (partial) charging of adsorbed PTCDA. Indeed, we have found an increasing metal-to-molecule charge transfer, i.e., decreasing Δq values, per PTCDA molecule in the sequence Ag(111), Ag(100), Ag(110), namely, values of $-1.00 e$, $-1.33 e$, and $-1.35 e$, respectively (see also Table 7.7 below). Note that Bader analysis tends to overestimate the absolute charges.⁵³¹ The general trend in the Δq values, however, should remain unaffected thereby. The charge that is donated from the metal to the PTCDA molecule accumulates in a metal/molecule hybrid state, which very much resembles the LUMO of the free molecule [see also Fig. 7.5(b) for a representation on the LUMO].^{j)} This charge accumulation is visualized in terms of $\Delta\rho(\mathbf{r})$ plots in Fig. 7.12, third row, below. Further consequences of the LUMO filling relevant to the surface bonding which are beyond electrostatic interactions will be discussed in Sec. 7.6. At this point, we state that our DFT results concerning the metal-to-molecule charge transfer support the above conclusions drawn from the UPS data.

Indications for a metal-to-molecule charge transfer can also be deduced from the work function shifts $\Delta\Phi_{\text{PTCDA}}$ upon PTCDA adsorption on the coinage metal surfaces. Respective available values have been compiled in Table 7.5 above. $\Delta\Phi_{\text{PTCDA}}$ increases by 0.53 eV, i.e., from -0.40 eV to $+0.13$ eV, in the series Au(111),⁶⁰ Cu(111),⁶⁰ Ag(111),⁵⁹ and Ag(100), and thus exhibits the reversed trend in comparison to the respective d_{vdW} values. This trend in $\Delta\Phi_{\text{PTCDA}}$ is explained as follows. Due to the negatively charged molecular layer above the surface, the energetic cost increases for the excitation of metal electrons from the Fermi edge to the vacuum level. This effect is more pronounced for a larger magnitude of charge transfer. Thus, more positive values of $\Delta\Phi_{\text{PTCDA}}$ are expected for more negative values of Δq (and vice versa), as is indeed the case here.

ⁱ⁾The Bader analysis^{504,505} derives the atomic (partial) charges from the electron density distribution $\rho(\mathbf{r})$ while the Mulliken population analysis^{526,527} relies on the basis functions, which are used to represent the wave function, and on the density matrix.⁵²⁸ Thus, the Mulliken procedure exhibits a strong dependence on the employed basis set.⁵²⁸⁻⁵³⁰

^{j)}A more detailed analysis of the charge transfer reveals that the electrons donated from the metal indeed accumulate on both the perylene core and the functional groups. The fractions of the net charges Δq which are located on the functional groups amount to 37 %, 38 %, and 42 % in the series of PTCDA on Ag(111), Ag(100), and Ag(110), respectively, and thus are higher than may be anticipated solely from the appearance of the PTCDA LUMO. The electron-withdrawing effect of the functional groups³⁰ as well as local interactions with the surface may play a role here.

The Helmholtz equation allows to calculate the surface dipole μ from the work function shift $\Delta\Phi_{\text{PTCDA}}$ via the relation:^{38,62,201,532}

$$\Delta\Phi_{\text{PTCDA}} = \frac{e N_{\text{PTCDA}} \theta_{\text{PTCDA}} \mu}{\epsilon_0}, \quad (7.5)$$

where e is the elementary charge, N_{PTCDA} is the surface density of PTCDA molecules for a nominal monolayer on a given (coinage metal) surface, θ_{PTCDA} is the surface coverage of PTCDA in percent of a full monolayer, and ϵ_0 is the vacuum permittivity. Using the relation:^{62,201}

$$\mu = -\Delta q d, \quad (7.6)$$

the charge transfer Δq can be obtained. The parameter d denotes the charge separation and is given by $d \approx 2d(\text{C}_{\text{peryl}})$ in the present case because the (partial) charge on the adsorbed molecule at an adsorption height of $+d(\text{C}_{\text{peryl}})$ with respect to the surface induces an image charge of opposite polarity below the surface, i.e., within the subsurface layers, at a (effective) position of $-d(\text{C}_{\text{peryl}})$.⁶² Note that the dipole moment μ is defined as pointing from positive to negative charge here.⁶² Therefore, a positive μ value refers to an increase in Φ upon PTCDA adsorption (by electron accumulation above the substrate surface, $\Delta\Phi > 0$), and denote an increased metal-to-molecule charge transfer, that is, an increased electron transfer ($\Delta q < 0$). Employing the respective values for $\Delta\Phi_{\text{PTCDA}}$, θ_{PTCDA} (see Table 7.5), N_{PTCDA} [$8.38 \times 10^{13} \text{ cm}^{-2}$ on Ag(111)⁹⁸ and $7.49 \times 10^{13} \text{ cm}^{-2}$ on Ag(100)¹²⁰], and $d(\text{C}_{\text{peryl}}) \approx d(\text{C total})$ (see Table 7.1), surface dipoles of $\mu = +0.32 \text{ D}$ and $\mu = +0.31 \text{ D}$ are obtained for PTCDA/Ag(111) and PTCDA/Ag(100), for example, which nominally correspond to Δq values of $-0.16 e$ and $-0.18 e$, respectively. Although the so-obtained values are comparably small and deviate by about $1 e$ from our calculated net Δq values (see Table 7.7), they follow the anticipated trend of being larger in the case of the more open Ag(100) surface. The discrepancies in the absolute values may be ascribed to the potentially inadequate choice of the d values, for example.

The substantial deviation between the Δq values calculated from the work function shifts and those obtained from DFT calculations also results from the fact that the above deduction does not account for the push-back effect⁵³³ (also known as pillow effect^{534,535}). The push-back effect originates from the repulsion of the metal surface electrons by the electrons of the adsorbed PTCDA molecules which reduces the electron ‘overspill’ into the vacuum and thereby also the surface dipole, with the consequence of a lower Φ .^{62,477,533,536,537} In the case of molecular adsorption on the Au(111) surface, for example, the lowering of Φ due to the push-back effect typically amounts to values in the range of 1 eV .^{477,478} Because the push-back effect counteracts the charge-transfer induced increase of the work function, the above Δq values obtained from DFT are systematically too large. Δq values derived for PTCDA on Au(111) and Cu(111) employing Eqs. (7.5) and (7.6) are in fact positive because $\Delta\Phi_{\text{PTCDA}} < 0$ (see Table 7.5). Obviously, the push-back effect outweighs the electron transfer here. Hence, disregarding the push-back effect is a gross simplification of the actual electronic modifications at the metal/organic interface. Nonetheless, the general trend observed for $\Delta\Phi_{\text{PTCDA}}$ is in line with our hitherto conclusions.

Evidence of metal-to-molecule charge transfer by core level spectroscopy

UPS data in conjunction with our DFT results have provided strong evidence of the metal-to-molecule charge transfer for PTCDA adsorption on the low-index Ag surfaces and on the Cu(111) surface. For PTCDA/Cu₃Au(111), however, UPS data are not available. Nevertheless, in our discussion of the surface bonding mechanism for PTCDA on coinage metal surfaces in Sec. 7.3,

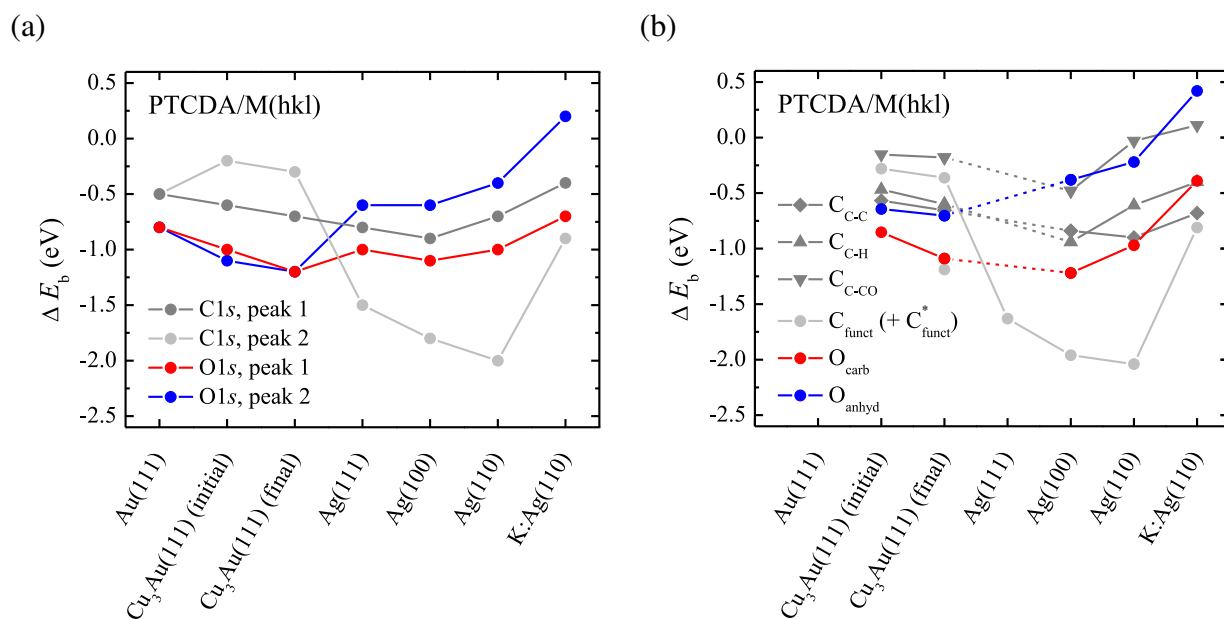


FIG. 7.8. Peak shifts ΔE_b in XPS for the C1s and O1s levels of PTCDA in the (sub-)monolayer regime on various coinage metal surfaces.^{43,59,117,307,468} Graphical representation of the data compiled in Table 7.6. Lines are guides to the eye. (a) Effective ΔE_b values for the peaks at lower and higher E_b in the C1s and O1s XP spectra which can roughly be understood as representing the C_{peryl} and C_{funct} components of the C1s level, and as representing the O_{carb} and O_{anhyd} components of the O1s level. (b) ΔE_b values for the individual components contributing to the C1s and O1s XP spectra (where available). Dark gray: C_{peryl} , light gray: C_{funct} , red: O_{carb} , blue: O_{anhyd} . \blacklozenge , \blacktriangle , and \blacktriangledown symbols represent the $\text{C}_{\text{C-C}}$, $\text{C}_{\text{C-H}}$, and $\text{C}_{\text{C-CO}}$ atoms within the perylene core of PTCDA, respectively. Note that in the case of PTCDA/Ag(111) the ΔE_b values for the individual C_{peryl} components are not available because fitting models for the reported monolayer XP spectra are missing.^{59,468}

we have postulated a (small) electron transfer from the metal to the molecule also for PTCDA/ $\text{Cu}_3\text{Au}(111)$, especially in the final state (see also Sec. 6.7), in contrast to the situation of PTCDA/Au(111) where an essentially physisorptive bonding with is assumed^{59,60,153} and the overall adsorption height is larger.⁵⁴ We will now gain evidence of a (partial) metal-to-molecule charge transfer also on this surface from the peak shifts in XPS. In the following, we will demonstrate that the individual binding energy shifts ΔE_b observed in XPS for PTCDA (sub-)monolayers in comparison to the multilayers correlate (qualitatively) with the metal-to-molecule charge transfer and charge redistributions Δq at the interface upon adsorption, as obtained from Bader analysis for PTCDA/Ag(*hkl*).^{504,505} This correlation is remarkable because the observed XPS shifts are a combination of initial and final state effects^{157,202} while the Bader analysis only includes initial state effects.

First, we will discuss the observed trends in the ΔE_b values as a combination of screening effects and shifts due to the altered chemical environment. The contributions from the chemical shifts become more important with increasing metal/molecule interaction. As a general trend, an increased metal-to-molecule charge transfer leads to a smaller binding energy, i.e., to a more negative ΔE_b . As will be elucidated below, this particularly holds for the C_{funct} component. Schöll *et al.* have attributed (large) shifts of several hundred milli-electronvolts (up to almost 2 eV in extreme cases) towards lower E_b values in the XP spectra of NTCDA/Ag(111) to well or fully screened core levels

TABLE 7.6. Peak shifts ΔE_b in XPS for the C1s and O1s levels of PTCDA in the (sub-)monolayer regime on various coinage metal surfaces. The ΔE_b values have been deduced (with an accuracy of about ± 0.1 eV) from the observed peak positions in the (sub-)monolayer regime (with θ_{PTCDA} as the nominal PTCDA coverage) with respect to those in the multilayer regime, i.e., $\Delta E_{b,i} = E_{b,\text{mono},i} - E_{b,\text{multi},i}$. The peaks at lower and higher E_b in the C1s and O1s XP spectra are labeled 1 and 2, respectively, and can roughly be understood as representing the C_{peryl} and C_{funct} components of the C1s level, and as representing the O_{carb} and O_{anhyd} components of the O1s level. Where available, the shifts for the individual components contributing to the C1s and O1s XPS levels are given explicitly. Note that for PTCDA on Au(111), $\text{Cu}_3\text{Au}(111)$, Ag(111), and Cu(111), respectively, all $E_{b,\text{mono},i}$ values have been referenced against the reported peak positions in PTCDA multilayers on Ag(111),^{59,307} because respective multilayer XPS data for the other surfaces are not available (t.w. = this work, n.a. = not available/applicable).

	Au(111)	$\text{Cu}_3\text{Au}(111)$ (<i>initial</i>)	$\text{Cu}_3\text{Au}(111)$ (<i>final</i>)	Ag(111)	Ag(100)	Ag(110)	K:Ag(110)	Cu(111)	Cu (<i>polycryst.</i>)
θ_{PTCDA}	1 ML	0.8 ML	0.8 ML	0.9–1 ML	0.8 ML	0.9 ML	0.9 ML	1 ML	1 ML
Ref(s).	59	t.w.	t.w.	59,468	t.w.	t.w.	t.w.	43	117
	ΔE_b (eV) ^a	ΔE_b (eV) ^a	ΔE_b (eV) ^a	ΔE_b (eV) ^a	ΔE_b (eV)	ΔE_b (eV)	ΔE_b (eV)	ΔE_b (eV) ^a	ΔE_b (eV) ^b
C1s, peak 1	-0.5	-0.6	-0.7	-0.8	-0.9	-0.7	-0.4	0.3	-0.2
C1s, peak 2	-0.5	-0.2	-0.3	-1.5	-1.8	-2.0	-0.9	n.a.	n.a.
O1s, peak 1	-0.8	-1.0	-1.2	-1.0	-1.1	-1.0	-0.7	0.3	-0.5
O1s, peak 2	-0.8	-1.1	-1.2	-0.6	-0.6	-0.4	0.2	0.6	-0.1
$C_{\text{C-C}}$	n.a.	-0.57	-0.66	n.a.	-0.84	-0.90	-0.68	n.a.	n.a.
$C_{\text{C-H}}$	n.a.	-0.47	-0.60	n.a.	-0.94	-0.61	-0.40	n.a.	n.a.
$C_{\text{C-CO}}$	n.a.	-0.15	-0.18	n.a.	-0.48	-0.03	0.11	n.a.	n.a.
C_{funct}	n.a.	-0.28	-0.36	-1.63	-1.96	-2.04	-0.81	n.a.	n.a.
C_{funct}^*	n.a.	n.a.	-1.19 ^c	n.a.	n.a.	n.a.	n.a.	n.a.	n.a.
O_{carb}	n.a.	-0.85	-1.09	n.a.	-1.22	-0.97	-0.39	n.a.	n.a.
O_{anhyd}	n.a.	-0.64	-0.70	n.a.	-0.38	-0.22	0.42	n.a.	n.a.

^aPeak positions and binding energies for the C and O components of a condensed film of PTCDA molecules on the Ag(111) surface, with a coverage of 10 ML and well above, have been reported in Refs. 59 and 307, respectively. Here, these E_b values serve as a reference for the energetic positions of the respective XPS levels in the bulk phase and also in the multilayer regime on Au(111), $\text{Cu}_3\text{Au}(111)$, Ag(111), and Cu(111). Potential work function effects are neglected.

^bReferenced against the peak positions for the C and O components of a 35 ML thick PTCDA film on polycrystalline Cu, as reported in Ref. 117.

^cReferenced against the binding energy E_b for the C_{funct} component of a condensed film of PTCDA molecules on the Ag(111) surface, as reported in Ref. 307.

(due to the metal-to-molecule charge transfer; sometimes also referred to as “shake-down” satellites) of chemisorbed adsorbates.⁴⁶⁷ Furthermore, for PTCDA/Ag(111) in the monolayer regime, Häming *et al.* have observed asymmetric peak profiles and continuous satellite contributions in XPS besides peak shifts towards lower E_b , indicating a comparably strong adsorbate-substrate interaction.⁴⁶⁸ They have explained these findings by the presence of metal/molecule hybrid states around E_F which exhibit a considerable metallic character due to a strong adsorbate-substrate coupling.⁴⁶⁸

Table 7.6 reports the peak shifts ΔE_b for the C1s and O1s levels of PTCDA in the (sub-)monolayer regime on various coinage metal surfaces with respect to the multilayer regime. The ΔE_b values, that is, $\Delta E_{b,i} = E_{b, \text{mono}, i} - E_{b, \text{multi}, i}$, have been determined on the basis of our XPS data which have been reported in the course of the present work as well as by comparing the respective peak positions in XP spectra reported earlier by other authors (see Refs. 43, 59, 117, 307, 468). Note that the peak positions in the (sub-)monolayer regime have been referenced against the reported peak positions in PTCDA multilayers on Ag(111)^{59,307} in those cases where respective multilayer data are not existent, that is, for PTCDA on Au(111), Cu₃Au(111), and Cu(111). Note further that the E_b values observed in XPS of the individual components vary only within ± 0.2 eV for PTCDA multilayers on the low-index Ag surfaces [(111),³⁰⁷ (100), and (110); see also Sec. C.3.3 in the appendix of the present work], for which the respective XPS data are indeed available. Considering also the estimated error of ± 0.1 eV in the determination of the E_b values, this validates the above-described approach and renders the so-obtained ΔE_b values as well as the below-discussed trends meaningful.

Where available, the shifts for the individual components contributing to the C1s and O1s XPS levels are compared. If only two peaks could be separated in the XP spectra, the peak positions at lower and higher E_b in the C1s and O1s XP spectra (labeled 1 and 2, respectively, in Table 7.6; see Fig. 6.27 for exemplary XP spectra, for instance) are considered. They can roughly be understood as representing the C_{peryl} and C_{funct} components of the C1s level, and as representing the O_{carb} and O_{anhyd} components of the O1s level. Yet, the validity of these peak assignments to the individual components is much better in the case of the C1s level, as contrasting the respective ΔE_b values in Table 7.6 reveals (see also below). For better comparison of the ΔE_b values for PTCDA on the various coinage metal surfaces, Fig. 7.8 visualizes the data from Table 7.6 in a graphical representation. The respective data for PTCDA/Cu(111) and PTCDA/Cu (polycrystalline), however, has been omitted here. In the former case, positive values of ΔE_b have been found which is in contrast to the findings on all other surfaces. Thus, we postulate that this finding is due to an improper calibration of the binding energy scale for the XP spectra of PTCDA/Cu(111) in Ref. 43 rather than due to a chemical or physical origin. Indeed, negative ΔE_b have been determined for PTCDA on polycrystalline Cu (see Table 7.6). However, since the adsorption configuration in this case is unknown, these data are omitted for the discussion below, as well.

C1s peak shifts

We first focus on the shifts of the C1s peaks 1 and 2 [see Fig. 7.8(a)]. C1s peak 1, which represents the C_{peryl} atoms, shifts towards lower binding energies in the sequence Au(111), Cu₃Au(111) (initial state), Cu₃Au(111) (final state), Ag(111), and Ag(100). One reason for the lowering of E_b are screening effects due to the presence of the metal surface. In the final state, the core hole, which is created upon photoemission of a core level electron, is stabilized by its image charge, that is, by charge redistributions/polarization effects, in the substrate.⁵⁹ Yet, the screening effect of the metal is expected to be of similar magnitude on all coinage metal surfaces, assuming potential effects due to the variations in the adsorption heights (about 0.7 Å overall; see also Table 7.1) to

be of lower order. We have determined an increase in the C1s peaks 1 shift of about 0.4 eV, i.e., about a doubling, in the above series. Hence, additional effects must play a role here which, in turn, are a combination of initial and final state effects presumably. A lowering of E_b indicates an enhanced shielding of the nuclear charge and thus an increased electron density at (or near) the electron-emitting atom (initial state effect). Besides, the additional and *delocalized* electronic charge density based on the (partial) filling of the PTCDA LUMO (see above) may further screen and thus stabilize the photohole left behind by the emitted photoelectron, leading to a decreased binding energy (final state effect). Therefore, the observed trend of ΔE_b for C1s peak 1 may be well explained by the increasing metal-to-molecule charge transfer, i.e., an increasing filling of the PTCDA LUMO [which is mainly located on the perylene core, see Fig. 7.5(b)], in the above-stated series of Au(111), Cu₃Au(111) (initial state), Cu₃Au(111) (final state), Ag(111), and Ag(100). In turn, the ΔE_b (C1s, peak 1) values observed for PTCDA/Cu₃Au(111) in both states, especially in comparison to that for PTCDA/Au(111), prove (a) that a charge transfer indeed occurs from the metal to the molecule, and that (b) the magnitude of charge transfer increases upon transition from the initial to the final state, as has already been concluded from the lower d values in the latter case.

The smaller absolute value of ΔE_b (C1s, peak 1) in the case of PTCDA/Ag(110) than for PTCDA on the Ag(100) and Ag(111) surfaces is interpreted as being indicative of an *additional*, substantial charge transfer also from the molecule to the metal, that is, in the opposite direction as discussed for far. Thus, a *molecule-to-metal* charge transfer is postulated to occur via local interactions between C and O atoms in PTCDA and substrate surface atoms (see Secs. 7.5 and 7.6), in addition to the metal-to-molecule charge transfer due to the filling of the PTCDA LUMO with electrons from the metal substrate (see above). The further decrease in magnitude of ΔE_b (C1s, peak 1) for PTCDA/K:Ag(110) is ascribed to the presence of K atoms in the surface layer and will be elucidated in Sec. 7.7.

Considering the trend for ΔE_b (C1s, peak 2), which essentially represents the C_{funct} atoms, we have observed two regimes. On the (111) surfaces of Au and Cu₃Au(111), the C1s peak 2 exhibits (slightly) *smaller* shifts to lower binding energies than peak 1 (by +0.4 eV, see Table 7.6). On the low-index Ag surfaces, in contrast, the respective shift is *larger* by about 1 eV in comparison to C1s peak 1 [the discussion of the ΔE_b (C1s, peak 2) value for PTCDA/K:Ag(110) is postponed to Sec. 7.7]. This can be understood as follows. Since the contributions of the C_{funct} to the PTCDA LUMO is comparably small [see Fig. 7.5(b)], a (partial) filling affects the E_b values, and thus also the ΔE_b values, of these atoms to a lesser extent than those of the C_{peryl} atoms. However, where (comparably) strong chemisorptive bonding occurs, i.e., for PTCDA adsorption on the low-index Ag surfaces as evidenced by both XSW and UPS, substantial intramolecular structural and electronic modifications take place, leading to a hindered orbital conjugation between the p_z orbitals of C_{funct} and O_{carb}, for instance. Therefore, the electron-withdrawal by the more electronegative O atoms is reduced such that the electron density at the C_{funct} atoms is increased as compared to the situation in the free and non-distorted molecule. Higher electron densities at the electron-emitting atoms result in lower binding energies of the core electron. Thus, strongly negative values of ΔE_b (C1s, peak 2), and equivalently of ΔE_b (C_{funct}), are taken as a prove for substantial chemical bonding at the PTCDA/coinage metal interface.

This argumentation has already been employed for the bonding situation of PTCDA/Cu₃Au(111) in the final state (see Sec. 6.7). Figure 7.8(b) re-captures this point. Here, the ΔE_b values of the individual components are considered instead of ΔE_b of the two “effective” peaks in the respective C1s and O1s XP spectra. Notably, two data points are displayed for C_{funct} in the case of PTCDA/Cu₃Au(111) (final state) one of which corresponds to the C_{funct}^{*} component (at $\Delta E_b = -1.19$ eV). The C_{funct}^{*} component is understood as representing the C_{funct} atoms in PTCDA in a (strongly)

chemisorptively bound state on the $\text{Cu}_3\text{Au}(111)$ surface (see also Sec. 6.6.2). This conclusion is drawn from the fact that the $\Delta E_b(\text{C}_{\text{funct}}^*)$ value (being well below -1 eV) by tendency resembles the determined $\Delta E_b(\text{C}_{\text{funct}})$ values for PTCDA on the low-index Ag surfaces, where chemisorption is present.^{32,59,98} It is further supported by the only small difference of the obtained $d_{\text{vdW}}(i)$ values for PTCDA/ $\text{Cu}_3\text{Au}(111)$ in the final state in comparison to those for (chemisorbed) PTCDA/ $\text{Cu}(111)$, for example [which agree within maximal 0.08 Å; see also Sec. 7.3, in particular Fig. 7.6(a) on page 193 of the present work for a graphical illustration concerning the $d_{\text{vdW}}(\text{C}_{\text{peryl}})$ values].

Correlation between the XPS peak shifts and the local valence electron density

We will demonstrate now that the observed peak shifts ΔE_b can indeed be explained by an increased (valence) charge density at the electron-emitting atoms. For this purpose, we have analyzed the (averaged) local changes of the electron density, $\Delta q(i)$, for the individual components i in PTCDA on Ag surfaces by means of a Bader analysis.^{504,505} Table 7.7 compiles the determined values and contrasts them with the experimentally obtained $\Delta E_b(i)$ values. Figure 7.9 reports the identical data in a more illustrative manner. Note that the Δq values for the different atoms of one individual type are subject to a spreading. For all components except of the C_{peryl} atoms (in particular the $\text{C}_{\text{C-H}}$ atoms; see the footnotes of Table 7.7 for the explicit values), the spread is in a range of well below $\pm 0.010 e$, generally justifying the subsumption of the values for each individual atoms to averaged $\Delta q(i)$ values according to the respective components observed in the XP spectra of PTCDA, in particular in the multilayers regime.³⁰⁷

As a general trend, more negative values of ΔE_b correlate well with more negative Δq values. For example, the largest shift in magnitude of -2.04 eV in ΔE_b , that is, for C_{funct} in PTCDA/Ag(110), is correlated with the largest value in magnitude of $-0.091 e$ in Δq . For PTCDA/Ag(100), the largest values in magnitude of both parameters, being -1.96 eV and $-0.070 e$ for ΔE_b and Δq , respectively, are found for the C_{funct} atoms, too [with the exception of $\Delta q(\text{C}_{\text{C-H}}) = -0.084 e$]. Comparing $\Delta E_b(\text{C}_{\text{funct}})$ and $\Delta q(\text{C}_{\text{funct}})$ for PTCDA on the (111), (100), and (110) surfaces of Ag, in turn, shows that both parameters exhibit increasing values in magnitude in this sequence, again in agreement with our above conclusion of increasing charge transfer.

When comparing the binding energy shifts of the experimentally distinguishable atoms within the perylene core, namely, of the $\text{C}_{\text{C-H}}$, $\text{C}_{\text{C-C}}$, and $\text{C}_{\text{C-CO}}$ atoms, for PTCDA on *one* particular Ag(hkl) surface, the above-stated correlation of $\Delta E_b(i)$ and $\Delta q(i)$ is not strictly obeyed. We speculate that this is due to inaccuracies in both the Bader analysis and the XPS fitting models, where the three groups of C atoms are reflected in one $\text{C}1s$ XPS peak which hardly shows any discernible features, such as shoulders.^{59,468} Hence, a further discussion of these values is waived here.

O1s peak shifts

Concerning the O atoms in PTCDA, the O_{carb} atoms exhibit larger shifts towards lower binding energies than the O_{anhyd} atoms (see Fig. 7.8). Note that the ΔE_b values of O_{carb} are the second largest in magnitude after those of C_{peryl} . This is consistent with comparably large $\Delta q(\text{O}_{\text{carb}})$ values (see Table 7.7 or Fig. 7.9). In analogy to above, the larger absolute value of $\Delta E_b(\text{O}_{\text{carb}})$ in comparison to $\Delta E_b(\text{O}_{\text{anhyd}})$ is explained with the relative contributions of the O_{carb} and O_{anhyd} orbitals to the PTCDA LUMO [see Fig. 7.5(b)], which are in fact zero in the latter case. Thus, in a rough approximation, only screening effects of the metal substrate apply to the O_{anhyd} atoms. In the case of PTCDA on the low-index Ag surfaces, also local O–Ag interactions play a role. These local interactions result in a charge donation from the molecule to the metal, which reflects in more positive ΔE_b in comparison to PTCDA on the $\text{Au}(111)$ and $\text{Cu}_3\text{Au}(111)$ substrates. Apparently, this effect is more pronounced for PTCDA on Ag(110) than on Ag(100). This will be elucidated in detail in the following section.

TABLE 7.7. Peak shifts ΔE_b in XPS for the C1s and O1s levels and metal-to-molecule charge transfer/charge redistributions Δq for PTCDA in the (sub-)monolayer regime on the low-index Ag surfaces. θ_{PTCDA} denotes the PTCDA coverage of the Ag surface in monolayers. The ΔE_b values have been deduced from the observed peak positions for the individual components in the (sub-)monolayer regime (with the nominal PTCDA coverage θ_{PTCDA}) with respect to those in the multilayer regime, i.e., $\Delta E_{b,i} = E_{b,\text{mono},i} - E_{b,\text{multi},i}$. For PTCDA/Ag(100) and PTCDA/Ag(110), the respective XPS data are depicted in Appendix C of the present work. Binding energies for the C and O components of a condensed film of PTCDA molecules on the Ag(111) surface, with a coverage of 10 ML and well above, have been reported in Refs. 59 and 307, respectively. In Refs. 59 and 468 the XP spectra for the C1s and O1s levels of PTCDA on Ag(111) in the (sub-)monolayer regime have been reported, too. Unfortunately, respective XPS fitting models have not been provided. Therefore, $E_{b,\text{mono},i}$ values for the individual C and O components and hence also the corresponding $\Delta E_{b,\text{mono},i}$ values are not available for PTCDA/Ag(111) at this point. The charge transfer Δq has been obtained by means of a Bader analysis^{504,505} of the electron density $\rho(r)$. The stated Δq values refer to the (averaged) relative gain (negative sign) or loss (positive sign) of electrons per individual atom within the PTCDA molecule upon adsorption on the respective Ag surface. In addition, the net charge transfer per PTCDA molecule is given (t.w. = this work, n.a. = not available/applicable).

	Ag(111)		Ag(100)		Ag(110)	
	0.9–1 ML	1 ML	0.8 ML	1 ML	0.9 ML	1 ML
θ_{PTCDA}	0.9–1 ML	1 ML	0.8 ML	1 ML	0.9 ML	1 ML
Ref(s).	59, 307, 468	t.w.	t.w.	t.w.	t.w.	t.w.
	ΔE_b (eV)	Δq ($10^{-2} e$) ^{a,b}	ΔE_b (eV)	Δq ($10^{-2} e$) ^a	ΔE_b (eV)	Δq ($10^{-2} e$) ^a
C _{C–C}	n.a.	–2.27	–0.84	–1.38	–0.90	–1.93
C _{C–H}	n.a.	–3.70	–0.94	–8.43	–0.61	–6.81
C _{C–CO}	n.a.	–1.91	–0.48	2.27	–0.03	0.76
C _{funct}	–1.63	–4.66	–1.96	–7.02	–2.04	–9.13
O _{carb}	n.a.	–4.71	–1.22	–6.32	–0.97	–5.55
O _{anhyd}	n.a.	0.31	–0.38	1.36	–0.22	0.75
H	n.a.	–1.00	n.a.	–1.63	n.a.	–1.39
PTCDA (<i>net</i> ; in e)	n.a.	–1.00	n.a.	–1.33	n.a.	–1.35

^aNote that the Δq values for the different atoms of one individual component are subject to a spreading. Typically, the spread is in a range of well below $\pm 1.00 \times 10^{-2} e$. For the C_{peryl} atoms, however, the variation in Δq exceeds this range and amounts to $\pm 3.84 \times 10^{-2} e$ to $\pm 5.92 \times 10^{-2} e$ in the case of PTCDA/Ag(111), $\pm 3.62 \times 10^{-2} e$ to $\pm 4.71 \times 10^{-2} e$ in the case of PTCDA/Ag(100), and even $\pm 0.61 \times 10^{-2} e$ to $\pm 14.01 \times 10^{-2} e$ in the case of PTCDA/Ag(110), respectively. The maximal value holds for the C_{C–H} atoms in each case.

^bThe differences in the (averaged) Δq values for the individual components of molecules A and B for PTCDA/Ag(111) amount to maximal $0.007 e$ and are thus well within the spreading of Δq for the individual atoms (see also footnote *a* of this table). Hence, the individual (averaged) Δq values for molecules A and B are not reported separately.

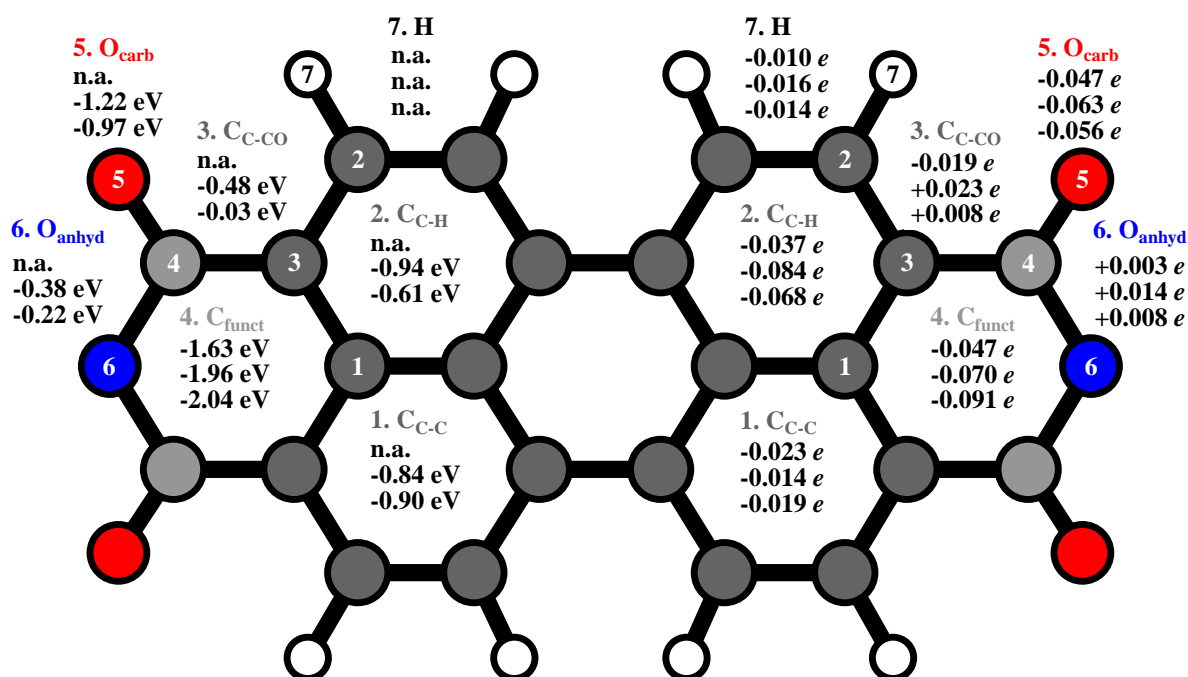


FIG. 7.9. Comparison of peak shifts ΔE_b in XPS for the $C1s$ and $O1s$ levels (left) and metal-to-molecule charge transfer/charge redistributions Δq (right) for PTCDA in the (sub-)monolayer regime on the low-index Ag surfaces. Values are given for PTCDA/Ag(111), PTCDA/Ag(100), and PTCDA/Ag(110) from top to bottom, respectively. The ΔE_b values have been deduced from the observed peak positions for the individual components in the (sub-)monolayer regime with respect to those in the multilayer regime (see Table 7.7). Note that $\Delta E_{b, \text{mono}, i}$ values are not available for PTCDA/Ag(111).⁴⁶⁸ The charge transfer Δq has been obtained by means of a Bader analysis^{504,505} of the electron density $\rho(\mathbf{r})$. The stated Δq values refer to the (averaged) relative gain (negative sign) or loss (positive sign) of electrons per individual atom within the PTCDA molecule upon adsorption on the respective Ag surface (n.a. = not available/applicable).

7.5 Surface bonding via the functional groups: relevance of local interactions

We will now discuss potential local interactions between the atoms within the functional groups, namely, the C_{funct} , O_{carb} , and O_{anhyd} atoms, and individual surface atoms as a second relevant, chemical bonding channel besides that related to the metal-to-molecule charge transfer. Local interactions between the functional groups and the surface (atoms) are only indicated for PTCDA on the Ag surfaces by the lower d values of the respective atoms in comparison to $d(C_{\text{peryl}})$. In turn, from the (presumably) at least identical or even larger $d(O_{\text{carb}})$, $d(O_{\text{anhyd}})$ and $d(C_{\text{funct}})$ values compared to $d(C_{\text{peryl}})$ for PTCDA on Au(111), $\text{Cu}_3\text{Au}(111)$, and Cu(111), we conclude that local interactions via the functional groups are *not* relevant in these cases. The same conclusion is drawn from the respective d_{vdW} values [see Fig. 7.6(b) above]. Hence, the following discussion will only deal with PTCDA/Ag(hkl). As will be evidenced below, the relevant interactions are, in particular, realized by local $O_{\text{carb}}-\text{Ag}$ bonds and, to a lesser extent, local $O_{\text{anhyd}}-\text{Ag}$ bonds. $C_{\text{funct}}-\text{Ag}$ bonds, however, do not play a role although $d_{\text{vdW}}(C_{\text{funct}}) \leq d_{\text{vdW}}(C_{\text{peryl}})$.

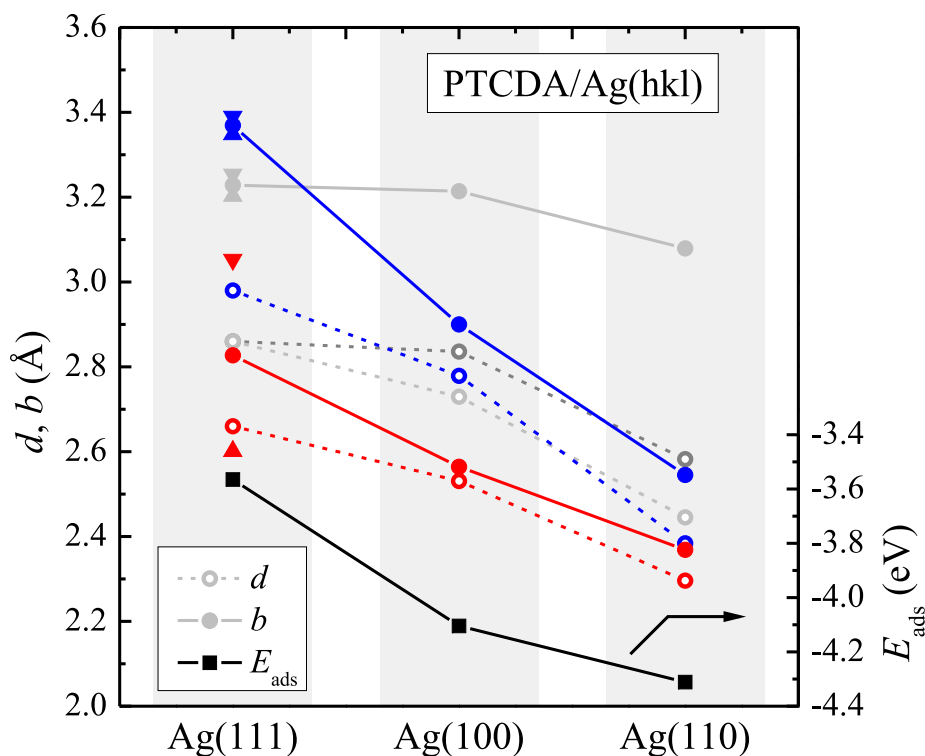


FIG. 7.10. Averaged vertical heights d (dashed lines, \circ) and bond lengths b to neighboring surface atoms (solid lines, \bullet) for PTCDA adsorption on the low-index Ag surfaces. Triangle symbols \blacktriangle and \blacktriangledown refer to the two non-equivalent molecules A and B for PTCDA on the Ag(111) surface, respectively. Dark gray: C_{pearl} , light gray: C_{funct} , red: O_{carb} , blue: O_{anhyd} . Note that the b values for the C_{pearl} atoms were not determined. Error bars are omitted for clarity; lines are guides to the eye. The calculated adsorption energy E_{ads} per molecule is also indicated (black solid line, \blacksquare). Adapted from Ref. 66.

Structural considerations

Based on the structural arguments outlined in Sec. 7.1, we can already rationalize the following aspects: The O atoms in PTCDA are pulled towards the surface with respect to the perylene core (1) in a commensurate PTCDA superstructure, (2) for an (nearly) on-top registry with the substrate surface atoms, and (3) to a greater extent for the more open surfaces, i.e., in the series PTCDA on Ag(111), Ag(100), and Ag(110) (see Fig. 7.10). Findings (1) and (2) represent necessary conditions for the formation of local O—Ag bonds. Fulfilling these conditions assures the well-defined and close proximity of the involved binding partner for *all* PTCDA molecules within the PTCDA overlayer. Finding (3) can be explained by the increased coordinative unsaturation and the thereby enhanced reactivity of the surface atoms. The coordination number (CN) of the surface atoms decreases as $9 > 8 > 7$ in the sequence Ag(111), Ag(100), Ag(110). The correlation of CN and length/strength of local bonding has recently also been pointed out taking the example of formate (HCOO^-) on low-index Cu surfaces.³⁷ We conclude that the magnitude of local (covalent, see below) O—Ag bond formation and thus the bond strength increases while the bond length decreases in the above-stated sequence.

In the following, we will consider the bond lengths b rather than the adsorption heights d because, in contrast to incommensurate PTCDA superstructures on other coinage metal surfaces, they

are in fact well-defined here, and because they allow a more meaningful interpretation of the bonding situation. For this purpose, the lateral and vertical positions of the atoms of interest, namely, C_{funct} , O_{carb} , O_{anhyd} , and Ag surface atoms, have to be considered explicitly. The lateral positions of the atoms have been taken from the determined superstructures (see Sec. 7.1).^{k)} The vertical positions of C and O are available from our XSW experiments and those by Hauschild *et al.*⁵⁵

The vertical positions of the (individual) Ag surface atoms could not be accessed by means of XSW. Hence, we have taken the Ag positions from our DFT calculations (see Sec. 7.2). Remarkably, the Ag surfaces exhibit a substantial buckling upon PTCDA adsorption (see Fig. 7.11). The Ag atoms below the center of the perylene core (and below the O_{anhyd} atoms) are repelled and *pushed into* the surface, while the Ag atoms below the O_{carb} atoms are pulled out. Apparently, the interaction between the Ag atoms and the C backbone turns locally Pauli-repulsive when the PTCDA molecule is pulled towards the surface by the O—Ag bonds. The overall amplitude of the surface buckling is largest for Ag(110), being 0.22 Å, compared to that for Ag(100) and Ag(111), 0.19 Å and 0.17 Å, respectively.^{l), m)} In the sequence Ag(111), Ag(100), Ag(110), the surface atoms are less tightly bound to the bulk in this series because of the decreased CN (see above), which is reflected by their displacements due to the interaction with the PTCDA. Yet, for the (110) surface, the repulsion of the Ag atoms directly below the perylene core is smaller compared to (100) and

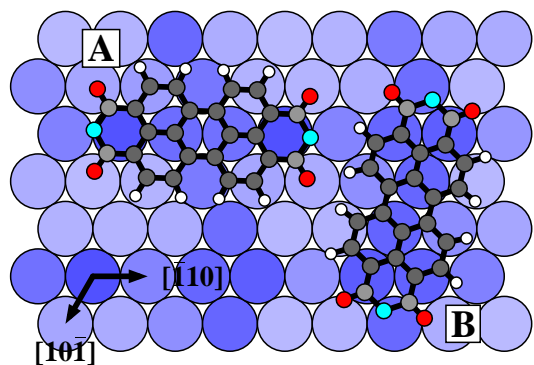
^{k)}The (lateral) intramolecular positions of C and O in PTCDA have been deduced under the assumption that they are identical to those in PTCDA in bulk polymorph α .¹⁰⁸

^{l)}Note that, in the context of the present work, the term “amplitude of the surface buckling” refers to the peak-to-peak value, i.e., to the difference between the maximal and minimal z values of the Ag surface atoms.

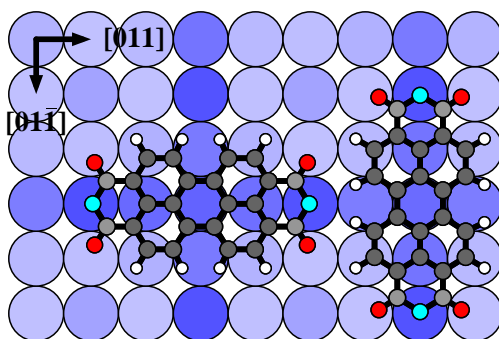
^{m)}The vertical positions of the Ag surface atoms with respect to the surface lattice plane, d_B , range from -0.12 Å to $+0.10$ Å for Ag(110), from -0.12 Å to $+0.07$ Å for Ag(100), and from -0.07 Å to $+0.10$ Å for Ag(111). Our DFT calculations of the clean surfaces have shown relaxations of -0.005 Å, 0.000 Å, and $+0.042$ Å in the same series (in combination with a small buckling with an overall amplitude of 0.018 Å in the latter case). For instance, surface relaxations of -0.08 Å, $0.00(3)$ Å, and 0.00 Å have been found experimentally with LEED- $I(V)$ for the topmost layers of the clean Ag(110),⁵³⁸ Ag(100),⁵³⁹ and Ag(111) surfaces,⁵⁴⁰ respectively (see also Ref. 422 for a collection of both theoretically and experimentally determined surface relaxations of *fcc* metals). Note that, in contrast to our DFT results, the experimental values for the surface relaxation merely represent the variation in the layer spacing between the surface layer and the subjacent layer in comparison to that to that in the bulk (as given by the d_{hkl} value). Thus, they may *not entirely* comply with the displacement of the surface atoms from the surface lattice plane, d_B , due to (potential) multilayer surface relaxations, i.e., relaxations of the sub-surface layers, which have not been considered here.^{538, 539}

FIG. 7.11 (following page). Hard sphere models of the lateral and vertical molecular configurations of PTCDA on (a) Ag(111),^{55, 98, 124} (b) Ag(100),¹²⁰ and (c) Ag(110).^{98, 485} Top views (top), side views along the long (middle) and along the short molecular axis (bottom). Ag atoms are shown in different shades of blue in order to indicate the vertical deviation Δd from their position in the relaxed uncovered surface (dashed line, d_0); H atoms are shown in white, $C_{\text{funct}}/C_{\text{peryl}}$ in light gray/dark gray, and $O_{\text{carb}}/O_{\text{anhyd}}$ in red/blue. In the side views, d denotes the vertical adsorption height; the vertical scale is enlarged by a factor of 4 and referenced against the Bragg plane (dashed line, d_B). The adsorption configuration of PTCDA is taken from the XSW experiments and the surface buckling from DFT calculations. O—Ag interactions (bonds) are illustrated by black dotted lines. For (a) Ag(111), the side views refer to molecule A. For reasons of clarity, the depicted PTCDA molecule has exactly been aligned with the $[\bar{1}10]$ substrate direction although, in our calculations as well as in previous investigations,¹²⁴ it has been found at a small angle (2°) with respect to the substrate lattice. As a consequence of the alignment, the vertical positions of the respective Ag surface atoms have been averaged. In the top views, we show only the molecules within one unit cell of the periodic structure for clarity. Adapted from Ref. 66.

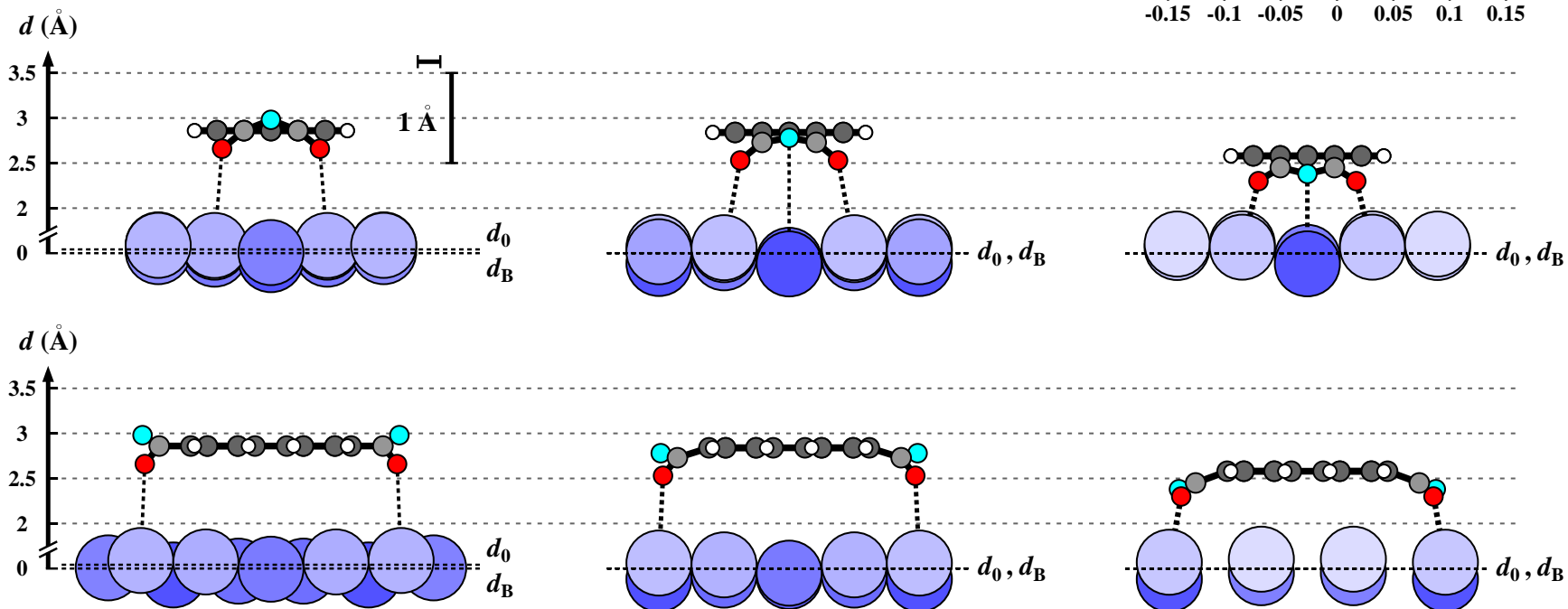
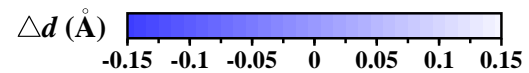
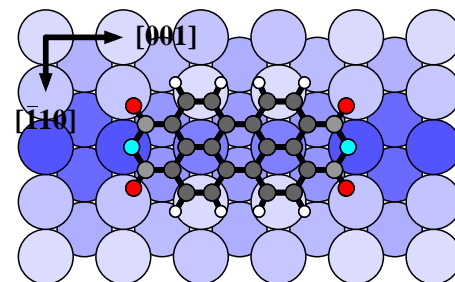
(a) Ag(111)



(b) Ag(100)



(c) Ag(110)



(111), as is revealed by the (slightly) lighter blue color of the respective surface atoms in Fig. 7.11 (top views) in the case of PTCDA/Ag(110). This indicates additional attractive interactions for these atoms, as will be discussed in Sec. 7.6.

For the calculation of the average b values between the O_{carb} , O_{anhyd} , as well as C_{funct} atoms, and the neighboring Ag surface atoms, we have considered two Ag neighbors in the case of (off-)bridge adsorption sites and one for (off-)on-top adsorption sites, respectively. As can be seen from Fig. 7.10 (solid lines), $b(C_{\text{funct}}-\text{Ag})$ does not alter much for the three Ag faces and is too long for a covalent interaction [minimal 3.08(7) Å; to be compared to a value of 2.18 Å for the sum of the covalent radii of C and Ag, see Table 7.4].¹⁴⁴ Obviously, the C_{funct} atoms do not form a bond of their own with Ag surface atoms. The comparably low $d(C_{\text{funct}})$ values may thus result from the fact that C_{funct} simply follow the downward movement of the O atoms in order to maintain as far as possible a planar geometry of the atoms within the functional groups (with a maximal excursion of 0.04 Å, see Table 7.10 below), which is favored due to mesomeric effects.

For both types of O atoms, however, $b(\text{O}-\text{Ag})$ shortens, the more open the substrate surface is. In particular, $b(O_{\text{anhyd}}-\text{Ag})$ reduces from 3.37(4) Å, which is in fact equal to the sum of the vdW radii of O and Ag (see Table 7.4),¹⁴¹ to 2.55(2) Å, that is, by about 25 %, from Ag(111) to Ag(110). Finally, $b(O_{\text{anhyd}}-\text{Ag})$ is close to $b(O_{\text{carb}}-\text{Ag})$, being 2.37(4) Å for PTCDA/Ag(110). The reduction of the difference in $b(\text{O}-\text{Ag})$ for O_{carb} and O_{anhyd} points to a stronger hybridization of the electronic states of the adsorbed PTCDA with metal states, as is also visualized by DFT in Fig. 7.12 below, due to the closer proximity of the binding partners and the thus larger overlap of the respective (valence) states (see also Sec. 2.1.3). This leads to a larger distortion of the C backbone and to a subsequent loss of the mesomeric stabilization within the molecule. Apparently, the energetic cost of the deformation is counterbalanced by the energy gain through the formation of covalent O—Ag bonds. This holds for all O atoms, although for O_{anhyd} the interaction is less pronounced as judged from the larger b values throughout.

Electronic considerations

Based on our DFT results on the electronic structure of PTCDA/Ag(hkl), we will now clarify the chemical nature of the O—Ag bonds. The formation of *covalent* O—Ag bonds can be derived from Fig. 7.12 (top). The electron density $\rho(\mathbf{r})$ between the O_{carb} and the nearest Ag surface atoms increases from Ag(111) over Ag(100) to Ag(110). Here, $\rho_{\text{BCP}}(\mathbf{r})$ at the bond critical point⁵⁴¹ (BCP, of the type 3, -1) is found to be approximately $0.25 \text{ e}^-/\text{Å}^3$ in the latter case, while for PTCDA on Ag(100) and Ag(111), smaller values are found ($0.20 \text{ e}^-/\text{Å}^3$ and $0.12 \text{ e}^-/\text{Å}^3$, respectively; see also

FIG. 7.12 (following page). Total electron density $\rho(\mathbf{r})$ and electron density difference $\Delta\rho(\mathbf{r})$ for PTCDA on the low-index Ag surfaces, that is, (a) Ag(111), (b) Ag(100), and (c) Ag(110). First and second rows: side views along the long molecular axis; third row: top views; fourth row: side views along the short molecular axis. The horizontal cuts have been made 0.8 Å below the perylene core of the PTCDA molecule. Light gray: Ag, white: H, dark gray: C_{peryl} , light gray: C_{funct} , red: O_{carb} , blue: O_{anhyd} . (d) Lowest unoccupied molecular orbital (LUMO) of gas-phase PTCDA. The black and white arrows indicate the positions of the vertical and horizontal cuts. Note that in (a) the PTCDA molecule is rotated against the $[\bar{1}10]$ substrate direction by 2°. Adapted from Ref. 66.

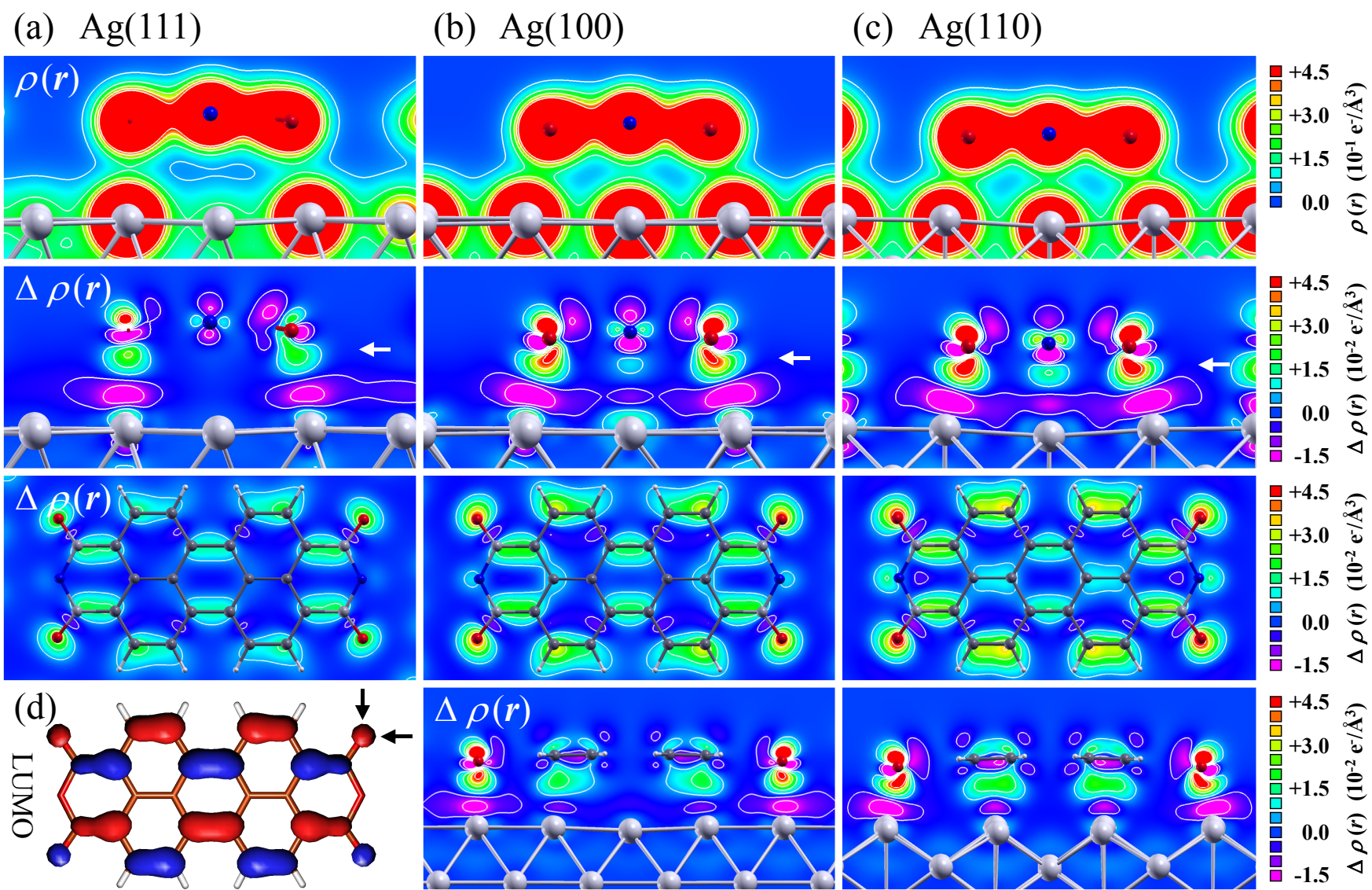


Table 7.9 below).^{n), o)} Additionally, electrons accumulate between the O_{anhyd} and the Ag atoms in the same series. For the $O_{\text{anhyd}}-\text{Ag}$ bonds, $\rho_{\text{BCP}}(\mathbf{r})$ values of about $0.06 \text{ e}^-/\text{\AA}^3$, $0.12 \text{ e}^-/\text{\AA}^3$, and $0.17 \text{ e}^-/\text{\AA}^3$ are found on average in the sequence Ag(111), Ag(100), and Ag(110). This proves the above-noted evolution of substantial $O_{\text{carb}}-\text{Ag}$ bonds, in particular, and $O_{\text{anhyd}}-\text{Ag}$ bonds with decreasing CN of the Ag surface atoms. Note at this point already that a similar trend can be perceived also concerning the accumulation of electrons between the perylene core of adsorbed PTCDA, in particular on the periphery of the molecule, and the nearest Ag surface atoms, indicating the formation of local C—Ag bonds in addition (see the following section for a detailed discussion of this finding).

The development of O—Ag bonds can also be identified in the electron density difference $\Delta\rho(\mathbf{r})$ (see Fig. 7.12, second row), which is defined as $\rho(\mathbf{r})$ of the bonded system PTCDA/Ag(*hkl*) minus $\rho(\mathbf{r})$ of the free (but distorted) PTCDA molecule and minus $\rho(\mathbf{r})$ of the bare (but buckled) Ag(*hkl*) surface [see Eq. (7.2)]. The electron density enhances around the O atoms, while it is reduced directly above the surface, indicating (polar) covalent O—Ag bonds. Presumably, these bonds are of coordinative nature. We speculate that the electron-enriched O atoms donate electrons to the subjacent Ag surface atoms via an overlap of their p_z orbitals with metal states. Thereby, the ‘overspill’ of electron density from the metal into the vacuum, which is present on the clean surface, is diminished, leading to the observed decrease in $\rho(\mathbf{r})$ directly above the surface. Again, this effect is most prominent for the most open (110) surface. Therefore, an important aspect of PTCDA bonding on the Ag(*hkl*) surfaces, besides the metal-to-molecule charge transfer, is the formation of the covalent O—Ag bonds.

7.6 Interplay of the bonding channels

We have so-far identified two relevant (chemical) bonding channels. In this section, their mutual interplay will be discussed, among others. However, further bonding channels have to be considered, too. The following bonding channels can in principle be relevant for PTCDA on coinage metal surfaces, as will be shown below:

1. Van der Waals interactions.
2. Intermolecular interactions.
3. Metal-to-molecule charge transfer.
4. Local covalent O—M bonds.
5. Local covalent C—M bonds.

Bonding channels 3 and 4 of the above list, which may not be exhaustive, have been elucidated in detail in Secs. 7.3 to 7.5. The other potential bonding channels will be addressed in the following.

Van der Waals interactions

Van der Waals (vdW) interactions are inherent between atoms and/or molecules.^{85, 146} Hence, the basic relevance of vdW interactions is indisputable here. Yet, their relative contribution to the overall surface bonding and their character, being either attractive or repulsive, may vary for the

ⁿ⁾For instance, these $\rho_{\text{BCP}}(\mathbf{r})$ values for the $O_{\text{carb}}-\text{Ag}$ may be compared to values of $0.38 \text{ e}^-/\text{\AA}^3$ for O—Fe bonds in Wüstite (FeO)⁵⁴² or about $0.10 \text{ e}^-/\text{\AA}^3$ for N—Cu bonds in various Cu(I) complexes with N-containing ligands.⁵⁴³

^{o)} $\rho_{\text{BCP}}(\mathbf{r})$ values are given in electrons per cubic ångströms ($\text{e}^-/\text{\AA}^3$, with a charge of $-1 e$ per electron) throughout the present work.

TABLE 7.8. Adsorption energies E_{ads} for PTCDA on the low-index Ag surfaces, as obtained from DFT calculations. The calculations were performed at DFT-GGA level employing the PBE functional⁴⁹⁸ and D3(BJ) dispersion corrections.⁵⁰¹ The total adsorption energy is given as the sum of the two individual contributions from the functional and the dispersion corrections, respectively, i.e., $E_{\text{ads}} = E_{\text{ads}}^{\text{PBE}} + E_{\text{ads}}^{\text{D3(BJ)}}$. The ratio $f_{\text{vdW}} = E_{\text{ads}}^{\text{D3(BJ)}}/E_{\text{ads}}$, that is, the fraction of the dispersion energy on the total adsorption energy, allows to estimate the percentage of the vdW interactions on the overall surface bonding. Note that all E values are given in eV and hold for the adsorption of one molecule within a full PTCDA monolayer. In order to obtain E values in kJ mol^{-1} a conversion factor of $1 \text{ eV} = 96.485 \text{ kJ mol}^{-1}$ applies.

	E_{ads} (eV)	$E_{\text{ads}}^{\text{PBE}}$ (eV)	$E_{\text{ads}}^{\text{D3(BJ)}}$ (eV)	f_{vdW} (%)
PTCDA/Ag(111)	-3.57	0.17	-3.73	$\approx 100^a$
PTCDA/Ag(100)	-4.10	-0.55	-3.55	87
PTCDA/Ag(110)	-4.31	-1.14	-3.17	74

^aIn the strict mathematical sense, a f_{vdW} value of 105 % is obtained here. This is of course unphysical and thus an artifact of the DFT calculation, i.e., of the partitioning of E_{ads} into the two individual contributions from the functional and the dispersion corrections, respectively. Because $E_{\text{ads}}^{\text{D3(BJ)}}$ is larger in magnitude than E_{ads} —implying that only dispersion interactions are relevant for the surface bonding in this case—, we conclude that the fraction of the dispersion energy on the total adsorption energy, f_{vdW} , is close to 100 % for PTCDA/Ag(111) in actual fact.

different surfaces. Of course, (nearly) pure vdW bonding occurs in cases of physisorption,¹⁵⁷ that is, for PTCDA/Au(111).^{54,60} For chemisorbed PTCDA on the other coinage metal surfaces within the scope of the present work, at least one of the bonding channels 3 to 5 has to apply in addition.

The importance of vdW interactions for the overall surface bonding can be estimated from our DFT results for PTCDA/Ag(hkl). The calculated adsorption energies E_{ads} for PTCDA on the low-index Ag surfaces (see Sec. 7.2 for details) are given in Table 7.8 and have also been plotted in Fig. 7.10 above. We find that E_{ads} increases in magnitude with decreasing coordination number (CN) of the Ag surface atoms, i.e., by about 20 % in the series Ag(111), Ag(100), Ag(110). This is explained by the enhanced reactivity of the surface atoms due to the increased coordinative unsaturation, resulting in stronger surface bonding as judged from the smaller d and b values. Note at this point that the absolute values of E_{ads} may be overestimated by the PBE-D3(BJ) functional employed here [see also footnote p) on page 215 of this chapter].^{544,545} In particular, theoretically determined E_{ads} for PTCDA/Ag(hkl) ranging from about -2.0 eV to -3.5 eV have been reported,^{153,546,547} being smaller by as much as $\approx 45 \%$ (in the most extreme case) in comparison to our value of -3.57 eV . Yet, the obtained general trend in E_{ads} versus CN, and thereby versus the surface reactivity, should remain valid regardless of the absolute values of the adsorption energy.

Partitioning the obtained E_{ads} values into contributions from the pure PBE functional,⁴⁹⁸ which does not include dispersion effects,^{155,544,p)} and those from the D3(BJ) dispersion correction⁵⁰¹ yields a measure for the percentage of dispersion/vdW interactions to the total energy gain upon surface bonding via $f_{\text{vdW}} = E_{\text{ads}}^{\text{D3(BJ)}}/E_{\text{ads}}$ where $E_{\text{ads}} = E_{\text{ads}}^{\text{PBE}} + E_{\text{ads}}^{\text{D3(BJ)}}$. As presented in Table 7.8, E_{ads} and $E_{\text{ads}}^{\text{PBE}}$ increase in magnitude in the sequence Ag(111), Ag(100), Ag(110), while $E_{\text{ads}}^{\text{D3(BJ)}}$ decreases in magnitude (see also Fig. 7.10). Hence, chemical interactions become more relevant on the more open surfaces and the vdW interactions become less relevant (not only in relative

^{p)}Note in this context that the PBE functional predicts weak binding in noble gas dimers⁵⁴⁴ which may be interpreted as an indication for dispersion effects being already considered to a small extent.⁵⁴⁸ The PBE functional is generally known to be “overattractive”.⁵⁴⁴ In particular, the overbinding of chemisorbed atoms and molecules on surfaces (in terms of the chemisorption energies) is on the order of several tenths of an electronvolt.⁵⁴⁵

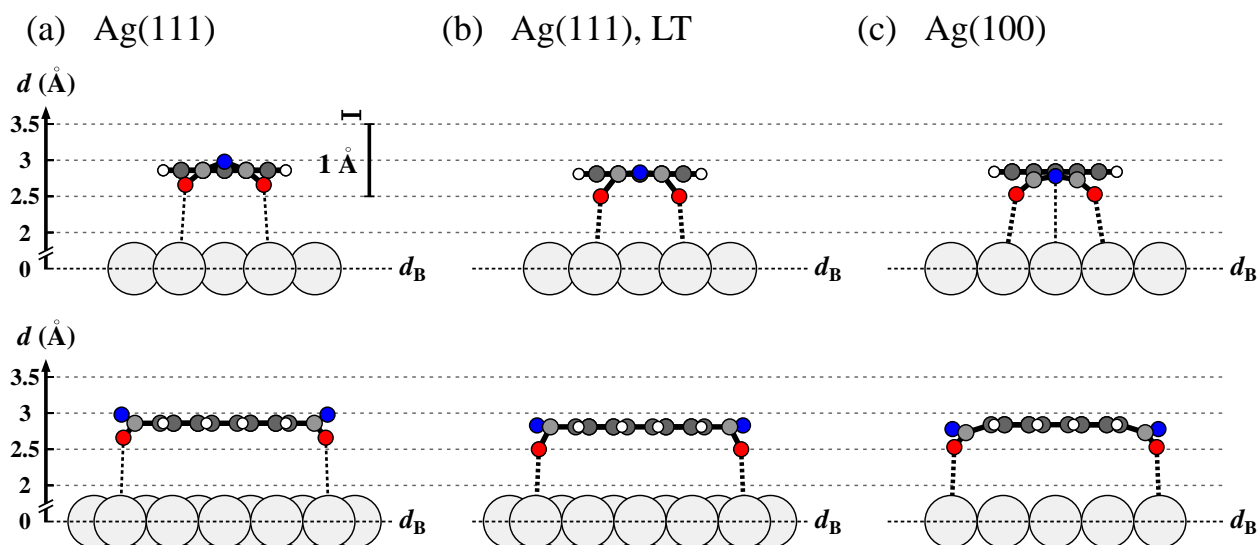


FIG. 7.13. Comparison of the adsorption configurations of PTCDA (a) on the Ag(111) surface in the RT phase,⁵⁵ (b) on the Ag(111) surface in the (disordered) LT phase,¹⁴⁰ and (c) on the Ag(100) surface. The top row shows side views along the long molecular axis while the bottom row shows side views along the short molecular axis. H atoms are shown in white, C_{funct} and C_{peryl} atoms in light gray and dark gray, and O_{carb} and O_{anhyd} atoms in red and blue, respectively. d denotes the vertical adsorption height; the vertical scale is enlarged by a factor of 4 and referenced against the Bragg plane (dashed line, d_B). O—Ag interactions are illustrated by black dotted lines. For (a, b) Ag(111), the side views refer to molecule A. For reasons of clarity, the depicted PTCDA molecule in (a) has exactly been aligned with the $[\bar{1}10]$ substrate direction although, in our calculations as well as in previous investigations,¹²⁴ it has been found at a small angle (2°) with respect to the substrate lattice. Note that for the PTCDA phases on Ag(111) the C_{funct} and C_{peryl} atoms could not be distinguished experimentally.⁵⁵

terms but also in absolute terms; see Table 7.8) due to the lower surface atom density, that is, due to the smaller number of Ag surface atoms underneath one PTCDA molecule. Yet, even in the case of strong chemisorption, which is strongest for PTCDA/Ag(110) [see Secs. 7.3 and 7.4; besides PTCDA/Cu(111) and PTCDA/K:Ag(110) according to UPS^{60,68}], vdW interactions still contribute by about $\geq 70\%$ to E_{ads} , leaving for the chemical interactions only an amount of a little more than 1 eV. Nevertheless, the chemical interactions beyond vdW are decisive for the adsorption heights and molecular distortions, and thus determine the surface bonding of PTCDA on coinage metal surfaces, except for the case of PTCDA/Au(111).

Intermolecular interactions

Before the implications of chemical interactions will be elucidated further, we will briefly discuss also the relevance of intermolecular interactions using the example of PTCDA/Ag(111) in the disordered (LT) phase. This aspect has already been addressed in a recent publication by Kilian *et al.* (see Ref. 140). Here, we amend their findings by quantitative DFT results and also by a comparison to the situation for PTCDA adsorbed on another low-index Ag surface, namely, on Ag(100).

Figure 7.13 depicts the corresponding adsorption configuration of PTCDA/Ag(111) in the disordered LT phase and contrasts it with those of PTCDA/Ag(111) in the ordered (RT) phase and PTCDA/Ag(100). While the determined adsorption heights of the distinguishable atoms deviate by up to 0.16 \AA between the two phases on Ag(111),⁵⁵ they agree within 0.05 \AA for Ag(111) (LT) and

TABLE 7.9. Electron densities $\rho(\mathbf{r})$ at bond critical points (BCP, of the type 3, -1) for PTCDA on the low-index Ag surfaces, as obtained from DFT calculations. Averaged values are given for (potential) bonds between individual C and O atoms in PTCDA, respectively, and the nearest Ag surface atoms. For the C_{C-C} atoms, two sets of atoms have been distinguished, namely, the C_{C-C} atoms on the central, long axis of the PTCDA molecule (on-axis) and the C_{C-C} atoms off the central, long axis (off-axis). On the one hand, the on-axis C_{C-C} atoms are located closer (by tendency) to on-top positions with respect to the Ag surface atoms than the off-axis C_{C-C} atoms (see also Fig. 7.11). On the other hand, the $2p_z$ orbitals of the on-axis C_{C-C} atoms do not contribute to the PTCDA LUMO (see also Fig. 7.12). In addition, respective $\rho_{\text{BCP}}(\mathbf{r})$ values for (potential) hydrogen bonds, $C=O\cdots H-C$, between neighboring PTCDA molecules at the Ag surfaces are given. All values in $e^-/\text{\AA}^3$.

	PTCDA		
	Ag(111)	Ag(100)	Ag(110)
$C_{C-C}-\text{Ag}$ (long axis)	0.091	0.129	0.149
$C_{C-C}-\text{Ag}$ (off long axis)	0.061	0.073	0.034
$C_{C-H}-\text{Ag}$	0.115	0.170	0.210
$C_{C-CO}-\text{Ag}$	0.079 ^a	0.060	0.036
$C_{\text{funct}}-\text{Ag}$	0.063	0.050	0.039
$O_{\text{carb}}-\text{Ag}$	0.117 ^b	0.201	0.253
$O_{\text{anhyd}}-\text{Ag}$	0.057 ^c	0.121	0.173
$C=O\cdots H-C^d$	0.131	0.037	0.015

^aSubstantially different (averaged) $\rho_{\text{BCP}}(\mathbf{r})$ values have been found for the respective $C_{C-CO}-\text{Ag}$ bonds of the two non-equivalent PTCDA molecules, namely, $0.058 e^-/\text{\AA}^3$ for molecule A and $0.099 e^-/\text{\AA}^3$ for molecule B.

^bSubstantially different (averaged) $\rho_{\text{BCP}}(\mathbf{r})$ values have been found for the respective $O_{\text{carb}}-\text{Ag}$ bonds of the two non-equivalent PTCDA molecules, namely, $0.149 e^-/\text{\AA}^3$ for molecule A and $0.086 e^-/\text{\AA}^3$ for molecule B.

^cSlightly different (averaged) $\rho_{\text{BCP}}(\mathbf{r})$ values have been found for the respective $O_{\text{anhyd}}-\text{Ag}$ bonds of the two non-equivalent PTCDA molecules, namely, $0.047 e^-/\text{\AA}^3$ for molecule A and $0.067 e^-/\text{\AA}^3$ for molecule B.

^dOnly $C=O\cdots H-C$ hydrogen bonds with $b(O\cdots H) \leq 2.50 \text{\AA}$ have been considered here.⁵⁴⁹ A value of $\approx 2.50 \text{\AA}$ corresponds to the sum of the vdW radii of O and H atoms in the plane of the aromatic core of PTCDA.¹⁴¹

Ag(100) (see also Table 7.1 above). The $d(\text{C total})$ values are in fact identical, being $2.81(2) \text{\AA}$.⁵⁵ Due to these practically identical d values, we postulate that $d(\text{C}_{\text{peryl}})$ and $d(\text{C}_{\text{funct}})$, which were not determined in the case of PTCDA/Ag(111),⁵⁵ are (nearly) equal for both Ag(111) (LT) and Ag(100), too, yielding an arch-like configuration. Furthermore, we conclude that local O-Ag bonds play a more prominent role in the surface bonding for PTCDA/Ag(111) in the disordered than in the RT phase (see Sec. 7.5).

This is explained as follows. In the disordered phase of PTCDA on Ag(111), (small) dendritic clusters consisting of maximal a few hundreds of molecules are formed, as judged from the STM images reported in Ref. 140. The relative molecular arrangement is less well-defined in terms of the azimuthal orientation, and the molecular packing is less dense.¹⁴⁰ The (average) number of neighboring PTCDA molecules, and thus are the intermolecular interactions, is strongly reduced in comparison to the ordered HB phase.⁴⁶⁴ For example, the formation of $C=O\cdots H-C$ hydrogen bonds is hindered due to geometric reasons (see also Fig. 7.3). $\rho_{\text{BCP}}(\mathbf{r})$ for hydrogen bonds in ordered PTCDA monolayers on Ag(111) amounts to $0.131 e^-/\text{\AA}^3$ on average, as revealed by our DFT results, and in fact exceeds that for the $O_{\text{carb}}-\text{Ag}$ bonds by more than 10% (see Table 7.9). According to a correlation of $\rho_{\text{BCP}}(\mathbf{r})$ values with the corresponding energy gain presented by

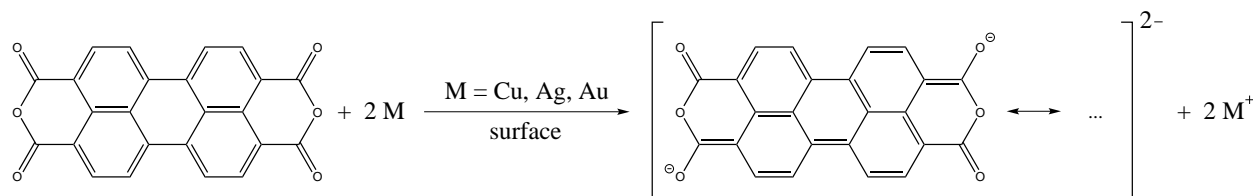


FIG. 7.14. Formation of a quinoid-like structure of PTCDA upon metal-to-molecule charge transfer on a coinage metal surface (surface atom $M = \text{Cu, Ag, Au}$), presented in terms of a chemical equation. The resulting semiquinoid-like structure of the molecule for $\Delta q = -2e$ may be described by resonance structures one of which is shown in square brackets.

Parthasarathi *et al.*,⁵⁵⁰ this corresponds to a stabilization energy of about 20 kJ mol^{-1} or 0.2 eV for the $\text{C}=\text{O}\cdots\text{H}-\text{C}$ hydrogen bonds.

If the formation of hydrogen bonds is diminished, as is also the case for PTCDA/Ag(100) [$\rho_{\text{BCP}}(\text{C}=\text{O}\cdots\text{H}-\text{C}) = 0.037 \text{ e}^-/\text{\AA}^3$, see Table 7.9], the electron density *on* the molecule is enhanced, as may be deduced from the electron density differences $\Delta\rho(\mathbf{r})$ for PTCDA on the low-index Ag surfaces presented in Fig. 7.12, in particular from the top views, in conjunction with the increased net charge Δq of the molecule [$-1.33e$ for PTCDA/Ag(100) as compared to $-1.00e$ for PTCDA/Ag(111); see also Table 7.7]. Thereby, the formation of coordinative $\text{O}-\text{Ag}$ bonds via charge donation from the molecule towards the metal is favored (see also Sec. 7.5). This conclusion is supported by the strong resemblance of the UP spectra of disordered PTCDA/Ag(111) on the one hand and PTCDA/Ag(100) as well as PTCDA/Ag(110) on the other hand (see Fig. 7.7 above). We hence can conclude that a reduction in the intermolecular interactions facilitates the strengthening of the surface bonding via the O atoms and also via the perylene core. We further propose that, as a general principle, all relevant, individual bonding channels influence each other.

Charge transfer and intramolecular distortions

The interdependence of the individual interactions is most pronounced for the “chemical” bonding channels 3–5 of the list at the beginning of this section (see page 214), namely, the metal-to-molecule charge transfer on the one hand and the local bond formation on the other hand. The donation of metal electrons to the adsorbed PTCDA leads to the (partial) filling of the LUMO, and thereby changes the electron density of the molecule towards that of a quinoid structure.^{97,153,551} Figure 7.14 depicts the hypothetical case of $\Delta q = -2e$ leading to a semiquinoid-like character of the PTCDA molecule.⁹⁾

The metal-to-molecule charge transfer leads, among others, to a weakening of the $\text{C}_{\text{funct}}=\text{O}_{\text{carb}}$ double bonds to which the former LUMO is antibonding, that is, to the formal reduction of the bond order [see Fig. 7.5(b)]. Similar effects have recently been reported for the adsorption of 6,13-pentacenequinone and 5,7,12,14-pentacenetetrone as O-containing, oxidized pentacene derivatives on the (111) surfaces of Au, Ag, and Cu.⁴⁰ The weakening of the $\text{C}_{\text{funct}}=\text{O}_{\text{carb}}$ double bonds reflects in the charge depletion between these atoms in the $\Delta\rho(\mathbf{r})$ plots for PTCDA/Ag(*hkl*) in Fig. 7.12 (third row), for example. The lowering of the bond order has also been evidenced with HREELS for these systems (see also Sec. 2.2.2).^{122,137–139} For instance, the frequency of the $\text{C}=\text{O}$ stretching vibration shifts towards lower wavenumbers by about 150 cm^{-1} to 200 cm^{-1} for a submonolayer

⁹⁾An increased quinoid character reduces the band gap in organic conjugated polymers.⁵⁵² The same should apply to organic molecules. Thus, the decrease in the HOMO–(F-)LUMO splitting for PTCDA on coinage metal surfaces observed in UPS^{59,60} (see Secs. 2.2.2 and 7.4) may indicate an increased quinoid character of adsorbed PTCDA.

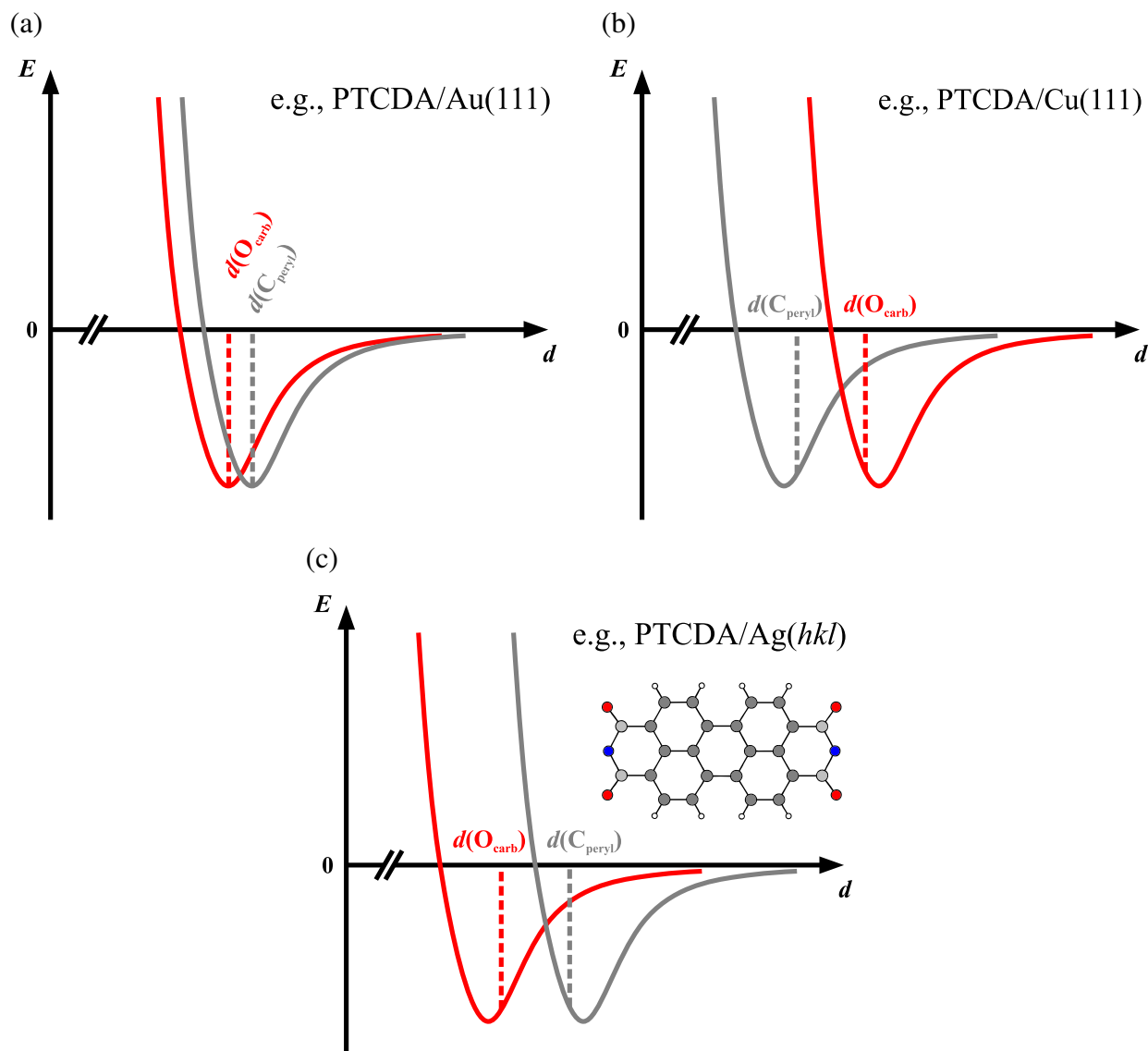


FIG. 7.15. Schematic representation of the potential energy E as a function of the adsorption height d for PTCDA, i.e., for the C_{pery1} (dark gray) and the O_{carb} atoms (red), in particular, on coinage metal surfaces for different scenarios (not to scale). Realized values for $d(C_{\text{pery1}})$ and $d(O_{\text{carb}})$ in the individual scenarios are marked by dashed lines. (a) C_{pery1} and O_{carb} atoms essentially exhibit the same d values, representing the scenario of a (nearly) planar adsorption configuration of the PTCDA molecule. (b) C_{pery1} atoms exhibit a lower d value than the O_{carb} atoms, representing the scenario of a boat-like adsorption configuration of the PTCDA molecule. (c) C_{pery1} atoms exhibit a larger d value than the O_{carb} atoms, representing the scenario of either a saddle-like or an arch-like adsorption configuration of the PTCDA molecule. A ball-and-stick model of the PTCDA molecule is shown as an inset in (c).

of PTCDA on Ag(110) in comparison to the multilayer regime (1569 cm^{-1} for the submonolayer versus $1740\text{--}1771\text{ cm}^{-1}$ for PTCDA multilayers).^{137–139} Thus, it is well within the expected regime for the antisymmetric stretching mode in carboxylate species $\text{R}-\text{COO}^-$ ($1550\text{--}1610\text{ cm}^{-1}$,⁵⁵³ with $\text{R} =$ organic moiety) in which both O atoms formally have the same bond order (being smaller than 2).^{137, r)} Thus, the charge transfer enhances the flexibility of the PTCDA molecule and thereby facilitates intramolecular distortions.

At first, we consider the adsorption configurations of PTCDA on Au(111), $\text{Cu}_3\text{Au}(111)$ in the initial and final state, and Cu(111). Indeed, the vertical distortion increases in this sequence to a final value of $\Delta d_{\text{PTCDA}/\text{Cu}(111)} = 0.23(6)\text{ \AA}$ (see Table 7.1).^{s)} The adsorption configurations becomes increasingly boat-like. The perylene core is lowered by $0.61(3)\text{ \AA}$ due to an increased charge transfer and thus a stronger bond. Because the O atoms do not interact with the respective surfaces via local bonds here, their ideal distance from the surface is larger due to Pauli repulsion. Thus, the O atoms do not readily follow the downward movement of the perylene core. The corresponding binding potential for PTCDA on the pure and alloyed (111) surfaces of Au and Cu can schematically be split into the contributions of these two bonding channels as sketched in Fig. 7.15: For PTCDA/Au(111) as a physisorbed system, the minima of the two potentials felt by the C_{peryl} and O_{carb} atoms (and equivalently by the O_{anhyd} atoms) are located at a nearly equal distance d from the surface [see Fig. 7.15(a)]. In the cases of PTCDA on $\text{Cu}_3\text{Au}(111)$ and pure Cu(111) as chemisorbed systems, the minimum felt by the O_{carb} atoms is at a *larger* distance d than for the C_{peryl} atoms [see Fig. 7.15(b)], as judged from the respective boat-like adsorption configurations. Hence, the overall adsorption height of the molecule as well as the adsorption configuration can be understood as a compromise between attractive $\text{C}_{\text{peryl}}-\text{M}$ interactions and repulsive $\text{O}_{\text{carb}}-\text{M}$ interactions, where $\text{M} = \text{Au}$ or $\text{M} = \text{Cu}$, in particular.

The situation for PTCDA on the low-index Ag surfaces is at variance to the above conclusions. Here, the charge transfer supports the formation of covalent $\text{O}-\text{Ag}$ bonds, also by enhancing the flexibility of the PTCDA molecule as elucidated above. For shorter $\text{O}-\text{Ag}$ bonds, the distortion of the C backbone of PTCDA increases to a maximal value of $0.13(11)\text{ \AA}$ (see Fig. 7.10). As a consequence of the generally small values of $b(\text{O}_{\text{carb}}-\text{Ag})$ and also $b(\text{O}_{\text{anhyd}}-\text{Ag})$, the substrate/perylene core interactions become locally repulsive, as is evidenced by the partial depression of Ag surface atoms and the surface buckling. Thus, the minimum felt by the O_{carb} atoms is at a *smaller* distance d from the surface than for the C_{peryl} atoms [see Fig. 7.15(c)], in contrast to the situation where local $\text{O}-\text{M}$ interactions do not evolve ($\text{M} = \text{Cu}, \text{Ag}, \text{Au}$). The buckling amplitude of the top-layer Ag atoms is larger (ranging from 0.17 \AA to 0.22 \AA ; see Sec. 7.5) and $b(\text{O}-\text{Ag})$ is shorter (ranging from $2.83(1)\text{ \AA}$ to $2.37(4)\text{ \AA}$) for lower surface atom coordination numbers,³⁷ i.e., in the sequence Ag(111), Ag(100), Ag(110).

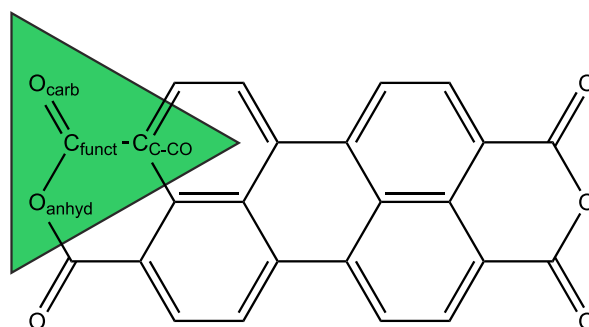
For PTCDA/Ag(*hkl*), the adsorption configuration can be understood as a compromise between attractive $\text{O}_{\text{carb}}-\text{Ag}$ interactions and repulsive $\text{C}_{\text{peryl}}-\text{Ag}$ interactions. Thus, we conclude that the neither the O_{carb} nor the C_{peryl} atoms are located in the “optimal” vertical positions which are determined by the respective individual binding potentials [see Fig. 7.15(c)]. Instead, a deviation of the realized d values from the “optimal” vertical positions of the individual atoms within the

^{r)}The explicit frequencies $\nu(\text{C}_{\text{funct}}=\text{O}_{\text{carb}})$ of the $\text{C}=\text{O}$ stretching mode in PTCDA submonolayers on Ag(110), Ag(100), and Ag(111) have been determined with HREELS as 1568 cm^{-1} ,^{137,138} 1556 cm^{-1} ,¹³⁹ and either 1542 cm^{-1} or $1600\text{--}1750\text{ cm}^{-1}$,¹³⁸ respectively. Note that the peak at $\approx 1540\text{ cm}^{-1}$ in the HREEL spectrum of PTCDA/Ag(111) has later been ascribed to a breathing mode of the central carbon ring in PTCDA, in fact.⁵⁸ For multilayer films of PTCDA on Ag(110), the infrared-active $\text{C}=\text{O}$ stretching modes have been found at 1740 cm^{-1} and 1771 cm^{-1} .¹³⁷ Yet, a detailed discussion of the $\nu(\text{C}_{\text{funct}}=\text{O}_{\text{carb}})$ values (and the potentially underlying trend) is waived here.

^{s)}The adsorption configuration of PTCDA on Au(111) is assumed to be (nearly) planar, as has been reasoned in Sec. 7.1.

TABLE 7.10. Deviations from the planarity of the functional groups $C_{C-CO}-C_{\text{funct}}O_{\text{carb}}O_{\text{anhyd}}$ (marked in green in the valence bond structure which is shown on the right-hand side) in PTCDA adsorbed on various coinage metal surfaces $M(hkl)$. $\Delta d_{C_{\text{funct}}}$ denotes the distance of the C_{funct} atoms from the plane defined by the O_{carb} , O_{anhyd} , and C_{C-CO} atoms, and thus the excursion from the planar arrangement. Positive values of $\Delta d_{C_{\text{funct}}}$ refer to a position above this plane, that is, further away from the surface, and negative values to a movement towards the surface. Values have been calculated on the basis of structural results from XSW, assuming that the C–C and C–O bond lengths are identical to those in PTCDA in bulk polymorph α ,¹⁰⁸ and further assuming that $d(C_{C-CO}) = d(C_{\text{peryl}})$ or $d(C_{C-CO}) = d(C \text{ total})$ in cases where $d(C_{\text{peryl}})$ has not been determined explicitly (t.w. = this work, n.a. = not available/applicable).

PTCDA/ $M(hkl)$		
	Ref.	$\Delta d_{C_{\text{funct}}} (\text{\AA})$
Au(111)	54	n.a.
Cu ₃ Au(111) (<i>initial</i>)	t.w.	−0.02
Cu ₃ Au(111) (<i>final</i>)	t.w.	−0.06
Cu(111)	43	−0.10
Ag(111)	55	0.04
Ag(111), LT	55	0.11
Ag(100)	t.w.	0.03
Ag(110)	t.w.	0.03
K:Ag(110)	t.w.	0.08



PTCDA molecule is anticipated. We propose that the vertical shifts of the Ag surface atoms with respect to the surface lattice planes, which amount to about $\pm 0.1 \text{ \AA}$ in all three cases [see above and also footnote m) on page 210 of this chapter], represent a valid measure for this deviation. Hence, judging from the buckling amplitudes obtained from DFT, the realized values for $d(C_{\text{peryl}})$ and $d(O_{\text{carb}})$ deviate by about (minus or plus) 0.1 \AA from the minima of the respective potentials. We conclude here that the strength of the $O_{\text{carb}}-\text{Ag}$ bonds, and to some extent also of the $O_{\text{anhyd}}-\text{Ag}$ bonds, plays a decisive role for the adsorption height and for the distortion of the PTCDA molecule on Ag surfaces. The importance of the interactions between O and Ag atoms is also indicated by the E_{ads} values which nicely follow the trends in d and b in relation to the substrate faces (see Fig. 7.10 above).⁴⁸⁷ This is particularly true for $b(O_{\text{carb}}-\text{Ag})$ and $b(O_{\text{anhyd}}-\text{Ag})$. We emphasize again that a commensurate registry and (nearly) on-top positions of the O atoms are required in order to make this bonding channel relevant for the overall surface bonding mechanism.

The enhanced flexibility of the PTCDA molecule causes, besides the increasing distortion $\Delta d(C)$ of the C backbone (see Table 7.1), a distortion of the intrinsically planar functional groups $C_{C-CO}-C_{\text{funct}}O_{\text{carb}}O_{\text{anhyd}}$. The excursion of the C_{funct} atoms, $\Delta d_{C_{\text{funct}}}$, from the plane defined by the O_{carb} , O_{anhyd} , and C_{C-CO} atoms can be calculated for the different systems from the respective d values. The results are compiled in Table 7.10. The planarity of the functional groups is distorted within about $\pm 0.1 \text{ \AA}$, leading to a loss of the mesomeric stabilization and potentially to a partial rehybridization of the involved atoms from sp^2 towards sp^3 . The energetic cost of the intramolecular deformations is apparently counterbalanced by the energy gain through either stronger bonding via the perylene core for PTCDA on the Cu₃Au(111) and Cu(111) surfaces (see Secs. 7.3 and 7.4), or through the formation of covalent O–Ag bonds for PTCDA on the low-index Ag surfaces (see Sec. 7.5). Interestingly, smaller values of $\Delta d_{C_{\text{funct}}}$ are obtained in the latter case,

i.e., on Ag(111), Ag(100), and Ag(110), where charge transfer and the formation of O—Ag bonds co-occur.^{b)} This finding points to a complex *cooperative* interplay of the two bonding channels: The overriding principle appears to be a conservation of the π conjugation in the functional groups $C_{C-CO}-C_{\text{funct}}O_{\text{carb}}O_{\text{anhyd}}$ (and potentially also in the entire molecular backbone).

Local C—Ag interactions

We have already stated in the context of Fig. 7.11 in Sec. 7.5 that the Ag surface buckles upon PTCDA adsorption with an increasing amplitude in the sequence Ag(111), Ag(100), Ag(110). In particular, the Ag atoms below the center of the perylene core are repelled and pushed into the surface, while only the Ag atoms below the C_{C-H} atoms are attracted and pulled out. Furthermore, in the above-introduced schematic picture of the bonding, the realized $d(C_{\text{peryl}})$ values in PTCDA/Ag(*hkl*) are smaller than the d value for the minimum of the binding potential given by the perylene core alone [see Fig. 7.15(c), gray dashed line].

We emphasize, however, that the charge donation is still of bonding character for all Ag surfaces, despite the (local) Pauli repulsion of surface atoms by the perylene core. Figure 7.12 (third and fourth row) shows the accumulation of charge also between the C_{peryl} atoms on the periphery of the PTCDA molecule and the Ag surface atoms, and thus the formation of covalent/coordinate bonds. The repulsion of the Ag atoms from the perylene core into the surface is only observed where the electron density of the metal/molecule hybrid state is marginal, i.e., underneath the long central axis of the PTCDA molecule (see Fig. 7.11), which coincides with the nodal plane of the LUMO. In the case of PTCDA/Ag(110), however, a strong hybridization of the molecular states with metal states causes an accumulation of electron density also below the long central axis of the adsorbed molecule, indicating additional attractive interactions with the surface. This explains the above-mentioned smaller depression of the Ag atoms in this case (see Sec. 7.5).

In order to assess the (relative) strength of the respective C—Ag bonds, we have determined the $\rho_{\text{BCP}}(C-Ag)$ values. Note at this point that we refer to the local interactions of C and Ag atoms at the surface solely as C—Ag, implying a covalent bond between only *two* binding partners, although the interaction may as well be π -like [$\parallel \cdots Ag$ interactions, with \parallel representing a (formal) C=C double bond], i.e., including (at least) two C atoms and one Ag atom, as is the case for the $C_{C-H}-Ag$ interactions in PTCDA/Ag(110), for example [see Fig. 7.12(c), bottom]. Judging from the obtained $\rho_{\text{BCP}}(C-Ag)$ values (see Table 7.9), the strength of the strongest C—Ag interactions, namely, of the $C_{C-H}-Ag$ bonds, exceeds that of the (weaker) $O_{\text{anhyd}}-Ag$ bonds and even reaches that of the (stronger) $O_{\text{carb}}-Ag$ bonds within 20% or less (We have assumed an identical, linear ρ_{BCP} -bond strength correlation for both C—Ag and O—Ag bonds here⁵⁶). Remarkably, $\rho_{\text{BCP}}(C-Ag)$ for the $C_{C-H}-Ag$ bonds in PTCDA/Ag(110) is larger (by ≈ 5 percent) than $\rho_{\text{BCP}}(O-Ag)$ for the $O_{\text{carb}}-Ag$ in PTCDA/Ag(100). This emphasizes the relevance of these local C—Ag interactions to the overall surface bonding mechanism for PTCDA on the low-index Ag surfaces. In conclusion, the interaction between the substrate and the central π system has to be seen as a combination of metal-to-molecule charge transfer on the one hand and attractive or Pauli-repulsive C—Ag or π interactions on the other hand (the π interactions being delocalized to a small extent). The local C—Ag and/or $\parallel \cdots Ag$ bonds partly involve a charge transfer in the inversed direction, i.e., from the molecule to the metal, due to the coordinative nature of the bonds which counteracts the above-noted metal-to-molecule charge transfer.

^{b)} Assuming that $d(C_{\text{peryl}})$ and $d(C_{\text{funct}})$ are (nearly) equal for PTCDA on Ag(111) in the disordered phase (LT) and Ag(100) again (see above) yields an excursion of $\Delta d_{C_{\text{funct}}} \approx 0.03 \text{ \AA}$ also in the former case. Thus, the preceding observation applies also to disordered PTCDA/Ag(111) in the LT phase.

Although the above argumentation has solely focused on the Ag surfaces so far, we assume that similar C–M interactions (M = Cu, Au) also play a role for the bonding of PTCDA on Cu₃Au(111) in the final state (see also Sec. 6.7) and on Cu(111). It has already been concluded in Secs. 7.3 and 7.4 from the available XSW, UPS,⁶⁰ and XPS data for these systems that, due to the relatively small adsorption heights [$\approx 85\%$ of the sum of the vdW radii of C and M, being $\approx 3\%$ larger than that for PTCDA/Ag(111); see Table 7.2], a substantial metal-to-molecule charge transfer occurs. In the present cases of final-state PTCDA/Cu₃Au(111) and PTCDA/Cu(111), the donated charge is in principle (fully) available for the formation of local, dative C–M bonds because, in contrast to the case of PTCDA/Ag(*hkl*), the excess electrons are *not* accumulated in respective O–M bonds. Thus, we suggest at this point that the C–M interactions may even be more pronounced here than for PTCDA on the low-index Ag surfaces, which would have to be proven by DFT calculations.

Synergism of bonding channels

The interplay of the chemical bonding channels for all systems discussed in the present work can be summarized as follows:

1. There is a metal-to-adsorbate charge transfer over the entire molecule (bonding channel 3 of the list at the beginning of this section, see page 214).
2. The charge transfer enhances the flexibility of the PTCDA molecule and facilitates intramolecular distortions.
 - a. For incommensurate PTCDA superstructures, i.e., on Cu₃Au(111) and Cu(111), the molecule distorts boat-like, allowing for an enhanced metal–perylene core interaction.
 - b. For commensurate PTCDA superstructures, i.e., on the low-index Ag surfaces, local covalent bonds evolve between the O, especially the O_{carb}, and the Ag surface atoms (bonding channel 4), leading to saddle- [on Ag(111)] and arch-like adsorption configurations [on Ag(100) and Ag(110)].
3. The interaction on the perylene core turns (or may turn) partially Pauli-repulsive.
4. Attractive C_{peryl}–M interactions (may) evolve on some of the perylene core atoms (bonding channel 5, M = Cu, Ag, Au).

The relevance of the above-listed bonding channels increases with the surface reactivity, that is, with decreasing Φ . The non-planar adsorption configurations are supported by the charge donation (**ad 1**), which results in a (partial) rehybridization of the molecular orbitals. This, in turn, allows the PTCDA O atoms to move either not as close to the surface (**ad 2.a**) or closer to the surface than the perylene core (**ad 2.b**). In both cases, however, the perylene core moves closer to the surface than anticipated for an undistorted, planar adsorption configuration, further facilitating the charge transfer. On the one hand, the charge transfer supports the formation of local O–Ag bonds in the case of PTCDA/Ag(*hkl*) (**ad 2.b**). On the other hand, the formation of local C–M bonds is supported, too (**ad 4**), which compensate for or even outweigh (potential) local Pauli repulsion between surface atoms and the perylene core for PTCDA on Ag(111), Ag(100), and Ag(110) (**ad 3**). This is particularly true for PTCDA on the more open Ag surfaces, i.e., for pronounced metal-to-molecule charge transfer and strong O–Ag bonding. Presumably, local C–M interactions are

also present for PTCDA/Cu₃Au(111) in the final state and for PTCDA/Cu(111). Both the local O—Ag and C—M bonds (M = Cu, Ag, Au) are of coordinative/dative nature.¹⁰⁾

Thus, there is a simultaneous charge transfer in both directions across the metal/organic interface. The bonding mechanism of PTCDA to coinage metal surfaces, hence, proceeds in a complex and *synergistic* interaction cycle, bearing similarities to the Blyholder model (see Sec. 2.1.1).¹⁰ For the more reactive/open surfaces, the covalent O—Ag and (postulated) C—M bonds are significantly shorter as a consequence of a reinforced interaction cycle. In conclusion, the bonding of PTCDA on coinage metal surfaces can be well described with one *universal* bonding mechanism, where the delicate balance between the different bonding channels and hence their individual relevance depends on both the electronic properties of the (clean) substrate surface and the lateral geometric structure of the metal/organic interface.

7.7 Manipulation of bonding channels

Now that we have established a conclusive and universal picture of the surface bonding mechanism for PTCDA/M(*hkl*) (M = Cu, Ag, Au) it is a valid question to be raised how the synergistic interplay of the individual bonding channels may be influenced. We have probed the relevance and also the coupling of both the metal-to-molecule charge transfer and local, covalent interactions by varying the substrate elemental composition and orientation (see above). In addition, we have investigated the feasibility of manipulating bonding channels via the coadsorption of reactive metal atoms, using the example of K + PTCDA/Ag(110) or, more precisely, PTCDA/K:Ag(110). The above-established synergistic interaction cycle will be reasoned and shown to be valid also for this system on the basis of structural arguments in conjunction with XP- and UV-spectroscopic results, proving the postulated coupling of the individual bonding channels.

In principle, the coadsorbed potassium may be expected to interact via at least two different bonding channels. On the one hand, K atoms as a potential electron donor may donate charge to the adsorbed PTCDA molecules, possibly competing with the charge transfer from the substrate. On the other hand, local O—K interactions may be expected which have been proven to be present in K-doped PTCDA multilayer films or crystals by means of XPS, UPS, and infrared spectroscopy^{64,554,555} as well as by DFT.⁶⁵ In both cases, the surface bonding to the Ag substrate (atoms)

¹⁰⁾ For reasons of clarity, we recite the definitions of a coordinative or dative bond here. According to the International Union of Pure and Applied Chemistry (IUPAC), coordination, i.e., the formation of a coordinative bond, is defined as follows:⁸⁵

The formation of a covalent bond, the two shared electrons of which have come from only one of the two parts of the molecular entity linked by it, as in the reaction of a Lewis acid and a Lewis base to form a Lewis adduct; alternatively, the bonding formed in this way. In the former sense, it is the reverse of unimolecular heterolysis.

A dative bond is defined by the IUPAC as:⁸⁵

The coordination bond formed upon interaction between molecular species, one of which serves as a donor and the other as an acceptor of the electron pair to be shared in the complex formed [...]. In spite of the analogy of dative bonds with covalent bonds, in that both types imply sharing a common electron pair between two vicinal atoms, the former are distinguished by their significant polarity, lesser strength, and greater length. The distinctive feature of dative bonds is that their minimum-energy rupture in the gas phase or in inert solvent follows the heterolytic bond cleavage path.

Following the IUPAC definition of a “coordinative bond”, the synonym “dative bond” has become obsolete because the origin of the bonding electrons has by itself no bearing on the character of the bond formed.⁸⁵ Yet, within the framework of the present work, both terms are used synonymously.

is presumably weakened. Although the overall interplay of the bonding channels is considered as synergistic, we expect the presence of additional bonding channels to decrease the relevance of those bonding channels “intrinsic” to PTCDA/Ag(110) in the surface bonding mechanism.

Experimental findings

As has been already described in Sec. 7.1, the coadsorbed K atoms are incorporated in the Ag(110) surface, forming a local (1×3) surface reconstruction (see Fig. 7.2). K-induced surface reconstructions of type $(1 \times n)$ with $n = 2, 3$, depending on the K coverage, are known to occur also on the clean Ag(110) surface.^{282,556–558} These reconstructions are caused by a charge donation from the K atoms to the Ag substrate [yielding (partially) positively charged K atoms at the surface] which destabilizes the intrinsic (1×1) surface due to electronic re-organizations.^{559–561} Note that the equivalent quantity of K atoms which is present in a full monolayer of PTCDA/K:Ag(110) and which amounts to $\theta_K = 0.18(2)$ ML, as has been determined with SPA-LEED in conjunction with XPS (where 1 ML corresponds to one K atom per Ag surface atom; see also Sec. 4.2 as well as Secs. D.3.1 and D.3.2 in the appendix of the present work), induces a (1×2) reconstruction on the *clean* surface²⁸² while a local (1×3) reconstruction is found for the *PTCDA-covered* Ag(110) surface. Therefore, a substantial interaction of the K atoms with the PTCDA is anticipated which causes the change in the periodicity of the reconstruction. This interaction proceeds via both direct and indirect ways as will be evidenced below.

First, however, we deduce the individual relevant bonding channels from the adsorption configuration. Figure 7.16 contrasts the adsorption configurations of PTCDA on the pure Ag(110) and the modified K:Ag(110) surface. Upon incorporation of K in the Ag surface layer, the adsorption configuration has changed from *arch*-like to *saddle*-like or, by tendency, to a nearly planar one [$\Delta d = d_{\max} - d_{\min} = 0.16(16)$ Å is comparably small, see Table 7.1]. The d values of the O_{carb} and O_{anhyd} atoms are larger by 0.32(13) Å and 0.40(10) Å in PTCDA/K:Ag(110) in comparison to the K-free system (see also Table 7.1). The perylene core has moved upwards by 0.07(2) Å. The C_{funct} atoms now exhibit a 0.30(12) Å larger d value which causes, in conjunction with the realized d values of the other atoms in PTCDA, a substantial deformation of the functional groups away from a planar arrangement of the involved atoms [$\Delta d_{C_{\text{funct}}} = 0.08$ Å; see Table 7.10 in Sec. 7.6]. Two aspects can be rationalized from the determined adsorption heights: (1) The O–Ag interactions have been weakened, or even been lifted, by the presence of K within the surface, judging from the increased d values. (2) Subsequently, the perylene core has relaxed away from the surface, although strong bonding is still anticipated from the realized $d(C_{\text{peryl}})$ value [2.65(2) Å or 76(1) % of the sum of the vdW radii, being second smallest for PTCDA on the investigated coinage metal surfaces; see Tables 7.1 and 7.2]. These findings are in good agreement with our above-established model of the coupling of the two bonding channels for PTCDA (see Fig. 7.15, in particular) and will be elucidated in the following.

Bonding on the functional groups

According to our structural model for PTCDA/K:Ag(110) (see Fig. 7.2 above), which is based on a combination of XSW, XPS, STM,⁶⁸ and SPA-LEED results (see Sec. C.3 in the appendix of the present work), the O_{anhyd} are located nearly on-top of the K atoms in the surface layer. In fact, XSW has revealed that the K atoms are located within the Ag surface layer. Furthermore, the determined binding energy shifts ΔE_b in XPS of (about) 0.2 eV, 0.58 eV, and 0.64 eV for the C_{peryl} , O_{carb} , and O_{anhyd} components (see also Table 7.6 and Fig. 7.8) suggest that the K atoms within the substrate surface layer are located closest to the O_{anhyd} which exhibit the largest ΔE_b value (see

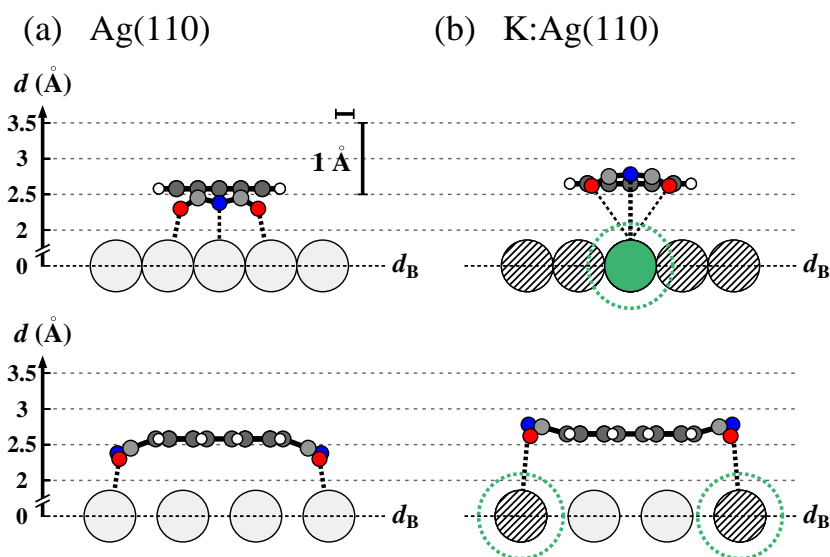


FIG. 7.16. Comparison of the adsorption configurations of PTCDA (a) on the pure Ag(110) and (b) on the K-modified Ag(110) surface. The top row shows side views along the long molecular axis while the bottom row shows side views along the short molecular axis. K atoms are shown in green, H atoms in white, C_{funct} and C_{peryl} atoms in light gray and dark gray, and O_{carb} and O_{anhyd} atoms in red and blue, respectively. d denotes the vertical adsorption height; the vertical scale is enlarged by a factor of 4 and referenced against the Bragg plane (dashed line, d_B). O—Ag and O—K interactions are illustrated by black dotted lines, respectively. For reasons of clarity, the depicted PTCDA molecule on the K:Ag(110) surface in (b) has exactly been aligned with the [001] substrate direction although it has been found at a small angle (2°) with respect to the substrate lattice in the experiment.⁶⁸ The shaded atoms represent ideal surface positions which potentially are not occupied by Ag atoms and thus vacant. Note that the K atoms are depicted with the same metallic radius as the Ag atoms; the intrinsic metallic radius of K atoms is indicated by green dashed circles.¹⁴²

also Sec. 7.1). The shifting towards higher binding energies can be explained by a combination of both initial and final state effects.⁶⁸ On the one hand, the presence of positively charged K atoms increases the energy required to excite a photoelectron from a core level due to the induced electrostatic field (initial state effect, chemical shift¹⁵⁷). On the other hand, the positive charge of the K atoms diminishes the screening of the created core hole by surrounding electrons (in the metal substrate or within the molecule) because a re-organization of the electron density will require more energy (final state effect, relaxation shift¹⁵⁷). Note that, given the above reasoning, the observed shifts towards higher E_b do *not* imply a reduced metal-to-molecule charge transfer in comparison to the situation without K, as has also been proven by means of UPS (see below).⁶⁸

While the O_{anhyd} atoms in PTCDA are located (nearly) on-top of K atoms, the surface positions underneath the O_{carb} atoms may be vacant. This is required by stoichiometric considerations regarding the absolute quantities of K and Ag atoms at the surface. Here, we assume that the uppermost terraces in Fig. 7.2 (light gray Ag atoms) have been built from Ag atomic rows originating from the next lower layer (medium gray, the “original”, unreconstructed surface layer) which, in turn, have been replaced by (a lower number of) K atoms. Hence, we conclude that the $O_{\text{carb}}-\text{Ag}$ bonds (and the $O_{\text{anhyd}}-\text{Ag}$ bonds, as well; see also below) which are present in pure PTCDA/Ag(110) have indeed been eliminated, simply due to the absence of Ag atoms as binding partners. Therefore, the O atoms have relaxed towards higher d values for PTCDA/K:Ag(110). In particular, the O_{carb} atoms reside at almost the same height as the perylene core (within 0.03 \AA) in PTCDA/

K:Ag(110), presumably in order to minimize the overall molecular distortion in favor of maximal π conjugation. Potentially, the increased π conjugation within the molecule may also explain the upward shifting in E_b of the C1s peak 2 and the C_{funct} component, respectively, of more than 1 eV observed in XPS when going from PTCDA/Ag(110) to PTCDA/K:Ag(110).

However, the initial O—Ag interactions have been replaced (partially) by O—K interactions. This becomes apparent from the respective bond length $b(\text{O—K})$ which have been calculated from the lateral and vertical positions of both the O atoms in PTCDA and the K atoms within the surface layer. The lateral O positions have been deduced from the structural model, considering the 2° rotation of the long molecular axis away from the [001] substrate direction and assuming the (lateral) intramolecular coordinates of PTCDA bulk polymorph α to apply here, too.^{68,108} The vertical positions have been taken from XSW. Ideal, i.e., bulk-determined surface positions, which were occupied by Ag atoms in the unreconstructed surface, have been assumed for the K atoms because XSW revealed a vertical position within 0.02 Å around the ideal position on the Bragg plane. The choice of the lateral position has already been reasoned above. We find $b(\text{O}_{\text{carb}}\text{—K})$ and $b(\text{O}_{\text{anhyd}}\text{—K})$ values of 3.45(9) Å and 2.82(10) Å, respectively.^{v)} All values are considerably smaller than the sum of the vdW radii of O and K, 4.40 Å (see also Table 2.3),¹⁴¹ indicating substantial O—K interactions, in particular for the O_{anhyd} atoms. In fact, the determined $b(\text{O}_{\text{anhyd}}\text{—K})$ value is only 5(4) % larger than the sum of the covalent radii¹⁴⁴ and is well within the range expected for ionic interactions (2.72–3.06 Å;^{145,146} see Table 2.3).^{w)} In general, O—K bonds are expected to be more ionic in character than O—Ag bonds due to the larger differences in electronegativity between the binding partners.^{x)} Hence, we conclude that the length of the local bonds between the O_{anhyd} atoms and the underlying metal atoms increases simply due the larger size of the K atoms compared to Ag (see Table 2.3). At the same time, the bond character changes from covalent to ionic. Because the “new” $\text{O}_{\text{anhyd}}\text{—K}$ bonds are *shorter in relative terms* than the “former” $\text{O}_{\text{anhyd}}\text{—Ag}$ bonds [63(2) % versus 71(1) % of the sum of the corresponding vdW radii; see also Table 7.2], we further conclude that the $\text{O}_{\text{anhyd}}\text{—K}$ bonds are stronger.^{56,57}

Bonding on the perylene core

We now discuss the bonding via the perylene core: Following the schematic model of two major bonding channels for PTCDA on the Ag(110) surface as depicted in Fig. 7.15(c) (via the perylene core and via local O—Ag bonds), the removal of the O—Ag bonds in the case of PTCDA/K:Ag(110) was expected to result in a lifting of the perylene core away from the surface. The reason behind this is to avoid Pauli repulsion (see Fig. 7.11 and also Secs. 7.3 and 7.6). From the depression of the Ag surface atoms of maximal -0.12 Å with respect to the surface lattice plane d_B [see footnote m) on page 210 of this chapter], a lifting of this magnitude was expected for the C_{peryl} atoms. Note that, under the plausible assumption of identical PTCDA adsorption sites, the surface geometry underneath the perylene core should be very similar in the cases with and without K, in principle allowing for essentially identical interactions (The small rotation of the long molecular

^{v)} Assuming that K atoms are present also underneath the O_{carb} (in ideal positions), $b(\text{O}_{\text{carb}}\text{—K})$ amounts to 2.74(11) Å on average for this O—K interaction. This might be the case for a small excess of K atoms at/within the surface. In principle, the PTCDA/K:Ag(110) structure forms under variation of the K coverage within a range of about ± 10 %. In fact, XPS points at a K : PTCDA ratio of about 3.0(3) : 1 which, however, is not compatible with our structural model and the coverage calibration with SPA-LEED, being too large by ≈ 50 %. Therefore, we conclude that, besides the ordered PTCDA/K:Ag(110) structure, small three-dimensional K clusters are formed which LEED is invisible to.

^{w)} The O—K distance in the KO_2 molecule has been determined as 2.10–2.55 Å with both experimental and theoretical methods.^{562–564} In the solid state, the O—K distances in KO_2 are 2.71 Å and 2.92 Å, respectively.⁵⁶⁵

^{x)} The electronegativities χ of O, K, and Ag amount to 3.50, 0.91, and 1.42 according to the formalism proposed by Allred and Rochow, for example.^{146,524}

axis of 2° away from the [001] substrate direction may be negligible here). However, XSW has revealed a lifting of only $0.07(2) \text{ \AA}$, being about 40 % smaller. Hence, the bonding via the perylene core is enhanced for PTCDA/K:Ag(110) in comparison to pure PTCDA/Ag(110) since the loss of the O—Ag bonds is partially compensated.

This finding can be understood as follows. Due to the (partial) electron transfer from K to Ag at the surface (see above), excess charge is in principle available at the metal/organic interface which reinforces this bonding channel. An enhanced metal-to-molecule charge transfer in PTCDA/K:Ag(110) (via the perylene core; see also Sec. 7.3) can indeed be deduced from UPS. Firstly, we anticipate at this point that the (unfortunately unavailable) Φ value of the bare K:Ag(110) surface is very low and thus much lower than that of the pure Ag(110) surface due to the reactive character of the K atoms [the work functions Φ of K (polycryst.) and Ag(110) amount to 2.30 eV^{519} and 4.52 eV^{510} respectively; see also Table 7.5].²⁰ Since we have observed a shift in Φ of only -0.58 eV for PTCDA/K:Ag(110) in comparison to pure PTCDA/Ag(110),⁶⁸ we conclude that there is a substantially *larger* increase in the substrate work function upon PTCDA adsorption, $\Delta\Phi_{\text{PTCDA}}$, for K:Ag(110) than for pure Ag(110). A larger increase in Φ indicates a more pronounced metal-to-molecule charge transfer (see also Sec. 7.4). Secondly, the HOMO peak is shifted by 470 meV towards higher binding energy E_b in comparison to the pure PTCDA/Ag(110) system while the F-LUMO is shifted by 360 meV .⁶⁸ Mere work function effects can be excluded since the shifting is differential, pointing to a reorganization of the molecule/metal hybrid states and thus an altered bonding situation (in accordance with the determined adsorption configuration). We attribute the slightly smaller shifting towards higher E_b of the F-LUMO peak in comparison to the HOMO peak (by 110 meV) for PTCDA/K:Ag(110) to the increased adsorption height [$\Delta d(C_{\text{peryl}}) = +0.07(2) \text{ \AA}$],⁶⁸ because the (F-)LUMO as the acceptor state is more sensitive to the realized d value than the HOMO according to the Newns-Anderson model and shifts, in relative terms, to smaller E_b values.⁸⁶

The enhanced metal-to-molecule charge transfer (see above) results in a greater electrostatic interaction between the PTCDA molecule, that is, mainly the perylene core, and the metal substrate. Also the change in character of the local O—M bonds ($M = \text{Ag, K}$) from covalent (dative) to ionic reinforces this bonding channel: Because the charge donation from the molecule to the metal via the (local) O—M bonds is reduced in the case of PTCDA/K:Ag(110) compared to pure PTCDA/Ag(110) due to their rather ionic character, a more negative net charge Δq of the adsorbed PTCDA molecule is expected, further intensifying the electrostatic interaction. Hence, competing effects occur here. On the one hand, an enhanced metal-peryrene core interaction is expected to lead to a smaller adsorption height $d(C_{\text{peryl}})$.^{56,57} On the other hand, a larger $d(C_{\text{peryl}})$ value is favored due to the Pauli repulsion, as judged from the observed buckling of the pure, K-free Ag surface. The experimentally determined value of $+0.07(2) \text{ \AA}$ is thus understood as being a compromise between these two conditions. In addition, one may speculate that the local C—Ag bonds, which have been proven to exist for PTCDA/Ag(110) (see Sec. 7.6) and are anticipated also for PTCDA/K:Ag(110), may gain strength, too, due to the potentially increased electron density on the adsorbed molecule.

In conclusion, the bonding situation at the surface in PTCDA/K:Ag(110) can be envisaged as being similar to that depicted in Fig. 7.15(b) but considering, in particular, the potential energy E as a function of d for the O_{anhyd} atoms instead of the O_{carb} atoms (shown in red). The perylene core is located closer to the surface than the O_{anhyd} but as close as given by the minimum of the schematic binding potential. This is simply due steric reasons, namely, due to the larger size of the K atoms in comparison to Ag atoms, with the consequence of $d(\text{O}_{\text{anhyd}}) > d(C_{\text{peryl}})$. Thus, the perylene core is located (slightly) further away from the surface when comparing PTCDA/Ag(110)

with and without K being incorporated in the surface although the two major bonding channels, namely, via the perylene core and via local O—M interactions, are strengthened by the potassium.

To summarize, the presence of K influences the surface bonding of PTCDA on Ag(110) in (at least) two ways: (1) in a direct manner by replacing the original (covalent) O—Ag bonds with (presumably ionic) O—K bonds, and (2) in an indirect manner by enhancing the metal-to-molecule charge transfer, that is, the bonding via the perylene core. Therefore, the example of PTCDA/K:Ag(110) shows that it is *not* possible to selectively manipulate one of the relevant bonding channels. Hence, the above-proposed model of a synergistic interaction cycle for PTCDA adsorption on coinage metal surfaces is once again valid here.

7.8 Final general conclusions

In this chapter, we have established a conclusive and universal bonding mechanism for the surface bonding of PTCDA on coinage metal surfaces. This bonding mechanism allows to describe the surface bonding, in both a qualitative and a semi-quantitative manner, for varying surface reactivities, that is, for varying elemental compositions and orientations of the surface. The essential constituents of the bonding mechanism are:

1. Metal-to-molecule charge transfer, which also facilitates the formation of local bonds (see points 2. and 3. below) due to an increased electron density on the molecule and an enhanced flexibility allowing for intramolecular distortions.
2. Local O—M bonds ($M = \text{Ag}, \text{K}$), which necessitate a commensurate registry between the adsorbate and the substrate *and* an (nearly) on-top positioning of the O atoms in PTCDA with respect to the metal surface atoms.
3. Local C—M bonds ($M = \text{Cu}, \text{Ag}$), in cases of strong bonding.

These bonding channels grow in relevance with increasing surface reactivity, i.e., with decreasing work function Φ . They overcompensate intermolecular interactions, which favor a herringbone arrangement of the PTCDA molecules—independent of the surface orientation and regardless of potential bonding to the surface—and pervasive van der Waals interactions (although, energy-wise, the latter still are the main contribution to the surface bonding) in determining both the molecular orientation, and thus the lateral structure, as well as the adsorption configuration. The local O—M and C—M bonds are of covalent and dative character. Yet, in the case of PTCDA/K:Ag(110), largely ionic O—K bonds are presumed.

There is a delicate coupling between all the individual bonding channels, and the bonding mechanism of PTCDA to coinage metal surfaces proceeds in a complex, synergistic interaction cycle. The synergistic cycle is reinforced on the more reactive surfaces. It is schematically depicted in Fig. 7.17, using the example of PTCDA/Ag(110). The bonding mechanism bears similarities to classical bonding models for small molecules on surfaces, such as the Blyholder model¹⁰ or the Hoffmann model,^{12,13,89} and also to the Dewar-Chatt-Duncanson model describing the bonding in metal π -complexes.^{78,79} We suggest that our proposed picture also holds for other π -conjugated functionalized planar molecules on surfaces.^{40,520}

7.9 Outlook

As stated above, we suggest that our proposed bonding mechanism with its relevant constituents (bonding channels) also applies to the adsorption of other organic, π -conjugated and functional-

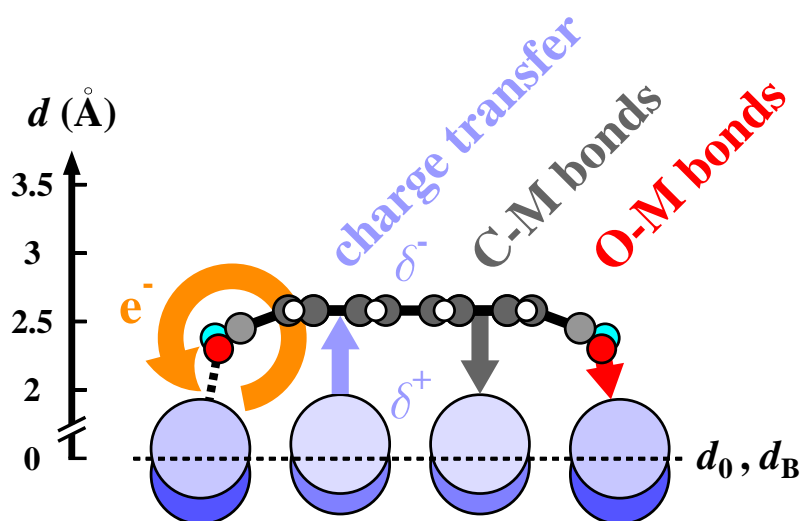


FIG. 7.17. Schematic representation of the bonding mechanism for PTCDA adsorption on coinage metal surfaces, using the example of PTCDA/Ag(110). The PTCDA molecule is shown in a side view along the short molecular axis. Ag atoms are shown in different shades of blue in order to indicate the vertical deviation Δd from their position in the relaxed uncovered surface (dashed line, d_0 ; see also Fig. 7.11); H atoms are shown in white, C_{funct} and C_{peryl} atoms in light gray and dark gray, and O_{carb} and O_{anhyd} atoms in red and blue, respectively. d denotes the vertical adsorption height; the vertical scale is enlarged by a factor of 4 and referenced against the Bragg plane (dashed line, d_B). Vertical positions of the C and O atoms in PTCDA have been taken from XSW, and those of the Ag atoms from DFT. O—Ag interactions are illustrated by black dotted lines. The orange curved arrow illustrates the (potential) charge flow (e^-) across the metal/organic interface. The metal-to-molecule charge transfer is marked as a pale-blue arrow. δ^+ and δ^- denote the partial charges. Covalent, dative C—M and O—M bonds (M = Cu, Ag) are represented by gray and red arrows, respectively; in case of K coadsorption, largely ionic O—K bonds are formed.

ized molecules on (metal) surfaces.^{40,520} Recently, a experimental and theoretical study on the adsorption of pentacene-derived quinones, i.e., oxidized derivatives of hydroxy-substituted pentacene, has been reported (Ref. 40), for example, where the relevance of charge transfer, rehybridization, and local metal/molecule interactions for the surface bonding was emphasized, too. As an outlook for future mechanistic studies on adsorption on surfaces, we propose the following additional experiments in order to further validate (or maybe disprove) our above-postulated, conclusive bonding mechanism. Besides investigating the adsorption properties of other (prototype) organic molecules, the below-mentioned investigations which still focus on the surface bonding mechanism of PTCDA, in particular, will or should be considered:

1. The adsorption heights of the O atoms in PTCDA on the Au(111) surface should be determined with XSW, in addition to the already known adsorption height of the C atoms.⁵⁴ We expect a (nearly) planar adsorption configuration. The experimental challenge of the $O1s$ XPS signal being overlaid by an Au Auger line experienced in earlier investigations⁵⁴ may be overcome in two ways, potentially: (1) detecting the photoelectrons at an angle of close to 90° with respect to the surface normal, which reduces the contributions from the substrate to the observed spectra and thus the impact of the Auger line on the XPS signal of interest to a minimum (due to enhanced surface sensitivity); or (2) shifting the Bragg energy E_B and thereby the required photon energy by cooling and (slightly) tilting the sample in the XSW experiment, which virtually shifts the Au line away from the XPS signal under investigation.

2. UPS investigations of PTCDA/Cu₃Au(111) may further prove the altering in the bonding situation (from physisorption to chemisorption) upon the transition from the initial to the final state, and also the increased metal-to-molecule charge transfer in the latter case, in addition to the indications from core level spectroscopy and the determined adsorption configurations. Furthermore, (potential) shifts of the Shockley surface states of Cu₃Au(111) and Cu(111) upon PTCDA adsorption should be quantified with 2PPE because such shifts can be regarded as a measure for the adsorption height, and thus also for the character and the strength of the metal/molecule interaction.¹³⁵
3. The buckling of the low-index Ag surfaces upon PTCDA adsorption which is observed in DFT calculations, should be verified by means of LEED- $I(V)$.⁵⁶⁶ Besides, one may attempt to establish LEED- $I(V)$ as a method for determining adsorption configurations (for commensurate registry), having the respective data for PTCDA/Ag(hkl) as benchmark data from XSW at hand.⁵⁶⁷
4. The adsorption configuration of PTCDA in the herringbone phase on the Ag(110) surface, which can also be prepared in the monolayer and which is *not* commensurate,^{269,568} should be determined with XSW. Based on our elaborate picture of the bonding mechanism, we expect a larger adsorption height of the perylene core as well as the disappearance of local O—Ag bonds in comparison to the (commensurate) brick-wall phase of PTCDA/Ag(110).
5. The adsorption configuration of PTCDA on the Cu(100) surface should also be determined with XSW. Here, a commensurate superstructure is present (see Refs. 569 and 570, in particular),^{117,315,316,569,570} in contrast to PTCDA/Cu(111). Due to the lower Φ of the clean Cu(100) surface in comparison to Cu(111),^{63,507} a smaller adsorption height is expected. Furthermore, local, covalent O—Cu and/or C—Cu bonds may evolve as a consequence of both the (potentially) strong bonding⁵²⁰ and the commensurate registry. This could be judged from the realized adsorption configuration.
6. The adsorption configuration of PTCDA on insulator surfaces, such as NaCl^{571,572} or KCl,⁵⁷³ should be determined, too. This would allow to (experimentally) prove the applicability of our proposed bonding mechanism for PTCDA adsorption also on others than metal surfaces. Recent DFT calculations by Aldahhak *et al.*, for instance, have indeed suggested an arch-like adsorption configuration of PTCDA on both NaCl and KCl with an intramolecular vertical distortion of up to 0.48 Å;⁵⁷⁴ that is, the O atoms are substantially closer to the surface than the perylene core,⁵⁷⁴ indicating strong local interactions between the O atoms and metal cations at the surface (the alkali halide surfaces are predicted to buckle at an overall amplitude of about 0.2 Å⁵⁷⁴). Besides, a metal-to-molecule charge transfer of 0.79 e has been observed in the calculations for PTCDA/NaCl(100).⁵⁷⁴

8

Summary

The aim of the present work was to establish a comprehensive bonding mechanism for the adsorption of the organic prototype molecule PTCDA on coinage metal surfaces. PTCDA was chosen as a testing probe for the influence of the surface reactivity on the lateral structure formation and the realized adsorption configuration(s) of aromatic molecules on metal surfaces. Due to its chemical constitution, the PTCDA molecule allowed studying the effects of both the π -conjugated system and the presence of functional groups, including heteroatoms, on the interfacial bonding. Conclusions on the relevant metal/molecule interactions were drawn from the results of structural investigations (XSW, LEED, STM) in combination with spectroscopic results (XPS, UPS) and theoretical calculations (DFT).

Summary of the experimental findings

Within the framework of the present study, the available experimental data for PTCDA/M(*hkl*), in particular for the monolayer regime, has been amended by structural clarifications and refinements as well as, to a certain extent, by electronic properties for the following systems:

- (a) PTCDA/Cu(111).
- (b) PTCDA/Cu₃Au(111).
- (c) PTCDA/Ag(100).
- (d) PTCDA/Ag(110).
- (e) PTCDA/K:Ag(110).

In particular, the adsorption configurations have been determined for the latter four systems [systems (b)–(e)]. They have been compared and related to the already available adsorption configurations of PTCDA on the (111) surfaces of Au,⁵⁴ Ag^{32,43,55,151} and Cu.⁴³ In the following, the individual results and conclusion will be summarized.

PTCDA on Cu(111)

Two herringbone (HB) phases have been identified for PTCDA/Cu(111) in the monolayer regime with SPA-LEED (**ad a**), one main phase α and a minority phase β . Both of them exhibit point-on-line (p-o-l) commensurability with respect to the Cu(111) surface. In contrast to earlier STM results by Wagner *et al.*,¹¹⁵ a commensurate PTCDA superstructure has not been observed. This is explained such that a potentially commensurate structure of PTCDA on Cu(111) would only be kinetically stabilized, as is also the case for the minor HB phase β . This β phase could only be prepared selectively (in small domains) by thermal annealing of essentially disordered films prepared at low temperatures. Neglecting potential effects of the substrate-surface lattice constants, the lack of commensurability between the PTCDA overlayer and the substrate surface evidences

a weaker metal/molecule interaction for PTCDA/Cu(111) in comparison to PTCDA on the low-index Ag surfaces, for example, where commensurate superstructures are present.^{98,120} Nonetheless, a metal-to-molecule charge transfer exists,⁶⁰ explaining also the reported boat-like adsorption configuration (see also below).⁴³ This charge transfer is interpreted as causing a reconstruction on the intrinsically unreconstructed Cu(111) surface upon PTCDA adsorption which had not been observed before.

PTCDA on Cu₃Au(111)

The Cu₃Au(111) surface has been shown to behave rather Au-like (**ad b**). The *clean* surface is depleted in Cu atoms and enriched in Au atoms (leading to a reduced long-range order), and the surface stoichiometry amounts to Cu_{0.61(2)}Au_{0.39(2)} as opposed to the expected value of Cu_{0.75}Au_{0.25}. In addition, the surface is relaxed in outward direction by about 15 % of the lattice plane spacing. This is understood as a consequence of the reduced Cu fraction in the surface layer due to both a weakening of the interlayer bonding and Pauli repulsion of the larger Au atoms, which may also adopt former Cu sites and/or interlattice sites at the surface. PTCDA forms three different HB structures (termed α , β , and γ), along with a quadratic (S or δ) phase after thermal annealing, in the monolayer on the Cu₃Au(111) surface two of which (α , β) are analogous to HB structures on the pure Au(111) surface. A PTCDA/Cu(111)-analogous phase (γ) is present only as a minority phase. Remarkably, the PTCDA-covered Cu₃Au(111) surface further relaxes outward by an additional 12 % of the lattice plane spacing as compared to the clean surface.

Furthermore, the Cu fraction in the surface layer increases again with time of x-ray beam exposure. Over two hours, the surface stoichiometry reaches a value of Cu_{0.69(4)}Au_{0.31(4)} eventually, which is close to the ideal surface stoichiometry of Cu_{0.75}Au_{0.25}. Our measurements indicate that the top-layer position of the PTCDA-covered Cu₃Au(111) surface is not altered upon this modification of the surface stoichiometry. At the same time, however, the bonding situation at the metal/organic interface changes as reflects in the adsorption configurations. In the *final* state, i.e., in the “Cu-rich” state of the Cu₃Au(111) surface, the perylene core is 0.24(5) Å lower than in the *initial* state, i.e., in the “Au-rich” state. The adsorption configuration is boat-like in both states, but the intramolecular distortion perpendicular to the surface in the final state is twice the size of that in the initial state. Thus, the adsorption configuration transforms from rather Au-analogous towards Cu-analogous while the lateral structure remains unaffected. The observed binding energy shifts in XPS support the interpretation of a stronger, chemisorptive bonding of PTCDA/Cu₃Au(111) in the final state as opposed to a largely physisorbed bonding in the initial state. Furthermore, a metal-to-molecule charge transfer can be concluded from the determined ΔE_b values. As stated above, the top-layer position of the PTCDA-covered Cu₃Au(111) surface is not altered upon the initial- to final-state transition.

PTCDA on Ag(100) and Ag(110)

Arch-like adsorption configurations have been found for PTCDA on the (100) and (110) surfaces of Ag (**ad c**, **ad d**). Considering also the (saddle-like) adsorption configuration of PTCDA on Ag(111),^{32,55} a clear trend has become evident. With decreasing coordination number (CN) of the Ag surface atoms and decreasing work function Φ in the series Ag(111), Ag(100), Ag(110), the adsorption heights of both the C and O atoms in PTCDA decrease, too, being ≥ 18 % lower than the sum of the van der Waals (vdW) radii of the involved atoms, namely, C and O atoms on the one hand and Ag atoms on the other hand. This is accompanied by an increasing metal-to-molecule charge transfer and the evolution of covalent, dative O—Ag bonds in the same sequence, as UPS⁵⁹ and DFT have evidenced. Furthermore, C—Ag bonds with increasing strength are formed, also being covalent and dative in character.

The formation of local bonds is favored by the commensurate registry of the PTCDA molecules with the substrate in combination with the close proximity of the respective binding partners, i.e., by the (nearly) on-top adsorption sites of O and C atoms or C=C double bonds with respect to the Ag surface atoms. Although the interaction via the perylene core is of bonding character, local Pauli repulsion of some of the Ag surface atoms underneath the PTCDA molecule is observed in DFT.

Coadsorption of K and PTCDA on Ag(110)

We have shown that K atoms can be incorporated in the Ag(110) surface underneath the O_{anhyd} atoms in PTCDA via coadsorption of K at PTCDA/Ag(110) and subsequent (mild) thermal annealing (**ad e**). The adsorption configuration of the PTCDA molecule changes from arch-like to saddle-like, with a comparably small vertical distortion. The perylene core is lifted by 0.07(2) Å in comparison to situation without K while the O atoms move upwards by about 0.3–0.4 Å. Local, presumably ionic O–K bonds are formed which are longer than the original O–Ag bonds due to the larger size of K compared to Ag. At the same time, the bond on the perylene core is modified by competing effects: On the one hand, the adsorption height increases in order to minimize the (local) Pauli repulsion between Ag surface atoms and C atoms within the perylene core. On the other hand, the electrostatic interaction with the surface may be enhanced, limiting the upward relaxation of the molecule. The electron density on the molecule is presumably increased because, firstly, the dative O–Ag bonds, which lead to a charge transfer also from the molecule to the metal, are no longer present and, secondly, the metal-to-molecule charge transfer may be intensified by additional electrons from the potassium. The postulated electron donation from K to adsorbed PTCDA, in particular to the perylene core, potentially occurs via the Ag substrate (atoms).

Bonding mechanism for PTCDA adsorption

Within the present work, a conclusive and universal bonding mechanism for PTCDA adsorption on coinage metal surfaces has been deduced from our and earlier experimental findings. This bonding mechanism allows to explain the observed trends in the adsorption configurations, and thereby also in the lateral arrangements of the molecules on the surface (and vice versa), for the different surfaces under investigation in a qualitative and even semi-quantitative manner. The essential constituents to the surface bonding are: (1) vdW interactions, (2) intermolecular interactions, such as hydrogen bond-like and/or quadrupole interactions, (3) metal-to-molecule charge transfer, i.e., electrostatic interactions, (4) local O–M bonds (M = Ag, K), that is, covalent and dative O–Ag bonds or ionic O–K bonds, only in cases of commensurate registry and sufficiently close proximity of the binding partners, and (5) local C–M bonds [M = Ag, Cu (potentially)] of covalent and dative character in cases of strong surface bonding. On the more reactive surfaces (lower Φ), namely, Cu₃Au(111) in the Cu-rich state, Cu(111), and the low-index Ag surfaces (also with K), the “chemical” bonding channels (3)–(5) outweigh the bonding channels (1) and (2) in their relevance. Thus, the “chemical” bonding channels determine the adsorption configurations and the lateral structure of the PTCDA molecules although vdW interactions are still the predominant contribution to the interfacial interaction in terms of the adsorption energy E_{ads} .

There is a mutual interdependence of the individual bonding channels. The bonding mechanism of PTCDA to coinage metal surfaces proceeds in a complex, synergistic interaction cycle: The metal-to-molecule charge transfer enhances the flexibility of the molecular backbone by a (partial) rehybridization of the molecular orbitals and hence favors non-planar adsorption configurations. Thereby, a smaller distance of the perylene core from the surface is realized, further facilitating the substrate–perylene core interaction. The charge transfer also supports the formation of local O–M

and C—M bonds (see above). This, in turn, leads (or may lead) to a charge transfer also from the molecule to the metal and hence to a bidirectional charge donation across the metal/organic interface, indeed reinforcing the interaction cycle in a synergistic manner.

Outlook

We suggest that our proposed bonding mechanism with its relevant constituents (bonding channels) also applies to the adsorption of other organic, π -conjugated and functionalized molecules on (metal) surfaces.^{40,520} Regarding the surface bonding mechanism of PTCDA on coinage metal surfaces, in particular, we suggest to determine the adsorption configuration of PTCDA on Cu(100) with XSW, for example. In contrast to PTCDA/Cu(111), a commensurate superstructure is present on this surface.^{117,315,316,569,570} As a consequence of both the (potentially) strong bonding⁵²⁰ and the commensurate registry, a smaller overall adsorption height and the formation of local, covalent O—Cu and/or C—Cu bonds can be anticipated, as will be revealed by the realized adsorption configuration.

A

XSWAVES: An x-ray standing wavefield absorption data evaluation routine for Origin 8

A customized computer routine, *XSWAVES: An x-ray standing wavefield absorption data evaluation routine for Origin 8*, for the evaluation of XSW profiles has been developed for the purposes of the present work. The XSWAVES routine runs on the commercially available computer program Origin (version 8.0).²⁹² This chapter outlines the usage as well as the computational details of this routine. The physical background of the XSW technique has already been described in detail in Sec. 3.1.

A.1 Purpose of XSWAVES

In principle, several customized routines for the evaluation of XSW data have been developed over the last decades.^{575–578} Yet, not all of them are readily available and/or meet the requirements which apply to our experimental data. We have traditionally used the computer program DARE written by Zegenhagen for the XSW data evaluation.⁵⁷⁶ Due to insuperable limitations, such as the impossibility to consider technical or experimental imperfections (e.g., width in energy of the x-ray beam, mosaicity of the substrate crystals, and others) or the inaccessibility of the source code, not to mentioned inconvenient handling, however, we have developed a new and convenient fitting routine, namely, XSWAVES. This routine overcomes the aforementioned limitations and is transparent in terms of the computational details (open source). Hence, XSWAVES provides full access to all employed parameters. Note that the independent XSW program Torricelli has been developed in parallel by Mercurio for the same reasons.^{326,330}

XSWAVES employs the dynamical theory of x-ray diffraction. Its algorithm is based on the formulae provided in Sec. 3.1. XSWAVES is a free and open-source routine which is available at http://www.thch.uni-bonn.de/pctc/sokolowski/XSWAVES/XSWAVES_index.html (as of 2013). It runs on Origin, version 8.0.^{292,579,580} XSWAVES is unfortunately not (yet) compatible with earlier versions of Origin (minor changes in the source code syntax of XSWAVES may solve this issue); compatibility with more recent versions has not been tested. The operation of XSWAVES will be described in Sec. A.2 below.

XSWAVES makes use of the nonlinear least square fitting (NLSF) engine in Origin which, in turn, is based on the Levenberg-Marquardt algorithm^{581,582} for adjusting the fitting parameter values in an iterative procedure by reducing χ^2 , which is the goodness of fit and describes the level of agreement between the experimental data and the fitted curve.⁵⁸⁰ Thus, XSWAVES employs a robust and both well-established and well-documented fitting algorithm,^{580–582} thereby diminish-

ing the chance to obtain the parameters of only a local minimum in χ^2 as a fitting result. Further advantages of implementing our fitting routine in Origin are (a) the user-friendly interface, (b) advanced data organization and graphing options, and not least (c) a wide availability of Origin in the scientific community. In order to offer XSWAVES to a broad audience within the XSW community, experimental data, such as XSW photoelectron yield curves, and necessary model parameters are input through simple *.txt-type files. A batch processing option has been implemented in XSWAVES for the automated evaluation of large data sets (up to several hundred individual XSW profiles).

A.2 Installation and operation

The XSWAVES routine consists of a several files (see also Sec. A.4), namely, of:

- (a) XSWAVES_v2.5.c,
- (b) XSWAVES_ReflectivityFit_v2_5.fdf,
- (c) XSWAVES_AbsorptionProfileFit_v_2_5.fdf, and
- (d) XSWAVES_AbsorptionProfileFit_Special_v_2_5.fdf.

In addition, exemplary parameter and XSW data files (*.txt) are provided for testing purposes (see also Sec. A.5 for their explicit structure). The file XSWAVES_v2.5.c contains the main routine while the files of type *.fdf are the actual fitting algorithms for the experimentally obtained reflectivity curves $R_{\text{exp}}(E)$ and the photoelectron yield curves $Y_{Z,j,\text{exp}}(E)$, respectively, which are called by XSWAVES and then executed in the Origin NLSF engine. The *.fdf files are responsible for the actual data evaluation and may be used for fitting in Origin independent of the main routine, in principle (see below for the tasks of the main routine). Note at this point that two individual fitting algorithms are available for the evaluation of the photoelectron yield curves $Y_{Z,j,\text{exp}}(E)$, one of which is termed ‘Special’ [file (d) of the above list]. In contrast to the ‘normal’ fitting algorithm [file (c) of the above list], this algorithm allows to fit the experimental XSW photoelectron yield curves by a linear combination of *two individual* XSW profiles, corresponding to two different (adsorption) sites or configurations (see also Sec. A.3 below).

The main routine (XSWAVES_v2.5.c) is responsible for all data processing apart from the actual fitting process, such as import, organization, and graphing. It is written in Origin C which is an ANSI C compatible programming language that also includes elements of C++ and C#. ⁵⁷⁹ The fitting algorithms (*.fdf) are also written in this programming language. Origin C provides built-in C++ classes for programmatic access to most Origin objects. ⁵⁷⁹ It also includes a wide selection of numerical computational routines from the NAG C Library. ^{579,583} The XSWAVES_v2.5.c code is compiled with Origin C’s integrated development environment *Code Builder*. ⁵⁷⁹




Furthermore, the simulation routine *XSWAVES Simulator* (XSWAVES_simulator_v2.5.c) is provided which allows to simulate the theoretically expected reflectivity curves $R(E)$ and (normalized) photoelectron yield curves $Y_{Z,j,\text{norm}}(E)$ for a given set of parameters f_c , p_c , and w . Here, f_c is the coherent fraction, p_c the coherent position, and w the full width at half maximum (FWHM) of the Gaussian function which is used to resemble instrumental broadening and/or experimental effects, such as the mosaicity of the substrate crystal. ^{a)} XSWAVES Simulator uses a similar algorithm as

^{a)}Using XSWAVES Simulator, also the reflectivity curves of the Si(111) crystals of the double-crystal monochromator can be calculated along with the substrate reflectivity. Both the “perfect” (i.e., intrinsic) and the instrumentally broadened XSW profiles can be calculated, as well. This allows to study the effect of (inevitable) instrumental broadening in detail.

XSWAVES but it does not employ the NLSF engine. Therefore, all convolutions which need to be computed during the calculations can be performed by fast Fourier transform⁵⁸⁴ (FFT) directly in the Origin C code. This is at variance to the computation in the XSWAVES fitting routine where one of the convolutions is performed by explicitly solving the actually underlying integral function due to computational reasons (see Sec. A.3 below).^{585,586}


Installation

XSWAVES requires Origin, version 8.0 (it may be compatible with more recent versions of Origin, too).²⁹² The following steps need to be performed for XSWAVES installation:

1. Start Origin 8.0.
2. The fitting routines (*.fdf) have to be added to the NLSF engine which is called *NLFit* in Origin versions 8.0 and higher. For this purpose, open NLFit via “Analysis > Fitting > Non-linear Curve Fit > Open Dialog”. Then, either choose “Category > <New...>” or click the “Create/Edit Fitting Functions” button () which opens the *Fitting Function Organizer*. Alternatively to this whole procedure, simply press the F9 key. Once the Fitting Function Organizer has opened, activate the directory “-----USER DEFINED-----” and choose “New Category”. Enter a name to your choice (e.g., XSWAVES) and confirm by clicking “Add”. Browse to the directory where the provided *.fdf files have been saved and add them. The three *.fdf files should now appear as available fitting functions in your newly created Category (directory). Afterwards, close the Fitting Function Organizer and NLFit.
3. Open Code Builder via “View > Code Builder” or by clicking the corresponding button () in the toolbar. Open XSWAVES_v2.5.c via “File > Open” or via the keystroke combination Ctrl+O (the user may have to create a new workspace in advance via “File > New Workspace”), then add this file to the workspace via “File > Add to Workspace” or via the keystroke combination Ctrl+W. Finally, compile the routine via “Tools > Build”, the keystroke combination Shift+F8, or clicking the *Build* button in the toolbar (). As a result, the *Output* window (“View > Output” or keystroke combination Alt+2) should read:

```
compiling...
XSWAVES_v2.5.c
Linking...
Done!
```

Subsequently, close Code Builder and return to Origin. Note that it is mandatory to close Code Builder prior to running XSWAVES. If Code Builder is still open while executing XSWAVES, the fitting algorithm will be severely slowed down due to cross-communication between the NLSF engine and Code Builder (“Debug mode”).

4. In principle, there are two ways of running XSWAVES. In a classical way, XSWAVES can be started from the *Script Window* (“Window > Script Window”) in Origin with the command “xswaves”. Note that for this procedure the XSWAVES C-code routine XSWAVES_v2.5.c has to be compiled according to step 3 above prior to first usage after *every* restart of Origin. Thus, for reasons of convenience, we suggest to customize the *Custom Routine* button () of the Origin toolbar.⁵⁷⁹ After customization, the Custom Routine button allows to start XSWAVES with just one click since the mandatory compiling will be done automatically. The Custom Routine button is customized by overwriting the original Custom.ogs file in the user’s default Origin *User Files Folder* (e.g., C:\...\OriginLab\Origin8\User Files\)

the already customized Custom.ogs file which is provided together with XSWAVES. (For backup purposes, the user may wish to create a copy of the original Custom.ogs file prior to overwriting.)

Basically, the installation of XSWAVES Simulator is performed accordingly, following steps 1, 3, and 4 from above. Only a corresponding adapted Custom Routine is not (yet) available. Note that both XSWAVES and XSWAVES Simulator compute R and (normalized) $Y_{Z,j}$ as a function of the photon energy E and not as a function of the scattering angle θ_{sc} .

General operation

XSWAVES allows to fully control the fitting process of the XSW data. In general, there are two ways of controlling the fitting routine. On the one hand, experimental data is retrieved through the upload of simple *.txt files. These exhibit a three-column structure where the first column holds the photon energy E , the second column holds the experimental data $R_{exp}(E)$ or $Y_{Z,j,exp}(E)$ (not normalized),^{b)} and the third column holds the corresponding error in $R_{exp}(E)$ or $Y_{Z,j,exp}(E)$, respectively. Note that proper data analysis requires a normalization of the (raw) experimental data to the intensity of the primary x-ray beam, I_0 , which is inevitable for obtaining reliable results, *prior to* the upload into XSWAVES. On the other hand, numerical values may be input in dialog boxes where appropriate, for example, as starting values for the fitting parameters f_c and p_c or as nondipolar correction terms. Likewise, several fitting options, such as parameter constraints, may be chosen. This is done by entering “0” or “1” at the respective points of the XSWAVES run where “0” or “1” refers to, e.g., “no” or “yes”, or “fixed” or “free” (see also below).

As a general procedure, XSWAVES fits the experimental reflectivity curve $R_{exp}(E)$ in a first step (see also Fig. A.1 below for a schematic representation of an XSWAVES run). The fitting of $R_{exp}(E)$ yields the characteristics of the Gaussian function which resembles instrumental broadening and sample quality, for example, and which the theoretically predicted reflectivity curve for the perfect crystal is convoluted with (see Sec. A.3 below).

In a second step, the so-obtained characteristic parameters will then be employed in the fitting of the corresponding experimental XSW profile $Y_{Z,j,exp}(E)$ (see also Sec. A.3 below). Therefore, a typical XSWAVES run consists of the fitting of both the reflectivity curve and the XSW profile. The below-listed Origin *Workbooks*, *Graphs* and *Notes* will be created by XSWAVES during one run (with i = sequential number, see also below).

- (a) Workbook “Fit # i - ExpReflectivity - <input file>”: contains the imported data of the experimental reflectivity curve $R_{exp}(E)$ and, eventually, the data points of the corresponding fitting curve, as well as the data of the corresponding normalized curves.
- (b) Graph “Fit # i - ExpReflectivity - <input file>”: displays the exp. reflectivity data $R_{exp}(E)$ and the respective fitting curve (including the fitting parameters).
- (c) Workbook “Fit # i - FitParameters - Reflectivity”: stores all relevant parameters which were used and/or optimized during the fitting of the reflectivity curve $R_{exp}(E)$ with their corresponding errors, if applicable.

^{b)} $R_{exp}(E)$ and $Y_{Z,j,exp}(E)$ are denoted as “not normalized” here although all experimental XSW data were standardly normalized to the intensity of the primary x-ray beam, I_0 . However, they are still on an arbitrary y scale due to experimental reasons. For example, the XSW photoelectron yield curve $Y_{Z,j,exp}(E)$ has not yet been normalized to 1 for photon energies far from the Bragg energy E_B . See also footnote d) on page 250 of this chapter.

- (d) Workbook “Fit # i - signal - ExpXSWProfile - <input file>”: contains the imported data of the experimental XSW profile $Y_{Z,j,\text{exp}}(E)$ and, eventually, the data points of the corresponding fitting curve, as well as the data of the corresponding normalized curves.
- (e) Graph “Fit # i - signal - ExpXSWProfile - <input file>”: contains the imported data of the experimental XSW profile $Y_{Z,j,\text{exp}}(E)$ and, eventually, the data points of the corresponding fitting curve, as well as the data of the corresponding normalized curves.
- (f) Workbook “Fit # i - signal - FitParameters - XSW Profile”: stores all relevant parameters which were used and/or optimized during the fitting of the XSW profile $Y_{Z,j,\text{exp}}(E)$ with their corresponding errors, if applicable.
- (g) Graph “Fit # i - signal - Result”: presents the normalized experimental curves $R(E)$ and $Y_{Z,j,\text{norm}}(E)$ together with their corresponding fitting curves and the most important fitting parameters as a final result.
- (h) Workbook “XSWAVES - Results - <date, time>”: contains the individual fitting-parameter results of all fits of one particular XSWAVES run conveniently compiled in a single table.
- (i) Notes “XSWAVES Log File - <date, time>”: stores the text output of XSWAVES, which is also announced in the Origin Script Window during the respective XSWAVES run, for reasons of easy traceability.

Here, i denotes the number of the i -th fitting procedure of one or more individual XSW profiles within one XSWAVES run (starting with 1 and increasing for consecutive XSW profile fittings), <input file> the name of the input *.txt file, and <date, time> the date and the starting time of the respective XSWAVES run.

In the so-called single-run mode of XSWAVES (where only one experimental reflectivity curve $R_{\text{exp}}(E)$ is fitted; see also below) i necessarily equals 1 for the reflectivity data. However, i may exceed 1 for the XSW profile fitting results even in the case of the single-run mode. In fact, there may be cases where more than one XSW profile is deduced from one data set, namely, if the respective XPS signal can be decomposed into several individual components (often referred to as differential analysis). A repetitive re-fitting of the (identical) curves $R_i(E)$ for the fitting of all individual curves $Y_{Z,j,i}(E)$ is not mandatory then, and thus it will be waived in XSWAVES (see below). The same is true if the user wishes to re-fit one particular curve $Y_{Z,j,i}(E)$, for instance, with different parameters. Therefore, it is indeed possible that several XSW profiles $Y_{Z,j,i}(E)$ and/or fitting results # i with different i values belong to one and the same $R_i(E)$ with $i = 1$. This reasons the above nomenclature (# i) of the created Origin Workbooks and Graphs.

Detailed description of the XSWAVES run

We will now exemplarily describe a single run of XSWAVES, i.e., the fitting process of an individual data set. The user will be guided through the XSWAVES run by several dialog boxes. The three most relevant points of the XSWAVES run will be illustrated by screen shots of the XSWAVES graphical user interface (GUI), i.e., the dialog boxes, representing the standard procedure with default fitting parameters. Figure A.1 illustrates the general fitting process in an XSWAVES run by means of a schematic flow chart.

1. Upon the start of XSWAVES, a dialog box appears (not shown). Here, the user may choose between the classical, single-run mode of XSWAVES ($\hat{=}$ “0”) or an fully automated *Batch Processing* mode ($\hat{=}$ “1”). The Batch Processing mode requires to upload all necessary parameters needed during the XSWAVES run in form of a single *.txt file, in addition to the oblig-

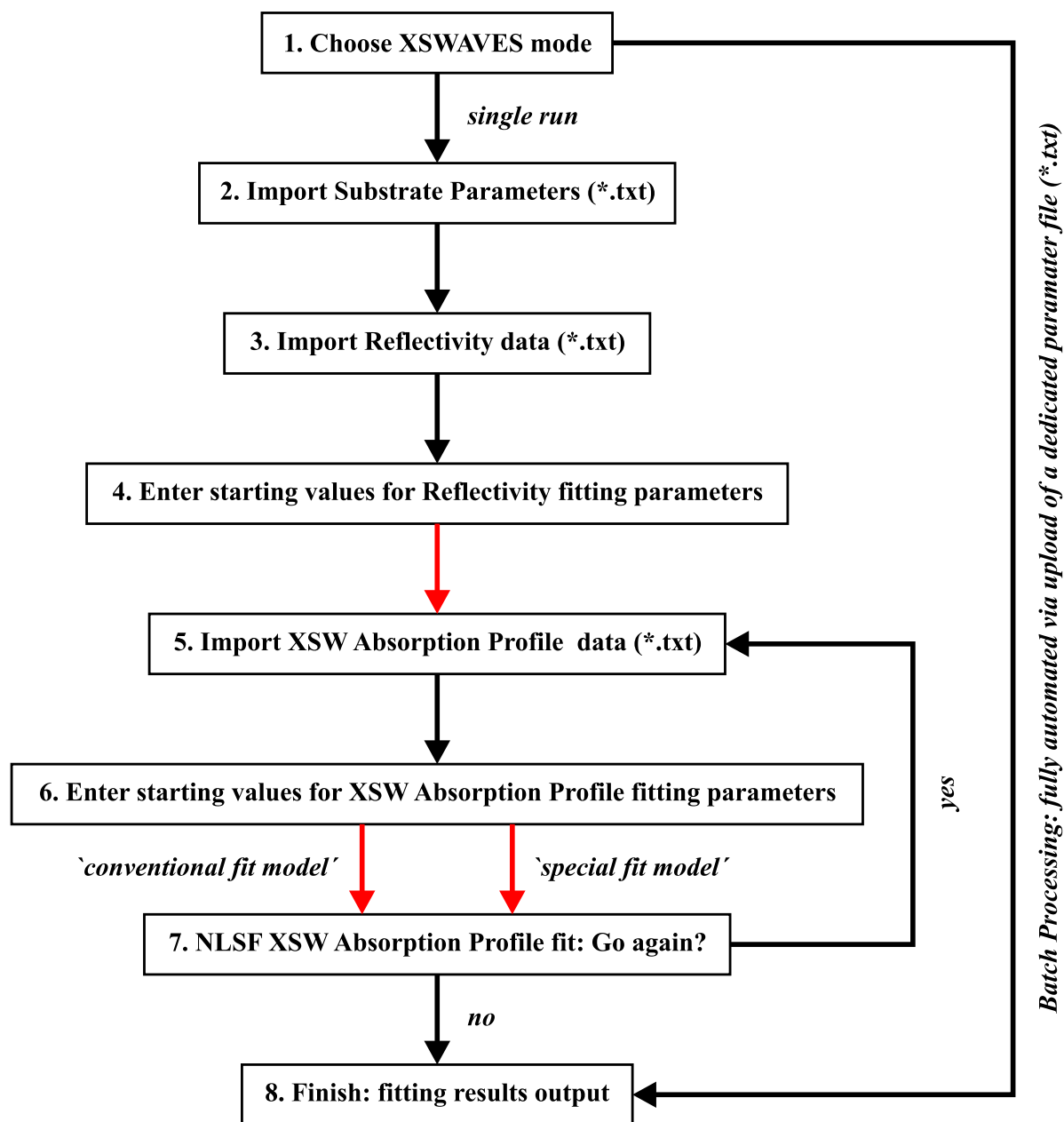


FIG. A.1. Flow chart of the XSWAVES routine. Red arrows indicate those steps in the fitting process in which the actual fitting algorithms (*.fdf) are called by the main routine (XSWAVES_v2.5.c) and then executed by the NLSF engine incorporated in Origin. See text for further details.

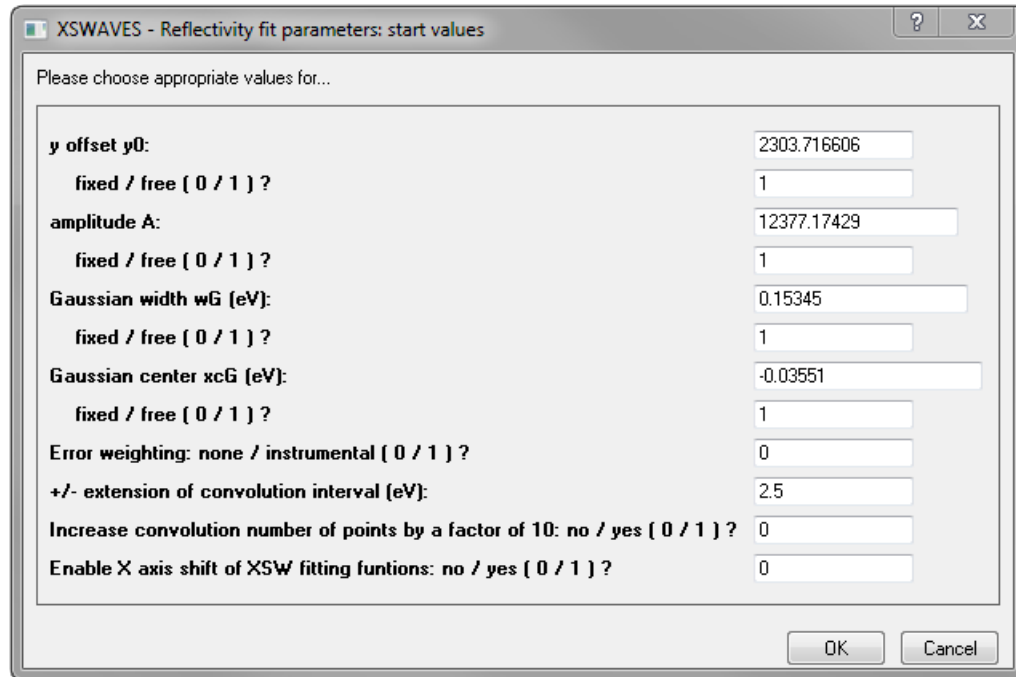


FIG. A.2. XSWAVES dialog box for the fitting of the experimental reflectivity curve $R_{\text{exp}}(E)$. See text for further details.

atory input and parameter files (see also below; a Microsoft Excel template for creating such Batch Processing parameter files is provided). We recommend the Batch Processing mode to advanced and experienced users only, because a step-by-step control of the XSWAVES run will not be possible. If the Batch Processing mode is chosen, an additional Workbook termed “XSWAVES Batch Processing Parameters - <date, time>” is created which contains all imported parameters employed in the fitting process(es).

2. In a second dialog box (not shown), the user is asked to upload a “Substrate Parameters” input file (*.txt). The Substrate Parameters file provides all parameters, such as the structure factors F_0 and F_H , which are needed for the calculation of the theoretical $R(E)$ and $Y_{Z,j,\text{norm}}(E)$ curves for the respective substrate or system in use. An exemplary Substrate Parameters file can be found in Sec. A.5.1.
3. After having chosen a Substrate Parameters input file, a third dialog box pops up (not shown), which asks the user for the “Reflectivity” input file (*.txt). At this point, the first experimental data is fed to the XSWAVES routine. This reflectivity data will now be fitted according to the algorithm outlined in Sec. A.3.
4. XSWAVES suggests appropriate starting values for relevant parameters of the reflectivity fitting in a fourth dialog box, as shown in Fig. A.2. The user may adapt these starting values and/or exclude them from being fitted by choosing “0” ($\hat{=}$ “fixed”; lines 1 to 8 from the top in Fig. A.2). In particular, the parameters refer to the scaling (offset, amplitude) of the fitting curve and the characteristics of the Gaussian function (width, center) which the theoretically predicted curve for the perfect crystal is convoluted with (see Sec. A.3 below). Furthermore, several options related to actual fitting algorithm may be set (lines 9 to 12 from the top). The meaning of the individual parameters will become clearer from the explanations given in Sec. A.3. The user may confirm by clicking “OK”, and the actual fitting process starts. Note

Please choose appropriate values for...

Fit # 1 - XSW signal name:	signal
coherent fraction CF:	0.5
fixed / free (0 / 1) ?	1
coherent position CP:	0.5
fixed / free (0 / 1) ?	1
Q:	0
fixed / free (0 / 1) ?	0
Delta:	0
fixed / free (0 / 1) ?	0
y offset y0:	0
fixed / free (0 / 1) ?	0
amplitude A:	2739.82741
fixed / free (0 / 1) ?	1
Gaussian width wG (eV):	0.0944
fixed / free (0 / 1) ?	0
Gaussian center xcG (eV):	-0.1089
fixed / free (0 / 1) ?	0
Error Weighting: none / instrumental (0 / 1) ?	1
+/- extension of convolution interval (eV):	2.5
Increase convolution number of points by a factor of 10: no / yes (0 / 1) ?	0
Use 'special fit model': no / yes (0 / 1) ?	0

OK Cancel

FIG. A.3. XSWAVES dialog box for the fitting of the experimental XSW photoelectron yield curve $Y_{Z,j,\text{exp}}(E)$. See text for further details.

that the overall fitting process for both $R_i(E)$ and $Y_{Z,j,i}(E)$ may last a few minutes, depending on the computer power and the number of data points in the experimental curves to be fitted.

The progress of the fitting process, and of the XSWAVES run in general, can be monitored in two ways. On the one hand, information, in particular on the current fitting status, are provided in the “Status Bar” (left end) at the very bottom of the Origin window. On the other hand, more general information on the current XSWAVES run (input parameters, fitting results, etc.) are minuted in both the Script Window and the XSWAVES Log File. Note that the XSWAVES Log File is accessible only after the XSWAVES run has finished. The XSWAVES user is recommended to have the Script Window open during the XSWAVES run.

- Once the fitting of the experimental reflectivity $R_{\text{exp}}(E)$ has finished, the user is asked to provide the “XSW Absorption Profile” input file (*.txt) in a fifth dialog box (not shown). The term “XSW Absorption Profile” is used synonymously to “XSW photoelectron yield curve” here due to historical reasons in the development of the XWAVES routine.
- Having chosen the data input file, a sixth dialog box gives access to the relevant parameters of the fitting of the XSW photoelectron yield $Y_{Z,j,\text{exp}}(E)$, in analogy to the reflectivity fitting

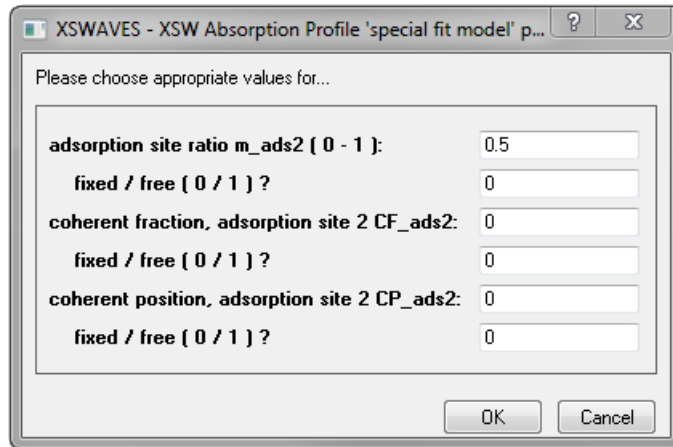


FIG. A.4. XSWAVES dialog box for the fitting of the experimental XSW photoelectron yield curve $Y_{Z,j,\text{exp}}(E)$ by a linear combination of two individual XSW profiles ('special fit model'). See text for further details.

(see also above). The respective dialog box is shown in Fig. A.3. The user may enter a name to choice for the XSW profile to be fitted (line 1 from the top in Fig. A.3). Starting values for the fitting parameters coherent fraction f_c ($\hat{=}$ "CF") and coherent position p_c ($\hat{=}$ "CP") may be chosen, and these parameters may also be excluded from the fitting (lines 2 to 5 from the top). The nondipolar correction terms Q ($\hat{=}$ "Q") and Δ ($\hat{=}$ "Delta") may be entered and, if desired, may also be a subject to the fitting by choosing "1" ($\hat{=}$ "free"; lines 6 to 9 from the top). Besides, scaling parameters (offset, amplitude) of the fitting curve and the characteristics of the Gaussian function (width, center) employed in the convolution may be accessed in lines 10 to 17 from the top. The width and center of the Gaussian function are taken from the fitting of the experimental reflectivity $R_{\text{exp}}(E)$ and constrained by default (the constraints may be lifted). Furthermore, the same options related to actual fitting algorithm are available as in the reflectivity fitting (except of the "X axis shift" option; lines 18 to 20 from the top). These options are set to the same choice as during the preceding reflectivity fitting by default, too. Finally, the user may activate the so-called 'special fit model' by choosing "1" ($\hat{=}$ "yes"; line 21 from the top, i.e., lowest line). Clicking the "OK" button starts the actual fitting of the experimental XSW profile.

The 'special fit model' allows to fit a given XSW photoelectron yield curve $Y_{Z,j,\text{exp}}(E)$ by a linear combination of *two individual* XSW profiles, corresponding to two different (adsorption) sites or configurations. If activated, the user may enter values for the additional fitting parameters coherent fraction f_c ($\hat{=}$ "CF_ads2") and coherent position p_c ($\hat{=}$ "CP_ads2") as well as the relative contribution ($\hat{=}$ "m_ads2", ranging from 0 to 1) of the second XSW profile. This is done in a dedicated dialog box, as shown in Fig. A.4. We strongly suggest that the XSWAVES user constrains one or more of the parameters "CF", "CP", "CF_ads2", "CP_ads2", and "m_ads2" here. Otherwise the fitting process will hardly converge.

7. As a final step, after the fitting of the XSW profile has finished, the user may decide whether or not to repeat the XSW profile fitting via input in another dialog box (not shown). If "1" ($\hat{=}$ "yes") is chosen, the XSWAVES run continues with the re-appearing of the fifth dialog box (see step 5), that is, the user may choose another "XSW Absorption Profile" input file (*.txt). Then, the XSWAVES run proceeds with the $i + 1$ -th fitting as described above in step 6. If "0" ($\hat{=}$ "no") is chosen, XSWAVES terminates and the user has full access to

the fitting results via the Origin Workbooks, Graphs and Notes created by the routine (see above).

A.3 Computational algorithm

The computational algorithm behind XSWAVES employs the dynamical theory of x-ray diffraction.^{160,164} The reader is referred to Sec. 3.1 for a review of this theory as well as of the physical foundations of the XSW technique. At this point, only the most relevant formulae will be stated. Their implementation in the fitting algorithms will be highlighted. The source codes of the individual fitting algorithms (of file type *.fdf) are given in the subsequent section, in particular in Sec. A.4.1 for the reflectivity data, in Sec. A.4.2 for the XSW Absorption Profile data, and in Sec. A.4.3 for the XSW Absorption Profile data employing the ‘special fit model’, i.e., fitting a linear combination of two individual XSW profiles, respectively. For reasons of simplicity, we will give a short notation of type “section number, l(l). line number(s)” rather than the full name of the respective fitting routines when referring to the corresponding implementation in the source codes.

Note at this point that the nomenclature/notation for the individual parameters used by Woodruff in Ref. 29 has been employed in the XSWAVES code. It differs slightly from the notation employed in Section 3.1 which, in turn, is mainly based on the notation used by Zegenhagen in Ref. 28. For example, the phase ν (termed as is done in Ref. 28) of the complex electric-field amplitude ratio E_H/E_0 , which has been introduced in Eq. (3.8), is denoted as “Phi” (Φ in Ref. 29) here. See Tables A.1 and A.2, respectively, for a conversion in the notation of the relevant terms (function, parameters, and variables) from that employed in the text to that in the source code(s) and vice versa. For reasons of clarity, this information are presented in two tables with identical content in different order.

Note further that, in the strict sense, XSWAVES may only be used for the evaluation of XSW data on substrates with centrosymmetric and cubic lattices so far. The reasons are the following. For centrosymmetric crystals, such as *fcc* crystals, the structure factors F_H and $F_{\bar{H}}$ are equal if the origin of the Bravais lattice is taken at a center of symmetry (see also Sec. 3.1.2).¹⁶⁰ This is exploited in the XSWAVES code, therefore centrosymmetry is a necessary condition here. However, $F_H = F_{\bar{H}}$ may be a good approximation in general,¹⁶⁰ i.e., also for non-centrosymmetric crystals. The requirement for cubic symmetry is due to the fact that, so far, only *one* lattice constant a_{bulk} can be entered. From the lattice constant, the volume V_{uc} of the crystal unit cell is calculated via $V_{\text{uc}} = (a_{\text{bulk}})^3$ within the XSWAVES routine. That is, $a_{\text{bulk}} = b_{\text{bulk}} = c_{\text{bulk}}$ and $\alpha_{\text{bulk}} = \beta_{\text{bulk}} = \gamma_{\text{bulk}} = 90^\circ$ are assumed here concerning the lattice parameters of the bulk material (constants and angles, respectively). V_{uc} enters the calculation of the substrate reflectivity R through Eqs. (3.16), (3.17), and (3.18). These limitations will possibly be removed by small modifications to the source code(s) in future versions of XSWAVES.

TABLE A.1. List of abbreviations of the functions, parameters, and variables used for the calculation of the reflectivity $R(E)$ and the XSW photoelectron yield $Y_{Z,j}(E)$ as employed in the text of the present work. The corresponding notation of the respective terms which has been employed in the XSWAVES source code is given in parentheses. See Sec. 3.1 for a detailed explanation of the individual functions, parameters, and variables (n.a. = not applicable).

Function, parameter, or variable	Meaning
A (“A”)	Normalization factor
b (“b”)	Asymmetry parameter of the Bragg reflection
Γ (“Sigma”)	Constant of proportionality
Δ (“Delta”)	Phase difference (nondipolar cor. parameter)
E (“x”)	Photon energy
E_B (“E_Bragg”)	Bragg energy
ΔE_{conv} (“ConvolutionExtension_constraint”)	Additional extension of the convolution interval
E_H/E_0 (“EH_E0”)	Ratio of the electric-field amplitudes E_H and E_0
$\text{Im}(E_H/E_0)$ (“EH_E0_imag”)	Imaginary part of the ratio E_H/E_0
$\text{Re}(E_H/E_0)$ (“EH_E0_real”)	Real part of the ratio E_H/E_0
$\exp(-M_Z)$ (“DW”)	Debye-Waller factor
ϵ (n.a.)	Auxiliary variable in the convolution integral
η (“eta”)	Displacement of E_B from the midpoint of $R(E)$
$F(E) = \Upsilon_{\text{ideal}}(E)$ (“F”)	$\Upsilon_{\text{theo}}(E) * [R_{\text{mono}}(E)]^2$ (“response function”)
F_0 (“F0”)	Structure factor for the (000) reflection
F'_0 (“F0_real”)	Real part of the structure factor F_0
F''_0 (“F0_imag”)	Imaginary part of the structure factor F_0
F_H (“FH”)	Structure factor for the reflection def. by H_{hkl}
F'_H (“FH_real”)	Real part of the structure factor F_H
F''_H (“FH_imag”)	Imaginary part of the structure factor F_H
f_c (“CF”)	Coherent fraction
$f_{c,2}$ (“CF_ads2”)	Coherent fraction for the second XSW profile
$G(E, t)$ (“G”)	Gaussian function
m_2 (“m_ads2”)	Rel. contribution of the second XSW profile
μ (“xcG”)	Center of the Gaussian function
P (“P”)	Polarization factor
p_c (“CP”)	Coherent position
$p_{c,2}$ (“CP_ads2”)	Coherent position for the second XSW Profile
ψ (“Psi”)	Phase of the nondipolar correction parameter S_1
Q (“Q”)	Forward/backward asymmetry parameter
$R_{\text{mono}}(E)$ (“Reflectivity_mono”)	Reflectivity of the monochromator crystal

(continued on next page)

(continued from previous page)

Function, parameter, or variable	Meaning
$[R_{\text{mono}}(E)]^2$ (“Reflectivity_mono_squared”)	Reflectivity of the double-crystal monochrom.
$R_{\text{theo}}(E)$ (“Reflectivity”)	Reflectivity of the substrate crystal
$ S_1 $ (“SI”)	Magnitude of the nondipolar cor. parameter S_1
S_R (“SR”)	Nondipolar correction parameter
σ (“wG”)	Width of the Gaussian function
t (“t”)	Energy shift, employed in the convolution
t_{final} (“t_final”)	Upper bound of integration
t_{initial} (“t_initial”)	Lower bound of integration
$[t_{\text{initial}}, t_{\text{final}}]$ (n.a.)	Convolution interval
Δt (“dt”)	Step size in energy for numerical integration
θ_B (“theta_Bragg”)	Bragg angle
$Y_{\text{exp}}(E)$ (“y”)	Experimental $R(E)$ or $Y_{Z,j}(E)$ (not normalized)
ΔY_{exp} (“y0”)	Offset
$Y_i(E)$ (n.a.)	$R(E)$ or norm. $Y_{Z,j}(E)$ ($i = \text{theo, ideal, real}$)
$\{Y_{\text{theo}}(E) * [R_{\text{mono}}(E)]^2 * G(E)\}$ (“dIntegral”)	Convolution term
$\nu(E)$ (“Phi”)	Phase of the x-ray standing wavefield

TABLE A.2. List of terms used in the XSW source code for the calculation of the reflectivity $R(E)$ and the XSW photoelectron yield $Y_{Z,j}(E)$ in alphabetical order. The corresponding notation of the individual terms (function, parameter, or variable, respectively) as employed in the text of the present work is given in square brackets. Note that, in principle, this table presents the same information as Table A.1 but in different order for reasons of clarity. See Sec. 3.1 for a detailed explanation of the individual functions, parameters, and variables (n.a. = not applicable).

Term in XSWAVES source code	Meaning
A [A]	Normalization factor
b [b]	Asymmetry parameter of the Bragg reflection
CF [f_c]	Coherent fraction
CF_ads2 [$f_{c,2}$]	Coherent fraction for the second XSW profile
ConvolutionExtension_constraint [ΔE_{conv}]	Additional extension of the convolution interval
CP [p_c]	Coherent position
CP_ads2 [$p_{c,2}$]	Coherent position for the second XSW Profile
Delta [Δ]	Phase difference (nondipolar cor. parameter)

(continued on next page)

(continued from previous page)

Term in XSWAVES source code	Meaning
dIntegral $\left[\left\{ \Upsilon_{\text{theo}}(E) * [R_{\text{mono}}(E)]^2 * G(E) \right\} \right]$	Convolution term
dt $[\Delta t]$	Step size in energy for numerical integration
DW $[\exp(-M_Z)]$	Debye-Waller factor
E_Bragg $[E_B]$	Bragg energy
EH_E0 $[E_H/E_0]$	Ratio of the electric-field amplitudes E_H and E_0
EH_E0_imag $[\text{Im}(E_H/E_0)]$	Imaginary part of the ratio E_H/E_0
EH_E0_real $[\text{Re}(E_H/E_0)]$	Real part of the ratio E_H/E_0
eta $[\eta]$	Displacement of E_B from the midpoint of $R(E)$
F $[F(E) = \Upsilon_{\text{ideal}}(E)]$	$\Upsilon_{\text{theo}}(E) * [R_{\text{mono}}(E)]^2$ (“response function”)
F0 $[F_0]$	Structure factor for the (000) reflection
F0_imag $[F_0'']math>$	Imaginary part of the structure factor F_0
F0_real $[F_0']$	Real part of the structure factor F_0
FH $[F_H]$	Structure factor for the reflection def. by \mathbf{H}_{hkl}
FH_imag $[F_H'']math>$	Imaginary part of the structure factor F_H
FH_real $[F_H']$	Real part of the structure factor F_H
G $[G(E, t)]$	Gaussian function
m_ads2 $[m_2]$	Rel. contribution of the second XSW profile
P $[P]$	Polarization factor
Phi $[\nu(E)]$	Phase of the x-ray standing wavefield
Psi $[\psi]$	Phase of the nondipolar correction parameter S_I
Q $[Q]$	Forward/backward asymmetry parameter
Reflectivity $[R_{\text{theo}}(E)]$	Reflectivity of the substrate crystal
Reflectivity_mono $[R_{\text{mono}}(E)]$	Reflectivity of the monochromator crystal
Reflectivity_mono_squared $[R_{\text{mono}}(E)]^2$	Reflectivity of the double-crystal monochrom.
SI $[S_I]$	Magnitude of the nondipolar cor. parameter S_I
Sigma $[\Gamma]$	Constant of proportionality
SR $[S_R]$	Nondipolar correction parameter
t $[t]$	Energy shift, employed in the convolution
t_final $[t_{\text{final}}]$	Upper bound of integration
t_initial $[t_{\text{initial}}]$	Lower bound of integration
theta_Bragg $[\theta_B]$	Bragg angle
wG $[\sigma]$	Width of the Gaussian function
x $[E]$	Photon energy
xcG $[\mu]$	Center of the Gaussian function
y $[\Upsilon_{\text{exp}}(E)]$	Experimental $R(E)$ or $Y_{Z,j}(E)$ (not normalized)
y0 $[\Delta \Upsilon_{\text{exp}}]$	Offset

General fitting function

The general fitting function common to all three fitting routines (*.fdf) is:^{c)}

$$\Upsilon_{\text{exp}}(E) = A \cdot \left\{ \Upsilon_{\text{theo}}(E) * [R_{\text{mono}}(E)]^2 * G(E) \right\} + \Delta\Upsilon_{\text{exp}}. \quad (\text{A.1})$$

In the above equation, $\Upsilon(E)$ denotes the [non-normalized, experimentally obtained (exp) or normalized, theoretically predicted (theo)] signal of interest, that is, either the reflectivity $R(E)$ or the (normalized) XSW photoelectron yield $Y_{Z,j}(E)$;^{d)} E is the photon energy, A is a normalization factor, $[R_{\text{mono}}(E)]^2$ is the squared reflectivity of the Si(111) crystals in the double-crystal monochromator (see also below), $G(E)$ is a Gaussian function, and $\Delta\Upsilon_{\text{exp}}$ is an offset. This general fitting function eventually computes in XSWAVES as:

$$\begin{aligned} \Upsilon_{\text{exp}}(E) &= A \cdot \left\{ \Upsilon_{\text{theo}}(E) * [R_{\text{mono}}(E)]^2 * G(E) \right\} + \Delta\Upsilon_{\text{exp}} \\ \Leftrightarrow y &= A \cdot \text{“dIntegral”} + y_0, \end{aligned} \quad (\text{A.2})$$

with $y = \Upsilon_{\text{exp}}(E)$ (termed “y” in the source codes; “x” denotes the photon energy), $y_0 = \Delta\Upsilon_{\text{exp}}$ ($\hat{=}$ “y0”), and the term “dIntegral” being a substitution for the term in braces in Eq. (A.1) (see source codes A.4.1, l. 222, A.4.2, l. 276, and A.4.3, l. 282). A (termed “A” in the source codes) and $y_0 = \Delta\Upsilon_{\text{exp}}$ are fitting parameters by default if they are not explicitly constrained by the user. Further (potential) fitting parameters are contained in the functions $G(E)$ and $\Upsilon_{\text{theo}}(E) = Y_{Z,j,\text{norm}}(E)$ (see below). The (experimentally obtained) individual data points which are subjected to the fitting may be weighted by their corresponding errors in the fitting process if desired.

We will now explain the line of reasoning behind Eq. (A.1). It is not possible to measure the theoretically predicted $R(E)$ or (normalized) $Y_{Z,j,\text{norm}}(E)$ curves for a given substrate/system in the experiment. This is because the experimentally obtained curves are broadened in comparison to those predicted by theory. The reasons are as follows: On the one hand, the x-ray beam is not perfectly monochromatic but exhibits a finite width in energy. This is considered through the term $[R_{\text{mono}}(E)]^2$, as will be explained below. On the other hand, the real sample is not perfect due to effects such as mosaic spread within the substrate single crystal. Furthermore, there is so-called instrumental broadening by instrumental factors, such as imperfect focusing of the x-ray beam or the given width of the slits in the beam path.¹⁶⁴ This instrumental broadening is described by a Gaussian function $G(E)$ (termed “G” in the source codes; see A.4.1, l. 196, A.4.2, l. 250, and A.4.3, l. 256):^{585,586}

$$G(E) = \frac{1}{\sigma \sqrt{2\pi}} \exp \left[-\frac{1}{2} \left(\frac{E - \mu}{\sigma} \right)^2 \right], \quad (\text{A.3})$$

where σ ($\hat{=}$ “wG”) determines the width [via $w = 2\sqrt{2\ln 2}\sigma$ as the full width at half maximum (FWHM)] and μ ($\hat{=}$ “xcG”) is the position of the center of the Gaussian peak.^{e)} Note that the

^{c)}See Appendix F of the present work for an evaluation of the validity of this approach which (incorrectly) employs convolutions instead of cross-correlations in order to account for broadening effects. See also footnote f) on page 253 of this chapter.

^{d)}Note at this point that the experimentally obtained reflectivity $R_{\text{exp}}(E)$ is on an arbitrary y scale due to experimental reasons, in contrast to the theoretically predicted reflectivity curves $R_{\text{theo}}(E)$. Furthermore, in the present context, the theoretically predicted XSW photoelectron yield $Y_{Z,j,\text{norm}}(E)$ is standardly normalized to 1 for photon energies far from the Bragg energy E_B . See also footnote b) on page 240 of this chapter.

^{e)}The parameter μ represents the *intrinsic* position of the center of the Gaussian peak and thereby an energy shift (see also below). In the source codes, the arithmetic expression $E - \mu$ in the exponential is replaced by $(E - \mu) - t$

integral of the above Gaussian function, i.e., the peak area, equals 1 due to the choice of the normalization factor as $1/(\sigma\sqrt{2\pi})$. The two parameters σ and μ are fitted to the experimental data during the analysis of $R_{\text{exp}}(E)$, and they are kept fixed during the the analysis of $Y_{Z,j,\text{exp}}(E)$ as a default setting. In particular, μ represents an energy shift. Thus, it can be understood as a shift of the calculated curves on the x axis which allows to align their maxima with those of the experimentally obtained curves. Fitted values of μ range from about -5 eV to 5 eV, typically.

XSWAVES plots the fitting result as a function of E . If the user wishes to plot the fitting result as a function of $E - E_{\text{B}}$ (which may be the more common representation), the x axis can be manually converted as:

$$E - E_{\text{B}} = E - E'_{\text{B}} - \mu, \quad (\text{A.4})$$

where E_{B} denotes the experimentally observed Bragg energy and E'_{B} the Bragg energy calculated from the lattice constants a_{bulk} reported in the literature. The two values may indeed differ by a few electronvolts due to small differences in the lattice constants or due to small deviation from the anticipated Bragg angle $\theta_{\text{B}} = 88^\circ$. For instance, a deviation of only $\pm 0.005 \text{ \AA}$ in a_{bulk} causes a shift of $\Delta E_{\text{B}} \approx \mp 5.3$ eV for the (220) reflection of Ag [$a_{\text{bulk}} = 4.0853 \text{ \AA}$,²⁸⁹ $d_{220} = 1.444 \text{ \AA}$, and $E'_{\text{B}} = 4294.59$ eV, respectively; see also Eq. (3.5)]. At the same time, $\Delta\theta_{\text{B}} = \pm 1^\circ$ results in a shift in E_{B} of -2.0 eV and 3.2 eV, respectively.

In principle, the option to automatically convert the x -axis scaling may be easily implemented in future versions of XSWAVES. So far, an option called “Enable X axis shift of the XSW fitting functions” (see Fig. A.2) is available in XSWAVES, version 2.5. However, this option does *not* address the aforementioned issue, but it is intended to save computation time in the fitting process. If activated, the x axis, i.e., the E scale of the *theoretically predicted* curves for both the reflectivity and the XSW profile, is shifted according to $E''_{\text{B}} = E'_{\text{B}} + \mu_{\text{initial}}$, resulting in a near alignment of the maxima of the theoretically predicted and experimentally obtained reflectivity curves *prior to* the actual fitting. Here, E''_{B} denotes the *shifted* calculated Bragg energy and μ_{initial} the center position of the Gaussian function initialized (that is, educatedly guessed) by the XSWAVES algorithm. After this computational step, the starting value of μ_{initial} is re-set to 0 eV for the subsequent fitting step. Therefore the convolution interval, that is, the interval in which the integral function behind the convolution is solved during the fitting process, can be chosen smaller. By default, it is set equal to the energy interval that was also employed in the experiment plus or minus 2.5 eV for the upper and lower bound of integration, respectively (see also below).

The presence of the term $[R_{\text{mono}}(E)]^2$ in Eq. (A.1), which describes the finite width in energy of the incident x-ray beam on the sample, is reasoned as follows. The x-ray light which is produced by the undulator is monochromatized by means of a Si(111) double-crystal monochromator [see Fig. A.5(a)]. We assume that the intensity $I(E)$ of the x-ray beam emitted from the undulator is constant over the energy window of a typical XSW experiment ($\Delta E \leq 10$ eV) as depicted in Fig. A.5(b), and we neglect potential dispersion effects here. The Si(111) crystals, which are considered as perfect crystals here, in the monochromator now act as band-pass filters,⁵⁸⁷ that is, the effective beam intensity $I_{\text{eff}}(E)$ is modulated as given by the reflectivity of the Si(111) monochromator crystals [see Fig. A.5(c), dark-gray full line]. Because the monochromator consists of

[see also Eq. (A.10) below]. The parameter t (with the dimension of an energy; termed “ t ” in the source codes), which represents an *additional* energy shift, will be required for performing the final convolution step [see Eqs. (A.8) and (A.9) below] due to computational reasons; t may have values within a range of some electronvolts around the Bragg energy E_{B} or, more precisely, around the center of the experimental curves.

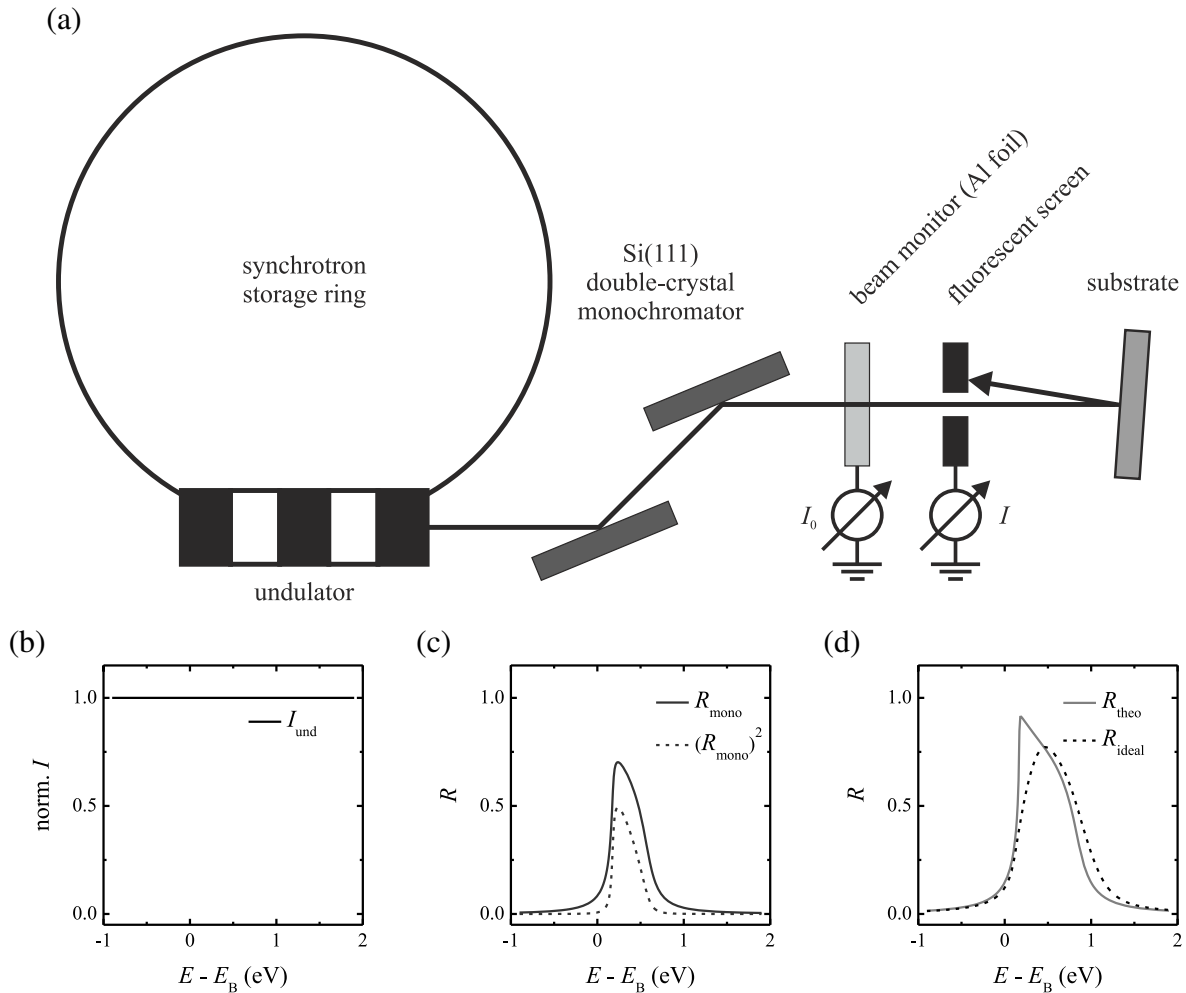


FIG. A.5. Schematic layout of beamline ID32 of the European Synchrotron Radiation Facility (ESRF) and theoretical reflectivity curves of the monochromator and substrate crystals. (a) The x-ray beam is created in an undulator and monochromatized in a Si(111) double-crystal monochromator (dark gray). The intensity I_0 of the incident beam is monitored through an Al foil (light gray) in the beam path. The intensity I of the Bragg-reflected beam is monitored via the drain current from a fluorescent screen (black). The substrate is depicted in medium gray. (b) Normalized intensity I_{und} of the x-ray beam obtained from the undulator. (c) Reflectivity R_{mono} (dark gray line) and squared reflectivity $(R_{\text{mono}})^2$ (dark-gray dashed line) of the Si(111) crystals in the double-crystal monochromator. (d) Reflectivity R_{theo} (medium gray line) and ideal reflectivity $R_{\text{ideal}} = R_{\text{theo}} * (R_{\text{mono}})^2$ (black dashed line) of the substrate crystal. The reflectivity curves $R(E)$ in (c) and (d) have been calculated with the XSWAVES routine for the scenario of XSW investigations on a perfect Ag(100) crystal, employing the (200) Bragg reflection with $d_{200} = 2.043 \text{ \AA}$ at a Bragg angle θ_B of 88° (Bragg energy $E_B = 3036.74 \text{ eV}$). Adapted from Ref. 587.

two Si(111) crystals, this modulation occurs in two analogous steps, and the intensity of the x-ray beam on the sample can be expressed as:

$$I_{\text{eff, norm}}(E) = 1 \cdot R_{\text{mono},1}(E) \cdot R_{\text{mono},2}(E) = [R_{\text{mono}}(E)]^2, \quad (\text{A.5})$$

with $R_{\text{mono},i}$ as the reflectivity of the respective monochromator crystal i . In the above equation, the term $[R_{\text{mono}}(E)]^2$ denotes the total reflectivity of the double-crystal monochromator (termed “Reflectivity_mono_squared” in the source codes). Thus, the normalized effective intensity of the x-ray beam on the sample, $I_{\text{eff, norm}}$, is determined by the squared reflectivity of the two individual Si(111) monochromator crystals [see Fig. A.5(c), dark-gray dashed line]. In the above equation, it has been exploited that [see also Eq. (3.9)]:^{28,29,326}

$$R_{\text{mono},1}(E) \cdot R_{\text{mono},2}(E) = \frac{|E_H^{\text{mono},1}|^2}{|E_0^{\text{mono},1}|^2} \cdot \frac{|E_H^{\text{mono},2}|^2}{|E_0^{\text{mono},2}|^2} = \frac{|E_H^{\text{mono},2}|^2}{|E_0^{\text{mono},1}|^2} = [R_{\text{mono}}(E)]^2, \quad (\text{A.6})$$

where $E_0^{\text{mono},i}$ and $E_H^{\text{mono},i}$ are the complex electric-field amplitudes of the incident and emergent electromagnetic waves on the monochromator crystals i . As is apparent from Fig. A.5(a), $E_0^{\text{mono},2} = E_H^{\text{mono},1}$ is valid necessarily.³²⁶ Furthermore, it has been assumed here that $R_{\text{mono},1}(E) = R_{\text{mono},2}(E) = R_{\text{mono}}(E)$ (termed “Reflectivity_mono” in the source codes).³²⁶ This requires that the two monochromator crystal are perfectly identical and also perfectly parallel to each other, guaranteeing that $\theta_{\text{B, mono},1} = \theta_{\text{B, mono},2}$ (θ_{B} denotes the Bragg angle).³²⁶

The experimentally obtained signal $\Upsilon_{\text{exp}}(E)$ is always broadened in comparison to the theoretically predicted signal. In mathematical terms, broadening effects are considered through a convolution.^{f)} In the present case, the theoretically predicted signal has to be convoluted with both the total reflectivity of the double-crystal monochromator and the instrumental function. Having $\Upsilon_{\text{theo}}(E)$, $[R_{\text{mono}}(E)]^2$, and $G(E)$ at hand (the explicit calculation of the former two functions will be treated below), the convolution term of Eq. (A.2) is computed in two steps. In principle, the order of the two individual convolution steps is permutable. However, systematic tests have shown that, in computational terms, the most robust and fastest fitting algorithm consisted in the convolution sequence presented in the following, in fact.

In the first step, $\Upsilon_{\text{theo}}(E)$ and $[R_{\text{mono}}(E)]^2$ are convoluted to give the ideal signal $\Upsilon_{\text{ideal}}(E)$, i.e., the reflectivity of the substrate crystal or the XSW profile of interest, respectively, in the absence of any further broadening effects besides the finite width of the x-ray beam. $\Upsilon_{\text{ideal}}(E)$ is referred to as $F(E)$ ($\hat{=}$ “F”) in the source codes:^{g)}

$$\Upsilon_{\text{ideal}}(E) = F(E) = \Upsilon_{\text{theo}}(E) * [R_{\text{mono}}(E)]^2. \quad (\text{A.7})$$

The above convolution is computed using an FFT algorithm provided in Origin C (denoted as “fft_fft_convolution”; see source codes A.4.1, ll. 152–190, A.4.2, ll. 204–244, and A.4.3, ll. 210–250). Note that the convolution is performed such that the integral of $\Upsilon_{\text{theo}}(E)$ over E is retained

^{f)}In the strict physical sense, this only applies to broadening effects which can be described by an even, i.e., symmetric function. If the relevant broadening effects can only be described by an odd, i.e., asymmetric function, they have to be considered through a cross-correlation. This has not been done here. See Appendix F of the present work for a validation of controversial approximations in the computational algorithm behind the data evaluation routine XSWAVES³²⁹ regarding this point.

^{g)} $F(E)$ ($\hat{=}$ “F”) is also (incorrectly) denoted as “response function” within the source codes. This is due to historical reasons in the development of the XWAVES routine. Usually, the term “response function” refers to the function(s) which the actual signal $[\Upsilon_{\text{theo}}(E)$ in the present case] is convoluted with.

in this step, i.e., $\int F(E) dE = \int \Upsilon_{\text{theo}}(E) dE$. In a second step, $F(E)$ is convoluted with the instrumental function in order to give the real (normalized) signal $\Upsilon_{\text{real}}(E) = \Upsilon_{\text{theo}}(E) * [R_{\text{mono}}(E)]^2 * G(E)$. This final convolution is performed by explicitly solving the actual integral function behind the convolution:^{585,586}

$$\Upsilon_{\text{real}}(E) = F(E) * G(E) = \int_{-\infty}^{\infty} F(\epsilon) G(E - \epsilon) d\epsilon, \quad (\text{A.8})$$

with ϵ being an auxiliary variable with the dimension of an energy. This convolution step cannot be computed using the same FFT algorithm as in the first convolution step above because Origin fitting routines (of type *.fdf) require an *explicit* equation [$y = \dots$; see also Eq. (A.2)] as a final fitting function. The “fft_fft_convolution” algorithm provided in Origin is not compatible with this requirement. Hence, the convolution of Eq. (A.8) is computed by solving the integral in an interval around the Bragg energy E_B or, more precisely, around the center of the experimental curves by *numerical integration* according to the trapezoidal rule (see source codes A.4.1, ll. 194–220, A.4.2, ll. 248–274, and A.4.3, ll. 254–280):⁵⁸⁶

$$\begin{aligned} \Upsilon_{\text{real}}(E) &= F(E) * G(E) = \text{dIntegral} \\ &= \sum_{t=t_{\text{initial}}}^{t_{\text{final}}-\Delta t} \frac{1}{2} \cdot [F(t)G(E, t) + F(t + \Delta t)G(E, t + \Delta t)] \cdot \Delta t, \end{aligned} \quad (\text{A.9})$$

where

$$G(E, t) = \frac{1}{\sigma \sqrt{2\pi}} \exp \left[-\frac{1}{2} \left(\frac{(E - \mu) - t}{\sigma} \right)^2 \right]. \quad (\text{A.10})$$

The parameter t (with the dimension of an energy; termed “t” in the source codes) represents an *additional* energy shift. Again, the integral of $\Upsilon_{\text{theo}}(E)$ over E is retained, i.e., $\int \Upsilon_{\text{real}}(E) dE = \int \Upsilon_{\text{theo}}(E) dE$, in this step because the peak area of $G(E, t)$ is normalized to 1 (see also above). In Eq. (A.9), $t_{\text{initial}} = E_{\text{min}} - \Delta E_{\text{conv}}$ (termed “t_initial” in the source codes) and $t_{\text{final}} = E_{\text{max}} + \Delta E_{\text{conv}}$ (termed “t_final”) are the lower and upper bounds of integration, respectively. They calculate from the minimal and maximal photon energies employed in the experiment, E_{min} and E_{max} , and a small offset ΔE_{conv} (termed “ConvolutionExtension_constraint” in the XSWAVES C code). This offset extends the convolution interval $[t_{\text{initial}}, t_{\text{final}}]$, i.e., the interval in which the integral function behind the convolution is solved during the fitting process, by a few electronvolts in order to avoid undesirable artifacts in the fitting curve for high and low values of E . By default, $\Delta E_{\text{conv}} \geq 2.5 \text{ eV}$ where a value of 2.5 eV holds for $\mu = 0 \text{ eV}$; otherwise, ΔE_{conv} automatically increases with the magnitude of μ . This ensures that the relevant features of both the experimentally obtained and the theoretically predicted curves are well within the convolution interval $[t_{\text{initial}}, t_{\text{final}}]$. If desired, the user may set ΔE_{conv} to a value of choice through the option “+/- extension of the convolution interval (eV)” (see Fig. A.2). Note that, in principle, the value of ΔE_{conv} should increase with σ , too. However, $\sigma < 0.2 \text{ eV}$ holds in a typical XSW experiment, being one order of magnitude smaller than the default (minimal) ΔE_{conv} value. Hence, the impact of the actual σ value on the choice of ΔE_{conv} is small and has been neglected here.

The parameter Δt (termed “dt” in the source codes) is the step size in solving the integral of Eq. (A.8) through the trapezoidal rule. It is restricted to values of $\leq 0.1 \text{ eV}$ and maximal one fourth of the experimental step size in photon energy, $\Delta t \leq 1/4 \Delta E$. If desired, the user may

decrease Δt by a factor of ten via the option “Increase convolution number of points by a factor of 10” (see Figs. A.2 and A.3). It has been verified that the default choice of both Δt and ΔE_{conv} are appropriate for obtaining reliable fitting results. This was done by systematically varying the values of the two parameters (resulting in $\Delta f_c, \Delta p_c < 1 \times 10^{-3}$) and also by exemplarily comparing fitting results obtained with XSWAVES with those of other fitting algorithms.^{330,576}

Having performed the two convolution steps, the general and final fitting function as given in Eqs. (A.1) and (A.2) above can eventually be computed. For $\Upsilon(E) = R(E)$, the parameters σ and μ are obtained as a fitting result (besides A and $\Delta \Upsilon_{\text{exp}}$). They are then transferred automatically to the fitting of the XSW profile [$\Upsilon(E) = Y_{Z,j}(E)$] as fixed parameters by default (if desired, σ and μ can be chosen as fitting parameters in this evaluation step, as well). For $\Upsilon(E) = Y_{Z,j}(E)$, the fitting yields the values of f_c and p_c and thereby the desired structural information.

Calculation of the theoretical curves $R(E)$ and $Y_{Z,j}(E)$

So far, we have presumed that the individual theoretical curves $R(E)$ and $Y_{Z,j}(E)$ are known. The explicit calculation of these curves and their computation will be described in the following. As already stated, details on the theoretical background are reviewed in Sec. 3.1. For reasons of convenience, we will recite the most relevant equations here and designate the corresponding lines of the source code of the fitting routines (*.fdf; see Sec. A.4). Concerning the reflectivity $R(E)$, however, we will only highlight the calculation and computation of the reflectivity $R_{\text{theo}}(E)$ of the substrate and not also that of the monochromator crystals, $R_{\text{mono}}(E)$, because they are completely identical in both cases. The reader is referred to Sec. 3.1 (and also to Tables A.1 and A.2 of this chapter, regarding the conversion of the notation of the individual parameters, in particular) for a detailed description of the meaning of the individual parameters which are employed here.

The reflectivity $R(E)$ calculates as [see also Eq. (3.16)]:¹⁶⁰

$$R(E) = \frac{|E_H|^2}{|E_0|^2} = |b| \left| \eta \pm (\eta^2 - 1)^{\frac{1}{2}} \right|^2, \quad (\text{A.11})$$

with $R(E) \hat{=}$ “Reflectivity”, $b \hat{=}$ “b”, and $\eta = \eta(E) \hat{=}$ “eta” as the equivalent notation in the source codes (see A.4.1, ll. 68–100, A.4.2, ll. 78–125, and A.4.3, ll. 84–131). Note that the above equation is valid under the assumption that $F_H = F_{\bar{H}}$ which, in the strict sense, holds for centrosymmetric crystals only.¹⁶⁰ The complex parameter $\eta(E)$ itself describes the displacement of the scattering condition from the midpoint of the reflectivity curve $R(E)$ and calculates as [see also Eq. (3.17)]:²⁹

$$\eta(E) = \frac{-2(\Delta E/E) \sin^2 \theta_B + \Gamma F_0}{|P| \Gamma (F_H F_{\bar{H}})^{\frac{1}{2}}}, \quad (\text{A.12})$$

with $\Delta E = E - E_B \hat{=}$ “Delta_E”, $E \hat{=}$ “E_photon”, $\theta_B \hat{=}$ “theta_Bragg”, $\Gamma \hat{=}$ “Sigma”, $F_0 \hat{=}$ “F0”, $P \hat{=}$ “P”, and $(F_H F_{\bar{H}})^{\frac{1}{2}} = F_H \hat{=}$ “FH”, respectively, as the equivalent notation in the source codes (see A.4.1, l. 84, A.4.2, l. 110, and A.4.3, l. 116). The explicit calculations of the parameters P and b employed in the above equations are treated in Secs. 3.1.2 and 3.1.3, respectively. The b value as well as the θ_B value are provided by the Substrate Parameters input file while the parameter P may either be provided as a numerical value, too, or be calculated from θ_B in the case of π polarization (see Sec. 3.1.2). The parameter Γ , which is the constant of proportionality between the Fourier

coefficients of the charge density, i.e., the electron density within the crystal, and the dielectric constant, is given by [see also Eq. (3.18)]:^{28,29,160}

$$\Gamma = \frac{r_e \lambda^2}{\pi V_{uc}} = \left(\frac{e^2}{4\pi \epsilon_0 m_e c^2} \right) \frac{\lambda^2}{\pi (a_{bulk})^3}, \quad (\text{A.13})$$

where $r_e = (e^2/4\pi \epsilon_0 m_e c^2)$ is the classical electron radius and $V_{uc} = (a_{bulk})^3$ is the volume of the crystal unit cell. Here, the calculation of V_{uc} is based on the assumption that the substrate (or monochromator) crystal has a cubic crystal system. This parameter Γ , which is termed ‘‘Sigma’’ in the XSWAVES source codes, is calculated directly within the C-code routine of XSWAVES (XSWAVES_v2.5.c) from the a_{bulk} value, which in turn is provided by the Substrate Parameters input file, and passed to the actual fitting algorithms (*.fdf) as a numerical value.

Having calculated the reflectivity $R(E)$, the (normalized) XSW photoelectron yield $Y_{Z,j, \text{norm}}(E)$ (termed ‘‘XSWProfile’’ in the source codes) calculates as [see also Eq. (3.37)]:¹⁸⁸

$$Y_{Z,j, \text{norm}}(E) = \frac{I(z_{hkl})}{I_0} = 1 + S_R R(E) + 2 |S_I| \sqrt{R(E)} f_c \cos(\nu - 2\pi p_c + \psi), \quad (\text{A.14})$$

or as a linear combination of two individual XSW profiles (‘special fit model’):

$$\begin{aligned} Y_{Z,j, \text{norm}}(E) &= (1 - m_2) \left[1 + S_R R(E) + 2 |S_I| \sqrt{R(E)} f_c \cos(\nu - 2\pi p_c + \psi) \right] \\ &\quad + m_2 \left[1 + S_R R(E) + 2 |S_I| \sqrt{R(E)} f_{c,2} \cos(\nu - 2\pi p_{c,2} + \psi) \right] \\ &= 1 + S_R R(E) + 2 |S_I| \sqrt{R(E)} \\ &\quad \cdot \left[(1 - m_2) f_c \cos(\nu - 2\pi p_c + \psi) + m_2 f_{c,2} \cos(\nu - 2\pi p_{c,2} + \psi) \right], \end{aligned} \quad (\text{A.15})$$

with $S_R \hat{=}$ ‘‘SR’’, $|S_I| \hat{=}$ ‘‘SI’’, $f_c \hat{=}$ ‘‘CF’’, $p_c \hat{=}$ ‘‘CP’’, $\nu = \nu(E) \hat{=}$ ‘‘Phi’’, and $\psi \hat{=}$ ‘‘Psi’’, respectively, as the equivalent notation in the source codes (see A.4.2, l. 150 and A.4.3, l. 156, respectively). Furthermore, the relative contribution of the second XSW profile, which represents a different (adsorption) site or configurations, is denoted as $m_2 \hat{=}$ ‘‘m_ads2’’ (with values ranging from 0 to 1) while the corresponding coherent fraction and position are denoted as $f_{c,2} \hat{=}$ ‘‘CF_ads2’’, $p_{c,2} \hat{=}$ ‘‘CP_ads2’’, respectively.

In order to compute $Y_{Z,j, \text{norm}}(E)$ according to Eqs. (A.14) and (A.15), additional parameters are needed, namely, the phase $\nu(E)$ of the x-ray standing wavefield on the one hand and the nondipolar correction terms S_R , $|S_I|$, and ψ on the other hand. $\nu(E)$ calculates as [see also Eqs. (3.10) and (3.11)]:²⁸

$$\nu = \begin{cases} \zeta & \text{for } \text{Re}(E_H/E_0) > 0, \\ \zeta + \pi & \text{for } \text{Re}(E_H/E_0) < 0, \end{cases} \quad (\text{A.16})$$

where

$$\zeta = \arctan \left[\frac{\text{Im} \left(\frac{E_H}{E_0} \right)}{\text{Re} \left(\frac{E_H}{E_0} \right)} \right] = \arg \left(\frac{E_H}{E_0} \right), \quad (\text{A.17})$$

with $\text{Re}(E_H/E_0) \hat{=}$ ‘‘EH_E0_real’’, $\text{Im}(E_H/E_0) \hat{=}$ ‘‘EH_E0_imag’’, and $E_H/E_0 \hat{=}$ ‘‘EH_E0’’, which is the ratio of the complex electric-field amplitudes, as the equivalent notation in the source codes

(see A.4.2, ll. 127–148 and A.4.3, ll. 133–154). Here, E_H/E_0 is computed as [with the convention that $\sqrt{|b|}$ denotes the principal square root of $|b|$ and thus has a positive sign;²⁹ see also Eq. (3.15)]:^{28,29,160}

$$\frac{E_H}{E_0} = \sqrt{R} \exp(i\nu) = -\sqrt{|b|} (\eta \pm (\eta^2 - 1)^{\frac{1}{2}}). \quad (\text{A.18})$$

The nondipolar corrections are considered in XSWAVES initially through the parameters Q (termed “ Q ” in the source codes) and Δ ($\hat{=}$ “Delta”) which can be set by the user (see Fig. A.3 above). These two parameters are converted into the parameters S_R , $|S_I|$, and ψ within the fitting routines (*.fdf) according to [see also Eqs. (3.31), (3.32), and (3.33)]:¹⁷⁶

$$S_R = \frac{1 + Q}{1 - Q}, \quad (\text{A.19})$$

$$|S_I| = \frac{(1 + \tan^2 \psi)^{\frac{1}{2}}}{1 - Q}, \quad (\text{A.20})$$

and

$$\tan \psi = Q \tan \Delta. \quad (\text{A.21})$$

These conversions are computed in the source codes A.4.2, ll. 100–103 and A.4.3, ll. 106–109, respectively. At this point, all parameters required for the calculation of both the reflectivity $R(E)$ and the normalized XSW photoelectron yield $Y_{Z,j,\text{norm}}(E)$ are available so that the general fitting function can eventually be computed [see Eqs. (A.1) and (A.2) above]. All further lines of the source codes, which have not been addressed yet, are less important for the fundamental understanding of the overall computational algorithm in XSWAVES, e.g., they define parameters and variables, or they compute auxiliary calculations [apart from the lines where $R_{\text{mono}}(E)$ is computed, of course]. Therefore, these lines are not explicitly discussed here.

Performance of XSWAVES

In order to ensure that the XSWAVES routine does not suffer from computational or numerical errors, its performance has been thoroughly tested. In particular, this was done employing both synthetic and experimental data. The synthetic data were created with XSWAVES Simulator and also with a dedicated algorithm in Microsoft EXCEL which was written and kindly provided by Dr. Bruce Cowie (Australian Synchrotron, Clayton, VIC, Australia). Besides, the measured photoelectron yield curves $Y_{Z,j,\text{exp}}(E)$ of the C total and O total XPS signals of PTCDA/Ag(100), PTCDA/Ag(110) (see Sec. C.3.4 in Appendix C for both), and K + PTCDA/Ag(110) (see Sec. D.3.3 in Appendix D of the present work) were taken as experimental reference data here. The XSWAVES fitting results were compared with those obtained when employing the programs DARE⁵⁷⁶ or Torricelli.^{326,330}

We found that the deviations in the fitting results of the coherent fractions and positions, Δf_c and Δp_c , respectively, between the individual fitting routines or analysis programs amount to maximal ± 0.02 . Thus, the deviations are well within the error margins of a typical XSW measurement. In particular, we found that $\Delta p_c \ll 0.01$ when fitting the synthetic data (where f_c and p_c are known *a priori*) with XSWAVES. Hence, we conclude that computational or numerical errors can

be excluded and that the analysis of XSW data with the XSWAVES fitting routine yields highly reliable results.

A.4 Source codes

In this section, the source codes of the above-noted, actual fitting algorithms (*.fdf) are given in versions 2.5 for both the reflectivity and the XSW profile (including the ‘special fit model’, i.e., the linear combination of two individual XSW profiles). Keywords are marked in blue and comments are marked in green, respectively. These algorithms are called from the XSWAVES routine and computed by the NLSF engine of Origin. The source code of the actual XSWAVES routine (XSWAVES_v2.5.c) is not reproduced here because this routine does not carry out sophisticated calculations, in contrast to the fitting algorithms. This C routine essentially handles data import, organization, and graphing only. It is available in full at http://www.thch.uni-bonn.de/pctc/sokolowski/XSWAVES/XSWAVES_index.html (as of 2013).

The fitting results for XSW data which are presented in this work have been obtained with XSWAVES, versions 2.4 and 2.5, i.e., the latest versions (as of 2013).³²⁹ Both versions yield identical results and differ only slightly in the implementation of a few formulae of the dynamical theory of x-ray diffraction (see also Sec. A.3).³²⁹ The modifications from version 2.4 to version 2.5 have been made in order to improve the completeness and the consistency of the source codes. It has been ensured that they do not affect the fitting results.

The only exceptions are the evaluation of the influence of the nondipolar correction terms Q and Δ on the fitting results f_c and p_c (see Appendix E of the present work) where XSWAVES, version 2.3, has been employed instead. This version assumes π polarization of the x-ray light. This is indeed true for the scattering event at the substrate. However, σ polarization is present with respect to the scattering geometry at the Si(111) double-crystal monochromator. This has been neglected in XSWAVES, version 2.3, and π polarization has been assumed here, too. Yet, this causes uncertainties in f_c of maximal ± 0.01 and uncertainties in p_c of well less than ± 0.005 , as has been verified by comparing exemplarily the fitting results obtained with the different versions of XSWAVES. Thus, the discrepancies in the fitting results from different XSWAVES versions are in fact negligible, justifying the general assumption of π polarization in earlier XSWAVES versions.

A.4.1 Fitting algorithm for Reflectivity data (XSWAVES_ReflectivityFit_v2_5.fdf)

```

1
2 [General Information]
3 Function Name = XSWAVES_ReflectivityFit_v2_5
4 Brief Description = fit to experimental reflectivity (including convolution with Gaussian
   function)
5 Function Source = fgroup.NewFunction
6 Function Type = User-Defined
7 Function Form = Equations
8 Number Of Parameters = 27
9 Number Of Independent Variables = 1
10 Number Of Dependent Variables = 1
11 Analytical Derivatives for User-Defined = 0

```



```

38
39 Dataset dsReflectivity;           // substrate reflectivity
40 dsReflectivity.Create(nSize);
41
42 //Dataset dsReflectivity_mono;     // monochromator reflectivity
43 //dsReflectivity_mono.Create(nSize);
44
45 Dataset dsReflectivity_mono_squared; // squared monochromator reflectivity
46 dsReflectivity_mono_squared.Create(nSize);
47
48 Dataset dsReflectivity_mono_squared_modified; // squared monochromator
    reflectivity, "wrapped around" and normalised
49 dsReflectivity_mono_squared_modified.Create(nSize);
50
51 Dataset dsResponse;
52 dsResponse.Create(nSize);
53
54 // Parameters for reflectivity calculation
55
56 // substrate Reflectivity
57
58 double Delta_E[10000];           // deviation from calculated Bragg energy in
    eV
59 double E_photon[10000];          // photon energy in eV = E_Bragg +
    Delta_E
60
61 // definition of complex structure factors F0, FH
62 complex F0(F0_real,F0_imag);
63 complex FH(FH_real,FH_imag);
64
65 // temperatue correction of reflected intensity
66 FH = FH*DW;
67
68 // Calculation of eta and Reflectivity = |b| * |eta +/- (eta^2 - 1)^0.5|^2
69
70 complex eta[10000];              // eta = ((-2.0*pow(sin(theta_Bragg),2.0)*Delta_E[ii]/
    E_photon[ii] + Sigma * F0) / (|P| * Sigma * FH)
71 complex z0[10000];              // z0 = ((-2.0*pow(sin(theta_Bragg),2.0)*Delta_E[ii]/
    E_photon[ii] + Sigma * F0)
72 complex z1[10000];              // z1 = eta^2
73 complex z2[10000];              // z2 = eta^2 - 1
74 complex z3[10000];              // z3 = (eta^2 - 1)^0.5
75 double d1[10000];               // d1 = | eta +/- (eta^2 - 1)^0.5 |
76 double d2[10000];               // d2 = Re(eta)
77 double Reflectivity[10000];     // Reflectivity = |b| * | eta +/- (eta^2 - 1)^0.5|^2
78
79 for (int ii = 0; ii < nSize; ii++)
80 {
81     Delta_E[ii] = (t_initial + ii * dt) - E_Bragg; // in eV
82     E_photon[ii] = (t_initial + ii * dt);

```



```

83  z0[ii] = -2.0*pow(sin(theta_Bragg),2.0)*Delta_E[ii]/E_photon[ii] + Sigma * F0;
84  eta[ii] = z0[ii] / (abs(P) * Sigma * FH);
85  z1[ii] = cpow(eta[ii],2.0+0i);
86  z2[ii] = z1[ii] - 1;
87  z3[ii] = sqrt(z2[ii]);
88  d2[ii] = eta[ii].m_re;
89
90  if (d2[ii] < 0)
91  {
92    d1[ii] = cabs( eta[ii] + z3[ii] );
93    Reflectivity[iii] = abs(b) * pow( d1[iii], 2.0 );
94  }
95  else
96  {
97    d1[ii] = cabs( eta[ii] - z3[ii] );
98    Reflectivity[iii] = abs(b) * pow( d1[iii], 2.0 );
99  }
100 }
101
102 // monochromator Reflectivity
103
104 double Delta_E_mono[10000]; // deviation from calculated Bragg
    energy in eV
105 double E_photon_mono[10000]; // photon energy in eV = E_Bragg
    + Delta_E
106
107 // definition of complex structure factors F0, FH
108 complex F0_mono(F0_real_mono,F0_imag_mono);
109 complex FH_mono(FH_real_mono,FH_imag_mono);
110
111 // temperatue correction of reflected intensity
112 FH_mono = FH_mono * DW_mono;
113
114 // Calculation of eta and Reflectivity = |b| * |eta +/- (eta^2 - 1)^0.5|^2
115
116 complex eta_mono[10000]; // eta = ((-2.0*pow(sin(theta_Bragg),2.0)*
    Delta_E[ii]/E_photon[ii] + Sigma * F0) / (|P| * Sigma * FH)
117 complex z0_mono[10000]; // z0 = ((-2.0*pow(sin(theta_Bragg),2.0)*Delta_E
    [ii]/E_photon[ii] + Sigma * F0)
118 complex z1_mono[10000]; // z1 = eta^2
119 complex z2_mono[10000]; // z2 = eta^2 - 1
120 complex z3_mono[10000]; // z3 = (eta^2 - 1)^0.5
121 double d1_mono[10000]; // d1 = | eta +/- (eta^2 - 1)^0.5 |
122 double d2_mono[10000]; // d2 = Re(eta)
123 double Reflectivity_mono[10000]; // Reflectivity = |b| * | eta +/- (eta^2 - 1)^0.5
    |^2
124 double Reflectivity_mono_squared[10000]; // Reflectivity^2 = ( |b| * | eta +/- (eta^2
    - 1)^0.5 |^2 ) ^2
125 double Reflectivity_mono_squared_modified[10000]; // Reflectivity^2 = ( |b| * | eta
    +/- (eta^2 - 1)^0.5 |^2 ) ^2, "wrapped around" and normalised

```

```

126
127 for (int jj = 0; jj < nSize; jj ++)
128 {
129     Delta_E_mono[jj] = (t_initial + jj * dt) - E_Bragg_mono; // in eV
130     E_photon_mono[jj] = (t_initial + jj * dt);
131     z0_mono[jj] = -2.0*pow(sin(theta_Bragg_mono),2.0)*Delta_E_mono[jj]/
        E_photon_mono[jj] + Sigma_mono * F0_mono;
132     eta_mono[jj] = z0_mono[jj] / (abs(P_mono) * Sigma_mono * FH_mono);
133     z1_mono[jj] = cpow(eta_mono[jj],2.0+0i);
134     z2_mono[jj] = z1_mono[jj] - 1;
135     z3_mono[jj] = sqrt(z2_mono[jj]);
136     d2_mono[jj] = eta_mono[jj].m_re;
137
138     if (d2_mono[jj] < 0)
139     {
140         d1_mono[jj] = cabs( eta_mono[jj] + z3_mono[jj] );
141         Reflectivity_mono[jj] = abs(b_mono) * pow( d1_mono[jj], 2.0 );
142     }
143     else
144     {
145         d1_mono[jj] = cabs( eta_mono[jj] - z3_mono[jj] );
146         Reflectivity_mono[jj] = abs(b) * pow( d1_mono[jj], 2.0 );
147     }
148
149     Reflectivity_mono_squared[jj] = pow ( Reflectivity_mono[jj], 2.0 );
150 }
151
152 //***** Statistics on squared monochromator reflectivity data: used for
        modification of the the data in order to perform convolution *****
153
154 for(int kk = 0; kk < nSize; kk++)
155 {
156     dsReflectivity[kk] = Reflectivity[kk];
157     //dsReflectivity_mono[kk] = Reflectivity_mono[kk];
158     dsReflectivity_mono_squared[kk] = Reflectivity_mono_squared[kk];
159 }
160
161 // Prepare everthing for the convolution of substrate reflectivity and squared
        monochromator reflectivity
162
163 // Take response function and "wrap it around" so that the point with the max
        value is now the first point in the response dataset. Also normalize sum to 1
164 // Also find the row index of the maximum value in the response (= squared
        monochromator reflectivity)
165
166 BasicStats bsStats; // Data structure of the output statistics
167 Data_sum(&dsReflectivity_mono_squared, &bsStats); // returns sum of data in
        specified dataset
168 double Reflectivity_mono_squared_sum = bsStats.total; // sum of data

```

```

169 int Reflectivity_mono_squared_Max_iRow = bsStats.iMax;    // index of row which
    holds maximum of squared monochromator reflectivity
170
171 for (int ll = 0; ll < nSize; ll++)
172 {
173     if (ll >= Reflectivity_mono_squared_Max_iRow)
174     {
175         Reflectivity_mono_squared_modified[ll - Reflectivity_mono_squared_Max_iRow] =
            Reflectivity_mono_squared[ll] / Reflectivity_mono_squared_sum;
176         dsReflectivity_mono_squared_modified[ll - Reflectivity_mono_squared_Max_iRow] =
            Reflectivity_mono_squared_modified[ll - Reflectivity_mono_squared_Max_iRow];
177     }
178     if (ll < Reflectivity_mono_squared_Max_iRow)
179     {
180         Reflectivity_mono_squared_modified[nSize + ll -
            Reflectivity_mono_squared_Max_iRow] = Reflectivity_mono_squared[ll] /
            Reflectivity_mono_squared_sum;
181         dsReflectivity_mono_squared_modified[nSize + ll -
            Reflectivity_mono_squared_Max_iRow] = Reflectivity_mono_squared_modified[nSize
            + ll - Reflectivity_mono_squared_Max_iRow];
182     }
183 }
184
185 int convolution1;
186 vector x1 = dsReflectivity;
187     vector y1 = dsReflectivity_mono_squared_modified;
188
189     convolution1 = fft_fft_convolution(nSize, x1, y1);
190     dsResponse = x1;
191
192 //+++++
193
194 // response function
195
196 G1 = 1 / (wG * sqrt(2.0 * PI)) * exp(-0.5*((x - xcG) - t)^2/wG^2);
197
198 // ideal Reflectivity curve: Assign function values F(t) by dataset index [mm] of
    dataset "dsResponse".
199 for(int mm = 0; mm < nSize; mm++)
200 {
201     F[mm] = dsResponse[mm];
202 }
203
204 // The following lines actually perform a integrate to the function, the trapezoidal
    rule is used.
205
206 do
207 {
208     // response function
209

```

```
210 G2 = 1 / (wG * sqrt(2.0 * PI)) * exp( -0.5*((x - xcG) - (t + dt))^2/wG^2 );
211
212 // employing trapezoidal rule for integration
213
214 dInt = 0.5 * (G1 * F[round((t - t_initial) / dt, 0)] + G2 * F[round((t + dt - t_initial) /
dt, 0)]) * dt ;
215 dIntegral += dInt;
216 t += dt;
217
218 G1 = G2;
219
220 }while (t < t_final - 1e-9);
221
222 y = A * dIntegral + y0;
223
224 [Constraints]
225
226 [Parameters Initialization]
227
228 [Initializations]
229
230 [After Fitting]
231
232 [Independent Variables]
233 x =
234
235 [Dependent Variables]
236 y =
237
238 [Controls]
239 General Linear Constraints = 1
240 Initialization Scripts = 0
241 Scripts After Fitting = 0
242 Number Of Duplicates = N/A
243 Duplicate Offset = N/A
244 Duplicate Unit = N/A
245 Generate Curves After Fitting = 1
246 Curve Point Spacing = Uniform on X-Axis Scale
247 Generate Peaks After Fitting = 1
248 Generate Peaks During Fitting = 1
249 Generate Peaks with Baseline = 1
250 Paste Parameters to Plot After Fitting = 1
251 Paste Parameters to Notes Window After Fitting = 1
252 Generate Residuals After Fitting = 0
253 Keep Parameters = 0
254 Enable Parameters Initialization = 0
255 Compile On Param Change Script = 0
256
257 [Compile Function]
258 Compile = 1
```

```
259 Compile Parameters Initialization = 1
260 OnParamChangeScriptsEnabled = N/A
261
262 [Origin C Function Header]
263 #pragma warning(error : 15618)
264 #include <origin.h>
265
266 // Add your special include files here.
267 // For example, if you want to fit with functions from the NAG library,
268 // add the header file for the NAG functions here.
269
270 #include <..\originlab\fft.h> // path points to C:\Program Files\
    OriginLab\Origin8\OriginC\OriginLab\fft.h; used for convolution of data
271
272 // Add code here for other Origin C functions that you want to define in this file,
273 // and access in your fitting function.
274
275 // You can access C functions defined in other files, if those files are loaded and
    compiled
276 // in your workspace, and the functions have been prototyped in a header file that
    you have
277 // included above.
278
279 // You can access NLSF object methods and properties directly in your function
    code.
280
281 // You should follow C-language syntax in defining your function.
282 // For instance, if your parameter name is P1, you cannot use p1 in your function
    code.
283 // When using fractions, remember that integer division such as 1/2 is equal to 0,
    and not 0.5
284 // Use 0.5 or 1/2.0 to get the correct value.
285
286 // For more information and examples, please refer to the "User-Defined Fitting
    Function"
287 // section of the Origin Help file.
288
289 [Origin C Parameter Initialization Header]
290 #include <origin.h>
291
292 // Add your special include files here.
293 // For example, if you want to use functions from the NAG library,
294 // add the header file for the NAG functions here.
295
296 // Add code here for other Origin C functions that you want to define in this file,
297 // and access in your parameter initialization.
298
299 // You can access C functions defined in other files, if those files are loaded and
    compiled
```

```

300 // in your workspace, and the functions have been prototyped in a header file that
      you have
301 // included above.
302
303 // You can access NLSF object methods and properties directly in your function
      code.
304 // You should follow C-language syntax in defining your function.
305 // For instance, if your parameter name is P1, you cannot use p1 in your function
      code.
306 // When using fractions, remember that integer division such as 1/2 is equal to 0,
      and not 0.5
307 // Use 0.5 or 1/2.0 to get the correct value.
308
309 // For more information and examples, please refer to the "User-Defined Fitting
      Function"
310 // section of the Origin Help file.
311
312 [References]
313

```

A.4.2 Fitting algorithm for XSW Absorption Profile data (XSWAVES_AbsorptionProfileFit_v_2_5.fdf)

```

1
2 [General Information]
3 Function Name = XSWAVES_AbsorptionProfileFit_v_2_5
4 Brief Description = fit to experimental XSW absorption profile (including convolution with
      Gaussian function)
5 Function Source = fgroup.NewFunction
6 Function Type = User-Defined
7 Function Form = Equations
8 Number Of Parameters = 31
9 Number Of Independent Variables = 1
10 Number Of Dependent Variables = 1
11 Analytical Derivatives for User-Defined = 0
12 FunctionPrev = \\pcfs2\abt-soko\bauer\OriginLab\Origin8-s0601w\User Files\fitfunc\
      XSWAVES_AbsorptionProfileFit_v_2_3.fdf
13
14 [Fitting Parameters]
15 Naming Method = User-Defined
16 Names = CF,CP,Q,Delta,y0_XSWProfile,A_XSWProfile,wG_XSWProfile,xcG_XSWProfile,
      t_XSWinitial,t_XSWfinal,dt_XSW,E_Bragg,theta_Bragg,Sigma,F0_real,F0_imag,
      FH_real,FH_imag,DW,b,P,E_Bragg_mono,theta_Bragg_mono,Sigma_mono,
      F0_real_mono,F0_imag_mono,FH_real_mono,FH_imag_mono,DW_mono,b_mono,
      P_mono
17 Meanings = coherent fraction,coherent position,non-dipolar parameter Q,non-dipolar
      parameter Delta,y offset,amplitude,Gaussian width,Gaussian center,lower bound of
      integration,upper bound of integration,integration stepsize,Bragg energy (eV),Bragg angle
      (rad),Sigma,structure factor Re(F0),structure factor Im(F0),structure factor Re(FH),

```



```

44 //dsPhi.Create(nSize);
45
46 Dataset dsXSWProfile;           // XSW absorption profile
47 dsXSWProfile.Create(nSize);
48
49 //Dataset dsReflectivity_mono;   // monochromator reflectivity
50 //dsReflectivity_mono.Create(nSize);
51
52 Dataset dsReflectivity_mono_squared; // squared monochromator reflectivity
53 dsReflectivity_mono_squared.Create(nSize);
54
55 Dataset dsReflectivity_mono_squared_modified; // squared monochromator
    reflectivity, "wrapped around" and normalised
56 dsReflectivity_mono_squared_modified.Create(nSize);
57
58 Dataset dsResponse;             // Response = convolution of Gaussian and
    squared Monochromator Reflectivity
59 dsResponse.Create(nSize);
60
61 // Parameters for reflectivity and phase calculation
62
63 // substrate Reflectivity and phase
64
65 double Delta_E1,Delta_E2;       // deviation from calculated Bragg
    energy in eV
66 double E_photon1,E_photon2;     // photon energy in eV = E_Bragg
    + Delta_E
67
68 double Delta_E[10000];          // deviation from calculated Bragg energy in
    eV
69 double E_photon[10000];        // photon energy in eV = E_Bragg +
    Delta_E
70
71 // definition of complex structure factors F0, FH
72 complex F0(F0_real,F0_imag);
73 complex FH(FH_real,FH_imag);
74
75 // temperatue correction of reflected intensity
76 FH = FH*DW;
77
78 // Calculation of eta and Reflectivity = |b| * |eta +- (eta^2 -1)^0.5|^2 (for
    centrosymmetric crystals) and phase Phi = arctan (Im(E_H / E_0) / Re (E_H
    / E_0)) [+ Pi if Re(E_H/E_0 < 0)]
79 // references: B.W. Batterman, H. Cole, Reviews of Modern Physics 36 (1964)
    681-717.
80 //     J. Zegenhagen, Surface Science Reports 18 (1993) 199-271.
81 //     D.P. Woodruff, Progress in Surface Science 57 (1998) 1-60.
82 //     D.P. Woodruff, Reports on Progress in Physics 68 (2005) 743-798.
83

```



```

84 complex eta[10000];          // eta = ((-2.0*pow(sin(theta_Bragg),2.0)*Delta_E[ii]/
    E_photon[ii] + Sigma * F0) / (|P| * Sigma * FH)
85 complex z0[10000];          // z0 = ((-2.0*pow(sin(theta_Bragg),2.0)*Delta_E[ii]/
    E_photon[ii] + Sigma * F0)
86 complex z1[10000];          // z1 = eta^2
87 complex z2[10000];          // z2 = eta^2 - 1
88 complex z3[10000];          // z3 = (eta^2 - 1)^0.5
89 double d1[10000];           // d1 = | eta +/- (eta^2 - 1)^0.5 |
90 double d2[10000];           // d2 = Re(eta)
91 double Reflectivity[10000]; // Reflectivity = |b| * | eta +/- (eta^2 - 1)^0.5 |^2
92
93 double Phi[10000];           // Phi = phase difference between incoming and outgoing
    wave
94 complex EH_E0[10000];        // EH_E0 = EH / E0 = eta +/- (eta^2 - 1)^0.5 (=
    ratio of complex electric field amplitudes)
95 double EH_E0_real[10000];    // real part of EH / E0 (= ratio of complex electric
    field amplitudes)
96 double EH_E0_imag[10000];    // imaginary part of EH / E0 (= ratio of complex
    electric field amplitudes)
97
98 double XSWProfile[10000];    // absorption = 1 + S_R * R + |S_I| * 2 * CF * sqrt(
    R) * cos (Phi - 2 * Pi * CP + Psi)
99
100 // non-dipolar parameters
101 double SR = (1 + Q) / (1 - Q);
102 double SI = sqrt(1 + pow(Q,2.0) * pow(tan(Delta),2.0)) / (1 - Q);
103 double Psi = atan(Q * tan(Delta));
104
105 for (int ii = 0; ii < nSize; ii++)
106 {
107     Delta_E[ii] = (t_XSWinitial + ii * dt_XSW) - E_Bragg; // in eV
108     E_photon[ii] = (t_XSWinitial + ii * dt_XSW);
109     z0[ii] = -2.0*pow(sin(theta_Bragg),2.0)*Delta_E[ii]/E_photon[ii] + Sigma * F0;
110     eta[ii] = z0[ii] / (abs(P) * Sigma * FH);
111     z1[ii] = cpow(eta[ii],2.0+0i);
112     z2[ii] = z1[ii] - 1;
113     z3[ii] = sqrt(z2[ii]);
114     d2[ii] = eta[ii].m_re;
115
116     if (d2[ii] < 0)
117     {
118         d1[ii] = cabs( eta[ii] + z3[ii] );
119         Reflectivity[ii] = abs(b) * pow( d1[ii], 2.0 );
120     }
121     else
122     {
123         d1[ii] = cabs( eta[ii] - z3[ii] );
124         Reflectivity[ii] = abs(b) * pow( d1[ii], 2.0 );
125     }
126 }

```

```

127 // phase Phi
128
129 if (d2[ii] < 0)
130 {
131     EH_E0[ii] = -sqrt(abs(b)) * (eta[ii] + z3[ii]);
132 }
133 else
134 {
135     EH_E0[ii] = -sqrt(abs(b)) * (eta[ii] - z3[ii]);
136 }
137
138 EH_E0_real[ii] = EH_E0[ii].m_re;
139 EH_E0_imag[ii] = EH_E0[ii].m_im;
140
141 if (EH_E0_real[ii] < 0)
142 {
143     Phi[ii] = PI + atan (EH_E0_imag[ii] / EH_E0_real[ii]);
144 }
145 else
146 {
147     Phi[ii] = atan (EH_E0_imag[ii] / EH_E0_real[ii]);
148 }
149
150 XSWProfile[ii] = 1 + SR * Reflectivity[ii] + SI * 2 * CF * sqrt(Reflectivity[ii]) * cos(Phi[ii]
    + Psi - (2 * Pi * CP))
151 }
152
153 // monochromator Reflectivity
154
155 double Delta_E_mono[10000]; // deviation from calculated Bragg
    energy in eV
156 double E_photon_mono[10000]; // photon energy in eV = E_Bragg
    + Delta_E
157
158 // definition of complex structure factors F0, FH
159 complex F0_mono(F0_real_mono,F0_imag_mono);
160 complex FH_mono(FH_real_mono,FH_imag_mono);
161
162 // temperatue correction of reflected intensity
163 FH_mono = FH_mono * DW_mono;
164
165 // Calculation of eta and Reflectivity = |b| * |eta +- (eta^2 - 1)^0.5|^2 and phase
    Phi
166
167 complex eta_mono[10000]; // eta = ((-2.0*pow(sin(theta_Bragg),2.0)*
    Delta_E[ii]/E_photon[ii] + Sigma * F0) / (|P| * Sigma * FH)
168 complex z0_mono[10000]; // z0 = ((-2.0*pow(sin(theta_Bragg),2.0)*Delta_E
    [ii]/E_photon[ii] + Sigma * F0)
169 complex z1_mono[10000]; // z1 = eta^2
170 complex z2_mono[10000]; // z2 = eta^2 - 1

```

```

171 complex z3_mono[10000];           // z3 = (eta^2 - 1)^0.5
172 double d1_mono[10000];           // d1 = | eta +/- (eta^2 - 1)^0.5 |
173 double d2_mono[10000];           // d2 = Re(eta)
174 double Reflectivity_mono[10000]; // Reflectivity = |b| * | eta +/- (eta^2 - 1)^0.5
    |^2
175 double Reflectivity_mono_squared[10000]; // Reflectivity^2 = ( |b| * | eta +/- (eta^2
    - 1)^0.5 |^2 ) ^2
176 double Reflectivity_mono_squared_modified[10000]; // Reflectivity^2 = ( |b| * | eta
    +/- (eta^2 - 1)^0.5 |^2 ) ^2, "wrapped around" and normalised
177
178 for (int jj = 0; jj < nSize; jj ++)
179 {
180     Delta_E_mono[jj] = (t_XSWinitial + jj * dt_XSW) - E_Bragg_mono; // in eV
181     E_photon_mono[jj] = (t_XSWinitial + jj * dt_XSW);
182     z0_mono[jj] = -2.0*pow(sin(theta_Bragg_mono),2.0)*Delta_E_mono[jj]/
        E_photon_mono[jj] + Sigma_mono * F0_mono;
183     eta_mono[jj] = z0_mono[jj] / (abs(P_mono) * Sigma_mono * FH_mono);
184     z1_mono[jj] = cpow(eta_mono[jj],2.0+0i);
185     z2_mono[jj] = z1_mono[jj] - 1;
186     z3_mono[jj] = sqrt(z2_mono[jj]);
187     d2_mono[jj] = eta_mono[jj].m_re;
188
189     if (d2_mono[jj] < 0)
190     {
191         d1_mono[jj] = cabs( eta_mono[jj] + z3_mono[jj] );
192         Reflectivity_mono[jj] = abs(b_mono) * pow( d1_mono[jj], 2.0 );
193     }
194     else
195     {
196         d1_mono[jj] = cabs( eta_mono[jj] - z3_mono[jj] );
197         Reflectivity_mono[jj] = abs(b) * pow( d1_mono[jj], 2.0 );
198     }
199
200     Reflectivity_mono_squared[jj] = pow ( Reflectivity_mono[jj], 2.0 );
201
202 }
203
204 ***** Statistics on squared monochromator reflectivity data: used for
    modification of the the data in order to perform convolution *****
205
206 for(int kk = 0; kk < nSize; kk++)
207 {
208     //dsReflectivity[kk] = Reflectivity[kk];
209     //dsPhi = Phi[kk];
210     dsXSWProfile[kk] = XSWProfile[kk];
211     //dsReflectivity_mono[kk] = Reflectivity_mono[kk];
212     dsReflectivity_mono_squared[kk] = Reflectivity_mono_squared[kk];
213 }
214

```

```

215 // Prepare everything for the convolution of substrate reflectivity and squared
      // monochromator reflectivity
216
217 // Take response function and "wrap it around" so that the point with the max
      // value is now the first point in the response dataset. Also normalize sum to 1
218 // Also find the row index of the maximum value in the response (= squared
      // monochromator reflectivity)
219
220 BasicStats bsStats; // Data structure of the output statistics
221 Data_sum(&dsReflectivity_mono_squared, &bsStats); // returns sum of data in
      // specified dataset
222 double Reflectivity_mono_squared_sum = bsStats.total; // sum of data
223 int Reflectivity_mono_squared_Max_iRow = bsStats.iMax; // index of row which
      // holds maximum of squared monochromator reflectivity
224
225 for (int ll = 0; ll < nSize; ll++)
226 {
227     if (ll >= Reflectivity_mono_squared_Max_iRow)
228     {
229         Reflectivity_mono_squared_modified[ll - Reflectivity_mono_squared_Max_iRow] =
230         Reflectivity_mono_squared[ll] / Reflectivity_mono_squared_sum;
231         dsReflectivity_mono_squared_modified[ll - Reflectivity_mono_squared_Max_iRow] =
232         Reflectivity_mono_squared_modified[ll - Reflectivity_mono_squared_Max_iRow];
233     }
234     if (ll < Reflectivity_mono_squared_Max_iRow)
235     {
236         Reflectivity_mono_squared_modified[nSize + ll -
237         Reflectivity_mono_squared_Max_iRow] = Reflectivity_mono_squared[ll] /
238         Reflectivity_mono_squared_sum;
239         dsReflectivity_mono_squared_modified[nSize + ll -
240         Reflectivity_mono_squared_Max_iRow] = Reflectivity_mono_squared_modified[nSize
241         + ll - Reflectivity_mono_squared_Max_iRow];
242     }
243 }
244
245 int convolution1;
246 vector x1 = dsXSWProfile;
247 vector y1 = dsReflectivity_mono_squared_modified;
248
249 convolution1 = fft_fft_convolution(nSize, x1, y1);
250 dsResponse = x1;
251
252 //+++++
253 // Gaussian (= response function) at data point 1
254
255 G1 = 1 / (wG_XSWProfile * sqrt(2.0 * PI)) * exp( -0.5*((x - xcG_XSWProfile) - t)^2/
256         wG_XSWProfile^2 );

```

```

252 // convoluted XSW absorption profile: Assign function values F(t) by dataset index
    [mm] of dataset "dsResponse".
253 for(int mm = 0; mm < nSize; mm++)
254 {
255     F[mm] = dsResponse[mm];
256 }
257
258 // The following lines actually perform a integrate to the function, the trapezoidal
    rule is used.
259
260 do
261 {
262     // Gaussian (= response function) at data point 2
263
264     G2 = 1 / (wG_XSWProfile * sqrt(2.0 * PI)) * exp( -0.5*((x - xcG_XSWProfile) - (t +
        dt_XSW))^2/wG_XSWProfile^2 );
265
266     // employing trapezoidal rule for integration
267
268     dInt = 0.5 * (G1 * F[round((t - t_XSWinitial) / dt_XSW, 0)] + G2 * F[round((t +
        dt_XSW - t_XSWinitial) / dt_XSW, 0)]) * dt_XSW ;
269     dIntegral += dInt;
270     t += dt_XSW;
271
272     G1 = G2;
273 }while (t < t_XSWfinal - 1e-9);
274
275 y = A_XSWProfile * dIntegral + y0_XSWProfile;
276
277 [Constraints]
278
279 [Parameters Initialization]
280
281 [Initializations]
282
283 [After Fitting]
284
285 [Independent Variables]
286 x =
287
288 [Dependent Variables]
289 y =
290
291 [Controls]
292 General Linear Constraints = 1
293 Initialization Scripts = 0
294 Scripts After Fitting = 0
295 Number Of Duplicates = N/A
296 Duplicate Offset = N/A

```

```
298 Duplicate Unit = N/A
299 Generate Curves After Fitting = 1
300 Curve Point Spacing = Uniform on X-Axis Scale
301 Generate Peaks After Fitting = 1
302 Generate Peaks During Fitting = 1
303 Generate Peaks with Baseline = 1
304 Paste Parameters to Plot After Fitting = 1
305 Paste Parameters to Notes Window After Fitting = 1
306 Generate Residuals After Fitting = 0
307 Keep Parameters = 0
308 Enable Parameters Initialization = 0
309 Compile On Param Change Script = 0
310
311 [Compile Function]
312 Compile = 1
313 Compile Parameters Initialization = 1
314 OnParamChangeScriptsEnabled = N/A
315
316 [Origin C Function Header]
317 #pragma warning(error : 15618)
318 #include <origin.h>
319
320 // Add your special include files here.
321 // For example, if you want to fit with functions from the NAG library,
322 // add the header file for the NAG functions here.
323
324 #include <..\originlab\fft.h> // path points to C:\Program Files\
    OriginLab\Origin8\OriginC\OriginLab\fft.h; used for convolution of data
325
326 // Add code here for other Origin C functions that you want to define in this file,
327 // and access in your fitting function.
328
329 // You can access C functions defined in other files, if those files are loaded and
    compiled
330 // in your workspace, and the functions have been prototyped in a header file that
    you have
331 // included above.
332
333 // You can access NLSF object methods and properties directly in your function
    code.
334
335 // You should follow C-language syntax in defining your function.
336 // For instance, if your parameter name is P1, you cannot use p1 in your function
    code.
337 // When using fractions, remember that integer division such as 1/2 is equal to 0,
    and not 0.5
338 // Use 0.5 or 1/2.0 to get the correct value.
339
340 // For more information and examples, please refer to the "User-Defined Fitting
    Function"
```

```

341 // section of the Origin Help file.
342
343 [Origin C Parameter Initialization Header]
344 #include <origin.h>
345
346 // Add your special include files here.
347 // For example, if you want to use functions from the NAG library,
348 // add the header file for the NAG functions here.
349
350 // Add code here for other Origin C functions that you want to define in this file,
351 // and access in your parameter initialization.
352
353 // You can access C functions defined in other files, if those files are loaded and
    compiled
354 // in your workspace, and the functions have been prototyped in a header file that
    you have
355 // included above.
356
357 // You can access NLSF object methods and properties directly in your function
    code.
358 // You should follow C-language syntax in defining your function.
359 // For instance, if your parameter name is P1, you cannot use p1 in your function
    code.
360 // When using fractions, remember that integer division such as 1/2 is equal to 0,
    and not 0.5
361 // Use 0.5 or 1/2.0 to get the correct value.
362
363 // For more information and examples, please refer to the "User-Defined Fitting
    Function"
364 // section of the Origin Help file.
365
366 [References]
367

```

A.4.3 Fitting algorithm for XSW Absorption Profile data: ‘special fit model’ (XSWAVES_AbsorptionProfileFit_Special_v_2_5.fdf)

```

1
2 [General Information]
3 Function Name = XSWAVES_AbsorptionProfileFit_Special_v_2_5
4 Brief Description = fit to experimental XSW absorption profile (including convolution with
    Gaussian function)
5 Function Source = fgroup.NewFunction
6 Number Of Parameters = 34
7 Function Type = User-Defined
8 Function Form = Equations
9 Path =
10 Number Of Independent Variables = 1
11 Number Of Dependent Variables = 1

```



```

35 double t = t_XSWinitial;           // The integration interval ranges over experimental
    photon energy range +/- some eV. The latter is necessary to ensure the quality
    of the fit at the boundaries of the experimental photon energy range.
36
37 double dSize = (t_XSWfinal - t_XSWinitial) / dt_XSW + 1.0; // number of simulated
    data points in the reflectivity curves; it might be a number with fractional digits
    ...
38 int nSize = round(dSize,0);           // number of simulated data points in
    the reflectivity curves as rounded integer
39
40 double t_XSWmean = 0.5 * (t_XSWinitial + t_XSWfinal); // This parameter is used to
    define the "center" of the substrate Reflectivity and phase Phi curves during the
    calculation of the convolution integral
41
42 double F[10000], G1, G2, Response[10000];           // F = convoluted XSW absorption
    profile (dynamical theory), G = Gaussian, Response = convolution of theoretical
    XSW absorption profile and squared Monochromator Reflectivity
43
44 // Definition of datasets to create
45
46 //Dataset dsReflectivity;           // substrate reflectivity
47 //dsReflectivity.Create(nSize);
48
49 //Dataset dsPhi;           // substrate phase Phi
50 //dsPhi.Create(nSize);
51
52 Dataset dsXSWProfile;           // XSW absorption profile
53 dsXSWProfile.Create(nSize);
54
55 //Dataset dsReflectivity_mono;           // monochromator reflectivity
56 //dsReflectivity_mono.Create(nSize);
57
58 Dataset dsReflectivity_mono_squared;           // squared monochromator reflectivity
59 dsReflectivity_mono_squared.Create(nSize);
60
61 Dataset dsReflectivity_mono_squared_modified; // squared monochromator
    reflectivity, "wrapped around" and normalised
62 dsReflectivity_mono_squared_modified.Create(nSize);
63
64 Dataset dsResponse;           // Response = convolution of Gaussian and
    squared Monochromator Reflectivity
65 dsResponse.Create(nSize);
66
67 // Parameters for reflectivity and phase calculation
68
69 // substrate Reflectivity and phase
70
71 double Delta_E1,Delta_E2;           // deviation from calculated Bragg
    energy in eV

```

```

72 double E_photon1,E_photon2;           // photon energy in eV = E_Bragg
    + Delta_E
73
74 double Delta_E[10000];               // deviation from calculated Bragg energy in
    eV
75 double E_photon[10000];             // photon energy in eV = E_Bragg +
    Delta_E
76
77 // definition of complex structure factors F0, FH
78 complex F0(F0_real,F0_imag);
79 complex FH(FH_real,FH_imag);
80
81 // temperature correction of reflected intensity
82 FH = FH*DW;
83
84 // Calculation of eta and Reflectivity = |b| * |eta +/- (eta^2 - 1)^0.5|^2 (for
    centrosymmetric crystals) and phase Phi = arctan (Im(E_H / E_0) / Re (E_H
    / E_0)) [+ Pi if Re(E_H/E_0 < 0)]
85 // references: B.W. Batterman, H. Cole, Reviews of Modern Physics 36 (1964)
    681-717.
86 // J. Zegenhagen, Surface Science Reports 18 (1993) 199-271.
87 // D.P. Woodruff, Progress in Surface Science 57 (1998) 1-60.
88 // D.P. Woodruff, Reports on Progress in Physics 68 (2005) 743-798.
89
90 complex eta[10000];                 // eta = ((-2.0*pow(sin(theta_Bragg),2.0)*Delta_E[ii]/
    E_photon[ii] + Sigma * F0) / (|P| * Sigma * FH)
91 complex z0[10000];                 // z0 = ((-2.0*pow(sin(theta_Bragg),2.0)*Delta_E[ii]/
    E_photon[ii] + Sigma * F0)
92 complex z1[10000];                 // z1 = eta^2
93 complex z2[10000];                 // z2 = eta^2 - 1
94 complex z3[10000];                 // z3 = (eta^2 - 1)^0.5
95 double d1[10000];                 // d1 = | eta +/- (eta^2 - 1)^0.5 |
96 double d2[10000];                 // d2 = Re(eta)
97 double Reflectivity[10000];       // Reflectivity = |b| * | eta +/- (eta^2 - 1)^0.5 |^2
98
99 double Phi[10000];                 // Phi = phase difference between incoming and outgoing
    wave
100 complex EH_E0[10000];             // EH_E0 = EH / E0 = eta +/- (eta^2 - 1)^0.5 (=
    ratio of complex electric field amplitudes)
101 double EH_E0_real[10000];         // real part of EH / E0 (= ratio of complex electric
    field amplitudes)
102 double EH_E0_imag[10000];         // imaginary part of EH / E0 (= ratio of complex
    electric field amplitudes)
103
104 double XSWProfile[10000];          // absorption = 1 + S_R * R + |S_I| * 2 * CF * sqrt(
    R) * cos (Phi - 2 * Pi * CP + Psi)
105
106 // non-dipolar parameters
107 double SR = (1 + Q) / (1 - Q);
108 double SI = sqrt(1 + pow(Q,2.0) * pow(tan(Delta),2.0)) / (1 - Q);

```

```

109 double Psi = atan(Q * tan(Delta));
110
111 for (int ii = 0; ii < nSize; ii ++)
112 {
113     Delta_E[ii] = (t_XSWinitial + ii * dt_XSW) - E_Bragg; // in eV
114     E_photon[ii] = (t_XSWinitial + ii * dt_XSW);
115     z0[ii] = -2.0*pow(sin(theta_Bragg),2.0)*Delta_E[ii]/E_photon[ii] + Sigma * F0;
116     eta[ii] = z0[ii] / (abs(P) * Sigma * FH);
117     z1[ii] = cpow(eta[ii],2.0+0i);
118     z2[ii] = z1[ii] - 1;
119     z3[ii] = sqrt(z2[ii]);
120     d2[ii] = eta[ii].m_re;
121
122     if (d2[ii] < 0)
123     {
124         d1[ii] = cabs( eta[ii] + z3[ii] );
125         Reflectivity[ii] = abs(b) * pow( d1[ii], 2.0 );
126     }
127     else
128     {
129         d1[ii] = cabs( eta[ii] - z3[ii] );
130         Reflectivity[ii] = abs(b) * pow( d1[ii], 2.0 );
131     }
132
133     // phase Phi
134
135     if (d2[ii] < 0)
136     {
137         EH_E0[ii] = -sqrt(abs(b)) * (eta[ii] + z3[ii]);
138     }
139     else
140     {
141         EH_E0[ii] = -sqrt(abs(b)) * (eta[ii] - z3[ii]);
142     }
143
144     EH_E0_real[ii] = EH_E0[ii].m_re;
145     EH_E0_imag[ii] = EH_E0[ii].m_im;
146
147     if (EH_E0_real[ii] < 0)
148     {
149         Phi[ii] = PI + atan (EH_E0_imag[ii] / EH_E0_real[ii]);
150     }
151     else
152     {
153         Phi[ii] = atan (EH_E0_imag[ii] / EH_E0_real[ii]);
154     }
155
156     XSWProfile[ii] = (1 - m_ads2) * (1 + SR * Reflectivity[ii] + SI * 2 * CF * sqrt(Reflectivity
    [ii]) * cos(Phi[ii] + Psi - (2 * Pi * CP))) + m_ads2 * (1 + SR * Reflectivity[ii] + SI * 2 *

```

```

    CF_ads2 * sqrt(Reflectivity[ii]) * cos(Phi[ii] + Psi - (2 * Pi * CP_ads2)));
157 }
158
159 // monochromator Reflectivity
160
161 double Delta_E_mono[10000];           // deviation from calculated Bragg
    energy in eV
162 double E_photon_mono[10000];         // photon energy in eV = E_Bragg
    + Delta_E
163
164 // definition of complex structure factors F0, FH
165 complex F0_mono(F0_real_mono,F0_imag_mono);
166 complex FH_mono(FH_real_mono,FH_imag_mono);
167
168 // temperatue correction of reflected intensity
169 FH_mono = FH_mono * DW_mono;
170
171 // Calculation of eta and Reflectivity = |b| * |eta +/- (eta^2 - 1)^0.5|^2 and phase
    Phi
172
173 complex eta_mono[10000];              // eta = ((-2.0*pow(sin(theta_Bragg),2.0)*
    Delta_E[ii]/E_photon[ii] + Sigma * F0) / (|P| * Sigma * FH)
174 complex z0_mono[10000];              // z0 = ((-2.0*pow(sin(theta_Bragg),2.0)*Delta_E
    [ii]/E_photon[ii] + Sigma * F0)
175 complex z1_mono[10000];              // z1 = eta^2
176 complex z2_mono[10000];              // z2 = eta^2 - 1
177 complex z3_mono[10000];              // z3 = (eta^2 - 1)^0.5
178 double d1_mono[10000];               // d1 = | eta +/- (eta^2 - 1)^0.5 |
179 double d2_mono[10000];               // d2 = Re(eta)
180 double Reflectivity_mono[10000];     // Reflectivity = |b| * | eta +/- (eta^2 - 1)^0.5
    |^2
181 double Reflectivity_mono_squared[10000]; // Reflectivity^2 = ( |b| * | eta +/- (eta^2
    - 1)^0.5 |^2 ) ^2
182 double Reflectivity_mono_squared_modified[10000]; // Reflectivity^2 = ( |b| * | eta
    +/- (eta^2 - 1)^0.5 |^2 ) ^2, "wrapped around" and normalised
183
184 for (int jj = 0; jj < nSize; jj ++)
185 {
186     Delta_E_mono[jj] = (t_XSWinitial + jj * dt_XSW) - E_Bragg_mono; // in eV
187     E_photon_mono[jj] = (t_XSWinitial + jj * dt_XSW);
188     z0_mono[jj] = -2.0*pow(sin(theta_Bragg_mono),2.0)*Delta_E_mono[jj]/
        E_photon_mono[jj] + Sigma_mono * F0_mono;
189     eta_mono[jj] = z0_mono[jj] / (abs(P_mono) * Sigma_mono * FH_mono);
190     z1_mono[jj] = cpow(eta_mono[jj],2.0+0i);
191     z2_mono[jj] = z1_mono[jj] - 1;
192     z3_mono[jj] = sqrt(z2_mono[jj]);
193     d2_mono[jj] = eta_mono[jj].m_re;
194
195     if (d2_mono[jj] < 0)

```

```

196 {
197     d1_mono[jj] = cabs( eta_mono[jj] + z3_mono[jj] );
198     Reflectivity_mono[jj] = abs(b_mono) * pow( d1_mono[jj], 2.0 );
199 }
200 else
201 {
202     d1_mono[jj] = cabs( eta_mono[jj] - z3_mono[jj] );
203     Reflectivity_mono[jj] = abs(b) * pow( d1_mono[jj], 2.0 );
204 }
205
206 Reflectivity_mono_squared[jj] = pow ( Reflectivity_mono[jj], 2.0 );
207
208 }
209
210 //***** Statistics on squared monochromator reflectivity data: used for
modification of the the data in order to perform convolution *****
211
212 for(int kk = 0; kk < nSize; kk++)
213 {
214     //dsReflectivity[kk] = Reflectivity[kk];
215     //dsPhi = Phi[kk];
216     dsXSWProfile[kk] = XSWProfile[kk];
217     //dsReflectivity_mono[kk] = Reflectivity_mono[kk];
218     dsReflectivity_mono_squared[kk] = Reflectivity_mono_squared[kk];
219 }
220
221 // Prepare everything for the convolution of substrate reflectivity and squared
monochromator reflectivity
222
223 // Take response function and "wrap it around" so that the point with the max
value is now the first point in the response dataset. Also normalize sum to 1
224 // Also find the row index of the maximum value in the response (= squared
monochromator reflectivity)
225
226 BasicStats bsStats; // Data structure of the output statistics
227 Data_sum(&dsReflectivity_mono_squared, &bsStats); // returns sum of data in
specified dataset
228 double Reflectivity_mono_squared_sum = bsStats.total; // sum of data
229 int Reflectivity_mono_squared_Max_iRow = bsStats.iMax; // index of row which
holds maximum of squared monochromator reflectivity
230
231 for (int ll = 0; ll < nSize; ll++)
232 {
233     if (ll >= Reflectivity_mono_squared_Max_iRow)
234     {
235         Reflectivity_mono_squared_modified[ll - Reflectivity_mono_squared_Max_iRow] =
236         Reflectivity_mono_squared[ll] / Reflectivity_mono_squared_sum;
237         dsReflectivity_mono_squared_modified[ll - Reflectivity_mono_squared_Max_iRow] =
238         Reflectivity_mono_squared_modified[ll - Reflectivity_mono_squared_Max_iRow];

```

```

237 }
238 if (ll < Reflectivity_mono_squared_Max_iRow)
239 {
240     Reflectivity_mono_squared_modified[nSize + ll -
241     Reflectivity_mono_squared_Max_iRow] = Reflectivity_mono_squared[ll] /
242     Reflectivity_mono_squared_sum;
243     dsReflectivity_mono_squared_modified[nSize + ll -
244     Reflectivity_mono_squared_Max_iRow] = Reflectivity_mono_squared_modified[nSize
245     + ll - Reflectivity_mono_squared_Max_iRow];
246 }
247 }
248
249 int convolution1;
250 vector x1 = dsXSWProfile;
251 vector y1 = dsReflectivity_mono_squared_modified;
252
253 convolution1 = fft_fft_convolution(nSize, x1, y1);
254 dsResponse = x1;
255
256 //+++++
257
258 // Gaussian (= response function) at data point 1
259
260 G1 = 1 / (wG_XSWProfile * sqrt(2.0 * PI)) * exp( -0.5*((x - xcG_XSWProfile) - t)^2/
261     wG_XSWProfile^2 );
262
263 // convoluted XSW absorption profile: Assign function values F(t) by dataset index
264 // [mm] of dataset "dsResponse".
265 for(int mm = 0; mm < nSize; mm++)
266 {
267     F[mm] = dsResponse[mm];
268 }
269
270 // The following lines actually perform a integrate to the function, the trapezoidal
271 // rule is used.
272
273 do
274 {
275     // Gaussian (= response function) at data point 2
276
277     G2 = 1 / (wG_XSWProfile * sqrt(2.0 * PI)) * exp( -0.5*((x - xcG_XSWProfile) - (t +
278     dt_XSW))^2/wG_XSWProfile^2 );
279
280     // employing trapezoidal rule for integration
281
282     dInt = 0.5 * (G1 * F[round((t - t_XSWinitial) / dt_XSW, 0)] + G2 * F[round((t +
283     dt_XSW - t_XSWinitial) / dt_XSW, 0)]) * dt_XSW ;
284     dIntegral += dInt;
285     t += dt_XSW;
286 }
287

```

```
278     G1 = G2;
279
280 }while (t < t_XSWfinal - 1e-9);
281
282 y = A_XSWProfile * dIntegral + y0_XSWProfile;
283
284 [Initializations]
285
286 [After Fitting]
287
288 [Controls]
289 General Linear Constraints = 0
290 Initialization Scripts = 0
291 Scripts After Fitting = 0
292 Number Of Duplicates = N/A
293 Duplicate Offset = N/A
294 Duplicate Unit = N/A
295 Generate Curves After Fitting = 1
296 Curve Point Spacing = Uniform on X-Axis Scale
297 Generate Peaks After Fitting = 1
298 Generate Peaks During Fitting = 1
299 Generate Peaks with Baseline = 1
300 Paste Parameters to Plot After Fitting = 1
301 Paste Parameters to Notes Window After Fitting = 1
302 Generate Residuals After Fitting = 0
303 Keep Parameters = 0
304 Compile On Param Change Script = 0
305 Enable Parameters Initialization = 0
306
307 [Compile Function]
308 Compile = 1
309 Compile Parameters Initialization = 1
310 OnParamChangeScriptsEnabled = 0.
311
312 [Parameters Initialization]
313
314 [Origin C Function Header]
315 #pragma warning(error : 15618)
316 #include <origin.h>
317
318 // Add your special include files here.
319 // For example, if you want to fit with functions from the NAG library,
320 // add the header file for the NAG functions here.
321
322 #include <..\originlab\fft.h> // path points to C:\Program Files\
    OriginLab\Origin8\OriginC\OriginLab\fft.h; used for convolution of data
323
324 // Add code here for other Origin C functions that you want to define in this file,
325 // and access in your fitting function.
326
```

```
327 // You can access C functions defined in other files, if those files are loaded and
    // compiled
328 // in your workspace, and the functions have been prototyped in a header file that
    // you have
329 // included above.
330
331 // You can access NLSF object methods and properties directly in your function
    // code.
332
333 // You should follow C-language syntax in defining your function.
334 // For instance, if your parameter name is P1, you cannot use p1 in your function
    // code.
335 // When using fractions, remember that integer division such as 1/2 is equal to 0,
    // and not 0.5
336 // Use 0.5 or 1/2.0 to get the correct value.
337
338 // For more information and examples, please refer to the "User-Defined Fitting
    // Function"
339 // section of the Origin Help file.
340
341 [Origin C Parameter Initialization Header]
342 #include <origin.h>
343
344 // Add your special include files here.
345 // For example, if you want to use functions from the NAG library,
346 // add the header file for the NAG functions here.
347
348 // Add code here for other Origin C functions that you want to define in this file,
349 // and access in your parameter initialization.
350
351 // You can access C functions defined in other files, if those files are loaded and
    // compiled
352 // in your workspace, and the functions have been prototyped in a header file that
    // you have
353 // included above.
354
355 // You can access NLSF object methods and properties directly in your function
    // code.
356 // You should follow C-language syntax in defining your function.
357 // For instance, if your parameter name is P1, you cannot use p1 in your function
    // code.
358 // When using fractions, remember that integer division such as 1/2 is equal to 0,
    // and not 0.5
359 // Use 0.5 or 1/2.0 to get the correct value.
360
361 // For more information and examples, please refer to the "User-Defined Fitting
    // Function"
362 // section of the Origin Help file.
363
364 [Constraints]
```


365
366 [References]
367

A.5 Exemplary input files

This section provides exemplary input files (*.txt) for both parameter and data input. The data input files are organized in three columns: the first column holds the photon energy, the second column holds the experimentally determined value of the reflectivity $R(E)$ or of the XSW photoelectron yield $Y_{Z,j}(E)$, respectively, and the third column holds the corresponding error (see Secs. A.5.2 and A.5.3 below). The tabulator character (“tab”) or the space character serve as valid separator signs between the individual column entries here.

The Substrate Parameters input file (see Sec. A.5.1) contains information about both the substrate and the monochromator crystals (structure factors and Debye-Waller factors, for example; see also Appendix B) which are required for the simulation of the theoretical $R(E)$ and $Y_{Z,j}(E)$ curves. Note that some of the entries in this file, such as the energy of x-ray beam, the chemical element, the employed reflection, the Bragg energy, or the temperature, are for information purposes only, and that they are not processed during the XSWAVES run. For example, the Bragg energy E_B will be calculated from the Bragg angle θ_B and the lattice plane spacing d_{hkl} (denoted as “d_H” here) via Eq. (3.5) with $n = 1$. Note that the structure of the exemplary Substrate Parameters input file, which is stated below (see Sec. A.5.1), must by all means be preserved in Substrate Parameters input file if customized by the XSWAVES user. For example, the Bragg angle θ_B must always be given as the fourth token on input line 11. Otherwise, the parameter import and/or the assignment to the individual physical quantities will not work correctly and, hence, proper execution of the XSWAVES routine will fail.

A.5.1 Exemplary Substrate Parameters input file (*.txt)

```

1 energy of X-ray beam (eV)    3036.74
2
3 Substrate:
4
5 element                      Ag
6 surface orientation          Ag(100)
7 employed reflection          (200)
8 lattice constant a_bulk (Angstrom)  4.0853
9 lattice plane spacing d_H (Angstrom)  2.04265
10 Bragg energy (eV)           3036.74
11 Bragg angle (°)             88.0
12 structure factors F0_real =   151.4378854
13     F0_imaginary =   15.32511429
14     FH_real =       105.4210862
15     FH_imaginary =   15.32511429
16 substrate temperature (K)    298.15
17 Debye-Waller factor DW = exp(-M)  0.95628
18 asymmetry parameter b        -1

```

```

19 polarisation factor P          2.000000          // use values P > 1 for auto-calculation:
    P = cos(2*theta_Bragg) (= pi polarisation); values P <= 1 are computed as given (P =
    1 for sigma polarisation).
20
21 Monochromator:
22
23 element          Si
24 surface orientation    Si(111)
25 employed reflection    (111)
26 lattice constant a_bulk_mono (Angstrom)    5.43088
27 lattice plane spacing d_H_mono (Angstrom) 3.1355
28 structure factors F0_real_mono = 113.78228
29     F0_imaginary_mono = 15.37005501
30     FH_real_mono = -60.87274884
31     FH_imaginary_mono = -10.86827013
32 substrate temperature (K)    77
33 Debye-Waller factor DW_mono = exp(-M)    0.99461
34 asymmetry parameter b_mono    -1
35 polarisation factor P_mono    1.000000          // use values P > 1 for auto-calculation:
    P = cos(2*theta_Bragg) (= pi polarisation); values P <= 1 are computed as given (P =
    1 for sigma polarisation).
36
37 Comments:
38 Parameters used for the calculation of the Darwin-Prins curves of both, the substrate as well
    as the monochromator crystals.
39
40 Structure factors are derived by linear interpolation of tabulated values (Internatinal tables
    for Crystallography and homepage of the Center of X-Ray Optics of the Lawrence
    Berkeley National Laboratory).
41
42 Debye-Waller factors are taken from the paper of Peng et al. [L.-M. Peng et al., Acta Cryst.
    A52 (1996) 456-470.] who tabulated calculated B parameters over a wide range of
    temperatures - directly for T = 77 K or through linear fit.
43

```

A.5.2 Exemplary Reflectivity input file (*.txt)

```

1 3.03375 3287.72995125777 57.9476261706422
2 3.0339 3661.95826630127 60.8554009467888
3 3.03405 4171.21215786334 64.80444760304
4 3.0342 4856.30909020758 69.8550685197308
5 3.03435 5825.23418007494 76.495666814121
6 3.0345 7275.30319902481 85.3382313890915
7 3.03465 9653.10498469611 98.0731138337957
8 3.0348 13935.1921122513 117.815953684057
9 3.03495 23726.649533169 153.587438006299
10 3.0351 52966.5949280329 229.183123525725
11 3.03525 114889.398338035 337.71723578385
12 3.0354 185160.479714888 428.395351726468

```

13 3.03555 196960.100334957 441.863436800023
14 3.0357 174306.229380854 415.755555451606
15 3.03585 138643.844159529 371.343165841528
16 3.036 91926.3880862305 301.81356751398
17 3.03615 49778.8286176365 222.295593997406
18 3.0363 26413.4087604765 161.987542674728
19 3.03645 16249.0269324174 127.287820565295
20 3.0366 11216.5297359357 105.731661432857
21 3.03675 8399.24491414196 91.507204968549
22 3.0369 6666.79194192656 81.6614007082413
23 3.03705 5514.88886140247 74.342473781079
24 3.0372 4709.86146718147 68.8176265328452
25 3.03735 4117.95449125596 64.3744794549561
26 3.0375 3668.05653956222 60.7807494159754
27 3.03765 3331.81396200453 58.0522352282794
28 3.0378 3053.41987616923 55.5718649703128
29

A.5.3 Exemplary XSW Absorption Profile input file (*.txt)

1 3.03375 14232.8372754776 119.289750663903
2 3.0339 13945.275095694 115.997407662181
3 3.03405 13531.0175707469 108.968009427397
4 3.0342 13191.0136237364 115.681241530982
5 3.03435 12722.5967340754 111.944145029755
6 3.0345 12025.0711791256 100.14452851448
7 3.03465 11497.8364637079 93.4026586702011
8 3.0348 10512.1551076943 99.4812347555978
9 3.03495 9459.05410664034 94.8189094467834
10 3.0351 8205.19115718528 83.9428106808316
11 3.03525 8190.62972097278 87.7026863497751
12 3.0354 11919.4215442999 100.819208706668
13 3.03555 20236.4577953715 138.988850220767
14 3.0357 29474.2460703678 145.280313228238
15 3.03585 34526.0927131867 173.589261994653
16 3.036 34817.3585464092 168.023866479682
17 3.03615 30696.2990606724 161.984447871402
18 3.0363 26408.938309919 158.754640197051
19 3.03645 23951.6599804188 155.789639661321
20 3.0366 22250.8681056257 152.559355797933
21 3.03675 21626.3857743629 133.889447118014
22 3.0369 20555.2249615916 131.969471577815
23 3.03705 19657.8779685335 146.766395375684
24 3.0372 19457.7408764479 128.697668455598
25 3.03735 19195.1826874669 136.712667544383
26 3.0375 18850.5071467244 133.44595150437
27 3.03765 18586.3431321852 131.497411697146
28 3.0378 18406.286069039 134.635689657468
29

B

Calculation of structure factors and Debye-Waller factors

The simulation of theoretical XSW photoelectron yield curves (see Sec. 3.1) as well as the evaluation of experimentally obtained XSW profiles requires to explicitly consider the structure of the substrate crystal. This is done by means of the so-called structure factor which enters the calculation of the reflectivity R [see Eq. (3.14), for example]. Thermal effects are taken into account through the Debye-Waller factor. The calculation of both the structure factor and the Debye-Waller factor are treated in this chapter.

B.1 Structure factor

The structure factor F_H for the reflection defined by the diffraction vector \mathbf{H}_{hkl} usually is a complex quantity:^{160,164}

$$F_H = F'_H + i F''_H, \quad (\text{B.1})$$

where F'_H denotes the real part and F''_H the imaginary part of F_H . The structure factor F_H calculates as:^{160,164}

$$F_H = \sum_n f_n \exp(2\pi i \mathbf{H}_{hkl} \cdot \mathbf{r}_n) = \sum_n (f_0 + \Delta f' + i \Delta f'')_n \exp(2\pi i \mathbf{H}_{hkl} \cdot \mathbf{r}_n), \quad (\text{B.2})$$

with f_n being the atomic scattering factor of the n -th atom within the unit cell. The summation over n in Eq. (B.2) involves the positions \mathbf{r}_n of the different atoms in the unit cell, and hence it varies from one structure to another.¹⁶⁴ The atomic scattering factor f_n depends on the scattering angle θ and the wavelength λ of the incident x-rays as:¹⁶⁴

$$f_n = f_n \left(\frac{\sin \theta}{\lambda} \right) = f_n \left(\frac{1}{2 d_{hkl}} \right). \quad (\text{B.3})$$

The right part of the above equation applies to the case of Bragg reflection [see Eq. (3.2); with $\theta = \theta_B$ and $n = 1$]. Here, θ denotes the (grazing) angle of incidence with respect to the lattice planes, i.e., the scattering angle, θ_B the Bragg angle, and d_{hkl} the spacing of the family $\{hkl\}$ of (Bragg) lattice planes. For small values of $(\sin \theta)/\lambda$, f_n approaches Z where Z is the number of electrons in the atom, that is, the atomic number, and it approaches 0 with increasing $(\sin \theta)/\lambda$ val-

ues.^{164, a)} So far, it has been assumed that (a) the x-ray wavelength is much smaller than any of the adsorption edge wavelength in the atom, and (b) the electron distribution in the atom has spherical symmetry.¹⁶⁴ If the first condition is not satisfied, a dispersion correction due to resonance and absorption effects is necessary.^{160, 164}

$$f_n = (f_0 + \Delta f' + i \Delta f'')_n. \quad (\text{B.4})$$

Here, f_n is the *corrected* atomic scattering factor; f_0 is the tabulated, *uncorrected* value of the atomic scattering factor, and $\Delta f'$ and $\Delta f''$ are the real and imaginary parts of the dispersion correction (the so-called Hönl corrections).^{160, 164} $\Delta f''$ represents a (small) shift in phase of the scattered radiation.¹⁶⁴ The angular dependence of $\Delta f'$ and $\Delta f''$ is much smaller than that of f_0 .¹⁶⁴ $\Delta f'$ and $\Delta f''$ are tabulated as a function of energy^{588, 589} in the form of the parameters f_1 and f_2 where:^{588, 589}

$$\Delta f' = f_1 - Z, \text{ and} \quad (\text{B.5})$$

$$\Delta f'' = f_2. \quad (\text{B.6})$$

Respective values for f_0 , f_1 , and f_2 of the different elements Z are tabulated in the *International Tables for Crystallography* (Ref. 341) and in the atomic scattering factor files of the (online) *X-Ray Database of the Center for X-Ray Optics* (CXRO, Lawrence Berkeley National Laboratory, Berkeley, CA, USA; Ref. 589). In the framework of the present work, these parameters have been linearly interpolated from the tabulated values for the respective $(\sin \theta)/\lambda$ or E_B values in use. Tables B.1, B.2, and B.3 summarize the so-obtained atomic scattering factors and structure factors employed in the present work for both the substrate crystals and the Si(111) monochromator crystals. A Si(111) double-crystal monochromator was in use at the beamline ID32 of the European Synchrotron Radiation Facility (ESRF) in Grenoble, France, where the XSW experiments presented in this work were performed.

The structure factors F_H and $F_{\bar{H}}$ are equal for centrosymmetric crystals if the origin of the Bravais lattice is taken at a center of symmetry.¹⁶⁰ The pure coinage metals²⁰ [Cu, Ag, and Au; *fcc* structure, space group $Fm\bar{3}m$ (no. 225)] as well as Cu_3Au ^{328, 369, 375} [simple cubic structure, space group $Pm\bar{3}m$ (no. 221)] and Si^{20, 343} [diamond structure, space group $Fm\bar{3}d$ (no. 227)] crystallize in cubic space groups which indeed are centrosymmetric.^{343, 593, 594} Thus, $F_H = F_{\bar{H}}$ applies in all aforementioned cases. Following Eq. (B.2), the specific F_0 and F_H values, with F_0 being the structure factor for the (000) reflection, calculate as:

$$F_0 = \begin{cases} 4f_{\text{Ag}} & \text{for Ag,} \\ 3f_{\text{Cu}} + f_{\text{Au}} & \text{for Cu}_3\text{Au,} \\ 8f_{\text{Si}} & \text{for Si,} \end{cases} \quad (\text{B.7})$$

and

$$F_H = \begin{cases} 4f_{\text{Ag}} & \text{for Ag,} \\ 3f_{\text{Cu}} + f_{\text{Au}} & \text{for Cu}_3\text{Au,} \\ 8 \cos\left(\frac{3\pi}{4}\right) f_{\text{Si}} & \text{for Si,} \end{cases} \quad (\text{B.8})$$

^{a)}Note that the parameter $(\sin \theta)/\lambda$ is equal to $1/(2d_{hkl})$ [see Eq. (3.2)] and thus proportional to the magnitude of the diffraction vector: $|\mathbf{H}_{hkl}| = 1/d_{hkl} = 2(\sin \theta)/\lambda$.

TABLE B.1. Structure factors F_0 , F_H and Debye-Waller factors $\exp(-M_Z)$ of Cu_3Au and Si as employed in the analysis of XSW data on clean $\text{Cu}_3\text{Au}(111)$ and on PTCDA/ $\text{Cu}_3\text{Au}(111)$. F_0 and F_H are given in terms of their real (F'_0 , F'_H) and imaginary parts (F''_0 , F''_H). They have been calculated from the respective atomic scattering factors $f_Z = (f_0 + \Delta f' + i\Delta f'')_Z$.^{85,589} B is the Debye parameter,^{590,591} E_B the Bragg energy, Z the chemical element (or binary alloy), a_{bulk} the bulk lattice constant, (hkl) the relevant Bragg reflection, and d_{hkl} the corresponding lattice plane spacing; the parameter $(\sin \theta)/\lambda$ is proportional to $|\mathbf{H}_{hkl}|$. Note that $F_H = F_{\bar{H}}$,¹⁶⁰ and that F_H values prior to correction for thermal vibrations are stated (see also footnote f of this table; n.a. = not available/applicable).

Cu ₃ Au(111)								
E_B (eV)	2865.04							
Z	Cu		Au		Cu ₃ Au		Si	
a_{bulk} (Å)	3.75 ^a		3.75 ^a		3.75 ^a		5.4309 ^b	
(hkl)	(000)	(111)	(000)	(111)	(000)	(111)	(000)	(111)
d_{hkl} (Å)	∞	2.165	∞	2.165	∞	2.165	∞	3.136
$(\sin \theta)/\lambda$ (Å ⁻¹)	0.000	0.231	0.000	0.231	0.000	0.231	0.000	0.159
f_0^c	29.000	22.393	79.000	64.772	n.a.	n.a.	14.000	10.538
$\Delta f'^d$	0.062	0.062	-20.835	-20.835	n.a.	n.a.	0.143	0.143
$\Delta f''^d$	3.623	3.623	31.202	31.202	n.a.	n.a.	2.105	2.105
F'_0, F'_H	116.247	89.818	232.659	175.747	145.350	107.290 ^f	113.147	-60.424
F''_0, F''_H	14.493	14.493	124.809	124.809	42.072	40.719 ^f	16.837	-11.906
B (Å ²) ^e	n.a.	0.774	n.a.	0.557	n.a.	n.a. ^f	n.a.	0.212
$\exp(-M)$	1.000	0.960	1.000	0.971	1.000	1.000 ^f	1.000	0.995

^aLattice constant of Cu_3Au , taken from Ref. 288. The bulk lattice constants of pure Cu and pure Au are $a_{\text{bulk}}(\text{Cu}) = 3.6149 \text{ \AA}^{287}$ and $a_{\text{bulk}}(\text{Au}) = 4.0782 \text{ \AA}^{455}$ respectively.

^bTaken from Ref. 592. The stated value holds for Si at room temperature ($T = 298 \text{ K}$). In the experiment, the Si(111) crystals of the monochromator were cooled with liquid nitrogen ($T = 77 \text{ K}$). Thermal contraction of the lattice constant $a_{\text{bulk}}(\text{Si})$ and consequential effects on other values derived thereof have been neglected here.

^cObtained through linear interpolation of tabulated values from Ref. 85.

^dObtained through linear interpolation of tabulated values from Ref. 589.

^eTaken from Refs. 590 (for Cu_3Au , $T = 298 \text{ K}$) and 591 (Si, $T = 77 \text{ K}$).

^fDue to computational reasons in the evaluation routine XSWAVES (see Appendix A of the present work), the stated structure factor F_H of $\text{Cu}_3\text{Au}(111)$ already includes the correction for thermal vibrations; that is, the (different) Debye-Waller factors of Cu and Au have already been considered in the calculation of F_H through $f_{Z,\text{corrected}} = f_Z \exp(-M_Z)$. As a consequence, a B value is not available and $\exp(-M)$ has been set to 1, respectively.

TABLE B.2. Same as Table B.1, but for PTCDA/Ag(100) (table caption applies accordingly): Structure factors F_0 , F_H and Debye-Waller factors $\exp(-M_Z)$ of Ag and Si as employed in the analysis of XSW data on PTCDA/Ag(100). For this system, the (200) as well as the (111) reflection have been used in the XSW measurements for triangulation purposes.

E_B (eV)	Ag(100), (111) reflection				Ag(100), (200) reflection			
	2629.89				3036.74			
Z	Ag		Si		Ag		Si	
a_{bulk} (Å)	4.0853 ^a		5.4309 ^b		4.0853 ^a		5.4309 ^b	
(hkl)	(000)	(111)	(000)	(111)	(000)	(200)	(000)	(111)
d_{hkl} (Å)	∞	2.359	∞	3.136	∞	2.043	∞	3.136
$(\sin \theta)/\lambda$ (Å ⁻¹)	0.000	0.212	0.000	0.159	0.000	0.245	0.000	0.159
f_0^c	47.000	37.435	14.000	10.538	47.000	35.496	14.000	10.538
$\Delta f'^d$	-6.943	-6.943	-0.075	-0.075	-9.141	-9.141	0.223	0.223
$\Delta f''^d$	4.744	4.744	2.437	2.437	3.831	3.831	1.921	1.921
F'_0, F'_H	160.229	121.970	111.404	-59.191	151.438	105.421	113.782	-60.873
F''_0, F''_H	18.978	18.978	19.494	-13.784	15.325	15.325	15.370	-10.868
B (Å ²) ^e	n.a.	0.746	n.a.	0.212	n.a.	0.746	n.a.	0.212
$\exp(-M)$	1.000	0.967	1.000	0.995	1.000	0.956	1.000	0.995

^aTaken from Ref. 289.

^bTaken from Ref. 592. The stated value holds for Si at room temperature ($T = 298$ K). In the experiment, the Si(111) crystals of the monochromator were cooled with liquid nitrogen ($T = 77$ K). Thermal contraction of the lattice constant $a_{\text{bulk}}(\text{Si})$ and consequential effects on other values derived thereof have been neglected here.

^cObtained through linear interpolation of tabulated values from Ref. 85.

^dObtained through linear interpolation of tabulated values from Ref. 589.

^eTaken from Ref. 591 (for Ag, $T = 298.15$ K, and for Si, $T = 77$ K). The B value of Ag was obtained by linear interpolation of the tabulated values.⁵⁹¹

TABLE B.3. Same as Table B.1, but for PTCDA/Ag(110) (table caption applies accordingly): Structure factors F_0 , F_H and Debye-Waller factors $\exp(-M_Z)$ of Ag and Si as employed in the analysis of XSW data on PTCDA/Ag(110) and also on K + PTCDA/Ag(110) [or, more precisely, PTCDA/K:Ag(110)].

E_B (eV)	Ag(110), (220) reflection			
	4294.59			
Z	Ag		Si	
a_{bulk} (Å)	4.0853 ^a		5.4309 ^a	
(hkl)	(000)	(220)	(000)	(111)
d_{hkl} (Å)	∞	1.444	∞	3.136
$(\sin \theta)/\lambda$ (Å ⁻¹)	0.000	0.346	0.000	0.159
f_0^c	47.000	30.093	14.000	10.538
$\Delta f'^d$	-3.576	-3.576	0.410	0.410
$\Delta f''^d$	11.805	11.805	1.048	1.048
F'_0, F'_H	173.696	106.067	115.281	-61.932
F''_0, F''_H	47.221	47.221	8.387	-5.931
B (Å ²) ^e	n.a.	0.746	n.a.	0.212
$\exp(-M)$	1.000	0.914	1.000	0.995

^aTaken from Ref. 289.

^bTaken from Ref. 592. The stated value holds for Si at room temperature ($T = 298$ K). In the experiment, the Si(111) crystals of the monochromator were cooled with liquid nitrogen ($T = 77$ K). Thermal contraction of the lattice constant $a_{\text{bulk}}(\text{Si})$ and consequential effects on other values derived thereof have been neglected here.

^cObtained through linear interpolation of tabulated values from Ref. 85.

^dObtained through linear interpolation of tabulated values from Ref. 589.

^eTaken from Ref. 591 (for Ag, $T = 298.15$ K, and for Si, $T = 77$ K). The B value of Ag was obtained by linear interpolation of the tabulated values.⁵⁹¹

for $H = (111)$ in the case of Cu_3Au and Si and for $H = (111), (200), (220)$ in the case of Ag, respectively. Note again that in the above equations the individual atomic scattering factors $f_Z = f_Z((\sin \theta)/\lambda, E)$ depend on the magnitude of the diffraction vector \mathbf{H}_{hkl} [through Eq. (B.3)], in addition to the x-ray beam energy, and thus differ for the calculation of F_0 and F_H .

B.2 Debye-Waller factor

In order to include thermal vibrations of the scatterers, i.e., the atoms, in the calculation of the respective structure factor F_H , f_n needs to be replaced by $f_n \exp(-M_n)$, where the exponential is the so-called Debye-Waller factor, in the above equations.¹⁶⁰ The Debye-Waller factor $\exp(-M)$ is given as:^{157, 164, 209}

$$\exp(-M) = \exp\left(-8\pi^2 \langle u^2 \rangle \frac{\sin^2 \theta}{\lambda^2}\right) = \exp\left(-B \frac{\sin^2 \theta}{\lambda^2}\right). \quad (\text{B.9})$$

The factor $B = 8\pi^2 \langle u^2 \rangle$ in the above equation is called the temperature factor or Debye parameter and sometimes simply the Debye-Waller factor.⁵⁹¹ The displacement factor²⁰⁹ $\langle u^2 \rangle$ denotes the

mean square of the component of displacement, i.e., the vibrational amplitude, along the direction of \mathbf{H}_{hkl} .^{157,164} In the high-temperature limit ($T \gg \theta_D$), it can be related to the Debye temperature θ_D of the surface via:^{157,595}

$$\langle u^2 \rangle = \frac{3\hbar^2 T}{mk_B \theta_D^2}, \quad (\text{B.10})$$

where m is the mass of the scatterer and k_B is Boltzmann's constant. Equation (B.10) neglects correlations in adjacent vibrations.¹⁵⁷ Usually, $\langle u^2 \rangle$ is assumed to be isotropic and independent of the individual hkl values, which is particularly true for an atom whose surroundings have cubic symmetry.^{157,164}

The Debye-Waller factor has to be considered explicitly in the simulation and evaluation of XSW photoelectron yield curves for two reasons. On the one hand, it affects the relative peaks intensities at different energies due to the energy dependence of the diffraction vector \mathbf{H}_{hkl} ¹⁵⁷ and also the shape of the reflectivity curve R , for example, through Eq. (3.17).⁵⁵ Note that $\exp(-M) = 1$ for F_0 , the structure factor for the (000) reflection, due to $H = (000)$.^{b)} On the other hand, Debye-Waller factors smaller than one effectively reduce the atomic scattering cross sections, in particular for backscattering events which become relevant at large values of \mathbf{H}_{hkl} , and thereby also diminish multiple scattering.¹⁵⁷

The Debye parameter B is in principle available from both theory and experiment.^{591,596–599} Yet, the reported values may exhibit a large variance.^{c)} For Ag, for instance, B values have been determined, e.g., by monitoring the attenuation of x-ray or neutron diffraction peaks, which range from $0.65(5) \text{ \AA}^2$ to $0.87(7) \text{ \AA}^2$ at room temperature ($T \approx 300 \text{ K}$; see Ref. 600 and references therein, in particular).^{591,598–614} For reasons of consistency, we employed the B values from Peng *et al.*, who have derived the Debye parameters for numerous elements, including Si, Cu, Ag, and Au, from the experimentally determined phonon density of states (with a typical accuracy of 2–3 %),⁵⁹¹ in the calculation of the Debye-Waller factor for both Si and Ag in the present work. The tabulated $B(T)$ values have been linearly interpolated in order to hold for a temperature of 298.15 K.⁶⁰¹ The so-obtained value of $B(298.15 \text{ K}) = 0.746 \text{ \AA}^2$ for Ag (see Table B.3, for example) is well within the variation of the above-stated experimental values.⁵⁹¹

In principle, the Debye parameters B of Cu and Au in the ordered binary alloy Cu_3Au may differ from those in the pure metals due to the different surroundings of the atoms.¹⁶⁴ Several investigations on the Debye parameter(s) of Cu_3Au have been reported, using either theoretical methods³⁷⁴ or diffraction techniques.^{373,378,459,590,615,616} Within the present work, we employed the parameters given by Gehlen and Cohen, who have determined individual $\langle u^2 \rangle^{1/2}$ values for Cu and Au in Cu_3Au by x-ray diffraction ($T = 298 \text{ K}$),⁵⁹⁰ for the calculation of the respective Debye-Waller factors $\exp(-M_Z)$. The employed Debye-Waller factors of the elements of interest, i.e., Si, Cu, Ag, and Au, are compiled in Tables B.1, B.2, and B.3. Exemplary fittings with different values of $\exp(-M)$ have revealed that variations in the absolute values of the Debye-Waller factor $\exp(-M)$ within 5 % lead to a change in the fitting results of maximal $|\Delta f_c| = 0.03$ and $|\Delta p_c| \ll 0.01$ only, which is well within the typical accuracy of XSW. Thus, we conclude that potential systematic error due to the chosen $\exp(-M)$ values are negligible here.

^{b)}Note that $H = (000)$ is equivalent to $(\sin \theta)/\lambda = 0$ and $d_{hkl} = \infty$, respectively.

^{c)}In some cases, only θ_D , $\langle u^2 \rangle$, or $\langle u^2 \rangle^{1/2}$ values have been reported which yield B through Eq. (B.10) and the relation $B = 8\pi^2 \langle u^2 \rangle$ (see above).

C

PTCDA on Ag(100) and Ag(110)

The experimental results for PTCDA on the Ag(100) and Ag(110) surfaces will be briefly presented in this chapter for the sake of completeness. The main results have already been published in parts in Refs. 66 [Bauer *et al.*, Physical Review B **86**, 235431 (2012)] and 67 [Mercurio *et al.*, Physical Review B **87**, 045421 (2013)], respectively. A discussion of the data within the scope of this work is found in Chapter 7. Note that the XSW results which are stated here may slightly differ in their numerical values from those given in the publications for two reasons: firstly, due to a re-analysis of the experimental XSW data employing a more recent and slightly improved version of XSWAVES³²⁹ (version 2.5 here versus version 2.3^{a)} as in Ref. 66) and, secondly, due to the fact that Ref. 67 reports the results which were obtained by employing the independent XSW program Torricelli^{326,330} instead of the evaluation routine XSWAVES, as done here. Yet, these differences are well within the experimental accuracy.

C.1 Review of the literature

PTCDA forms commensurate structures in the monolayer regime on the (100) and (110) surfaces of Ag, as has already been described in Sec. 7.1. In particular, the PTCDA molecules arrange in an T-shape motif on Ag(100)¹²⁰ (often referred to as quadratic phase Q, with two molecules per unit cell) and in a (less dense) brick-wall structure on Ag(110) (BW phase, only one molecule per unit cell).^{98,617} Respective structural models are found in Figs. 7.1(b) and (c) in Chapter 7, page 179, of the present work. The corresponding lattice parameters are compiled in Table C.1.

In the multilayer regime, PTCDA forms herringbone (HB) structures on both surfaces as LEED and STM have proven (structure models not shown; see Table C.1 for the respective lattice parameters).^{120,568,618} Regarding the Ag(110) surface, a HB structure within the monolayer regime has been identified (also using LEED and STM), too, at first by Seidel *et al.*^{618,619} in 1998. This monolayer HB phase is obtained through thermal desorption of multilayers. Recently, a different structure of the monolayer HB phase has been reported by Wießner *et al.*²⁶⁹ and by Willenbockel *et al.*⁵⁶⁸ respectively, which deviates from that proposed earlier by Seidel *et al.*^{618, b)} The structural parameters reported by Seidel *et al.*,⁶¹⁸ however, do not agree with the more recent results. Presumably, this is due to an incorrect assignment, i.e., a confusion, of the crystallographic

^{a)}In XSWAVES, version 2.3, π polarization instead of σ polarization was (incorrectly) assumed to be present with respect to the scattering geometry at the Si(111) double-crystal monochromator, causing systematic variations of maximal ± 0.01 in the averaged fitting results of both f_c and p_c (see also Secs. 3.1.2 and A.4, in particular, for further details).

^{b)}We note that, despite their different lattice parameters, the monolayer HB phases reported by Wießner *et al.*²⁶⁹ and Willenbockel *et al.*⁵⁶⁸ are principally identical and show the same LEED pattern. The different lattice parameters are simply due to a different choice of the unit cell for the (nearly) identical superstructure.

TABLE C.1. Structural results for PTCDA on the Ag(100) and Ag(110) surfaces, as obtained from LEED and STM experiments, and proposed model parameters reported in the literature.^{98, 120, 568} The lattice constants b_i , the enclosed angle β , and the area of the unit cell, A_{uc} , are given. ϕ denotes the enclosed angle between the surface lattice vectors \mathbf{a}_1 and \mathbf{b}_1 , ϱ is the angle of inclination of the long molecular axis with respect to \mathbf{b}_1 (values in square brackets refer to the second molecule within the unit cell), and τ is the herringbone angle, i.e., the enclosed (acute) angle between the long molecular axes of the two symmetry-nonequivalent molecules in the unit cell. In addition, the two-dimensional space groups and the superstructure matrices \mathfrak{M} are given. Note that Willenbockel *et al.* (Ref. 568) have not given explicit errors for their structural parameters. Thus, typical error margins for structural parameters obtained from LEED analysis have been assumed. Note further that the lattice parameters and superstructure matrices from the literature have been transformed such that they agree with the conventions established by Barlow and Raval in Ref. 3 (Q = quadratic, HB = herringbone, BW = brick-wall, n.a. = not available/applicable).

	PTCDA/Ag(100)		PTCDA/Ag(110)		
	monolayer	multilayer	monolayer		multilayer
	Q phase	HB phase	BW phase	HB phase	HB phase
	(Ref. 120)	(Ref. 120)	(Ref. 98)	(Ref. 568)	(Ref. 568)
b_1 (Å)	16.34	12.2(3)	11.91	11.6(5)	11.9(5)
b_2 (Å)	16.34	19.8(7)	11.91	21.2(5)	19.8(5)
β (°)	90.0	90.0	93.4	91.1(10)	93.7(10)
A_{uc} (Å ²)	267.0	242(15)	141.6	246(12)	235(12)
ϕ (°)	45.0	45.0	43.3	41.8(7)	43.3(7)
ϱ (°)	45.0 [135.0]	40.5(14) [139.5(14)] ^a	46.7	n.a.	n.a.
τ (°)	90	81(2)	n.a.	n.a.	n.a.
Two-dim. space group	$p4gm$	$p2gg$	$p211$	n.a.	n.a.
\mathfrak{M}	$\begin{pmatrix} 4 & 4 \\ -4 & 4 \end{pmatrix}$	$\begin{pmatrix} 2.99(7) & 2.99(7) \\ -4.85(17) & 4.85(17) \end{pmatrix}$	$\begin{pmatrix} 3 & 2 \\ -3 & 2 \end{pmatrix}$	$\begin{pmatrix} 3.0(1) & 1.9(1) \\ -5.0(1) & 3.6(1) \end{pmatrix}$	$\begin{pmatrix} 3.0(1) & 2.0(1) \\ -5.0(1) & 3.3(1) \end{pmatrix}$

^aThe stated values for the angle ϱ have been deduced from the experimentally determined τ value of 81(2)° given in Ref. 120, considering also that the valid two-dimensional space group is $p2gg$.

axes of the Ag substrate surface in the report by Seidel *et al.* (as has been concluded by Willenbockel *et al.*,⁵⁶⁸ too). Thus, only the lattice parameters and superstructure matrices of the HB phases in the mono- and the multilayer regime corrected by Willenbockel *et al.*⁵⁶⁸ are included in Table C.1.

The monolayer HB phase of PTCDA on Ag(110) exhibits lower binding energies of the HOMO and the F-LUMO peaks in UPS as compared to the brick-wall phase (by about 100 meV), which has been explained by a combination of both increased intermolecular interactions and weaker bonding to the substrate.^{269,568} Further details on the two systems PTCDA/Ag(100) and PTCDA/Ag(110) in the monolayer regime, especially concerning the metal/molecule interaction, have already been reported and discussed earlier in this work. The reader is referred to Sec. 2.2.2 for a review of the electronic and vibrational properties of adsorbed PTCDA, in particular on the more widely investigated Ag(110) surface, and to Chapter 7 for a review of the adsorption configurations and the bonding mechanism derived thereof.

C.2 Experimental procedure

Different types of experiments have been performed, namely, (SPA-)LEED, UPS, XPS, and XSW, on PTCDA on the (100) and (110) surfaces of Ag. Except of the UPS measurements, all experiments were accomplished on the same Ag(100) or Ag(110) crystal, respectively. For the technical details of the UPS measurements on PTCDA/Ag(100), which were performed by Manuel Marks in the group of Professor Dr. Ulrich Höfer at Philipps-Universität Marburg (Marburg, Germany), the reader is referred to Sec. 4.3.5 and to Ref. 275, in particular.

SPA-LEED experiments

The Ag(100) and Ag(110) substrate crystals were prepared by repeated cycles of sputtering and annealing. The long-range structural order and the cleanliness of the prepared surfaces were checked by means of (SPA-)LEED and also XPS, if available. For the SPA-LEED experiments, the preparation parameters were as follows: (a) sputtering with Ar⁺ ions of 850 eV to 1000 eV kinetic energy for 15–30 min at an Ar partial pressure of 1×10^{-5} mbar under normal incidence, resulting in an ion current of 5–10 $\mu\text{A}/\text{cm}^2$ on the sample, and subsequent annealing at 1000 K for 60–120 min for Ag(100), and (b) sputtering with Ar⁺ ions of 875 eV to 1250 eV kinetic energy for 15–30 min at an Ar partial pressure of 5×10^{-5} mbar (with an ion current of 3–4 $\mu\text{A}/\text{cm}^2$ on the sample) and annealing at 1000 K for 15–60 min for Ag(110), respectively. PTCDA was deposited at rates of 0.5–1.0 ML min^{-1} on both surfaces. Typical heating and cooling rates for annealing, also for mild post-annealing, were 0.5–1.0 K s^{-1} (up to 3.0 K s^{-1} for the heating of the clean surfaces).

XPS and XSW experiments

The XPS and XSW experiments on both PTCDA mono- and multilayers on the Ag(100) and Ag(110) surfaces were performed in three individual beamtimes in two different UHV systems at room temperature (see Tables 4.3 and 4.5 in Sec. 4.3, pages 56 and 60, of the present work, respectively). The measurements on PTCDA/Ag(110) were done exclusively in XSW setup I, while those on PTCDA/Ag(100) were done in both XSW setup I (multilayer data) and II [(sub-)monolayer data]. In the following, we will exemplarily describe the preparation parameters in detail which

were employed in order to obtain PTCDA overlayers in the submonolayer regime suitable for XSW measurements.^{c)}

For PTCDA/Ag(110), the base pressure of XSW setup I was 7×10^{-10} mbar. The crystal was sputtered for 30–60 min Ar⁺ ions of 1.5 keV kinetic energy, using an ion current of 20 $\mu\text{A}/\text{cm}^2$ on the sample. Subsequently, the sample was annealed at 850 K for 30–60 min. PTCDA was evaporated from a homemade Knudsen cell with a deposition rate of 1.0 ML min^{-1} . After the deposition, the sample was annealed at 420 K for 10 min to improve the order within the adsorbate layer. The coverage of the PTCDA was deduced from the XPS intensity of the C1s signal in comparison to that of 1 ML of PTCDA on Ag(111),⁵⁵ yielding a coverage of 0.91(4) ML (preparation no. Feb'09-2a; see Table 4.3 in Sec. 4.3.2, page 56, of the present work). Note that, employing an analogous procedure—but without the post-annealing step—, another preparation with a coverage of 1.15(4) ML PTCDA was obtained (preparation no. Feb'09-1).

In the case of PTCDA/Ag(100), the preparation parameters were as follows: Base pressures of 8×10^{-10} mbar and 4×10^{-10} mbar for the preparation chamber and the experimental chamber of XSW setup II, respectively, sputtering with Ar⁺ ions of 850 eV kinetic energy and an ion current of 10 $\mu\text{A}/\text{cm}^2$ on the sample for 15–30 min, and subsequent annealing at 1000 K between 30 min and 90 min. PTCDA was deposited from a homemade Knudsen cell, which was carefully calibrated prior to the preparation using thermal programmed desorption (TPD) spectroscopy by monitoring a fragment of the PTCDA molecule ($m/z = 124$ u). The absolute PTCDA coverage was verified by means of XPS, yielding a coverage of 0.78(10) ML and 0.22(3) ML, respectively, for the two preparations reported here (preparations no. Feb'11-1 and no. Feb'11-2, respectively; see Table 4.3 in Sec. 4.3.2, page 56, of the present work). The deposition rates were 1.0 ML min^{-1} and below. The long-range order of the PTCDA layers was proven by the bright and sharp LEED patterns for both Ag(110) and Ag(100) (see Figs. C.1 and C.2 below).

All XPS and XSW data were conducted at room temperature. For determining the vertical positions of the atoms of interest, the (200) and (220) Bragg reflections of the Ag(100) and Ag(110) substrate crystals (for which the respective lattice planes are parallel to the surface) were employed in the XSW measurements under near-normal incidence of the x-ray beam [with $d_{200} = 2.043$ Å, $\theta_B = 88^\circ$, and $E_B = 3036.74$ eV for the (200) Bragg reflection and $d_{220} = 1.444$ Å, $\theta_B = 88^\circ$, and $E_B = 4294.59$ eV for the (220) Bragg reflection, respectively].^{d)} Furthermore, for determining the adsorption site(s) of PTCDA on Ag(100) via triangulation,^{29,159} we employed the (111) reflection of the Ag(100) substrate crystal, for which the respective lattice planes enclose an angle of 54.74° with the surface (with $d_{111} = 2.359$ Å, $\theta_B = 88^\circ$, and $E_B = 2629.89$ eV).

XP and Auger spectra of the substrate signals, namely, Ag3d_{3/2}, Ag3d_{5/2}, and AgM₅N₄₅N₄₅, were acquired with pass energies of 100 eV [in the case of PTCDA/Ag(100); XSW setup II] and 46.95 eV [in the case of PTCDA/Ag(110); XSW setup I], respectively. The C1s and O1s spectra of the adsorbed PTCDA molecules in the multilayer regime were conducted with a pass energy of 11.75 eV on both surfaces (XSW setup I). The C1s and O1s spectra of the adsorbed PTCDA molecules in the (sub-)monolayer regime were again conducted with pass energies of 100 eV [in the case of PTCDA/Ag(100); XSW setup II] and 46.95 eV [in the case of PTCDA/Ag(110); XSW setup I], respectively. For the XSW experiments, the same pass energies were employed as in the XPS measurements, except for the Ag3d signal in the case of PTCDA/Ag(100) where the

^{c)}The multilayer films (preparation no. Apr'08-1 in each case; see Table 4.3 in Sec. 4.3.2, page 56, of the present work) were prepared simply by depositing PTCDA at a rate of about 1.5 ML min^{-1} on the freshly cleaned, well-ordered substrates surfaces (see also below).

^{d)}Note that the (100) and (110) reflections, as are all further (*hkl*) Bragg reflections where the Miller indices *h*, *k*, *l* are not all odd or all even,²⁰⁹ are systematically extinct for the Ag substrates due to the *fcc* bulk structure.²⁰

pass energy amounted to 50 eV only. Several XSW data sets were acquired for the individual preparations on the different samples:

- (a) Two $Ag3d$, four $C1s$, and three $O1s$ data sets for preparation no. Feb'11-1, as well as
- (b) two $Ag3d$, two $AgM_5N_{45}N_{45}$, three $C1s$, and four $O1s$ data sets for preparation no. Feb'11-2 in the case of PTCDA/Ag(100).
- (c) Furthermore, one $AgM_5N_{45}N_{45}$ and four $O1s$ data sets for preparation no. Feb'11-2 in the case of PTCDA/Ag(100), employing the (111) Bragg reflection.
- (d) Three $C1s$ and three $O1s$ data sets for preparation no. Feb'09-1, as well as
- (e) one $Ag3d$, two $C1s$, and three $O1s$ data sets for preparation no. Feb'09-2a in the case of PTCDA/Ag(110).
- (f) Two $AgM_5N_{45}N_{45}$ data sets for preparation no. Feb'09-2b, i.e., in the case of K + PTCDA/Ag(110).

The XSW measurements of the $AgM_5N_{45}N_{45}$ Auger signal in the case of PTCDA/Ag(110) with K atoms being coadsorbed are regarded as being representative also for the pure PTCDA/Ag(110) interface. Indeed, the obtained XSW fitting results for the $AgM_5N_{45}N_{45}$ signal (see Table C.6 below) are in the expected range for well-ordered metal crystals (and also ideal metal surfaces) and similar to those obtained for the $Ag3d$ signal. This is remarkable because these XSW measurement were rather surface-sensitive (here, the escape depth of the Auger electrons amounted to 5.0 Å only; see also Table 4.2) and the K atoms have been shown to induce a reconstruction of the both the clean²⁸² and the PTCDA-covered Ag(110) surface (see also Sec. 7.1 as well as Secs. D.1 and D.3.1 in Appendix D of the present work). We can thus conclude at this point that coadsorption of K atoms at the PTCDA/Ag(110) interface does not lead to a substantial change in the (averaged) vertical positions of the Ag surface atoms.

C.3 Results

Measurements on the structural and electronic properties of PTCDA on the Ag(100) and the Ag(110) surface have been performed by a variety of methods, namely, by means of SPA-LEED, UPS, XPS, and XSW. Our experimental results will be briefly described in this section.

C.3.1 Lateral structure

Prior to all other experiments, the effective transfer widths $T_{w, \text{eff}}$ of the clean Ag(100) and Ag(110) surfaces were determined with SPA-LEED from the width of the (00) reflection (data not shown) in order to verify long-range surface order. For Ag(100), we obtained values of about 460 Å at in-phase conditions ($E = 81.2$ eV) and about 305 Å at out-of-phase conditions ($E = 110.5$ eV). For Ag(110), values of about 335 Å at in-phase conditions ($E = 72.1$ eV) and about 235 Å at out-of-phase conditions ($E = 112.8$ eV) were obtained.

The Q phase on Ag(100)¹²⁰ and the BW phase on Ag(110),⁹⁸ respectively, could be prepared by depositing a (sub-)monolayer equivalent of PTCDA on the Ag surfaces, as was proven with SPA-LEED (data not shown; see also Sec. C.1). Yet, thermal desorption of multilayers yielded pure herringbone (HB) phases, instead of the aforementioned Q and BW phases, also in the monolayer regime on both surfaces. In brief, this demonstrates that the energy which is gained by the denser and structurally more favorable packing within the monolayer HB arrangements overcompensates

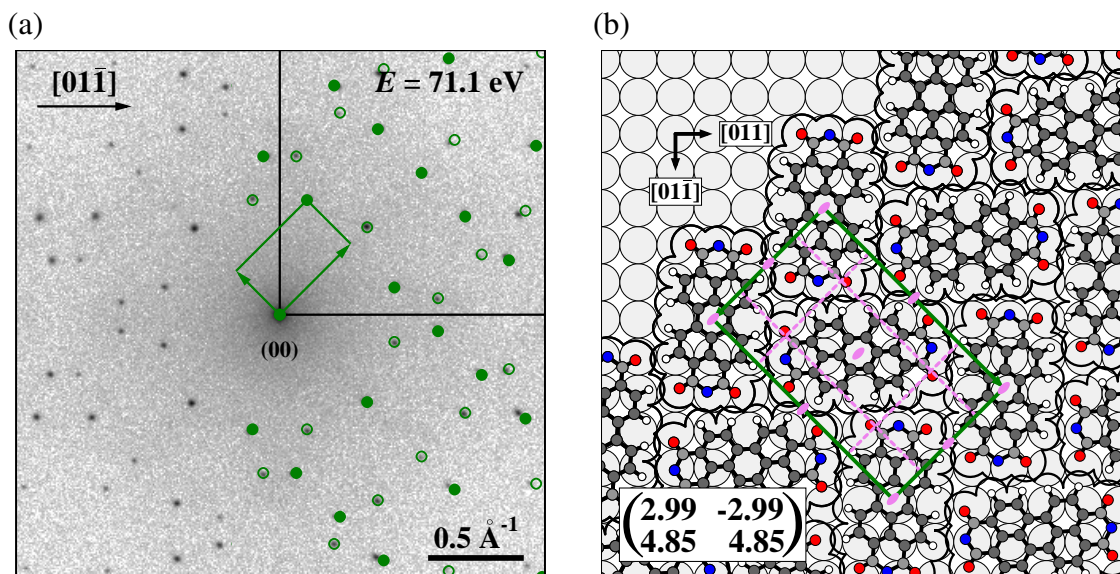


FIG. C.1. LEED pattern and structure model of the PTCDA herringbone phase in the monolayer regime on the Ag(100) surface. (a) LEED pattern of 1 ML PTCDA/Ag(100), prepared by thermal desorption of multilayers ($T = 648$ K for 5 min). The initial PTCDA coverage θ_{PTCDA} was ≈ 2 ML. The SPA-LEED measurement was performed with an electron energy of 71.1 eV at a sample temperature of 100 K. On the right-hand side of the LEED pattern, a simulation is superimposed. The superstructure spots are shown in green. Black lines indicate the reciprocal lattice vectors \mathbf{a}_i^* of the substrate. (b) Corresponding structural model for the PTCDA herringbone phase in the monolayer regime. The PTCDA molecules are shown as ball-and-stick models, including a two-dimensional projection of the molecular vdW surface. Green solid lines indicate the unit cells. The substrate directions are also indicated. The superstructure matrix is given as an inset. Symmetry operations are shown in violet.

the loss in adsorption energy (per molecule) due to the less favorable molecular adsorption sites as compared to the Q and BW arrangements. In the following, the corresponding experimental data are presented. In the case of PTCDA/Ag(110), the data allow for a refinement of the structural results by Wießner *et al.*²⁶⁹ and Willenbockel *et al.*⁵⁶⁸ Briefly summarized, we find lattice parameters which differ by maximal ± 0.3 Å and $\pm 3^\circ$ from those reported by Willenbockel *et al.*,⁵⁶⁸ for example, while the general structural motifs proposed by these authors are supported qualitatively by our SPA-LEED data.

PTCDA on Ag(100)

Figure C.1(a) shows a LEED pattern of 1 ML PTCDA/Ag(100) which was obtained by thermal desorption of multilayers. The initial PTCDA coverage amounted to ≈ 2 ML. The sample was annealed at $T = 648$ K for 5 min. This temperature is well above the desorption temperature of PTCDA in higher layers on coinage metal surfaces [which is typically in the range of about 525 K to 575 K for the second layer on the (111) surfaces of Au,⁴⁶⁵ Ag,¹¹³ and Cu,³³⁸ for example], which justifies the conclusion of only a monolayer coverage in the LEED pattern of Fig. C.1(a). This conclusion is further supported by the decreased intensity ratio between the superstructure spots and the fundamental substrate spots (by a factor of about 5 to 10): The corresponding one-dimensional LEED scans reveal a decrease in intensity of the superstructure spots while the intensity of the sub-

strate spots is increased (data not shown), indicating a smaller damping and thus a smaller surface coverage of PTCDA.^{e)}

The LEED pattern in Fig. C.1(a) is well explained by the structural parameters which have been reported for the HB phase of PTCDA in the multilayer on the Ag(100) surface (see Table C.2 and also Table C.1 above). Hence, we conclude that a HB phase of PTCDA can be prepared within the monolayer regime on Ag(100) by thermal desorption of multilayers, in analogy to the case of PTCDA/Ag(110).^{269,568,618,619} Figure C.1(b) shows the corresponding structural model. This HB phase may be considered as a *compressed* monolayer phase because the surface density of PTCDA molecules is 10 % higher as compared to the Q phase (see Table C.1). Note that within the error margins a point-on-line (p-o-l) commensurability of the PTCDA superstructure may exist, pointing to a non-negligible influence of the substrate on the exact structure (formation) within the HB monolayer phase. Further SPA-LEED experiments are needed at this point for a structural refinement.

PTCDA on Ag(110)

We have prepared HB phases of PTCDA on the Ag(110) surfaces in both the multi- and the monolayer regime. The respective LEED patterns are shown in Figs. C.2(a) and C.2(c). Judging from the bright and sharp superstructure spots, the PTCDA overlayers exhibit good long-range order. Only in the case of Fig. C.2(a), a small azimuthal broadening of the superstructure spots may be discerned. Both LEED patterns are well explained by the simulations shown in blue [Fig. C.2(a), multilayer regime] and green [Fig. C.2(c), monolayer regime], respectively. The corresponding structural models of the HB phases are presented in Figs. C.2(b) and C.2(d). We note that spots which originate from the BW phase of PTCDA on the Ag(110) surface can also be (faintly) observed in Fig. C.2(a) (marked in red).

The LEED pattern in Fig. C.2(a) was obtained from a 3 ML thick PTCDA film on the Ag(110) surface, which had been mildly post-annealed at 430 K for 15 min. Depending on the position of the electron beam of the SPA-LEED instrument on the sample surface, the relative intensities of the HB and BW phase spots varied significantly, that is, from essentially pure HB phase to mainly pure BW phase (data not shown). This indicates a (macroscopically) inhomogeneous surface coverage of PTCDA molecules and may also be taken as an indication of Stranski-Krastanov growth.⁶² The latter finding can be reasoned by the lattice mismatch between the *commensurate* BW phase preferentially grown in the monolayer and the *incommensurate* HB phase in higher layers. The symmetry of the HB PTCDA superstructure is $p211$ and may even be $p2gg$ within the error margin. In the latter case, extinction rules apply^{157,210} and, indeed, the diffraction spots $\{h0\}$ and $\{0k\}$ for which h or k is odd are systematically very weak. It cannot be unambiguously decided at this point, i.e., on the basis of the available LEED data alone, whether the interfacial PTCDA layer underneath the HB structure of the higher layers still adopts the BW structure or whether it has transitioned into the HB structure (see also below). It is likely, however, that the BW phase of PTCDA is still present in the interfacial layer because the respective LEED spots originating from the BW phase (although with varying intensities, most probably due to damping effects of the inhomogeneously thick PTCDA film) have been observed across large portions of the sample surface.

The HB phase in the monolayer [see Fig. C.2(c)] was prepared (as a pure phase) by thermal annealing of a multilayer above the desorption temperature of the higher layers, that is, at 555 K for 5 min. The intensity ratio between the superstructure and the substrate spots observed here is

^{e)}Note that nearby superstructure spots, which could not be resolved, may also (falsely) contribute to the observed intensity of the substrate spots. However, this does *not* affect the drawn conclusion.

TABLE C.2. Structural results for the herringbone phases of PTCDA on the Ag(100) and Ag(110) surfaces, as obtained from SPA-LEED experiments, and proposed model parameters. The lattice constants b_i , the enclosed angle β , and the area of the unit cell, A_{uc} , are given. ϕ denotes the enclosed angle between the surface lattice vectors \mathbf{a}_1 and \mathbf{b}_1 , ϱ is the angle of inclination of the long molecular axis with respect to \mathbf{b}_1 (values in square brackets refer to the second molecule within the unit cell), and τ is the herringbone angle, i.e., the enclosed (acute) angle between the long molecular axes of the two symmetry-nonequivalent molecules in the unit cell. In addition, the two-dimensional space groups and the superstructure matrices \mathfrak{M} are given. Note that the stated parameters for the monolayer herringbone phase of PTCDA/Ag(100) have been adopted from those given by Ikononov *et al.* in Ref. 120 for the herringbone phase in the multilayer regime (see also Table C.1; HB = herringbone, t.w. = this work).

	PTCDA/Ag(100)		PTCDA/Ag(110)	
	monolayer		monolayer	multilayer
	HB phase		HB phase	HB phase
	(adopted from Ref. 120)		(t.w.)	(t.w.)
b_1 (Å)	12.2(3)	11.9(4)	12.0(4)	
b_2 (Å)	19.8(7)	20.9(5)	19.6(5)	
β (°)	90.0	91.1(7)	90.7(10)	
A_{uc} (Å ²)	242(15)	249(10)	234(10)	
ϕ (°)	45.0	-43.3(5)	-44.8(7)	
ϱ (°)	40.5(14) [139.5(14)] ^a	41.0 [139.0]	41.0 [139.0]	
τ (°)	81(2)	82	82	
Two-dim. space group ^{b,c}	$p2gg$	$p211$	$p211 [p2gg]$	
\mathfrak{M}	$\begin{pmatrix} 2.99(7) & 2.99(7) \\ -4.85(17) & 4.85(17) \end{pmatrix}$	$\begin{pmatrix} 3.00(8) & -2.00(8) \\ 4.86(10) & 3.79(9) \end{pmatrix}$	$\begin{pmatrix} 2.94(10) & -2.07(6) \\ 4.72(10) & 3.44(10) \end{pmatrix}$	

^aThe stated values for the angle ϱ have been deduced from the experimentally determined τ value of 81(2)° given in Ref. 120, considering also that the valid two-dimensional space group is $p2gg$.

^bOnly the atomic positions within the adsorbate layers are considered for the determination of the two-dimensional space groups whereas the substrate surface atoms are neglected. The symmetry of the respective interface structures in their entireties, i.e., including the substrate atoms, reduces to space group $p1$ for all PTCDA phases.

^cStatements in square brackets hold under the assumption of truly rectangular units cells. Indeed, an enclosed angle β of 90° was found within the error margins for the unit cell of the multilayer HB phase of PTCDA on Ag(110).

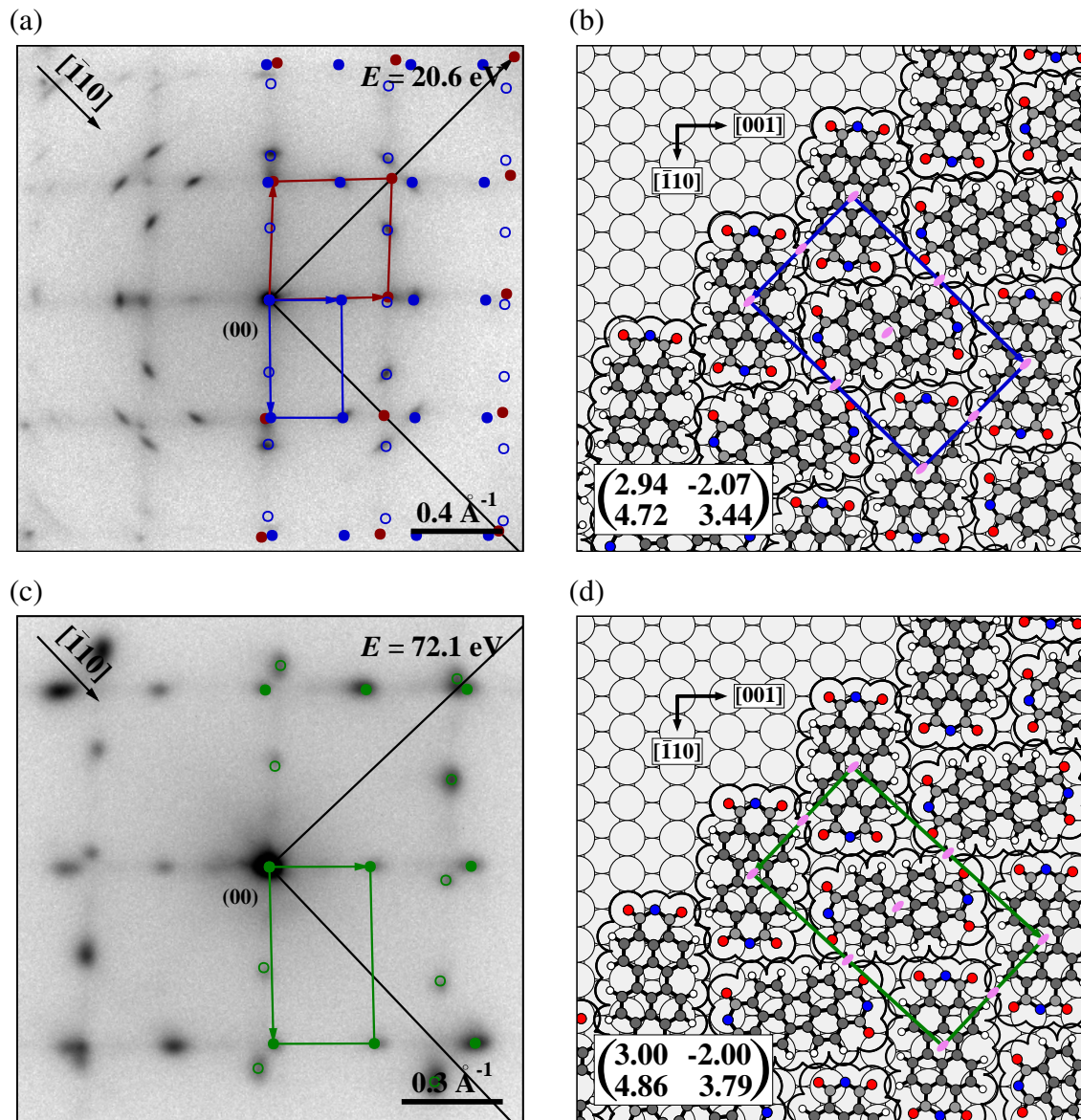


FIG. C.2. LEED patterns and structure models of the PTCDA herringbone phases in the multilayer and the monolayer regime on the Ag(110) surface. (a) LEED pattern of 3 ML PTCDA/Ag(110) after mild thermal annealing ($T = 430$ K for 15 min). The SPA-LEED measurement was performed with an electron energy of 20.6 eV at a sample temperature of 195 K. (b) Corresponding structural model for the PTCDA herringbone phase in the multilayer regime. (c) LEED pattern of 1 ML PTCDA/Ag(110), prepared by thermal desorption of multilayers ($T = 555$ K for 5 min). The initial PTCDA coverage θ_{PTCDA} was ≥ 2 ML. The SPA-LEED measurement was performed with an electron energy of 72.1 eV at a sample temperature of 250 K. (d) Corresponding structural model for the PTCDA herringbone phase in the monolayer regime. In (a) and (c), simulations are superimposed on the right-hand side of the LEED patterns. The superstructure spots are shown in blue for the herringbone phase in the multilayer regime and in green for the herringbone phase in the monolayer regime, respectively. In addition, those spots which originate from the brick-wall structure (present in the first layer) are marked in dark red in (a). Black lines indicate the reciprocal lattice vectors \mathbf{a}_i^* of the substrate. In (b) and (d), the PTCDA molecules are shown as ball-and-stick models, including a two-dimensional projection of the molecular vdW surface. Blue and green solid lines indicate the respective unit cells. The substrate directions are also indicated. The superstructure matrices are given as insets. Symmetry operations are shown in violet.

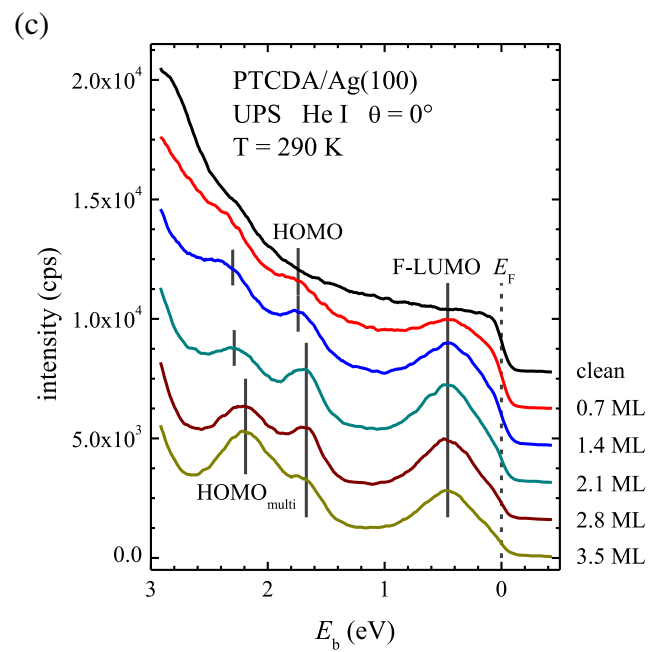
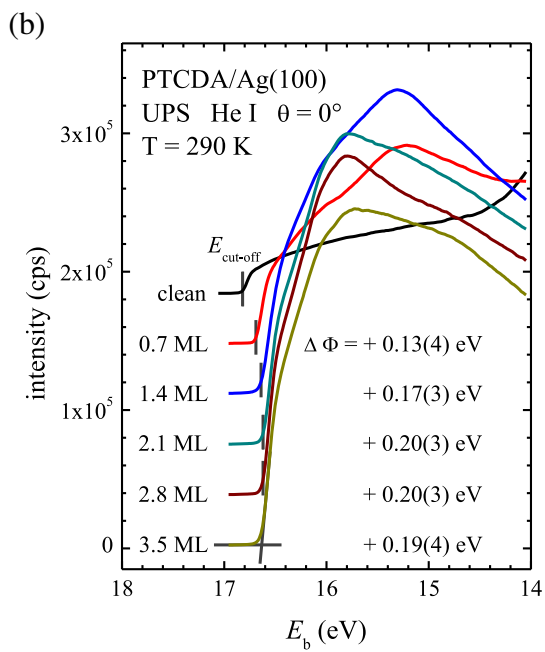
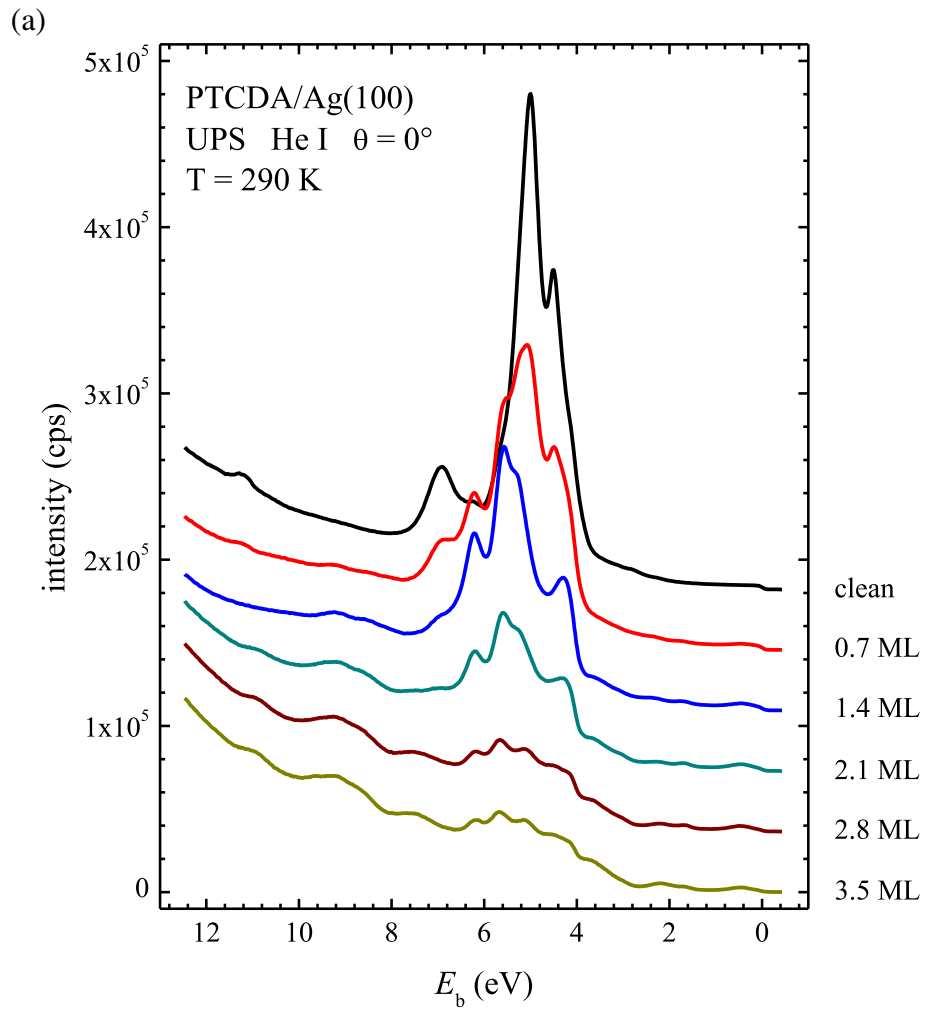
identical [within 10 %, as deduced from one-dimensional LEED scans (data not shown)] to that of about 1 ML PTCDA/Ag(110) in the BW phase. This finding corroborates the conclusion of only a monolayer coverage of PTCDA molecules on the Ag(110) surfaces. This monolayer phase is less dense than the multilayer HB phase (by $\approx 6\%$) but compressed in comparison to the BW phase (by $\approx 14\%$; see Table C.2 in conjunction with Table C.1). Furthermore, the monolayer HB phase is commensurate in one direction.¹⁵⁷ Note that, due to symmetry the commensurate vector of the surface unit cell of the monolayer HB phase concurs with one of the unit cell vectors of the BW phase. This can be rationalized through symmetry deliberations from Figs. C.2(d) and 7.1(c) (see Sec. 7.1, page 179, of the present work).

Brief conclusions and outlook

The above results for both systems, namely, PTCDA/Ag(100) and PTCDA/Ag(110), need to be validated in further systematic LEED studies. In particular, the question of a potential restructuring of the first layer towards a HB arrangement in the presence of PTCDA coverages exceeding 1 ML, already prior to or with only very mild thermal treatment (i.e., below the desorption temperature of the higher layers), should be addressed. Indications for the re-structuring of the (covered) first layer at higher PTCDA coverages on the Ag(110) surface have indeed been obtained from STM experiments.⁶¹⁹

Furthermore, we briefly comment on the stability and thus on the energetics of the more open Q and BW phases in comparison to the respective monolayer HB phases on the Ag(100) and Ag(110) surfaces. As has been stated above, the packing densities of the commensurate Q and BW phases are only $\approx 10\%$ smaller than those of the incommensurate HB phases. We thus conclude that the gain in adsorption energy per molecule due to the favored molecular adsorption sites in the Q and BW phases (as a consequence of the commensurate registry) is of comparable size and thus small. Looking at it the other way round, we conclude that mainly site-unspecific contributions add to the molecular adsorption energy. This is consistent with the observed large mobility of the PTCDA molecules on the Ag(100) and Ag(110) surfaces and the comparably small diffusion barriers.^{120,485,620–622} In turn, one may anticipate that the Q and BW phases of PTCDA are metastable—at least in the presence of a sufficiently large reservoir of PTCDA molecules on the surface—, and/or that the growth of the HB phases is kinetically hindered at low PTCDA coverages.

FIG. C.3 (following page). Coverage-dependent UP spectra of PTCDA on the Ag(100) surface. (a) Overview UP spectra. (b) UP spectra of the cut-off region, i.e., for high binding energies E_b and low kinetic energies E_{kin} of the photoelectrons, respectively. Work function shifts $\Delta\Phi_{PTCDA}$ as a function of PTCDA coverage, as deduced from the observed cut-off energy $E_{cut-off}$ [via Eq. (3.57) in conjunction with Eq. (3.50)], are stated in the figure. For $\theta_{PTCDA} = 3.5$ ML, the extrapolation of the cut-off region to the background level is shown exemplarily. (c) Close-up of the UP spectra shown in (a) in an energy interval close to the Fermi energy E_F . Spectral features are assigned to valence states of adsorbed PTCDA. The presented UPS data have been carefully smoothed. The PTCDA coverages in monolayers are indicated in the figures. All UP spectra were conducted at an angle of 0° with respect to the surface normal (i.e., at normal emission) and at a sample temperature of 290 K, employing He I UV light ($E = 21.22$ eV).^{275,334}



C.3.2 Electronic structure of the valence bands in PTCDA

In order to investigate the electronic structure of the valence bands in PTCDA on the Ag(100) surface, UP spectra have been recorded. The UPS measurements on PTCDA/Ag(100) were performed by Manuel Marks in the group of Professor Dr. Ulrich Höfer at Philipps-Universität Marburg (Marburg, Germany) within a joint research project on the electronic structure at the metal/organic interface. The reader is referred to Sec. 4.3.5 on page 65 of the present work for the experimental details. We will briefly present the experimentally obtained UP spectra and their evaluation at this point. An independent analysis of the data is found in Ref. 275.

Figure C.3(a) shows overview UP spectra of the clean Ag(100) surface (top, depicted in black) and PTCDA overlayers with coverages ranging from 0.7 ML to 3.5 ML. The spectra are dominated by the spectral features at binding energies E_b of about 4–8 eV, which originate from the Ag4*d* states.^{59,60} With increasing PTCDA coverages, the intensity of these features as a whole decreases. Besides, the relative intensities are altered, and new features and/or peak shifts occur. A detailed investigation of these findings is waived here. We focus on two further aspects of the data: (1) the cut-off region [see Fig. C.3(b)], and (2) the region close to the Fermi energy E_F [see Fig. C.3(c)].

Applying Eq. (3.57) in conjunction with Eq. (3.50), the work function shifts $\Delta\Phi_{\text{PTCDA}}$ upon PTCDA adsorption were obtained. The explicit values are stated in Fig. C.3(b). Starting from $\Phi = 4.40(2)$ eV for the clean Ag(100) surfaces, the work function increases with PTCDA coverage θ_{PTCDA} and reaches a final value of about 4.60 eV for $\theta_{\text{PTCDA}} \gtrsim 2$ ML (because $\Delta\Phi_{\text{PTCDA}} \approx 0.20$ eV). Note at this point that the absolute Φ values may be subject to a systematic error (of $\approx -0.21(15)$ eV; see also Sec. 4.3.5) due to the chosen determination of the cut-off energy $E_{\text{cut-off}}$ by linear extrapolation of the low kinetic-energy side of the secondary-electron peak [see also Fig. C.3(b)]. Yet because mainly work function *shifts* $\Delta\Phi$ are considered in the framework of the present work, these (small) systematic errors cancel out and thus can be neglected here.

Spectral features which can be attributed to adsorbed PTCDA were observed for $E_b < 4$ eV. Figure C.3(c) displays a close-up of the binding energy interval around E_F . The spectral features increase in intensity with θ_{PTCDA} and shift in their E_b values, except for the peak at minimal E_b . This peak is assigned to the former LUMO (F-LUMO) of PTCDA.

The exact peak positions were obtained by peak fitting of the experimentally obtained UP spectra with pseudo-Voigt functions, as shown in Fig. C.4. Fittings of the data for 0.7 ML PTCDA/Ag(100) [UP spectrum depicted as red open circles; see Fig. C.4(a)] and 1.4 ML PTCDA/Ag(100) [UP spectrum depicted as blue open circles; see Fig. C.4(a)], employing two different approaches concerning the background correction of the data, yielded identical peak positions for all peaks within 0.04 eV. This renders the obtained E_b values very reliable. In Fig. C.4(a), the UP spectrum of the clean substrate was subtracted from the UP data for PTCDA/Ag(100) while in Fig. C.4(b) a spline-type background was employed.

As mentioned above, the peak at $E_b = 0.46(1)$ eV originates from the PTCDA (F-)LUMO. Because this peak lies below E_F entirely, the (F-)LUMO of PTCDA in the (sub-)monolayer regime on Ag(100) is concluded to be completely filled (see Sec. 7.4 for a detailed discussion). The other peaks are identified in analogy to the UPS results reported for PTCDA on Ag(111) and Ag(110):^{59,60} The peak at $E_b = 1.74(1)$ eV is assigned to the HOMO of PTCDA in the (sub-)monolayer regime^{f)} while the peak at $E_b = 2.30(2)$ eV is assigned to the HOMO of PTCDA in the multilayer regime.⁵⁹ Interestingly, the HOMO_{multi} feature is already (weakly) observed in

^{f)}Since the F-LUMO state is concluded to be completely filled and therefore the true HOMO state in the case of ≤ 1 ML PTCDA on Ag(100), the state observed at $E_b = 1.74(1)$ eV should correctly be termed former HOMO (F-HOMO) or HOMO-1 for reasons of consistency. However, this nomenclature may lead to confusion, especially in the latter case, when comparing UP spectra of adsorbed PTCDA (e.g., on different surfaces or for different coverages)

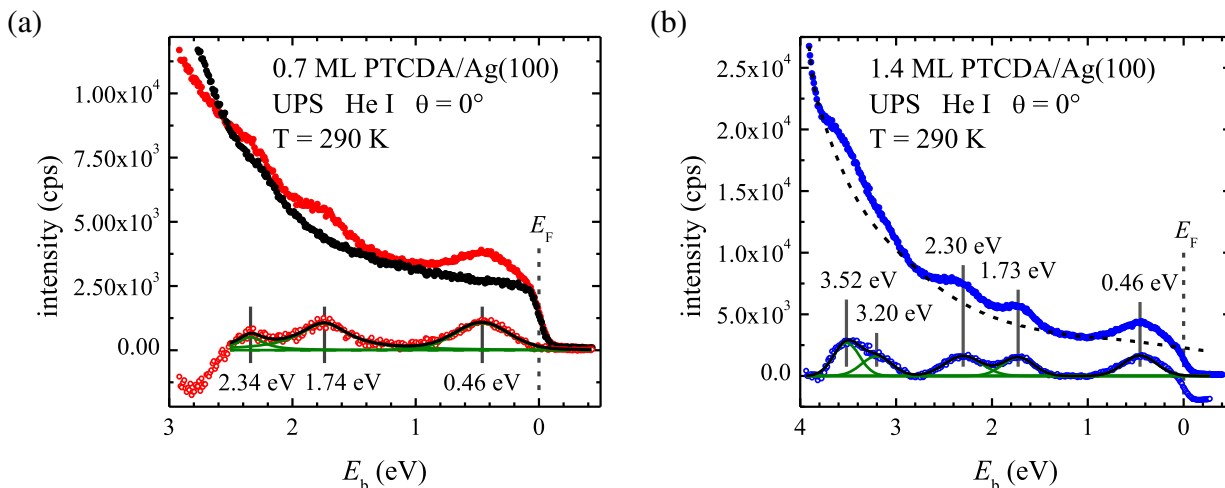


FIG. C.4. Fitting of the spectral features in the UP spectra of PTCDA on the Ag(100) surface for (a) $\theta_{\text{PTCDA}} = 0.7$ ML (spectrum depicted as red filled circles) and (b) $\theta_{\text{PTCDA}} = 1.4$ ML (spectrum depicted as blue filled circles). The peaks were fitted by a linear combination of Gaussian and Lorentzian profiles, i.e., by pseudo-Voigt functions (depicted in green). The sum of all components is represented by a black line. Fitted peak positions are marked in the figures. The background-corrected UP spectra are shown as red and blue open circles, respectively. The UP spectrum of the clean Ag(100) surface (depicted as black filled circles) was subtracted from the experimentally obtained UP spectrum for PTCDA/Ag(100) in (a), while the background in (b) was modeled by a spline function (black dashed line). The Fermi energy E_F is indicated by a vertical, gray dashed line. All UP spectra were conducted at an angle of 0° with respect to the surface normal (i.e., at normal emission) and at a sample temperature of 290 K, employing He I UV light ($E = 21.22$ eV).^{275,334}

the UP spectrum of 0.7 ML PTCDA/Ag(100) [see Fig. C.4(a)] although the nominal coverage is below that of a full monolayer. The spectral features at $E_b = 3.20(10)$ eV and $E_b = 3.52(5)$ eV are ascribed to the (former) HOMO–1 levels of PTCDA.⁵⁹

C.3.3 Electronic structure of the core levels in PTCDA

We have performed core level spectroscopy on PTCDA multi- and (sub-)monolayers on both the Ag(100) and the Ag(110) surface. In addition, the Ag3d XP and AgM₅N₄₅N₄₅ Auger signals were investigated. In principle, data acquisition and treatment were analogous to the general procedure employed for PTCDA/Cu₃Au(111), as has already been described in Secs. 6.3.2, 6.5.2 (for the above-mentioned substrate signals), and 6.6.2 (for the adsorbate signals, i.e., C1s and O1s) of the present work, respectively. A detailed discussion of the XPS data concerning the observed shifts in binding energy E_b of the C1s and O1s levels in the (sub-)monolayer regime as compared to the multilayer regime (and also in comparison to PTCDA on other coinage metal surfaces) is given in Sec. 7.4. At this point, the corresponding experimental data are presented. All XP spectra were acquired at photon energies about 10 eV to 15 eV below the Bragg energies of the substrate Bragg reflections of interest. LEED patterns of the individual PTCDA (sub-)monolayer preparations, which were employed in the XPS as well as in the XSW investigations (see Sec. C.3.4 below), are shown in Figs. C.5 and C.6. All observed LEED spots are explained by the well-known monolayer

with as well as without the LUMO state being (partially) filled. Furthermore, this terminology is not established in the literature and thus waived here, too.

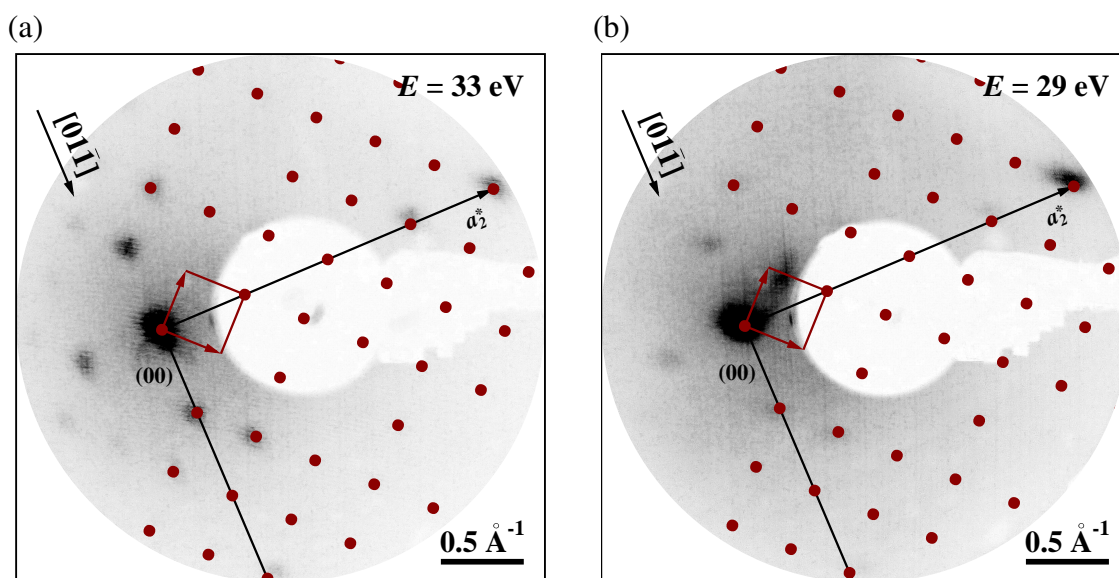


FIG. C.5. LEED patterns of the PTCDA submonolayers on the Ag(100) surface which were employed in the XPS and XSW experiments (taken at the ESRF prior to the XPS and XSW experiments): (a) 0.78(10) ML PTCDA/Ag(100) (preparation no. Feb'11-1; $E = 33$ eV) and (b) 0.22(3) ML PTCDA/Ag(100) (preparation no. Feb'11-2; $E = 29$ eV). The spots of the PTCDA Q phase can be identified in addition to the substrate spots. On the right-hand side of the LEED patterns, simulations are superimposed. Q-phase spots are shown in dark red. Black lines indicate the reciprocal lattice vectors a_i^* of the substrate.

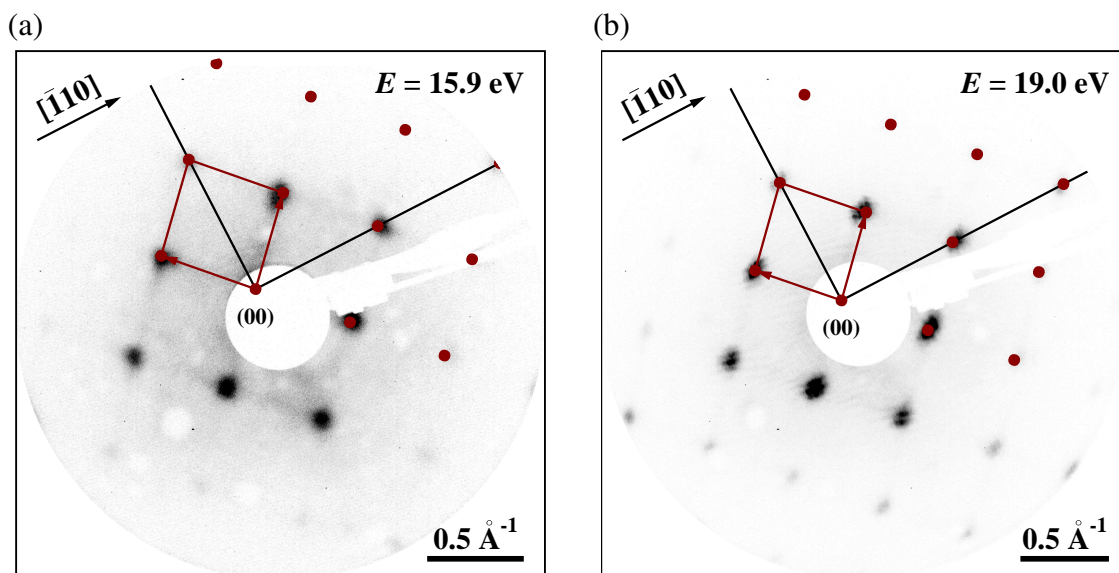


FIG. C.6. Same as Fig. C.5 but for PTCDA/Ag(110): LEED patterns of the PTCDA (sub-)monolayers on the Ag(110) surface which were employed in the XPS and XSW experiments (taken at the ESRF prior to the XPS and XSW experiments): (a) 1.15(4) ML PTCDA/Ag(110) (preparation no. Feb'09-1; $E = 15.9$ eV, $T = 360$ K) and (b) 0.91(4) ML PTCDA/Ag(110) (preparation no. Feb'09-2a; $E = 19.0$ eV, $T = 345$ K). The spots of the PTCDA brick-wall phase can be identified. On the upper right-hand side of the LEED patterns, simulations are superimposed. BW-phase spots are shown in dark red. Black lines indicate the reciprocal lattice vectors a_i^* of the substrate.

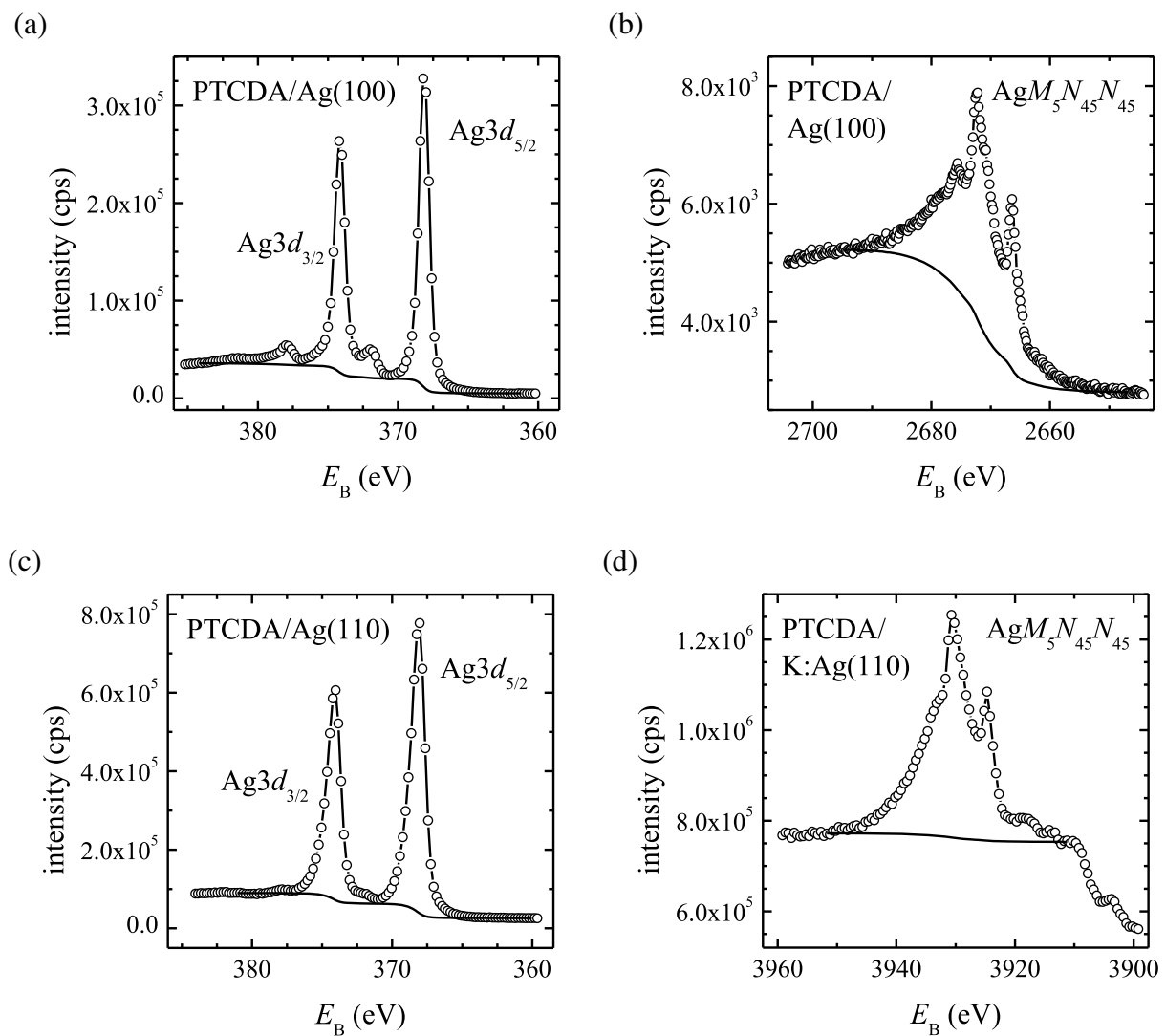


FIG. C.7. XP and Auger spectra of the substrate levels for the Ag(100) and Ag(110) surfaces. (a) $Ag3d_{3/2}$ and $Ag3d_{5/2}$ XPS signals as well as (b) $AgM_5N_{45}N_{45}$ Auger signal of the PTCDA-covered Ag(100) surface [$\theta_{\text{PTCDA}} = 0.22(3)$ ML]. The spectra were acquired with a photon energy of $E = 3024.0$ eV at an effective angle of 86° of the photoelectron analyzer with respect to the surface normal (XSW setup II). (c) $Ag3d_{3/2}$ and $Ag3d_{5/2}$ XPS signals as well as (d) $AgM_5N_{45}N_{45}$ Auger signal of the PTCDA-covered and, in the latter case, K-modified Ag(110) surface [$\theta_{\text{PTCDA}} = 0.91(4)$ ML]. These spectra were acquired with a photon energy of $E = 4280.0$ eV at an effective angle of 45° of the photoelectron analyzer with respect to the surface normal (XSW setup I). The employed backgrounds of Shirley type are shown as black lines.

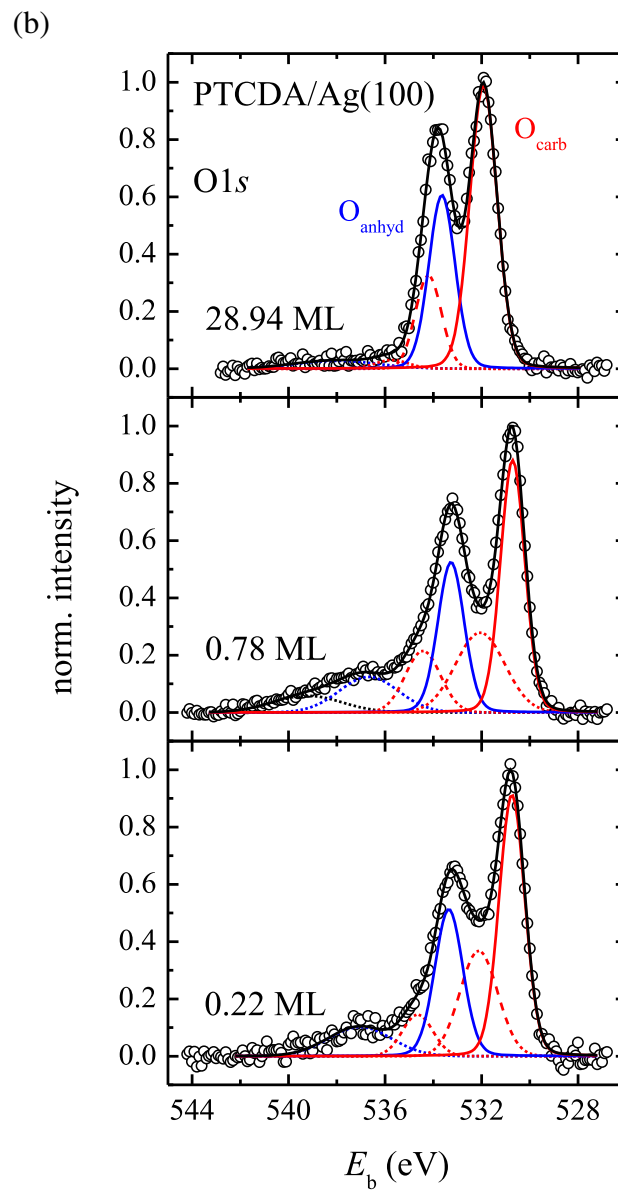
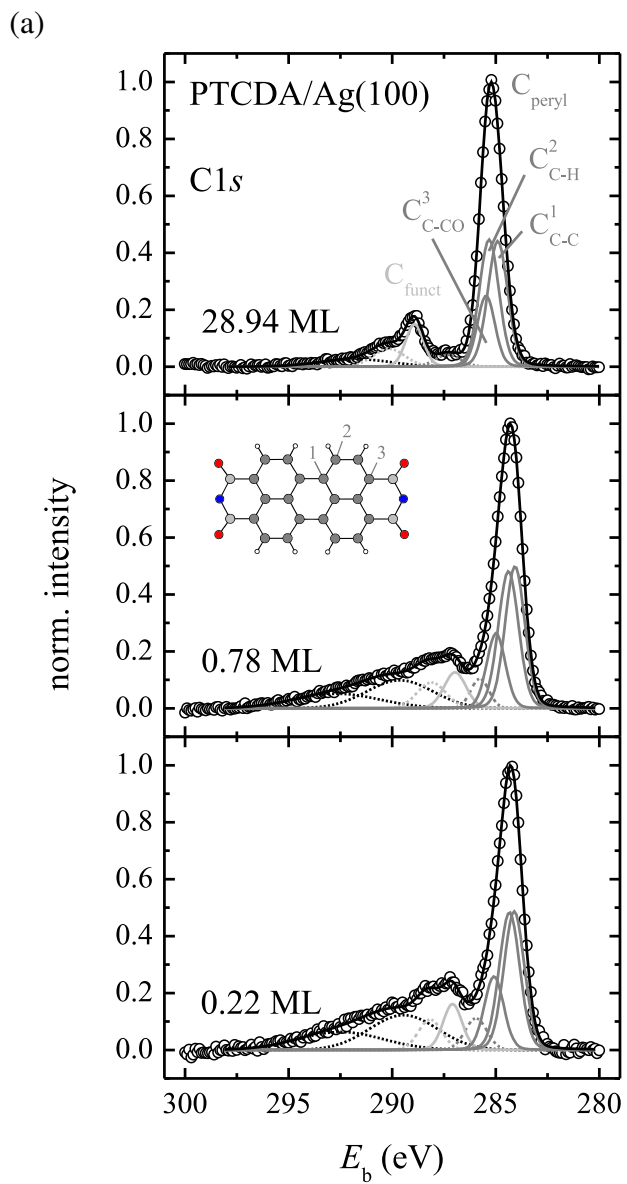
structures of PTCDA, namely, the Q phase in the case of PTCDA/Ag(100)¹²⁰ and the brick-wall phase in the case of PTCDA/Ag(110).⁹⁸

Figure C.7 shows exemplary Ag3*d* XP and AgM₅N₄₅N₄₅ Auger spectra of the PTCDA-covered surfaces of Ag(100) and Ag(110). The individual experimental parameters are given in Sec. C.2 and also in the figure caption. In the case of the AgM₅N₄₅N₄₅ signal of the Ag(110) substrate [see Fig. C.7(d)], the surface had additionally been modified through the coadsorption of K atoms (see also Appendix D). However, we did not observe substantial differences in the substrate XP and Auger spectra between pure PTCDA/Ag(110) and K + PTCDA/Ag(110). Hence, it can be concluded that the involved levels of the Ag(110) substrate were not affected by the presence of K atoms at the interface. The satellite peaks in the Ag3*d* XP spectrum of PTCDA-covered Ag(100) at about 4 eV higher E_b values than the main lines are ascribed to energy losses to due plasmon excitation [see Fig. C.7(a)].³¹⁰

The C1*s* and O1*s* spectra of PTCDA for different coverages on the two Ag surfaces under investigation are displayed in Figs. C.8 and C.9. The lower signal-to-noise of the data for the Ag(110) surface is due to the smaller photoemission cross sections at the higher photon energy (see also Sec. C.2), a smaller transmission of the analyzer, and the different data acquisition geometry (see also Sec. 4.1.2). Sophisticated fittings models, including the chemically differentiable main components of the C1*s* and the O1*s* level, respectively, as well as the corresponding satellite features, were developed in each case. The restrictions for developing appropriate XPS fitting models have been outlined in Sec. 4.3.2. For example, the expected stoichiometric ratio of the PTCDA molecule, i.e., C_{peryl} : C_{funct} = 20 : 4 and O_{carb} : O_{anhyd} = 4 : 2, had to be fulfilled by the integral peak intensities. All XPS fitting models are in good agreement with the experimental data. The respective fitting parameters are summarized in Tables C.3 and C.4.

The fitting models for the multilayer XPS data are based on earlier work of Schöll *et al.*³⁰⁷ on PTCDA/Ag(111) in the multilayer regime. Note at this point that the E_b values observed in XPS of the individual components agree within ± 0.2 eV for PTCDA multilayers on the three low-index Ag surfaces (111),³⁰⁷ (100), and (110). Considering also the estimated error of ± 0.1 eV in the determination of E_b , we conclude that, in principle, all fitting models give the same E_b values for the individual components, thereby rendering themselves self-consistent. As a general trend, we observed a (differential) shift of the individual components towards lower E_b at the transition

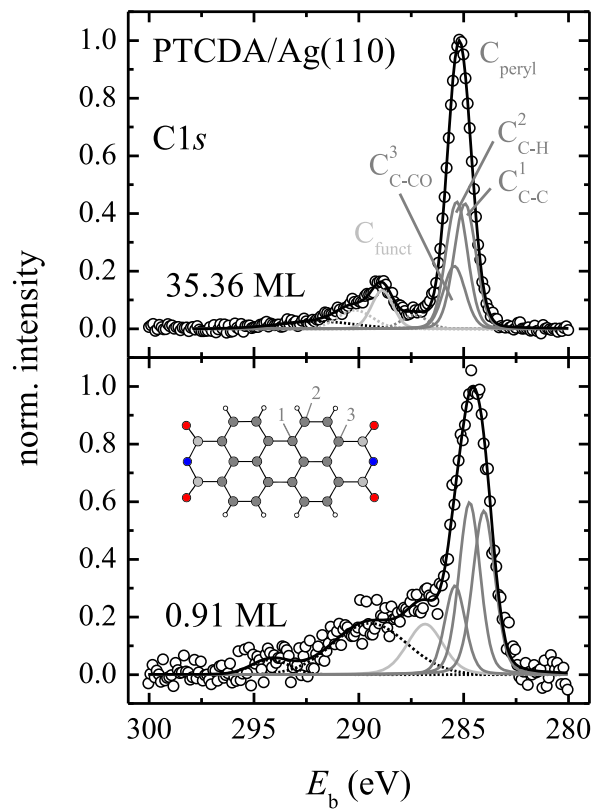
FIG. C.8 (following page). Normalized XP spectra of the (a) C1*s* and (b) O1*s* levels of PTCDA on the Ag(100) surface with corresponding fitting models for different coverages. The PTCDA coverages amounted to 28.94(94) ML, 0.78(10) ML, and 0.22(3) ML, respectively (from top row to bottom row). All XP spectra were acquired with a photon energy of $E = 3024.0$ eV at an effective angle of 86° of the photoelectron analyzer with respect to the surface normal (XSW setup II), except for the multilayer XP spectra which were acquired at an effective angle of 45° (XSW setup I). The individual XP spectra were corrected with a linear or Shirley background function. Contributions from the carbon atoms within the perylene core and within the functional groups are shown in dark gray (C_{C–C}, C_{C–H}, and C_{C–CO}) and light gray (C_{funct}), respectively, while the contributions from the chemically nonequivalent oxygen atoms are shown in red (O_{carb}) and blue (O_{anhyd}). The main photoemission peaks are drawn as full lines, the (corresponding) satellite peaks as dashed lines, in respective colors. Unassigned satellite peaks are depicted in black. In addition, the resulting sum of all components is shown as a black line. A ball-and-stick model of the PTCDA molecule is shown as an inset in (a). Note that for the evaluation of the XSW data all C atoms of the perylene core were combined to give the C_{peryl} signal.



from the multilayer to the (sub-)monolayer regime (see Sec. 7.4 for details). Besides, the satellite components exhibited increased intensities in the (sub-)monolayer XP spectra.

FIG. C.9 (following page). Same as Fig. C.8 but for PTCDA/Ag(110): Normalized XP spectra of the (a) C1s and (b) O1s levels of PTCDA on the Ag(110) surface with corresponding fitting models for different coverages. The PTCDA coverages amounted to 35.36(71) ML and 0.91(4) ML, respectively (from top row to bottom row). The XP spectra for the (sub-)monolayer were acquired with a photon energy of $E = 4280.0$ eV at an effective angle of 45° of the photoelectron analyzer with respect to the surface normal (XSW setup I), while the XP spectra for the multilayer regime were acquired with a photon energy of $E = 4276.0$ eV (also in XSW setup I but in a different beamtime). The individual XP spectra were corrected with a linear or Shirley background function. Contributions from the carbon atoms within the perylene core and within the functional groups are shown in dark gray (C_{C-C} , C_{C-H} , and C_{C-CO}) and light gray (C_{funct}), respectively, while the contributions from the chemically nonequivalent oxygen atoms are shown in red (O_{carb}) and blue (O_{anhyd}). The main photoemission peaks are drawn as full lines, the (corresponding) satellite peaks as dashed lines, in respective colors. Unassigned satellite peaks are depicted in black. In addition, the resulting sum of all components is shown as a black line. A ball-and-stick model of the PTCDA molecule is shown as an inset in (a). Note that for the evaluation of the XSW data all C atoms of the perylene core were combined to give the C_{peryl} signal.

(a)



(b)

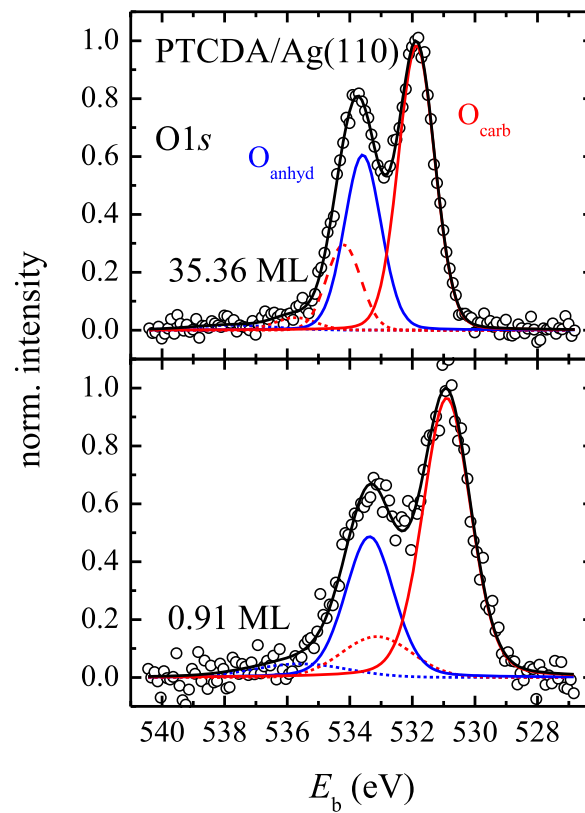


TABLE C.3. XPS fitting parameters for the C1s and O1s levels of PTCDA on the Ag(100) surface ($E = 3024.0$ eV). E_b denotes the binding energy, w the width of the peak, and A the relative peak area. The respective values are given for all components observed in the XP spectra for the different preparations, namely, for 28.94(94) ML (preparation no. Apr'08-1), 0.78(10) ML (preparation no. Feb'11-1), and 0.22(3) ML PTCDA/Ag(100) (preparation no. Feb'11-2). The corresponding XP spectra are shown in Fig. C.8. Note that the (sub-)monolayer XP spectra were acquired at an effective angle of 86° of the photoelectron analyzer with respect to the surface normal (XSW setup II), while the multilayer XP spectra were acquired at an effective angle of 45° (XSW setup I). The C1s and O1s main components, namely, C_{C-C} , C_{C-H} , C_{C-CO} , C_{funct} , O_{carb} , and O_{anhyd} , were fitted with pseudo-Voigt functions with 10 % Lorentzian contribution while the satellite components were fitted with pure Gaussian functions. $\Delta E_b = E_{b, \text{mono}} - E_{b, \text{multi}}$ denote the changes in E_b for the (sub-)monolayer regime with respect to the multilayer regime, i.e., with respect to the condensed PTCDA film (n.o. = not observed, n.a. = not applicable/available).

	28.94(94) ML PTCDA/Ag(100)			0.78(10) ML PTCDA/Ag(100)				0.22(3) ML PTCDA/Ag(100)			
	E_b (eV)	w (eV)	A (%)	E_b (eV)	w (eV)	A (%)	ΔE_b (eV)	E_b (eV)	w (eV)	A (%)	ΔE_b (eV)
C_{C-C}	284.91	1.13	29.98	284.07	1.12	23.40	-0.84	284.11	1.17	21.82	-0.80
C_{C-H}	285.33	1.12	29.98	284.39	1.16	23.40	-0.94	284.34	1.17	21.82	-0.99
C_{C-CO}	285.47	1.00	14.99	284.99	1.06	11.70	-0.48	285.08	1.10	10.91	-0.39
$C_{\text{peryl, sat}}$	287.32	1.44	3.47	285.77	1.02	4.29	-1.55	285.95	1.24	5.07	-1.37
C_{funct}	288.92	1.01	9.08	286.96	1.25	6.62	-1.96	287.08	1.08	6.71	-1.84
$C_{\text{funct, sat}}$	290.16	1.81	6.52	288.10	1.63	5.94	-2.06	288.16	1.33	5.21	-2.00
$C_{\text{sat 1}}$	291.76	3.94	5.98	289.63	3.74	14.76	-2.13	289.45	3.86	17.32	-2.31
$C_{\text{sat 2}}$	n.o.	n.o.	n.o.	292.66	4.82	9.89	n.a.	292.49	4.82	11.14	n.a.
O_{carb}	531.93	1.34	49.96	530.71	1.19	32.33	-1.22	530.74	1.26	38.21	-1.19
$O_{\text{carb, sat 1}}$	534.21	1.27	14.89	532.06	2.40	19.69	-2.15	532.12	1.85	21.60	-2.09
O_{anhyd}	533.65	1.28	29.39	533.27	1.29	20.86	-0.38	533.36	1.37	23.37	-0.29
$O_{\text{carb, sat 2}}$	535.72	1.62	1.77	534.43	1.72	10.86	-1.29	534.65	1.49	6.86	-1.07
$O_{\text{anhyd, sat}}$	538.02	4.00	3.99	536.68	2.88	10.50	-1.34	537.04	3.08	9.96	-0.98
O_{sat}	n.o.	n.o.	n.o.	539.22	3.36	5.76	n.a.	n.o.	n.o.	n.o.	n.a.

C.3.4 XSW photoelectron yield curves

By analogy to the general procedure for the XSW experiments in the case of PTCDA/Cu₃Au(111) (see Secs. 6.3.3, 6.5.3, 6.6.3, and 6.6.4 of the present work), we investigated the vertical structure at the metal/organic interfaces and, in particular, the adsorption configurations of PTCDA on the Ag(100) and Ag(110) surfaces. The above-introduced XPS fitting models were employed for the differential analysis of the C1s and O1s signals (see Sec. C.3.3). The Ag3d XPS and the AgM₅N₄₅N₄₅ Auger signal were used to characterize the substrate crystals and their surfaces, respectively. Note that all XSW experiments on PTCDA/Ag(100) were performed in XSW setup II, where $\theta_p = 0^\circ$ (see Sec. 4.1.2; with the consequence that $Q, \Delta = 0$), while the XSW experiments on PTCDA/Ag(110) were performed in XSW setup I, where $\theta_p = 45^\circ$ and thus nondipolar correction terms apply ($Q, \Delta \neq 0$; see Sec. 3.1.4 for the theoretical background and Table 4.6 in Sec. 4.3.3, page 63, of the present work for the explicit values).

XSW results for the substrate signals

Figure C.10 presents exemplary XSW photoelectron yield curves of the substrate signals for all available preparations of PTCDA/Ag(100) and PTCDA/Ag(110), also including K coadsorption in the latter case (see also Appendix D of the present work, in particular Sec. D.3.3). Note that the obtained XSW photoelectron yield profile in Fig. C.10(d), i.e., for the AgM₅N₄₅N₄₅ Auger signal of PTCDA/K:Ag(110), is regarded as being representative also for that of the pure PTCDA/Ag(110) interface. This conclusion is justified by the determined f_c and p_c values which are close to 1 and 0, respectively, as expected for well-ordered metal crystals (and also for ideal metal surfaces). In general, the obtained fitting curves are in excellent agreement with the experimental data. Only the data points for the minimal and maximal values of the normalized $Y_{Z,j}$ may slightly be over- or underestimated in some cases, respectively.

The derived fitting parameters coherent fraction f_c and coherent position p_c are presented in Tables C.5 and C.6. Judging from the obtained fitting results for both the Ag3d and the AgM₅N₄₅N₄₅ signal, the vertical positions d of the Ag atoms in both Ag(100) and Ag(110) are 0.00 Å within the error margins (because $p_c \approx 0$), except for Ag3d of the Ag(110) substrate crystal. Note, however, that nondipolar correction terms have been considered for the Ag(110) Ag3d signal due to the experimental geometry (see Table 4.7 in Sec. 4.3.3, page 64, of the present work for the explicit values). Neglecting these correction terms, i.e., setting both parameters Q and Δ to 0, leads to $f_c = 0.99(1)$, $p_c = 0.02(1)$, and $d = 0.03(1)$ Å as a result here. Apparently, the fitting results for the Ag3d signal depend on the choice of Q and Δ . Hence, the obtained deviation of $p_c(\text{Ag}3d)$ from 0 may in fact be an artifact of our data analysis and will hence not be discussed further here.

Our theoretical investigations have predicted a buckling of the Ag surfaces upon PTCDA adsorption (see Sec. 7.5). In particular, the Ag(100) surface is expected to buckle at an amplitude of 0.19 Å according to DFT. This should reflect in the f_c values if the prediction was correct and if the XSW experiments were surface-sensitive enough. In fact, we probed only the topmost Ag layer of the Ag(100) substrate crystal in our XSW experiments for the Ag3d signal [with an escape depth of only 2.1 Å or 1.0 Ag layers (and 0.5 Å or 0.2 Ag layers for the AgM₅N₄₅N₄₅ signal); see also Table 4.2]. Judging from the obtained coherent fraction of 0.90(1)—where a value of 1 is expected for an ideally flat surface—and employing a simple two-level scenario (with only two distinct values of the vertical position d being equally adopted by the surface atoms), a buckling of the topmost Ag(100) surface layer of ± 0.10 Å may indeed be anticipated. Our theoretical results on the surface buckling fully support this interpretation. Note that a similar analysis of the

surface buckling cannot be done for the Ag(110) substrate because the escape depth of the Ag3d photoelectrons amounts to as much as 28.9 Å or, equivalently, 20.0 Ag layers here.^{g)}

XSW results for the adsorbate signals

Exemplary XSW photoelectron yield curves for the different preparations of PTCDA on the (100) and (110) Ag surfaces are displayed in Figs. C.11 to C.14. As in the case of the XPS measurements (see Sec. C.3.3), the lower signal-to-noise of the data for the Ag(110) surface is due to the smaller photoemission cross sections at the higher photon energy (see also Sec. C.2), a smaller transmission of the analyzer, and the different data acquisition geometry (see above and also Sec. 4.1.2). Nonetheless, a good agreement with the experimental data was achieved in the fittings of all XSW curves. Employing the XPS fitting models from Sec. C.3.3, a differential analysis of the XSW data was performed. The so-obtained results are summarized in Table C.5 for PTCDA/Ag(100) and in Table C.6 for PTCDA/Ag(110), respectively.

The details of the XSW data analysis have been explained in general in Sec. 4.3.3 already. The analysis performed here is principally the same as that for PTCDA/Cu₃Au(111) (see Secs. 6.6.3 and 6.6.4). Only a few technical details will be amended to the general procedure in the following. Firstly, in the case of 0.78(10) ML PTCDA/Ag(100) (preparation no. Feb'11-1), a satellite component (O_{sat}) was observed in the XP spectra [see Fig. C.8(b), middle row]. Note at this point that this component was not observed in the XP spectra of PTCDA overlayers with higher or lower coverages. This peak was fitted as an individual component to the sets of XPS data in the XSW data analysis, with its relative intensity in the XP spectra being free to the fit. The so-obtained XSW fitting results indicate that this satellite peak may be ascribed to the O_{carb} atoms (the determined p_c values agree within 0.01; see Table C.5).^{h)} However, the determined f_c value (of 1) for O_{sat} is larger than the result for the substrate signal (see also above), questioning the validity of the XSW analysis for this component. Secondly, concerning PTCDA/Ag(110), a very weak $C_{\text{sat } 2}$ component [with a relative intensity of only 3.50%; see Fig. C.9(a), bottom row, at $E_b \approx 294$ eV and Table C.6] was observed in the C1s XP spectrum of PTCDA in the submonolayer regime. This component was fitted to the XP spectra of the XSW measurements but, due to its weakness, it was not evaluated separately as an individual component in the XSW analysis.

The first preparation of PTCDA/Ag(110) (preparation no. Feb'09-1) exhibited a coverage which was slightly higher than a full monolayer, namely, $\theta_{\text{PTCDA}} = 1.15(4)$ ML according to XPS (see Table 4.3 in Sec. 4.3.2, page 56, of the present work). Remarkably, solely diffraction spots originating from the monolayer brick-wall phase could be discerned in the corresponding LEED patterns [see Fig. C.6(a) above]. However, the more intense diffuse background of the LEED patterns, especially around the specular (00) reflection, in comparison to the LEED pattern of the PTCDA submonolayer in Fig. C.6(b) indicates the presence of additional molecules in a disordered phase and/or very small islands in the second layer on the Ag(110) surface. We performed XSW measurements also on this preparation (see Fig. C.13 for the corresponding XSW photoelectron yield curves). The individual C1s and O1s XP spectra of the respective XSW data sets were fitted with the fitting models for the (sub-)monolayer XP spectra for reasons of simplicity.

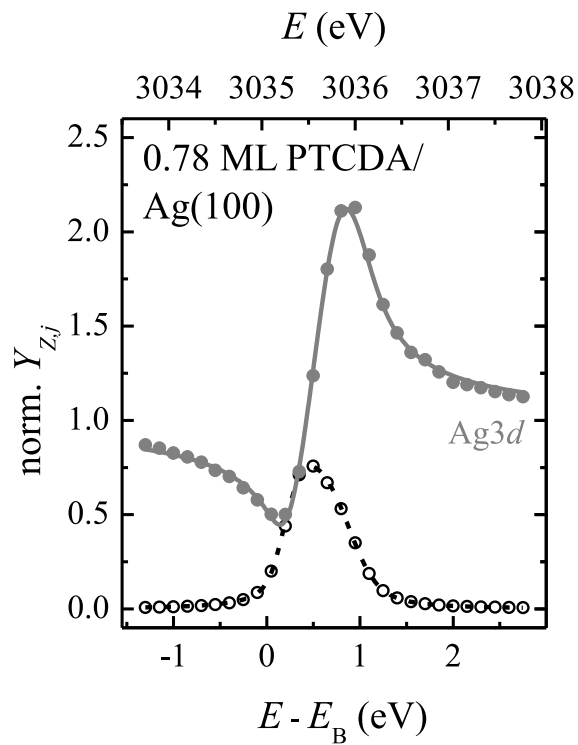
The fitting results for the so-obtained XSW photoelectron yield curves are also included in Table C.6. Obviously, the obtained coherent fractions f_c are lower [by up to 0.19(8) in the worst case, that is, for C_{funct}] than for the submonolayer preparation (preparation no. Feb'09-2a; see also

^{g)}The escape depth of the Ag $M_5N_{45}N_{45}$ Auger electrons amounts to only 5.0 Å or, equivalently, 3.5 Ag layers due to their lower kinetic energy (see also Table 4.2).

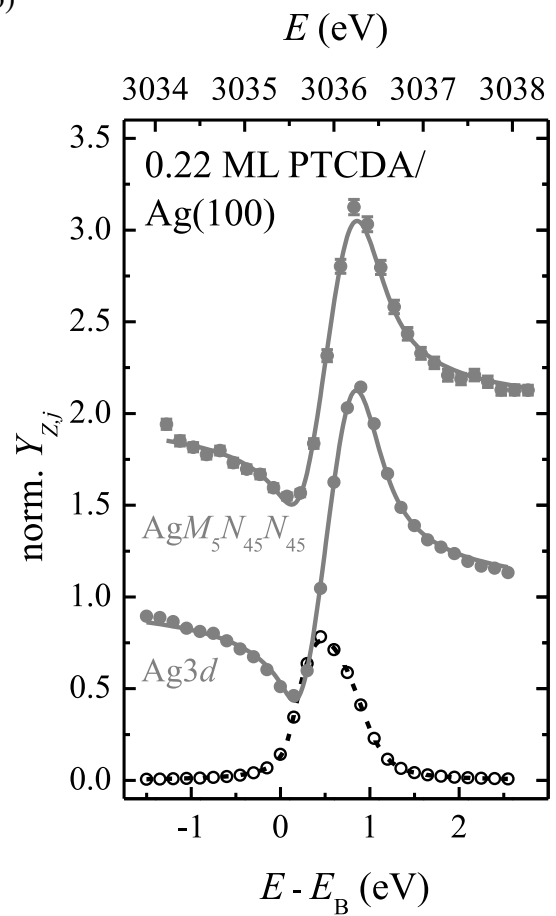
^{h)}An exemplary XSW photoelectron yield curve is not shown here.

FIG. C.10 (following page). Typical XSW photoelectron yield curves of the substrate signals for the PTCDA-covered Ag(100) and Ag(110) surfaces. The Ag3d XP and AgM₅N₄₅N₄₅ Auger signals were employed in the respective XSW experiments. (a) Ag3d for 0.78(10) ML PTCDA/Ag(100) (preparation no. Feb'11-1), (b) Ag3d as well as AgM₅N₄₅N₄₅ for 0.22(3) ML PTCDA/Ag(100) (preparation no. Feb'11-2), (c) Ag3d for 0.91(4) ML PTCDA/Ag(110) (preparation no. Feb'09-2a), and (d) AgM₅N₄₅N₄₅ for 0.91(4) ML PTCDA/K:Ag(110) (preparation no. Feb'09-2b). Note that the obtained XSW photoelectron yield profile in (d), i.e., for PTCDA/Ag(110) with K atoms being coadsorbed, is regarded as being representative also for the pure PTCDA/Ag(110) interface. Experimental data points are shown as filled circles while respective fits to the data are shown as solid lines. The curves in (b) have been vertically offset for clarity. In all cases, error bars are so small that they are (almost) hidden by the data points. In addition, the measured reflectivity curve of the substrate employing the (a, b) (200) or (c, d) (220) lattice planes (open circles), respectively, and the corresponding fit (dashed line) are shown in each case. Error bars have been omitted for clarity here. Note that only the topmost surface layer has been probed in these experiments.

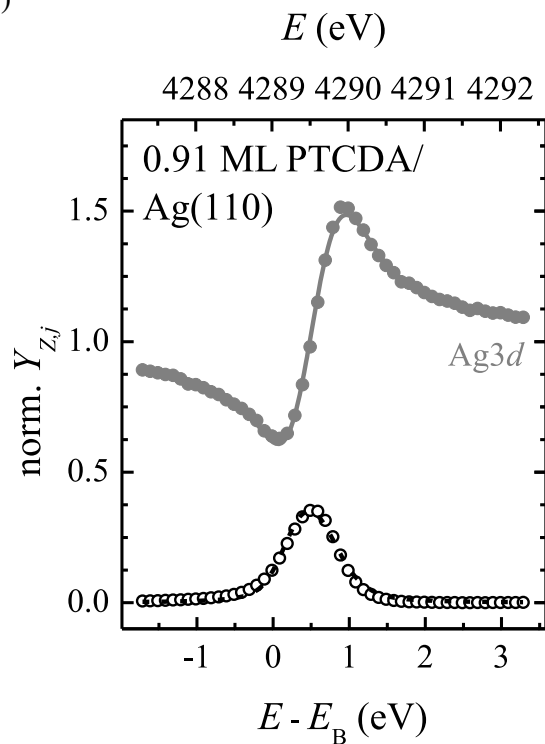
(a)



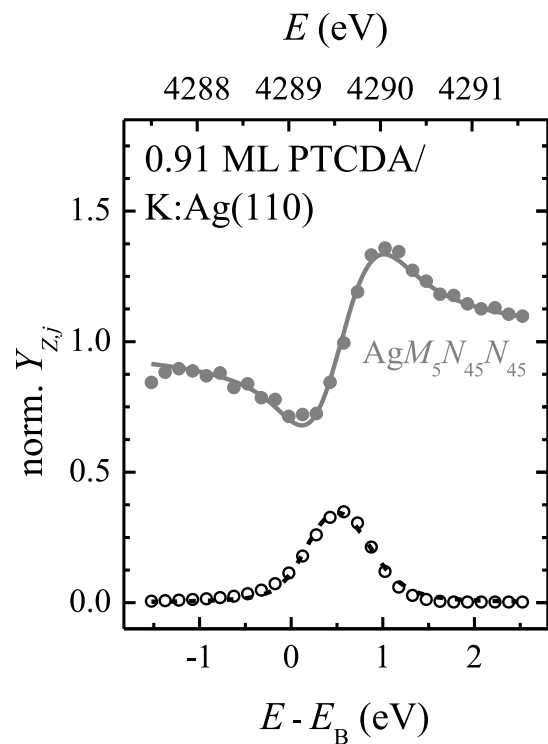
(b)



(c)



(d)



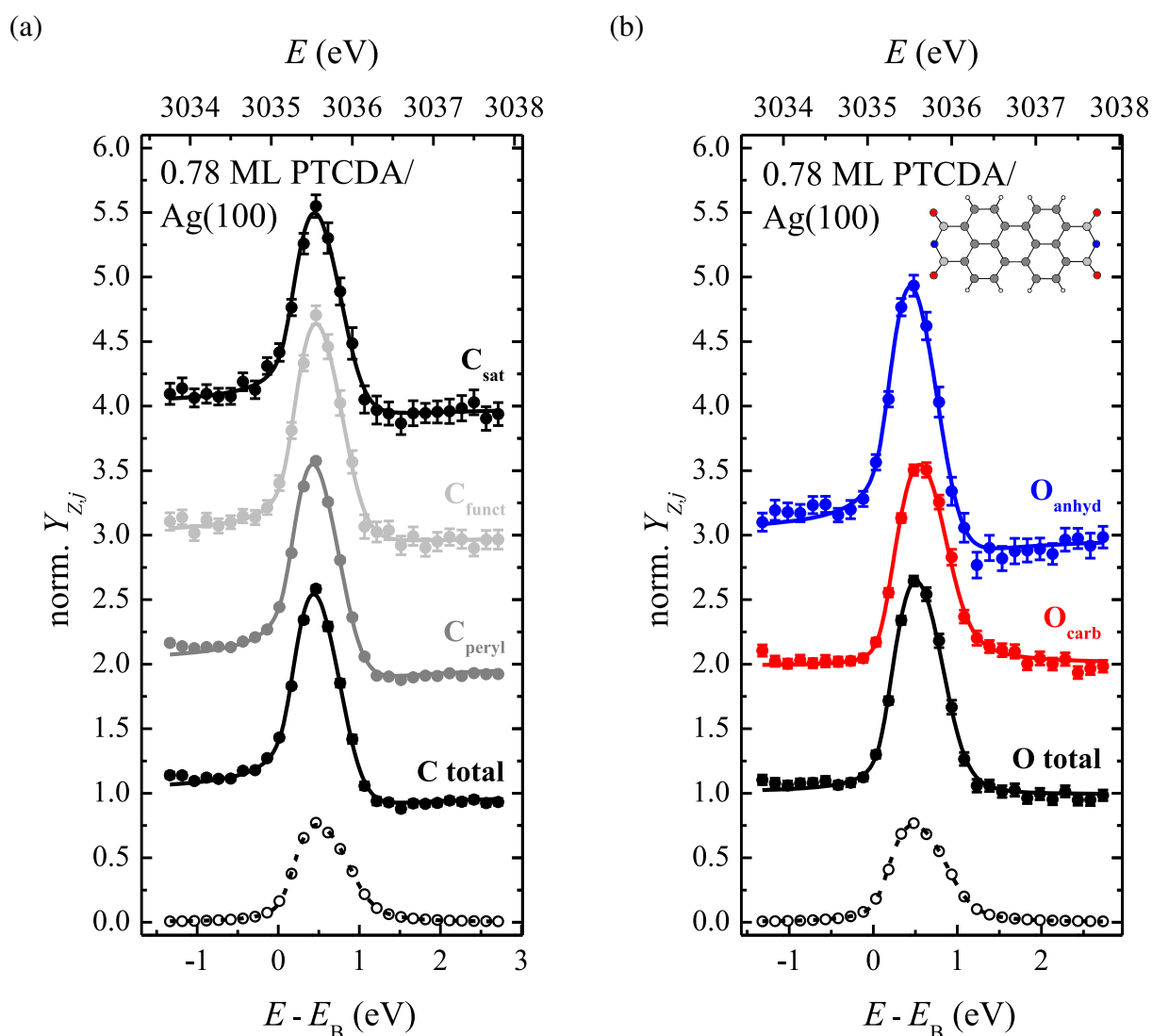


FIG. C.11. Typical XSW photoelectron yield curves of carbon and oxygen in PTCDA on the Ag(100) surface for the first preparation [$\theta_{\text{PTCDA}} = 0.78(10)$ ML; preparation no. Feb'11-1]. The (a) C1s and the (b) O1s signals were employed in the respective XSW experiments. The XP fitting models allowed for a differential analysis of the XSW data regarding the individual components: (a) C_{ptyl} (dark gray), C_{func} (light gray), and C_{sat} (black) for the C1s signal, and (b) O_{carb} (red) and O_{anhyd} (blue) for the O1s signal. In addition, the summed data of the individual C1s and O1s components are shown in black. Experimental data points are shown as filled circles while respective fits to the data are shown as solid lines. The curves have been vertically offset for clarity. In some cases, error bars are so small that they are almost hidden by the data points. In addition, the measured reflectivity of the substrate employing the (200) lattice planes (open circles) and the corresponding fit (dashed line) are shown. Error bars have been omitted for clarity here. A color-coded ball-and-stick model of the PTCDA molecule is shown as an inset in (b).

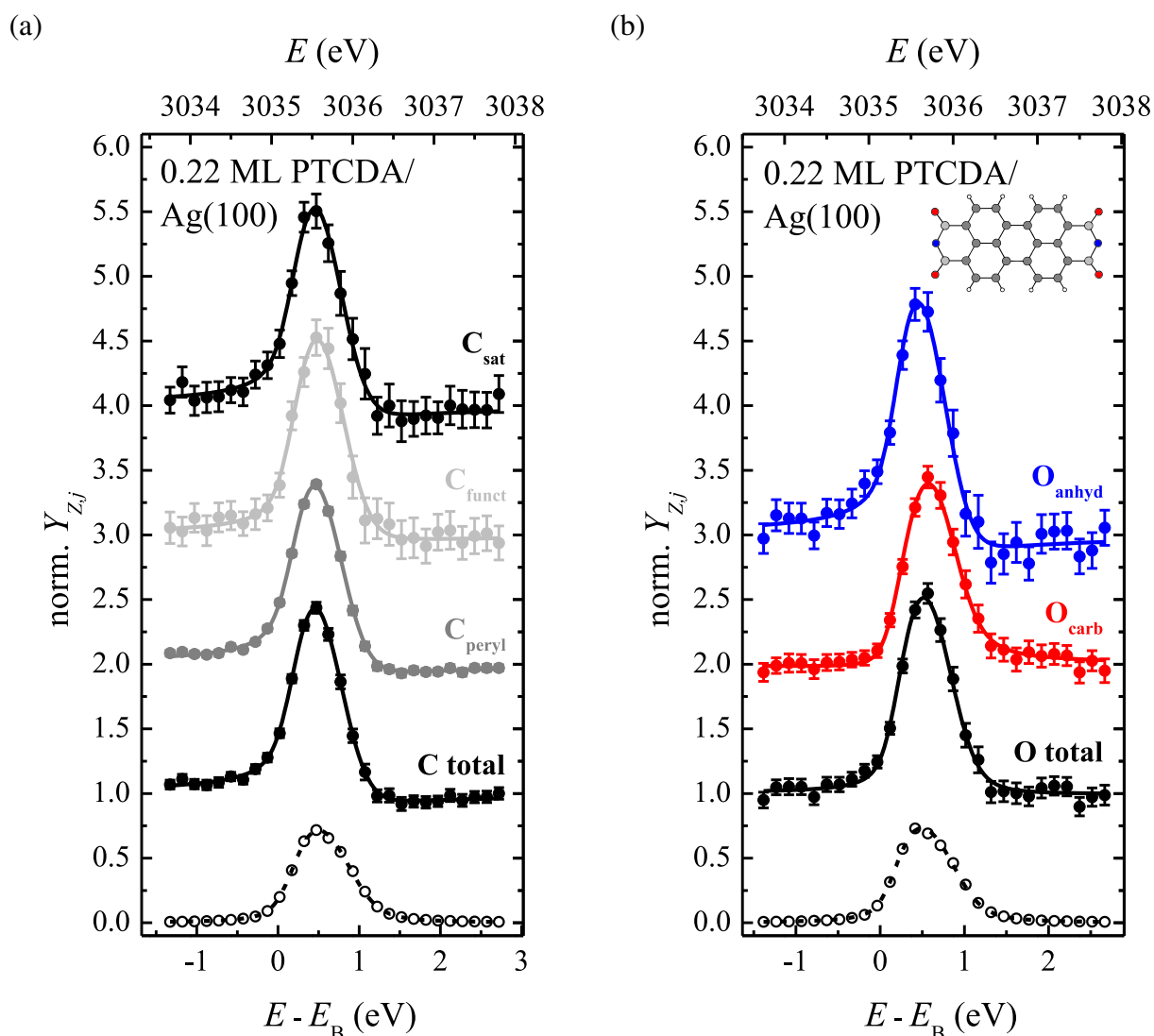


FIG. C.12. Same as Fig. C.11 but for the second preparation (with lower coverage): Typical XSW photoelectron yield curves of carbon and oxygen in PTCDA on the Ag(100) surface for the second preparation [$\theta_{\text{PTCDA}} = 0.22(3)$ ML; preparation no. Feb'11-2]. The (a) C1s and the (b) O1s signals were employed in the respective XSW experiments. The XP fitting models allowed for a differential analysis of the XSW data regarding the individual components: (a) C_{ptyl} (dark gray), C_{func} (light gray), and C_{sat} (black) for the C1s signal, and (b) O_{carb} (red) and O_{anhyd} (blue) for the O1s signal. In addition, the summed data of the individual C1s and O1s components are shown in black. Experimental data points are shown as filled circles while respective fits to the data are shown as solid lines. The curves have been vertically offset for clarity. In some cases, error bars are so small that they are almost hidden by the data points. In addition, the measured reflectivity of the substrate employing the (200) lattice planes (open circles) and the corresponding fit (dashed line) are shown. Error bars have been omitted for clarity here. A color-coded ball-and-stick model of the PTCDA molecule is shown as an inset in (b).

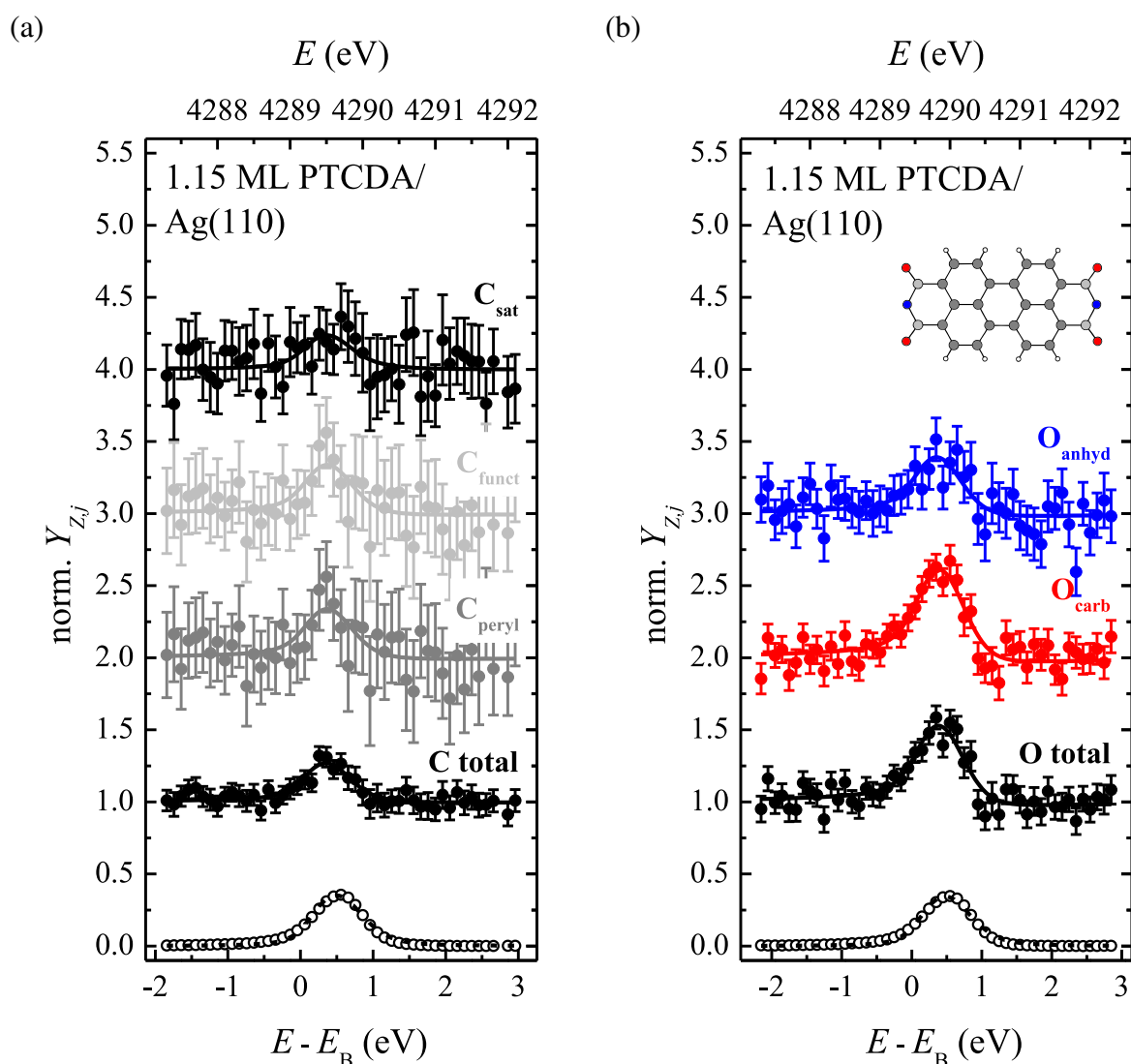


FIG. C.13. Same as Fig. C.11 but for PTCDA/Ag(110): Typical XSW photoelectron yield curves of carbon and oxygen in PTCDA on the Ag(110) surface for the first preparation [$\theta_{\text{PTCDA}} = 1.15(4)$ ML; preparation no. Feb'09-1]. The (a) C1s and the (b) O1s signals were employed in the respective XSW experiments. The XP fitting models allowed for a differential analysis of the XSW data regarding the individual components: (a) C_{ptyl} (dark gray), C_{func} (light gray), and C_{sat} (black) for the C1s signal, and (b) O_{carb} (red) and O_{anhyd} (blue) for the O1s signal. In addition, the summed data of the individual C1s and O1s components are shown in black. Experimental data points are shown as filled circles while respective fits to the data are shown as solid lines. The curves have been vertically offset for clarity. In addition, the measured reflectivity of the substrate employing the (220) lattice planes (open circles) and the corresponding fit (dashed line) are shown. Error bars have been omitted for clarity here. A color-coded ball-and-stick model of the PTCDA molecule is shown as an inset in (b).

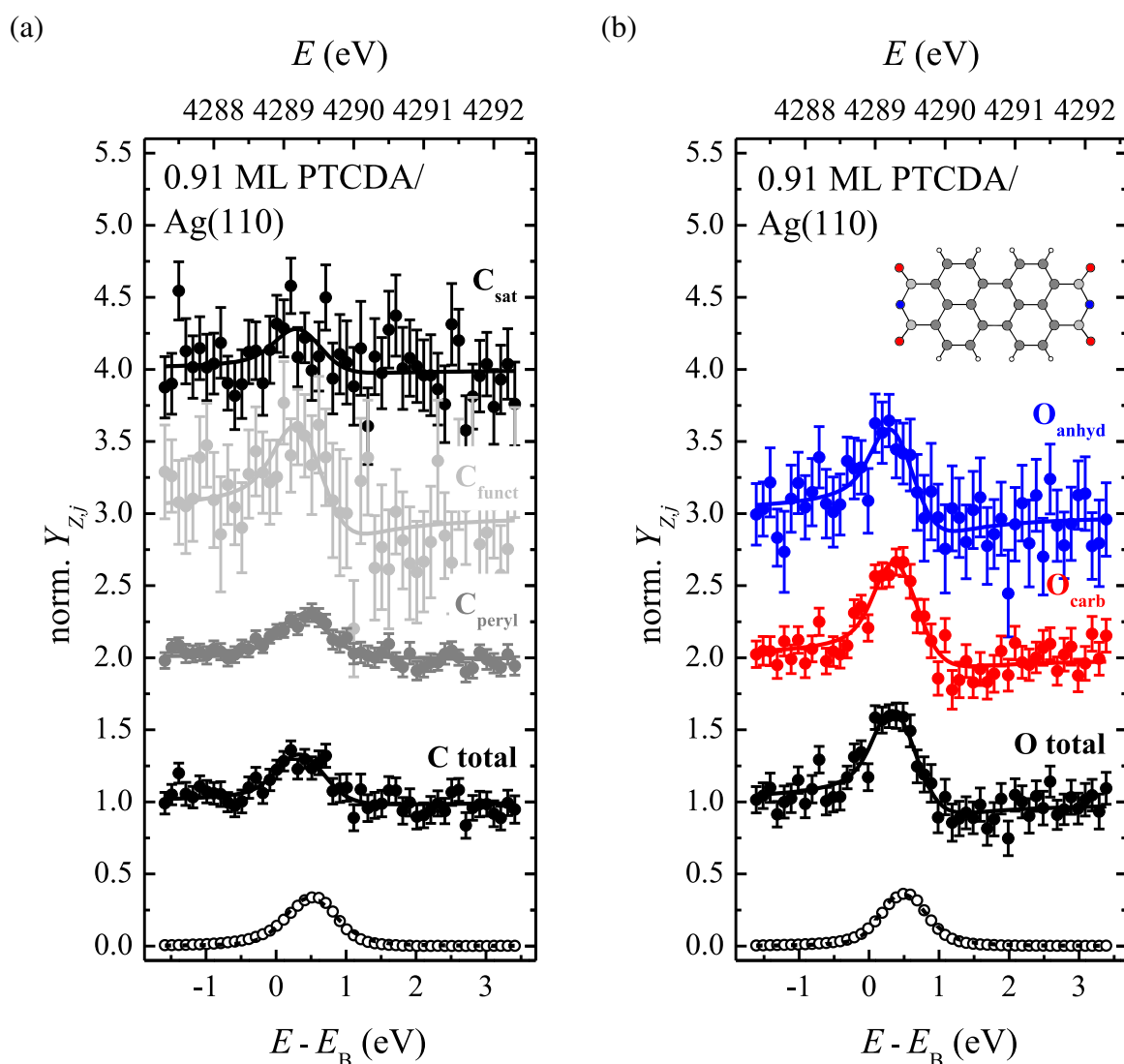


FIG. C.14. Same as Fig. C.13 but for the second preparation (with lower coverage): Typical XSW photoelectron yield curves of carbon and oxygen in PTCDA on the Ag(110) surface for the second preparation [$\theta_{\text{PTCDA}} = 0.91(4)$ ML; preparation no. Feb'09-2a]. The (a) C1s and the (b) O1s signals were employed in the respective XSW experiments. The XP fitting models allowed for a differential analysis of the XSW data regarding the individual components: (a) C_{panyl} (dark gray), C_{func} (light gray), and C_{sat} (black) for the C1s signal, and (b) O_{carb} (red) and O_{anhyd} (blue) for the O1s signal. In addition, the summed data of the individual C1s and O1s components are shown in black. Experimental data points are shown as filled circles while respective fits to the data are shown as solid lines. The curves have been vertically offset for clarity. In addition, the measured reflectivity of the substrate employing the (220) lattice planes (open circles) and the corresponding fit (dashed line) are shown. Error bars have been omitted for clarity here. A color-coded ball-and-stick model of the PTCDA molecule is shown as an inset in (b).

Fig. C.14 for the corresponding XSW photoelectron yield curves). This is in full agreement with the picture of additional molecules being present in the second layer which most likely exhibit a different (relative) vertical position with respect to the extended Bragg planes than the PTCDA molecules in the first layer. Assuming their contribution to the XSW result to be 13 %, as indicated by XPS, the adsorption heights of these molecules was calculated from the XSW results for the two preparations according to the procedure employed for PTCDA/Cu₃Au(111) already (see Sec. 6.6.4). Besides, we assumed the adsorption configuration of the PTCDA molecules in the monolayer to be completely unaltered by the additional molecules in the second layer. Taking the C_{peryl} atoms as a criterion, we found a spacing of 3.26(2) Å between the first and the second PTCDA layer on the Ag(110) surface (see Table C.6). This is in very good agreement with the (102) layer spacing in bulk PTCDA (e.g., 3.22 Å for the α phase;¹⁰⁷ see also Table 2.1).

Briefly summarizing our results concerning the adsorption configurations, PTCDA adsorbs in an arch-like configuration on both Ag(100) and Ag(110), with all O atoms being closer to the surface than the C_{peryl} atoms. The overall adsorption height d is lower on the more open Ag(110) surface. The implications of these findings for the surface bonding mechanism and the underlying bonding channels—in particular, metal-to-molecule charge transfer and local O—Ag interactions—are discussed at large in Chapter 7. Schematic illustrations of the adopted adsorption configurations are also found in that chapter (see Fig. 7.4 in Sec. 7.1, page 182, of the present work, for example).

Values of the coherent fractions

Finally, we briefly comment on the values of the coherent fractions f_c which were obtained from the XSW data analysis. In the case of PTCDA/Ag(110), we systematically found f_c values which are the smallest within the available datasets of PTCDA on Ag(111),⁵⁵ Ag(100) (see Table C.5), and Ag(110) (see Table C.6), and also smaller than those usually obtained for organic adsorbates (see also Refs. 43 and 42, for example). In particular, the f_c values of the C and O atoms in PTCDA on Ag(110) are reduced by about 20 % and 50 % with respect to those on Ag(100) (see Tables C.5 and C.6). From the quality of the LEED patterns [see Fig. C.6(b), in particular], we can exclude that this is due to lateral disorder effects. It is much more likely that the effect is related to the significantly smaller lattice plane spacing in the case of the employed (220) reflection [by about 30 % and 40 %, respectively, in comparison to the (200) and (111) reflections].⁶⁶ This causes f_c as well as p_c to be more sensitive to vertical displacements of the atoms with respect to the extended lattice planes.^{28, 159} Hence, thermal vibrations lead to a stronger reduction of the f_c values.⁶⁶ In addition, a small fraction of molecules at defect sites (which are more likely on this most open surface), which are in structurally different adsorption configurations and lead to an incoherent contribution to the NIXSW curves, could play a role here.⁶⁶ However, the p_c values are not affected by this.

TABLE C.5. XSW results for the adsorption configuration of PTCDA on the Ag(100) surface. Results are given for a PTCDA submonolayer with higher coverage [$\theta_{\text{PTCDA}} = 0.78(10)$ ML; preparation no. Feb' 11-1], a PTCDA submonolayer with lower coverage [$\theta_{\text{PTCDA}} = 0.22(3)$ ML; preparation no. Feb' 11-2], and as a combined result (i.e., weighted average) of both preparations. The Ag3*d*, AgM₅N₄₅N₄₅ (denoted as AgMNN), C1*s*, and O1*s* levels were measured, respectively. The parameters f_c and p_c are the coherent fractions and positions, respectively, which were obtained from the fits to the photoelectron yield curves. The d values denote the averaged vertical adsorption height of the specific atoms. Here, d is calculated at $d = (n + p_c) d_{hkl}$ with $n = 0$ for the substrate levels and $n = 1$ for the adsorbate levels. d_{hkl} is the lattice plane spacing of the employed (200) Bragg reflection of the Ag substrate crystal. $\Delta d' = d_{0.22(3)\text{ML}} - d_{0.78(10)\text{ML}}$ denotes the changes in the averaged vertical adsorption heights for the PTCDA submonolayer with lower coverage with respect to that with higher coverage. $\Delta d = d_{\text{max}} - d_{\text{min}}$ is the absolute (overall) vertical distortion of the (intrinsically planar) PTCDA molecule, $\Delta d(\text{C}) = d(\text{C}_{\text{funct}}) - d(\text{C}_{\text{peryl}})$ is the vertical displacement of the C atoms, and $\Delta d(\text{O}) = d(\text{O}_{\text{anhyd}}) - d(\text{O}_{\text{carb}})$ is the vertical displacement of the O atoms, respectively. For the specification of the atoms, see Figs. C.11(b) and C.12(b), for example. The values for C total and O total were obtained by performing the fitting of the XSW photoelectron yield curves to the sum of the integral intensities of all components contributing to the respective XPS signal (n.a. = not available/applicable).

θ_{PTCDA}	PTCDA/Ag(100)									
	0.78(10) ML			0.22(3) ML				combined results		
	f_c	p_c	d (Å)	f_c	p_c	d (Å)	$\Delta d'$ (Å)	f_c	p_c	d (Å)
Ag3 <i>d</i>	0.90(1)	0.00(1)	-0.01(1)	0.89(1)	0.00(1)	-0.01(1)	0.00(1)	0.90(1)	0.00(1)	-0.01(1)
AgMNN	n.a.	n.a.	n.a.	0.86(1)	0.00(1)	0.00(2)	n.a.	0.86(1)	0.00(1)	0.00(2)
C total	0.56(2)	0.37(1)	2.81(1)	0.44(8)	0.38(1)	2.82(3)	0.01(3)	0.51(8)	0.38(1)	2.81(2)
C _{peryl}	0.57(1)	0.39(1)	2.84(1)	0.41(8)	0.39(2)	2.83(3)	-0.01(3)	0.50(10)	0.39(1)	2.84(2)
C _{funct}	0.61(4)	0.34(1)	2.73(1)	0.55(3)	0.33(1)	2.73(1)	0.00(1)	0.59(5)	0.34(1)	2.73(1)
C _{sat}	0.54(4)	0.36(1)	2.78(3)	0.49(10)	0.38(1)	2.82(3)	0.04(4)	0.52(7)	0.37(2)	2.79(3)
C _{sat 1}	0.58(7)	0.38(3)	2.83(5)	0.45(4)	0.39(2)	2.84(3)	0.01(6)	0.53(9)	0.39(2)	2.83(4)
C _{sat 2}	0.52(5)	0.32(4)	2.69(9)	0.56(18)	0.37(1)	2.79(2)	0.10(9)	0.54(11)	0.34(4)	2.73(8)
O total	0.59(2)	0.29(1)	2.64(3)	0.52(5)	0.29(1)	2.64(2)	0.00(4)	0.55(6)	0.29(1)	2.64(2)
O _{carb}	0.55(2)	0.25(1)	2.55(3)	0.46(6)	0.23(1)	2.52(1)	-0.03(3)	0.50(7)	0.24(1)	2.53(2)
O _{anhyd}	0.79(3)	0.36(1)	2.77(2)	0.76(3)	0.36(1)	2.78(3)	0.01(4)	0.77(3)	0.36(1)	2.78(2)
O _{sat}	1.00(1)	0.24(16)	2.54(34)	n.a.	n.a.	n.a.	n.a.	n.a.	n.a.	n.a.
Δd (in Å)			0.29(3)			0.31(3)				0.31(3)
$\Delta d(\text{C})$ (in Å)			-0.10(1)			-0.10(3)				-0.11(2)
$\Delta d(\text{O})$ (in Å)			0.22(4)			0.26(3)				0.25(3)

TABLE C.6. Same as Table C.5 but for PTCDA/Ag(110): XSW results for the adsorption configuration of PTCDA on the Ag(110) surface. Results are given for PTCDA overlayers with coverages around 1 ML, namely, with $\theta_{\text{PTCDA}} = 1.15(4)$ ML (preparation no. Feb'09-1) and $\theta_{\text{PTCDA}} = 0.91(4)$ ML (preparation no. Feb'09-2a). In addition, the extrapolated results for the second layer are given. The Ag3*d*, AgM₅N₄₅N₄₅ (denoted as AgMNN), C1*s*, and O1*s* levels were measured, respectively. The parameters f_c and p_c are the coherent fractions and positions, respectively, which were obtained from the fits to the photoelectron yield curves. The d values denote the averaged vertical adsorption height of the specific atoms. Here, d is calculated at $d = (n + p_c) d_{hkl}$ with $n = 0$ for the substrate levels and $n = 1$ for the adsorbate levels. d_{hkl} is the lattice plane spacing of the employed (220) Bragg reflection of the Ag substrate crystal. $\Delta d' = d_{\text{second layer}} - d_{0.91(4)\text{ML}}$ denotes the differences in the averaged vertical adsorption heights between the first and the second monolayer of PTCDA. $\Delta d = d_{\text{max}} - d_{\text{min}}$ is the absolute (overall) vertical distortion of the (intrinsically planar) PTCDA molecule, $\Delta d(\text{C}) = d(\text{C}_{\text{funct}}) - d(\text{C}_{\text{peryl}})$ is the vertical displacement of the C atoms, and $\Delta d(\text{O}) = d(\text{O}_{\text{anhyd}}) - d(\text{O}_{\text{carb}})$ is the vertical displacement of the O atoms, respectively. For the specification of the atoms, see Figs. C.13(b) and C.14(b), for example. The values for C total and O total were obtained by performing the fitting of the XSW photoelectron yield curves to the sum of the integral intensities of all components contributing to the respective XPS signal (n.a. = not available/applicable).

θ_{PTCDA}	PTCDA/Ag(110)									
	1.15(4) ML			0.91(4) ML			second layer [0.15(4) ML] ^a			
	f_c	p_c	d (Å)	f_c	p_c	d (Å)	f_c	p_c	d (Å)	$\Delta d'$ (Å)
Ag3 <i>d</i>	n.a.	n.a.	n.a.	0.80(1)	-0.04(1)	-0.06(1)	n.a.	n.a.	n.a.	n.a.
AgMNN	n.a.	n.a.	n.a.	0.87(7) ^b	-0.01(1) ^b	-0.02(2) ^b	n.a.	n.a.	n.a.	n.a.
C total	0.31(5)	0.80(2)	2.59(2)	0.38(5)	0.77(1)	2.56(1)	0.39(8)	0.07(2)	5.88(3)	3.32(3)
C _{peryl}	0.33(4)	0.80(1)	2.60(2)	0.38(7)	0.79(1)	2.58(1)	0.17(8)	0.04(1)	5.84(2)	3.26(2)
C _{funct}	0.24(8)	0.78(3)	2.56(5)	0.43(1)	0.69(8)	2.45(11)	1.52(8)	0.09(9)	5.91(13)	3.46(18)
C _{sat}	0.32(7)	0.80(3)	2.59(4)	0.39(1)	0.77(1)	2.55(1)	0.44(7)	0.09(3)	5.91(4)	3.36(4)
O total	0.15(4)	0.67(2)	2.41(3)	0.26(3)	0.61(2)	2.33(3)	0.77(6)	0.03(3)	5.82(4)	3.49(5)
O _{carb}	0.10(7)	0.58(6)	2.28(9)	0.24(2)	0.59(3)	2.30(4)	0.82(7)	0.10(7)	5.92(10)	3.62(11)
O _{anhyd}	0.33(11)	0.72(3)	2.59(4)	0.33(6)	0.65(1)	2.38(1)	1.05(13)	0.89(3)	5.62(4)	3.24(4)
Δd (in Å)			0.32(9)			0.28(4)			0.29(14)	
$\Delta d(\text{C})$ (in Å)			-0.04(5)			-0.13(11)			0.07(13)	
$\Delta d(\text{O})$ (in Å)			0.21(10)			0.08(4)			-0.30(11)	

^aCalculated from the XSW results for PTCDA/Ag(110) with $\theta_{\text{PTCDA}} > 1$ and $\theta_{\text{PTCDA}} < 1$, assuming 13 % contribution of the second layer [0.15(4) ML] to the former results.

^bThe stated f_c , p_c , and d values were determined from XSW data acquired on PTCDA/K:Ag(110), i.e., on a K-modified (and PTCDA-covered) Ag(110) surface (preparation no. Feb'09-2b). Yet, these values are regarded as being representative also for the pure and the PTCDA-covered Ag(110) surface (preparation no. Feb'09-2a), respectively.

C.4 Adsorption site determination of PTCDA on Ag(100) by means of XSW

In addition to the adsorption configuration (see Sec. C.3.4), we determined the previously unknown adsorption site of the PTCDA molecules in the Q phase on the Ag(100) surface via triangulation by means of XSW.^{29, 159} For this purpose, photoelectron yield curves of the O1s signal with respect to the (111) lattice planes of the Ag substrate were measured under near-normal incidence, i.e., at a Bragg angle of $\theta_B \approx 88^\circ$. It will be elucidated in detail in the context of Figs. C.18 and C.19 further below, how this approach allowed for unambiguously determining the PTCDA adsorption site in Q phase PTCDA/Ag(100). First, however, the experimental characteristics and results will be presented.

The (111) lattice planes make an angle of $\varphi = 54.74^\circ$ with the surface and thus with the (200) lattice planes, which were employed above for determining the vertical adsorption heights [see Fig. C.18(b), for example]. In order to achieve near-normal incidence of the x-ray beam on the (111) Bragg planes, the surface normal had to be tilted away from the (nearly) antiparallel alignment with the beam direction. In particular, the sample surface was turned towards the electron analyzer (see Fig. 4.3 in Sec. 4.1.2, page 46, of the present work for a schematic representation of the employed experimental setup, XSW setup II). Note at this point that the angle of incidence of the x-ray beam as well as the direction of photoelectron detection are fixed in the experiment (90° in XSW setup II), with consequences in particular for the XPS measurements (see below).

Because the (111) Bragg planes, which were employed in the XSW experiments here, are not parallel to the surface in contrast to the (200) Bragg planes, the asymmetry of the Bragg reflection had to be considered here via the parameter b (see Sec. 3.1.3 for details).¹⁾ We calculated b as -0.906 from Eq. (3.25) by setting $\theta_B = 88^\circ$ and $\varphi_{\text{asym}} = -\varphi = -54.74^\circ$ in compliance with the convention.^{164, 180, 181} The so-obtained results for the coherent fractions f_c and coherent positions p_c systematically deviate from those obtained for the hypothetical case of $b = -1$ by maximal $\Delta f_c = -0.01$ and $\Delta p_c = -0.02$, respectively. Hence, due to the unambiguity of our results concerning the adsorption site of PTCDA on Ag(100) (see below), the actual choice of the parameter b is not at all a decisive factor here.

Furthermore, due to the turning of the sample towards the analyzer, the escape depth $d_e = d_e(E_{\text{kin}}, \theta)$ of the detected photoelectrons (see Sec. 3.2.3) and thus the probing depth of the XPS experiments were increased. Therefore, the XPS measurements (as well as the XSW measurements) were less surface-sensitive than in the case of the previously described experiments on PTCDA/Ag(100) (22.0 Å or, equivalently, 10.8 Ag layers in the case of the Ag3d signal, as compared to only 2.1 Å or 1.0 Ag layers before). As a consequence, the intensity of the substrate peaks in XPS and, accordingly, the background levels in the O1s XP spectra increased.

XPS data

Figure C.15 shows the normalized XP spectrum of the O1s level of PTCDA/Ag(100), acquired with a photon energy of 2615.0 eV, i.e., about 15 eV below the Bragg energy of the (111) reflection ($\theta_B = 88^\circ$; see also Sec. C.2), and a pass energy of 100 eV at an effective angle of detection of 33.3° . Similar to the XP spectrum taken at higher photon energy [$E = 3024.0$ eV; see Fig. C.8(b)], the O_{carb} and O_{anhyd} components can be clearly discerned. The spectrum was fitted with five components in total, namely, two main components and three satellite components (see

¹⁾For the symmetric Bragg case, i.e., if the employed Bragg planes are parallel to the surface and if the incident and the reflected beams run through the same surface, $b = -1$ applies.¹⁶⁰

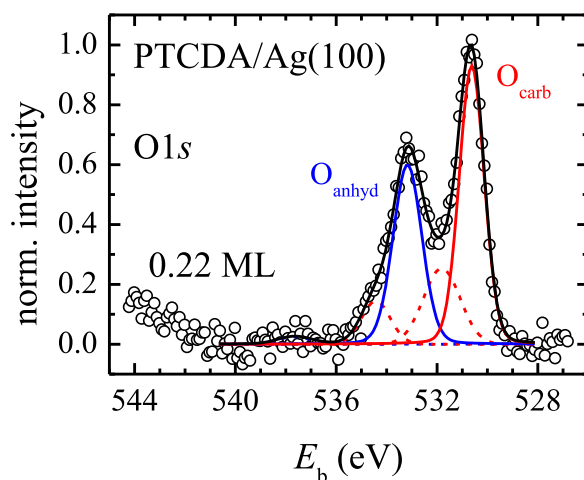


FIG. C.15. Normalized XP spectrum of the O1s level of PTCDA on the Ag(100) surface with corresponding fitting model. The PTCDA coverage amounted to 0.22(3) ML. The XP spectrum was acquired with a photon energy of $E = 2615.0$ eV at an effective angle of about 33° of the photoelectron analyzer with respect to the surface normal (XSW setup II). The spectrum was corrected with a linear background function. Contributions from the chemically nonequivalent oxygen atoms are shown in red (O_{carb}) and blue (O_{anhyd}), respectively. The main photoemission peaks are drawn as full lines, the corresponding satellite peaks as dashed lines, in respective colors. In addition, the resulting sum of all components is shown as a black line. Note that the $O_{\text{anhyd, sat}}$ component (dashed blue line, $E_b \approx 537.7$ eV) is fully overlaid by the black line. See Fig. C.8, for example, for a ball-and-stick model of the PTCDA molecule.

TABLE C.7. XPS fitting parameters for the O1s level of PTCDA on the Ag(100) surface at lower photon energy ($E = 2615.0$ eV). E_b denotes the binding energy, w the width of the peak, and A the relative peak area. The respective values are given for all components observed in the XP spectrum for a coverage of 0.22(3) ML PTCDA/Ag(100) (preparation no. Feb'11-2). The corresponding XP spectrum is shown in Fig. C.15. Note that this submonolayer XP spectrum was acquired at an effective angle of 33.3° of the photoelectron analyzer with respect to the surface normal (XSW setup II and tilted sample), and that this XPS fitting model was employed in the differential analysis of the O1s XSW data for PTCDA/Ag(100) with respect to the (111) lattice planes. The O1s main components, namely, O_{carb} and O_{anhyd} , were fitted with pseudo-Voigt functions with 10 % Lorentzian contribution while the satellite components were fitted with pure Gaussian functions. ΔE_b values denote the changes in E_b in comparison to the O1s XP spectrum of this preparation at higher photon energies and an effective angle of detection of 86° ($E = 3024.0$ eV; see Table C.3).

0.22(3) ML PTCDA/Ag(100)				
	E_b (eV)	w (eV)	A (%)	ΔE_b (eV)
O_{carb}	530.62	1.17	43.01	-1.31
$O_{\text{carb, sat 1}}$	531.81	1.71	16.35	-2.40
O_{anhyd}	533.17	1.35	31.87	-0.48
$O_{\text{carb, sat 2}}$	534.43	1.34	7.31	-1.29
$O_{\text{anhyd, sat}}$	537.65	1.56	1.46	-0.37

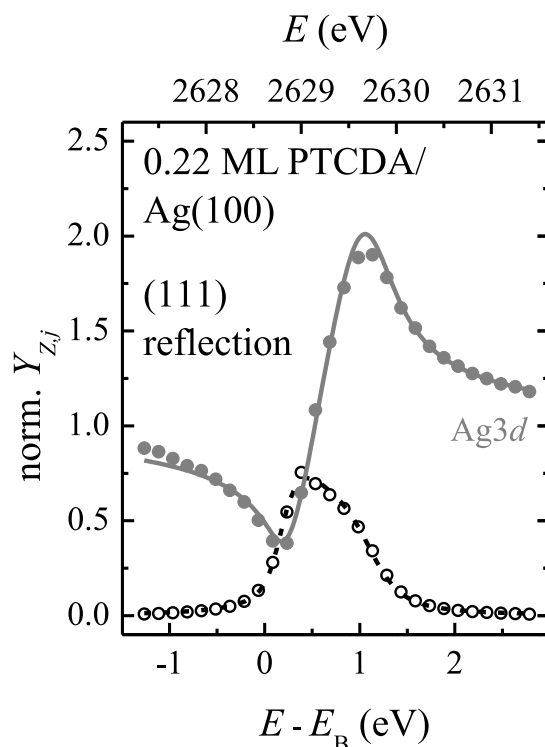


FIG. C.16. Typical XSW photoelectron yield curve of the $Ag3d$ signal for PTCDA on the $Ag(100)$ surface, employing the (111) Bragg reflection of the substrate crystal. Experimental data points are shown as filled circles while the respective fit to the data is shown as a solid line. The error bars are so small that they are hidden by the data points. In addition, the measured reflectivity of the substrate employing the (111) lattice planes (open circles) and the corresponding fit (dashed line) are shown. Error bars have been omitted for clarity here.

Table C.7 for the fitting parameters). The fitting model fulfills the expected stoichiometric ratio of $O_{carb} : O_{anhyd} = 4 : 2$.

Notably, the $O_{anhyd, sat}$ component at $E_b = 576.65$ eV exhibits a very low intensity relative to the other components (i.e., below 1.5 % of the total $O1s$ intensity). This is ascribed to the increased background intensity due to the experimental geometry and the thus higher contributions of inelastically scattered photoelectrons from the substrate as compared to the XPS data for the higher angle of detection (see also above). The more intense background, which further increases for binding energies above 544 eV (see Fig. C.15), overlays the (intrinsically weak) $O_{anhyd, sat}$ component here.

XSW data

We recorded XSW photoelectron yield curves for the $Ag3d$ and $O1s$ XPS levels in the tilted sample geometry, i.e., with respect to the (111) Bragg planes. Exemplary XSW curves together with their corresponding fitting curves are shown in Figs. C.16 and C.17. The fitting curves are in very good overall agreement with the experimental data. As a minor impairment, only the first few data points are systematically underestimated which can be ascribed in parts, at least for the very first data point of the individual XSW photoelectron yield curve, to a systematic error in the normalization of the data to the intensity I_0 of the incident beam (see Sec. 6.3.3 for further details). Besides, a few data points at $E - E_B \approx 1$ eV, i.e., around the maximum of the XSW curve, are not

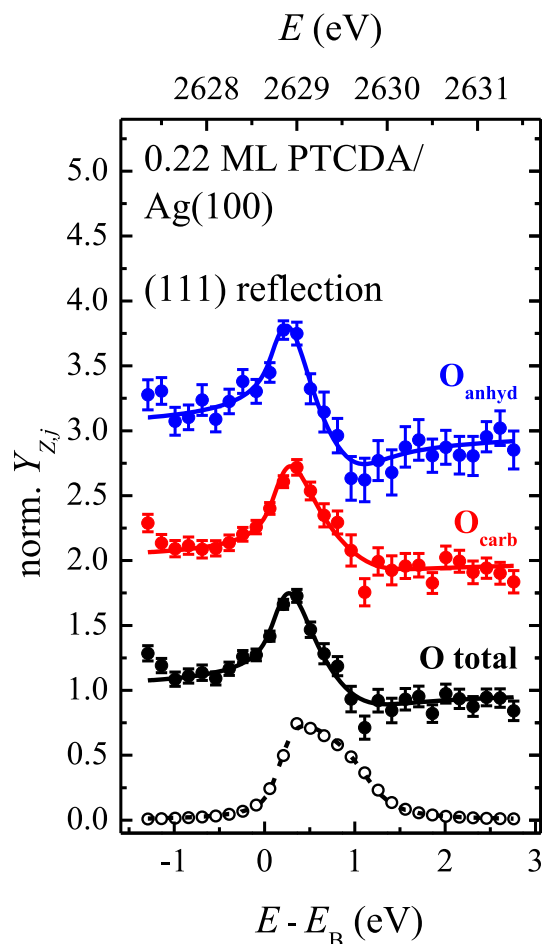


FIG. C.17. Typical XSW photoelectron yield curves of oxygen in PTCDA on the Ag(100) surface, employing the (111) Bragg reflection of the substrate crystal [$\theta_{\text{PTCDA}} = 0.22(3)$ ML; preparation no. Feb' 11-2]. The $O1s$ signal was measured in the respective XSW experiments. The XP fitting model allowed for a differential analysis of the XSW data regarding the individual components, namely, O_{carb} (red) and O_{anhyd} (blue) for the $O1s$ signal. In addition, the summed data of the individual $O1s$ components are shown in black. Experimental data points are shown as filled circles while respective fits to the data are shown as solid lines. The curves have been vertically offset for clarity. In addition, the measured reflectivity of the substrate employing the (111) lattice planes (open circles) and the corresponding fit (dashed line) are shown. Error bars have been omitted for clarity here. A color-coded ball-and-stick model of the PTCDA molecule is shown in Fig. C.12(b), for example.

TABLE C.8. XSW results concerning the adsorption site of PTCDA on the Ag(100) surface, employing the (111) Bragg reflection of the substrate crystal. The stated results were obtained on a PTCDA submonolayer with a coverage of $\theta_{\text{PTCDA}} = 0.22(3)$ ML (preparation no. Feb'11-2). In addition, the theoretically expected results for different high-symmetry adsorption sites of the two PTCDA molecules per unit cell on Ag(100) (as defined by the centers of the two molecules) are given, which have been calculated on the basis of the XSW results employing the (200) Bragg reflection (see Table C.5). The Ag3*d* and O1*s* levels were measured. The parameters f_c and p_c are the coherent fractions and positions, respectively, which were obtained from the fits to the photoelectron yield curves in the case of the experimental data. The calculation of the theoretically expected data is described in the text. Note that, regarding the adsorption in bridge sites, $f_c = 0$ applies for reasons of symmetry. For the specification of the atoms, see Figs. C.11(b) and C.12(b), for example. The values for O total were obtained by performing the fitting of the XSW photoelectron yield curves to the sum of the integral intensities of all components contributing to this XPS signal (n.a. = not available/applicable).

$\theta_{\text{PTCDA}} / \text{adsorption site}$	PTCDA/Ag(100) – (111) reflection							
	experimental data		calculated data					
	0.22(3) ML		on-top		fourfold hollow		bridge	
	f_c	p_c	f_c	p_c	f_c	p_c	f_c	p_c
Ag3 <i>d</i>	0.89(1)	−0.02(1)	n.a.	n.a.	n.a.	n.a.	n.a.	n.a.
O total	0.40(2)	0.64(1)	0.39(4)	0.65(3)	0.39(4)	0.15(3)	0.00	n.a.
O _{carb}	0.32(2)	0.64(2)	0.27(4)	0.62(4)	0.27(4)	0.12(4)	0.00	n.a.
O _{anhyd}	0.57(3)	0.64(1)	0.76(5)	0.68(3)	0.76(5)	0.18(3)	0.00	n.a.

described as adequately as the others. Despite these minor impairments, the fitting of the Ag3d XSW curve yielded very reasonable results for a well-ordered metal crystal, namely, $f_c = 0.89(1)$ and $p_c = -0.02(1)$ (see Table C.8), thereby rendering the obtained values reliable and meaningful.

For both the O_{carb} and the O_{anhyd} atoms, identical coherent positions were obtained from the fitting ($p_c = 0.64$; see Table C.8). Yet, the determination of the adsorption configuration in Sec. C.3.4 above has revealed that the PTCDA molecule distorts on the Ag(100) surface [i.e., $p_c^{(200)}(O_{\text{carb}}) \neq p_c^{(200)}(O_{\text{anhyd}})$], with the chemically nonequivalent O atoms being at different vertical heights [with a vertical splitting of $\Delta d(\text{O}) = 0.25(3)$ Å; see Table C.5]. As a consequence, different coherent positions $p_c^{(111)}$ must necessarily be present for the two nonequivalent O species also with respect to the (111) lattice planes, which, however, is *not* found in our analysis of the experimental XSW data. Apparently, our XPS fitting model does not allow for (correctly) distinguishing between the O_{carb} and the O_{anhyd} atoms when employed on all O1s XPS signals of one XSW data set. Again, the increased background level and, in particular, the almost vanishing $O_{\text{anhyd, sat}}$ component may play a decisive role here. Nevertheless, the adsorption site of the PTCDA molecules on the Ag(100) surface can unambiguously be determined from our XSW results, as will be demonstrated in the following.

Triangulation

For determining the adsorption sites of atoms and molecules on surfaces with XSW, the respective photoelectron yield curves must be measured with respect to more than one, non-parallel family of Bragg planes.^{29, 159, 623} Here, the (200) and (111) lattice planes were employed (see also above). The lines of intersection of these two families of lattice planes run along the $[01\bar{1}]$ direction of the Ag substrate [see Fig. C.18(a)]. As a second requirement, the atoms or molecules of interest may not be incoherently distributed with respect to the employed families of lattice planes. As can be seen from Figs. C.18(a) and (b), the O atoms in PTCDA, in particular the O_{anhyd} , exhibit a well-defined registry with the Ag(100) surface, and thus also with respect to the (200) lattice planes (shown for on-top adsorption), *and* with respect to the (111) lattice planes. This makes them the ideal candidate for the determination of the PTCDA adsorption site. Note at this point that, in the context of the present work, the term “adsorption site of the PTCDA molecule” refers to the lateral position of the center of gravity of the molecule, i.e., the lateral position of the central benzene ring in PTCDA, with respect to the Ag surface atoms.

The relative positions of the C atoms with respect to the (111) lattice planes, however, cover the full range of possible $p_c^{(111)}$ values [0–1 modulo the (111) lattice planes], rendering the resulting coherent fractions f_c so small that they are not expected to be physically meaningful. For example, an f_c value of only 0.32 is expected for C total even under the assumption of perfect “vertical” order [i.e., $f_c^{(111)} = 1$] for the individual C atoms within the two PTCDA molecules per unit cell of the Q phase of PTCDA/Ag(100). The relative positions of the C atoms with respect to the (111) lattice planes can hence be considered as being (almost) incoherent in sum.

In principle, the coherent positions of the atoms of interest with respect to at least *three* independent families of lattice planes have to be determined for an unambiguous result concerning the adsorption site. Due to the high (fourfold) symmetry of the substrate surface, however, a second measurement is sufficient to distinguish the different high-symmetry adsorption sites,¹⁵⁹ namely, on-top, fourfold hollow, or bridge site. These positions are marked exemplarily by diamonds and lines at the top in Fig. C.18(a). Other adsorption sites (of lower symmetry) can be excluded on rational grounds: PTCDA forms a commensurate structure with fourfold symmetry (two-dimensional space group $p4gm$;¹²⁰ see also Table C.1) in the monolayer regime on the Ag(100) surface. This has been evidenced with LEED.¹²⁰ Therefore, it is very likely that the

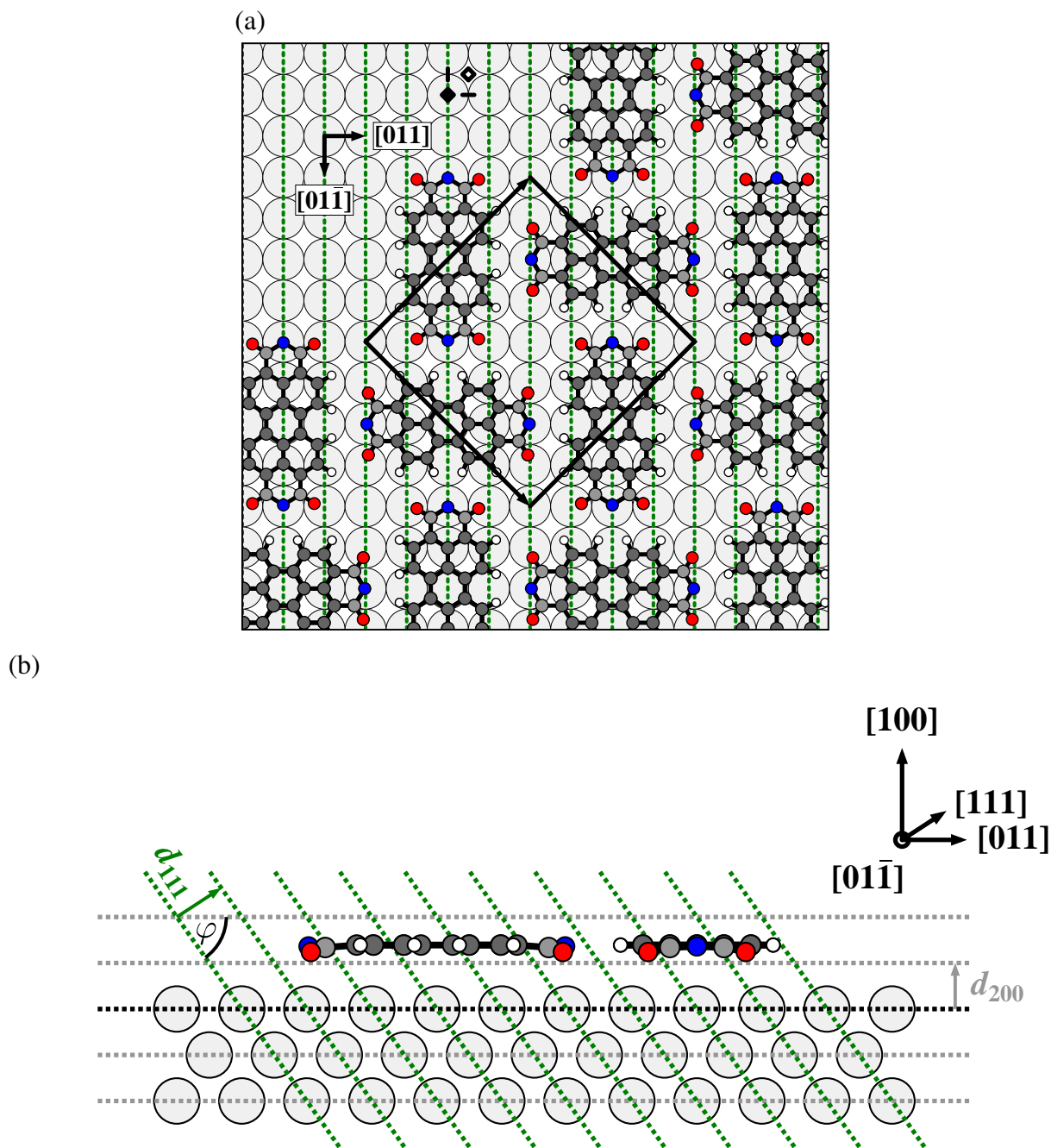


FIG. C.18. Schematic illustration of the adsorption site determination for PTCDA on the Ag(100) surface. The PTCDA molecules are shown such that their centers are located in on-top positions with respect to the underlying Ag surface atoms. (a) Top view of the Q phase of PTCDA/Ag(100) in the (sub-)monolayer regime.¹²⁰ The PTCDA molecules are shown as ball-and-stick models. Black solid lines indicate the respective unit cell. The substrate directions are also indicated. The lines of intersection of the (111) lattice planes with the (100) surface plane of the Ag substrate crystal are marked by green dashed lines. High-symmetry adsorption sites are exemplarily marked by a filled diamond (\blacklozenge) for an on-top site, by an open diamond (\diamond) for a fourfold hollow site, and short, black horizontal and vertical lines for bridge sites. (b) Side view (along the $[0\bar{1}1]$ direction) of two symmetry-nonequivalent PTCDA molecules in the Q phase on the Ag(100) surface. The (111) and (200) lattice planes are depicted as green and gray dashed lines, respectively, which make an angle of $\varphi = 54.74^\circ$. d_{hkl} denotes the lattice plane spacing. The substrate directions are indicated in the inset.

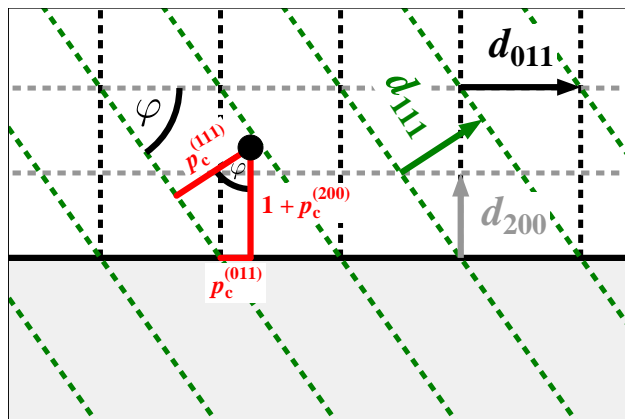


FIG. C.19. Schematic illustration for the calculation of the theoretically expected coherent positions $p_c^{(111)}$ with respect to the (111) lattice planes (green dashed lines) of the Ag(100) substrate crystal (side view along the $[0\bar{1}1]$ direction). An atom (●) is adsorbed in an arbitrary position on the surface (black solid line) of the Ag(100) substrate crystal (depicted as a gray area). The corresponding $p_c^{(111)}$ values can be obtained by geometrical considerations from the (known) coherent positions $p_c^{(200)}$ and $p_c^{(011)}$ with respect to the (200) and (011) lattice planes, respectively (gray and black dashed lines; see text for further details). Note that the (110) reflection is systematically extinct²⁰⁹ for Ag crystals due to their *fcc* bulk structure.²⁰ The spacings d_{hkl} of the individual sets of lattice planes are marked by arrows in respective colors. The (111) and (200) lattice planes enclose an angle of $\varphi = 54.74^\circ$.

PTCDA molecules are adsorbed in high-symmetry sites. Strictly speaking, only on-top and four-fold hollow sites are possible in conjunction with the valid space group $p4gm$ if also the Ag surface atoms are taken into account. Adsorption in bridge positions would already lead to a reduced symmetry [$p2gg$; see also Fig. C.18(a)], for instance.

Having determined the coherent positions $p_c^{(200)}(\text{O})$ with respect to the (200) lattice planes, the coherent positions $p_c^{(111)}(\text{O})$ with respect to the (111) lattice planes which are expected for the different adsorption sites can be calculated. The situation is schematically depicted in Fig. C.19. From geometrical considerations, it follows that:

$$p_c^{(111)} = \left[1 + p_c^{(200)} \right] \cos \varphi + p_c^{(011)} \sin \varphi. \quad (\text{C.1})$$

The respective values of $p_c^{(111)}(\text{O})$ for PTCDA adsorption in the different surface sites were deduced from the structural models under the assumption that the lateral intramolecular coordinates are identical to those in the α phase of bulk PTCDA.¹⁰⁸ The calculated results for the different adsorption sites tested here, namely, on-top, fourfold hollow, and bridge, are compiled in Table C.8 and contrasted with the experimentally obtained results. In addition, the expected coherent fractions $f_c^{(111)}(\text{O})$ have been estimated from the measured $f_c^{(200)}(\text{O})$ values via:

$$f_c^{(111)} = \frac{f_c^{(200)}}{f_{c,\text{ideal}}^{(200)}} f_{c,\text{ideal}}^{(111)}, \quad (\text{C.2})$$

where $f_{c,\text{ideal}}^{(hkl)}$ denotes the ideal coherent fraction under the assumption of perfect vertical order of a given atomic species against the (200) lattice planes [and thus also against the (111) lattice planes; see below]. Note that $f_{c,\text{ideal}}^{(200)} = 1$ applies for the individual O atoms, namely, for the O_{carb} and the O_{anhyd} atoms. The $f_{c,\text{ideal}}^{(200)}$ value for the O total signal amounts to 0.94 and is thus smaller

than 1 due to the vertical splitting of $0.25(3) \text{ \AA}$ of the O_{carb} and O_{anhyd} atoms with respect to the surface, i.e., the (200) lattice planes (see also Table C.5 above). The respective $f_{\text{c,ideal}}^{(111)}$ values were obtained by adding the results vectors of all O atoms of the individual component in the Argand-diagram representation of the data, by analogy to the procedure employed for the final state of PTCDA/Cu₃Au(111) (see Sec. 6.6.4). In this approach, we assumed that the $f_{\text{c}}^{(111)}$ values are solely determined by the vertical order against the (200) lattice planes, $f_{\text{c}}^{(200)}$, and that lateral deviations from the ideal adsorption site(s) [which the $f_{\text{c}}^{(200)}$ values are not sensitive to] can be neglected. In other words, the relative reduction in the real, i.e., experimentally determined $f_{\text{c}}^{(hkl)}$ values in comparison to the ideally expected $f_{\text{c,ideal}}^{(hkl)}$ values for a given component is independent of the employed family $\{hkl\}$ of lattice planes here and thus constant. Hence, the ratio $f_{\text{c}}^{(200)}/f_{\text{c,ideal}}^{(200)}$, which is present on the right-hand side of Eq. (C.2) and which amounts to 0.59(6) for O total, for instance, serves as a correction or scaling factor in order to predict more realistic $f_{\text{c}}^{(111)}(\text{O})$ values from the calculated, ideal $f_{\text{c,ideal}}^{(111)}(\text{O})$ values, that is, coherent fractions with respect to the (111) lattice planes which may actually be observed in the experiment for one particular adsorption site of the PTCDA molecules. These predicted $f_{\text{c}}^{(111)}(\text{O})$ values can then be compared to the factual, experimentally determined values of the coherent fraction.

The above assumption of $f_{\text{c}}^{(hkl)}/f_{\text{c,ideal}}^{(hkl)}$ being constant for all values of $\{hkl\}$ is justified by the fact that the experimentally obtained $f_{\text{c}}^{(111)}$ values are in fact larger than the calculated ones in most cases (see Table C.8). Apparently, the underlying effects which lead to a reduced order along the [200] or the [111] direction partly cancel out. Only for the O_{anhyd} atoms, the experimental $f_{\text{c}}^{(111)}$ value is smaller than the calculated ones for on-top and fourfold-hollow adsorption. We attribute this to an improper differential decomposition of the O total XSW photoelectron yield curve into the two chemically nonequivalent O species due to the inappropriate XPS fitting model (see above).

However, this does not question our result concerning the PTCDA adsorption site. By comparing the experimental and the calculated values, it is obvious that only on-top adsorption is in agreement with our experimental findings. The results for $p_{\text{c}}^{(111)}(\text{O total})$ agree within 0.01 here (see Table C.8). For the O_{carb} and O_{anhyd} components, the discrepancies between theory and experiment amount to maximal 0.04 which is close to the experimental accuracy. The $p_{\text{c}}^{(111)}(\text{O})$ results for fourfold-hollow adsorption are shifted by 0.5 [or, equivalently, by π in the Argand diagram (not shown)] to smaller values in comparison to those for on-top adsorption since the relation $p_{\text{c}}^{(011)}(\text{fourfold hollow}) = p_{\text{c}}^{(011)}(\text{on-top}) + 1/2$ applies here. This holds because the lateral positions of the fourfold-hollow and the on-top adsorption sites differ exactly by half the spacing d_{011} of the (011) lattice planes when projected on the [011] direction [see Fig. C.18(a), in particular].

For reasons of symmetry, the adsorption in bridge positions results in an incoherent distribution of the O atoms with respect to the (111) lattice planes [$f_{\text{c}}^{(111)}(\text{O}) = 0$]. Note in this context that the XSW result of O for PTCDA in bridge positions can be understood as the vector sum [in an Argand diagram (not shown)] of the adsorption in on-top and in fourfold-hollow positions. This is due to the fact that two domains with equal area portions are possible (and realized) here [again due to reasons of symmetry; see Fig. C.18(a)], which differ in $p_{\text{c}}^{(011)}$ by exactly 0.5 (see Table C.8), i.e., by 1/2 of the layer spacing d_{011} . One of these two domains corresponds to the adsorption in on-top sites concerning the lateral position along the [011] direction, while the other domain corresponds to the adsorption in fourfold-hollow sites. The two associated vectors in the Argand diagram exactly cancel out when added with equal portions. As a consequence, the coherent fraction equals 0 for the adsorption in bridge sites, and the coherent position is hence not defined.

The on-top adsorption of the PTCDA molecules with respect to the Ag surface causes that the O atoms also adopt (nearly) on-top positions [see also Sec. 7.1 and Fig. C.18(a)]. The implications

of this registry for the relevant bonding channels, in particular for the formation of local, covalent O—Ag bonds, and also for the overall bonding mechanism have been discussed at large in Chapter 7. Here, we emphasize that our experimental finding of on-top adsorption is in perfect agreement with our theoretical results. According to DFT, the adsorption of the PTCDA molecule in the Q phase in an on-top site is favored by 0.64 eV over the adsorption in a fourfold hollow site (which corresponds to about 15 % of the total adsorption energy per molecule; see also Table 7.8 on page 215 of the present work), for example, with a 0.13 Å lower overall adsorption height judging from the obtained $d(\text{C}_{\text{peryl}})$ values. We propose that the theoretical predictions concerning both adsorption site and configuration can be traced back to the shorter and hence stronger O—Ag bonds in the former case of on-top adsorption (see Secs. 7.5 and 7.6).

D

Coadsorption of K and PTCDA on Ag(110)

The experimental results for PTCDA on the Ag(110) surface have been presented in the previous chapter. For the sake of completeness, we will now proceed with a brief presentation also of the experimental data concerning the coadsorption of K atoms and PTCDA molecules on Ag(110). The system K + PTCDA/Ag(110) was investigated because the interplay of the relevant bonding channels at the metal/organic interface could be both probed and tuned by the coadsorption of a reactive metal. The main results have already been published in Ref. 68 [Mercurio *et al.*, Physical Review B **87**, 121409(R) (2013)]. A detailed discussion of the data is found in Chapter 7.

Note that the data in the publication (Ref. 68) were analyzed employing the independent XSW program Torricelli.^{326,330} Here, the data were analyzed using the evaluation routine XSWAVES³²⁹ instead. Within the error margins, identical results were obtained for the two cases.

D.1 Review of the literature

Alkali metal atoms are known to induce reconstructions when adsorbed on *fcc* metal surfaces, in particular on transition metal surfaces.⁵⁶¹ In particular, K atoms induce a $(1 \times n)$ missing-row-type reconstruction of the Ag(110) surface depending on the K coverage.²⁸² For $0.04 \text{ ML} \leq \theta_K \leq 0.19 \text{ ML}$, a (1×2) superstructure is formed, while a (1×3) superstructure forms in the case of lower and higher coverages.²⁸² Note that a coverage of $\theta_K = 1 \text{ ML}$ corresponds to one K atoms per Ag surface atom [at the Ag(110) surface] here. In these structures, every second or third row of densely packed Ag atoms, which are present at the (clean) Ag(110) surface along the $[\bar{1}10]$ direction, is removed and (only) partly replaced by (the larger) K atoms.²⁸²

Two models are available which explain the tendency of alkali metal atoms to induce missing-row-type reconstructions of *fcc* (110) surfaces.^{560,561,624,625} In the long-range interaction model proposed by Fu and Ho,⁵⁶⁰ the reconstructed surface is energetically stabilized due to a charge transfer, i.e., an electron donation, from the alkali metal to the Ag surface atoms. This electron donation produces an increased surface electron concentration which is accumulated in delocalized, *sp*-like states.^{282,560} Because the reconstructed surface exhibits a larger surface facet area as compared to the unreconstructed surface, the corresponding induced charge distribution is smoother, i.e., more extended, leading to a lowering in the kinetic energy of the delocalized electrons.⁵⁶⁰ Within the framework of the short-range model presented by Jacobsen and Nørskov,⁶²⁵ the observed reconstructions originate from the gain in adsorption energy of the alkali metal atoms due to their larger coordination numbers at the reconstructed surface.⁶²⁵

Also the effect of alkali metal coadsorption together with PTCDA on coinage metal surfaces has been studied to some extent already.^{64,65,554,555,626–632} Except for the work of Álvarez *et al.*,⁶³² all experimental data have been collected on PTCDA overlayers with coverages exceeding 1 ML (in some cases quite considerably). Common to all studies, however, was the result that there is a

strong chemical interaction between the reactive, electron-donating alkali atoms and the electron-accepting PTCDA molecules, and, in structural terms, that the alkali atoms are located in the proximity of the O atoms in PTCDA. The latter finding may indicate the relevance of (local) metal–oxygen interactions in these “alkali-doped” PTCDA films. In our studies, we have focused on the structural and electronic properties of PTCDA in the presence of K atoms in the (*sub-*)*monolayer* regime on the Ag(110) surface.

D.2 Experimental procedure

For our experiments on K + PTCDA/Ag(110) presented here, we always started from well-ordered pure PTCDA/Ag(110) layers. Their preparation has already been described in Sec. C.2. Then, potassium was evaporated from commercially available K metal dispensers (see Sec. 4.2 for further details). As a final preparation step, (mild) post-annealing was performed; annealing temperatures of ≥ 450 K, which were usually applied for 5 min, led to well-ordered surface structures, as judged from the bright and sharp LEED patterns. The employed heating and cooling rates amounted to $0.5\text{--}1.0$ K s^{-1} , typically.

We did not attempt (on a systematic basis) to prepare the mixed layers of K and PTCDA with a different chronological order of evaporation of the two materials. The reasons were as follows. On the one hand, a simultaneous evaporation of both materials did not allow for a precise control and/or variation of the K : PTCDA ratio on the surface for experimental reasons. On the other hand, the evaporation of K prior to that of PTCDA was waived as a standard preparation procedure here. In this scenario, the formation of mixed (ordered) phases of K and PTCDA on the Ag(110) surface might potentially be hindered by the already formed, K-induced surface reconstruction²⁸² due to kinetic stabilization. However, individual experiments have shown for the latter case of the K atoms being evaporated first that, in principle, the same surface structure of K + PTCDA/Ag(110) [or, more precisely, PTCDA/K:Ag(110); see Sec. D.3.1 below] can be obtained as in the case of PTCDA being evaporated first, i.e., as for the reverse order of evaporation of the two materials.

For the SPA-LEED experiments, we evaporated potassium at a deposition rate of $0.13(1)$ K atoms per Ag surface atom [at the Ag(110) surface] and minute, judging from the observed LEED patterns in conjunction with the XPS results (see also Sec. 4.2 as well as Secs. D.3.1 and D.3.2 below). The evaporation source in the SPA-LEED had been thoroughly calibrated by making use of the coverage-dependent change in the periodicity of the surface reconstruction along the [001] direction.²⁸² For the XPS and XSW experiments, the deposition of K in XSW setup I was performed at a rate of $0.28(1)$ K atoms per Ag surface atom and minute. This preparation (preparation no. Feb'09-2b; see Table 4.3 in Sec. 4.3.2, page 56, of the present work) was post-annealed at $T = 450\text{--}470$ K for 2 min prior to the XPS and XSW measurements.

In principle, the parameters for both XPS and XSW employed here were the same as for pure PTCDA/Ag(110). The reader is referred to Sec. C.2 at this point for the details and the explicit values. The investigated XPS levels of potassium, namely, $K1s$ and $K2p$, were recorded with a pass energy of 46.95 eV, that is, with the same pass energy as the other adsorbate XPS signals ($C1s$ and $O1s$) also of the pure PTCDA/Ag(110) system. Note that the $K2p$ and $C1s$ XPS signals were always recorded as one combined XP spectrum because their binding energies differ by about 10 eV only [see Table 4.1 in Sec. 4.3.2, page 54, of the present work and also Fig. D.6(a) below, for example]. Note further that the individual $C1s$, $K2p$, and $O1s$ XP spectra, in particular in the XSW measurements, had to be recorded with lower statistics, lower data point density, smaller binding energy windows, and also with larger step sizes in photon energy in comparison to the

pure system because the PTCDA overlayer on the K-modified Ag(110) surface was subject to beam damage. After about 30–40 min of x-ray radiation, an altering of the line shapes, intensities, and peak positions became apparent in the XP spectra. Thus, the recording times of the individual spectra were limited to maximal 30 min in our XPS and XSW experiments.

Several XSW data sets were acquired for K + PTCDA/Ag(110), namely, two $\text{Ag}M_5N_{45}N_{45}$, six $\text{K}1s$, five $\text{O}1s$, as well as four combined $\text{K}2p$ and $\text{C}1s$ data sets. The individual XSW fitting results of these data sets were averaged to give the below-stated values for the coherent fractions f_c and coherent positions p_c , respectively, for the corresponding atoms.

D.3 Results

Measurements on the structural and electronic properties of PTCDA plus K on the Ag(110) surface have been performed by a variety of methods, namely, by means of SPA-LEED, STM, UPS (also angle-resolved), XPS, and XSW. Our experimental results obtained with SPA-LEED, XPS, and XSW will be briefly described in this section for reasons of completeness. The STM and (AR)UPS data have been acquired by Giuseppe Mercurio, Martin Willenbockel, Christian Weiss, Dr. Tomoki Sueyoshi, Dr. Ruslan Temirov and Dr. Serguei Soubatch from the group of Professor Dr. Frank Stefan Tautz from Forschungszentrum Jülich (Jülich, Germany). These data have been published in detail in Refs. 68 and 326 already which the reader is referred to for further information. At this point, we only recapitulate the most important results from these two methods where appropriate.

D.3.1 Lateral structure

The lateral structure of PTCDA on the Ag(110) surface upon coadsorption of K atoms was investigated by means of SPA-LEED. As will be elucidated in the following, results obtained from STM (not shown here; see Refs. 68 and 326), XPS (see Sec. D.3.2 below), and XSW (see Sec. D.3.3 below) were also employed in order to clarify the exact surface structure of K + PTCDA/Ag(110) or, more precisely, PTCDA/K:Ag(110). The latter nomenclature is meant to emphasize the fact that the K atoms are incorporated in the Ag(110) surface and thus underneath the PTCDA molecules. Due to the incorporation of K atoms, the PTCDA-covered Ag(110) surface exhibits a complex reconstruction.

Structural clarification

Figure D.1 shows a typical two-dimensional LEED pattern of PTCDA/K:Ag(110) with the corresponding simulation. This structure was prepared by depositing K atoms onto a well-ordered brick-wall (BW) phase of 0.5 ML PTCDA/Ag(110) and subsequent annealing at 450 K for 5 min. The LEED pattern is composed of lines of close-lying diffraction spots along the [001] direction. Identical LEED patterns were obtained when starting from up to 1.0 ML PTCDA/Ag(110) in the BW phase or even from PTCDA/Ag(110) in the more closely packed monolayer herringbone (HB) phase (see Sec. C.3.1). The K coverage could be varied within $\pm 10\%$ relative to the PTCDA coverage for this structure. For lower K coverages, areas with PTCDA in the K-free BW phase remained on the surface, as judged from the respective LEED patterns [and is also the case for the LEED pattern in Fig. D.1(a) to some extent; see also below]. For higher K coverages, the diffraction spots were smeared out along the the [001] direction, indicating poor long-range order, that is, statistical deviation from the well-defined, complex structural arrangement in this direction (the structural arrangement will be addressed in more detail below). Besides, additional diffraction spots from other

phases, which were only present for lower K coverages and/or insufficient annealing, and which were also weak in intensity and/or smeared out, were observed in some preparations. However, these additional phases are not of further interest at this point. Thus, their discussion is waived here.

Note that in the LEED pattern of Fig. D.1(a) also weak spots originating from the pure PTCDA BW phase can indeed be observed [marked in dark red in Fig. D.1(b)]. Yet, in other preparations and in particular for higher PTCDA coverages (and accordingly higher K coverages), the K + PTCDA structure was obtained as a single, *pure* phase [see the one-dimensional LEED scans in Fig. D.2 below, for example, where BW diffraction spots are not present]. We attribute the presence of the K-free BW phase at lower PTCDA coverages to a non-homogeneous distribution of both PTCDA molecules and K atoms on the Ag(110) surface. This inhomogeneous distribution may arise from a non-equal deposition rate for different spots on the sample surface due to the actual geometric conditions in the SPA-LEED setup in these experiments (see also Sec. 4.1.1), the very narrow deposition angle of the K getter source, and/or an enhanced diffusion of the K atoms and thus a phase separation upon annealing of the sample. Such inhomogeneities were indeed observed with LEED when the sample was moved.

We will now analyze the LEED pattern from Fig. D.1(a) in detail. All observed spots can unambiguously be described by a single K + PTCDA phase with superstructure matrix $\mathfrak{M} = \begin{pmatrix} 3 & 0 \\ 0 & 26 \end{pmatrix}$ [depicted in orange in Fig. D.1(b)]. Due to its columnar or stripe-like appearance in STM (as a consequence of the surface reconstruction described below; data not shown),^{68,326} this phase will be referred to as stripe phase in the following. Because the stripe phase as a single, pure phase is commensurate to the (K:)Ag(110) surface, it must be concluded that both the PTCDA molecules and the K atoms are in commensurate registry to the Ag(110) surface and also to each other.

Remarkably, some of the superstructure spots are much more intense than the others. These spots are marked in purple in Fig. D.1(b). Considering only these spots, a superstructure matrix of type $\mathfrak{M} = \begin{pmatrix} 3.00(3) & 0.00(1) \\ -1.29(4) & 3.71(3) \end{pmatrix}$ applies which describes the so-called “apparent unit cell”. Table D.1 compiles the corresponding lattice parameters. The apparent unit cell can accommodate only one PTCDA molecule, while the unit cell of the stripe phase contains seven PTCDA molecules. The exact filling of the unit cell will be described further below. At this point, however, we emphasize that taking seven times the apparent unit cell along the [001] direction results in the following superstructure matrix:

$$\mathfrak{M}' = \begin{pmatrix} 1 & 0 \\ 0 & 7 \end{pmatrix} \cdot \begin{pmatrix} 3.00(3) & 0.00(1) \\ -1.29(4) & 3.71(3) \end{pmatrix} = \begin{pmatrix} 3.00(3) & 0.00(1) \\ -9.01(31) & 25.97(21) \end{pmatrix} \approx \begin{pmatrix} 3 & 0 \\ -9 & 26 \end{pmatrix}, \quad (\text{D.1})$$

which is an alternative representation of the stripe phase with $\mathfrak{M} = \begin{pmatrix} 3 & 0 \\ 0 & 26 \end{pmatrix}$ simply (see above and also Table D.1). Thus, the apparent unit cell can be understood as an *effective*, mono-

FIG. D.1 (following page). LEED pattern of PTCDA plus K in the (sub-)monolayer regime on the Ag(110) surface and corresponding simulation. (a) Two-dimensional LEED pattern of 0.5 ML PTCDA/K:Ag(110) after annealing at 450 K for 5 min ($E = 24.5$ eV). The measurement were performed at 175 K. (b) Corresponding simulation of the LEED pattern in (a). LEED spots originating from the stripe phase are depicted in orange while the (weak) LEED spots from the remaining, pure PTCDA brick-wall phase are depicted in dark red. In addition, those LEED spots of the stripe-phase superstructure which can be considered as representing the apparent (or averaged) unit cell containing only one PTCDA molecule are marked in purple. Black lines indicate the reciprocal lattice vectors \mathbf{a}_i^* of the substrate.

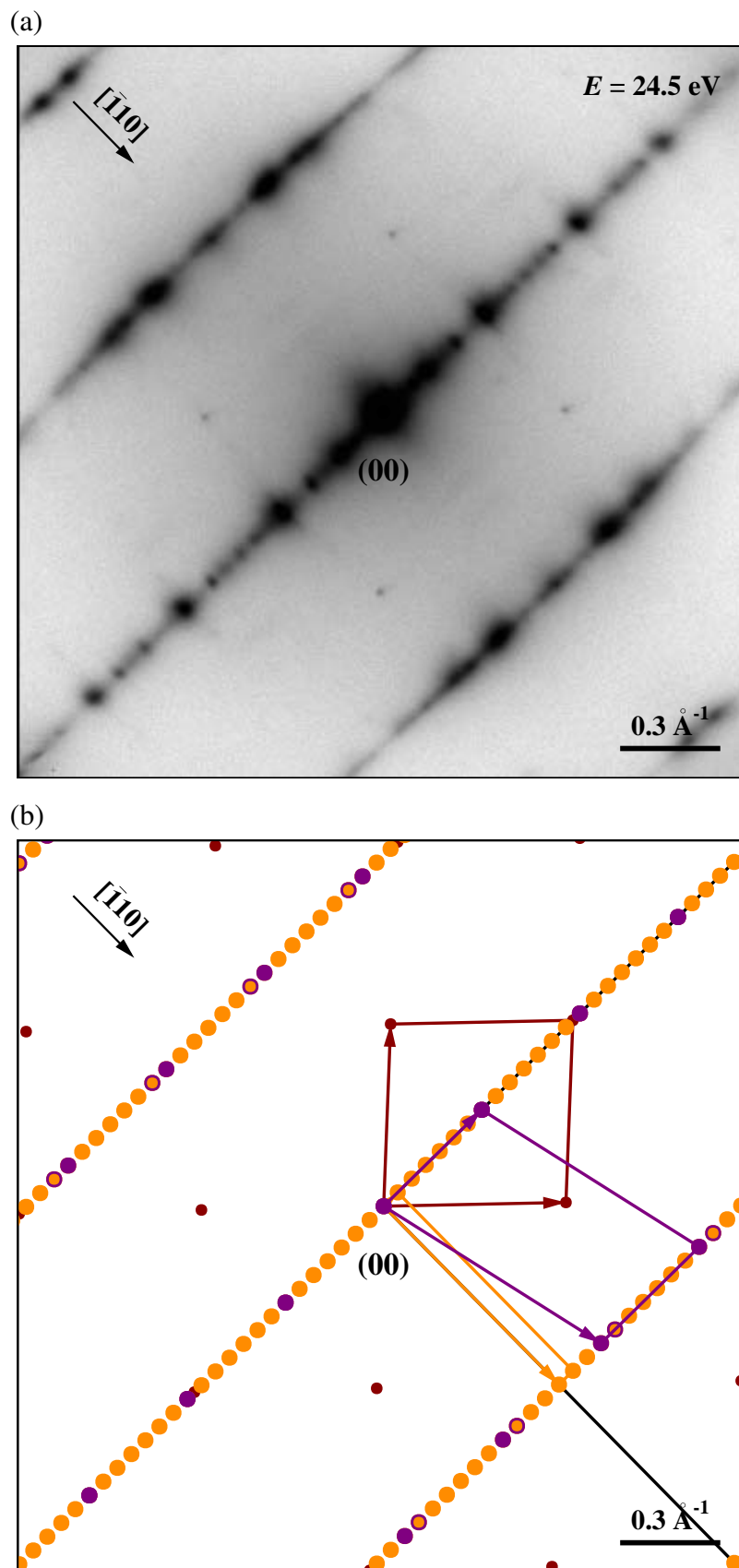


TABLE D.1. Structural results for the apparent unit cell and the stripe phase of PTCDA plus K on the Ag(110) surface, as obtained from SPA-LEED experiments, and proposed model parameters. The lattice constants b_i , the enclosed angle β , the area of the unit cell, A_{uc} , and the number of molecules per unit cell are given. In addition, the two-dimensional space groups and the superstructure matrices \mathfrak{M} are stated (n.a. = not applicable/available).

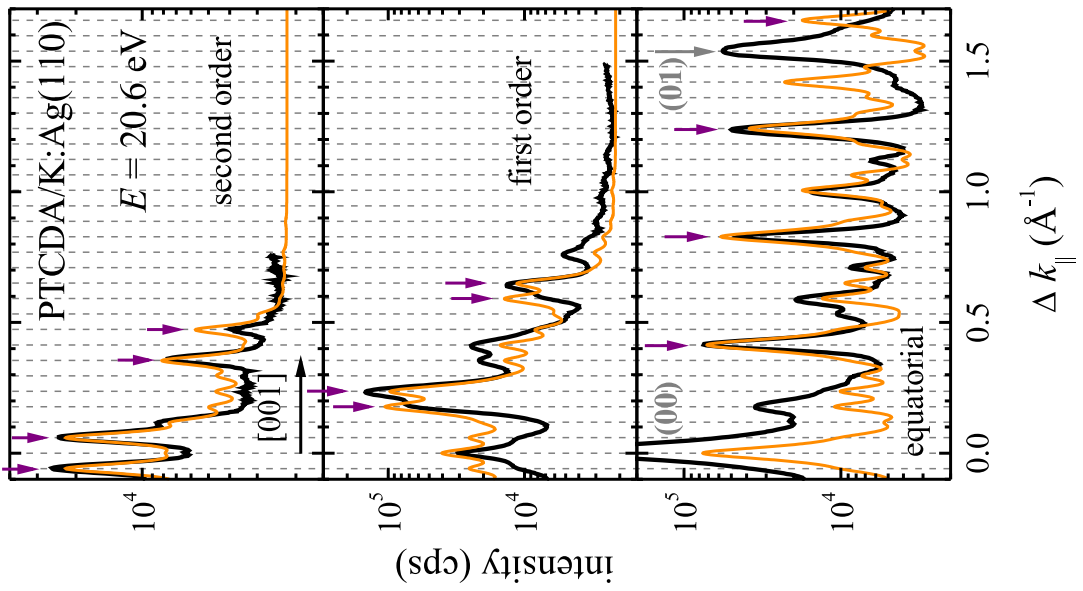
	PTCDA/K:Ag(110)	
	apparent unit cell	stripe phase
b_1 (Å)	8.7(1)	8.7
b_2 (Å)	15.6(1)	110.3
β (°)	103.8(5)	90.0
A_{uc} (Å ²)	131(16)	956
molecules per unit cell	1	7
Two-dim. space group	n.a.	$p211$
\mathfrak{M}	$\begin{pmatrix} 3.00(3) & 0.00(1) \\ -1.29(4) & 3.71(3) \end{pmatrix}$	$\begin{pmatrix} 3.00 & 0.00 \\ 0.00 & 26.00 \end{pmatrix}$

molecular unit cell, which describes the *average* distances between neighboring PTCDA molecules on the K:Ag(110) along the two substrate directions [001] and $[\bar{1}10]$. Note that the realized distances between neighboring PTCDA molecules along [001] amount to either $3.5 a_2$ for neighboring PTCDA molecules across step edges (which result from the K-induced surface reconstruction; see also below) or $4.0 a_2$ for neighboring molecules on a terrace where $a_2 = 4.085 \text{ \AA}$ is the respective surface lattice constant of the Ag(110) substrate (see Fig. 7.2 in Sec. 7.1, page 180, of the present work for a schematic representation of the structure model).²⁸⁹

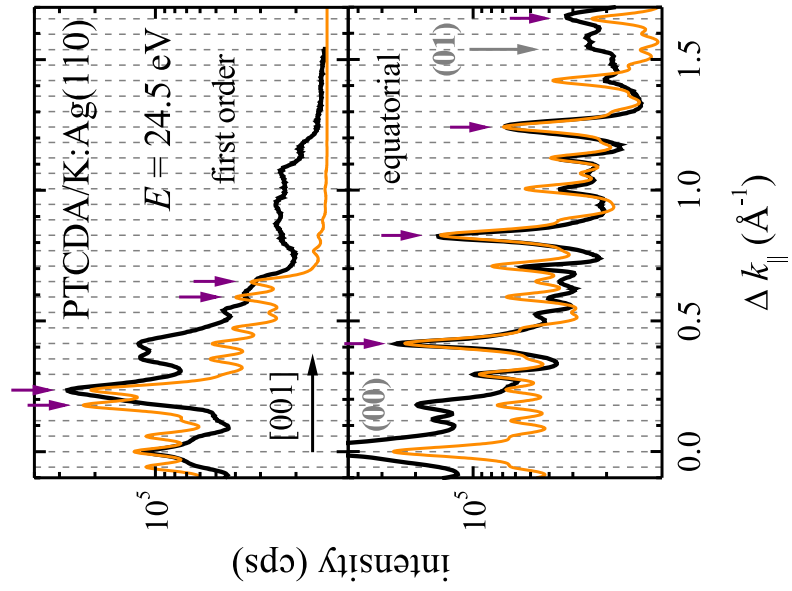
However, the apparent unit cell does *not* represent a structure which is actually realized on the K:Ag(110) surface. This is deduced from the presence of the additional spots of lower intensity in the LEED pattern of PTCDA/K:Ag(110) besides the more intense spots originating from the apparent unit cell. These diffraction spots cannot be explained by the apparent unit-cell structure. Figure D.2 shows one-dimensional LEED scans along the [001] direction for different values

FIG. D.2 (following page). High-resolution one-dimensional LEED scans of PTCDA plus K on the Ag(110) surface along the [001] direction for two individual preparations at two different electron energies, namely, (a) at $E = 20.6 \text{ eV}$ ($\theta_{\text{PTCDA}} = 0.5 \text{ ML}$, after mild thermal annealing at 450 K for 5 min; acquired at a sample temperature of $T_{\text{sample}} = 175 \text{ K}$) and (b) at $E = 24.5 \text{ eV}$ ($\theta_{\text{PTCDA}} = 1.0 \text{ ML}$, after thermal annealing at 570 K for 5 min; $T_{\text{sample}} = 195 \text{ K}$ during data acquisition). In the case of (a), these line scans along the [001] direction represent cuts through the two-dimensional LEED pattern shown in Fig. D.1(a) along the diagonal from lower left to upper right. The line scans were recorded through the specular reflection (bottom; termed “equatorial” here) as well as along the corresponding parallel lines of higher-order diffraction spots, i.e., along lines with greater values of k_{\parallel} with respect to the $[\bar{1}10]$ direction [middle and top; see also the upper left corner of the two-dimensional LEED pattern in Fig. D.1(a)]. Experimental data are shown as black solid lines. In addition, theoretical simulations within the framework of the kinematic approximation²¹⁵ of the experimentally observed LEED data are shown in dark orange, assuming a superstructure with matrix $\mathfrak{M} = \begin{pmatrix} 3 & 0 \\ 0 & 26 \end{pmatrix}$ to be present on the surface, namely, the stripe phase. Substrate spots are marked in gray while those superstructure spots which originate from the apparent unit cell are marked in purple.

(a)



(b)



of k_{\parallel} with respect to the $[\bar{1}10]$ direction, recorded at two different electron energies on two individual preparations. Regarding the two-dimensional LEED pattern from Fig. D.1(a), these line scans represent cuts through the LEED pattern along the diagonal from lower left to upper right. Considering the line scans through the specular reflection, in particular (termed “equatorial” in Fig. D.2), it becomes obvious that six well-resolved satellite spots of lower intensity are present in between the more intense spots of the apparent unit cell, corresponding to a (projected) periodicity of seven PTCDA molecules along the $[001]$ direction. This finding is in full agreement with the above statement that the unit cell of the stripe phase contains seven PTCDA molecules. From the widths of the first-order spots of the apparent unit cell (at $k_{\parallel} = 0.414 \text{ \AA}^{-1}$), effective transfer widths of about 220 \AA and 245 \AA were derived for the employed electron energies of $E = 20.6 \text{ eV}$ and $E = 24.5 \text{ eV}$, respectively. These values correspond to about twice the extension of the stripe-phase unit cell along the $[001]$ direction.

Now the question arises what this comparably large periodicity along the $[001]$ direction originates from. Indications for a conclusive structural model were obtained from STM here. The STM images (data not shown) revealed that the PTCDA-covered Ag(110) surface reconstructs in a columnar or stripe-like motif upon the coadsorption of K atoms such that mono-atomic steps are induced at the surface. As a consequence, terraces are created which extend along the $[\bar{1}10]$ direction of the substrate, i.e., perpendicular to the $[001]$ direction. Along the $[001]$ direction, however, these terraces are limited in width to the lateral extensions of one or two PTCDA molecules (along their long molecular axis) only (and exclusively). Then, a step edge occurs, and the long-range ordered K + PTCDA structure continues on the next terrace. A statistical analysis of the available STM images showed that in 69 % of all cases the projected structure along the $[001]$ direction is given by a 1 down, 2 up, 2 down, 2 up sequence of PTCDA molecules (see Fig. 7.2 in Sec. 7.1, page 180, of the present work for a structural model of the stripe phase).^{a)} The down/up terminology employed here refers to the number of consecutive PTCDA molecules on a lower terrace and an upper terrace, respectively. As shown in orange in Fig. D.2, this structural model allowed to describe the experimentally observed LEED scans quite accurately (see Sec. D.4 below for the computational details). In conjunction with the findings from STM and also ARUPS,⁶⁸ the PTCDA molecules had to be slightly rotated against the $[001]$ direction by 2° with the pivot being on the O_{anhyd} atoms at the step edges in order to achieve this degree of agreement.

Surface reconstruction and K coverage

We now turn to the reconstruction of the Ag(110) surface upon K coadsorption and subsequent annealing. K atoms are known to induce either a (1×2) or a (1×3) reconstruction of the *clean* Ag(110) surface, depending on the K coverage (see also Sec. D.1).²⁸² In order to access the K coverage and thus also the K : PTCDA ratio at the Ag(110) surface in our experiments, we deposited an equivalent amount of K atoms on the clean surface which was found to be the maximal one allowed for the evolution of the well-ordered stripe phase in the case of PTCDA/K:Ag(110). A (1×2) reconstruction was observed in LEED for K/Ag(110) (data not shown). Hence, the surface coverage of K atoms was 0.19 ML or below in this experiment.²⁸² This is equivalent to a K : PTCDA ratio of maximal 2.1 : 1.

However, XPS hinted at an about 50 % larger ratio (see Sec. D.3.2 below), in apparent contradiction to the findings from LEED. Reconciling the results from both XPS and LEED, we thus conclude that the real K : PTCDA ratio was indeed close to the maximal value of 2.1 determined

^{a)}This analysis was performed and kindly provided by Martin Willenbockel from Forschungszentrum Jülich (Jülich, Germany).

with LEED (and not significantly smaller, as would still be consistent with the findings from LEED; see also Sec. D.1). Hence, the structural model in Fig. 7.2 employs a K : PTCDA ratio of exactly 2 : 1, considering also the above conclusion of a well-defined, commensurate registry between the K atoms and the PTCDA molecules at the Ag(110) surface.

In conjunction with our XPS results, showing the largest shifts in binding energy upon K coadsorption for the O atoms (see Sec. D.3.2), and with our XSW results (see Sec. D.3.3), we positioned the K atoms underneath the O_{anhyd} atoms of the adsorbed PTCDA molecules *within* the Ag(110) surface layer in our structural model. Hence, according to our model, a *local* (1 × 3) reconstruction of the Ag(110) surface in the case of PTCDA/K:Ag(110) is present, in fact, while a (1 × 2) reconstruction was observed for the clean surface (see above).²⁸²

Temperature dependence

The commensurability of the stripe phase of PTCDA/K:Ag(110) was also proven by temperature-dependent one-dimensional LEED measurements. We recorded line scans along the [001] direction for 1.0 ML PTCDA/K:Ag(110) (in the stripe phase; see Fig. D.3) for temperature T in the range from 300 K to 700 K and monitored the positions of the superstructure spots as a function of T . This layer had been prepared by an initial annealing step at 500 K for 5 min directly after K deposition on 1.0 ML PTCDA/Ag(110). However, the expected six satellite spots between the more intense apparent-unit-cell spots (see above) could not be resolved here. Therefore, we analyzed the observed, *effective* satellite spots here. These spots are effective in the sense that they most likely are composed of two individual peaks of the stripe phase, as can be deduced from the comparison with better-resolved LEED scans (shown in gray in Fig. D.3).

With increasing T , the superstructure diffraction spots shifts towards lower k_{\parallel} values due to thermal expansion (see below). In addition, the spot profiles sharpen, which is indicative of an increasing surface order upon thermal activation. However, for $T > 650$ K the spots broaden significantly and decrease in intensity at the same time. This effect is not reversible upon cooling. Thus, we conclude that the stripe phase is stable only for $T \leq 650$ K. Furthermore, we speculate that the stripe phase is the thermodynamically favored phase because there are no indications for the presence of other phases and/or a phase transition in this temperature range. Besides, the stripe phase can in principle be obtained by depositing PTCDA on the already K-modified Ag(110) surface, i.e., for the reverse chronological order of evaporation of the two materials, too, as individual experiments have shown (see also Sec. D.2). This finding further corroborates the above conjecture.

The observed spot profiles in Fig. D.3 were fitted with Lorentzian functions (depicted in green), yielding the corresponding explicit $k_{\parallel}(T)$ values. The fitting results for the spots positioned at about $k_{\parallel} = 0.41 \text{ \AA}^{-1}$ (apparent unit cell) and $k_{\parallel} = 0.56 \text{ \AA}^{-1}$ (stripe phase) are shown in a graphical representation in Fig. D.4. In addition, the expected spot positions $k_{\parallel}(T)$ based on the thermal expansion coefficients of pure Ag and pure K (as bulk materials) are plotted as dashed lines.²⁹⁰ The spot positions of the apparent unit cell agree well with the expectation for the case that the thermal expansion is analogous to that of the Ag substrate (shown in purple in Fig. D.4). This finding is only plausible for a *commensurate* registry between the K + PTCDA overlayer and the Ag(110) surface, in full agreement with the results obtained from the two-dimensional LEED patterns (see above).

Note that this agreement was not found for the stripe-phase spots (shown in orange in Fig. D.4), in apparent contradiction to the above conclusion. Here, the observed thermal expansion is larger than that of the Ag substrate, thereby leading to more pronounced shifts towards lower $k_{\parallel}(T)$ values

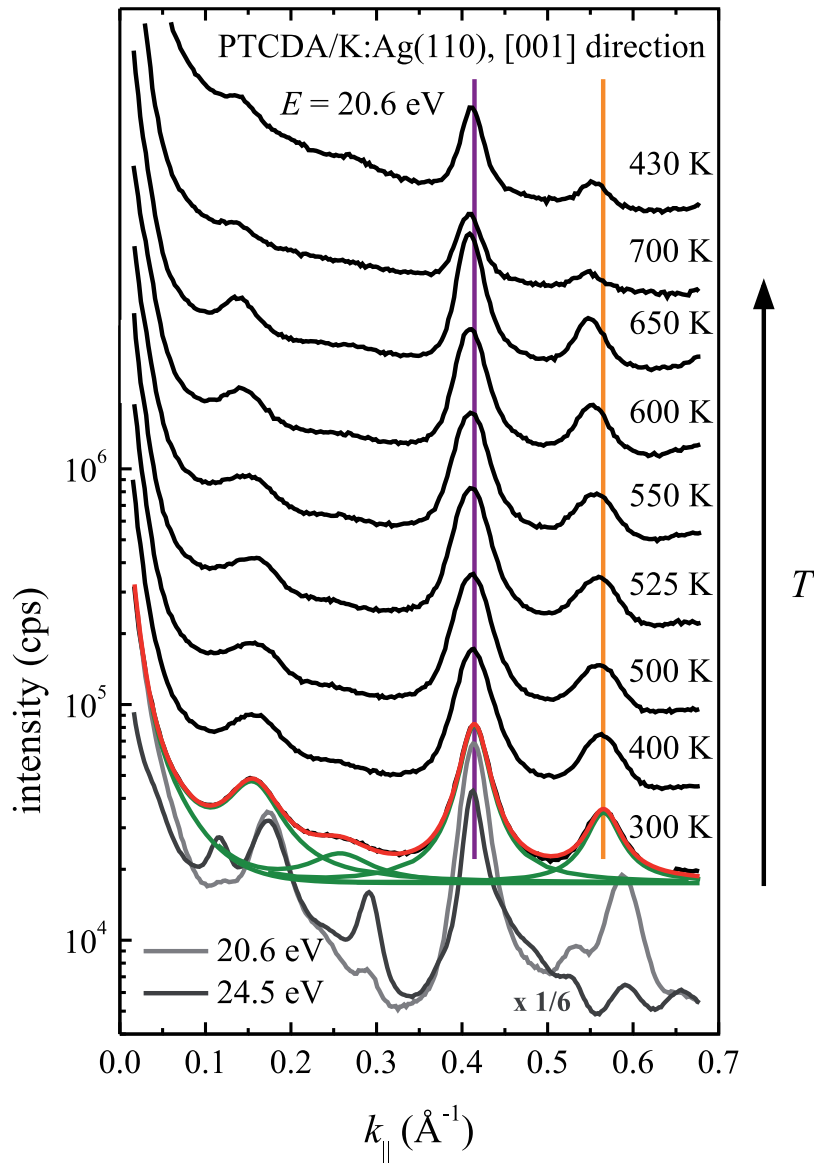


FIG. D.3. One-dimensional LEED scans of PTCDA plus K on the Ag(110) surface along the [001] direction as a function of temperature T ($\theta_{\text{PTCDA}} = 1.0 \text{ ML}$; note that, prior to the present experiment, the prepared layer had already been thermally annealed at 500 K for 5 min once). All measurements were performed at an electron energy of $E = 20.6 \text{ eV}$. The sample temperature $T = T_{\text{sample}}$ was varied in a range from 300 K to 700 K. The individual spot profiles were fitted with Lorentzian functions, as exemplarily shown in green for the line scan recorded at $T_{\text{sample}} = 300 \text{ K}$. The sum of all fitting curves to the individual spot profiles is represented by a red line. Spot positions of the LEED spots originating from the apparent unit cell and the stripe phase at $T_{\text{sample}} = 300 \text{ K}$ are marked in purple and orange, respectively. See Fig. D.4 for a graphical representation of the peak positions as a function of $T = T_{\text{sample}}$. Note that the LEED spot of the stripe phase at a k_{\parallel} value of about 0.56 \AA^{-1} is an effective peak in the sense that it is most likely composed of two individual peaks which were not resolved in this experiment. For reasons of comparison, high-resolution LEED scans from different preparations which were acquired at $E = 20.6 \text{ eV}$ [$T_{\text{sample}} = 175 \text{ K}$; see also Fig. D.2(a), bottom] and $E = 24.5 \text{ eV}$ [scaled by a factor of 1/6; $T_{\text{sample}} = 195 \text{ K}$; see also Fig. D.2(b), bottom] are shown in light and dark gray, respectively. These profiles were thoroughly corrected for thermal expansion effects of the Ag substrate²⁹⁰ here in order to allow for a direct comparison with the experimental data obtained at $T_{\text{sample}} = 300 \text{ K}$.

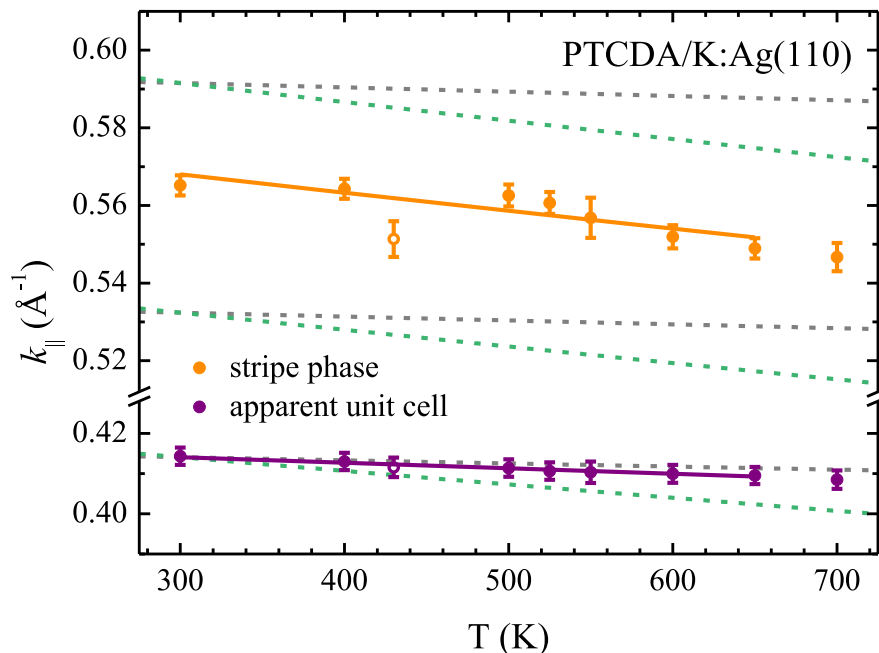


FIG. D.4. Graphical representation of the spot positions observed in LEED for PTCDA plus K on the Ag(110) surface as a function of temperature $T = T_{\text{sample}}$. The (effective) spot positions of both the apparent unit cell (shown in purple) and the stripe phase (shown in orange) were derived from fits to one-dimensional LEED spot profiles (see Fig. D.3). The LEED spot profiles were collected on a preparation with 1.0 ML PTCDA/K:Ag(110) along the [001] direction. Filled symbols refer to the spot positions during the heating cycle while open symbols refer to the spot positions during the subsequent cooling to room temperature. Full lines represent linear fits to the data. Gray and green dashed lines indicate the spot positions which had been expected assuming the thermal expansion coefficients of Ag and K, respectively, as bulk materials to apply here.²⁹⁰

with increasing T . This would indicate an incommensurate registry between the (K +)PTCDA overlayer and the (K-modified) Ag(110) surface, in principle. However, we postulate that the experimental data is deceptive at this point and that the trend derived from the apparent-unit-cell spots, i.e., the shifts of the diffraction spot positions being analogous to those expected for the Ag substrate due to the commensurate registry, is indeed correct. The behavior of the stripe-phase and the apparent-unit-cell spots as a function of T must principally be the same because they represent one and the same structure. Therefore, we attribute the observed discrepancies to the fact that potential relaxations of the surface layer (and maybe also of the PTCDA layer) upon thermal treatment led to intensity modulations of the intrinsic superstructure spots for the stripe phase. These intensity modulations resulted in apparent, additional shifts of the poorly resolved and thus only *effective* stripe-phase spots observed in this experiment.

D.3.2 Electronic structure of the core levels in PTCDA

In extension of the XPS investigations on PTCDA/Ag(110), which have already been presented in Sec. C.3.3, we performed core level spectroscopy also on PTCDA/K:Ag(110). The results for the adsorbate levels, namely, the C1s, O1s, K1s, and K2p signals, will be presented in this section. Note that the results for the substrate levels, i.e., for the the Ag3d XP and AgM₅N₄₅N₄₅

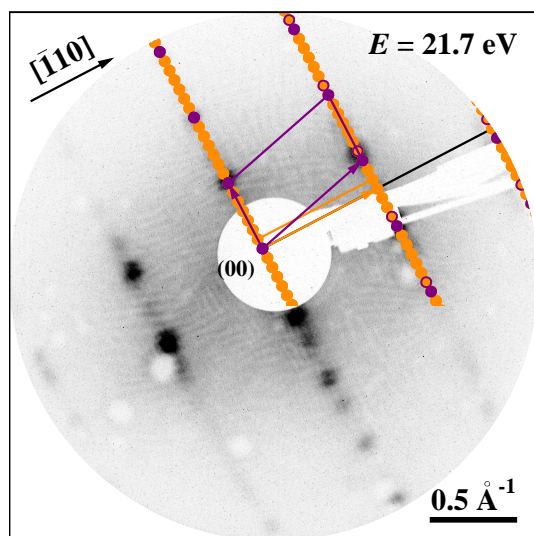


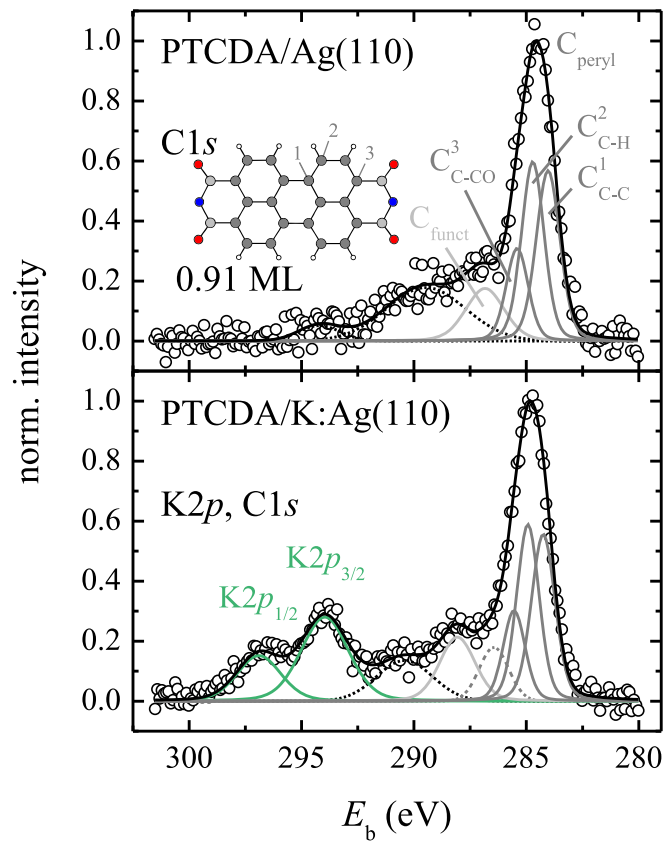
FIG. D.5. LEED pattern of PTCDA plus K on the Ag(110) surface as employed in the XPS and XSW experiments (taken at the ESRF prior to the XPS and XSW experiments; $E = 21.7$ eV, $T = 340$ K). The PTCDA coverage amounted to $\theta_{\text{PTCDA}} = 0.91(4)$ ML (preparation no. Feb'09-2b). The spots of the PTCDA/K:Ag(110) stripe phase can be identified. On the upper right-hand side of the LEED pattern, a simulation is superimposed. Spots originating from the apparent unit cell are shown in purple while stripe-phase superstructure spots are shown in orange. Black lines (one of which is hidden by the orange stripe-phase spots) indicate the reciprocal lattice vectors a_i^* of the substrate.

Auger signals, for both the pure PTCDA/Ag(110) and the PTCDA/K:Ag(110) system have been presented jointly in Sec. C.3.3 already, because substantial differences due to the presence of K atoms at the surface were not observed.

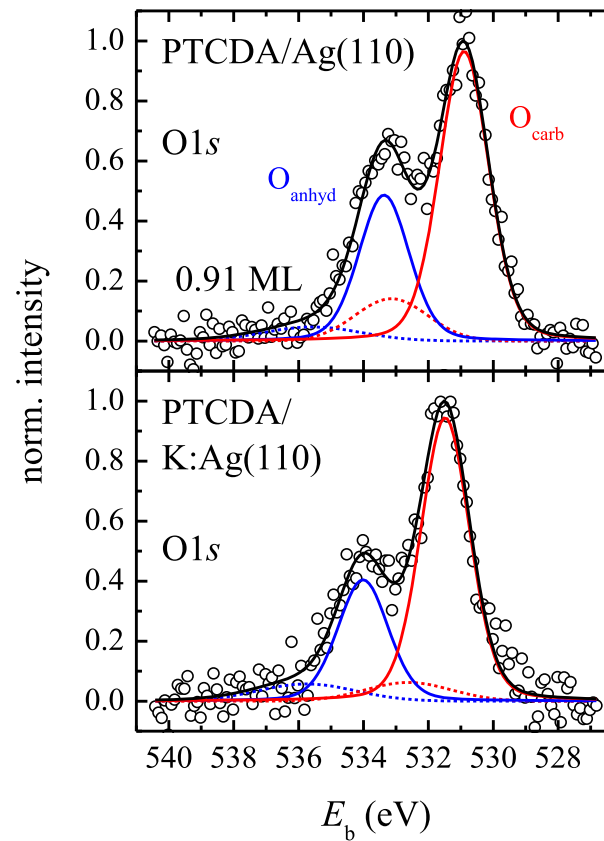
In principle, data acquisition and treatment were again analogous to the general procedure employed for PTCDA/Cu₃Au(111), as has already been described in Sec. 6.6.2 of the present work. A detailed discussion of the XPS data concerning the observed shifts in binding energy E_b for the adsorbate levels between the situation with and without K atoms being present at the PTCDA/Ag(110) interface can be found in Sec. 7.7. At this point, the corresponding experimental data are presented. All XP spectra were acquired at photon energies about 15 eV below the Bragg energy of the (220) Bragg reflection of the substrate (i.e., at $E = 4280.0$ eV). A LEED pattern of the PTCDA/K:Ag(110) sample, which was employed in the XPS as well as in the XSW investigations (see Sec. D.3.3 below), is shown in Fig. D.5. All observed LEED spots are explained by the above-described stripe phase. Hence, the XPS and XSW data were recorded on a phase-pure preparation of PTCDA/K:Ag(110) ($\theta_{\text{PTCDA}} = 0.91(4)$ ML; preparation no. Feb'09-2b), rendering the obtained results and the conclusions derived thereof meaningful.

FIG. D.6 (following page). Normalized XP spectra of the (a) K2p, C1s, and (b) O1s levels of PTCDA plus K on the Ag(110) surface in the (sub-)monolayer regime [PTCDA/K:Ag(110); bottom] in comparison to those of pure PTCDA/Ag(110) (top). The PTCDA coverage amounted to 0.91(4) ML in both cases. The individual XP spectra were acquired with a photon energy of $E = 4280.0$ eV at an effective angle of 45° of the photoelectron analyzer with respect to the surface normal (XSW setup I). All XP spectra were corrected with a linear background function. Contributions from the carbon atoms within the perylene core and within the functional groups are shown in dark gray ($C_{\text{C-C}}$, $C_{\text{C-H}}$, and $C_{\text{C-CO}}$) and light gray (C_{func}), respectively, while the contributions from the chemically nonequivalent oxygen atoms are shown in red (O_{carb}) and blue (O_{anhyd}). Contributions from the potassium atoms are shown in green. The main photoemission peaks are drawn as full lines, the (corresponding) satellite peaks as dashed lines, in respective colors. Unassigned satellite peaks are depicted in black. In addition, the resulting sum of all components is shown as a black line. A ball-and-stick model of the PTCDA molecule is shown as an inset in (a). Note that for the evaluation of the XSW data all C atoms of the perylene core were combined to give the C_{peryl} signal.

(a)



(b)



XP spectra of the adsorbate levels

Figure D.6 displays the experimentally obtained XP spectra of the $C1s$, $K2p$, and $O1s$ levels for PTCDA/K:Ag(110) (bottom). For reasons of convenience, they are contrasted to the corresponding spectra for pure PTCDA/Ag(110) (top), which have already been shown in Fig. C.9 in Sec. C.3.3, page 312, of the present work also. The individual components were fitted with sophisticated fittings models, including the chemically differentiable main components of the $C1s$, $K2p$, and the $O1s$ level, respectively, as well as the corresponding satellite features. The restrictions for developing appropriate XPS fitting models have been outlined in Sec. 4.3.2. For example, the expected stoichiometric ratio of the PTCDA molecule, i.e., $C_{\text{peryl}} : C_{\text{funct}} = 20 : 4$ and $O_{\text{carb}} : O_{\text{anhyd}} = 4 : 2$, had to be fulfilled by the integral peak intensities. The intensity ratio of the $K2p_{1/2}$ and $K2p_{3/2}$ components was fixed to $2 : 4$ in accordance with their degeneracies due to spin-orbit coupling/splitting.³¹⁰ All XPS fitting models are in good agreement with the experimental data. The respective fitting parameters are summarized in Table D.2.

As a general trend, we observed a (differential) shift of the individual $C1s$ and $O1s$ components towards *higher* E_b upon K coadsorption (see Sec. 7.7 for details). Besides, the $C_{\text{peryl, sat}}$ satellite component can now be observed (at $E_b \approx 286.4$ eV), in contrast to the $C1s$ XP spectrum of pure PTCDA/Ag(110). This may be attributed to the large shift of the C_{funct} component for the situation with K atoms in comparison to that without K atoms (by +1.23 eV; see also Table D.2). In the latter case without K atoms, the C_{funct} component may simply have overlaid the $C_{\text{peryl, sat}}$ satellite component. In turn, the previously observed $C_{\text{sat 2}}$ satellite component (at $E_b \approx 294.2$ eV), which is missing in the combined $C1s$ and $K2p$ XP spectrum of PTCDA/K:Ag(110), may be overlaid by the $K2p_{3/2}$ component. It may thus have been overlooked. However, this does not challenge our XPS and XSW results due to the low relative intensity of this component (about 2 % only; see also Table D.2).

The peak positions of the $K2p_{1/2}$ and $K2p_{3/2}$ signals in XPS at *lower* binding energies E_b (by about 0.3–0.7 eV) for PTCDA/K:Ag(110) in comparison to tabulated values for the respective XPS levels of pure K^{162,633, b)} are in apparent contradiction to the postulation of (partially) positively charged K atoms being present at/within the Ag surface layer (also in the presence of the adsorbed PTCDA molecules). The (partial) positive charge on the K atoms results from the charge transfer, i.e., an electron donation, from the alkali metal to the Ag surface atoms, which is the driving force behind the surface reconstruction according to the long-range interaction model proposed by Fu and Ho.⁵⁶⁰ However, positively charged K atoms should in principle exhibit *higher* binding energies for the respective core levels in XPS than neutral K atoms. Thus, we speculate that screening effects by the surrounding Ag substrate (atoms) outweigh the expected increase in E_b here.

In addition, an exemplary XP spectrum of the $K1s$ level is shown in Fig. D.7. Because the integral intensity of this signal, i.e., the photoelectron yield Y_{K1s} , was obtained by numerical integration for the evaluation of the $K1s$ XSW data, the development of an explicit fitting model for the $K1s$ XP level was waived.

K : PTCDA ratio

The K : PTCDA ratio, which was present in the prepared PTCDA/K:Ag(110) system, was deduced from the N_K/N_C stoichiometric ratio and thus from the relative intensities, i.e., the photoelectron yields $Y_{Z,j}$, of the $C1s$ and $K2p$ signals in the XP spectrum of Fig. D.6(a), bottom, by analogy to

^{b)}For example, E_b values of 294.3 eV and 294.7 eV have been reported for the $K2p_{3/2}$ level in pure K,^{162,633} respectively, while we have determined a value of 293.97 eV for $K2p_{3/2}$ in PTCDA/K:Ag(110) (see also Table D.2).

TABLE D.2. XPS fitting parameters for the C1s, K2p, and O1s levels of PTCDA on the Ag(110) surface in the (sub-)monolayer regime [$E = 4280.0$ eV; $\theta_{\text{PTCDA}} = 0.91(4)$ ML; preparation no. Feb'09-2b]. E_b denotes the binding energy, w the width of the peak, and A the relative peak area. The respective values are given for all components observed in the individual XP spectra. For reasons of comparison, also the values for pure PTCDA/Ag(110) at different coverages are given (preparation nos. Feb'09-2a and Apr'08-1, respectively; see also Table C.4 in Sec. C.3.3, page 315, of the present work). The corresponding XP spectra are shown in Figs. D.6 and C.9, respectively. All XP spectra were acquired at an effective angle of 45° of the photoelectron analyzer with respect to the surface normal (XSW setup I). Note that the multilayer XPS data were acquired with a slightly different photon energy of $E = 4276.0$ eV. The C1s, K2p, and O1s main components, namely, C_{C-C} , C_{C-H} , C_{C-CO} , C_{funct} , $K2p_{1/2}$, $K2p_{3/2}$, O_{carb} , and O_{anhyd} , were fitted with pseudo-Voigt functions with 20 % Lorentzian contribution (10 % for the multilayer data), while the satellite components were fitted with pure Gaussian functions. $\Delta E_b = E_{b, \text{mono}} - E_{b, \text{multi}}$ denotes the changes in E_b for the (sub-)monolayer regime with respect to the multilayer regime, i.e., with respect to the condensed PTCDA film. $\Delta E_{b, K} = E_{b, \text{PTCDA/K:Ag(110)}} - E_{b, \text{PTCDA/Ag(110)}}$ denotes the differences in E_b between the situations with and without K atoms being coadsorbed in the (sub-)monolayer regime (n.o. = not observed, n.a. = not applicable/available).

	35.36(71) ML PTCDA/Ag(110)			0.91(4) ML PTCDA/Ag(110)				0.91(4) ML PTCDA/K:Ag(110)				
	E_b (eV)	w (eV)	A (%)	E_b (eV)	w (eV)	A (%)	ΔE_b (eV)	E_b (eV)	w (eV)	A (%)	ΔE_b (eV)	$\Delta E_{b, K}$ (eV)
C_{C-C}	284.93	1.23	29.93	284.03	1.25	24.43	-0.90	284.25	1.25	25.26	-0.68	0.22
C_{C-H}	285.33	1.21	29.93	284.72	1.19	24.43	-0.61	284.93	1.18	25.26	-0.40	0.21
C_{C-CO}	285.44	1.23	14.96	285.41	1.15	12.21	-0.03	285.55	1.15	12.63	0.11	0.14
$C_{\text{peryl, sat}}$	287.34	1.46	3.72	n.o.	n.o.	n.o.	n.a.	286.44	1.54	9.18	-0.90	n.a.
C_{funct}	288.88	1.21	9.00	286.84	2.03	12.21	-2.04	288.07	1.87	14.48	-0.81	1.23
$C_{\text{funct, sat}}$	290.18	1.95	6.72	n.o.	n.o.	n.o.	n.a.	n.o.	n.o.	n.o.	n.a.	n.a.
$C_{\text{sat 1}}$	291.98	4.19	5.74	289.47	4.15	23.22	-2.51	290.42	2.93	13.18	-1.56	0.95
$C_{\text{sat 2}}$	n.o.	n.o.	n.o.	294.21	2.16	3.50	n.a.	n.o.	n.o.	n.o.	n.a.	n.a.
$K2p_{3/2}$	294.30 ^a	n.a.	n.a.	n.a.	n.a.	n.a.	n.a.	293.97	2.50	66.67	-0.33	n.a.
$K2p_{1/2}$	297.30 ^a	n.a.	n.a.	n.a.	n.a.	n.a.	n.a.	296.90	2.30	33.33	-0.40	n.a.
O_{carb}	531.87	1.37	50.57	530.90	1.81	55.80	-0.97	531.48	1.78	60.31	-0.39	0.58
$O_{\text{carb, sat 1}}$	534.20	1.29	13.67	533.14	2.64	10.86	-1.06	532.62	3.12	6.35	-1.58	-0.52
O_{anhyd}	533.59	1.39	31.47	533.37	1.83	28.50	-0.22	534.01	1.84	26.72	0.42	0.64
$O_{\text{carb, sat 2}}$	535.74	1.56	2.41	n.o.	n.o.	n.o.	n.a.	n.o.	n.o.	n.o.	n.a.	n.a.
$O_{\text{anhyd, sat}}$	537.71	3.13	1.88	535.57	3.53	4.84	-2.14	535.75	3.53	6.62	-1.96	0.18

^aTaken from Refs. 162, 302.

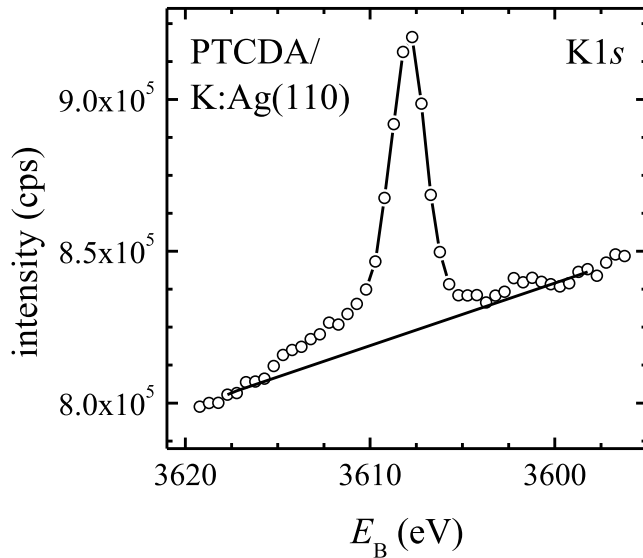


FIG. D.7. $K1s$ XPS spectrum of PTCDA/K:Ag(110) [$\theta_{\text{PTCDA}} = 0.91(4)$ ML]. The spectrum was acquired with a photon energy of $E = 4280.0$ eV at an effective angle of 45° of the photoelectron analyzer with respect to the surface normal (XSW setup I). The employed linear background is shown as a black line.

Eq. (4.6). The employed inelastic mean free paths $\lambda_{\text{IMFP}}(E_{\text{kin},Z,j})$ (within the PTCDA overlayer) and photoionization cross sections $\sigma_{Z,j}(E_{\text{kin},Z,j})$ are tabulated in Tables 4.1 and 4.4, respectively. Here, a *homogenous* distribution of the C and K atoms was (falsely) assumed. This analysis yielded a K : PTCDA ratio of 2.87(27) : 1 [corresponding to $\theta_{\text{K}} = 0.26(2)$ ML in the case of 1 ML PTCDA/Ag(110) as the initial PTCDA coverage]. Under the assumption that the K atoms are located within the Ag surface layer, as derived from XSW, and thus underneath the PTCDA molecules, an additional damping factor according to Eq. (3.53) applies for $Y_{\text{K}2p}$. Considering the actual, layered PTCDA/K:Ag(110) interface structure, a K : PTCDA ratio of 3.03(29) : 1 was obtained [corresponding to $\theta_{\text{K}} = 0.27(3)$ ML].

This ratio of about 3 K atoms per PTCDA molecule on the Ag(110) surface is not compatible with the finding from LEED, saying that the K : PTCDA ratio amounts to only 2.1 : 1 [corresponding to $\theta_{\text{K}} = 0.19$ ML] or less (see Sec. D.3.1). The discrepancy between the results from LEED and XPS may potentially be explained by effects such as the formation of K nanocrystallites on the Ag(110) surfaces, to which the LEED pattern is not sensitive, or the (statistical) decoration of step edges at the Ag(110) surface with the excess K atoms. However, both scenarios have in common that the excess K atoms are not involved in the formation of the ordered K + PTCDA stripe phase. Thus, our structural model for PTCDA/K:Ag(110) is indeed based on an K : PTCDA ratio of 2.0(2) : 1 (including the observed possible variation of $\pm 10\%$) within the stripe-phase domains (see Fig. 7.2).

Position of the K atoms

Eventually, we will discuss the position(s) of the K atoms at the reconstructed Ag(110) surface relative to those of the adsorbed PTCDA molecules and the Ag surface atoms. We have already concluded from the SPA-LEED results that a commensurate registry exists between the K atoms and the PTCDA molecules at the K-modified Ag(110) surface (see Sec. D.3.1). Furthermore, the K : PTCDA ratio has been rationalized to amount to 2.0(2) : 1 from both SPA-LEED and XPS results (see above). Now the question arises where the K atoms are located in this complex K + PTCDA superstructure. Indications have been obtained from XPS in conjunction with STM and XSW results.

Anticipating the result from XSW, the K atoms are incorporated *within* the reconstructed, PTCDA-covered Ag(110) surface layer, as is also the case for the clean Ag(110) surface upon K adsorption.²⁸² The result that the K atoms are located *underneath* the PTCDA molecules is supported by the finding from STM that the K atoms can hardly be imaged for the PTCDA/K:Ag(110) stripe phase while this is indeed possible for another K + PTCDA phase, the so-called X phase, on the Ag(110) surface.^{68,326} XPS revealed that the shifts in binding energy $\Delta E_{b,K}$ for PTCDA/K:Ag(110) in comparison to pure PTCDA/Ag(110) are larger for the O1s main components than for the C1s main components (about +0.6 eV versus +0.2 eV; see also Table D.2). Furthermore, the line widths of the XP levels of the C1s and the O1s main components, respectively, are identical within 8 % for PTCDA on the pure Ag(110) surface and on K:Ag(110). This strongly favors an *identical* positioning of all distinguishable atoms relative to the K atoms because selective proximity and/or interactions between the K atoms and individual C or O atoms within the adsorbed PTCDA molecules are expected to result in line broadening or even the appearance of additional peaks in the XP spectra.

Thus, although the exact positions of the K atoms along the $[\bar{1}10]$ direction as well as the positions of the PTCDA molecules relative to the substrate along this direction are not known with absolute certainty, the structural model in Fig. 7.2 with the K atoms underneath the O_{anhyd} atoms of PTCDA indeed represents the most likely arrangement for the PTCDA/K:Ag(110) interface. It appears plausible that the PTCDA molecules adopt the same adsorption site as on pure Ag(110) due to the strong surface bonding [see Sec. 7.7 for a discussion of the bonding mechanism for PTCDA/K:Ag(110)]. Only a small rotation of the molecules against the [001] direction of 2° was deduced from the STM and SPA-LEED data (see also Sec. D.3.1; a compatible value of 7° for the angle of rotation was also deduced from ARUPS data),⁶⁸ which is not present for pure PTCDA/Ag(110). Hence, the positioning of the individual atoms within the PTCDA molecule, especially those within the perylene core, relative to the surface atoms is assumed to be (nearly) identical for both PTCDA/Ag(110) and PTCDA/K:Ag(110).

D.3.3 XSW photoelectron yield curves

The vertical structure at the metal/organic interface in the PTCDA/K:Ag(110) system, in particular, (a) the adsorption configuration of PTCDA on the K-modified Ag(110) surface as well as (b) the vertical positions of the K atoms were investigated by means of XSW. The data acquisition and treatment were conducted by analogy to the general procedure for the XSW experiments in the case of PTCDA/Cu₃Au(111) (see Secs. 6.3.3, 6.5.3, 6.6.3, and 6.6.4 of the present work) and the pure system, PTCDA/Ag(110) (see Sec. C.3.4), in particular. All XSW experiments on PTCDA/K:Ag(110) were performed in XSW setup I [as was the case for PTCDA/Ag(110), too], where $\theta_p = 45^\circ$ and thus non-nondipolar correction terms apply ($Q, \Delta \neq 0$; see Sec. 3.1.4 for the theoretical background and Table 4.6 in Sec. 4.3.3, page 63, of the present work for the explicit values).

Note that the XSW results for the substrate signals, i.e., for both the Ag3d XPS signal and the AgM₅N₄₅N₄₅ Auger signal, of PTCDA/Ag(110) with and without K atoms being coadsorbed have already been presented in the context of the K-free system (see Sec. C.3.4). The obtained experimental data were considered to be representative of the well-ordered metal crystal in both cases. This is justified by the comparably large escape depth of the Ag3d photoelectrons of almost 30 Å (see also Sec. C.3.4),^{c)} and also by the obtained fitting results for the coherent fractions f_c

^{c)}The escape depth of the AgM₅N₄₅N₄₅ Auger electrons amounts to only 5.0 Å [see also footnote g) in Appendix C, page 317, of the present work].

and the coherent positions p_c , which are close to 1 and 0, respectively (see Table C.5 in Sec. C.3.4, page 325, of the present work).

XSW results for the C1s and O1s signals

Typical XSW photoelectron yield curves of the C1s and O1s XPS signals in PTCDA/K:Ag(110) are shown in Fig. D.8. These XSW curves exhibit a larger scattering in the experimental data points as compared to those of pure PTCDA/Ag(110) (see Fig. C.14 in Sec. C.3.4, page 323, of the present work). This is due to the lower statistics during data acquisition which had to be accepted here in order to minimize beam damage on the PTCDA overlayer upon x-ray illumination (see also Sec. D.2 above).

Nonetheless, the obtained fitting curves are in good agreement with the experimental data. The corresponding fitting parameters for f_c and p_c are summarized in Table D.3 and also contrasted to those obtained for the K-free system. Noticeably, the f_c values in PTCDA/K:Ag(110) [except for $f_c(\text{O}_{\text{carb}})$] are systematically smaller by up to 20 % [$\Delta f_c^{\text{max}} = -0.07(10)$] than those in PTCDA/Ag(110). We attribute this general finding to a (potentially) non-homogeneous K coverage across the substrate surface with the consequence of varying adsorption configurations of the PTCDA molecules (see below for the actual adsorption configuration), leading to a reduction in f_c on average.

The adsorption configuration of PTCDA has changed from arch-like on the pure Ag(110) surface to saddle-like on the K-modified Ag(110) surface (see Fig. 7.16 in Sec. 7.7, page 226, of the present work for a graphical representation of the respective adsorption configurations, for example). In addition, the adsorption heights d of *all* atoms within the PTCDA molecule have increased (see also Table D.3). The overall adsorption height of the molecule on the K-modified Ag(110) surface, as judged from the respective $d(\text{C}_{\text{peryl}})$ values, is larger by 0.07(2) Å as compared to the situation without K atoms. The O_{carb} and O_{anhyd} atoms now reside further away from the surface by as much as 0.32(13) Å and 0.40(10) Å, respectively, in the presence of K atoms within the surface layer (see below). A detailed discussion of the bonding mechanism for PTCDA/K:Ag(110) is given in Sec. 7.7.

XSW results for the K1s and K2p signals

Eventually, we turn to the XSW data of the K atoms in PTCDA/K:Ag(110). Both the K1s and the K2p XPS signals have been employed in our XSW measurements. Typical XSW photoelectron yield curves for the two XPS signals are displayed in Fig. D.9. Both XSW curves principally exhibit the same overall shape. Indeed, fitting these data yields identical results in d within ± 0.02 Å [± 0.01 in p_c ; see also Table D.3], rendering the obtained results self-consistent and thus reliable in the sense that, apparently, they are not corrupted by the employed, theoretically determined nondipolar parameters.

It follows from the averaged $p_c(\text{K})$ value of $\approx 0.00(4)$ that the K atoms reside on the (extended) (220) lattice planes of the Ag(110) substrate. In principle, the adsorption height d of the K atoms is calculated at $d = (n + p_c) d_{hkl}$ with $n = 0, 1, 2, \dots$, where d_{hkl} is the lattice plane spacing of the employed (220) Bragg reflection of the Ag substrate crystal. Since n is a variable parameter, the absolute adsorption height of the K atoms can only be derived from further structural arguments here. For our argumentation, we assume the K atoms to be in commensurate registry with both the Ag atoms and the PTCDA molecules at the surface, as deduced from LEED, and to be located in closest proximity to the O_{anhyd} atoms, as indicated by the observed E_b shifts in XPS (see Sec. D.3.2 above). Reasonable values for the bond lengths $b(\text{O}_{\text{anhyd}}-\text{K})$, which can be obtained from the

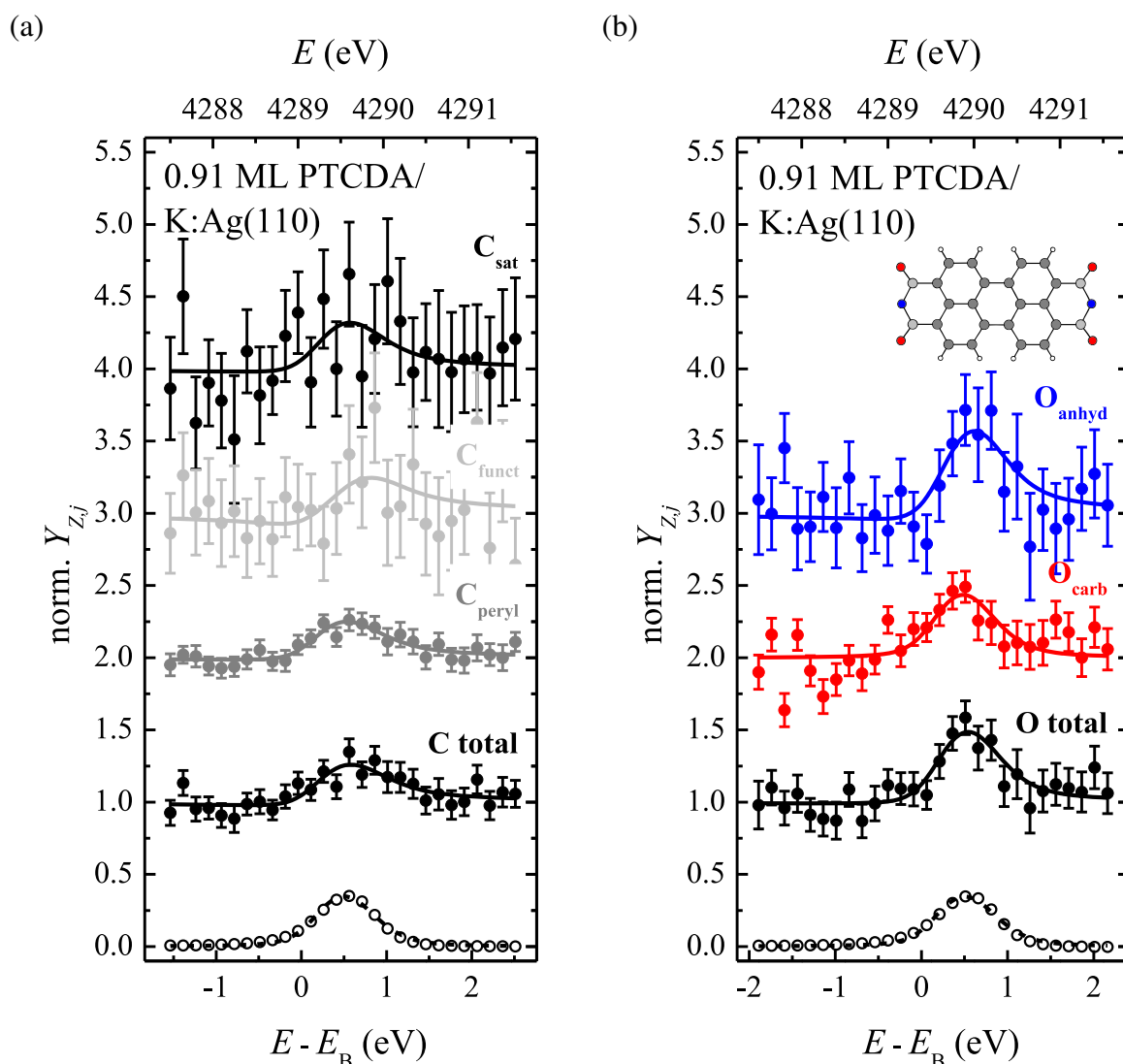


FIG. D.8. Typical XSW photoelectron yield curves of carbon and oxygen in PTCDA plus K on the Ag(110) surface [$\theta_{\text{PTCDA}} = 0.91(4)$ ML; preparation no. Feb'09-2b, which was obtained from preparation no. Feb'09-2a by additional deposition of K atoms and subsequent (mild) annealing]. The (a) $C 1s$ and the (b) $O 1s$ signals were employed in the respective XSW experiments. The XP fitting models allowed for a differential analysis of the XSW data regarding the individual components: (a) C_{peryl} (dark gray), C_{funct} (light gray), and C_{sat} (black) for the $C 1s$ signal, and (b) O_{carb} (red) and O_{anhyd} (blue) for the $O 1s$ signal. In addition, the summed data of the individual $C 1s$ and $O 1s$ components are shown in black. Experimental data points are shown as filled circles while respective fits to the data are shown as solid lines. The curves have been vertically offset for clarity. In addition, the measured reflectivity of the substrate employing the (220) lattice planes (open circles) and the corresponding fit (dashed line) are shown. Error bars have been omitted for clarity here. A color-coded ball-and-stick model of the PTCDA molecule is shown as an inset in (b).

TABLE D.3. XSW results for the adsorption configuration of PTCDA plus K on the Ag(110) surface [PTCDA/K:Ag(110); $\theta_{\text{PTCDA}} = 0.91(4)$ ML; preparation no. Feb'09-2b]. In addition, the XSW results for pure PTCDA/Ag(110) are given for reasons of comparison (preparation no. Feb'09-2a; repeated from Table C.6 in Sec. C.3.4, page 326, of the present work). The Ag3*d*, AgM₅N₄₅N₄₅ (denoted as AgMNN), K1*s*, K2*p*, C1*s*, and O1*s* levels were measured, respectively. The parameters f_c and p_c are the coherent fractions and positions, respectively, which were obtained from the fits to the photoelectron yield curves. The d values denote the averaged vertical adsorption height of the specific atoms. Here, d is calculated at $d = (n + p_c) d_{hkl}$ with $n = 0$ for the Ag and K levels, and $n = 1$ for the adsorbate levels, i.e., C1*s* and O1*s*. d_{hkl} is the lattice plane spacing of the employed (220) Bragg reflection of the Ag substrate crystal. $\Delta d' = d_{\text{PTCDA/K:Ag(110)}} - d_{\text{PTCDA/Ag(110)}}$ denotes the differences in the averaged vertical adsorption heights between the situations with and without K atoms being coadsorbed. $\Delta d = d_{\text{max}} - d_{\text{min}}$ is the absolute (overall) vertical distortion of the (intrinsically planar) PTCDA molecule, $\Delta d(\text{C}) = d(\text{C}_{\text{funct}}) - d(\text{C}_{\text{peryl}})$ is the vertical displacement of the C atoms, and $\Delta d(\text{O}) = d(\text{O}_{\text{anhyd}}) - d(\text{O}_{\text{carb}})$ is the vertical displacement of the O atoms, respectively. For the specification of the atoms, see Figs. C.13(b) and C.14(b), for example. The values for C total and O total were obtained by performing the fitting of the XSW photoelectron yield curves to the sum of the integral intensities of all components contributing to the respective XPS signal (n.a. = not available/applicable).

θ_{PTCDA}	PTCDA/Ag(110)			PTCDA/K:Ag(110)			
	0.91(4) ML			0.91(4) ML			
	f_c	p_c	d (Å)	f_c	p_c	d (Å)	$\Delta d'$ (Å)
Ag3 <i>d</i>	0.80(1)	-0.04(1)	-0.06(1)	n.a.	n.a.	n.a.	n.a.
AgMNN	n.a.	n.a.	n.a.	0.87(7)	-0.01(1)	0.02(2)	n.a.
K1 <i>s</i>	n.a.	n.a.	n.a.	0.32(5)	0.01(3)	0.02(4)	n.a.
K2 <i>p</i>	n.a.	n.a.	n.a.	0.26(6)	-0.01(2)	-0.02(3)	n.a.
C total	0.38(5)	0.77(1)	2.56(1)	0.36(1)	0.84(1)	2.66(2)	0.10(2)
C _{peryl}	0.38(7)	0.79(1)	2.58(1)	0.37(2)	0.83(1)	2.65(2)	0.07(2)
C _{funct}	0.43(1)	0.69(8)	2.45(11)	0.38(10)	0.90(2)	2.75(3)	0.30(12)
C _{sat}	0.39(1)	0.77(1)	2.55(1)	0.36(1)	0.85(4)	2.67(6)	0.12(6)
O total	0.26(3)	0.61(2)	2.33(3)	0.23(7)	0.85(6)	2.67(8)	0.34(9)
O _{carb}	0.24(2)	0.59(3)	2.30(4)	0.25(7)	0.81(8)	2.62(12)	0.32(13)
O _{anhyd}	0.33(6)	0.65(1)	2.38(1)	0.26(8)	0.92(7)	2.78(10)	0.40(10)
Δd (in Å)			0.28(4)			0.16(16)	
$\Delta d(\text{C})$ (in Å)			-0.13(11)			0.10(4)	
$\Delta d(\text{O})$ (in Å)			0.08(4)			0.16(16)	

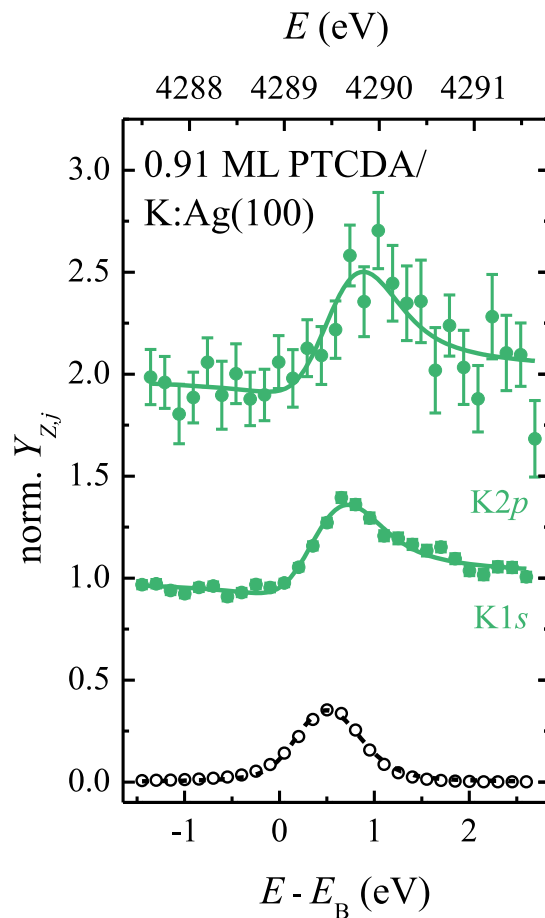


FIG. D.9. Typical XSW photoelectron yield curves of K in PTCDA/K:Ag(110). The K1s (bottom) and K2p XPS signals (top) were employed in the respective XSW experiments. Experimental data points are shown as filled circles while respective fits to the data are shown as solid lines. The curves have been vertically offset for clarity. In the case of K1s, error bars are so small that they are almost hidden by the data points. In addition, the measured reflectivity of the substrate employing the (220) lattice planes (open circles) and the corresponding fit (dashed line) are shown. Error bars have been omitted for clarity here.

individual d values in conjunction with the (relative) lateral positions (see also Sec. 7.7), are only obtained for $n = 0, 4, 5$. We propose those $b(\text{O}_{\text{anhyd}}-\text{K})$ values to be reasonable which are in the range from about 2.7 \AA to 4.4 \AA . This range has been defined from the sum of the covalent (r_{cov}) and van der Waals radii (r_{vdW}) of the involved atoms as the lower and upper bounds, respectively (see also Tables 2.3 in Sec. 2.2.2, page 16, and 7.4 in Sec. 7.3, page 190, of the present work).

For $n = 4, 5$ the K atoms would reside above the PTCDA overlayer at the metal/organic interface. This can in fact be ruled out on the basis of two other independent experimental findings. On the one hand, the reconstruction of the Ag(110) surface and the large periodicity of the K + PTCDA superstructure, which has been observed for the stripe phase with LEED and STM, could hardly be explained. On the other hand, the K atoms being above the PTCDA molecules should in principle be visible in the STM images, as is indeed the case for another phase of K + PTCDA/Ag(110) (the so-called X phase).^{68,326} However, the K atoms in the stripe phase can only be imaged under very special tunneling conditions, i.e., by employing a resonance of the electronic levels in the K atoms.^{68,326} Therefore, only positions of the K atoms *within* the Ag(110) surface layer (for $n = 0$) are plausible, in turn, further validating the above conclusions on the geometrical structure of the PTCDA/K:Ag(110) interface. Due to this incorporation of the K atoms into the Ag surface layer (see Fig. 7.2), the K-modified substrate surface has indeed been termed “K:Ag(110)” in the course of the present work.

D.4 Simulation of the one-dimensional SPA-LEED scans for PTCDA/K:Ag(110)

The computational details of the theoretical simulations of the one-dimensional SPA-LEED scans for PTCDA/K:Ag(110), as shown in Fig. D.2, have already been reported at large in the supplemental material of Ref. 68. For reasons of completeness, these computational details are reproduced here along with the underlying source code.

D.4.1 Computational details

The theoretical simulations were performed with the computer program Mathematica, version 4.2, from Wolfram Research.⁶³⁴ A superstructure with matrix $\mathfrak{M} = \begin{pmatrix} 3 & 0 \\ 0 & 26 \end{pmatrix}$, i.e., a superstructure with a periodicity corresponding to 7 PTCDA molecules along the [001] direction, was assumed to be present on the Ag(110) surface, as indicated from our LEED results (see Sec. D.3.1 above). In conjunction with our findings from STM,^{68,326} the superstructure was modeled by a 1 down, 2 up, 2 down, 2 up sequence of PTCDA molecules along the [001] direction [STM data not shown; see Fig. D.2 on page 342 of this chapter for the experimental LEED data as well as Fig. 7.2 in Sec. 7.1, page 180, of the present work for a structural model of the stripe phase]. The down/up terminology employed here refers to the number of consecutive PTCDA molecules on a lower terrace and an upper terrace, respectively.

The SPA-LEED profiles were simulated in the framework of the kinematic approximation²¹⁵ of electron scattering. The PTCDA molecule, or more precisely, the periodic adsorption unit was modeled as a point-like object. For reasons of simplicity, the K as well as the Ag surface atoms were not considered explicitly, and all atomic form factors were set to 1. The intensity $I(\mathbf{k}_{\parallel}, \mathbf{k}_{\perp})$ of the observed diffraction spots was calculated as:

$$I(\mathbf{k}_{\parallel}, \mathbf{k}_{\perp}) = G(\mathbf{k}_{\parallel}) |F(\mathbf{k}_{\parallel}, \mathbf{k}_{\perp})|^2 \exp\left(-2M |\mathbf{k}_{\parallel}|^2\right), \quad (\text{D.2})$$

where $G(\mathbf{k}_{\parallel})$ is the lattice factor, $F(\mathbf{k}_{\parallel}, \mathbf{k}_{\perp})$ is the structure factor, $\exp\left(-2M |\mathbf{k}_{\parallel}|^2\right)$ is the Debye-Waller factor, and \mathbf{k}_{\parallel} and \mathbf{k}_{\perp} are the parallel and vertical components of the scattering vector $\mathbf{k} = (\mathbf{k}_{\parallel}, \mathbf{k}_{\perp})$ relative to the surface, respectively. The lattice factor $G(\mathbf{k}_{\parallel})$ was given by a sum of δ functions which were convoluted with a Lorentzian of width σ in order to mimic the experimentally observed line shape and to account for (instrumental) broadening:

$$G(\mathbf{k}_{\parallel}) = \sum_j \sigma^2 \left[\sigma^2 + (|\mathbf{k}_{\parallel}| - j)^2 \right]^{-1}. \quad (\text{D.3})$$

The variable j in Eq. (D.3) refers to the position of the respective diffraction spot in reciprocal space. The structure factor $F(\mathbf{k}_{\parallel}, \mathbf{k}_{\perp})$ was calculated as the sum over all molecules i within the unit cell which were described by their position vectors \mathbf{R}_i :

$$F(\mathbf{k}_{\parallel}, \mathbf{k}_{\perp}) = \sum_i \exp[i(\mathbf{k}_{\parallel}, \mathbf{k}_{\perp}) \cdot \mathbf{R}_i]. \quad (\text{D.4})$$

The Debye-Waller factor $\exp\left(-2M |\mathbf{k}_{\parallel}|^2\right)$ served as an effective means for the description of thermal effects and the angular dependence of the atomic form factors. The parameter M is an

adjustable factor and was chosen such that the best agreement with the experimental data was achieved.

As outlined above, the calculations were performed for the periodic adsorbate structure with $\mathfrak{M} = (3\ 0\ | 0\ 26)$ (see also Fig. 7.2). The existence of two rotational and two mirror domains due to the symmetry of the substrate was considered. The PTCDA molecules in the adsorbate layer were rotated by 2° against the [001] direction of the substrate with the pivot being at the O_{anhyd} atoms at the step edges, as deduced from the STM measurements.^{68,326} Vertical relaxations of the PTCDA molecules of up to 0.1 Å were allowed during the fitting process. The presence of multiple scattering effects involving reciprocal substrate vectors was tested but dismissed since no improvement was found for the agreement of the simulated LEED profiles with the experimental data.

Given the simplicity of the simulations, we found very good agreement between theory and experimental data (see Fig. D.2). The intensity of the most intense superstructure spots was fitted very well (marked with purple arrows in Fig. D.2). In general, the relative intensities of the less intense satellite spots were correctly reproduced, although in some cases the absolute intensities were over- or underestimated. Especially, the absolute intensities of the superstructure spots in the vicinity of the specular reflection, i.e., for small values of Δk_{\parallel} in the equatorial line scans [see Figs. D.2(a) and (b), bottom], were underestimated. This can be rationalized by the large contribution of the substrate to the intensity of the (00) spot that could in principle be modeled by a Lorentzian-shaped background (which has been neglected here). The more pronounced reduction of spot intensities for greater values of Δk_{\parallel} in the non-equatorial line scans [see Figs. D.2(a) and (b), both middle and top] in comparison to the equatorial scans is due to the higher sensitivity of these line scans to structural disorder in the adsorbate layer.

In summary, the simulations agree well with the experimentally observed SPA-LEED data. Hence, the structural model which is given in Fig. 7.2 of Sec. 7.1, page 180, of the present work is strongly supported by our electron diffraction data.

D.4.2 Source code

An exemplary source code of a Mathematica routine for simulating the one-dimensional LEED profile of PTCDA/K:Ag(110) in the monolayer regime will be presented in this section. Namely, the source code which allowed to calculate the theoretical LEED profile in Fig. D.2(b), middle ($E = 24.5$ eV, labeled “first-order”), will be shown on the following pages. Comments within the source code are marked/enclosed by “(*)” and “*”, respectively.

```

In[49] := (*****
(* Berechnung von SPA-LEED Profilen *)
(* M. Sokolowski, O. Bauer, ab 11/2010, Version 17.06.11 (21) *)
(* fortgeführt von O. Bauer, ab 01/2012, Version 13.01.12 *)
(*****

(* Model according to SPA-
LEED with two alternating different domains D ("dreifach": 1 down / 2 up)
and V ("vierfach": 2 down / 2 up) on the K + PTCDA /Ag (110) surface *)

(* calculation of spots for ky = (0,1,2)*1/3 ay *)
(* kx (=k, in units of 1/ax) along the [001]-direction,
i.e. perpendicular to close packed rows in reciprocal units of ax = 4.09 Angström *)
(* kz perpendicular to surface with step height of az = 1.44 Angström, i.e. in units 1/az *)
(* This version does include rotation of the molecules around O_anhydride at the step edges,
resembling "midway" appearance in STM *)
(* This version does include disorder and thermal effects as well as the
angular dependence of atom form factors via an effective Debye-Waller factor*)
(* complex numbers are used in this routine *)

ClearAll;

(* definition of experimental parameters *)

ax = 4.0853 ;
ay = 4.0853 / 2 ^ 0.5 ;
az = ax / 2 ^ 1.5 ;
ene = 24.5 ; (* electron energy in eV: 20.6, 24.5, 27.3 *)
k0 = (ene / 150.4) ^ 0.5 ; (* 1/lambda in inv. Ang., factor 2*Pi is omitted *)
ky = 1 * 1 / 3 ; (* in units of 1/ay *)

(* position of PTCDA molecules within the domains in units of ax, ay and az *)
(* Lambda is an additional periodicity *)

Lambda = 7
pha = 0.0
alpha = 2 ;
(* rotation angle of the PTCDA molecule versus [001] substrate direction, in ° (STM: 2 °) *)
derotx = (1 - Cos[Pi / 180 * alpha]) * 1 / 2 * 11.322 / ax ;
(* displacement of the molecular center due to rotation by angle alpha,
pivot is the O_anhydride atom at the step edge, in units of ax *)
deroty = Sin[Pi / 180 * alpha] * 1 / 2 * 11.322 / ay ;
(* displacement of the molecular center due to rotation by angle alpha,
pivot is the O_anhydride atom at the step edge, in units of ay *)
(* The position of the O_anhydride atom at the step edge is calculated relative to the
center of the molecule, assuming PTCDA alpha X-Ray structure (K.Tojo, et al.) *)

dex = -1 / 6 + 1 / 6
rx = {0.0, 3.5 - derotx + dex, 7.5 + derotx - dex,
11 - derotx + dex, 15 + derotx - dex, 18.5 - derotx + dex, 22.5 + derotx - dex} ;
drx = Table[0.0 * Cos[2 * Pi * ((i - 1) / Lambda + pha)], {i, 7}];
trx = rx + drx;

dey = dex;
ry = {0.0, 1.5 - deroty + dey, 2.5 + deroty - dey,
1 - deroty + dey, 2 + deroty - dey, 0.5 - deroty + dey, 1.5 + deroty - dey} ;
(* {3.0, 4.5+dey, 5.5-dey,4+dey,5-dey,3.5+dey,4.5-dey } *)
dry = Table[0.0 * Cos[2 * Pi * ((i - 1) / Lambda + pha)], {i, 7}];
try = ry; (*try=ry+dry;*)

dez = 0.07; (* 0.05-0.1 *)

```

```

dez1 = -1*dez;
dez2 = +1*dez;
dez3 = -1*dez;
dez4 = -0*dez; (* dez4=-1*dez or dez4=-0*dez (for ky=1/3) *)
dez5 = +1*dez; (* dez5=+0*dez or dez5=+1*dez (for ky=1/3) *)
dez6 = -1*dez;
dez7 = +1*dez;
rz = {0+dez1, 1.0+dez2, 1.0+dez3, 0+dez4, 0+dez5, 1.0+dez6, 1.0+dez7};
(* {0,1.0+dez,1.0-dez,0-dez,0,1.0-dez,1.0+dez *}
drz = Table[0.0*Cos[2*Pi*(i-1)/Lambda+pha]], {i, 7}];
trz = rz + drz;

xz = Table[{trx[[i]], trz[[i]]}, {i, 7}]
nxz = Table[{rx[[i]], rz[[i]]}, {i, 7}]
xy = Table[{trx[[i]], try[[i]]}, {i, 7}]
nxy = Table[{rx[[i]], ry[[i]]}, {i, 7}]
yz = Table[{try[[i]], trz[[i]]}, {i, 7}]
nyz = Table[{ry[[i]], rz[[i]]}, {i, 7}]

(* parameters for profile width & thermal/disorder/atom form factor effects*)
fwhm = 0.020;
sigma = 0.60*fwhm;
M = 7.5 (* effective DW factor = exp(-2 M*k_parallel^2);
20.6 eV: 2 M = 0.4, 24.5 eV: 2 M = 0.85 for equatorial scans*)
n = 2; (* Lorentzian line shape exponent, in units of -1/2; n=2 Lorentzian; n=3 Lorentzian^3/2 *)

(*****
(* Calculation of the intensity, i.e. lattice factor G * structure factor F squared *)

kz = ((2*Cos[Pi/180*4/2]*k0)^2 - (k/ax)^2 - (ky/ay)^2)^0.5;
(* as required for SPA-LEED, in units of 1/lambda *)
(* Do we need to correct the first term with 2*Pi
here? => No since k0=1/lambda instead of 2*Pi/lambda, see above. *)

ha[k_] := 1/4 * ( Sum[2*sigma^(n)/2*(sigma^2+(k-j/26)^2)^(-n/2)*
((1/7.0)*Abs[Sum[Exp[I*2*Pi*(j/26*trx[[i]]+ky*try[[i]]+kz*trz[[i]]*az)]]^2) +
1/4 * ( Sum[2*sigma^(n)/2*(sigma^2+(k-j/26)^2)^(-n/2)*
((1/7.0)*Abs[Sum[Exp[I*2*Pi*(j/26*trx[[i]]-ky*try[[i]]+kz*trz[[i]]*az)]]^2) +
1/4 * ( Sum[2*sigma^(n)/2*(sigma^2+(k-j/26)^2)^(-n/2)*
((1/7.0)*Abs[Sum[Exp[I*2*Pi*(-j/26*trx[[i]]+ky*try[[i]]+kz*trz[[i]]*az)]]^2) +
1/4 * ( Sum[2*sigma^(n)/2*(sigma^2+(k-j/26)^2)^(-n/2)*
((1/7.0)*Abs[Sum[Exp[I*2*Pi*(-j/26*trx[[i]]-ky*try[[i]]+kz*trz[[i]]*az)]]^2)

```

$$2 \left. \right) \left. \right) * \text{Exp}[-2 * M * (k^2 + (0 * ky * 2 * \text{Pi} / ay)^2)];$$

```
(* First factor describes instrumental and disorder broadening (lattice factor G *)
(* index j refers to the specific spot on the k axis,
index i to the position vector of the molecule *)
(* symmetry-equivalent domains are included
(2 x rotation, 2 x mirroring) by changing the signs in kx and ky*)

(* Adding some background and scaling *)

fa[k_] := (50 * ha[k] + 1) * 15000.

(* going to the experimental k scale = 2*Pi/lambda in inv. Angstroems *)
(* kz remains unaffected by this correction/transformation,
as desired; this has been exemplarily tested. *)

faexp[k_] := fa[ax*k / (2 * Pi)] (* ax/2*Pi = 0.65 *)

Export["SPA-LEED_1D_20.dat", Table[{k, faexp[k]}, {k, -2.0, 2.0, 0.001}]];
(* Plot[faexp[k], {k, -0.1, 1.7}, PlotPoints -> 2000, PlotRange -> {0, 11000}] *)

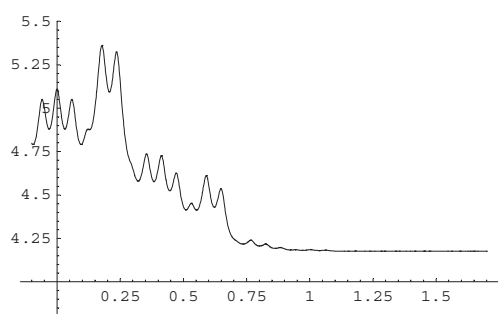
(* calculation of the profile on the log scale *)

logfaexp[k_] := Log[10, faexp[k]]
Plot[logfaexp[k], {k, -0.1, 1.7}, PlotPoints -> 2000, PlotRange -> {3.8, 5.5}]

(* Here we would need an additional routine plotting the positions of the molecules *)

(* ListPlot[xz, Prolog -> AbsolutePointSize[10]]
ListPlot[xy, Prolog -> AbsolutePointSize[10]] *)

Out[56]= 7
Out[57]= 0.
Out[61]= 0
Out[80]= {{0., -0.07}, {3.49916, 1.07}, {7.50084, 0.93},
{10.9992, 0.}, {15.0008, 0.07}, {18.4992, 0.93}, {22.5008, 1.07}}
Out[81]= {{0., -0.07}, {3.49916, 1.07}, {7.50084, 0.93},
{10.9992, 0}, {15.0008, 0.07}, {18.4992, 0.93}, {22.5008, 1.07}}
Out[82]= {{0., 0.}, {3.49916, 1.43161}, {7.50084, 2.56839}, {10.9992, 0.931608},
{15.0008, 2.06839}, {18.4992, 0.431608}, {22.5008, 1.56839}}
Out[83]= {{0., 0.}, {3.49916, 1.43161}, {7.50084, 2.56839}, {10.9992, 0.931608},
{15.0008, 2.06839}, {18.4992, 0.431608}, {22.5008, 1.56839}}
Out[84]= {{0., -0.07}, {1.43161, 1.07}, {2.56839, 0.93},
{0.931608, 0.}, {2.06839, 0.07}, {0.431608, 0.93}, {1.56839, 1.07}}
Out[85]= {{0., -0.07}, {1.43161, 1.07}, {2.56839, 0.93},
{0.931608, 0}, {2.06839, 0.07}, {0.431608, 0.93}, {1.56839, 1.07}}
Out[88]= 7.5
```



Out [96]= - Graphics -

E

Influence of the nondipolar parameters on the XSW fitting results

The fitting parameters coherent fraction f_c and the coherent position p_c obtained from the analysis of the experimental XSW photoelectron yield curves are influenced by the choice of the nondipolar parameters Q and Δ (see Sec. 3.1.4).^{176,190} Concerning the XSW experiments performed in the context of the present work, only the data collected in XSW setup I are affected where $\theta_p = 45^\circ$ (see Sec. 4.1.2, in particular Fig. 4.2 on page 45 of the present work), i.e., the XSW data on PTCDA/Ag(110) and K + PTCDA/Ag(110) (preparations Feb'09-1, Feb'09-2a, and Feb'09-2b, respectively; see Table 4.3 in Sec. 4.3.2, page 56, of the present work). The XSW data collected in XSW setup II are not affected because $\theta_p = 0^\circ$ applies there (see Sec. 4.1.2, in particular Fig. 4.3 on page 46 of the present work, for a schematic layout of the experimental setup and Sec. 3.1.4 for the theoretical background).

In principle, Q and Δ are available from XSW experiments.^{176,190,332} However, the experimentally obtained Q values may be subject to a large variation (by a factor of up to ≈ 2).^{190,332} From these experiments, it is apparent that the Q values do not only depend on the chemical element and the kinetic energy of the respective photoelectrons but also on the chemical surroundings,^{332,635} e.g., within a molecule and/or on a surface. However, experimentally determined Q values for the C1s and O1s XPS signals of PTCDA on the pure and K-modified Ag(110) surface are not available unfortunately (see also Sec. 4.3.3). Hence, we have employed theoretically predicted Q and Δ values (which apply to the free atoms in the strict sense) in the framework of the present work which were taken from the literature.^{197,199} In order to evaluate the impact of the chosen nondipolar parameter Q on the fitting results obtained for both f_c and p_c , systematic tests have been performed (see below). Explicit tests also for the Ag3d, K1s, and K2p signals have been waived here.

The variation in p_c due to the chosen Δ value amounts to 0.01 only (as compared to the situation with $\Delta = 0$), as can be deduced from Eq. (3.37) in conjunction with Eq. (3.33) using the theoretical Q values. This is equivalent to a variation in d of maximal 0.02 Å, considering the lattice plane spacing $d_{hkl} = 1.444$ Å of the (220) Bragg plane in Ag,²⁸⁹ and is thus negligible. Note that the fitting result for f_c is not affected by the choice of Δ .

In order to test the influence of the chosen Q value on the fitting results, the available data sets for the C1s total and the O1s total signals of both PTCDA/Ag(110) and K + PTCDA/Ag(110) have been re-fitted exemplarily while Q was varied in the range from 0.00 to 0.40 in steps of 0.02. Δ was kept constant at the theoretically derived values (see Table 4.6 in Sec. 4.3.3, page 63, of the present work for the explicit values).¹⁹⁹ Note that these test fittings were performed with XSWAVES, version 2.3, while all other fittings of XSW data within the framework of the present study were performed with XSWAVES, version 2.5. Due to slight imperfections of the earlier XSWAVES version in the computation of the parameter P , which accounts for the polarization of

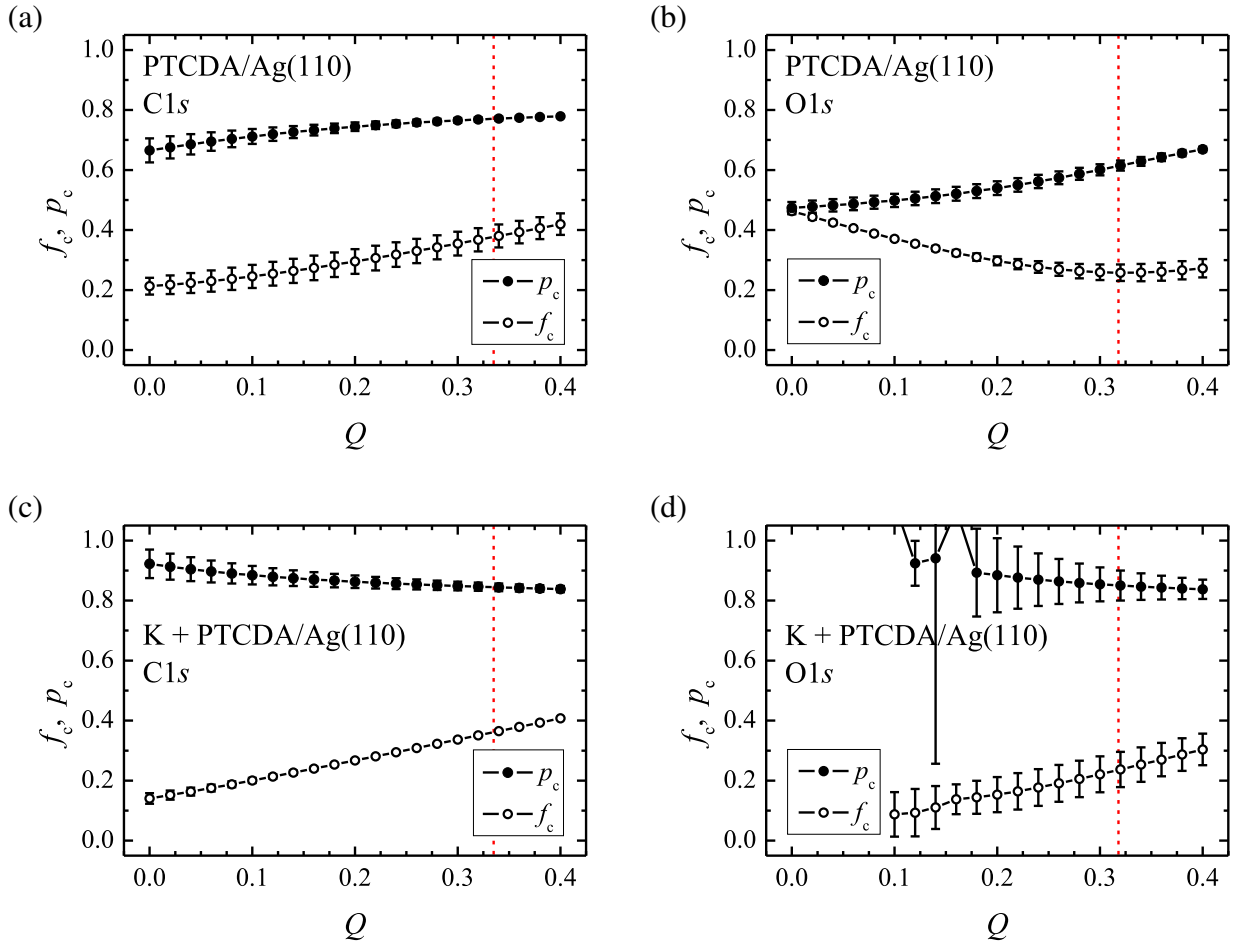


FIG. E.1. Impact of the nondipolar parameter Q on the averaged XSW fitting results for the coherent fraction f_c and the coherent position p_c in the cases of PTCDA/Ag(110) (top row) and K + PTCDA/Ag(110) (bottom row), respectively. (a, c) The C1s total and (b, d) the O1s total signals were employed in the present evaluation. The Q value was varied in steps of 0.02 in a range from 0.00 to 0.40. Note that in the case of (d), i.e., the O1s total signal of K + PTCDA/Ag(110), physically meaningful fitting results could not be obtained for $Q \lesssim 0.10$ because the corresponding fitting processes did not converge. The averaged results for f_c and p_c are shown as open and filled circles, respectively. Lines are guides to the eye. In some cases the error bars are so small that they are (almost) hidden by the data points. The red dashed lines mark the theoretically predicted Q values as obtained from tabulated values¹⁹⁷ for the respective kinetic energies of the photoelectrons and for the actual geometric circumstances in XSW setup I, i.e., for $\theta_p = 45^\circ$ (see Table 4.6 in Sec. 4.3.3, page 63, of the present work for the explicit values). The nondipolar parameters Δ were kept constant at the theoretically predicted values in all cases (see Table 4.6 in Sec. 4.3.3, page 63, of the present work for the explicit values).¹⁹⁹

the x-ray beam,³²⁹ small systematic variations in the fitting results were encountered. However, they amounted to maximal ± 0.01 in the averaged results of both f_c and p_c and are thus negligible.

Figure E.1 shows the obtained averaged fitting results for both the coherent fraction f_c (open circles) and the coherent position p_c (filled circles) for different values of Q in a graphical manner. The averaged p_c results remain essentially constant, in particular in the range of about ± 0.10 around the theoretically predicted Q values (marked by red dashed lines in Fig. E.1), except for the O1s total signal of PTCDA/Ag(110). Here, the averaged p_c result varies by about $\pm 10\%$ in this

range [see Fig. E.1(b)]. However, the averaged f_c results are strongly affected, that is, by a factor of 2 to 3 in all cases. This finding may partly explain the fact that the coherent fractions obtained for the individual C1s and the O1s XPS components of both PTCDA/Ag(110) and K + PTCDA/Ag(110) are much smaller in comparison to the cases of PTCDA on other coinage metal surfaces (by about 20 % and 50 % for C1s total and O1s total, respectively;⁶⁶ see also Secs. C.3.4 and D.3.3 in the appendix of the present work as well as Sec. 6.6.4). Note that in the case of the O1s total signal of K + PTCDA/Ag(110) [see Fig. E.1(d)] physically meaningful fitting results could not be obtained for $Q \lesssim 0.10$ because the corresponding fitting processes did not converge.

In conclusion, the variation of p_c with the actual choice of the Q value is found to be well within the experimental accuracy and thus negligible for the systems within the scope of the present work [$\Delta p_c = \pm 0.01(4)$ on average if $\Delta Q = \pm 0.10$ is considered for Q values in the (presumably) relevant range of 0.20 to 0.40¹⁹⁰]. The variation of f_c with Q may give rise to small systematic deviations of $\Delta f_c = \pm 0.05(4)$ on average if $\Delta Q = \pm 0.10$ is considered here. Yet, this potential systematic deviation does not question the general conclusions drawn from our XSW results within the framework of the present study. Note, however, that the degree of variation in the fitting results for both the coherent fraction and the coherent position due the actual choice of Q principally depends on the realized combination of the true f_c and p_c values in each individual case.

F

Validity of the computational algorithm of XSWAVES, version 2.5

Very recently, after the XSW data evaluation presented in this work had been finalized, Bocquet and Lee⁶³⁶ stated that the XSW data evaluation routines XSWAVES³²⁹ and Torricelli³³⁰ both exhibit an approximation within their computational algorithms which may affect the quality of the obtained XSW fitting curves and thus the validity of the obtained fitting results as well as the conclusions drawn thereof. In order to validate our XSW results, which are presented throughout this work, we have systematically examined the effect of the approximation on the obtained values of the coherent fraction f_c and the coherent position p_c , respectively.

Controversial approximations in the computational algorithm of XSWAVES

In the source code of XSWAVES, version 2.5 and earlier (see Sec. A.3 for details), the broadening of the perfect reflectivity $R(E)$ and the perfect (normalized) XSW photoelectron yield $Y_{Z,j}(E)$ curves—collectively referred to as $\Upsilon_{\text{theo}}(E)$ here—due to both the finite width of the x-ray beam and instrumental effects are described by a *convolution* of the perfect signal with the squared reflectivity of the Si(111) crystals in the double-crystal monochromator, $[R_{\text{mono}}(E)]^2$, and a Gaussian function, termed $G(E)$, giving the non-normalized, experimentally observable data curve [see also Eq. (A.2)]:

$$\Upsilon_{\text{exp}}(E) = A \cdot \left\{ \Upsilon_{\text{theo}}(E) * [R_{\text{mono}}(E)]^2 * G(E) \right\} + \Delta\Upsilon_{\text{exp}}. \quad (\text{F.1})$$

Here, $\Upsilon(E)$ denotes the [non-normalized, experimentally obtained (exp) or normalized, theoretically predicted (theo)] signal of interest, that is, either $R(E)$ or (normalized) $Y_{Z,j}(E)$, A is a normalization factor, and $\Delta\Upsilon_{\text{exp}}$ is an offset. The convolutions in the above equation are computed in two successive steps, namely, for the ideal signal (without instrumental broadening besides the finite width of the x-ray beam) as [see also Eq. (A.7)]:

$$\Upsilon_{\text{ideal}}(E) = F(E) = \Upsilon_{\text{theo}}(E) * [R_{\text{mono}}(E)]^2, \quad (\text{F.2})$$

and for the real, i.e., the normalized, theoretically predicted signal including broadening effects as [see also Eq. (A.8)]:

$$\Upsilon_{\text{real}}(E) = F(E) * G(E) = \int_{-\infty}^{\infty} F(\epsilon) G(E - \epsilon) d\epsilon, \quad (\text{F.3})$$

with ϵ being an auxiliary variable with the dimension of an energy. Note that $\Upsilon_{\text{ideal}}(E)$ is referred to as $F(E)$ ($\hat{=}$ “F”) in the source codes of the XSWAVES fitting routines (see also Sec. A.4).

In the strict physical sense, the Eqs. (F.2) and (F.3) only apply on those cases where $[R_{\text{mono}}(E)]^2$ and $G(E)$ are even, i.e., symmetric functions.^{a)} This is indeed the case for the Gaussian function $G(E)$. However, the squared reflectivity of the Si(111) crystals in the double-crystal monochromator, $[R_{\text{mono}}(E)]^2$, by nature is an odd, i.e., asymmetric function (see also Sec. 3.1.2 for details on the calculation of the reflectivity curve). Because a convolution mirrors the so-called response function, i.e., $[R_{\text{mono}}(E)]^2$ or $G(E)$ in the present case, around the y axis by definition,^{585,586} it does not correctly describe the broadening of the perfect signal by an *asymmetric* response functions. In order to avoid the physically incorrect and thus unwanted mirroring, Eqs. (F.2) and (F.3) should read as:

$$\Upsilon_{\text{ideal}}(E) = F(E) = \Upsilon_{\text{theo}}(E) * [R_{\text{mono}}(-E)]^2 \quad (\text{F.4})$$

and:

$$\Upsilon_{\text{real}}(E) = F(E) * G(-E) = \int_{-\infty}^{\infty} F(\epsilon) G(E + \epsilon) d\epsilon, \quad (\text{F.5})$$

respectively. As already noted above, the Gaussian function is symmetric [$G(E) = G(-E)$] and therefore Eqs. (F.3) and (F.5) are in fact equivalent. However, this is not true for Eqs. (F.2), and (F.4) because the squared reflectivity of the Si(111) crystals in the double-crystal monochromator, $[R_{\text{mono}}(E)]^2$, is not a symmetric function, i.e., $[R_{\text{mono}}(E)]^2 \neq [R_{\text{mono}}(-E)]^2$. Hence, the computation of the first convolution step according to Eq. (F.2) may result in systematic deviations in the fitting results from the true values.

Validity of the fitting results

In order to quantify the potential impact of the above-described approximation on the XSW fitting results, in particular regarding the f_c and p_c values, we have re-analyzed exemplary XSW data sets for every signal of interest of each and every system presented in this work, namely, for clean $\text{Cu}_3\text{Au}(111)$, PTCDA/ $\text{Cu}_3\text{Au}(111)$, PTCDA/ $\text{Ag}(100)$, PTCDA/ $\text{Ag}(110)$, and PTCDA/ $\text{K:Ag}(110)$. In summary, the effects of the computational approximations in XSWAVES on the relevant fitting parameters are well within the experimental errors and thus negligible. We emphasize that our conclusions drawn from the experimental results are hence fully valid and not challenged by the employed approximation at all.

Figure F.1 exemplarily contrasts the fitting results for the $\text{Cu}L_3M_{45}M_{45}$ and $\text{Au}3d_{5/2}$ signals at the clean $\text{Cu}_3\text{Au}(111)$ surface, as obtained with XSWAVES versions 2.5 and 2.6. Sub-figure (a) is a reproduction of Fig. 6.7 from Sec. 6.3.3, page 104, of the present work. Version 2.5 is the XSWAVES version which has standardly been used for the evaluation of XSW data throughout this work (see Appendix A). Version 2.6 has been improved and corrected for the above-described inaccuracies.

In XSWAVES, version 2.6, we have computed the second “broadening step”, i.e., the step of calculation due to instrumental effects, in the same way as in version 2.5 (see below for the reasoning) while the first “broadening step”, i.e., the step of calculation related to the finite width of

^{a)}Potential shifts of the two curves on the x axis are neglected here.

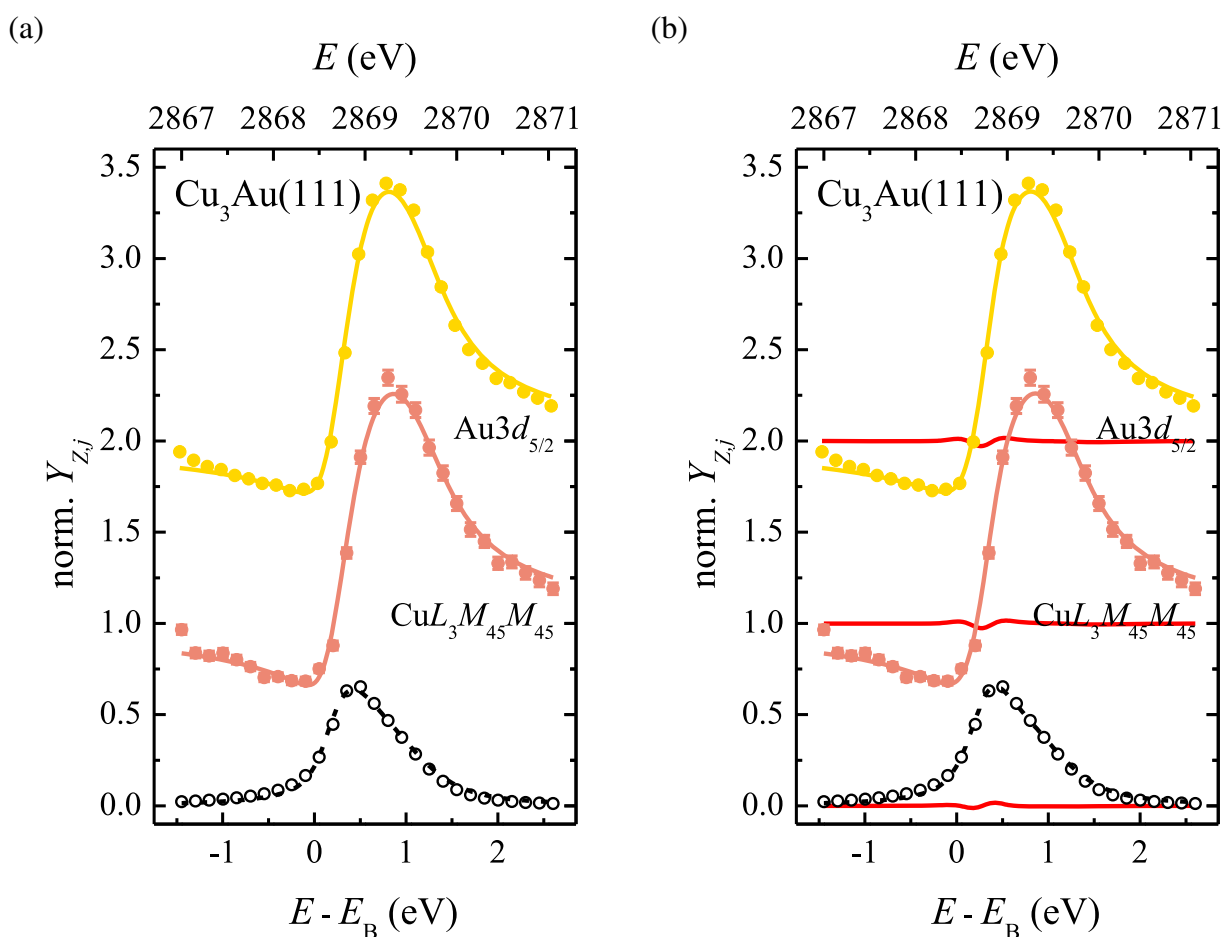


FIG. F.1. Exemplary XSW photoelectron yield curves fitted (a) with version 2.5 and (b) with version 2.6 of the XSWAVES evaluation routine. Sub-figure (a) is a reproduction of Fig. 6.7 from Sec. 6.3.3, page 104, of the present work: Typical XSW photoelectron yield curves of Cu and Au at the clean $\text{Cu}_3\text{Au}(111)$ surface. The $\text{Cu}L_3M_{45}M_{45}$ and $\text{Au}3d_{5/2}$ signals were employed in the respective XSW experiments. Experimental data points are shown as filled circles while respective fits to the data are shown as solid lines. The curves have been vertically offset for clarity. Error bars are so small that they are almost hidden by the data points. In addition, the measured reflectivity of the substrate employing the (111) lattice planes (open circles) and the corresponding fit (dashed line) are shown. Error bars have been omitted for clarity here. The red curves in (b) represent the differences of the respective fitting curves obtained with XSWAVES, version 2.6, from those shown in (a), as obtained with XSWAVES, version 2.5. Note that the difference curves corresponding to the individual XSW photoelectron yield curves have also been vertically offset for clarity.

the x-ray beam, has been computed as a cross-correlation [being equivalent to Eq. (F.4) above]:⁶³⁷

$$\Upsilon_{\text{ideal}}(E) = F(E) = \Upsilon_{\text{theo}}(E) \star [R_{\text{mono}}(E)]^2 = \int_{-\infty}^{\infty} \bar{\Upsilon}_{\text{theo}}(\epsilon) [R_{\text{mono}}(E + \epsilon)]^2 d\epsilon, \quad (\text{F.6})$$

where $\bar{\Upsilon}_{\text{theo}}(E)$ [or $\bar{\Upsilon}_{\text{theo}}(\epsilon)$] is the complex conjugate of $\Upsilon_{\text{theo}}(E)$ [or $\Upsilon_{\text{theo}}(\epsilon)$, respectively]. In doing so, the mirroring of the response function in the computational algorithm is avoided due to the nature of the cross-correlation.⁶³⁷ Note that $\bar{\Upsilon}_{\text{theo}}(E) = \Upsilon_{\text{theo}}(E)$ applies here [see also Eq. (F.4) above] because $\Upsilon_{\text{theo}}(E)$ is a real function. The same holds for $F(E)$ [see also Eq. (F.5)]. Furthermore, for the second “broadening step”:

$$\Upsilon_{\text{real}}(E) = F(E) \star G(E) = F(E) * G(E) \quad (\text{F.7})$$

applies because $G(E)$ is an even function.⁶³⁷ Hence, there has not been a necessity to improve the source codes of the XSWAVES computational algorithms concerning this step of calculation (see also above).

As can be seen from Fig. F.1, in particular Fig. F.1(b), the corrections to the XSWAVES source codes in version 2.6 lead to very subtle changes in the resulting XSW fitting curves (difference curves are depicted in red). In particular, small differences are observed for $E - E_B$ values in the region of about -0.5 eV to 1.0 eV, i.e., between the minima and maxima of the XSW photoelectron yield curves. However, these differences are in the range of $\Delta Y_{Z,j,\text{norm}} \leq \pm 0.03$ only, as compared to version 2.5. The overall shapes of the fitting curves remain unaffected. The corresponding variations in the fitting results are well within the experimental accuracy: $\Delta f_c = -0.001(2)$ and $\Delta p_c = 0.000(1)$, averaged over all XSW data sets which have been re-analyzed. Hence, the effects due to the employed approximations are negligible here, and all results discussed within the present work and all conclusions drawn from these XSW results remain fully valid.

The (absolute or relative) variations for the other relevant fitting parameters, i.e., for the position of the centers μ (termed “xcG” in the source codes; see Sec. A.3) and the widths σ ($\hat{=}$ “wG”) of the Gaussian function $G(E)$ as well as for the obtained χ^2 values amount to $\Delta\mu = +0.19(6)$ eV, $\Delta\sigma = -6(7)\%$, and $\Delta\chi^2 = -4(9)\%$ on average. In conclusion, the fitting curves and thus also our experimental data are rather insensitive to the two different computational approaches, that is, to the differences between $[R_{\text{mono}}(E)]^2$ and $[R_{\text{mono}}(-E)]^2$ [see Eqs. (F.2) and (F.4) above]. This can be understood as follows. Metal single crystal generally exhibit a lower degree of perfection as compared to semiconductor crystals, for example, due to their higher crystal mosaicity.^{28,29} Therefore, the corresponding reflectivity curves and also the XSW photoelectron yield profiles are broadened. This type of broadening is generally described by a Gaussian function (“instrumental broadening”; see also above). Hence, the observed overall broadening of the data curves in the case of metal substrates is mainly governed by these instrumental effects, outweighing the broadening effect due to the finite width of the x-ray beam. The broadening due to instrumental effects has been computed in the correct way already in XSWAVES, version 2.5, as opposed to the broadening due to the finite beam width. Based on the above reasoning, the impact on the fitting results of the corrections in XSWAVES, version 2.6, concerning the latter effect is expected not be crucial in the present case of metal substrates, as has indeed been proven here.

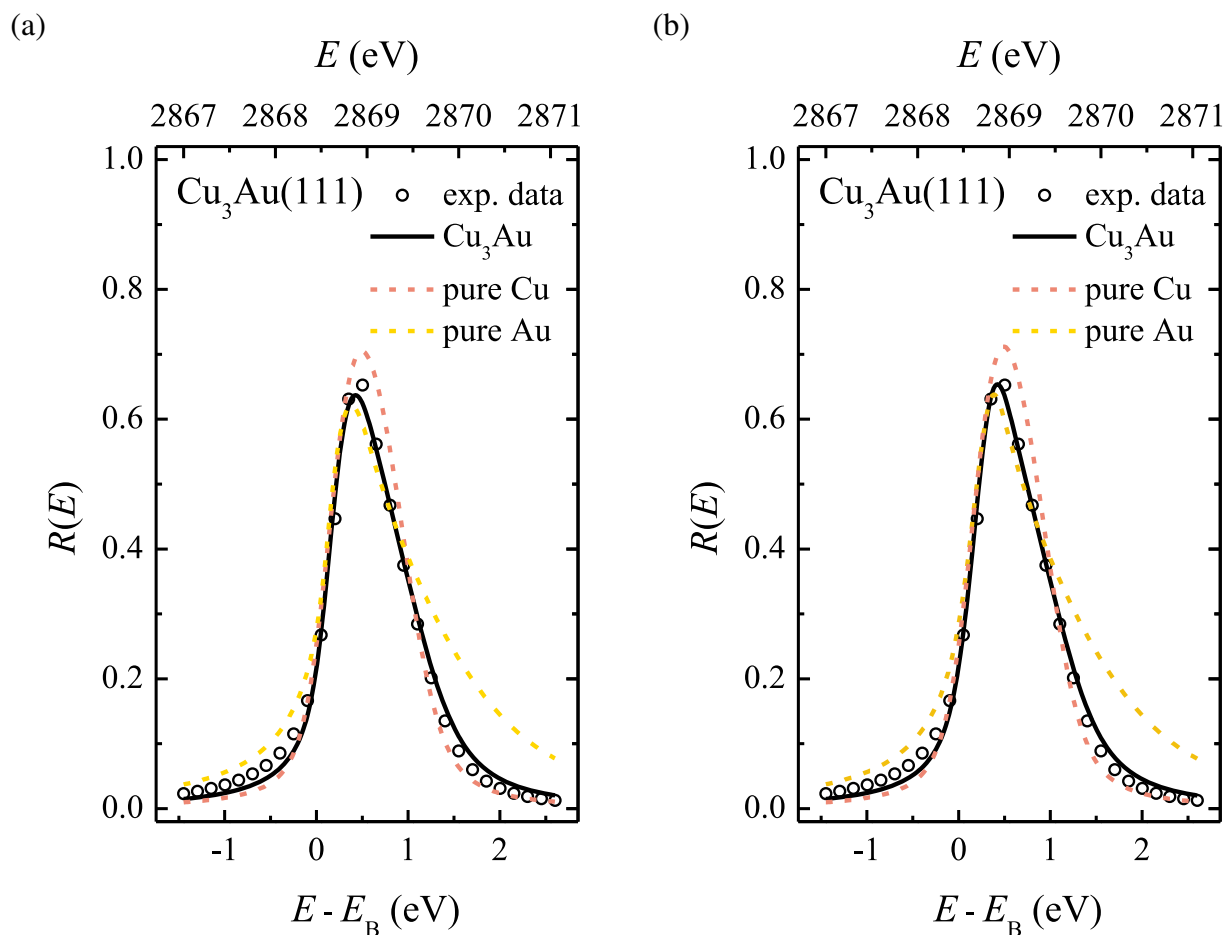


FIG. F.2. An exemplary Darwin-Prins curve fitted (a) with version 2.5 and (b) with version 2.6 of the XSWAVES evaluation routine. Sub-figure (a) is a reproduction of Fig. 6.8 from Sec. 6.3.3, page 105, of the present work: Typical Darwin-Prins curve $R(E)$ of the (clean) $\text{Cu}_3\text{Au}(111)$ substrate crystal (black open circles; error bars have been omitted for clarity). The reflectivity of the substrate was measured employing the (111) lattice planes. The corresponding fit, as obtained with one of the two employed versions of XSWAVES, is shown as a black solid line in (a) and (b), respectively. In addition, two fitting curves are shown in each case as dashed lines in respective colors where the substrate was modeled as being composed of either Cu or Au atoms only. Note that the $R(E)$ data shown here are the same as in Figs. 6.7, 6.8, and F.1, respectively.

Quality of the fitting: Darwin-Prins curves of $\text{Cu}_3\text{Au}(111)$

Finally, we comment on the quality of the fitting of the Darwin-Prins curves $R(E)$ of (clean or PTCDA-covered) $\text{Cu}_3\text{Au}(111)$. This aspect has already been discussed in Sec. 6.3.3 of the main part of the present work. In brief, we have observed that the maxima of the $R(E)$ curves are underestimated by their fitting curves [see Fig. F.2(a) (which is a reproduction of Fig. 6.8 from Sec. 6.3.3, page 105, of the main part of the present work) for a representation on an enlarged scale]. At the same time, the tails of the reflectivity curve are not correctly described, either. There, the overall agreement between the experimentally observed and the theoretically expected Darwin-Prins curves may have been improved by assuming a higher fraction of Cu atoms to be present in the employed $\text{Cu}_3\text{Au}(111)$ substrate crystal than expected from the nominal stoichiometric ratio $N_{\text{Cu}}/N_{\text{Au}}$. On the basis of the observed Bragg energy $E_{\text{B}} = 2865.04$ eV, however, an altered $N_{\text{Cu}}/N_{\text{Au}}$ ratio was excluded. Thus, it was concluded at that point that the non-perfect agreement between the experimental and the theoretical reflectivity curves are caused by alloy inhomogeneities, i.e., local disorder.

When fitted with XSWAVES, version 2.6—for which the implementation of the broadening effects has been corrected (see above)—the agreement between the fitting curves and the experimental data has indeed improved to a certain extent [see Fig. F.2(b); note again that the XSW fitting results regarding the f_{c} and p_{c} values remain unaffected thereby]. In particular, the maximum of the Darwin-Prins curve is described much better now by the fitting curve and underestimated only very slightly (while the tails of the reflectivity curve are still not described correctly). This finding further highly supports the above conclusion that the $\text{Cu}_3\text{Au}(111)$ substrate crystal indeed exhibits the correct stoichiometry $N_{\text{Cu}}/N_{\text{Au}}$ and that a Cu enrichment (or a Au depletion, respectively) in the bulk can be ruled out here. Note, however, that the general trends regarding the quality of the fitting curves remain valid also for XSWAVES, version 2.6, when assuming that the substrate crystal is composed of either Cu or Au atoms exclusively (see Sec. 6.3.3 for further details).

Bibliography

- ¹ A. NILSSON, L. G. M. PETERSSON, AND J. K. NØRSKOV (Eds.), *Chemical Bonding at Surfaces and Interfaces*, Elsevier, Amsterdam, The Netherlands (2008).
Cited on page(s): 1, 5.
- ² F. ROSEI, M. SCHUNACK, Y. NAITOH, P. JIANG, A. GOURDON, E. LAEGSGAARD, I. STENSGAARD, C. JOACHIM, AND F. BESENBACHER, *Properties of large organic molecules on metal surfaces*, *Progress in Surface Science* **71**, 95–146 (2003).
Cited on page(s): 1.
- ³ S. M. BARLOW AND R. RAVAL, *Complex organic molecules at metal surfaces: bonding, organisation and chirality*, *Surface Science Reports* **50**, 201–341 (2003).
Cited on page(s): 1, 49, 75, 296.
- ⁴ F. S. TAUTZ, *Structure and bonding of large aromatic molecules on noble metal surfaces: The example of PTCDA*, *Progress in Surface Science* **82**, 479–520 (2007).
Cited on page(s): 1, 3, 7, 10, 11, 12, 13, 75, 123, 182, 187.
- ⁵ G. ERTL, *Reactions at Surfaces: From Atoms to Complexity (Nobel Lecture)*, *Angewandte Chemie International Edition* **47**, 3524–3535 (2008).
Cited on page(s): 1, 5.
- ⁶ M. SCHWOERER AND H. C. WOLF, *Organische Molekulare Festkörper: Einführung in die Physik von π -Systemen*, 1st edition, Wiley-VCH, Weinheim, Germany (2005).
Cited on page(s): 1.
- ⁷ W. BRÜTTING (Ed.), *Physics of Organic Semiconductors*, Wiley-VCH, Weinheim, Germany (2005).
Cited on page(s): 1.
- ⁸ S. R. FORREST AND M. E. THOMPSON (Eds.), *Organic Electronics and Optoelectronics*, *Chemical Reviews* **107**, 923–1386 (2007).
Cited on page(s): 1.
- ⁹ D. P. WOODRUFF, *Surface Structure*, in *Chemical Bonding at Surfaces and Interfaces* (edited by A. Nilsson, L. G. M. Pettersson, and J. K. Nørskov), pp. 1–56, Elsevier, Amsterdam, The Netherlands (2008).
Cited on page(s): 1.
- ¹⁰ G. BLYHOLDER, *Molecular Orbital View of Chemisorbed Carbon Monoxide*, *The Journal of Physical Chemistry* **68**, 2772–2777 (1964).
Cited on page(s): 1, 5, 6, 224, 229.

- ¹¹ D. M. NEWNS, *Self-Consistent Model of Hydrogen Chemisorption*, *Physical Review* **178**, 1123–1135 (1969).
Cited on page(s): 1, 6, 174, 192.
- ¹² R. HOFFMANN, *How Chemistry and Physics Meet in the Solid State*, *Angewandte Chemie International Edition* **26**, 846–878 (1987).
Cited on page(s): 1, 8, 9, 194, 199, 229.
- ¹³ R. HOFFMANN, *A chemical and theoretical way to look at bonding on surfaces*, *Reviews of Modern Physics* **60**, 601 (1988).
Cited on page(s): 1, 8, 9, 194, 199, 229.
- ¹⁴ J. K. NØRSKOV, *Chemisorption on metal surfaces*, *Reports on Progress in Physics* **53**, 1253 (1990).
Cited on page(s): 1, 6, 7, 8, 192, 194.
- ¹⁵ B. HAMMER, Y. MORIKAWA, AND J. K. NØRSKOV, *CO Chemisorption at Metal Surfaces and Overlayers*, *Physical Review Letters* **76**, 2141–2144 (1996).
Cited on page(s): 1, 9, 10, 173, 174.
- ¹⁶ L. H. GADE, *Koordinationschemie*, 1st edition, Wiley-VCH, Weinheim, Germany (1998).
Cited on page(s): 1.
- ¹⁷ R. H. CRABTREE, *The Organometallic Chemistry of the Transition Metals*, 4th edition, John Wiley & Sons, Hoboken, NJ, USA (2005).
Cited on page(s): 1, 6, 113.
- ¹⁸ C. ELSCHENBROICH, *Organometallchemie*, Teubner Studienbücher Chemie, 5th edition, Teubner, Wiesbaden, Germany (2005).
Cited on page(s): 1, 6.
- ¹⁹ M. R. ALBERT AND J. T. YATES, JR., *The Surface Scientist's Guide to Organometallic Chemistry*, American Chemical Society, Washington, D.C., USA (1987).
Cited on page(s): 1.
- ²⁰ N. WIBERG, E. WIBERG, AND A. F. HOLLEMAN, *Lehrbuch der Anorganischen Chemie*, 101st edition, de Gruyter, Berlin, Germany (1995).
Cited on page(s): 1, 2, 3, 4, 11, 48, 60, 67, 72, 113, 144, 161, 162, 191, 228, 290, 298, 334.
- ²¹ N. ASHCROFT AND N. MERMIN, *Solid State Physics*, 1st edition, Brooks/Cole Thomson Learning, Pacific Grove, CA, USA (1976).
Cited on page(s): 1.
- ²² C. KITTEL, *Introduction to Solid State Physics*, 8th edition, John Wiley & Sons, Hoboken, NJ, USA (2004).
Cited on page(s): 1.
- ²³ P. S. BAGUS, K. HERMANN, AND J. C. W. BAUSCHLICHER, *A new analysis of charge transfer and polarization for ligand–metal bonding: Model studies of Al₄CO and Al₄NH₃*, *The Journal of Chemical Physics* **80**, 4378–4386 (1984).
Cited on page(s): 2.
- ²⁴ P. S. BAGUS, K. HERMANN, AND J. C. W. BAUSCHLICHER, *On the nature of the bonding of lone pair ligands to a transition metal*, *The Journal of Chemical Physics* **81**, 1966–1974 (1984).
Cited on page(s): 2.

- ²⁵ C. W. BAUSCHLICHER, JR., *On the uniqueness of the constrained space orbital variation (CSOV) technique*, *Chemical Physics* **106**, 391–398 (1986).
Cited on page(s): 2.
- ²⁶ P. S. BAGUS AND F. ILLAS, *Decomposition of the chemisorption bond by constrained variations: Order of the variations and construction of the variational spaces*, *The Journal of Chemical Physics* **96**, 8962–8970 (1992).
Cited on page(s): 2.
- ²⁷ M. P. MITORAJ, A. MICHALAK, AND T. ZIEGLER, *A Combined Charge and Energy Decomposition Scheme for Bond Analysis*, *Journal of Chemical Theory and Computation* **5**, 962–975 (2009).
Cited on page(s): 2.
- ²⁸ J. ZEGENHAGEN, *Surface structure determination with X-ray standing waves*, *Surface Science Reports* **18**, 202–271 (1993).
Cited on page(s): 2, 19, 20, 21, 22, 23, 24, 25, 26, 27, 62, 100, 102, 107, 119, 246, 253, 256, 257, 324, 372.
- ²⁹ D. P. WOODRUFF, *Normal incidence X-ray standing wave determination of adsorbate structures*, *Progress in Surface Science* **57**, 1–60 (1998).
Cited on page(s): 2, 19, 20, 21, 22, 23, 24, 25, 26, 27, 159, 246, 253, 255, 256, 257, 298, 327, 332, 372.
- ³⁰ R. BRÜCKNER, *Reaktionsmechanismen: organische Reaktionen, Stereochemie, moderne Synthesemethoden*, 2nd edition, Spektrum Akademischer Verlag, Heidelberg, Germany (2003).
Cited on page(s): 2, 172, 196, 200.
- ³¹ L. KILIAN, W. WEIGAND, E. UMBACH, A. LANGNER, M. SOKOLOWSKI, H. L. MEYERHEIM, H. MALTOR, B. C. C. COWIE, T. LEE, AND P. BÄUERLE, *Adsorption site determination of a large π -conjugated molecule by normal incidence x-ray standing waves: End-capped quaterthiophene on Ag(111)*, *Physical Review B* **66**, 075412 (2002).
Cited on page(s): 2.
- ³² A. HAUSCHILD, K. KARKI, B. C. C. COWIE, M. ROHLFING, F. S. TAUTZ, AND M. SOKOLOWSKI, *Molecular Distortions and Chemical Bonding of a Large π -Conjugated Molecule on a Metal Surface*, *Physical Review Letters* **94**, 036106 (2005).
Cited on page(s): 2, 3, 14, 16, 17, 67, 182, 184, 206, 233, 234.
- ³³ S. M. JOHNSTON, G. ROUSSEAU, V. DHANAK, AND M. KADODWALA, *The structure of acetate and trifluoroacetate on Cu(111)*, *Surface Science* **477**, 163 – 173 (2001).
Cited on page(s): 2.
- ³⁴ A. MULLIGAN, S. M. JOHNSTON, G. MILLER, V. DHANAK, AND M. KADODWALA, *A TPD and NIXSW investigation of furan and tetrahydrofuran adsorption on Cu(111)*, *Surface Science* **541**, 3 – 13 (2003).
Cited on page(s): 2.
- ³⁵ A. CHAUDHURI, M. ODELIUS, R. G. JONES, T.-L. LEE, B. DETLEFS, AND D. P. WOODRUFF, *The structure of the Au(111)/methylthiolate interface: New insights from near-edge x-ray absorption spectroscopy and x-ray standing waves*, *The Journal of Chemical Physics* **130**, 124708 (2009).
Cited on page(s): 2.

- ³⁶ A. CHAUDHURI, D. C. JACKSON, T. J. LEROTHOLI, R. G. JONES, T.-L. LEE, B. DETLEFS, AND D. P. WOODRUFF, *Structural investigation of Au(111)/butylthiolate adsorption phases*, *Physical Chemistry Chemical Physics* **12**, 3229–3238 (2010).
Cited on page(s): 2.
- ³⁷ D. KREIKEMEYER-LORENZO, W. UNTERBERGER, D. A. DUNCAN, M. K. BRADLEY, T. J. LEROTHOLI, J. ROBINSON, AND D. P. WOODRUFF, *Face-Dependent Bond Lengths in Molecular Chemisorption: The Formate Species on Cu(111) and Cu(110)*, *Physical Review Letters* **107**, 046102 (2011).
Cited on page(s): 2, 209, 220.
- ³⁸ N. KOCH, A. GERLACH, S. DUHM, H. GLOWATZKI, G. HEIMEL, A. VOLLMER, Y. SAKAMOTO, T. SUZUKI, J. ZEGENHAGEN, J. P. RABE, AND F. SCHREIBER, *Adsorption-Induced Intramolecular Dipole: Correlating Molecular Conformation and Interface Electronic Structure*, *Journal of the American Chemical Society* **130**, 7300–7304 (2008).
Cited on page(s): 2, 196, 197, 201.
- ³⁹ S. DUHM, S. HOSOUMI, I. SALZMANN, A. GERLACH, M. OEHZELT, B. WEDL, T.-L. LEE, F. SCHREIBER, N. KOCH, N. UENO, AND S. KERA, *Influence of intramolecular polar bonds on interface energetics in perfluoro-pentacene on Ag(111)*, *Physical Review B* **81**, 045418 (2010).
Cited on page(s): 2, 196, 197.
- ⁴⁰ G. HEIMEL, S. DUHM, I. SALZMANN, A. GERLACH, A. STROZECKA, J. NIEDERHAUSEN, C. BUERKER, T. HOSOKAI, I. FERNANDEZ-TORRENTE, G. SCHULZE, S. WINKLER, A. WILKE, R. SCHLESINGER, J. FRISCH, B. BROEKER, A. VOLLMER, B. DETLEFS, J. PFLAUM, S. KERA, K. J. FRANKE, N. UENO, J. I. PASCUAL, F. SCHREIBER, AND N. KOCH, *Charged and metallic molecular monolayers through surface-induced aromatic stabilization.*, *Nature Chemistry* **5**, 187–194 (2013).
Cited on page(s): 2, 196, 197, 218, 229, 230, 236.
- ⁴¹ J. STANZEL, W. WEIGAND, L. KILIAN, H. L. MEYERHEIM, C. KUMPF, AND E. UMBACH, *Chemisorption of NTCDA on Ag(111): a NIXSW study including non-dipolar and electron-stimulated effects*, *Surface Science* **571**, L311–L318 (2004).
Cited on page(s): 2, 15, 16, 26, 62, 102, 195.
- ⁴² C. STADLER, S. HANSEN, A. SCHÖLL, T.-L. LEE, J. ZEGENHAGEN, C. KUMPF, AND E. UMBACH, *Molecular distortion of NTCDA upon adsorption on Ag(111): a normal incidence x-ray standing wave study*, *New Journal of Physics* **9**, 50 (2007).
Cited on page(s): 2, 16, 195, 324.
- ⁴³ A. GERLACH, S. SELLNER, F. SCHREIBER, N. KOCH, AND J. ZEGENHAGEN, *Substrate-dependent bonding distances of PTCDA: A comparative x-ray standing-wave study on Cu(111) and Ag(111)*, *Physical Review B* **75**, 045401 (2007).
Cited on page(s): 2, 3, 14, 15, 67, 82, 84, 87, 105, 154, 156, 168, 169, 172, 182, 185, 186, 193, 202, 203, 204, 221, 233, 234, 324.
- ⁴⁴ A. GERLACH, F. SCHREIBER, S. SELLNER, H. DOSCH, I. A. VARTANYANTS, B. C. C. COWIE, T.-L. LEE, AND J. ZEGENHAGEN, *Adsorption-induced distortion of F16CuPc on Cu(111) and Ag(111): An x-ray standing wave study*, *Physical Review B* **71**, 205425 (2005).
Cited on page(s): 2.

- ⁴⁵ C. STADLER, S. HANSEN, F. POLLINGER, C. KUMPF, E. UMBACH, T.-L. LEE, AND J. ZEGENHAGEN, *Structural investigation of the adsorption of SnPc on Ag(111) using normal-incidence x-ray standing waves*, *Physical Review B* **74**, 035404 (2006).
Cited on page(s): 2, 65.
- ⁴⁶ C. STADLER, S. HANSEN, I. KRÖGER, C. KUMPF, AND E. UMBACH, *Tuning intermolecular interaction in long-range-ordered submonolayer organic films*, *Nature Physics* **5**, 153–158 (2009).
Cited on page(s): 2.
- ⁴⁷ H. YAMANE, A. GERLACH, S. DUHM, Y. TANAKA, T. HOSOKAI, Y. Y. MI, J. ZEGENHAGEN, N. KOCH, K. SEKI, AND F. SCHREIBER, *Site-Specific Geometric and Electronic Relaxations at Organic-Metal Interfaces*, *Physical Review Letters* **105**, 046103 (2010).
Cited on page(s): 2.
- ⁴⁸ I. KRÖGER, B. STADTMÜLLER, C. STADLER, J. ZIROFF, M. KOCHLER, A. STAHL, F. POLLINGER, T.-L. LEE, J. ZEGENHAGEN, F. REINERT, AND C. KUMPF, *Submonolayer growth of copper-phthalocyanine on Ag(111)*, *New Journal of Physics* **12**, 083038 (2010).
Cited on page(s): 2.
- ⁴⁹ I. KRÖGER, B. STADTMÜLLER, C. KLEIMANN, P. RAJPUT, AND C. KUMPF, *Normal-incidence x-ray standing-wave study of copper phthalocyanine submonolayers on Cu(111) and Au(111)*, *Physical Review B* **83**, 195414 (2011).
Cited on page(s): 2.
- ⁵⁰ I. KRÖGER, P. BAYERSDORFER, B. STADTMÜLLER, C. KLEIMANN, G. MERCURIO, F. REINERT, AND C. KUMPF, *Submonolayer growth of H₂-phthalocyanine on Ag(111)*, *Physical Review B* **86**, 195412 (2012).
Cited on page(s): 2.
- ⁵¹ C. TON-THAT, A. G. SHARD, S. EGGER, V. R. DHANAK, A. TANINAKA, H. SHINOHARA, AND M. E. WELLAND, *Orientation and constraints of endohedral lanthanum in La@C₈₂ molecules adsorbed on Cu(111)*, *Physical Review B* **68**, 045424 (2003).
Cited on page(s): 2.
- ⁵² R. A. J. WOOLLEY, K. H. G. SCHULTE, L. WANG, P. J. MORIARTY, B. C. C. COWIE, H. SHINOHARA, M. KANAI, AND T. J. S. DENNIS, *Does an Encapsulated Atom ‘feel’ the Effects of Adsorption?: X-ray Standing Wave Spectroscopy of Ce@C₈₂ on Ag(111)*, *Nano Letters* **4**, 361–364 (2004).
Cited on page(s): 2.
- ⁵³ K. SCHULTE, R. A. J. WOOLLEY, L. WANG, P. J. MORIARTY, P. R. BIRKETT, H. W. KROTO, AND B. C. C. COWIE, *XSW feasibility study of C₆₀Ph₅-OH on Ag(111): combining hard X-rays, low Z and, low coverage*, *Nuclear Instruments and Methods in Physics Research Section A: Accelerators, Spectrometers, Detectors and Associated Equipment* **547**, 208–215 (2005).
Cited on page(s): 2.
- ⁵⁴ S. K. M. HENZE, O. BAUER, T.-L. LEE, M. SOKOLOWSKI, AND F. S. TAUTZ, *Vertical bonding distances of PTCDA on Au(111) and Ag(111): Relation to the bonding type*, *Surface Science* **601**, 1566–1573 (2007).
Cited on page(s): 2, 3, 14, 15, 61, 87, 90, 105, 138, 144, 153, 168, 169, 182, 184, 185, 186, 193, 202, 215, 221, 230, 233.

- ⁵⁵ A. HAUSCHILD, R. TEMIROV, S. SOUBATCH, O. BAUER, A. SCHÖLL, B. C. C. COWIE, T.-L. LEE, F. S. TAUTZ, AND M. SOKOLOWSKI, *Normal-incidence x-ray standing-wave determination of the adsorption geometry of PTCDA on Ag(111): Comparison of the ordered room-temperature and disordered low-temperature phases*, *Physical Review B* **81**, 125432 (2010).
Cited on page(s): 2, 14, 15, 16, 17, 61, 67, 87, 140, 182, 184, 185, 186, 189, 192, 193, 194, 195, 199, 210, 216, 217, 221, 233, 234, 294, 298, 324.
- ⁵⁶ G. V. GIBBS, F. C. HILL, M. B. BOISEN, AND R. T. DOWNS, *Power law relationships between bond length, bond strength and electron density distributions*, *Physics and Chemistry of Minerals* **25**, 585–590 (1998).
Cited on page(s): 2, 18, 85, 113, 184, 191, 192, 222, 227, 228.
- ⁵⁷ G. V. GIBBS, K. M. ROSSO, D. F. COX, AND M. B. BOISEN, JR., *A physical basis for Pauling's definition of bond strength*, *Physics and Chemistry of Minerals* **30**, 317–320 (2003).
Cited on page(s): 2, 18, 85, 113, 184, 191, 192, 227, 228.
- ⁵⁸ M. EREMTCHENKO, J. A. SCHAEFER, AND F. S. TAUTZ, *Understanding and tuning the epitaxy of large aromatic adsorbates by molecular design*, *Nature* **425**, 602–605 (2003).
Cited on page(s): 3, 14, 220.
- ⁵⁹ Y. ZOU, L. KILIAN, A. SCHÖLL, T. SCHMIDT, R. FINK, AND E. UMBACH, *Chemical bonding of PTCDA on Ag surfaces and the formation of interface states*, *Surface Science* **600**, 1240–1251 (2006).
Cited on page(s): 3, 13, 18, 57, 84, 144, 145, 162, 166, 169, 184, 191, 192, 194, 197, 198, 199, 200, 202, 203, 204, 206, 207, 218, 234, 306, 307.
- ⁶⁰ S. DUHM, A. GERLACH, I. SALZMANN, B. BRÖKER, R. L. JOHNSON, F. SCHREIBER, AND N. KOCH, *PTCDA on Au(111), Ag(111) and Cu(111): Correlation of interface charge transfer to bonding distance*, *Organic Electronics* **9**, 111–118 (2008).
Cited on page(s): 3, 13, 18, 67, 84, 144, 165, 166, 169, 184, 191, 192, 194, 197, 199, 200, 202, 215, 216, 218, 223, 234, 306.
- ⁶¹ B. HAMMER AND J. K. NØRSKOV, *Why gold is the noblest of all the metals*, *Nature* **376**, 238–240 (1995).
Cited on page(s): 3, 10.
- ⁶² G. ATTARD AND C. BARNES, *Surfaces*, volume 59 of *Oxford Chemistry primers*, Oxford University Press, Oxford, UK (1998).
Cited on page(s): 3, 32, 36, 37, 40, 49, 52, 67, 131, 134, 142, 200, 201, 301.
- ⁶³ H. B. MICHAELSON, *The work function of the elements and its periodicity*, *Journal of Applied Physics* **48**, 4729–4733 (1977).
Cited on page(s): 3, 191, 192, 193, 200, 231.
- ⁶⁴ J. WÜSTEN, S. BERGER, K. HEIMER, S. LACH, AND C. ZIEGLER, *Interaction of alkali metals with perylene-3,4,9,10-tetracarboxylic-dianhydride thin films*, *Journal of Applied Physics* **98**, 013705–10 (2005).
Cited on page(s): 4, 224, 337.
- ⁶⁵ C. ZAZZA, S. MELONI, A. PALMA, M. KNUPFER, G. G. FUENTES, AND R. CAR, *Quasi-One-Dimensional K-O Chain in PTCDA Thin Films: Evidence from First-Principles Calculations*, *Physical Review Letters* **98**, 046401 (2007).
Cited on page(s): 4, 224, 337.

- ⁶⁶ O. BAUER, G. MERCURIO, M. WILLENBOCKEL, W. RECKIEN, C. HEINRICH SCHMITZ, B. FIEDLER, S. SOUBATCH, T. BREDOW, F. S. TAUTZ, AND M. SOKOLOWSKI, *Role of functional groups in surface bonding of planar π -conjugated molecules*, *Physical Review B* **86**, 235431 (2012).
Cited on page(s): 4, 177, 209, 210, 212, 295, 324, 367.
- ⁶⁷ G. MERCURIO, O. BAUER, M. WILLENBOCKEL, N. FAIRLEY, W. RECKIEN, C. H. SCHMITZ, B. FIEDLER, S. SOUBATCH, T. BREDOW, M. SOKOLOWSKI, AND F. S. TAUTZ, *Adsorption height determination of nonequivalent C and O species of PTCDA on Ag(110) using x-ray standing waves*, *Physical Review B* **87**, 045421 (2013).
Cited on page(s): 4, 51, 177, 295.
- ⁶⁸ G. MERCURIO, O. BAUER, M. WILLENBOCKEL, B. FIEDLER, T. SUEYOSHI, C. WEISS, R. TEMIROV, S. SOUBATCH, M. SOKOLOWSKI, AND F. S. TAUTZ, *Tuning and probing interfacial bonding channels for a functionalized organic molecule by surface modification*, *Physical Review B* **87**, 121409(R) (2013).
Cited on page(s): 4, 178, 180, 181, 216, 225, 226, 227, 228, 337, 339, 340, 344, 353, 357, 358, 359.
- ⁶⁹ R. B. WOODWARD AND R. HOFFMANN, *The Conservation of Orbital Symmetry*, *Angewandte Chemie International Edition in English* **8**, 781–853 (1969).
Cited on page(s): 5, 8.
- ⁷⁰ R. B. WOODWARD AND R. HOFFMANN, *Die Erhaltung der Orbitalsymmetrie*, Akademische Verlagsgesellschaft Geest & Portig K.-G., Leipzig, Germany (1970).
Cited on page(s): 5, 8.
- ⁷¹ L. E. ORGEL, *The Infrared Spectra of Substituted Metal Carbonyls*, *Inorganic Chemistry* **1**, 25–29 (1962).
Cited on page(s): 5.
- ⁷² A. NILSSON AND L. G. M. PETERSSON, *Adsorbate Electronic Structure and Bonding on Metal Surfaces*, in *Chemical Bonding at Surfaces and Interfaces* (edited by A. Nilsson, L. G. M. Pettersson, and J. K. Nørskov), pp. 57–142, Elsevier, Amsterdam, The Netherlands (2008).
Cited on page(s): 5, 6, 7, 194.
- ⁷³ G. BRODÉN, T. RHODIN, C. BRUCKER, R. BENBOW, AND Z. HURYCH, *Synchrotron radiation study of chemisorptive bonding of CO on transition metals – Polarization effect on Ir(100)*, *Surface Science* **59**, 593–611 (1976).
Cited on page(s): 6.
- ⁷⁴ G. DOYEN AND G. ERTL, *Theory of carbon monoxide chemisorption on transition metals*, *Surface Science* **43**, 197–229 (1974).
Cited on page(s): 6.
- ⁷⁵ J. L. WHITTEN AND H. YANG, *Theory of chemisorption and reactions on metal surfaces*, *Surface Science Reports* **24**, 55–124 (1996).
Cited on page(s): 6.
- ⁷⁶ A. FÖHLISCH, M. NYBERG, J. HASSELSTRÖM, O. KARIS, L. G. M. PETERSSON, AND A. NILSSON, *How Carbon Monoxide Adsorbs in Different Sites*, *Physical Review Letters* **85**, 3309–3312 (2000).
Cited on page(s): 6.

- ⁷⁷ M. NYBERG, A. FÖHLISCH, L. TRIGUERO, A. BASSAN, A. NILSSON, AND L. PETTERSSON, *Bonding in metal–carbonyls: A comparison with experiment and calculations on adsorbed CO*, Journal of Molecular Structure: THEOCHEM **762**, 123–132 (2006).
Cited on page(s): 6.
- ⁷⁸ M. J. S. DEWAR, *A review of π -Complex Theory*, Bulletin de la Societe Chimique de France **18**, C71–C79 (1951).
Cited on page(s): 6, 229.
- ⁷⁹ J. CHATT AND L. A. DUNCANSON, 586. *Olefin co-ordination compounds. Part III. Infra-red spectra and structure: attempted preparation of acetylene complexes*, Journal of the Chemical Society, pp. 2939–2947 (1953).
Cited on page(s): 6, 229.
- ⁸⁰ D. M. P. MINGOS, *A historical perspective on Dewar’s landmark contribution to organometallic chemistry*, Journal of Organometallic Chemistry **635**, 1–8 (2001).
Cited on page(s): 6.
- ⁸¹ P. W. ANDERSON, *Localized Magnetic States in Metals*, Physical Review **124**, 41–53 (1961).
Cited on page(s): 6, 174, 192.
- ⁸² T. BLIGAARD AND J. K. NØRSKOV, *Heterogeneous Catalysis*, in *Chemical Bonding at Surfaces and Interfaces* (edited by A. Nilsson, L. G. M. Pettersson, and J. K. Nørskov), pp. 255–321, Elsevier, Amsterdam, The Netherlands (2008).
Cited on page(s): 6, 9, 10, 173, 174, 194.
- ⁸³ B. I. LUNDQVIST, *Theoretical aspects of adsorption and heterogeneous catalysis*, Vacuum **33**, 639–649 (1983).
Cited on page(s): 6, 7, 8.
- ⁸⁴ D. CAHEN AND A. KAHN, *Electron Energetics at Surfaces and Interfaces: Concepts and Experiments*, Advanced Materials **15**, 271–277 (2003).
Cited on page(s): 7, 38.
- ⁸⁵ A. D. MCNAUGHT AND A. WILKINSON (Eds.), *IUPAC, Compendium of Chemical Terminology (the “Gold Book”)*, 2nd edition, Blackwell Scientific Publications, Oxford, UK (1997).
Cited on page(s): 7, 10, 96, 187, 196, 214, 224, 291, 292, 293.
- ⁸⁶ P. K. JOHANSSON, *Chemisorption of molecular hydrogen on simple metal surfaces*, Surface Science **104**, 510–526 (1981).
Cited on page(s): 7, 199, 228.
- ⁸⁷ H. HJELMBERG, *Hydrogen Chemisorption by the Spin-Density Functional Formalism. II. Rôle of the sp-conduction Electrons of Metal Surfaces*, Physica Scripta **18**, 481–493 (1978).
Cited on page(s): 7.
- ⁸⁸ S. S. SUNG AND R. HOFFMANN, *How carbon monoxide bonds to metal surfaces*, Journal of the American Chemical Society **107**, 578–584 (1985).
Cited on page(s): 8, 9.
- ⁸⁹ R. HOFFMANN, *Solids and Surfaces: A Chemist’s View of Bonding in Extended Structures*, 1st edition, Wiley-VCH, New York, NY, USA (1988).
Cited on page(s): 8, 229.

- ⁹⁰ R. HOFFMANN, *An Extended Hückel Theory. I. Hydrocarbons*, *The Journal of Chemical Physics* **39**, 1397–1412 (1963).
Cited on page(s): 8.
- ⁹¹ K. J. DONALD AND R. HOFFMANN, *Solid Memory: Structural Preferences in Group 2 Dihalide Monomers, Dimers, and Solids*, *Journal of the American Chemical Society* **128**, 11236–11249 (2006).
Cited on page(s): 8.
- ⁹² M. WOLFSBERG AND L. HELMHOLZ, *The Spectra and Electronic Structure of the Tetrahedral Ions MnO_4^- , CrO_4^{2-} , and ClO_4^-* , *The Journal of Chemical Physics* **20**, 837–843 (1952).
Cited on page(s): 8.
- ⁹³ B. HAMMER AND J. K. NØRSKOV, *Theoretical surface science and catalysis—calculations and concepts*, in *Impact of Surface Science on Catalysis* (edited by B. C. Gates and H. Knozinger), volume 45 of *Advances in Catalysis*, pp. 71–129, Academic Press, San Diego, CA, USA (2000).
Cited on page(s): 9, 10, 173.
- ⁹⁴ J. GREELEY, J. K. NØRSKOV, AND M. MAVRIKAKIS, *Electronic Structure and Catalysis on Metal Surfaces*, *Annual Review of Physical Chemistry* **53**, 319–348 (2002).
Cited on page(s): 9, 10, 173.
- ⁹⁵ B. HAMMER AND J. K. NØRSKOV, *Electronic factors determining the reactivity of metal surfaces*, *Surface Science* **343**, 211–220 (1995).
Cited on page(s): 10, 173.
- ⁹⁶ A. RUBAN, B. HAMMER, P. STOLTZE, H. L. SKRIVER, AND J. K. NØRSKOV, *Surface electronic structure and reactivity of transition and noble metals*, *Journal of Molecular Catalysis A: Chemical* **115**, 421–429 (1997).
Cited on page(s): 10, 173, 174, 194.
- ⁹⁷ M. ROHLFING, R. TEMIROV, AND F. S. TAUTZ, *Adsorption structure and scanning tunneling data of a prototype organic-inorganic interface: PTCDA on Ag(111)*, *Physical Review B* **76**, 115421 (2007).
Cited on page(s): 10, 13, 17, 18, 200, 218.
- ⁹⁸ K. GLÖCKLER, C. SEIDEL, A. SOUKOPP, M. SOKOLOWSKI, E. UMBACH, M. BÖHRINGER, R. BERNDT, AND W. D. SCHNEIDER, *Highly ordered structures and submolecular scanning tunnelling microscopy contrast of PTCDA and DM-PBDCI monolayers on Ag(111) and Ag(110)*, *Surface Science* **405**, 1–20 (1998).
Cited on page(s): 11, 12, 47, 57, 68, 72, 80, 84, 87, 120, 178, 179, 201, 206, 210, 234, 295, 296, 299, 310.
- ⁹⁹ S. HEUTZ, G. SALVAN, S. D. SILAGHI, T. S. JONES, AND D. R. T. ZAHN, *Raman Scattering as a Probe of Crystallinity in PTCDA and H_2Pc Single-Layer and Double-Layer Thin Film Heterostructures*, *The Journal of Physical Chemistry B* **107**, 3782–3788 (2003).
Cited on page(s): 10.
- ¹⁰⁰ SIGMA-ALDRICH, *Perylene-3,4,9,10-tetracarboxylic dianhydride Material Safety Data Sheet, Version 5.0*, Steinheim, Germany (2013).
Cited on page(s): 10, 11.

- ¹⁰¹ C. R. NEWMAN, C. D. FRISBIE, D. A. DA SILVA FILHO, J.-L. BRÉDAS, P. C. EWBank, AND K. R. MANN, *Introduction to Organic Thin Film Transistors and Design of n-Channel Organic Semiconductors*, Chemistry of Materials **16**, 4436–4451 (2004).
Cited on page(s): 10, 11.
- ¹⁰² T. KAMPEN, *Electronic structure of organic interfaces – a case study on perylene derivatives*, Applied Physics A: Materials Science & Processing **82**, 457–470 (2006).
Cited on page(s): 10, 140, 161, 172, 194, 195, 196.
- ¹⁰³ W. HERBST AND K. HUNGER, *Industrielle Organische Pigmente: Herstellung, Eigenschaften, Anwendung*, 2nd edition, VCH, Weinheim, Germany (1995).
Cited on page(s): 11.
- ¹⁰⁴ M. MÖBUS, M. SCHRECK, AND N. KARL, *Epitaxial growth of thin films of perylenetetracarboxylic dianhydride and coronene on NaCl(001)*, Thin Solid Films **175**, 89–93 (1989).
Cited on page(s): 11, 165.
- ¹⁰⁵ A. J. LOVINGER, S. R. FORREST, M. L. KAPLAN, P. H. SCHMIDT, AND T. VENKATESAN, *Structural and morphological investigation of the development of electrical conductivity in ion-irradiated thin films of an organic material*, Journal of Applied Physics **55**, 476–482 (1984).
Cited on page(s): 11, 12, 52, 75.
- ¹⁰⁶ S. R. FORREST, M. L. KAPLAN, AND P. H. SCHMIDT, *Organic-on-inorganic semiconductor contact barrier diodes. I. Theory with applications to organic thin films and prototype devices*, Journal of Applied Physics **55**, 1492–1507 (1984).
Cited on page(s): 11, 12, 52, 75.
- ¹⁰⁷ M. MÖBUS, N. KARL, AND T. KOBAYASHI, *Structure of perylene-tetracarboxylic-dianhydride thin films on alkali halide crystal substrates*, Journal of Crystal Growth **116**, 495–504 (1992).
Cited on page(s): 11, 12, 52, 75, 76, 165, 324.
- ¹⁰⁸ K. TOJO AND J. MIZUGUCHI, *Refinement of the crystal structure of α -3,4:9,10-perylenetetracarboxylic dianhydride, $C_{24}H_8O_6$, at 223 K*, Zeitschrift für Kristallographie – New Crystal Structures **217**, 253–254 (2002).
Cited on page(s): 11, 181, 210, 221, 227, 334.
- ¹⁰⁹ K. TOJO AND J. MIZUGUCHI, *Refinement of the crystal structure of β -3,4:9,10-perylenetetracarboxylic dianhydride, $C_{24}H_8O_6$, at 223 K*, Zeitschrift für Kristallographie – New Crystal Structures **217**, 255–256 (2002).
Cited on page(s): 11, 181.
- ¹¹⁰ T. OGAWA, K. KUWAMOTO, S. ISODA, T. KOBAYASHI, AND N. KARL, *3,4:9,10-Perylenetetracarboxylic dianhydride (PTCDA) by electron crystallography*, Acta Crystallographica Section B **55**, 123–130 (1999).
Cited on page(s): 11, 12, 76.
- ¹¹¹ G. R. DESIRAJU, *The C–H \cdots O hydrogen bond in crystals: what is it?*, Accounts of Chemical Research **24**, 290–296 (1991).
Cited on page(s): 11, 75, 123, 182, 187.
- ¹¹² M. LEONHARDT, O. MAGER, AND H. PORT, *Two-component optical spectra in thin PTCDA films due to the coexistence of α - and β -phase*, Chemical Physics Letters **313**, 24–30 (1999).
Cited on page(s): 12.

- ¹¹³ L. KILIAN, E. UMBACH, AND M. SOKOLOWSKI, *Molecular beam epitaxy of organic films investigated by high resolution low energy electron diffraction (SPA-LEED): 3,4,9,10-perylenetetracarboxylic acid-dianhydride (PTCDA) on Ag(111)*, *Surface Science* **573**, 359–378 (2004).
Cited on page(s): 12, 52, 72, 76, 80, 84, 134, 300.
- ¹¹⁴ L. KILIAN, E. UMBACH, AND M. SOKOLOWSKI, *A refined structural analysis of the PTCDA monolayer on the reconstructed Au(111) surface—“Rigid or distorted carpet?”*, *Surface Science* **600**, 2633–2643 (2006).
Cited on page(s): 12, 72, 87, 89, 90, 98, 120, 121, 162, 178.
- ¹¹⁵ T. WAGNER, A. BANNANI, C. BOBISCH, H. KARACUBAN, AND R. MÖLLER, *The initial growth of PTCDA on Cu(111) studied by STM*, *Journal of Physics: Condensed Matter* **19**, 056009 (2007).
Cited on page(s): 12, 67, 68, 69, 75, 77, 78, 82, 83, 84, 87, 178, 233.
- ¹¹⁶ S. MANNSFELD, M. TOERKER, T. SCHMITZ-HÜBSCH, F. SELLAM, T. FRITZ, AND K. LEO, *Combined LEED and STM study of PTCDA growth on reconstructed Au(111) and Au(100) single crystals*, *Organic Electronics* **2**, 121–134 (2001).
Cited on page(s): 12, 72, 87, 89, 90, 121, 127, 128, 178.
- ¹¹⁷ A. SCHMIDT, T. J. SCHUERLEIN, G. E. COLLINS, AND N. R. ARMSTRONG, *Ordered Ultrathin Films of Perylenetetracarboxylic Dianhydride (PTCDA) and Dimethylperylenebis(dicarboximide) (Me-PTCDI) on Cu(100): Characterization of Structure and Surface Stoichiometry by LEED, TDMS, and XPS*, *The Journal of Physical Chemistry* **99**, 11770–11779 (1995).
Cited on page(s): 12, 57, 202, 203, 204, 231, 236.
- ¹¹⁸ M. STÖHR, M. GABRIEL, AND R. MÖLLER, *Investigation of the growth of PTCDA on Cu(110): an STM study*, *Surface Science* **507–510**, 330–334 (2002).
Cited on page(s): 12, 82.
- ¹¹⁹ E. UMBACH, K. GLÖCKLER, AND M. SOKOLOWSKI, *Surface “architecture” with large organic molecules: interface order and epitaxy*, *Surface Science* **402–404**, 20–31 (1998).
Cited on page(s): 12.
- ¹²⁰ J. IKONOMOV, O. BAUER, AND M. SOKOLOWSKI, *Highly ordered thin films of perylene-3,4,9,10-tetracarboxylic acid dianhydride (PTCDA) on Ag(100)*, *Surface Science* **602**, 2061–2068 (2008).
Cited on page(s): 12, 47, 57, 178, 179, 201, 210, 234, 295, 296, 299, 302, 304, 310, 332, 333.
- ¹²¹ J. TABORSKI, P. VÄTERLEIN, H. DIETZ, U. ZIMMERMANN, AND E. UMBACH, *NEXAFS investigations on ordered adsorbate layers of large aromatic molecules*, *Journal of Electron Spectroscopy and Related Phenomena* **75**, 129–147 (1995).
Cited on page(s): 12.
- ¹²² M. EREMTCHENKO, D. BAUER, J. A. SCHAEFER, AND F. S. TAUTZ, *Polycyclic aromates on close-packed metal surfaces: functionalization, molecular chemisorption and organic epitaxy*, *New Journal of Physics* **6**, 4 (2004).
Cited on page(s): 13, 14, 196, 218.
- ¹²³ J. ZIROFF, F. FORSTER, A. SCHÖLL, P. PUSCHNIG, AND F. REINERT, *Hybridization of Organic Molecular Orbitals with Substrate States at Interfaces: PTCDA on Silver*, *Physical Re-*

view Letters **104**, 233004 (2010).

Cited on page(s): 13, 41, 199.

- ¹²⁴ A. KRAFT, R. TEMIROV, S. K. M. HENZE, S. SOUBATCH, M. ROHLFING, AND F. S. TAUTZ, *Lateral adsorption geometry and site-specific electronic structure of a large organic chemisorbate on a metal surface*, Physical Review B **74**, 041402(R) (2006).

Cited on page(s): 13, 178, 179, 197, 210, 216.

- ¹²⁵ N. NICOARA, E. ROMÁN, J. M. GÓMEZ-RODRÍGUEZ, J. A. MARTÍN-GAGO, AND J. MÉNDEZ, *Scanning tunneling and photoemission spectroscopies at the PTCDA/Au(111) interface*, Organic Electronics **7**, 287–294 (2006).

Cited on page(s): 13, 175, 197.

- ¹²⁶ J. KRÖGER, H. JENSEN, R. BERNDT, R. RURALI, AND N. LORENTE, *Molecular orbital shift of perylenetetracarboxylic-dianhydride on gold*, Chemical Physics Letters **438**, 249–253 (2007).

Cited on page(s): 13, 197.

- ¹²⁷ I. HILL, A. KAHN, Z. SOOS, R. PASCAL, AND JR, *Charge-separation energy in films of π -conjugated organic molecules*, Chemical Physics Letters **327**, 181–188 (2000).

Cited on page(s): 13.

- ¹²⁸ E. V. TSIPER, Z. G. SOOS, W. GAO, AND A. KAHN, *Electronic polarization at surfaces and thin films of organic molecular crystals: PTCDA*, Chemical Physics Letters **360**, 47–52 (2002).

Cited on page(s): 13.

- ¹²⁹ S. KRAUSE, M. B. CASU, A. SCHÖLL, AND E. UMBACH, *Determination of transport levels of organic semiconductors by UPS and IPS*, New Journal of Physics **10**, 085001 (2008).

Cited on page(s): 13.

- ¹³⁰ M. WIESSNER, J. ZIROFF, F. FORSTER, M. ARITA, K. SHIMADA, P. PUSCHNIG, A. SCHÖLL, AND F. REINERT, *Substrate-mediated band-dispersion of adsorbate molecular states*, Nature Communications **4**, 1514 (2013).

Cited on page(s): 13.

- ¹³¹ R. TEMIROV, S. SOUBATCH, A. LUICAN, AND F. S. TAUTZ, *Free-electron-like dispersion in an organic monolayer film on a metal substrate*, Nature **444**, 350–353 (2006).

Cited on page(s): 13.

- ¹³² C. H. SCHWALB, S. SACHS, M. MARKS, A. SCHÖLL, F. REINERT, E. UMBACH, AND U. HÖFER, *Electron Lifetime in a Shockley-Type Metal-Organic Interface State*, Physical Review Letters **101**, 146801 (2008).

Cited on page(s): 13.

- ¹³³ S. SACHS, C. H. SCHWALB, M. MARKS, A. SCHÖLL, F. REINERT, E. UMBACH, AND U. HÖFER, *Electronic structure at the perylene-tetracarboxylic acid dianhydride/Ag(111) interface studied with two-photon photoelectron spectroscopy*, The Journal of Chemical Physics **131**, 144701 (2009).

Cited on page(s): 13.

- ¹³⁴ C. H. SCHWALB, M. MARKS, S. SACHS, A. SCHÖLL, F. REINERT, E. UMBACH, AND U. HÖFER, *Time-resolved measurements of electron transfer processes at the PTCDA/Ag(111) interface*, The European Physical Journal B **75**, 23–30 (2010).

Cited on page(s): 13.

- ¹³⁵ M. MARKS, N. L. ZAITSEV, B. SCHMIDT, C. H. SCHWALB, A. SCHÖLL, I. A. NECHAEV, P. M. ECHENIQUE, E. V. CHULKOV, AND U. HÖFER, *Energy shift and wave function overlap of metal-organic interface states*, *Physical Review B* **84**, 081301 (2011).
Cited on page(s): 13, 175, 231.
- ¹³⁶ F. S. TAUTZ, M. EREMTCHENKO, J. A. SCHAEFER, M. SOKOLOWSKI, V. SHKLOVER, AND E. UMBACH, *Strong electron-phonon coupling at a metal/organic interface: PTCDA/Ag(111)*, *Physical Review B* **65**, 125405 (2002).
Cited on page(s): 14.
- ¹³⁷ F. S. TAUTZ, S. SLOBOSHANIN, J. A. SCHAEFER, R. SCHOLZ, V. SHKLOVER, M. SOKOLOWSKI, AND E. UMBACH, *Vibrational properties of ultrathin PTCDA films on Ag(110)*, *Physical Review B* **61**, 16933–16947 (2000).
Cited on page(s): 14, 218, 220.
- ¹³⁸ F. S. TAUTZ, S. SLOBOSHANIN, V. SHKLOVER, R. SCHOLZ, M. SOKOLOWSKI, J. A. SCHAEFER, AND E. UMBACH, *Substrate influence on the ordering of organic submonolayers: a comparative study of PTCDA on Ag(110) and Ag(111) using HREELS*, *Applied Surface Science* **166**, 363–369 (2000).
Cited on page(s): 14, 218, 220.
- ¹³⁹ F. S. TAUTZ, M. EREMTCHENKO, J. A. SCHAEFER, M. SOKOLOWSKI, V. SHKLOVER, K. GLÖCKLER, AND E. UMBACH, *A comparison of the chemisorption behaviour of PTCDA on different Ag surfaces*, *Surface Science* **502–503**, 176–184 (2002).
Cited on page(s): 14, 218, 220.
- ¹⁴⁰ L. KILIAN, A. HAUSCHILD, R. TEMIROV, S. SOUBATCH, A. SCHÖLL, A. BENDOUNAN, F. REINERT, T.-L. LEE, F. S. TAUTZ, M. SOKOLOWSKI, AND E. UMBACH, *Role of Intermolecular Interactions on the Electronic and Geometric Structure of a Large π -Conjugated Molecule Adsorbed on a Metal Surface*, *Physical Review Letters* **100**, 136103 (2008).
Cited on page(s): 14, 15, 16, 17, 179, 181, 182, 185, 186, 193, 197, 198, 199, 216, 217.
- ¹⁴¹ A. BONDI, *van der Waals Volumes and Radii*, *The Journal of Physical Chemistry* **68**, 441–451 (1964).
Cited on page(s): 14, 16, 163, 170, 184, 186, 190, 193, 196, 212, 217, 227.
- ¹⁴² M. TRÖMEL AND S. HÜBNER, *Metallradien und Ionenradien*, *Zeitschrift für Kristallographie – Crystalline Materials* **215**, 429–432 (2000).
Cited on page(s): 16, 97, 111, 112, 129, 163, 170, 180, 226.
- ¹⁴³ J. C. SLATER, *Atomic Radii in Crystals*, *The Journal of Chemical Physics* **41**, 3199–3204 (1964).
Cited on page(s): 16.
- ¹⁴⁴ B. CORDERO, V. GÓMEZ, A. E. PLATERO-PRATS, M. REVÉS, J. ECHEVERRÍA, E. CREMADES, F. BARRAGÁN, AND S. ALVAREZ, *Covalent radii revisited*, *Dalton Transactions*, 2832–2838 (2008).
Cited on page(s): 16, 186, 190, 212, 227.
- ¹⁴⁵ R. D. SHANNON, *Revised effective ionic radii and systematic studies of interatomic distances in halides and chalcogenides*, *Acta Crystallographica Section A* **32**, 751–767 (1976).
Cited on page(s): 16, 227.

- ¹⁴⁶ J. E. HUHEEY, *Anorganische Chemie: Prinzipien von Struktur und Reaktivität*, de Gruyter, Berlin, Germany (1988).
Cited on page(s): 16, 82, 111, 144, 184, 187, 196, 197, 214, 227.
- ¹⁴⁷ C. K. CHAN, E.-G. KIM, J.-L. BRÉDAS, AND A. KAHN, *Molecular n-Type Doping of 1,4,5,8-Naphthalene Tetracarboxylic Dianhydride by Pyronin B Studied Using Direct and Inverse Photoelectron Spectroscopies*, *Advanced Functional Materials* **16**, 831–837 (2006).
Cited on page(s): 16.
- ¹⁴⁸ D. R. ZAHN, G. N. GAVRILA, AND M. GORGOI, *The transport gap of organic semiconductors studied using the combination of direct and inverse photoemission*, *Chemical Physics* **325**, 99–112 (2006).
Cited on page(s): 16.
- ¹⁴⁹ P. K. NAYAK AND N. PERIASAMY, *Calculation of electron affinity, ionization potential, transport gap, optical band gap and exciton binding energy of organic solids using ‘solvation’ model and DFT*, *Organic Electronics* **10**, 1396–1400 (2009).
Cited on page(s): 16.
- ¹⁵⁰ R. RURALI, N. LORENTE, AND P. P. ORDEJÓN, *Comment on “Molecular Distortions and Chemical Bonding of a Large π -Conjugated Molecule on a Metal Surface”*, *Physical Review Letters* **95**, 209601 (2005).
Cited on page(s): 17.
- ¹⁵¹ A. HAUSCHILD, K. KARKI, B. C. C. COWIE, M. ROHLFING, F. S. TAUTZ, AND M. SOKOLOWSKI, *Hauschild et al. Reply*, *Physical Review Letters* **95**, 209602 (2005).
Cited on page(s): 17, 233.
- ¹⁵² W. JI, Z.-Y. LU, AND H.-J. GAO, *Multichannel interaction mechanism in a molecule-metal interface*, *Physical Review B* **77**, 113406 (2008).
Cited on page(s): 17.
- ¹⁵³ L. ROMANER, D. NABOK, P. PUSCHNIG, E. ZOJER, AND C. AMBROSCH-DRAXL, *Theoretical study of PTCDA adsorbed on the coinage metal surfaces, Ag(111), Au(111) and Cu(111)*, *New Journal of Physics* **11**, 053010 (2009).
Cited on page(s): 17, 18, 85, 144, 184, 200, 202, 215, 218.
- ¹⁵⁴ A. ABBASI AND R. SCHOLZ, *Ab Initio Calculation of the Dispersion Interaction between a Polyaromatic Molecule and a Noble Metal Substrate: PTCDA on Ag(110)*, *The Journal of Physical Chemistry C* **113**, 19897–19904 (2009).
Cited on page(s): 17, 199, 200.
- ¹⁵⁵ A. TKATCHENKO, L. ROMANER, O. T. HOFMANN, E. ZOJER, C. AMBROSCH-DRAXL, AND M. SCHEFFLER, *Van der Waals Interactions Between Organic Adsorbates and at Organic/Inorganic Interfaces*, *MRS Bulletin* **35**, 435–442 (2010).
Cited on page(s): 17, 215.
- ¹⁵⁶ E. KAWABE, H. YAMANE, R. SUMII, K. KOIZUMI, Y. OUCHI, K. SEKI, AND K. KANAI, *A role of metal d-band in the interfacial electronic structure at organic/metal interface: PTCDA on Au, Ag and Cu*, *Organic Electronics* **9**, 783–789 (2008).
Cited on page(s): 18.
- ¹⁵⁷ D. P. WOODRUFF AND T. A. DELCHAR, *Modern Techniques of Surface Science*, 2nd edition, Cambridge University Press, Cambridge, UK (1994).

- Cited on page(s): 19, 27, 32, 33, 36, 37, 38, 40, 41, 43, 59, 74, 107, 120, 128, 202, 215, 226, 293, 294, 301, 304.
- ¹⁵⁸ R. G. JONES, A. S. Y. CHAN, M. G. ROPER, M. P. SKEGG, I. G. SHUTTLEWORTH, C. J. FISHER, G. J. JACKSON, J. J. LEE, D. P. WOODRUFF, N. K. SINGH, AND B. C. C. COWIE, *X-ray standing waves at surfaces*, *Journal of Physics: Condensed Matter* **14**, 4059–4074 (2002).
Cited on page(s): 19.
- ¹⁵⁹ D. P. WOODRUFF, *Surface structure determination using x-ray standing waves*, *Reports on Progress in Physics* **68**, 743 (2005).
Cited on page(s): 19, 26, 29, 62, 64, 102, 107, 298, 324, 327, 332.
- ¹⁶⁰ B. W. BATTERMAN AND H. COLE, *Dynamical Diffraction of X Rays by Perfect Crystals*, *Reviews of Modern Physics* **36**, 681–717 (1964).
Cited on page(s): 20, 21, 22, 23, 24, 25, 27, 28, 246, 255, 256, 257, 289, 290, 291, 293, 327.
- ¹⁶¹ C. KUNZ (Ed.), *Synchrotron Radiation: Techniques and Applications*, volume 10 of *Topics in Current Physics*, Springer, Berlin, Germany (1979).
Cited on page(s): 20.
- ¹⁶² A. C. THOMPSON, J. KIRZ, D. T. ATTWOOD, E. M. GULLIKSON, M. R. HOWELLS, J. B. KORTRIGHT, Y. LIU, A. L. ROBINSON, J. H. UNDERWOOD, K.-J. KIM, I. LINDAU, P. PIANETTA, H. WINICK, G. P. WILLIAMS, AND J. H. SCOFIELD, *X-Ray Data Booklet*, 3rd edition, Center for X-ray Optics and Advanced Light Source, Lawrence Berkeley National Laboratory, University of California, Berkeley, CA, USA (2009).
Cited on page(s): 20, 51, 54, 55, 57, 58, 59, 145, 350, 351.
- ¹⁶³ J. FALTA AND T. MÖLLER (Eds.), *Forschung mit Synchrotronstrahlung: Eine Einführung in die Grundlagen und Anwendungen*, 1st edition, Vieweg + Teubner, Wiesbaden, Germany (2010).
Cited on page(s): 20.
- ¹⁶⁴ B. E. WARREN, *X-ray diffraction*, Dover Books on Physics, reprint of the Addison-Wesley Publishing Company, Reading, MA, USA, 1969 edition, Dover Publications, Mineola, NY, USA (1990).
Cited on page(s): 20, 28, 29, 33, 60, 246, 250, 289, 290, 293, 294, 327.
- ¹⁶⁵ W. H. ZACHARIASEN, *Theory of X-Ray Diffraction in Crystals*, Dover Phoenix edition, reprint of the 1967 Dover edition which was a republication of the John Wiley & Sons Publishing Company, New York, NY, USA, 1945 edition, Dover Publications, Mineola, NY, USA (2004).
Cited on page(s): 20.
- ¹⁶⁶ W. L. BRAGG, *The Diffraction of Short Electromagnetic Waves by a Crystal*, *Proceedings of the Cambridge Philosophical Society* **17**, 43–57 (1913).
Cited on page(s): 20.
- ¹⁶⁷ R. NEGISHI, T. FUKAMACHI, AND T. KAWAMURA, *X-ray standing wave as a result of only the imaginary part of the atomic scattering factor*, *Acta Crystallographica Section A* **55**, 267–273 (1999).
Cited on page(s): 22.
- ¹⁶⁸ L. E. BERMAN AND M. J. BEDZYK, *Angular distribution of the photoelectron yield excited by two coherently coupled photon beams*, *Physical Review Letters* **63**, 1172–1175 (1989).
Cited on page(s): 24, 29.

- ¹⁶⁹ K.-J. KIM, *Characteristics of Synchrotron Radiation*, in *X-ray Data Booklet* (edited by A. C. Thompson), 3rd edition, chapter 2.1A, pp. 2.1–2.16, Center for X-ray Optics and Advanced Light Source, Lawrence Berkeley National Laboratory, University of California, Berkeley, CA, USA (2009).
Cited on page(s): 24.
- ¹⁷⁰ D. P. WOODRUFF, B. C. C. COWIE, AND A. R. H. F. ETTEMA, *Surface structure determination using X-ray standing waves: a simple view*, *Journal of Physics: Condensed Matter* **6**, 10633–10645 (1994).
Cited on page(s): 26, 159.
- ¹⁷¹ M. J. BEDZYK AND L. CHENG, *X-ray Standing Wave Studies of Minerals and Mineral Surfaces: Principles and Applications*, in *Applications of Synchrotron Radiation in Low-Temperature Geochemistry and Environmental Science* (edited by P. A. Fenter, M. L. Rivers, N. C. Sturchio, and S. R. Sutton), volume 49 of *Reviews in Mineralogy and Geochemistry*, chapter 4, pp. 221–266, published jointly by the Mineralogical Society of America and The Geochemical Society, Washington, D.C., USA (2002).
Cited on page(s): 26.
- ¹⁷² L. CHENG, P. FENTER, M. J. BEDZYK, AND N. C. STURCHIO, *Fourier-Expansion Solution of Atom Distributions in a Crystal Using X-Ray Standing Waves*, *Physical Review Letters* **90**, 255503 (2003).
Cited on page(s): 26.
- ¹⁷³ J. ZEGENHAGEN, *X-ray standing waves imaging*, *Surface Science* **554**, 77–79 (2004).
Cited on page(s): 26.
- ¹⁷⁴ Z. ZHANG, P. FENTER, L. CHENG, N. STURCHIO, M. BEDZYK, M. MACHESKY, AND D. WESOLOWSKI, *Model-independent X-ray imaging of adsorbed cations at the crystal–water interface*, *Surface Science* **554**, L95–L100 (2004).
Cited on page(s): 26.
- ¹⁷⁵ A. G. SHARD AND B. C. C. COWIE, *A demonstration of Auger electron emission stimulated by secondary radiation: implications for x-ray standing-wave analysis of surfaces*, *Journal of Physics: Condensed Matter* **10**, L69 (1998).
Cited on page(s): 26, 62, 102, 107, 119.
- ¹⁷⁶ E. J. NELSON, J. C. WOICK, P. PIANETTA, I. A. VARTANYANTS, AND J. W. COOPER, *Quadrupole effects in core and valence photoelectron emission from crystalline germanium measured via a spatially modulated x-ray interference field*, *Physical Review B* **65**, 165219 (2002).
Cited on page(s): 27, 29, 30, 31, 32, 62, 257, 365.
- ¹⁷⁷ K.-G. HUANG, W. M. GIBSON, AND J. ZEGENHAGEN, *X-ray standing-wave analysis with high reflection order and near-normal incidence*, *Physical Review B* **40**, 4216–4219 (1989).
Cited on page(s): 27.
- ¹⁷⁸ A. CATICHA AND S. CATICHA-ELLIS, *Dynamical theory of x-ray diffraction at Bragg angles near $\pi/2$* , *Physical Review B* **25**, 971–983 (1982).
Cited on page(s): 27.
- ¹⁷⁹ W. GRAEFF AND G. MATERLIK, *Millielectron volt energy resolution in Bragg backscattering*, *Nuclear Instruments and Methods in Physics Research* **195**, 97–103 (1982).
Cited on page(s): 27.

- ¹⁸⁰ M. RENNIGER, *Asymmetrische Bragg-Reflexion am Idealkristall zur Erhöhung des Doppelspektrometer-Auflösungsvermögens*, *Zeitschrift für Naturforschung A: Astrophysik, Physik und Physikalische Chemie* **16 a**, 1110–1111 (1961).
Cited on page(s): 27, 29, 327.
- ¹⁸¹ P. B. HIRSCH AND G. N. RAMACHANDRAN, *Intensity of X-ray Reflexion from Perfect and Mosaic Absorbing Crystals*, *Acta Crystallographica* **3**, 187–194 (1950).
Cited on page(s): 27, 28, 327.
- ¹⁸² K. KOHRA, *An Application of Asymmetric Reflection for Obtaining X-ray Beams of Extremely Narrow Angular Spread*, *Journal of the Physical Society of Japan* **17**, 589–590 (1962).
Cited on page(s): 27, 29.
- ¹⁸³ K. KOHRA AND S. KIKUTA, *A Method of Obtaining an Extremely Parallel X-ray Beam by Successive Asymmetric Diffractions and Its Applications*, *Acta Crystallographica Section A* **24**, 200–205 (1968).
Cited on page(s): 27, 29.
- ¹⁸⁴ S. BRAUER, G. B. STEPHENSON, M. SUTTON, S. G. J. MOCHRIE, S. B. DIERKER, R. M. FLEMING, R. PINDAK, I. K. ROBINSON, G. GRÜBEL, J. ALS-NIELSEN, AND D. L. ABERNATHY, *Asymmetrically cut crystals as optical elements for highly collimated x-ray beams*, *Review of Scientific Instruments* **66**, 1506–1509 (1995).
Cited on page(s): 27.
- ¹⁸⁵ J. W. COOPER, *Multipole corrections to the angular distribution of photoelectrons at low energies*, *Physical Review A* **42**, 6942–6945 (1990).
Cited on page(s): 29, 30, 31.
- ¹⁸⁶ I. A. VARTANYANTS AND J. ZEGENHAGEN, *Photoelectric scattering from an X-ray interference field*, *Solid State Communications* **113**, 299 – 320 (1999).
Cited on page(s): 29.
- ¹⁸⁷ I. VARTANYANTS, T.-L. LEE, S. THIESS, AND J. ZEGENHAGEN, *Non-dipole effects in X-ray standing wave photoelectron spectroscopy experiments*, *Nuclear Instruments and Methods in Physics Research Section A: Accelerators, Spectrometers, Detectors and Associated Equipment* **547**, 196–207 (2005).
Cited on page(s): 29, 30, 31.
- ¹⁸⁸ D. P. WOODRUFF, *Non-dipole effects in high-energy photoelectron emission; identification and quantification using X-ray standing waves*, *Nuclear Instruments and Methods in Physics Research Section A: Accelerators, Spectrometers, Detectors and Associated Equipment* **547**, 187–195 (2005).
Cited on page(s): 29, 30, 31, 62, 256.
- ¹⁸⁹ J. W. COOPER, *Photoelectron-angular-distribution parameters for rare-gas subshells*, *Physical Review A* **47**, 1841–1851 (1993).
Cited on page(s): 29, 31.
- ¹⁹⁰ J. J. LEE, C. J. FISHER, D. P. WOODRUFF, M. G. ROPER, R. G. JONES, AND B. C. C. COWIE, *Non-dipole effects in photoelectron-monitored X-ray standing wave experiments: characterisation and calibration*, *Surface Science* **494**, 166–182 (2001).
Cited on page(s): 29, 30, 31, 32, 62, 365, 367.

- ¹⁹¹ M. O. KRAUSE, *Photo-Ionization of Krypton Between 300 and 1500 eV. Relative Subshell Cross Sections and Angular Distributions of Photoelectrons*, *Physical Review* **177**, 151–157 (1969).
Cited on page(s): 29.
- ¹⁹² F. WUILLEUMIER AND M. O. KRAUSE, *Photoionization of neon between 100 and 2000 eV: Single and multiple processes, angular distributions, and subshell cross sections*, *Physical Review A* **10**, 242–258 (1974).
Cited on page(s): 29.
- ¹⁹³ B. KRÄSSIG, M. JUNG, D. S. GEMMELL, E. P. KANTER, T. LEBRUN, S. H. SOUTHWORTH, AND L. YOUNG, *Nondipolar Asymmetries of Photoelectron Angular Distributions*, *Physical Review Letters* **75**, 4736–4739 (1995).
Cited on page(s): 29.
- ¹⁹⁴ M. JUNG, B. KRÄSSIG, D. S. GEMMELL, E. P. KANTER, T. LEBRUN, S. H. SOUTHWORTH, AND L. YOUNG, *Experimental determination of nondipolar angular distribution parameters for photoionization in the Ar K and Kr L shells*, *Physical Review A* **54**, 2127–2136 (1996).
Cited on page(s): 29.
- ¹⁹⁵ A. BECHLER AND R. H. PRATT, *Higher retardation and multipole corrections to the dipole angular distribution of 1s photoelectrons at low energies*, *Physical Review A* **39**, 1774–1779 (1989).
Cited on page(s): 31.
- ¹⁹⁶ A. BECHLER AND R. H. PRATT, *Higher multipole and retardation corrections to the dipole angular distributions of L-shell photoelectrons ejected by polarized photons*, *Physical Review A* **42**, 6400–6413 (1990).
Cited on page(s): 31.
- ¹⁹⁷ M. B. TRZHASKOVSKAYA, V. I. NEFEDOV, AND V. G. YARZHEMSKY, *Photoelectron angular distribution parameters for elements $Z = 1$ to $Z = 54$ in the photoelectron energy range 100–5000 eV*, *Atomic Data and Nuclear Data Tables* **77**, 97–159 (2001).
Cited on page(s): 31, 57, 58, 62, 63, 64, 365, 366.
- ¹⁹⁸ M. B. TRZHASKOVSKAYA, V. I. NEFEDOV, AND V. G. YARZHEMSKY, *Photoelectron angular distribution parameters for elements $Z = 55$ to $Z = 100$ in the photoelectron energy range 100–5000 eV*, *Atomic Data and Nuclear Data Tables* **82**, 257–311 (2002).
Cited on page(s): 31, 58, 62, 64.
- ¹⁹⁹ A. JABLONSKI, F. SALVAT, AND C. J. POWELL, *NIST Electron Elastic-Scattering Cross-Section Database*, NIST Standard Reference Database 64, version 3.1, National Institute of Standards and Technology, Gaithersburg, MD, USA (2003).
Cited on page(s): 31, 62, 63, 365, 366.
- ²⁰⁰ M. HENZLER AND W. GÖPEL, *Oberflächenphysik des Festkörpers*, Teubner Studienbücher Physik, 2nd edition, Teubner, Stuttgart, Germany (1994).
Cited on page(s): 32, 33, 34, 36, 37, 40, 41, 49, 78.
- ²⁰¹ K. W. KOLASINSKI, *Surface Science: Foundations of Catalysis and Nanoscience*, 2nd edition, John Wiley & Sons, Chichester, UK (2008).
Cited on page(s): 32, 36, 37, 40, 49, 131, 142, 200, 201.

- ²⁰² G. ERTL AND J. KÜPPERS, *Low Energy Electrons and Surface Chemistry*, 2nd edition, VCH, Weinheim, Germany (1985).
Cited on page(s): 32, 33, 35, 36, 37, 38, 39, 40, 41, 49, 53, 56, 59, 66, 96, 202.
- ²⁰³ J. B. PENDRY, *Low Energy Electron Diffraction: The Theory and Its Application to Determination of Surface Structure*, volume 2 of *Techniques of Physics*, Academic Press, London, UK (1974).
Cited on page(s): 32.
- ²⁰⁴ M. A. VAN HOVE AND S. Y. TONG, *Surface Crystallography by LEED: Theory, Computation and Structural Results*, volume 2 of *Springer Series in Chemical Physics*, Springer, Berlin, Germany (1979).
Cited on page(s): 32.
- ²⁰⁵ M. A. VAN HOVE, W. H. WEINBERG, AND C.-M. CHAN, *Low-Energy Electron Diffraction: Experiment, Theory and Surface Structure Determination*, volume 6 of *Springer Series in Surface Sciences*, Springer, Berlin, Germany (1986).
Cited on page(s): 32.
- ²⁰⁶ C. DAVISSON AND L. H. GERMER, *Diffraction of Electrons by a Crystal of Nickel*, *Physical Review* **30**, 705–740 (1927).
Cited on page(s): 32.
- ²⁰⁷ L. DE BROGLIE, XXXV. *A tentative theory of light quanta*, *Philosophical Magazine Series 6* **47**, 446–458 (1924).
Cited on page(s): 32.
- ²⁰⁸ W. BORCHARDT-OTT, *Kristallographie: Eine Einführung für Naturwissenschaftler*, 6th edition, Springer, Berlin, Germany (2002).
Cited on page(s): 33.
- ²⁰⁹ W. MASSA, *Kristallstrukturbestimmung*, Teubner Studienbücher Chemie, 4th edition, Teubner, Stuttgart, Germany (2005).
Cited on page(s): 33, 60, 293, 298, 334.
- ²¹⁰ B. HOLLAND AND D. WOODRUFF, *Missing spots in low energy electron diffraction*, *Surface Science* **36**, 488–493 (1973).
Cited on page(s): 33, 74, 120, 128, 301.
- ²¹¹ H. JAGODZIŃSKI, *Systematic absences in low energy electron diffraction*, *physica status solidi (a)* **49**, 119–126 (1978).
Cited on page(s): 33.
- ²¹² M. D. CHINN AND J. S. C. FAIN, *Low-energy electron diffraction from inert gas overlayers*, *Journal of Vacuum Science & Technology* **14**, 314–317 (1977).
Cited on page(s): 34.
- ²¹³ F. SOJKA, M. MEISSNER, C. ZWICK, R. FORKER, AND T. FRITZ, *Determination and correction of distortions and systematic errors in low-energy electron diffraction*, *Review of Scientific Instruments* **84**, 015111 (2013).
Cited on page(s): 34, 49.
- ²¹⁴ OCI VACUUM MICROENGINEERING, *Instruction Manual: LEED Software — Data Acquisition and Analysis, Version 5.50*, London, Ontario, Canada (2005).
Cited on page(s): 34.

- ²¹⁵ M. HORN-VON HOEGEN, *Growth of semiconductor layers studied by spot profile analysing low energy electron diffraction – Part I*, *Zeitschrift für Kristallographie* **214**, 591–629 (1999).
Cited on page(s): 34, 35, 36, 72, 80, 93, 342, 358.
- ²¹⁶ M. HORN-VON HOEGEN, *Growth of semiconductor layers studied by spot profile analysing low energy electron diffraction – Part II*, *Zeitschrift für Kristallographie* **214**, 684–721 (1999).
Cited on page(s): 34, 70.
- ²¹⁷ M. HENZLER, *LEED studies of surface imperfections*, *Applications of Surface Science* **11/12**, 450–469 (1982).
Cited on page(s): 36.
- ²¹⁸ G. COMSA, *Coherence length and/or transfer width?*, *Surface Science* **81**, 57–68 (1979).
Cited on page(s): 36.
- ²¹⁹ C. J. CHEN, *Introduction to Scanning Tunneling Microscopy*, volume 4 of *Oxford Series in Optical and Imaging Sciences*, Oxford University Press, Oxford, UK (1993).
Cited on page(s): 36, 37.
- ²²⁰ R. WIESENDANGER, *Scanning Probe Microscopy and Spectroscopy: Methods and Applications*, Cambridge University Press, Cambridge, UK (1994).
Cited on page(s): 36, 37.
- ²²¹ G. BINNIG, H. ROHRER, C. GERBER, AND E. WEIBEL, *Tunneling through a controllable vacuum gap*, *Applied Physics Letters* **40**, 178–180 (1982).
Cited on page(s): 36.
- ²²² G. BINNIG, H. ROHRER, C. GERBER, AND E. WEIBEL, *Surface Studies by Scanning Tunneling Microscopy*, *Physical Review Letters* **49**, 57–61 (1982).
Cited on page(s): 36.
- ²²³ G. BINNIG, H. ROHRER, C. GERBER, AND E. WEIBEL, *7 × 7 Reconstruction on Si(111) Resolved in Real Space*, *Physical Review Letters* **50**, 120–123 (1983).
Cited on page(s): 36.
- ²²⁴ J. BARDEEN, *Tunnelling from a Many-Particle Point of View*, *Physical Review Letters* **6**, 57–59 (1961).
Cited on page(s): 36.
- ²²⁵ J. TERSOFF AND D. R. HAMANN, *Theory of the scanning tunneling microscope*, *Physical Review B* **31**, 805–813 (1985).
Cited on page(s): 37.
- ²²⁶ C. J. CHEN, *Theory of scanning tunneling spectroscopy*, *Journal of Vacuum Science & Technology A: Vacuum, Surfaces, and Films* **6**, 319–322 (1988).
Cited on page(s): 37.
- ²²⁷ C. J. CHEN, *Origin of atomic resolution on metal surfaces in scanning tunneling microscopy*, *Physical Review Letters* **65**, 448–451 (1990).
Cited on page(s): 37.
- ²²⁸ J. A. NIEMINEN, E. NIEMI, AND K.-H. RIEDER, *Interference between competing tunneling channels and chemical resolution of STM*, *Surface Science* **552**, L47–L52 (2004).
Cited on page(s): 37.

- ²²⁹ J. REPP AND G. MEYER, *Molekulare Hüllen im Portrait: Rastertunnelmikroskop bildet Molekülorbitale ab*, *Physik in unserer Zeit* **37**, 266–271 (2006).
Cited on page(s): 37.
- ²³⁰ R. TEMIROV, S. SOUBATCH, O. NEUCHEVA, A. C. LASSISE, AND F. S. TAUTZ, *A novel method achieving ultra-high geometrical resolution in scanning tunnelling microscopy*, *New Journal of Physics* **10**, 053012 (2008).
Cited on page(s): 37.
- ²³¹ C. WEISS, C. WAGNER, C. KLEIMANN, M. ROHLFING, F. S. TAUTZ, AND R. TEMIROV, *Imaging Pauli Repulsion in Scanning Tunneling Microscopy*, *Physical Review Letters* **105**, 086103 (2010).
Cited on page(s): 37.
- ²³² C. WEISS, C. WAGNER, R. TEMIROV, AND F. S. TAUTZ, *Direct Imaging of Intermolecular Bonds in Scanning Tunneling Microscopy*, *Journal of the American Chemical Society* **132**, 11864–11865 (2010).
Cited on page(s): 37.
- ²³³ L. GROSS, *Recent advances in submolecular resolution with scanning probe microscopy*, *Nature Chemistry* **3**, 273–278 (2011).
Cited on page(s): 37.
- ²³⁴ J. M. HOLLAS, *High Resolution Spectroscopy*, 2nd edition, John Wiley & Sons, Chichester, UK (1998).
Cited on page(s): 37, 40.
- ²³⁵ D. BRIGGS AND M. P. SEAH (Eds.), *Practical Surface Analysis: Volume 1 — Auger and X-Ray Photoelectron Spectroscopy*, 2nd edition, John Wiley & Sons, Chichester, UK (1990).
Cited on page(s): 37, 38, 39, 40.
- ²³⁶ M. CARDONA AND L. LEY (Eds.), *Photoemission in Solids I: General Principles*, volume 26 of *Topics in Applied Physics*, Springer, Berlin, Germany (1978).
Cited on page(s): 37, 40.
- ²³⁷ M. P. SEAH, *The quantitative analysis of surfaces by XPS: A review*, *Surface and Interface Analysis* **2**, 222–239 (1980).
Cited on page(s): 37, 38, 39.
- ²³⁸ M. SEAH, *A review of the analysis of surfaces and thin films by AES and XPS*, *Vacuum* **34**, 463–478 (1984).
Cited on page(s): 37.
- ²³⁹ H. SIEGBAHN AND K. SIEGBAHN, *ESCA applied to liquids*, *Journal of Electron Spectroscopy and Related Phenomena* **2**, 319–325 (1973).
Cited on page(s): 38.
- ²⁴⁰ K. SIEGBAHN, C. NORDLING, G. JOHANSSON, J. HEDMAN, P. F. HEDÉN, K. HAMRIN, U. GELIUS, T. BERGMARK, L. O. WERME, M. R., AND B. Y., *ESCA Applied to Free Molecules*, North-Holland Publ. Co., Amsterdam, The Netherlands (1969).
Cited on page(s): 38.
- ²⁴¹ H. HERTZ, *Ueber einen Einfluss des ultravioletten Lichtes auf die elektrische Entladung*, *Annalen der Physik* **267**, 983–1000 (1887).
Cited on page(s): 38.

- ²⁴² A. EINSTEIN, *Über einen die Erzeugung und Verwandlung des Lichtes betreffenden heuristischen Gesichtspunkt*, *Annalen der Physik* **322**, 132–148 (1905).
Cited on page(s): 38.
- ²⁴³ T. KOOPMANS, *Über die Zuordnung von Wellenfunktionen und Eigenwerten zu den Einzelnen Elektronen Eines Atoms*, *Physica* **1**, 104–113 (1934).
Cited on page(s): 38.
- ²⁴⁴ K. SCHÖNHAMMER AND O. GUNNARSSON, *Shape of core level spectra in adsorbates*, *Solid State Communications* **23**, 691–693 (1977).
Cited on page(s): 39.
- ²⁴⁵ K. SCHÖNHAMMER AND O. GUNNARSSON, *Correlation effects on core level spectra of adsorbates*, *Solid State Communications* **26**, 399–402 (1978).
Cited on page(s): 39.
- ²⁴⁶ J. FUGGLE, E. UMBACH, D. MENZEL, K. WANDEL, AND C. BRUNDLE, *Adsorbate line shapes and multiple lines in XPS; comparison of theory and experiment*, *Solid State Communications* **27**, 65–69 (1978).
Cited on page(s): 39.
- ²⁴⁷ T. N. RHODIN AND J. W. GADZUK, *Electron spectroscopy and surface chemical bonding*, in *The Nature of the Surface Chemical Bond* (edited by T. N. Rhodin and G. Ertl), chapter 3, pp. 113–273, North-Holland, Amsterdam, The Netherlands (1979).
Cited on page(s): 39.
- ²⁴⁸ G. A. SOMORJAI, *Chemistry in Two Dimensions: Surfaces*, Cornell University Press, Ithaca, NY, USA (1981).
Cited on page(s): 39.
- ²⁴⁹ D. R. PENN, *Electron mean free paths for free-electron-like materials*, *Physical Review B* **13**, 5248–5254 (1976).
Cited on page(s): 39.
- ²⁵⁰ M. P. SEAH, *Quantification of AES and XPS*, in *Practical Surface Analysis: Volume 1 — Auger and X-Ray Photoelectron Spectroscopy* (edited by D. Briggs and M. P. Seah), 2nd edition, chapter 5, pp. 201–255, John Wiley & Sons, Chichester, UK (1990).
Cited on page(s): 39.
- ²⁵¹ M. P. SEAH AND W. A. DENCH, *Quantitative electron spectroscopy of surfaces: A standard data base for electron inelastic mean free paths in solids*, *Surface and Interface Analysis* **1**, 2–11 (1979).
Cited on page(s): 39.
- ²⁵² T. GRABER, F. FORSTER, A. SCHÖLL, AND F. REINERT, *Experimental determination of the attenuation length of electrons in organic molecular solids: The example of PTCDA*, *Surface Science* **605**, 878–882 (2011).
Cited on page(s): 39.
- ²⁵³ S. TANUMA, C. J. POWELL, AND D. R. PENN, *Calculations of electron inelastic mean free paths for 31 materials*, *Surface and Interface Analysis* **11**, 577–589 (1988).
Cited on page(s): 39.
- ²⁵⁴ S. TANUMA, C. J. POWELL, AND D. R. PENN, *Calculations of electron inelastic mean free paths. II. Data for 27 elements over the 50–2000 eV range*, *Surface and Interface Analysis* **17**,

- 911–926 (1991).
Cited on page(s): 39, 52, 54, 55.
- ²⁵⁵ S. TANUMA, C. J. POWELL, AND D. R. PENN, *Calculations of electron inelastic mean free paths. III. Data for 15 inorganic compounds over the 50–2000 eV range*, *Surface and Interface Analysis* **17**, 927–939 (1991).
Cited on page(s): 39.
- ²⁵⁶ S. TANUMA, C. J. POWELL, AND D. R. PENN, *Calculations of electron inelastic mean free paths (IMFPS). IV. Evaluation of calculated IMFPS and of the predictive IMFP formula TPP-2 for electron energies between 50 and 2000 eV*, *Surface and Interface Analysis* **20**, 77–89 (1993).
Cited on page(s): 39.
- ²⁵⁷ S. TANUMA, C. J. POWELL, AND D. R. PENN, *Calculations of electron inelastic mean free paths. V. Data for 14 organic compounds over the 50–2000 eV range*, *Surface and Interface Analysis* **21**, 165–176 (1994).
Cited on page(s): 39, 52.
- ²⁵⁸ S. TANUMA, C. J. POWELL, AND D. R. PENN, *Calculations of electron inelastic mean free paths. IX. Data for 41 elemental solids over the 50 eV to 30 keV range*, *Surface and Interface Analysis* **43**, 689–713 (2011).
Cited on page(s): 39.
- ²⁵⁹ A. JABLONSKI AND C. J. POWELL, *Information depth and the mean escape depth in Auger electron spectroscopy and x-ray photoelectron spectroscopy*, *Journal of Vacuum Science & Technology A: Vacuum, Surfaces, and Films* **21**, 274–283 (2003).
Cited on page(s): 39.
- ²⁶⁰ M. CARDONA AND L. LEY, *Introduction*, in *Photoemission in Solids I: General Principles* (edited by M. Cardona and L. Ley), volume 26 of *Topics in Applied Physics*, chapter 1, pp. 1–104, Springer, Berlin, Germany (1978).
Cited on page(s): 39.
- ²⁶¹ R. F. REILMAN, A. MSEZANE, AND S. T. MANSON, *Relative intensities in photoelectron spectroscopy of atoms and molecules*, *Journal of Electron Spectroscopy and Related Phenomena* **8**, 389–394 (1976).
Cited on page(s): 39.
- ²⁶² Z. KAJCSOS, W. MEISEL, P. GRIESBACH, AND P. GÜTLICH, *The effect of energy-dependent detector efficiency in electron spectroscopic methods: XPS, AES and DCEMS*, *Surface and Interface Analysis* **20**, 544–548 (1993).
Cited on page(s): 39.
- ²⁶³ D. WOODRUFF, *Adsorbate structure determination using photoelectron diffraction: Methods and applications*, *Surface Science Reports* **62**, 1–38 (2007).
Cited on page(s): 40, 59, 107.
- ²⁶⁴ W. HEISENBERG, *Über den anschaulichen Inhalt der quantentheoretischen Kinematik und Mechanik*, *Zeitschrift für Physik* **43**, 172–198 (1927).
Cited on page(s): 41.
- ²⁶⁵ J. ZIROFF, P. GOLD, A. BENDOUNAN, F. FORSTER, AND F. REINERT, *Adsorption energy and geometry of physisorbed organic molecules on Au(111) probed by surface-state photoemission*,

Surface Science **603**, 354–358 (2009).

Cited on page(s): 41.

- ²⁶⁶ P. PUSCHNIG, S. BERKEBILE, A. J. FLEMING, G. KOLLER, K. EMTSEV, T. SEYLLER, J. D. RILEY, C. AMBROSCH-DRAXL, F. P. NETZER, AND M. G. RAMSEY, *Reconstruction of Molecular Orbital Densities from Photoemission Data*, Science **326**, 702–706 (2009).

Cited on page(s): 41.

- ²⁶⁷ P. PUSCHNIG, E. M. REINISCH, T. ULES, G. KOLLER, S. SOUBATCH, M. OSTLER, L. ROMANER, F. S. TAUTZ, C. AMBROSCH-DRAXL, AND M. G. RAMSEY, *Orbital tomography: Deconvoluting photoemission spectra of organic molecules*, Physical Review B **84**, 235427 (2011).

Cited on page(s): 41.

- ²⁶⁸ B. STADTMÜLLER, M. WILLENBOCKEL, E. M. REINISCH, T. ULES, F. C. BOCQUET, S. SOUBATCH, P. PUSCHNIG, G. KOLLER, M. G. RAMSEY, F. S. TAUTZ, AND C. KUMPF, *Orbital tomography for highly symmetric adsorbate systems*, EPL (Europhysics Letters) **100**, 26008 (2012).

Cited on page(s): 41.

- ²⁶⁹ M. WIESSNER, D. HAUSCHILD, A. SCHÖLL, F. REINERT, V. FEYER, K. WINKLER, AND B. KRÖMKER, *Electronic and geometric structure of the PTCDA/Ag(110) interface probed by angle-resolved photoemission*, Physical Review B **86**, 045417 (2012).

Cited on page(s): 41, 231, 295, 297, 300, 301.

- ²⁷⁰ D. LÜFTNER, T. ULES, E. M. REINISCH, G. KOLLER, S. SOUBATCH, F. S. TAUTZ, M. G. RAMSEY, AND P. PUSCHNIG, *Imaging the wave functions of adsorbed molecules*, Proceedings of the National Academy of Sciences **111**, 605–610 (2014).

Cited on page(s): 41.

- ²⁷¹ N. V. SMITH, *Angular Dependent Photoemission*, in *Photoemission in Solids I: General Principles* (edited by M. Cardona and L. Ley), volume 26 of *Topics in Applied Physics*, chapter 6, pp. 237–264, Springer, Berlin, Germany (1978).

Cited on page(s): 41.

- ²⁷² E. W. PLUMMER AND W. EBERHARDT, *Angle-Resolved Photoemission as a Tool for the Study of Surfaces*, in *Advances in Chemical Physics, Volume XLIX* (edited by I. Prigogine and S. A. Rice), volume 49 of *Advances in Chemical Physics*, chapter 8, pp. 533–656, John Wiley & Sons, New York, NY, USA (1982).

Cited on page(s): 41.

- ²⁷³ R. J. SMITH, J. ANDERSON, AND G. J. LAPEYRE, *Adsorbate Orientation Using Angle-Resolved Polarization-Dependent Photoemission*, Physical Review Letters **37**, 1081–1084 (1976).

Cited on page(s): 41.

- ²⁷⁴ C. H. SCHMITZ, *On-surface synthesis of one- and two-dimensional polymers: polyamide films on Ag(111)*, Dissertation, Rheinische Friedrich-Wilhelms-Universität Bonn, Bonn, Germany (2011).

Cited on page(s): 43.

- ²⁷⁵ M. MARKS, *Über die Dynamik von Elektronen auf Silber-Einkristalloberflächen, an metal-organischen Grenzschichten und in PTCDA-Monolagen*, Dissertation, Philipps-Universität

- Marburg, Marburg, Germany (2012).
Cited on page(s): 43, 65, 66, 175, 297, 304, 306, 307.
- ²⁷⁶ J. ZEGENHAGEN, B. DETLEFS, T.-L. LEE, S. THIESS, H. ISERN, L. PETIT, L. ANDRÉ, J. ROY, Y. MI, AND I. JOUMARD, *X-ray standing waves and hard X-ray photoelectron spectroscopy at the insertion device beamline {ID32}*, *Journal of Electron Spectroscopy and Related Phenomena* **178–179**, 258–267, trends in X-ray Photoelectron Spectroscopy of solids (theory, techniques and applications) (2010).
Cited on page(s): 44, 46.
- ²⁷⁷ BEAMLINE ID32 OF THE EUROPEAN SYNCHROTRON RADIATION FACILITY (ESRF), <http://www.esrf.eu/UsersAndScience/Experiments/StructMaterials/ID32>, European Synchrotron Radiation Facility, Grenoble, France (2013).
Cited on page(s): 44.
- ²⁷⁸ G. ADMANS (Ed.), *ESRF Highlights 2011*, European Synchrotron Radiation Facility (ESRF), Grenoble, France (2012).
Cited on page(s): 44.
- ²⁷⁹ SPECS SURFACE NANO ANALYSIS GMBH, *PHOIBOS HV Series: PHOIBOS 150 HV and PHOIBOS 225 HV Analyzers for Hard X-ray Photoelectron Spectroscopy*, Product brochure, Berlin, Germany (2013).
Cited on page(s): 46.
- ²⁸⁰ SAES GETTERS, *Alkali Metal Dispensers*, Product brochure, Milano, Italy (2007).
Cited on page(s): 48.
- ²⁸¹ P. DELLA PORTA, C. EMILI, AND S. J. HELLIER, *Alkali Metal Generation and Gas Evolution from Alkali Metal Dispensers (IEEE Conference on Tube Techniques, New York, September 1968)*, SAES Technical Report TR18.
Cited on page(s): 48.
- ²⁸² F. MORESCO, M. ROCCA, T. HILDEBRANDT, V. ZIELASEK, AND M. HENZLER, *K adsorption on Ag(110): effect on surface structure and surface electronic excitations*, *Surface Science* **424**, 62–73 (1999).
Cited on page(s): 48, 178, 225, 299, 337, 338, 344, 345, 353.
- ²⁸³ C. WIEMAN, G. FLOWERS, AND S. GILBERT, *Inexpensive laser cooling and trapping experiment for undergraduate laboratories*, *American Journal of Physics* **63**, 317–330 (1995).
Cited on page(s): 48.
- ²⁸⁴ F. SOJKA, M. MEISSNER, C. ZWICK, R. FORKER, M. VYSHNEPOLSKY, C. KLEIN, M. H. VON HOEGEN, AND T. FRITZ, *To tilt or not to tilt: Correction of the distortion caused by inclined sample surfaces in low-energy electron diffraction*, *Ultramicroscopy* **133**, 35–40 (2013).
Cited on page(s): 49.
- ²⁸⁵ OMICRON NANOTECHNOLOGY, *New Calibration and Analysis Software for LEED*, Pico: The Omicron NanoTechnology Newsletter **16**, 12–13 (2012).
Cited on page(s): 49.
- ²⁸⁶ F. MEYER ZU HERINGDORF, *neutrans (Transfo: Correction for SPA-LEED Scans)*, version 0.99 (1999).
Cited on page(s): 49.

- ²⁸⁷ M. E. STRAUMANIS AND L. S. YU, *Lattice parameters, densities, expansion coefficients and perfection of structure of Cu and of Cu–In α phase*, Acta Crystallographica Section A **25**, 676–682 (1969).
Cited on page(s): 49, 85, 99, 111, 291.
- ²⁸⁸ H. DOSCH, L. MAILÄNDER, H. REICHERT, J. PEISL, AND R. L. JOHNSON, *Long-range order near the Cu₃Au(001) surface by evanescent x-ray scattering*, Physical Review B **43**, 13172–13186 (1991).
Cited on page(s): 49, 51, 60, 63, 64, 88, 97, 291.
- ²⁸⁹ L.-G. LIU AND W. A. BASSETT, *Compression of Ag and phase transformation of NaCl*, Journal of Applied Physics **44**, 1475–1479 (1973).
Cited on page(s): 49, 51, 60, 63, 64, 85, 180, 251, 292, 293, 342, 365.
- ²⁹⁰ W. D. HAYNES (Ed.), *CRC Handbook of Chemistry and Physics*, 92nd edition, CRC Press/Taylor & Francis, Boca Raton, FL, USA (2011).
Cited on page(s): 49, 161, 345, 346, 347.
- ²⁹¹ B. KRAUSE, A. C. DURR, F. SCHREIBER, H. DOSCH, AND O. H. SEECK, *Thermal stability and partial dewetting of crystalline organic thin films: 3,4,9,10-perylenetetracarboxylic dianhydride on Ag(111)*, The Journal of Chemical Physics **119**, 3429–3435 (2003).
Cited on page(s): 49.
- ²⁹² ORIGINLAB, *OriginPro*, version 8.0, service release 6 (SR6), OriginLab Corporation, Northampton, MA, USA (2009).
Cited on page(s): 50, 66, 131, 237, 239.
- ²⁹³ A. S. BUDDEN, A. G. GROZIN, A. ROHDE, B. JEFFRIES, C. PUGMIRE, C. BRENDES, D. PARFITT, E. EDMONDSON, J. STRUYF, L. ABBOTT, M. VYSKOCIL, S. BLUNDELL, S. WILKINSON, T. RÓSTEN, V. LABELLA, AND Z. KISIEL, *GLE (Graphics Layout Engine)*, version 4.2.3b (2010).
Cited on page(s): 50.
- ²⁹⁴ P. BAYERSDORFER, *Spot-Plotter*, version 1.2.1.4 (2008).
Cited on page(s): 50.
- ²⁹⁵ K. HERMANN AND M. A. VAN HOVE, *LEEDpat*, version 3.0 (2010).
Cited on page(s): 50.
- ²⁹⁶ W. DOMCKE AND L. S. CEDERBAUM, *Electronic recoil effects in high-energy photoelectron spectroscopy*, Journal of Electron Spectroscopy and Related Phenomena **13**, 161–173 (1978).
Cited on page(s): 51.
- ²⁹⁷ M. CINI, *Vibronic coupling and ion recoil effects in valence photoemission from chemisorbed molecules*, Physical Review B **29**, 547–554 (1984).
Cited on page(s): 51.
- ²⁹⁸ E. KUKK, K. UEDA, U. HERGENHAHN, X. J. LIU, G. PRÜMPER, H. YOSHIDA, Y. TAMENORI, C. MAKOCHEKANWA, T. TANAKA, M. KITAJIMA, AND H. TANAKA, *Violation of the Franck-Condon Principle due to Recoil Effects in High Energy Molecular Core-Level Photoionization*, Physical Review Letters **95**, 133001 (2005).
Cited on page(s): 51.
- ²⁹⁹ Y. TAKATA, Y. KAYANUMA, M. YABASHI, K. TAMASAKU, Y. NISHINO, D. MIWA, Y. HARADA, K. HORIBA, S. SHIN, S. TANAKA, E. IKENAGA, K. KOBAYASHI, Y. SENBA,

- H. OHASHI, AND T. ISHIKAWA, *Recoil effects of photoelectrons in a solid*, *Physical Review B* **75**, 233404 (2007).
Cited on page(s): 51.
- ³⁰⁰ Y. TAKATA, Y. KAYANUMA, S. OSHIMA, S. TANAKA, M. YABASHI, K. TAMASAKU, Y. NISHINO, M. MATSUNAMI, R. EGUCHI, A. CHAINANI, M. OURA, T. TAKEUCHI, Y. SENBA, H. OHASHI, S. SHIN, AND T. ISHIKAWA, *Recoil Effect of Photoelectrons in the Fermi Edge of Simple Metals*, *Physical Review Letters* **101**, 137601 (2008).
Cited on page(s): 51.
- ³⁰¹ N. FAIRLEY (CASA SOFTWARE LTD), *CasaXPS: Processing Software for XPS, AES, SIMS and More*, version 2.3.16, Casa Software Ltd, Teignmouth, Devon, UK (2010).
Cited on page(s): 51.
- ³⁰² J. F. MOULDER, W. F. STICKLE, P. E. SOBOL, AND K. BOMBEN, *Handbook of X-ray Photoelectron Spectroscopy*, 2nd edition, Perkin-Elmer Corporation, Physical Electronics Division, Eden Prairie, MN, USA (1992).
Cited on page(s): 51, 54, 55, 57, 58, 100, 351.
- ³⁰³ D. A. SHIRLEY, *High-Resolution X-Ray Photoemission Spectrum of the Valence Bands of Gold*, *Physical Review B* **5**, 4709–4714 (1972).
Cited on page(s): 51.
- ³⁰⁴ P. J. CUMPSON AND M. P. SEAH, *Random uncertainties in AES and XPS: I: Uncertainties in peak energies, intensities and areas derived from peak synthesis*, *Surface and Interface Analysis* **18**, 345–360 (1992).
Cited on page(s): 51.
- ³⁰⁵ P. J. CUMPSON AND M. P. SEAH, *Random uncertainties in AES and XPS: II: Quantification using either relative or absolute measurements*, *Surface and Interface Analysis* **18**, 361–367 (1992).
Cited on page(s): 51.
- ³⁰⁶ N. FAIRLEY (CASA SOFTWARE LTD), *CasaXPS Manual 2.3.16*, available in parts at <http://www.casaxps.com/>, Casa Software Ltd, Teignmouth, Devon, UK (2013).
Cited on page(s): 51, 142.
- ³⁰⁷ A. SCHÖLL, Y. ZOU, M. JUNG, T. SCHMIDT, R. FINK, AND E. UMBACH, *Line shapes and satellites in high-resolution x-ray photoelectron spectra of large π -conjugated organic molecules*, *The Journal of Chemical Physics* **121**, 10260–10267 (2004).
Cited on page(s): 52, 61, 140, 143, 144, 145, 202, 203, 204, 206, 207, 310.
- ³⁰⁸ A. HAUSCHILD, *The Adsorption Geometry of PTCDA on Ag(111) – an NIXSW Study*, Dissertation, Rheinische Friedrich-Wilhelms-Universität Bonn, Bonn, Germany (2007).
Cited on page(s): 52, 57.
- ³⁰⁹ S. TOUGAARD, *Accuracy of the non-destructive surface nanostructure quantification technique based on analysis of the XPS or AES peak shape*, *Surface and Interface Analysis* **26**, 249–269 (1998).
Cited on page(s): 53.
- ³¹⁰ D. BRIGGS AND J. C. RIVIÈRE, *Spectral Interpretation*, in *Practical Surface Analysis: Volume 1 — Auger and X-Ray Photoelectron Spectroscopy* (edited by D. Briggs and M. P. Seah),

2nd edition, chapter 3, pp. 85–141, John Wiley & Sons, Chichester, UK (1990).

Cited on page(s): 54, 58, 62, 310, 350.

- ³¹¹ C. D. WAGNER, *Photoelectron and Auger Energies and the Auger Parameter: A Data Set*, in *Practical Surface Analysis: Volume 1 — Auger and X-Ray Photoelectron Spectroscopy* (edited by D. Briggs and M. P. Seah), 2nd edition, chapter : Appendix 5, pp. 595–634, John Wiley & Sons, Chichester, UK (1990).

Cited on page(s): 54, 58.

- ³¹² K. L. SMITH AND K. M. BLACK, *Characterization of the treated surfaces of silicon alloyed pyrolytic carbon and SiC*, *Journal of Vacuum Science & Technology A: Vacuum, Surfaces, and Films* **2**, 744–747 (1984).

Cited on page(s): 54, 58.

- ³¹³ D. CLARK, D. KILCAST, D. ADAMS, AND W. MUSGRAVE, *An ESCA study of the molecular core binding energies of the fluorobenzenes*, *Journal of Electron Spectroscopy and Related Phenomena* **1**, 227–250 (1972–1973).

Cited on page(s): 54, 58.

- ³¹⁴ C. D. WAGNER, *Kinetic Energies of Auger Electrons: Experimental Data from Spectra Acquired by X-Ray Excitation*, in *Practical Surface Analysis: Volume 1 — Auger and X-Ray Photoelectron Spectroscopy* (edited by D. Briggs and M. P. Seah), 2nd edition, chapter : Appendix 9, pp. 645–650, John Wiley & Sons, Chichester, UK (1990).

Cited on page(s): 54, 55.

- ³¹⁵ T. J. SCHUERLEIN AND N. R. ARMSTRONG, *Formation and characterization of epitaxial phthalocyanine and perylene monolayers and bilayers on Cu(100): Low-energy electron diffraction and thermal desorption mass spectrometry studies*, *Journal of Vacuum Science & Technology A: Vacuum, Surfaces, and Films* **12**, 1992–1997 (1994).

Cited on page(s): 57, 231, 236.

- ³¹⁶ M. ANDREASSON, M. TENGELIN-NILSSON, L. ILVER, AND J. KANSKI, *Photoelectron spectroscopic studies of ultra-thin CuPc and PTCDA layers on Cu(100)*, *Synthetic Metals* **158**, 45–49 (2008).

Cited on page(s): 57, 231, 236.

- ³¹⁷ K. DILLER, F. KLAPPENBERGER, M. MARSCHALL, K. HERMANN, A. NEFEDOV, C. WÖLL, AND J. V. BARTH, *Self-metalation of 2H-tetraphenylporphyrin on Cu(111): An x-ray spectroscopy study*, *The Journal of Chemical Physics* **136**, 014705 (2012).

Cited on page(s): 59.

- ³¹⁸ D. VERNER, D. YAKOVLEV, I. BAND, AND M. TRZHASKOVSKAYA, *Subshell Photoionization Cross Sections and Ionization Energies of Atoms and Ions from He to Zn*, *Atomic Data and Nuclear Data Tables* **55**, 233–280 (1993).

Cited on page(s): 59.

- ³¹⁹ B. LUNDQVIST, *Characteristic structure in core electron spectra of metals due to the electron-plasmon coupling*, *Physik der kondensierten Materie* **9**, 236–248 (1969).

Cited on page(s): 59.

- ³²⁰ R. MANNE AND T. ÅBERG, *Koopmans' theorem for inner-shell ionization*, *Chemical Physics Letters* **7**, 282–284 (1970).

Cited on page(s): 59.

- ³²¹ C. FADLEY, *Photoelectric cross sections and multi-electron transitions in the sudden approximation*, Chemical Physics Letters **25**, 225–230 (1974).
Cited on page(s): 59.
- ³²² S. P. KOWALCZYK, L. LEY, R. L. MARTIN, F. R. MCFEELY, AND D. A. SHIRLEY, *Relaxation and final-state structure in XPS of atoms, molecules, and metals*, Faraday Discussions of the Chemical Society **60**, 7–17 (1975).
Cited on page(s): 59.
- ³²³ R. G. HAYES, *A simple approximate sum rule for correlation-state structure in {XPS}*, Journal of Electron Spectroscopy and Related Phenomena **22**, 365–372 (1981).
Cited on page(s): 59.
- ³²⁴ E. T. JENSEN, *Surface Physics*, in *Springer Handbook of Atomic, Molecular, and Optical Physics* (edited by G. W. F. DRAKE), volume LVIII of *Springer Handbooks*, 2nd edition, chapter 89, pp. 1343–1354, Springer, New York, NY, USA (2006).
Cited on page(s): 59.
- ³²⁵ C. D. WAGNER, L. E. DAVIS, M. V. ZELLER, J. A. TAYLOR, R. H. RAYMOND, AND L. H. GALE, *Empirical atomic sensitivity factors for quantitative analysis by electron spectroscopy for chemical analysis*, Surface and Interface Analysis **3**, 211–225 (1981).
Cited on page(s): 59.
- ³²⁶ G. MERCURIO, *Study of Molecule-Metal Interfaces by Means of the Normal Incidence X-ray Standing Wave Technique*, Schriften des Forschungszentrums Jülich, Reihe Schlüsseltechnologien, volume 49, Dissertation, Rheinisch-Westfälische Technische Hochschule Aachen, Aachen, Germany (2012).
Cited on page(s): 60, 62, 178, 237, 253, 257, 295, 337, 339, 340, 353, 357, 358, 359.
- ³²⁷ O. BAUER, *Die Adsorptionsgeometrie von PTCDA auf der (100)- und der (110)-Oberfläche einkristallinen Silbers: Untersuchungen mithilfe der Absorption im stehenden Röntgenwellenfeld*, Degree dissertation, Rheinische Friedrich-Wilhelms-Universität Bonn, Bonn, Germany (2007).
Cited on page(s): 60.
- ³²⁸ H.-J. MEYER, *Festkörperchemie*, in *Moderne Anorganische Chemie* (edited by E. RIEDEL), 2nd edition, chapter 3, pp. 351–555, de Gruyter, Berlin, Germany (2003).
Cited on page(s): 60, 87, 99, 109, 111, 290.
- ³²⁹ O. BAUER AND M. SOKOLOWSKI, *XSWAVES: An XSW Data Evaluation Routine for Origin 8*, version 2.5, available at http://www.thch.uni-bonn.de/pctc/sokolowski/XSWAVES/XSWAVES_index.html, Rheinische Friedrich-Wilhelms-Universität Bonn, Bonn, Germany (2013).
Cited on page(s): 61, 62, 104, 253, 258, 295, 337, 366, 369.
- ³³⁰ G. MERCURIO, *Torricelli: An XSW data analysis and simulation program*, Forschungszentrum Jülich, Jülich, Germany (2012).
Cited on page(s): 62, 237, 255, 257, 295, 337, 369.
- ³³¹ N. M. KABACHNIK AND I. P. SAZHINA, *Non-dipolar effects in angular distributions of photoinduced Auger electrons*, Journal of Physics B: Atomic, Molecular and Optical Physics **29**, L515–L519 (1996).
Cited on page(s): 62, 107.

- ³³² F. SCHREIBER, K. A. RITLEY, I. A. VARTANYANTS, H. DOSCH, J. ZEGENHAGEN, AND B. C. C. COWIE, *Non-dipolar contributions in XPS detection of X-ray standing waves*, *Surface Science* **486**, L519–L523 (2001).
Cited on page(s): 65, 365.
- ³³³ IMAGE METROLOGY, *SPIP: Scanning Probe Image Processor*, version 4.8.7.0 (2009).
Cited on page(s): 65.
- ³³⁴ H. LÜTH, *Solid Surfaces, Interfaces and Thin Films*, Graduate Texts in Physics, Springer, Berlin, Germany (2010).
Cited on page(s): 66, 198, 304, 307.
- ³³⁵ G. WEDLER, *Lehrbuch der Physikalischen Chemie*, 4th edition, Wiley-VCH, Weinheim, Germany (1997).
Cited on page(s): 66.
- ³³⁶ A. BEN HAMED, *Bestimmung der Struktur der Monolage von PTCDA auf der Cu(111)-Oberfläche mittels Spot Profile Analysis Low Energy Electron Diffraction*, Bachelor's dissertation, Rheinische Friedrich-Wilhelms-Universität Bonn, Bonn, Germany (2011).
Cited on page(s): 67.
- ³³⁷ T. WAGNER, H. KARACUBAN, A. BANNANI, C. BOBISCH, AND R. MÖLLER, *Thermal desorption of PTCDA on Cu(111)*, *Journal of Physics: Conference Series* **100**, 052068 (2008).
Cited on page(s): 67.
- ³³⁸ T. WAGNER, H. KARACUBAN, AND R. MÖLLER, *Analysis of complex thermal desorption spectra: PTCDA on copper*, *Surface Science* **603**, 482–490 (2009).
Cited on page(s): 67, 76, 77, 78, 80, 84, 131, 300.
- ³³⁹ J. WOLLSCHLÄGER, E. Z. LUO, AND M. HENZLER, *Thermal roughness of the homogeneous and inhomogeneous Cu(311) surface studied by high-resolution low-energy electron diffraction*, *Physical Review B* **44**, 13031–13041 (1991).
Cited on page(s): 69.
- ³⁴⁰ J. WOLLSCHLÄGER, E. LUO, AND M. HENZLER, *Epitaxial growth and thermal behaviour of Pb overlayers on Cu(311) studied by high-resolution low-energy electron diffraction*, *Surface Science* **257**, 274–288 (1991).
Cited on page(s): 69.
- ³⁴¹ P. J. BROWN, A. G. FOX, E. N. MASLEN, M. A. O'KEEFE, AND B. T. M. WILLIS, *Intensity of diffracted intensities*, in *International Tables for Crystallography, Volume C: Mathematical, physical and chemical tables, Part 6: Interpretation of diffracted intensities* (edited by E. Prince), 1st online edition, chapter 6.1, pp. 554–595, International Union of Crystallography, http://xrpp.iucr.org/cgi-bin/itr?url_ver=Z39.88-2003&rft_dat=what%3Dchapter%26volid%3DCb%26chnumo%3D601%26chvers%3Dv0001 (2006).
Cited on page(s): 70, 290.
- ³⁴² T. WAGNER, *Organische Heteroschichten: Untersuchung der Wechselwirkung organischer Moleküle auf metallischen Oberflächen*, Dissertation, Universität Duisburg-Essen, Duisburg, Germany (2006).
Cited on page(s): 72, 127.

- ³⁴³ U. MÜLLER, *Anorganische Strukturchemie*, Teubner Studienbücher Chemie, 4th edition, Teubner, Stuttgart, Germany (2004).
Cited on page(s): 72, 290.
- ³⁴⁴ C. WAGNER, R. FORKER, AND T. FRITZ, *On the Origin of the Energy Gain in Epitaxial Growth of Molecular Films*, *The Journal of Physical Chemistry Letters* **3**, 419–424 (2012).
Cited on page(s): 74.
- ³⁴⁵ G. EHRLICH AND F. G. HUDDA, *Atomic View of Surface Self-Diffusion: Tungsten on Tungsten*, *The Journal of Chemical Physics* **44**, 1039–1049 (1966).
Cited on page(s): 78.
- ³⁴⁶ R. L. SCHWOEBEL AND E. J. SHIPSEY, *Step Motion on Crystal Surfaces*, *Journal of Applied Physics* **37**, 3682–3686 (1966).
Cited on page(s): 78.
- ³⁴⁷ H. IBACH, *Physics of Surfaces and Interfaces*, Springer, Berlin, Germany (2006).
Cited on page(s): 78, 83.
- ³⁴⁸ T. A. WITTEN AND L. M. SANDER, *Diffusion-limited aggregation*, *Physical Review B* **27**, 5686–5697 (1983).
Cited on page(s): 78.
- ³⁴⁹ T. MICHELY, M. HOHAGE, M. BOTT, AND G. COMSA, *Inversion of growth speed anisotropy in two dimensions*, *Physical Review Letters* **70**, 3943–3946 (1993).
Cited on page(s): 78.
- ³⁵⁰ H. BRUNE, H. RÖDER, K. BROMANN, K. KERN, J. JACOBSEN, P. STOLTZE, K. JACOBSEN, AND J. NØRSKOV, *Anisotropic corner diffusion as origin for dendritic growth on hexagonal substrates*, *Surface Science* **349**, L115–L122 (1996).
Cited on page(s): 78.
- ³⁵¹ S. SCHMITT, *Adsorbatinduzierte richtungsabhängige Facettierung und selbstorganisierte Domänen-Musterbildung auf vizinalen Ag(111)-Oberflächen*, Dissertation, Julius-Maximilians-Universität Würzburg, Würzburg, Germany (2007).
Cited on page(s): 80.
- ³⁵² M. VAN HOVE, R. KOESTNER, P. STAIR, J. BIBÉRIAN, L. KESMODEL, I. BARTOŠ , AND G. SOMORJAI, *The surface reconstructions of the (100) crystal faces of iridium, platinum and gold: I. Experimental observations and possible structural models*, *Surface Science* **103**, 189–217 (1981).
Cited on page(s): 80, 81, 83, 98, 99, 110, 111.
- ³⁵³ C. WÖLL, S. CHIANG, R. J. WILSON, AND P. H. LIPPEL, *Determination of atom positions at stacking-fault dislocations on Au(111) by scanning tunneling microscopy*, *Physical Review B* **39**, 7988–7991 (1989).
Cited on page(s): 80, 81, 82, 99, 107.
- ³⁵⁴ J. V. BARTH, H. BRUNE, G. ERTL, AND R. J. BEHM, *Scanning tunneling microscopy observations on the reconstructed Au(111) surface: Atomic structure, long-range superstructure, rotational domains, and surface defects*, *Physical Review B* **42**, 9307–9318 (1990).
Cited on page(s): 80, 81, 82, 99, 107.
- ³⁵⁵ I.-S. HWANG, R. E. MARTINEZ, C. LIU, AND J. A. GOLOVCHENKO, *Soft incommensurate reconstruction on Pb/Si(111): Structure, stress modulation, and phase transition*, *Physical Re-*

- view B **51**, 10193–10196 (1995).
Cited on page(s): 81.
- ³⁵⁶ A. FASOLINO, G. SANTORO, AND E. TOSATTI, *Surface Phonons and the Incommensurate Reconstruction of Clean Mo (100)*, *Journal de Physique Colloques* **42**, C6–846–C6–848 (1981).
Cited on page(s): 81.
- ³⁵⁷ M. CORSO, L. FERNÁNDEZ, F. SCHILLER, AND J. E. ORTEGA, *Au(111)-Based Nanotemplates by Gd Alloying*, *ACS Nano* **4**, 1603–1611, pMID: 20146459 (2010).
Cited on page(s): 81, 82, 99, 107.
- ³⁵⁸ U. HARTEN, A. M. LAHEE, J. P. TOENNIES, AND C. WÖLL, *Observation of a Soliton Reconstruction of Au(111) by High-Resolution Helium-Atom Diffraction*, *Physical Review Letters* **54**, 2619–2622 (1985).
Cited on page(s): 81, 82, 99.
- ³⁵⁹ Ž. CRLJEN, D. ŠOKČEVIĆ, R. BRAKO, AND P. LAZIĆ, *DFT calculations of (111) surfaces of Au, Cu, and Pt: stability and reconstruction*, *Vacuum* **71**, 101–106 (2003).
Cited on page(s): 82, 83, 110.
- ³⁶⁰ M. KIEL, K. DUNCKER, C. HAGENDORF, AND W. WIDDRA, *Molecular structure and chiral separation in α -sexithiophene ultrathin films on Au(111): Low-energy electron diffraction and scanning tunneling microscopy*, *Physical Review B* **75**, 195439 (2007).
Cited on page(s): 82, 115.
- ³⁶¹ A. HÖFER, K. DUNCKER, M. KIEL, S. WEDEKIND, AND W. WIDDRA, *Adsorption of α -sexithiophene on Au(001): Molecule-induced partial lifting of the substrate reconstruction*, *Physical Review B* **83**, 075414 (2011).
Cited on page(s): 82, 115.
- ³⁶² J. T. SUN, L. GAO, X. B. HE, Z. H. CHENG, Z. T. DENG, X. LIN, H. HU, S. X. DU, F. LIU, AND H.-J. GAO, *Surface reconstruction transition of metals induced by molecular adsorption*, *Physical Review B* **83**, 115419 (2011).
Cited on page(s): 82, 115, 162.
- ³⁶³ P. W. MURRAY, M. O. PEDERSEN, E. LÆGSGAARD, I. STENSGAARD, AND F. BESENBACHER, *Growth of C₆₀ on Cu(110) and Ni(110) surfaces: C₆₀-induced interfacial roughening*, *Physical Review B* **55**, 9360–9363 (1997).
Cited on page(s): 82.
- ³⁶⁴ W. OSTWALD, *Über die vermeintliche Isomerie des roten und gelben Quecksilberoxyds und die Oberflächenspannung fester Körper*, *Zeitschrift für Physikalische Chemie, Stöchiometrie und Verwandtschaftslehre* **34**, 495–503 (1900).
Cited on page(s): 83.
- ³⁶⁵ Ž. CRLJEN, P. LAZIĆ, D. ŠOKČEVIĆ, AND R. BRAKO, *Relaxation and reconstruction on (111) surfaces of Au, Pt, and Cu*, *Physical Review B* **68**, 195411 (2003).
Cited on page(s): 83, 84, 110.
- ³⁶⁶ M. MANSFIELD AND R. J. NEEDS, *Application of the Frenkel-Kontorova model to surface reconstructions*, *Journal of Physics: Condensed Matter* **2**, 2361–2374 (1990).
Cited on page(s): 84, 110.

- ³⁶⁷ L. VEGARD, *Die Konstitution der Mischkristalle und die Raumfüllung der Atome*, Zeitschrift für Physik **5**, 17–26 (1921).
Cited on page(s): 87, 99, 109, 111.
- ³⁶⁸ E. RIEDEL, unter Mitwirkung von C. Janiak, *Anorganische Chemie*, 5th edition, de Gruyter, Berlin, Germany (2002).
Cited on page(s): 87, 99, 109, 111.
- ³⁶⁹ H. OKAMOTO, D. CHAKRABARTI, D. LAUGHLIN, AND T. MASSALSKI, *The Au-Cu (Gold-Copper) system*, Journal of Phase Equilibria (formerly: Bulletin of Alloy Phase Diagrams) **8**, 454–474 (1987).
Cited on page(s): 87, 88, 97, 290.
- ³⁷⁰ K. R. MECKE AND S. DIETRICH, *Segregation profiles in Cu₃Au above the order-disorder transition*, Physical Review B **52**, 2107–2116 (1995).
Cited on page(s): 87.
- ³⁷¹ D. T. KEATING AND B. E. WARREN, *Long-Range Order in Beta-Brass and Cu₃Au*, Journal of Applied Physics **22**, 286–290 (1951).
Cited on page(s): 87, 109.
- ³⁷² V. S. SUNDARAM, B. FARRELL, R. S. ALBEN, AND W. D. ROBERTSON, *Order-Disorder Transformation at the (100) Surface of Cu₃Au*, Physical Review Letters **31**, 1136–1139 (1973).
Cited on page(s): 87, 88.
- ³⁷³ V. SUNDARAM, R. ALBEN, AND W. ROBERTSON, *The order-disorder transformation at a (100) surface of Cu₃Au: Theory and experiment*, Surface Science **46**, 653–671 (1974).
Cited on page(s): 87, 88, 294.
- ³⁷⁴ N. MARDESICH, C. N. J. WAGNER, AND A. J. ARDELL, *Long-range order in Cu₃Au and dilute Cu₃Au-Co alloys*, Journal of Applied Crystallography **10**, 468–472 (1977).
Cited on page(s): 87, 88, 294.
- ³⁷⁵ B. E. WARREN, *X-Ray Studies of Order-Disorder*, in *X-ray diffraction*, Dover Books on Physics, reprint of the Addison-Wesley Publishing Company, Reading, MA, USA, 1969 edition, chapter 12, pp. 206–250, Dover Publications, Mineola, NY, USA (1990).
Cited on page(s): 87, 88, 97, 106, 109, 110, 290.
- ³⁷⁶ Z. W. WILCHINSKY, *X-Ray Measurement of Order in the Alloy Cu₃Au*, Journal of Applied Physics **15**, 806–812 (1944).
Cited on page(s): 88.
- ³⁷⁷ J. M. COWLEY, *X-Ray Measurement of Order in Single Crystals of Cu₃Au*, Journal of Applied Physics **21**, 24–30 (1950).
Cited on page(s): 88.
- ³⁷⁸ P. BARDHAN AND J. B. COHEN, *A structural study of the alloy Cu₃Au above its critical temperature*, Acta Crystallographica Section A **32**, 597–614 (1976).
Cited on page(s): 88, 294.
- ³⁷⁹ S. E. NAGLER, R. F. SHANNON, C. R. HARKLESS, M. A. SINGH, AND R. M. NICKLOW, *Time-Resolved X-Ray Scattering Study of Ordering and Coarsening in Cu₃Au*, Physical Review Letters **61**, 718–721 (1988).
Cited on page(s): 88.

- ³⁸⁰ B. D. BUTLER AND J. B. COHEN, *The structure of Cu₃Au above the critical temperature*, *Journal of Applied Physics* **65**, 2214–2219 (1989).
Cited on page(s): 88.
- ³⁸¹ R. F. SHANNON, S. E. NAGLER, C. R. HARKLESS, AND R. M. NICKLOW, *Time-resolved x-ray-scattering study of ordering kinetics in bulk single-crystal Cu₃Au*, *Physical Review B* **46**, 40–54 (1992).
Cited on page(s): 88, 91, 92.
- ³⁸² G. K. WERTHEIM, *Partial densities of states of alloys: Cu₃Au*, *Physical Review B* **36**, 4432–4434 (1987).
Cited on page(s): 88.
- ³⁸³ G. K. WERTHEIM, L. F. MATTHEISS, AND D. N. E. BUCHANAN, *Partial densities of states of ordered Cu₃Au*, *Physical Review B* **38**, 5988–5992 (1988).
Cited on page(s): 88.
- ³⁸⁴ T. K. SHAM, Y. M. YIU, M. KUHN, AND K. H. TAN, *Electronic structure of ordered and disordered Cu₃Au: The behavior of the Au 5d bands*, *Physical Review B* **41**, 11881–11886 (1990).
Cited on page(s): 88.
- ³⁸⁵ M. KUHN AND T. K. SHAM, *Charge redistribution and electronic behavior in a series of Au-Cu alloys*, *Physical Review B* **49**, 1647–1661 (1994).
Cited on page(s): 88.
- ³⁸⁶ C. JANSSON AND S. TOUGAARD, *Quantitative x-ray photoelectron spectroscopy of CuAu, CoNi, and CuNi alloys using theoretical photoionization cross sections or reference spectra*, *Journal of Vacuum Science & Technology A: Vacuum, Surfaces, and Films* **12**, 2332–2336 (1994).
Cited on page(s): 88.
- ³⁸⁷ P. WEINBERGER, V. DRCHAL, L. SZUNYOGH, J. FRITSCHER, AND B. I. BENNETT, *Electronic and structural properties of Cu-Au alloys*, *Physical Review B* **49**, 13366–13372 (1994).
Cited on page(s): 88.
- ³⁸⁸ R. W. G. WYCKOFF, *The Structure of Crystals*, American Chemical Society Monograph Series, 2nd edition, Chemical Catalog Company, New York, NY, USA (1931).
Cited on page(s): 88, 97, 112, 163.
- ³⁸⁹ H. C. POTTER AND J. M. BLAKELY, *LEED, Auger spectroscopy, and contact potential studies of copper-gold alloy single crystal surfaces*, *Journal of Vacuum Science & Technology* **12**, 635–642 (1975).
Cited on page(s): 88, 93, 97, 108, 191, 192.
- ³⁹⁰ X.-M. ZHU, R. FEIDENHANS'L, H. ZABEL, J. ALS-NIELSEN, R. DU, C. P. FLYNN, AND F. GREY, *Grazing-incidence x-ray scattering on the Cu₃Au(111) phase transition*, *Physical Review B* **37**, 7157–7160 (1988).
Cited on page(s): 88.
- ³⁹¹ Y. MA, S. LORDI, C. FLYNN, AND J. EADES, *Dynamical calculations for {RHEED} from a partially-ordered Cu₃Au(111) surface*, *Surface Science* **302**, 241–257 (1994).
Cited on page(s): 88.

- ³⁹² Y. HUANG, M. GAJDARDZISKA-JOSIFOVSKA, AND J. M. COWLEY, *REM in a UHV TEM for the observation of dynamic phase transformation processes on the Cu₃Au(111) surface*, *Ultramicroscopy* **57**, 391–408 (1995).
Cited on page(s): 88, 89, 108.
- ³⁹³ S. BONHAM AND C. FLYNN, *Resonant RHEED study of Cu₃Au(111) surface order*, *Surface Science* **366**, L760–L764 (1996).
Cited on page(s): 88.
- ³⁹⁴ S. W. BONHAM AND C. P. FLYNN, *Resonant RHEED measurements of surface order on Cu₃Au(111) films*, *Physical Review B* **57**, 4099–4110 (1998).
Cited on page(s): 88.
- ³⁹⁵ R. COURTHS, M. LAU, T. SCHEUNEMANN, H. GOLLISCH, AND R. FEDER, *From the Shockley surface state on Cu(111) to sp-like surface resonances on Cu₃Au(111)*, *Physical Review B* **63**, 195110 (2001).
Cited on page(s): 88, 174, 175, 194.
- ³⁹⁶ C. LEKKA, N. BERNSTEIN, M. MEHL, AND D. PAPACONSTANTOPOULOS, *Electronic structure of the Cu₃Au(111) surface*, *Applied Surface Science* **219**, 158 – 166 (2003).
Cited on page(s): 88.
- ³⁹⁷ A. STIERLE, A. STEINHÄUSER, A. RÜHM, F. U. RENNER, R. WEIGEL, N. KASPER, AND H. DOSCH, *Dedicated Max-Planck beamline for the in situ investigation of interfaces and thin films*, *Review of Scientific Instruments* **75**, 5302–5307 (2004).
Cited on page(s): 88, 89, 107, 108, 111.
- ³⁹⁸ J. ZEGENHAGEN, F. RENNER, A. REITZLE, T. LEE, S. WARREN, A. STIERLE, H. DOSCH, G. SCHERB, B. FIMLAND, AND D. KOLB, *In situ X-ray analysis of solid/electrolyte interfaces: electrodeposition of Cu and Co on Si(111):H and GaAs(001) and corrosion of Cu₃Au(111)*, *Surface Science* **573**, 67–79 (2004).
Cited on page(s): 88.
- ³⁹⁹ F. U. RENNER, A. STIERLE, H. DOSCH, D. M. KOLB, T.-L. LEE, AND J. ZEGENHAGEN, *Initial corrosion observed on the atomic scale*, *Nature* **439**, 707–710 (2006).
Cited on page(s): 88, 89.
- ⁴⁰⁰ F. U. RENNER, A. STIERLE, H. DOSCH, D. M. KOLB, T. L. LEE, AND J. ZEGENHAGEN, *In situ x-ray diffraction study of the initial dealloying and passivation of Cu₃Au(111) during anodic dissolution*, *Physical Review B* **77**, 235433 (2008).
Cited on page(s): 88, 89.
- ⁴⁰¹ T. M. BUCK, G. H. WHEATLEY, AND L. MARCHUT, *Order-Disorder and Segregation Behavior at the Cu₃Au(001) Surface*, *Physical Review Letters* **51**, 43–46 (1983).
Cited on page(s): 88.
- ⁴⁰² E. MCRAE AND R. MALIC, *Observations of the Cu₃Au(001) phase transition using a novel low energy electron diffraction system*, *Surface Science* **148**, 551–580 (1984).
Cited on page(s): 88.
- ⁴⁰³ K. JAMISON, D. LIND, F. DUNNING, AND G. WALTERS, *Polarized LEED investigation of the order/disorder transition at a Cu₃Au(100) surface*, *Surface Science Letters* **159**, L451–L459 (1985).
Cited on page(s): 88.

- ⁴⁰⁴ S. B. DICENZO, P. H. CITRIN, E. H. HARTFORD, AND G. K. WERTHEIM, *Au surface density of states and surface core-level shifts in $Cu_3Au(001)$* , *Physical Review B* **34**, 1343–1345 (1986).
Cited on page(s): 88.
- ⁴⁰⁵ Z. Q. WANG, S. C. WU, J. QUINN, C. K. C. LOK, Y. S. LI, F. JONA, AND J. W. DAVENPORT, *Experimental band structure of Cu_3Au* , *Physical Review B* **38**, 7442–7447 (1988).
Cited on page(s): 88.
- ⁴⁰⁶ H. DOSCH, L. MAILÄNDER, A. LIED, J. PEISL, F. GREY, R. L. JOHNSON, AND S. KRUMMACHER, *Experimental Evidence for an Interface Delocalization Transition in Cu_3Au* , *Physical Review Letters* **60**, 2382–2385 (1988).
Cited on page(s): 88.
- ⁴⁰⁷ S. KRUMMACHER, N. SEN, W. GUDAT, R. JOHNSON, F. GREY, AND J. GHIJSEN, *Comparative study of the electronic structure of the ordered and disordered $Cu_3Au(100)$ and $Cu_3Au(110)$ surfaces*, *Zeitschrift für Physik B Condensed Matter* **75**, 235–243 (1989).
Cited on page(s): 88.
- ⁴⁰⁸ H. REICHERT, P. J. ENG, H. DOSCH, AND I. K. ROBINSON, *Thermodynamics of Surface Segregation Profiles at $Cu_3Au(001)$ Resolved by X-Ray Scattering*, *Physical Review Letters* **74**, 2006–2009 (1995).
Cited on page(s): 88.
- ⁴⁰⁹ F. M. ZHANG, B. V. KING, AND D. J. O’CONNOR, *Low Energy Ion Scattering Investigation of the Order-Disorder Transition in the First Atomic Layer of the $Cu_3Au(100)$ Surface*, *Physical Review Letters* **75**, 4646–4649 (1995).
Cited on page(s): 88.
- ⁴¹⁰ L. HOUSSIAU AND P. BERTRAND, *Direct observation of the rippling and the order-disorder transition at the $Cu_3Au(100)$ surface by TOF-ion scattering*, *Surface Science* **352–354**, 978 – 982 (1996).
Cited on page(s): 88, 113.
- ⁴¹¹ L. HOUSSIAU AND P. BERTRAND, *Order-disorder phase transition of the $Cu_3Au(100)$ surface studied by ToF-ion scattering*, *Nuclear Instruments and Methods in Physics Research Section B: Beam Interactions with Materials and Atoms* **118**, 467–472 (1996).
Cited on page(s): 88, 113.
- ⁴¹² C. ERN, W. DONNER, A. RÜHM, H. DOSCH, B. TOPERVERG, AND R. JOHNSON, *Surface density oscillations in disordered binary alloys: X-ray reflectivity study of $Cu_3Au(001)$* , *Applied Physics A: Materials Science & Processing* **64**, 383–390 (1997).
Cited on page(s): 88.
- ⁴¹³ M. HAYOUN, V. PONTIKIS, AND C. WINTER, *Computer simulation study of surface segregation on Cu_3Au* , *Surface Science* **398**, 125–133 (1998).
Cited on page(s): 88.
- ⁴¹⁴ H. DOSCH AND H. REICHERT, *Ordering, disordering and segregation at binary interfaces: model system $Cu_3Au(001)$* , *Acta Materialia* **48**, 4387–4393 (2000).
Cited on page(s): 88.
- ⁴¹⁵ L. G. DIAS, A. A. LEITÃO, C. A. ACHETE, R.-P. BLUM, H. NIEHUS, AND R. B. CAPAZ, *Chemical identification in the $Cu_3Au(100)$ surface using scanning tunneling microscopy and*

- first-principles calculations*, Surface Science **601**, 5540–5545 (2007).
Cited on page(s): 88, 97.
- ⁴¹⁶ E. MCRAE, T. BUCK, R. MALIC, W. WALLACE, AND J. SANCHEZ, *Ordering and layer composition at the Cu₃Au(110) surface*, Surface Science **238**, L481–L485 (1990).
Cited on page(s): 88, 89, 108.
- ⁴¹⁷ Y. HUANG AND J. COWLEY, *A study of the Cu₃Au(110) surface structure by RHEED*, Surface Science **285**, 42–58 (1993).
Cited on page(s): 88, 89, 108.
- ⁴¹⁸ H. OVER, G. GILAROWSKI, AND H. NIEHUS, *The composition and structure of Cu₃Au(110)-(4 × 1): a low-energy electron diffraction analysis*, Surface Science **381**, L619–L622 (1997).
Cited on page(s): 88, 89, 108.
- ⁴¹⁹ H. NIEHUS, *Surface and sub-surface alloy formation connected with ordered superstructures*, in *Surface Alloys and Alloys Surfaces* (edited by D. P. Woodruff), volume 10 of *The Chemical Physics of Solid Surfaces*, chapter 10, pp. 364–403, Elsevier, Amsterdam, The Netherlands (2002).
Cited on page(s): 88.
- ⁴²⁰ M. A. VASILIEV, *Surface effects of ordering in binary alloys*, Journal of Physics D: Applied Physics **30**, 3037–3070 (1997).
Cited on page(s): 88, 89.
- ⁴²¹ L. VITOS, A. RUBAN, H. SKRIVER, AND J. KOLLÁR, *The surface energy of metals*, Surface Science **411**, 18–202 (1998).
Cited on page(s): 88, 108.
- ⁴²² J. WAN, Y. L. FAN, D. W. GONG, S. G. SHEN, AND X. Q. FAN, *Surface relaxation and stress of fcc metals: Cu, Ag, Au, Ni, Pd, Pt, Al and Pb*, Modelling and Simulation in Materials Science and Engineering **7** (1999).
Cited on page(s): 88, 108, 111, 113, 163, 164, 210.
- ⁴²³ A. R. MIEDEMA, *Surface Segregation in Alloys of Transition-Metals*, Zeitschrift für Metallkunde **69**, 455–461 (1978).
Cited on page(s): 88, 108.
- ⁴²⁴ W. TYSON AND W. MILLER, *Surface free energies of solid metals: Estimation from liquid surface tension measurements*, Surface Science **62**, 267–276 (1977).
Cited on page(s): 88, 108.
- ⁴²⁵ C. G. SHAW AND S. C. FAIN, JR., *Quantitative Auger electron spectroscopy of copper-gold alloys*, in *Proceedings of the Seventh International Vacuum Congress and the Third International Conference on Solid Surfaces of the International Union for Vacuum Science, Technique and Applications* (edited by R. Dobrozemsky, F. Rüdener, F. P. Viekböck and A. Breth), volume III, pp. 2315–2318, published in Vienna, Austria, by R. Dobrozemsky *et al.*, printed in Horn, Austria, by F. Berger & Söhne (1977).
Cited on page(s): 89, 98, 100, 108.
- ⁴²⁶ M. D. MOREIRA, G. N. FONTES, H. NIEHUS, C. A. ACHETE, AND R. B. CAPAZ, *First-principles calculations and XPS measurements of gold segregation at the Cu₃Au(111) surface*, Journal of Vacuum Science & Technology B: Microelectronics and Nanometer Structures **30**,

- 051802 (2012).
Cited on page(s): 89, 100, 108, 112, 113.
- ⁴²⁷ A. A. LEITÃO, M. D. MOREIRA, L. G. DIAS, A. M. SILVA, R. B. CAPAZ, AND C. A. ACHETE, *Ab initio studies of pristine and oxidized Cu₃Au(100) and (111) surfaces*, *Journal of Materials Science* **47**, 7594–7600 (2012).
Cited on page(s): 89, 100, 171.
- ⁴²⁸ A. M. SILVA, C. ACHETE, AND R. B. CAPAZ, *First-principles study of oxygen-induced copper segregation in Cu₃Au(111)*, *Chemical Physics* **410**, 99–102 (2013).
Cited on page(s): 89, 100, 162, 171.
- ⁴²⁹ J. M. MCDAVID AND S. C. FAIN, JR., *Segregation at Cu–Au alloy surfaces*, *Surface Science* **52**, 161–173 (1975).
Cited on page(s): 89, 98, 100, 108.
- ⁴³⁰ A. PAREEK, S. BORODIN, A. BASHIR, G. N. ANKAH, P. KEIL, G. A. ECKSTEIN, M. ROHWERDER, M. STRATMANN, Y. GRÜNDER, AND F. U. RENNER, *Initiation and Inhibition of Dealloying of Single Crystalline Cu₃Au(111) Surfaces*, *Journal of the American Chemical Society* **133**, 18264–18271 (2011).
Cited on page(s): 89.
- ⁴³¹ T. K. SHAM, Z.-F. LIU, AND K. H. TAN, *Photoemission studies of Ru₃(CO)₁₂ adsorption on Cu₃Au*, *The Journal of Chemical Physics* **93**, 4447–4452 (1990).
Cited on page(s): 89.
- ⁴³² M. ALEMANI, *Low Temperature STM Investigation of Molecular Manipulation, Decoupling and Switching*, Dissertation, Freie Universität Berlin, Berlin, Germany (2006).
Cited on page(s): 89.
- ⁴³³ G. GRAHAM, *Oxygen adsorption on Cu₃Au(100) above 350 K*, *Surface Science* **137**, L79–L83 (1984).
Cited on page(s): 89.
- ⁴³⁴ H. NIEHUS AND C. ACHETE, *Surface structure investigation of nitrogen and oxygen on Cu₃Au(100)*, *Surface Science* **289**, 19–29 (1993).
Cited on page(s): 89, 162.
- ⁴³⁵ Y. HUANG AND J. COWLEY, *Structure of the sulfur-adsorbed Cu₃Au(110) surface*, *Surface Science* **289**, 340–356 (1993).
Cited on page(s): 89.
- ⁴³⁶ K. MORGENSTERN, H. NIEHUS, AND G. COMSA, *Reconstruction of the oxygen covered Cu₃Au(110) surface investigated by low energy ion back scattering and LEED*, *Surface Science* **338**, 1–10 (1995).
Cited on page(s): 89, 116, 162.
- ⁴³⁷ M. OKADA, K. MORITANI, T. FUKUYAMA, H. MIZUTANI, A. YOSHIGOE, Y. TERAOKA, AND T. KASAI, *Comparative study of oxidation on Cu and Cu₃Au surfaces with a hyperthermal O₂ molecular beam*, *Surface Science* **600**, 4228–4232 (2006).
Cited on page(s): 89.
- ⁴³⁸ M. OKADA, M. HASHINOKUCHI, M. FUKUOKA, T. KASAI, K. MORITANI, AND Y. TERAOKA, *Protective layer formation during oxidation of Cu₃Au(100) using hyperthermal*

- O₂ molecular beam*, Applied Physics Letters **89**, 201912 (2006).
Cited on page(s): 89.
- ⁴³⁹ M. OKADA AND Y. TERAOKA, *Active oxidation of Cu₃Au(110) using hyperthermal O₂ molecular beam*, Applied Surface Science **256**, 5676–5680 (2010).
Cited on page(s): 89.
- ⁴⁴⁰ H. NIEHUS, T. BAUMANN, M. VOETZ, AND K. MORGENSTERN, *Clean and Oxygen-covered Cu₃Au(110): A Surface Structure Investigation with STM and NCISS*, Surface Review and Letters **3**, 1899–1908 (1996).
Cited on page(s): 89, 116, 162.
- ⁴⁴¹ G. ERTL, *Untersuchung von Oberflächenreaktionen mittels Beugung langsamer Elektronen (LEED): I. Wechselwirkung von O₂ und N₂O mit (110)-, (111)- und (100)-Kupfer-Oberflächen*, Surface Science **6**, 208–232 (1967).
Cited on page(s): 89.
- ⁴⁴² G. GRUZALSKI, D. ZEHNER, J. WENDELKEN, AND R. HATHCOCK, *LEED observations of oxygen ordering on Cu(110)*, Surface Science **151**, 430–446 (1985).
Cited on page(s): 89.
- ⁴⁴³ J. MUNDENAR, A. BADDORF, E. PLUMMER, L. SNEDDON, R. DIDIO, AND D. ZEHNER, *Oxygen chemisorption on copper (110)*, Surface Science **188**, 15–31 (1987).
Cited on page(s): 89.
- ⁴⁴⁴ F. M. CHUA, Y. KUK, AND P. J. SILVERMAN, *Oxygen chemisorption on Cu(110): An atomic view by scanning tunneling microscopy*, Physical Review Letters **63**, 386–389 (1989).
Cited on page(s): 89.
- ⁴⁴⁵ D. J. COULMAN, J. WINTTERLIN, R. J. BEHM, AND G. ERTL, *Novel mechanism for the formation of chemisorption phases: The (2 × 1)O-Cu(110) “added row” reconstruction*, Physical Review Letters **64**, 1761–1764 (1990).
Cited on page(s): 89.
- ⁴⁴⁶ K. MORGENSTERN, M. VOETZ, AND H. NIEHUS, *Nitrogen-induced reconstruction of the Cu₃Au(110) surface*, Physical Review B **54**, 17870–17876 (1996).
Cited on page(s): 89, 116, 162.
- ⁴⁴⁷ R. SPITZL, H. NIEHUS, AND G. COMSA, *Structure investigation of the nitrogen induced Cu(110)-(2 × 3) phase with 180° low energy impact collision ion scattering spectroscopy*, Surface Science Letters **250**, L355–L362 (1991).
Cited on page(s): 89.
- ⁴⁴⁸ H. NIEHUS, R. SPITZL, K. BESOCKE, AND G. COMSA, *N-induced (2 × 3) reconstruction of Cu(110): Evidence for long-range, highly directional interaction between Cu-N-Cu bonds*, Physical Review B **43**, 12619–12622 (1991).
Cited on page(s): 89.
- ⁴⁴⁹ R. LEE AND H. FARNSWORTH, *LEED studies of adsorption on clean (100) copper surfaces*, Surface Science **3**, 461–479 (1965).
Cited on page(s): 89.
- ⁴⁵⁰ H. C. ZENG, R. A. MCFARLANE, R. N. S. SODHI, AND K. A. R. MITCHELL, *LEED crystallographic studies for the chemisorption of oxygen on the (100) surface of copper*, Canadian

- Journal of Chemistry **66**, 2054–2062 (1988).
Cited on page(s): 89.
- ⁴⁵¹ H. ZENG, R. MCFARLANE, AND K. MITCHELL, *A LEED crystallographic investigation of some missing row models for the Cu(100)–(2√2 × √2)R45°–O surface structure*, Surface Science Letters **208**, L7–L14 (1989).
Cited on page(s): 89.
- ⁴⁵² F. U. RENNER, *In-situ X-ray Study of the Initial Electrochemical Corrosion of Cu₃Au(111)*, Dissertation, Universität Stuttgart, Stuttgart, Germany (2004).
Cited on page(s): 89.
- ⁴⁵³ I. CHIZHOV, A. KAHN, AND G. SCOLES, *Initial growth of 3,4,9,10-perylenetetracarboxylic-dianhydride (PTCDA) on Au(111): a scanning tunneling microscopy study*, Journal of Crystal Growth **208**, 449–458 (2000).
Cited on page(s): 89, 90, 128, 133.
- ⁴⁵⁴ M. MEISSNER, M. GRUENEWALD, F. SOJKA, C. UDHARDT, R. FORKER, AND T. FRITZ, *Highly ordered growth of PTCDA on epitaxial bilayer graphene*, Surface Science **606**, 1709–1715 (2012).
Cited on page(s): 99.
- ⁴⁵⁵ A. MAELAND AND T. B. FLANAGAN, *Lattice spacings of gold–palladium alloys*, Canadian Journal of Physics **42**, 2364–2366 (1964).
Cited on page(s): 99, 111, 112, 163, 291.
- ⁴⁵⁶ M. TOLKIEHN, D. V. NOVIKOV, AND S. S. FANCHENKO, *Kinematical x-ray standing waves for crystal structure investigations*, Physical Review B **71**, 165404 (2005).
Cited on page(s): 106, 107.
- ⁴⁵⁷ A. R. SANDY, S. G. J. MOCHRIE, D. M. ZEHNER, K. G. HUANG, AND D. GIBBS, *Structure and phases of the Au(111) surface: X-ray-scattering measurements*, Physical Review B **43**, 4667–4687 (1991).
Cited on page(s): 107, 111, 164.
- ⁴⁵⁸ E. MCRAE AND T. BUCK, *Surface compositional ordering and domain walls in Cu₃Au*, Surface Science **227**, 67–72 (1990).
Cited on page(s): 108.
- ⁴⁵⁹ D. R. CHIPMAN, *X-Ray Study of the Local Atomic Arrangement in Partially Ordered Cu₃Au*, Journal of Applied Physics **27**, 739–746 (1956).
Cited on page(s): 109, 294.
- ⁴⁶⁰ O. BRAUN AND Y. KIVSHAR, *The Frenkel-Kontorova model: concepts, methods, and applications*, number XVIII in Theoretical and Mathematical Physics, Springer, Berlin, Germany (2004).
Cited on page(s): 110.
- ⁴⁶¹ A. PIDCOCK, R. E. RICHARDS, AND L. M. VENANZI, ¹⁹⁵Pt–³¹P nuclear spin coupling constants and the nature of the trans-effect in platinum complexes, J. Chem. Soc. A pp. 1707–1710 (1966).
Cited on page(s): 113.

- ⁴⁶² C. JANIÁK, *Komplex- und Koordinationschemie*, in *Moderne Anorganische Chemie* (edited by E. RIEDEL), 2nd edition, chapter 2, pp. 167–349, de Gruyter, Berlin, Germany (2003).
Cited on page(s): 113.
- ⁴⁶³ A. ZANGWILL, *Physics at Surfaces*, Cambridge University Press, Cambridge, UK (1988).
Cited on page(s): 113.
- ⁴⁶⁴ M. MURA, X. SUN, F. SILLY, H. T. JONKMAN, G. A. D. BRIGGS, M. R. CASTELL, AND L. N. KANTOROVICH, *Experimental and theoretical analysis of H-bonded supramolecular assemblies of PTCDA molecules*, *Physical Review B* **81**, 195412 (2010).
Cited on page(s): 128, 217.
- ⁴⁶⁵ P. FENTER, F. SCHREIBER, L. ZHOU, P. EISENBERGER, AND S. R. FORREST, *In situ studies of morphology, strain, and growth modes of a molecular organic thin film*, *Physical Review B* **56**, 3046–3053 (1997).
Cited on page(s): 131, 300.
- ⁴⁶⁶ T. WAGNER, A. BANNANI, C. BOBISCH, H. KARACUBAN, M. STÖHR, M. GABRIEL, AND R. MÖLLER, *Growth of 3,4,9,10-perylenetetracarboxylic-dianhydride crystallites on noble metal surfaces*, *Organic Electronics* **5**, 35–43 (2004).
Cited on page(s): 136.
- ⁴⁶⁷ A. SCHÖLL, Y. ZOU, T. SCHMIDT, R. FINK, AND E. UMBACH, *High-Resolution Photoemission Study of Different NTCDA Monolayers on Ag(111): Bonding and Screening Influences on the Line Shapes*, *The Journal of Physical Chemistry B* **108**, 14741–14748 (2004).
Cited on page(s): 140, 204.
- ⁴⁶⁸ M. HÄMING, A. SCHÖLL, E. UMBACH, AND F. REINERT, *Adsorbate-substrate charge transfer and electron-hole correlation at adsorbate/metal interfaces*, *Physical Review B* **85**, 235132 (2012).
Cited on page(s): 140, 202, 203, 204, 206, 207, 208.
- ⁴⁶⁹ S. VOLLMER, G. WITTE, AND C. WÖLL, *Determination of Site Specific Adsorption Energies of CO on Copper*, *Catalysis Letters* **77**, 97–101 (2001).
Cited on page(s): 140.
- ⁴⁷⁰ B. J. HINCH AND L. H. DUBOIS, *Stable and metastable phases of water adsorbed on Cu(111)*, *The Journal of Chemical Physics* **96**, 3262–3268 (1992).
Cited on page(s): 140.
- ⁴⁷¹ M. BOWKER, *The role of precursor states in adsorption, surface reactions and catalysis*, *Journal of Physics: Condensed Matter* **22**, 263002 (2010).
Cited on page(s): 142, 172.
- ⁴⁷² T. U. KAMPEN, G. GAVRILA, H. MÉNDEZ, D. R. T. ZAHN, A. R. VEAREY-ROBERTS, D. A. EVANS, J. WELLS, I. MCGOVERN, AND W. BRAUN, *Electronic properties of interfaces between perylene derivatives and GaAs(001) surfaces*, *Journal of Physics: Condensed Matter* **15**, S2679–S2692 (2003).
Cited on page(s): 145.
- ⁴⁷³ D. B. BUTRYMOWICZ, J. R. MANNING, AND M. E. READ, *Diffusion in Copper and Copper Alloys, Part II. Copper-Silver and Copper-Gold Systems*, *Journal of Physical and Chemical Reference Data* **3**, 527–602 (1974).
Cited on page(s): 161.

- ⁴⁷⁴ P. ARMENTROUT AND R. GEORGIADIS, *Periodic trends in gas phase M—H and M—C bond energies*, *Polyhedron* **7**, 1573–1581 (1988).
Cited on page(s): 161.
- ⁴⁷⁵ R. SCHLAF, B. A. PARKINSON, P. A. LEE, K. W. NEBESNY, AND N. R. ARMSTRONG, *HOMO/LUMO Alignment at PTCDA/ZnPc and PTCDA/ClInPc Heterointerfaces Determined by Combined UPS and XPS Measurements*, *The Journal of Physical Chemistry B* **103**, 2984–2992 (1999).
Cited on page(s): 161.
- ⁴⁷⁶ H. IBACH, *The role of surface stress in reconstruction, epitaxial growth and stabilization of mesoscopic structures*, *Surface Science Reports* **29**, 195–263 (1997).
Cited on page(s): 162.
- ⁴⁷⁷ A. KAHN, N. KOCH, AND W. GAO, *Electronic structure and electrical properties of interfaces between metals and π -conjugated molecular films*, *Journal of Polymer Science Part B: Polymer Physics* **41**, 2529–2548 (2003).
Cited on page(s): 166, 201.
- ⁴⁷⁸ G. WITTE, S. LUKAS, P. S. BAGUS, AND C. WOLL, *Vacuum level alignment at organic/metal junctions: “Cushion” effect and the interface dipole*, *Applied Physics Letters* **87**, 263502 (2005).
Cited on page(s): 166, 201.
- ⁴⁷⁹ K. H. FRANK, P. YANNOULIS, R. DUDDE, AND E. E. KOCH, *Unoccupied molecular orbitals of aromatic hydrocarbons adsorbed on Ag(111)*, *The Journal of Chemical Physics* **89**, 7569–7576 (1988).
Cited on page(s): 172, 196.
- ⁴⁸⁰ J. R. KITCHIN, J. K. NØRSKOV, M. A. BARTEAU, AND J. G. CHEN, *Modification of the surface electronic and chemical properties of Pt(111) by subsurface 3d transition metals*, *The Journal of Chemical Physics* **120**, 10240–10246 (2004).
Cited on page(s): 173.
- ⁴⁸¹ M. MAVRIKAKIS, B. HAMMER, AND J. K. NØRSKOV, *Effect of Strain on the Reactivity of Metal Surfaces*, *Physical Review Letters* **81**, 2819–2822 (1998).
Cited on page(s): 173, 174.
- ⁴⁸² R. G. JORDAN AND G. S. SOHAL, *Observation of a surface state on Cu₃Au(111)*, *Journal of Physics C: Solid State Physics* **15**, L663–L667 (1982).
Cited on page(s): 175.
- ⁴⁸³ S. D. KEVAN AND R. H. GAYLORD, *High-resolution photoemission study of the electronic structure of the noble-metal (111) surfaces*, *Physical Review B* **36**, 5809–5818 (1987).
Cited on page(s): 175.
- ⁴⁸⁴ F. REINERT, G. NICOLAY, S. SCHMIDT, D. EHM, AND S. HÜFNER, *Direct measurements of the L-gap surface states on the (111) face of noble metals by photoelectron spectroscopy*, *Physical Review B* **63**, 115415 (2001).
Cited on page(s): 175.
- ⁴⁸⁵ M. BÖHRINGER, W. D. SCHNEIDER, K. GLÖCKLER, E. UMBACH, AND R. BERNDT, *Adsorption site determination of PTCDA on Ag(110) by manipulation of adatoms*, *Surface Science*

- 419**, L95–L99 (1998).
Cited on page(s): 178, 210, 304.
- ⁴⁸⁶ A. TKATCHENKO AND M. SCHEFFLER, *Accurate Molecular Van Der Waals Interactions from Ground-State Electron Density and Free-Atom Reference Data*, *Physical Review Letters* **102**, 073005 (2009).
Cited on page(s): 184.
- ⁴⁸⁷ V. G. RUIZ, W. LIU, E. ZOJER, M. SCHEFFLER, AND A. TKATCHENKO, *Density-Functional Theory with Screened van der Waals Interactions for the Modeling of Hybrid Inorganic-Organic Systems*, *Physical Review Letters* **108**, 146103 (2012).
Cited on page(s): 184, 189, 221.
- ⁴⁸⁸ M. J. FRISCH, G. W. TRUCKS, H. B. SCHLEGEL, G. E. SCUSERIA, M. A. ROBB, J. R. CHEESEMAN, J. A. MONTGOMERY, JR., T. VREVEN, K. N. KUDIN, J. C. BURANT, J. M. MILLAM, S. S. IYENGAR, J. TOMASI, V. BARONE, B. MENNUCCI, M. COSSI, G. SCALMANI, N. REGA, G. A. PETERSSON, H. NAKATSUJI, M. HADA, M. EHARA, K. TOYOTA, R. FUKUDA, J. HASEGAWA, M. ISHIDA, T. NAKAJIMA, Y. HONDA, O. KITAO, H. NAKAI, M. KLENE, X. LI, J. E. KNOX, H. P. HRATCHIAN, J. B. CROSS, V. BAKKEN, C. ADAMO, J. JARAMILLO, R. GOMPERS, R. E. STRATMANN, O. YAZYEV, A. J. AUSTIN, R. CAMMI, C. POMELLI, J. W. OCHTERSKI, P. Y. AYALA, K. MOROKUMA, G. A. VOTH, P. SALVADOR, J. J. DANNENBERG, V. G. ZAKRZEWSKI, S. DAPPRICH, A. D. DANIELS, M. C. STRAIN, O. FARKAS, D. K. MALICK, A. D. RABUCK, K. RAGHAVACHARI, J. B. FORESMAN, J. V. ORTIZ, Q. CUI, A. G. BABOUL, S. CLIFFORD, J. CIOSLOWSKI, B. B. STEFANOV, G. LIU, A. LIASHENKO, P. PISKORZ, I. KOMAROMI, R. L. MARTIN, D. J. FOX, T. KEITH, M. A. AL-LAHAM, C. Y. PENG, A. NANAYAKKARA, M. CHALLACOMBE, P. M. W. GILL, B. JOHNSON, W. CHEN, M. W. WONG, C. GONZALEZ, AND J. A. POPLE, *Gaussian 03, Revision C.02*, Gaussian, Inc., Wallingford, CT, USA (2004).
Cited on page(s): 188.
- ⁴⁸⁹ J. K. KANG AND C. B. MUSGRAVE, *Prediction of transition state barriers and enthalpies of reaction by a new hybrid density-functional approximation*, *The Journal of Chemical Physics* **115**, 11040–11051 (2001).
Cited on page(s): 188.
- ⁴⁹⁰ J. P. SENOSIAIN, J. H. HAN, C. B. MUSGRAVE, AND D. M. GOLDEN, *Use of quantum methods for a consistent approach to combustion modelling: Hydrocarbon bond dissociation energies*, *Faraday Discussions* **119**, 173–189 (2002).
Cited on page(s): 188.
- ⁴⁹¹ F. WEIGEND, F. FURCHE, AND R. AHLRICHS, *Gaussian basis sets of quadruple zeta valence quality for atoms H–Kr*, *The Journal of Chemical Physics* **119**, 12753–12762 (2003).
Cited on page(s): 188.
- ⁴⁹² F. WEIGEND AND R. AHLRICHS, *Balanced basis sets of split valence, triple zeta valence and quadruple zeta valence quality for H to Rn: Design and assessment of accuracy*, *Physical Chemistry Chemical Physics* **7**, 3297–3305 (2005).
Cited on page(s): 188.
- ⁴⁹³ G. SCHAFTENAAR AND J. NOORDIK, *Molden: a pre- and post-processing program for molecular and electronic structures*, *Journal of Computer-Aided Molecular Design* **14**, 123–134

- (2000).
Cited on page(s): 188.
- ⁴⁹⁴ G. KRESSE AND J. HAFNER, *Ab initio molecular dynamics for liquid metals*, *Physical Review B* **47**, 558–561 (1993).
Cited on page(s): 188.
- ⁴⁹⁵ G. KRESSE AND J. HAFNER, *Ab initio molecular-dynamics simulation of the liquid-metal–amorphous-semiconductor transition in germanium*, *Physical Review B* **49**, 14251–14269 (1994).
Cited on page(s): 188.
- ⁴⁹⁶ G. KRESSE AND J. FURTHMÜLLER, *Efficient iterative schemes for ab initio total-energy calculations using a plane-wave basis set*, *Physical Review B* **54**, 11169–11186 (1996).
Cited on page(s): 188.
- ⁴⁹⁷ G. KRESSE AND D. JOUBERT, *From ultrasoft pseudopotentials to the projector augmented-wave method*, *Physical Review B* **59**, 1758–1775 (1999).
Cited on page(s): 188.
- ⁴⁹⁸ J. P. PERDEW, K. BURKE, AND M. ERNZERHOF, *Generalized Gradient Approximation Made Simple*, *Physical Review Letters* **77**, 3865–3868 (1996).
Cited on page(s): 188, 215.
- ⁴⁹⁹ S. GRIMME, *Semiempirical GGA-type density functional constructed with a long-range dispersion correction*, *Journal of Computational Chemistry* **27**, 1787–1799 (2006).
Cited on page(s): 188.
- ⁵⁰⁰ S. GRIMME, J. ANTONY, S. EHRLICH, AND H. KRIEG, *A consistent and accurate ab initio parametrization of density functional dispersion correction (DFT-D) for the 94 elements H-Pu*, *The Journal of Chemical Physics* **132**, 154104 (2010).
Cited on page(s): 188.
- ⁵⁰¹ S. GRIMME, S. EHRLICH, AND L. GOERIGK, *Effect of the damping function in dispersion corrected density functional theory*, *Journal of Computational Chemistry* **32**, 1456–1465 (2011).
Cited on page(s): 188, 215.
- ⁵⁰² W. RECKIEN AND T. BREDOW, *Theoretical study of weak chemical interactions in solid formamide*, *Chemical Physics Letters* **508**, 54–58 (2011).
Cited on page(s): 188.
- ⁵⁰³ W. RECKIEN, B. KIRCHNER, F. JANETZKO, AND T. BREDOW, *Theoretical Investigation of Formamide Adsorption on Ag(111) Surfaces*, *The Journal of Physical Chemistry C* **113**, 10541–10547 (2009).
Cited on page(s): 188.
- ⁵⁰⁴ R. F. W. BADER, *Atoms in Molecules: A Quantum Theory*, Oxford University Press, New York, NY, USA (1990).
Cited on page(s): 189, 200, 202, 206, 207, 208.
- ⁵⁰⁵ G. HENKELMAN, A. ARNALDSSON, AND H. JÓNSSON, *A fast and robust algorithm for Bader decomposition of charge density*, *Computational Materials Science* **36**, 354–360 (2006).
Cited on page(s): 189, 200, 202, 206, 207, 208.

- ⁵⁰⁶ A. KOKALJ, *Computer graphics and graphical user interfaces as tools in simulations of matter at the atomic scale*, Computational Materials Science **28**, 155–168 (2003).
Cited on page(s): 189.
- ⁵⁰⁷ P. O. GARTLAND, S. BERGE, AND B. J. SLAGSVOLD, *Photoelectric Work Function of a Copper Single Crystal for the (100), (110), (111), and (112) Faces*, Physical Review Letters **28**, 738–739 (1972).
Cited on page(s): 191, 192, 231.
- ⁵⁰⁸ A. W. DWEYDARI AND C. H. B. MEE, *Oxygen adsorption on the (111) face of silver*, physica status solidi (a) **17**, 247–250 (1973).
Cited on page(s): 191, 192.
- ⁵⁰⁹ P. O. GARTLAND AND B. J. SLAGSVOLD, *Transitions conserving parallel momentum in photoemission from the (111) face of copper*, Physical Review B **12**, 4047–4058 (1975).
Cited on page(s): 191, 192.
- ⁵¹⁰ A. W. DWEYDARI AND C. H. B. MEE, *Work function measurements on (100) and (110) surfaces of silver*, physica status solidi (a) **27**, 223–230 (1975).
Cited on page(s): 191, 192, 228.
- ⁵¹¹ G. V. HANSSON AND S. A. FLODSTRÖM, *Photoemission study of the bulk and surface electronic structure of single crystals of gold*, Physical Review B **18**, 1572–1585 (1978).
Cited on page(s): 191, 192.
- ⁵¹² M. CHELVAYOHAN AND C. H. B. MEE, *Work function measurements on (110), (100) and (111) surfaces of silver*, Journal of Physics C: Solid State Physics **15**, 2305 (1982).
Cited on page(s): 191, 192.
- ⁵¹³ K. GIESEN, F. HAGE, F. J. HIMPEL, H. J. RIESS, AND W. STEINMANN, *Two-photon photoemission via image-potential states*, Physical Review Letters **55**, 300–303 (1985).
Cited on page(s): 191, 192.
- ⁵¹⁴ K. GIESEN, F. HAGE, F. J. HIMPEL, H. J. RIESS, AND W. STEINMANN, *Hydrogenic image-potential states: A critical examination*, Physical Review B **33**, 5241–5244 (1986).
Cited on page(s): 191, 192.
- ⁵¹⁵ K. GIESEN, F. HAGE, F. J. HIMPEL, H. J. RIESS, W. STEINMANN, AND N. V. SMITH, *Effective mass of image-potential states*, Physical Review B **35**, 975–978 (1987).
Cited on page(s): 191, 192.
- ⁵¹⁶ B. REIHL AND J. NICHOLLS, *Image-potential surface states on Ag(100): A reinvestigation*, Zeitschrift für Physik B Condensed Matter **67**, 221–224 (1987).
Cited on page(s): 191, 192.
- ⁵¹⁷ W. HANSEN, M. BERTOLO, AND K. JACOBI, *Physisorption of CO on Ag(111): investigation of the monolayer and the multilayer through HREELS, ARUPS, and TDS*, Surface Science **253**, 1–12 (1991).
Cited on page(s): 191, 192.
- ⁵¹⁸ M. CANEPA, P. CANTINI, L. MATTERA, S. TERRENI, AND F. VALDENAZZI, *Electronic States of the Ag(110)–O($n \times 1$) Phases Studied by Photoemission and Metastable Deexcitation Spectroscopies*, Physica Scripta **1992**, 226 (1992).
Cited on page(s): 191, 192.

- ⁵¹⁹ T. V. OIRSCHOT, M. V. D. BRINK, AND W. SACHTLER, *Photoelectric emission and phase transitions of evaporated metastable sodium, potassium and sodium-potassium alloy films*, *Surface Science* **29**, 189–202 (1972).
Cited on page(s): 191, 228.
- ⁵²⁰ M. WIESSNER, J. KÜBERT, V. FEYER, P. PUSCHNIG, A. SCHÖLL, AND F. REINERT, *Lateral band formation and hybridization in molecular monolayers: NTCDA on Ag(110) and Cu(100)*, *Physical Review B* **88**, 075437 (2013).
Cited on page(s): 192, 229, 230, 231, 236.
- ⁵²¹ Y.-M. KOO AND O.-K. SONG, *Spontaneous charge transfer from indium tin oxide to organic molecules for effective hole injection*, *Applied Physics Letters* **94**, 153302 (2009).
Cited on page(s): 195.
- ⁵²² A. HAUSCHILD AND M. SOKOLOWSKI, *Coverage and temperature dependence of ordered thin pentacene films on Ag(111) investigated with SPA-LEED*, 71st Annual Meeting 2007 of the DPG and Spring Meeting of the Condensed Matter Division, Regensburg, Germany, March 26–30, Poster O 44.10 (2007).
Cited on page(s): 196, 197.
- ⁵²³ C. BÜRKER, N. FERRI, A. TKATCHENKO, A. GERLACH, J. NIEDERHAUSEN, T. HOSOKAI, S. DUHM, J. ZEGENHAGEN, N. KOCH, AND F. SCHREIBER, *Exploring the bonding of large hydrocarbons on noble metals: Diindoperylene on Cu(111), Ag(111), and Au(111)*, *Physical Review B* **87**, 165443 (2013).
Cited on page(s): 196.
- ⁵²⁴ A. ALLRED AND E. ROCHOW, *A scale of electronegativity based on electrostatic force*, *Journal of Inorganic and Nuclear Chemistry* **5**, 264–268 (1958).
Cited on page(s): 196, 197, 227.
- ⁵²⁵ S. DUHM, C. BÜRKER, J. NIEDERHAUSEN, I. SALZMANN, T. HOSOKAI, J. DUVERNAY, S. KERA, F. SCHREIBER, N. KOCH, N. UENO, AND A. GERLACH, *Pentacene on Ag(111): Correlation of Bonding Distance with Intermolecular Interaction and Order*, *ACS Applied Materials & Interfaces* **5**, 9377–9381 (2013).
Cited on page(s): 197.
- ⁵²⁶ R. S. MULLIKEN, *Electronic Population Analysis on LCAO-MO Molecular Wave Functions. I*, *The Journal of Chemical Physics* **23**, 1833–1840 (1955).
Cited on page(s): 199, 200.
- ⁵²⁷ R. S. MULLIKEN, *Criteria for the Construction of Good Self-Consistent-Field Molecular Orbital Wave Functions, and the Significance of LCAO-MO Population Analysis*, *The Journal of Chemical Physics* **36**, 3428–3439 (1962).
Cited on page(s): 200.
- ⁵²⁸ K. B. WIBERG AND P. R. RABLEN, *Comparison of atomic charges derived via different procedures*, *Journal of Computational Chemistry* **14**, 1504–1518 (1993).
Cited on page(s): 200.
- ⁵²⁹ P. POLITZER AND R. S. MULLIKEN, *Comparison of Two Atomic Charge Definitions, as Applied to the Hydrogen Fluoride Molecule*, *The Journal of Chemical Physics* **55**, 5135–5136 (1971).
Cited on page(s): 200.

- ⁵³⁰ D. L. GRIER AND A. STREITWIESER, JR., *Electron density analysis of substituted carbonyl groups*, Journal of the American Chemical Society **104**, 3556–3564 (1982).
Cited on page(s): 200.
- ⁵³¹ F. DE PROFT, C. VAN ALSENOY, A. PEETERS, W. LANGENAEKER, AND P. GEERLINGS, *Atomic charges, dipole moments, and Fukui functions using the Hirshfeld partitioning of the electron density*, Journal of Computational Chemistry **23**, 1198–1209 (2002).
Cited on page(s): 200.
- ⁵³² K. CHRISTMANN, *Interaction of hydrogen with solid surfaces*, Surface Science Reports **9**, 1–163 (1988).
Cited on page(s): 201.
- ⁵³³ S. BRAUN, W. R. SALANECK, AND M. FAHLMAN, *Energy-Level Alignment at Organic/Metal and Organic/Organic Interfaces*, Advanced Materials **21**, 1450–1472 (2009).
Cited on page(s): 201.
- ⁵³⁴ H. VÁZQUEZ, Y. J. DAPPE, J. ORTEGA, AND F. FLORESI, *Energy level alignment at metal/organic semiconductor interfaces: “Pillow” effect, induced density of interface states, and charge neutrality level*, The Journal of Chemical Physics **126**, 144703 (2007).
Cited on page(s): 201.
- ⁵³⁵ P. C. RUSU, G. GIOVANNETTI, C. WEIJTENS, R. COEHOORN, AND G. BROCKS, *Work Function Pinning at Metal–Organic Interfaces*, The Journal of Physical Chemistry C **113**, 9974–9977 (2009).
Cited on page(s): 201.
- ⁵³⁶ X. CRISPIN, V. GESKIN, A. CRISPIN, J. E. CORNIL, R. LAZZARONI, W. R. SALANECK, AND J.-L. BRÉDAS, *Characterization of the Interface Dipole at Organic/ Metal Interfaces*, Journal of the American Chemical Society **124**, 8131–8141 (2002).
Cited on page(s): 201.
- ⁵³⁷ P. S. BAGUS, V. STAEMMLER, AND C. WÖLL, *Exchangelike Effects for Closed-Shell Adsorbates: Interface Dipole and Work Function*, Physical Review Letters **89**, 096104 (2002).
Cited on page(s): 201.
- ⁵³⁸ H. DAVIS AND J. NOONAN, *Multilayer relaxation in metallic surfaces as demonstrated by LEED analysis*, Surface Science **126**, 245–252 (1983).
Cited on page(s): 210.
- ⁵³⁹ H. LI, J. QUINN, Y. S. LI, D. TIAN, F. JONA, AND P. M. MARCUS, *Multilayer relaxation of clean Ag001*, Physical Review B **43**, 7305–7307 (1991).
Cited on page(s): 210.
- ⁵⁴⁰ F. SORIA, J. SACEDON, P. ECHENIQUE, AND D. TITTERINGTON, *LEED study of the epitaxial growth of the thin film Au(111)/Ag(111) system*, Surface Science **68**, 448–456 (1977).
Cited on page(s): 210.
- ⁵⁴¹ R. BADER, *Atoms in Molecules*, Encyclopedia of Computational Chemistry (edited by P. von Ragu é Schleyer, John Wiley and Sons, Chichester, UK) **1**, 64–86 (1998).
Cited on page(s): 212.
- ⁵⁴² G. V. GIBBS, R. T. DOWNS, D. F. COX, K. M. ROSSO, N. L. ROSS, A. KIRFEL, T. LIPPMANN, W. MORGENROTH, AND T. D. CRAWFORD, *Experimental Bond Critical Point and Local Energy Density Properties Determined for Mn–O, Fe–O, and Co–O Bonded Interactions*

- for Tephroite, Mn_2SiO_4 , Fayalite, Fe_2SiO_4 , and Co_2SiO_4 Olivine and Selected Organic Metal Complexes: Comparison with Properties Calculated for Non-Transition and Transition Metal M–O Bonded Interactions for Silicates and Oxides, *The Journal of Physical Chemistry A* **112**, 8811–8823 (2008).
Cited on page(s): 214.
- ⁵⁴³ S. DINDA AND A. G. SAMUELSON, *The Nature of Bond Critical Points in Dinuclear Copper(I) Complexes*, *Chemistry – A European Journal* **18**, 3032–3042 (2012).
Cited on page(s): 214.
- ⁵⁴⁴ S. GRIMME, *Density functional theory with London dispersion corrections*, *Wiley Interdisciplinary Reviews: Computational Molecular Science* **1**, 211–228 (2011).
Cited on page(s): 215.
- ⁵⁴⁵ B. HAMMER, L. B. HANSEN, AND J. K. NØRSKOV, *Improved adsorption energetics within density-functional theory using revised Perdew-Burke-Ernzerhof functionals*, *Physical Review B* **59**, 7413–7421 (1999).
Cited on page(s): 215.
- ⁵⁴⁶ J.-P. JALKANEN AND F. ZERBETTO, *Interaction Model for the Adsorption of Organic Molecules on the Silver Surface*, *The Journal of Physical Chemistry B* **110**, 5595–5601 (2006).
Cited on page(s): 215.
- ⁵⁴⁷ M. ROHLFING AND T. BREDOW, *Binding Energy of Adsorbates on a Noble-Metal Surface: Exchange and Correlation Effects*, *Physical Review Letters* **101**, 266106 (2008).
Cited on page(s): 215.
- ⁵⁴⁸ M. P. ANDERSSON, *Density Functional Theory with Modified Dispersion Correction for Metals Applied to Self-Assembled Monolayers of Thiols on Au(111)*, *Journal of Theoretical Chemistry* **Volume 2013**, Article ID 327839 (2013).
Cited on page(s): 215.
- ⁵⁴⁹ T. H. TANG, E. DERETAY, S. J. KNAK JENSEN, AND I. G. CSIZMADIA, *Hydrogen bonds: relation between lengths and electron densities at bond critical points*, *The European Physical Journal D – Atomic, Molecular, Optical and Plasma Physics* **37**, 217–222 (2006).
Cited on page(s): 217.
- ⁵⁵⁰ R. PARTHASARATHI, V. SUBRAMANIAN, AND N. SATHYAMURTHY, *Hydrogen Bonding without Borders: An Atoms-in-Molecules Perspective*, *The Journal of Physical Chemistry A* **110**, 3349–3351 (2006).
Cited on page(s): 218.
- ⁵⁵¹ S. HÜNIG, *Aromatic/quinoind systems: principles and applications*, *Pure and Applied Chemistry* **62**, 395–406 (1990).
Cited on page(s): 218.
- ⁵⁵² J. L. BRÉDAS, *Relationship between band gap and bond length alternation in organic conjugated polymers*, *The Journal of Chemical Physics* **82**, 3808–3811 (1985).
Cited on page(s): 218.
- ⁵⁵³ M. HESSE, H. MEIER, AND B. ZEEH, *Spektroskopische Methoden in der organischen Chemie*, Thieme, Stuttgart, Germany (2002).
Cited on page(s): 220.

- ⁵⁵⁴ J. WÜSTEN, K. HEIMER, S. LACH, AND C. ZIEGLER, *Alkali metals in perylene-3,4,9,10-tetracarboxylicdianhydride thin films*, *Journal of Applied Physics* **102**, 023708–5 (2007).
Cited on page(s): 224, 337.
- ⁵⁵⁵ K. HEIMER, J. WÜSTEN, S. LACH, AND C. ZIEGLER, *Interaction of alkali metals with perylene-3,4,9,10-tetracarboxylic-dianhydride thin films studied by IR spectroscopy*, *The Journal of Chemical Physics* **126**, 164709–5 (2007).
Cited on page(s): 224, 337.
- ⁵⁵⁶ B. HAYDEN, K. PRINCE, P. DAVIE, G. PAOLUCCI, AND A. BRADSHAW, *Alkali metal-induced reconstruction of Ag(110)*, *Solid State Communications* **48**, 325–328 (1983).
Cited on page(s): 225.
- ⁵⁵⁷ J. W. M. FRENKEN, R. L. KRANS, J. F. VAN DER VEEN, E. HOLUB-KRAPPE, AND K. HORN, *Missing-row surface reconstruction of Ag(110) induced by potassium adsorption*, *Physical Review Letters* **59**, 2307–2310 (1987).
Cited on page(s): 225.
- ⁵⁵⁸ W. JACOB, E. BERTEL, AND V. DOSE, *Potassium-induced empty electronic states on Ag(110)*, *Physical Review B* **35**, 5910–5912 (1987).
Cited on page(s): 225.
- ⁵⁵⁹ V. HEINE AND L. D. MARKS, *Competition between pairwise and multi-atom forces at noble metal surfaces*, *Surface Science* **165**, 65–82 (1986).
Cited on page(s): 225.
- ⁵⁶⁰ C. L. FU AND K. M. HO, *External-charge-induced surface reconstruction on Ag(110)*, *Physical Review Letters* **63**, 1617–1620 (1989).
Cited on page(s): 225, 337, 350.
- ⁵⁶¹ H. TOCHIHARA AND S. MIZUNO, *Composite surface structures formed by restructuring-type adsorption of alkali-metals on fcc metals*, *Progress in Surface Science* **58**, 1–74 (1998).
Cited on page(s): 225, 337.
- ⁵⁶² L. ANDREWS, *Matrix Reactions of K and Rb Atoms with Oxygen Molecules*, *The Journal of Chemical Physics* **54**, 4935–4943 (1971).
Cited on page(s): 227.
- ⁵⁶³ B. TREMBLAY, L. MANCERON, P. ROY, A.-M. LEQUÉRRÉ, AND D. ROY, *Vibrational spectra and structure of the {KO₂} complex in solid argon. A far-infrared study*, *Chemical Physics Letters* **228**, 410–416 (1994).
Cited on page(s): 227.
- ⁵⁶⁴ E. P. F. LEE AND T. G. WRIGHT, *A Study of the \tilde{X}^2A_2 State of KO₂ Using Ab Initio and Density Functional Theory: The Equilibrium Geometry and Vibrational Frequencies*, *The Journal of Physical Chemistry A* **102**, 1036–1040 (1998).
Cited on page(s): 227.
- ⁵⁶⁵ S. C. ABRAHAMS AND J. KALNAJS, *The crystal structure of α -potassium superoxide*, *Acta Crystallographica* **8**, 503–506 (1955).
Cited on page(s): 227.
- ⁵⁶⁶ G. HELD, W. BRAUN, H. P. STEINRÜCK, S. YAMAGISHI, S. J. JENKINS, AND D. A. KING, *Light-Atom Location in Adsorbed Benzene by Experiment and Theory*, *Physical Review Letters*

- 87**, 216102 (2001).
Cited on page(s): 231.
- ⁵⁶⁷ I. KRIEGER, *Die Adsorptionsgeometrie von PTCDA auf der Ag(100)-Oberfläche: eine explorative Untersuchung mit Hilfe von Beugung langsamer Elektronen*, Degree dissertation, Rheinische Friedrich-Wilhelms-Universität Bonn, Bonn, Germany (2013).
Cited on page(s): 231.
- ⁵⁶⁸ M. WILLENBOCKEL, B. STADTMÜLLER, K. SCHÖNAUER, F. C. BOCQUET, D. LÜFTNER, E. M. REINISCH, T. ULES, G. KOLLER, C. KUMPF, S. SOUBATCH, P. PUSCHNIG, M. G. RAMSEY, AND F. S. TAUTZ, *Energy offsets within a molecular monolayer: the influence of the molecular environment*, *New Journal of Physics* **15**, 033017 (2013).
Cited on page(s): 231, 295, 296, 297, 300, 301.
- ⁵⁶⁹ S. GÄRTNER, *Die Adsorption von PTCDA auf der sauberen und der oxidierten Cu(100)-Oberfläche*, Master's dissertation, Rheinische Friedrich-Wilhelms-Universität Bonn, Bonn, Germany (2012).
Cited on page(s): 231, 236.
- ⁵⁷⁰ S. GÄRTNER, B. FIEDLER, O. BAUER, A. MARELE, AND M. M. SOKOLOWSKI, *Lateral ordering of PTCDA on the clean and the oxygen pre-covered Cu(100) surface investigated by scanning tunneling microscopy and low energy electron diffraction*, *Beilstein Journal of Organic Chemistry* **10**, 2055–2064 (2014).
Cited on page(s): 231, 236.
- ⁵⁷¹ S. A. BURKE, W. JI, J. M. MATIVETSKY, J. M. TOPPLE, S. FOSTNER, H. J. GAO, H. GUO, AND P. GRÜTTER, *Strain Induced Dewetting of a Molecular System: Bimodal Growth of PTCDA on NaCl*, *Physical Review Letters* **100**, 186104 (2008).
Cited on page(s): 231.
- ⁵⁷² E. LE MOAL, M. MÜLLER, O. BAUER, AND M. SOKOLOWSKI, *Stable and metastable phases of PTCDA on epitaxial NaCl films on Ag(100)*, *Physical Review B* **82**, 045301 (2010).
Cited on page(s): 231.
- ⁵⁷³ M. MÜLLER, J. IKONOMOV, AND M. SOKOLOWSKI, *Structure of Epitaxial Layers of KCl on Ag(100)*, *Surface Science* **605**, 1090–1094 (2011).
Cited on page(s): 231.
- ⁵⁷⁴ H. ALDAHAK, W. SCHMIDT, AND E. RAULS, *Adsorption of PTCDA on NaCl(100) and KCl(100)*, *Surface Science* **617**, 242–248 (2013).
Cited on page(s): 231.
- ⁵⁷⁵ D. P. WOODRUFF, *Fortran routine*, a routine which allows to calculate the XSW profile for a given set of parameters, University of Warwick, Coventry, UK.
Cited on page(s): 237, 424.
- ⁵⁷⁶ J. ZEGENHAGEN, *DARE*, version of 18.01.2002, European Synchrotron Radiation Facility (ESRF), Grenoble, France (2002).
Cited on page(s): 237, 255, 257.
- ⁵⁷⁷ R. JONES, *XSWfit (IGOR Pro macro)*, an automated fitting procedure for XSW data which is based on the formalism originally developed by D.P. Woodruff in Fortran for calculating the XSW profile for a given set of parameters (see Ref. 575), University of Nottingham, Notting-

- ham, UK.
Cited on page(s): 237.
- ⁵⁷⁸ C. STADLER, I. KRÖGER, AND C. KUMPF, *gMinuit algorithm in Root (C++)*, XSW software, Julius-Maximilians-Universität Würzburg, Würzburg, Germany.
Cited on page(s): 237.
- ⁵⁷⁹ ORIGINLAB, *Programming in Origin: Origin C*, OriginLab Corporation, Northampton, MA, USA (2002).
Cited on page(s): 237, 238, 239.
- ⁵⁸⁰ ORIGINLAB, *Origin 8 User Guide*, OriginLab Corporation, Northampton, MA, USA (2007).
Cited on page(s): 237.
- ⁵⁸¹ K. LEVENBERG, *A Method for the Solution of Certain Non-Linear Problems in Least Squares*, Quarterly of Applied Mathematics **2**, 164–168 (1944).
Cited on page(s): 237.
- ⁵⁸² D. MARQUARDT, *An Algorithm for Least-Squares Estimation of Nonlinear Parameters*, Journal of the Society for Industrial and Applied Mathematics **11**, 431–441 (1963).
Cited on page(s): 237.
- ⁵⁸³ THE NUMERICAL ALGORITHMS GROUP (NAG), *The NAG C Library: The largest commercially available collection of numerical algorithms for C*, available at <http://www.nag.co.uk/numeric/CL/CLdescription.asp>, The Numerical Algorithms Group Ltd, Oxford, UK (2013).
Cited on page(s): 238.
- ⁵⁸⁴ J. W. COOLEY AND J. W. TUKEY, *An algorithm for the machine calculation of complex Fourier series*, Mathematics of Computation **19**, 297–301 (1965).
Cited on page(s): 239.
- ⁵⁸⁵ H. G. ZACHMANN, *Mathematik für Chemiker*, 5th edition, VCH, Weinheim, Germany (1994).
Cited on page(s): 239, 250, 254, 370.
- ⁵⁸⁶ I. N. BRONŠTEIN, K. A. SEMENDJAJEW, G. MUSIOL, AND H. MÜHLIG, *Taschenbuch der Mathematik*, 6th edition, Verlag Harri Deutsch, Frankfurt am Main, Germany (2005).
Cited on page(s): 239, 250, 254, 370.
- ⁵⁸⁷ I. KRÖGER, *Adsorption von Phthalocyaninen auf Edelmetalloberflächen*, Dissertation, Julius-Maximilians-Universität Würzburg, Würzburg, Germany (2010).
Cited on page(s): 251, 252.
- ⁵⁸⁸ B. HENKE, E. GULLIKSON, AND J. DAVIS, *X-Ray Interactions: Photoabsorption, Scattering, Transmission, and Reflection at $E = 50\text{--}30,000$ eV, $Z = 1\text{--}92$* , Atomic Data and Nuclear Data Tables **54**, 181–342 (1993).
Cited on page(s): 290.
- ⁵⁸⁹ THE CENTER FOR X-RAY OPTICS (CXRO) OF THE LAWRENCE BERKELEY NATIONAL LABORATORY, *X-Ray Database: X-Ray Interactions With Matter*, available at http://henke.lbl.gov/optical_constants/, The Center for X-Ray Optics, Lawrence Berkeley National Laboratory, Berkeley, CA, USA (2013).
Cited on page(s): 290, 291, 292, 293.

- ⁵⁹⁰ P. C. GEHLEN AND J. B. COHEN, *Nature of Long-Range Order in $Cu_{3+x}Au_{1-x}$* , *Journal of Applied Physics* **40**, 5193–5201 (1969).
Cited on page(s): 291, 294.
- ⁵⁹¹ L.-M. PENG, G. REN, S. L. DUDAREV, AND M. J. WHELAN, *Debye–Waller Factors and Absorptive Scattering Factors of Elemental Crystals*, *Acta Crystallographica Section A* **52**, 456–470 (1996).
Cited on page(s): 291, 292, 293, 294.
- ⁵⁹² C. R. HUBBARD, H. E. SWANSON, AND F. A. MAUER, *A silicon powder diffraction standard reference material*, *Journal of Applied Crystallography* **8**, 45–48 (1975).
Cited on page(s): 291, 292, 293.
- ⁵⁹³ P. VILLARS, K. CENZUAL, J. DAAMS, R. GLADYSHEVSKII, O. SHCHERBAN, V. DUBENSKYY, N. MELNICHENKO-KOBYLYUK, O. PAVLYUK, S. STOIKO, AND L. SYSA, *Cu_3Au* , in *Structure Types. Part 1: Space Groups (230) Ia-3d – (219) F43-c* (edited by P. VILLARS AND K. CENZUAL), volume 43 (Crystal Structures of Inorganic Compounds), subvolume A1 of *Landolt-Börnstein - Group III Condensed Matter*, pp. 1–1, Springer, Berlin, Germany (2004).
Cited on page(s): 290.
- ⁵⁹⁴ M. DRESSELHAUS, G. DRESSELHAUS, AND A. JORIO, *Group Theory: Application to the Physics of Condensed Matter*, 1st edition, Springer, Berlin, Germany (2008).
Cited on page(s): 290.
- ⁵⁹⁵ C. ZENER AND G. E. M. JAUNCEY, *Theory of the Effect of Temperature on the Reflection of X-Rays by Crystals. I. Isotropic Crystals*, *Physical Review* **49**, 17–18 (1936).
Cited on page(s): 294.
- ⁵⁹⁶ J. PRAKASH AND M. P. HEMKAR, *Debye-Waller Factors of fcc Metals*, *Journal of the Physical Society of Japan* **34**, 1583–1587 (1973).
Cited on page(s): 294.
- ⁵⁹⁷ J. PRAKASH AND M. P. HEMKAR, *Anharmonicity and Debye-Waller Factors of fcc Metals. II*, *Journal of the Physical Society of Japan* **36**, 1608–1613 (1974).
Cited on page(s): 294.
- ⁵⁹⁸ L. A. BERTOLO AND M. M. SHUKLA, *A calculation of Debye-Waller factors for F.C.C. metals*, *physica status solidi (b)* **77**, 433–439 (1976).
Cited on page(s): 294.
- ⁵⁹⁹ V. F. SEARS AND S. A. SHELLEY, *Debye–Waller factor for elemental crystals*, *Acta Crystallographica Section A* **47**, 441–446 (1991).
Cited on page(s): 294.
- ⁶⁰⁰ J. BASHIR, M. NASIR KHAN, Q. H. KHAN, N. M. BUTT, Z. BAISHENG, Y. JILIAN, J. LAN, AND Y. CHUNTANG, *Neutron diffraction investigations of thermal atomic displacements in Ta and Ag*, *Journal of Applied Crystallography* **27**, 418–419 (1994).
Cited on page(s): 294.
- ⁶⁰¹ R. ANDRIESSEN, *The influence of temperature on the intensity of x-ray reflection from silver*, *Physica* **2**, 417–424 (1935).
Cited on page(s): 294.

- ⁶⁰² J. BOSKOVITS, M. ROILAS, A. THEODOSSIOU, AND K. ALEXOPOULOS, *The characteristic temperature of silver from X-ray reflections*, *Acta Crystallographica* **11**, 845–847 (1958).
Cited on page(s): 294.
- ⁶⁰³ J. SPREADBOROUGH AND J. W. CHRISTIAN, *The Measurement of the Lattice Expansions and Debye Temperatures of Titanium and Silver by X-ray Methods*, *Proceedings of the Physical Society* **74**, 609–615 (1959).
Cited on page(s): 294.
- ⁶⁰⁴ C. W. HAWORTH, *Measurement of the Debye-Waller temperature factor for silver and α -iron*, *Philosophical Magazine* **5**, 1229–1234 (1960).
Cited on page(s): 294.
- ⁶⁰⁵ M. SIMERSKÁ, *The Temperature Dependence of the Debye Temperature Θ of Silver by X-ray Diffraction Measurements*, *Acta Crystallographica* **14**, 1259–1262 (1961).
Cited on page(s): 294.
- ⁶⁰⁶ K. ALEXOPOULOS, J. BOSKOVITS, S. MOURIKIS, AND M. ROILAS, *The characteristic temperature of silver, gold, platinum and lead from X-ray reflexions*, *Acta Crystallographica* **19**, 349–353 (1965).
Cited on page(s): 294.
- ⁶⁰⁷ J. ŠEDIVÝ AND H. ŠIACHOVÁ, *Röntgenographische Messung der charakteristischen Debye-Temperatur bei vielkristallinem Silber mit Anwendung der Korrektur auf primäre Extinktion*, *physica status solidi (b)* **20**, 249–254 (1967).
Cited on page(s): 294.
- ⁶⁰⁸ M. V. LINKOAHO, *The X-ray Debye Temperatures of V, Ni, Cu, Nb and Ag from the measured integrated intensities at 300 K and 4 K*, *Philosophical Magazine* **23**, 191–198 (1971).
Cited on page(s): 294.
- ⁶⁰⁹ N. SINGH AND P. K. SHARMA, *Debye-Waller Factors of Cubic Metals*, *Physical Review B* **3**, 1141–1148 (1971).
Cited on page(s): 294.
- ⁶¹⁰ R. C. G. KILLEAN AND E. J. LISHER, *The Debye temperatures of the face centred cubic metals. I. X-ray and neutron diffraction results*, *Journal of Physics F: Metal Physics* **5**, 1107–1112 (1975).
Cited on page(s): 294.
- ⁶¹¹ P. D. PATHAK AND N. P. SHAH, *Debye Temperature of Silver and Aluminium at High Temperatures – Some New Correlations*, *physica status solidi (a)* **55**, K159–K162 (1979).
Cited on page(s): 294.
- ⁶¹² Y. KASHIWASE, *Determination of X-Ray Debye Temperature of Fine Silver Particles by Means of Solid-State Detector and Continuous X-Rays*, *Japanese Journal of Applied Physics* **18**, 657–661 (1979).
Cited on page(s): 294.
- ⁶¹³ H. VEGA, G. FÖRSTERLING, AND K. KLEINSTÜCK, *Experimental proof on an anisotropic anharmonic DEBYE-WALLER factor for silver*, *Kristall und Technik* **15**, 815–822 (1980).
Cited on page(s): 294.

- ⁶¹⁴ C. K. SHEPARD, J. G. MULLEN, AND G. SCHUPP, *Debye-Waller factors of copper, silver, and lead*, *Physical Review B* **61**, 8622–8624 (2000).
Cited on page(s): 294.
- ⁶¹⁵ L. H. SCHWARTZ AND J. B. COHEN, *Nature of Long-Range Order in Cu₃Au and Cu₇₂Au₂₈*, *Journal of Applied Physics* **36**, 598–616 (1965).
Cited on page(s): 294.
- ⁶¹⁶ A. G. FOX, *The measurement of low-angle structure factors of Cu₃Au by high energy electron diffraction*, *Philosophical Magazine Part B* **50**, 477–491 (1984).
Cited on page(s): 294.
- ⁶¹⁷ C. SEIDEL, C. AWATER, X. D. LIU, R. ELLERBRAKE, AND H. FUCHS, *A combined STM, LEED and molecular modelling study of PTCDA grown on Ag(110)*, *Surface Science* **371**, 123–130 (1997).
Cited on page(s): 295.
- ⁶¹⁸ C. SEIDEL, J. POPPENSIEKER, AND H. FUCHS, *Real-time monitoring of phase transitions of vacuum deposited organic films by molecular beam deposition {LEED}*, *Surface Science* **408**, 223–231 (1998).
Cited on page(s): 295, 301.
- ⁶¹⁹ D. BRAUN, A. SCHIRMEISEN, AND H. FUCHS, *Molecular growth and sub-molecular resolution of a thin multilayer of {PTCDA} on Ag(110) observed by scanning tunneling microscopy*, *Surface Science* **575**, 3–11 (2005).
Cited on page(s): 295, 301, 304.
- ⁶²⁰ J. IKONOMOV, P. BACH, R. MERKEL, AND M. SOKOLOWSKI, *Surface diffusion constants of large organic molecules determined from their residence times under a scanning tunneling microscope tip*, *Physical Review B* **81**, 161412(R) (2010).
Cited on page(s): 304.
- ⁶²¹ J. IKONOMOV, C. H. SCHMITZ, AND M. SOKOLOWSKI, *Diffusion-limited island decay of PTCDA on Ag(100): Determination of the intermolecular interaction*, *Physical Review B* **81**, 195428 (2010).
Cited on page(s): 304.
- ⁶²² S. HAHNE, J. IKONOMOV, M. SOKOLOWSKI, AND P. MAASS, *Determining molecule diffusion coefficients on surfaces from a locally fixed probe: Analysis of signal fluctuations*, *Physical Review B* **87**, 085409 (2013).
Cited on page(s): 304.
- ⁶²³ J. A. GOLOVCHENKO, J. R. PATEL, D. R. KAPLAN, P. L. COWAN, AND M. J. BEDZYK, *Solution to the Surface Registration Problem Using X-Ray Standing Waves*, *Physical Review Letters* **49**, 560–563 (1982).
Cited on page(s): 332.
- ⁶²⁴ S. FOILES, *Reconstruction of fcc (110) surfaces*, *Surface Science* **191**, L779–L786 (1987).
Cited on page(s): 337.
- ⁶²⁵ K. W. JACOBSEN AND J. K. NØRSKOV, *Theory of Alkali-Metal-Induced Reconstruction of fcc (110) Surfaces*, *Physical Review Letters* **60**, 2496–2498 (1988).
Cited on page(s): 337.

- ⁶²⁶ V. SHKLOVER, F. S. TAUTZ, R. SCHOLZ, S. SLOBOSHANIN, M. SOKOLOWSKI, J. A. SCHAEFER, AND E. UMBACH, *Differences in vibronic and electronic excitations of PTCDA on Ag(111) and Ag(110)*, *Surface Science* **454–456**, 60–66 (2000).
Cited on page(s): 337.
- ⁶²⁷ N. SATO, H. YOSHIDA, AND K. TSUTSUMI, *Unoccupied electronic structure in organic thin films studied by inverse photoemission spectroscopy*, *Journal of Materials Chemistry* **10**, 85–89 (2000).
Cited on page(s): 337.
- ⁶²⁸ G. G. FUENTES AND M. KNUPFER, *Preparation and characterization of single-phase potassium-doped PTCDA thin films*, *Physical Review B* **70**, 233202 (2004).
Cited on page(s): 337.
- ⁶²⁹ J. WÜSTEN, C. ZIEGLER, AND T. ERTL, *Electron transport in pristine and alkali metal doped perylene-3,4,9,10-tetracarboxylic dianhydride (PTCDA) thin films*, *Physical Review B* **74**, 125205 (2006).
Cited on page(s): 337.
- ⁶³⁰ G. FUENTES AND M. KNUPFER, *Electronic structure and work function of potassium-doped PTCDA thin films*, *Applied Physics A: Materials Science & Processing* **84**, 329–333 (2006).
Cited on page(s): 337.
- ⁶³¹ J. WÜSTEN, S. BERGER, M. SALOMO, A. MÖNNICH, M. BAUER, S. LACH, M. AESCHLI-MANN, AND C. ZIEGLER, *Hot-electron dynamics in thin films of sodium-doped perylene-3,4,9,10-tetracarboxylic dianhydride*, *Physical Review B* **78**, 195326 (2008).
Cited on page(s): 337.
- ⁶³² L. ÁLVAREZ, S. PELÁEZ, R. CAILLARD, P. A. SERENA, J. A. MARTÍN-GAGO, AND J. MÉNDEZ, *Metal-organic extended 2D structures: Fe-PTCDA on Au(111)*, *Nanotechnology* **21**, 305703 (2010).
Cited on page(s): 337.
- ⁶³³ L.-G. PETERSSON AND S.-E. KARLSSON, *Clean and Oxygen Exposed Potassium Studied by Photoelectron Spectroscopy*, *Physica Scripta* **16**, 425–431 (1977).
Cited on page(s): 350.
- ⁶³⁴ WOLFRAM RESEARCH, *Mathematica 4*, version 4.2 (2002).
Cited on page(s): 358.
- ⁶³⁵ G. J. JACKSON, B. C. C. COWIE, D. P. WOODRUFF, R. G. JONES, M. S. KARIAPPER, C. FISHER, A. S. Y. CHAN, AND M. BUTTERFIELD, *Atomic Quadrupolar Photoemission Asymmetry Parameters from a Solid State Measurement*, *Physical Review Letters* **84**, 2346–2349 (2000).
Cited on page(s): 365.
- ⁶³⁶ F. C. BOCQUET AND T.-L. LEE, *private communication* (2014).
Cited on page(s): 369.
- ⁶³⁷ E. W. WEISSTEIN, *Cross-Correlation*, From MathWorld—A Wolfram Web Resource: <http://mathworld.wolfram.com/Cross-Correlation.html> (2014).
Cited on page(s): 372.

List of Abbreviations

Chemical abbreviations

DIP	Diindeno[1,2,3- <i>cd</i> :1',2',3'- <i>lm</i>]perylene, C ₃₂ H ₁₆
NTCDA	1,4,5,8-Naphthalenetetracarboxylic 1,8:4,5-dianhydride, C ₁₄ H ₄ O ₆
Pc	29 <i>H</i> ,31 <i>H</i> -Phthalocyanine, C ₃₂ H ₁₈ N ₈
MPc	Metal phthalocyanine, C ₃₂ H ₁₆ MN ₈
Pen	Pentacene, C ₂₂ H ₁₄
PFP	Tetradecafluoropentacene, also perfluoropentacene, C ₂₂ F ₁₄
PTCDA	3,4,9,10-Perylenetetracarboxylic 3,4:9,10-dianhydride, C ₂₄ H ₈ O ₆

General abbreviations

2PPE	Two-photon photoemission (spectroscopy)
AES	Auger electron spectroscopy
AO	Atomic orbital
ARUPS	Angle-resolved ultraviolet photoelectron spectroscopy
BCP	Bond critical point
BW	Brick-wall
CN	Coordination number
COOP	Crystal orbital overlap population
CTR	Crystal truncation rod
CXRO	Center for X-Ray Optics, Lawrence Berkeley National Laboratory, Berkeley, CA, USA
DFT	Density functional theory
DOS	Density of states
e ⁻	Electron
<i>fcc</i>	Face-centered cubic
FFT	Fast Fourier transform
F-HOMO	Former highest occupied molecular orbital
F-LUMO	Former lowest unoccupied molecular orbital
FWHM	Full width at half maximum
GGA	Generalized gradient approximation
GUI	Graphical user interface
HB	Herringbone

<i>hcp</i>	Hexagonal close-packed
HOMO	Highest occupied molecular orbital
HREELS	High-resolution electron energy loss spectroscopy
HWHM	Half width at half maximum
IMFP	Inelastic mean free path
IUPAC	International Union of Pure and Applied Chemistry
LDA	Local density approximation
LDOS	Local density of states
LEED	Low energy electron diffraction
LEED- <i>I(V)</i>	Energy-dependent low energy electron diffraction
LT	Low temperature
LUMO	Lowest unoccupied molecular orbital
MCP-LEED	Micro-channel plate low-energy electron diffraction
ML	Monolayer(s)
MO	Molecular orbital
MP2	Second-order Møller-Plesset perturbation theory
NICISS	Impact collision ion scattering spectroscopy with neutral particle detection
NIXSW	Normal incidence x-ray standing wave (technique) or normal incidence x-ray standing wavefield absorption (technique)
NLSF	Nonlinear least square fitting
OMBE	Organic molecular beam epitaxy
PAW	Projector-augmented wave method
PBE	Perdew-Burke-Ernzerhof
PBN	Pyrolytic boron nitride
PDOS	Projected density of states
PhD	Photoelectron diffraction
PID	Proportional-integral-derivative (controller)
PG	Pyrolytic graphite
p-o-l	Point-on-line
PVD	Physical vapor deposition
Q	Quadratic
QCM	Quartz crystal microbalance
QMS	Quadrupole mass spectrometer or quadrupole mass spectrometry
REM	Reflection electron microscopy
RGA	Residual gas analysis
RT	Room temperature
S	Square
SAM	Self-assembled monolayer

SOMO	Singly occupied molecular orbital
SPA-LEED	Spot profile analysis low energy electron diffraction
STM	Scanning tunneling microscopy or scanning tunneling microscope
STS	Scanning tunneling spectroscopy
TPD	Temperature programmed desorption (spectroscopy)
UHV	Ultrahigh vacuum
UPS	Ultraviolet photoelectron spectroscopy
vdW	Van der Waals
VASP	Vienna <i>Ab initio</i> Simulation Package
VT	Variable temperature
XPS	X-ray photoelectron spectroscopy
XRF	X-ray fluorescence (spectroscopy)
XSW	X-ray standing wave (technique) or x-ray standing wavefield absorption (technique)

Functions, parameters, and variables

A	Amplitude
A	Peak area
A	Surface area per atom
A_{uc}	Area of the surface unit cell
a	Twice the distance from the <i>fcc</i> hollow site to the nearest <i>hcp</i> hollow site on the (111) surface
a_0	Atomic row distance at the surface
a_{bulk}	Bulk lattice constant
\mathbf{a}_i	Surface lattice vector of the substrate in real space
\mathbf{a}_i^*	Surface lattice vector of the substrate in reciprocal space
a_i	Surface lattice constant of the substrate in real space
a_i^*	Surface lattice constant of the substrate in reciprocal space
a, b, c	Bulk lattice constants
α	Enclosed angle of the surface unit cell vectors of the substrate in real space
$\alpha^* = \pi - \alpha$	Enclosed angle of the surface unit cell vectors of the substrate in reciprocal space
α	Adjustable parameter in the <i>d</i> -band model
α, β, γ	Angles of inclination of the axes in the bulk unit cell
$b = \gamma_0/\gamma_H$	Asymmetry parameter of the Bragg reflection, given by the ratio of the direction cosines of the incident and emergent beams
b	Bond length
\mathbf{b}_i	Surface lattice vector of the adsorbate in real space

\mathbf{b}_i^*	Surface lattice vector of the adsorbate in reciprocal space
b_i	Surface lattice constant of the substrate in real space
b_i^*	Surface lattice constant of the substrate in reciprocal space
β	Enclosed angle of the surface unit cell vectors of the adsorbate in real space
$\beta^* = \pi - \beta$	Enclosed angle of the surface unit cell vectors of the adsorbate in reciprocal space
β	Dipolar asymmetry parameter
$C(f_a, f_d)$	Parameter employed in the calculation of the hybridization energy $E_{d\text{-hyb}}$, which depends on the fractional fillings of the involved states
c	Speed of light in vacuum
Γ	Constant of proportionality between the Fourier coefficients of the charge density and the dielectric constant
$\bar{\Gamma}$	Average or effective width of the surface regions with uniform periodicity/of the periodic structures
γ	Asymmetry parameter associated with the dipole–electric quadrupole interference
γ	Angle between the direction of incidence and of detection
γ	Surface energy
γ_0	Direction cosine of the incident beam with respect to the incident crystal surface
γ_H	Direction cosine of the Bragg-reflected beam with respect to the incident crystal surface
$D(E_{\text{kin}})$	Detection efficiency of the electron spectrometer
d	Distance or adsorption height
$d_e = d_e(E_{\text{kin}}, \theta)$	Escape depth
d_{hkl}	Lattice plane spacing or Bragg spacing of the family $\{hkl\}$ of lattice planes
$d_{h'k'l'}$	Lattice plane spacing or Bragg spacing
d_1	Overlayer thickness
d_z	Monoatomic step height
$\Delta = \phi_q - \phi_d$	Phase difference between the dipole and the quadrupole matrix elements ϕ_q and ϕ_d
δ	Asymmetry parameter associated with the magnetic–electric dipole term
δ_d, δ_p	Partial phase shifts of the final quadrupole-excited d and dipole-excited p states of the electron emitted from an initial s state
δ_{ij}	Kronecker's delta
E	Energy
E°	Standard electrode potential
E_A	Electron affinity

E_B	Bragg energy
E_a	Activation energy
E_{ads}	Adsorption energy
E_b	Binding energy (referenced against E_F)
E'_b	Binding energy (referenced against E_{vac})
$E_{\text{cut-off}}$	Cut-off energy
E_F	Fermi energy
E_{kin}	Kinetic energy (referenced against E_F)
E'_{kin}	Kinetic energy (referenced against E_{vac})
E_{vac}	Vacuum level
\mathbf{E}_i	Electric-field vector
E_0	Complex electric-field amplitude of the incident electromagnetic wave
E_H	Complex electric-field amplitude of the emergent electromagnetic wave
$\Delta E/E$	Resolving power or energy resolution
\mathbf{e}_0	Polarization unit vector of the electric field
e	Elementary charge
$\exp(-M_Z)$	Debye-Waller factor of element Z
ϵ	Energy
ϵ	Auxiliary variable in the convolution integral, with the dimension of an energy
ϵ_0	Vacuum permittivity or electric constant
ϵ_d	Center of the metal d -bands
$\epsilon = \epsilon_0 + \epsilon_H$	Total amplitude of the x-ray standing wavefield
ϵ_0	Complex amplitude of the incident electromagnetic wave
ϵ_H	Complex amplitude of the emergent or Bragg-reflected electromagnetic wave
η	Complex parameter, describing the displacement of the scattering condition from the midpoint of the reflectivity curve R
$F(\mathbf{k})$	Structure factor
F_0	Structure factor for the (000) reflection
F_H	Structure factor for the reflection defined by \mathbf{H}_{hkl}
F'_H, F''_H	Real and imaginary parts of F_H
f_0	Tabulated, uncorrected value of the atomic scattering factor f_Z , with $f_Z = (f_0 + \Delta f' + i \Delta f'')_Z$
$\Delta f', \Delta f''$	Real and imaginary parts of the dispersion correction, the so-called Hönl corrections, to f_0 (tabulated as a function of energy in the form of the parameters f_1 and f_2)
f_c	Coherent fraction
f_a	Fractional filling of the adsorbate level
f_d	Fractional filling of the metal d -bands

f_{vdW}	Fraction of the dispersion energy on the total adsorption energy, with $f_{\text{vdW}} = E_{\text{ads}}^{\text{D3(BJ)}}/E_{\text{ads}}$
f_Z	Atomic scattering factor (of element Z)
\mathbf{G}_{hkl}	Reciprocal lattice vector
$G(E_{\text{kin}})$	Transmission of the electron analyzer
$G(\mathbf{k})$	Lattice factor
\mathbf{H}_{hkl}	Scattering or diffraction vector
H_{ij}	Off-diagonal Hamiltonian matrix element (or Hamiltonian matrix element between orbitals i and j)
h	Planck's constant
\hbar	Reduced Planck's constant or Dirac's constant
h, k, l	Laue indices
h', k', l'	Miller indices
I	Current or intensity
I/I_0	Normalized intensity of the x-ray standing wavefield, also written as $I(\mathbf{r})/I_0$ or $I(z_{hkl})/I_0$
I_0	Intensity of the incident (or primary) beam
I_H	Intensity of the Bragg-reflected beam
$I_{\text{diff}}(\mathbf{K}_{\parallel})$	Normalized shape of the diffuse part of a diffraction spot profile
I_p	Ionization potential
I_t	Tunneling current
J_0	Photon flux on the sample
j	Total angular momentum quantum number
\mathbf{K}_i	Wavevector (with magnitude $K_i = \mathbf{K}_i = \lambda^{-1}$)
\mathbf{K}_0	Incident wavevector
\mathbf{K}_H	Emergent wavevector
$\mathbf{k} = \mathbf{k}_H - \mathbf{k}_0$	Scattering vector
\mathbf{k}_i	Wavevector (with magnitude $k_i = \mathbf{k}_i = 2\pi/\lambda$)
$\mathbf{k}_{i,\parallel}$	Parallel component of wavevector
$\mathbf{k}_{i,\perp}$	Perpendicular component of wavevector
\mathbf{k}_0	Incident wavevector
$k_0 = 2\pi/\lambda$	Magnitude of the incident wavevector or radius of the Ewald sphere
k_{01}	Distance between two neighboring fundamental diffraction spots
k_B	Boltzmann's constant
\mathbf{k}_H	Emergent wavevector
Δk_{hk}	Full width at half maximum of the (hk) diffraction spot
$\Delta k_{\parallel,\text{diff}}$	Width of the diffuse part of the diffraction spot profile
κ	Exponential inverse decay length

$L(\gamma)$	Angular asymmetry factor in photoemission
l	Orbital angular momentum quantum number
λ	Wavelength
λ_{IMFP}	Inelastic mean free path
M_{fi}	Matrix element between the initial and final states $ i\rangle$ and $ f\rangle$
\mathfrak{M}	Superstructure matrix in real space
\mathfrak{M}^*	Superstructure matrix in reciprocal space, with $\mathfrak{M}^* = \tilde{\mathfrak{M}}^{-1}$
m	Mass
m	Gaussian-to-Lorentzian ratio in pseudo-Voigt function, with $0 \leq m \leq 1$ where $m = 1$ is a pure Lorentzian function
m_e	Electron mass
μ	Center of the Gaussian function
μ	Surface force constant
N_Z	Atom density of element Z
\mathbf{n}	Surface normal
n	Order of diffraction
$n(E)$	Density of states
$n(\mathbf{r}, E)$	Local density of states
ν	Frequency
Ω	Solid angle
P	Polarization factor [with a value of unity for σ polarization and a value of $\cos(2\theta_B)$ for π polarization]
P	Misfit parameter
$P_2(\cos\theta_p)$	Second-order Legendre polynomial, with $P_2(\cos\theta_p) = (3\cos^2\theta_p - 1)/2$
$\hat{\mathbf{p}} = -i\hbar\nabla$	Momentum operator
p	Pressure
p_c	Coherent position
Φ	Work function
ϕ	Azimuthal angle
ϕ	Angle between the direction of photon propagation and the projection of the photoelectron wavevector in the plane perpendicular to \mathbf{e}_0
ϕ	Enclosed angle between the surface lattice vector \mathbf{a}_1 and \mathbf{b}_1
φ	Scattering angle (with respect to the surface normal)
φ_0	Angle of incidence (with respect to the surface normal)
φ_{asym}	Acute angle enclosed by the Bragg-reflecting lattice planes and the crystal surface
ψ	Phase of the nondipolar correction parameter S_1
Q	Forward/backward asymmetry parameter in the photoemission process

Δq	Charge (transfer)
\mathbf{R}	Position vector
$R = R(E, \theta_{sc})$	Reflectivity
\mathbf{r}	Position vector
r	Radius
r_e	Classical electron radius, with $r_e = (e^2/4\pi\epsilon_0 m_e c^2)$
$\rho(\mathbf{r})$	Electron density at point \mathbf{r}
$\Delta\rho(\mathbf{r})$	Electron density difference
ϱ	Angle of inclination of the long molecular axis with respect to \mathbf{b}_1
S	Scattering condition
S_{ij}	Overlap matrix element or overlap integral of orbitals i and j
$S_I = S_I \exp(i \psi)$	Nondipolar correction parameter with magnitude $ S_I $ and phase ψ
$ S_I $	Magnitude of the nondipolar correction parameter S_I
S_R	Nondipolar correction parameter
s_0	Unit vector in the incident beam direction
s_H	Unit vector in the diffracted beam direction
σ	Width of the Gaussian function
$\sigma = \sigma(E_{kin})$	Photoionization cross section
$d\sigma/d\Omega$	Differential photoionization cross section
T	Temperature
T_c	Critical temperature
T_w	Transfer width
$T(E, e U_{bias})$	Transmission coefficient of the tunneling junction
t	Time
t	Energy (shift), employed in the convolution
t_{final}	Upper bound of integration
$t_{initial}$	Lower bound of integration
$[t_{initial}, t_{final}]$	Convolution interval
Δt	Step size in energy for numerical integration
τ	Herringbone angle
τ	Surface stress
θ	Polar angle
θ	Emission/detection angle of the photoelectron with respect to the surface normal
θ	Scattering angle, i.e., the (grazing) angle of incidence (with respect to the lattice planes; also denoted as θ_{sc})
θ_0	Angle of the incident beam with respect to the surface normal
θ_B	Bragg angle (with respect to the lattice planes)

θ_D	Debye temperature (of the surface)
θ_H	Angle of the Bragg-reflected beam with respect to the surface normal
θ_p	Angle between the photoelectron detection direction and the polarization vector
θ_{sc}	Scattering angle (with respect to the lattice planes; also denoted as θ)
θ_Z	Surface coverage of element Z
ϑ_Z	Fractional surface coverage with element Z
U_{bias}	Bias voltage
$Y_{exp}(E)$	Experimental reflectivity [$R_{exp}(E)$] or XSW photoelectron yield [$Y_{Z,j}(E)$] (not normalized)
ΔY_{exp}	Offset
$Y_i(E)$	$R(E)$ or norm. $Y_{Z,j}(E)$ ($i = \text{theo, ideal, real}$)
$\langle u^2 \rangle$	Displacement factor (the mean square of the component of displacement, i.e., the vibrational amplitude, along the direction of \mathbf{H}_{hkl})
$\nu = \nu(E, \theta_{sc})$	Phase of the x-ray standing wavefield or phase relationship of the two complex electric-field amplitudes E_H and E_0
V_{ad}	Coupling matrix element, i.e., the overlap, between metal d -band state(s) $ d\rangle$ and adsorbate orbital $ a\rangle$
V_{ak}	Coupling matrix element between electronic state $ a\rangle$ of the adsorbate and one-electron metal state $ k\rangle$
V_{uc}	Volume of the crystal unit cell
\mathbf{v}	Velocity
W	(Average) potential energy
w	Width of peak profile, equals the FWHM of pure Lorentzian and Gaussian functions
$\omega = 2/\bar{\Gamma}$	Half width at half maximum of the diffuse part of the diffraction spot
x	Axis of abscissas or x coordinate
x_c	Center position of peak profile
χ	Electronegativity
χ^2	Goodness of fit
ξ	Correlation length of the surface height function or large-scale surface roughness
$Y_{Z,j}$	Photoelectron yield on photoemission from orbital j of element Z
$dY/d\Omega$	Differential/angle-resolved photoelectron yield
y	Axis of ordinates or y coordinate
y_0	Vertical offset
Z	Chemical element or atomic number
z	Axis of applicates or z coordinate

z_{hkl}	Vertical position of an atom relative to the Bragg planes
ζ	Component of the phase ν of the standing wavefield (complex argument of the ratio of the electric-field amplitudes, E_H/E_0)

List of Figures

	Page
Fig. 2.1. Blyholder model for CO chemisorption on metal surfaces.	6
Fig. 2.2. Schematic representation of chemisorption in the Newns-Anderson model. . .	7
Fig. 2.3. Hoffmann model for chemisorption on a metal surface.	8
Fig. 2.4. Hammer-Nørskov model for chemisorption of CO on metal surfaces.	9
Fig. 2.5. Valence bond structure and ball-and-stick model of PTCDA.	11
Fig. 2.6. Crystal structures of PTCDA.	11
Fig. 2.7. Adsorption configurations of PTCDA on the (111) surfaces of Au, Ag, and Cu. . .	15
Fig. 3.1. Principle of the formation of an x-ray standing wavefield.	23
Fig. 3.2. Shape of the Bragg reflection from a perfect crystal and typical XSW profiles. . .	25
Fig. 3.3. Asymmetric Bragg reflection and resulting values of b	28
Fig. 3.4. Influence of the nondipolar contributions on the angular distribution of photoemission from an initial s state.	30
Fig. 3.5. Ewald sphere construction and schematics of LEED.	34
Fig. 3.6. Energy level diagram for an STM tunneling junction.	37
Fig. 3.7. Principle of x-ray photoemission and successive effects.	38
Fig. 4.1. Cross-sectional top view of the SPA-LEED setup.	44
Fig. 4.2. Cross-sectional top view of XSW setup I.	45
Fig. 4.3. Cross-sectional top view of XSW setup II.	46
Fig. 5.1. Structural models of PTCDA on the Cu(111) surface, as proposed by Wagner <i>et al.</i>	69
Fig. 5.2. LEED patterns of PTCDA on the Cu(111) surface.	71
Fig. 5.3. High-resolution one-dimensional LEED scans and two-dimensional LEED patterns of PTCDA/Cu(111).	73
Fig. 5.4. Structural models of the PTCDA phases on the Cu(111) surface.	75
Fig. 5.5. LEED spot profiles of PTCDA on the Cu(111) surface.	77
Fig. 5.6. Temperature dependence of the structure formation for PTCDA on the Cu(111) surface.	78
Fig. 5.7. Model of the surface reconstruction present for PTCDA adsorption on Cu(111).	81
Fig. 6.1. Bulk structure and (111) surface of the ordered, binary alloy Cu ₃ Au.	88
Fig. 6.2. One-dimensional LEED scans and two-dimensional LEED patterns of the clean Cu ₃ Au(111) surface.	94
Fig. 6.3. STM image of the clean and ordered Cu ₃ Au(111) surface.	96
Fig. 6.4. Schematic models of the ideal and the real Cu ₃ Au(111) surface.	97
Fig. 6.5. Experimental depth profile of the Cu ₃ Au(111) substrate.	101
Fig. 6.6. XP and Auger spectra of the substrate levels for the clean Cu ₃ Au(111) surface. . .	102

Fig. 6.7.	Typical XSW photoelectron yield curves of Cu and Au at the clean $\text{Cu}_3\text{Au}(111)$ surface.	104
Fig. 6.8.	Typical Darwin-Prins curve of the (clean) $\text{Cu}_3\text{Au}(111)$ substrate crystal.	105
Fig. 6.9.	Schematic representation of the outward relaxation of the clean $\text{Cu}_3\text{Au}(111)$ surface.	111
Fig. 6.10.	One-dimensional LEED scans of the PTCDA-covered $\text{Cu}_3\text{Au}(111)$ surface in comparison to those of the clean surface.	114
Fig. 6.11.	Typical XSW photoelectron yield curves of Cu and Au at the PTCDA-covered $\text{Cu}_3\text{Au}(111)$ surface.	117
Fig. 6.12.	Close-up of the LEED pattern in Fig. 6.13(d).	123
Fig. 6.13.	LEED patterns of PTCDA monolayers on the $\text{Cu}_3\text{Au}(111)$ surface.	123
Fig. 6.14.	STM images of PTCDA (sub-)monolayers on the $\text{Cu}_3\text{Au}(111)$ surface.	125
Fig. 6.15.	LEED patterns of PTCDA layers on the $\text{Cu}_3\text{Au}(111)$ surface after thermal annealing.	126
Fig. 6.16.	STM images of PTCDA molecules on the $\text{Cu}_3\text{Au}(111)$ surface, revealing the molecular arrangement within the unit cell.	127
Fig. 6.17.	Structural models of the PTCDA phases on the $\text{Cu}_3\text{Au}(111)$ surface.	129
Fig. 6.18.	STM image of the δ phase of PTCDA on the $\text{Cu}_3\text{Au}(111)$ surface at domain boundaries.	130
Fig. 6.19.	Thermal desorption spectrum of PTCDA multilayers on the $\text{Cu}_3\text{Au}(111)$ surface.	131
Fig. 6.20.	STM image of a PTCDA overlayer on the $\text{Cu}_3\text{Au}(111)$ surface after thermal annealing.	132
Fig. 6.21.	Close-up STM image of a PTCDA overlayer on the $\text{Cu}_3\text{Au}(111)$ surface after thermal annealing.	132
Fig. 6.22.	LEED patterns of PTCDA multilayers on the $\text{Cu}_3\text{Au}(111)$ surface.	135
Fig. 6.23.	STM image of PTCDA multilayers on the $\text{Cu}_3\text{Au}(111)$ surface.	136
Fig. 6.24.	STM image of the wetting layers in PTCDA multilayers on the $\text{Cu}_3\text{Au}(111)$ surface.	137
Fig. 6.25.	LEED pattern of the PTCDA submonolayer on the $\text{Cu}_3\text{Au}(111)$ surface which was employed in the XPS and XSW experiments.	138
Fig. 6.26.	XP spectra of the $\text{C}1s$ and $\text{O}1s$ levels of PTCDA on the $\text{Cu}_3\text{Au}(111)$ surface as a function of x-ray beam exposure.	139
Fig. 6.27.	Normalized XP spectra of the $\text{C}1s$ and $\text{O}1s$ levels of PTCDA on the $\text{Cu}_3\text{Au}(111)$ surface with corresponding fitting models for short and long times of x-ray beam exposure.	140
Fig. 6.28.	Typical XSW photoelectron yield curves of carbon and oxygen in PTCDA on the $\text{Cu}_3\text{Au}(111)$ surface on a fresh spot.	148
Fig. 6.29.	Typical XSW photoelectron yield curves of carbon and oxygen in PTCDA on the $\text{Cu}_3\text{Au}(111)$ surface on an exposed spot.	149
Fig. 6.30.	Adsorption configurations of PTCDA on the $\text{Cu}_3\text{Au}(111)$ surface at different times of x-ray beam exposure.	153
Fig. 6.31.	Schematic representation of the XSW results for PTCDA on the $\text{Cu}_3\text{Au}(111)$ surface in an Argand diagram.	158
Fig. 6.32.	Schematic representation of the outward relaxation of the clean and the PTCDA-covered $\text{Cu}_3\text{Au}(111)$ surface.	163
Fig. 6.33.	Adsorption configurations of PTCDA on the (111) surfaces of Au, Cu_3Au , and Cu.	168

Fig. 6.34.	Schematic representation of the PTCDA adsorption configurations in the initial state and in the final state on the $\text{Cu}_3\text{Au}(111)$ surface, including the vdW radii of the individual atoms.	170
Fig. 6.35.	Schematic representation of the potential energy E as a function of the adsorption height d for PTCDA on the $\text{Cu}_3\text{Au}(111)$ surface.	173
Fig. 7.1.	Structural models for PTCDA in the monolayer regime on the (111), (100), and (110) surfaces of Ag.	179
Fig. 7.2.	Structural model for PTCDA in the monolayer regime on the K-modified Ag(110) surface.	180
Fig. 7.3.	Hydrogen bonds between individual PTCDA molecules in the herringbone arrangement.	181
Fig. 7.4.	Adsorption configurations of PTCDA on coinage metal surfaces.	182
Fig. 7.5.	Frontier orbitals of the PTCDA molecule in the gas phase.	188
Fig. 7.6.	Vertical bonding distances of PTCDA corrected for the different van der Waals radii of the surface atoms versus the work functions of the respective clean coinage metal surfaces.	193
Fig. 7.7.	UP spectra for PTCDA in the (sub-)monolayer regime on the low-index Ag surfaces.	198
Fig. 7.8.	Peak shifts in XPS for the $\text{C}1s$ and $\text{O}1s$ levels of PTCDA in the (sub-)monolayer regime on various coinage metal surfaces.	202
Fig. 7.9.	Comparison of peak shifts in XPS for the $\text{C}1s$ and $\text{O}1s$ levels and metal-to-molecule charge transfer for PTCDA in the (sub-)monolayer regime on the low-index Ag surfaces.	208
Fig. 7.10.	Averaged vertical heights d and bond lengths b to neighboring surface atoms for PTCDA adsorption on the low-index Ag surfaces.	209
Fig. 7.11.	Hard sphere models of the lateral and vertical molecular configurations of PTCDA on the low-index Ag surfaces.	210
Fig. 7.12.	Total electron density $\rho(\mathbf{r})$ and electron density difference $\Delta\rho(\mathbf{r})$ for PTCDA on the low-index Ag surfaces.	212
Fig. 7.13.	Comparison of the adsorption configurations of PTCDA on the Ag(111) and Ag(100) surfaces.	216
Fig. 7.14.	Formation of a quinoid-like structure of PTCDA upon metal-to-molecule charge transfer on a coinage metal surface.	218
Fig. 7.15.	Schematic representation of the potential energy E as a function of the adsorption height d for PTCDA on coinage metal surfaces for different scenarios.	219
Fig. 7.16.	Comparison of the adsorption configurations of PTCDA on the pure Ag(110) and on the K-modified Ag(110) surface.	226
Fig. 7.17.	Schematic representation of the bonding mechanism for PTCDA adsorption on coinage metal surfaces.	230
Fig. A.1.	Flow chart of the XSWAVES routine.	242
Fig. A.2.	XSWAVES dialog box for the fitting of the experimental reflectivity curve.	243
Fig. A.3.	XSWAVES dialog box for the fitting of the experimental XSW photoelectron yield curve.	244
Fig. A.4.	XSWAVES dialog box for the fitting of the experimental XSW photoelectron yield curve by a linear combination of two individual XSW profiles ('special fit model').	245

Fig. A.5.	Schematic layout of beamline ID32 of the European Synchrotron Radiation Facility (ESRF) and theoretical reflectivity curves of the monochromator and substrate crystals.	252
Fig. C.1.	LEED pattern and structure model of the PTCDA herringbone phase in the monolayer regime on the Ag(100) surface.	300
Fig. C.2.	LEED patterns and structure models of the PTCDA herringbone phases in the multilayer and the monolayer regime on the Ag(110) surface.	303
Fig. C.3.	Coverage-dependent UP spectra of PTCDA on the Ag(100) surface.	304
Fig. C.4.	Fitting of the spectral features in the UP spectra of PTCDA on the Ag(100) surface.	307
Fig. C.5.	LEED patterns of the PTCDA submonolayers on the Ag(100) surface which were employed in the XPS and XSW experiments.	308
Fig. C.6.	LEED patterns of the PTCDA (sub-)monolayers on the Ag(110) surface which were employed in the XPS and XSW experiments.	308
Fig. C.7.	XP and Auger spectra of the substrate levels for the Ag(100) and Ag(110) surfaces.	309
Fig. C.8.	Normalized XP spectra of the C1s and O1s levels of PTCDA on the Ag(100) surface with corresponding fitting models for different coverages.	310
Fig. C.9.	Normalized XP spectra of the C1s and O1s levels of PTCDA on the Ag(110) surface in the multilayer regime and the (sub-)monolayer regime with corresponding fitting models.	312
Fig. C.10.	Typical XSW photoelectron yield curves of the substrate signals for the PTCDA-covered Ag(100) and Ag(110) surfaces.	318
Fig. C.11.	Typical XSW photoelectron yield curves of carbon and oxygen in PTCDA on the Ag(100) surface for the first preparation.	320
Fig. C.12.	Typical XSW photoelectron yield curves of carbon and oxygen in PTCDA on the Ag(100) surface for the second preparation.	321
Fig. C.13.	Typical XSW photoelectron yield curves of carbon and oxygen in PTCDA on the Ag(110) surface for the first preparation.	322
Fig. C.14.	Typical XSW photoelectron yield curves of carbon and oxygen in PTCDA on the Ag(110) surface for the second preparation.	323
Fig. C.15.	Normalized XP spectrum of the O1s level of PTCDA on the Ag(100) surface with corresponding fitting model.	328
Fig. C.16.	Typical XSW photoelectron yield curve of the Ag3d signal for PTCDA on the Ag(100) surface, employing the (111) Bragg reflection of the substrate crystal.	329
Fig. C.17.	Typical XSW photoelectron yield curves of oxygen in PTCDA on the Ag(100) surface, employing the (111) Bragg reflection of the substrate crystal.	330
Fig. C.18.	Schematic illustration of the adsorption site determination for PTCDA on the Ag(100) surface.	333
Fig. C.19.	Schematic illustration for the calculation of the theoretically expected coherent positions with respect to the (111) lattice planes of the Ag(100) substrate crystal.	334
Fig. D.1.	LEED pattern of PTCDA plus K in the (sub-)monolayer regime on the Ag(110) surface and corresponding simulation.	340
Fig. D.2.	High-resolution one-dimensional LEED scans of PTCDA plus K on the Ag(110) surface.	342

Fig. D.3.	One-dimensional LEED scans of PTCDA plus K on the Ag(110) surface as a function of temperature.	346
Fig. D.4.	Graphical representation of the spot positions observed in LEED for PTCDA plus K on the Ag(110) surface as a function of temperature.	347
Fig. D.5.	LEED pattern of PTCDA plus K on the Ag(110) surface as employed in the XPS and XSW experiments.	348
Fig. D.6.	Normalized XP spectra of the K2 <i>p</i> , C1 <i>s</i> , and O1 <i>s</i> levels of PTCDA plus K on the Ag(110) surface in the (sub-)monolayer regime with corresponding fitting models in comparison to those of pure PTCDA/Ag(110).	348
Fig. D.7.	K1 <i>s</i> XP spectrum of PTCDA/K:Ag(110).	352
Fig. D.8.	Typical XSW photoelectron yield curves of carbon and oxygen in PTCDA plus K on the Ag(110) surface.	355
Fig. D.9.	Typical XSW photoelectron yield curves of K in PTCDA/K:Ag(110).	357
Fig. E.1.	Impact of the nondipolar parameter Q on the averaged XSW fitting results for the coherent fraction f_c and the coherent position p_c	366
Fig. F.1.	Exemplary XSW photoelectron yield curves fitted with version 2.5 and version 2.6 of the XSWAVES evaluation routine.	371
Fig. F.2.	An exemplary Darwin-Prins curve fitted with version 2.5 and version 2.6 of the XSWAVES evaluation routine.	373

List of Tables

	Page
Table 2.1. Lattice parameters of the α and β modifications of bulk PTCDA.	12
Table 2.2. Values for averaged vertical distances d of the carbon and oxygen atoms for PTCDA and NTCDA adsorbed on different coinage metal (111) surfaces. . .	15
Table 2.3. Radii of the elements of interest in the present work.	16
Table 4.1. Inelastic mean free paths within the PTCDA overlayers of the photoelectrons of interest in the present work.	54
Table 4.2. Inelastic mean free paths within the substrates of the photoelectrons of interest in the present work.	55
Table 4.3. PTCDA coverages of the systems under investigation in the present work. . .	56
Table 4.4. Photoionization cross sections for the spectroscopic levels of interest in the present work.	58
Table 4.5. Beamtimes and systems under investigation in the framework of the present work.	60
Table 4.6. Nondipolar parameters for the evaluation of the XSW photoelectron yield curves of the adsorbate XPS levels.	63
Table 4.7. Nondipolar parameters for the evaluation of the XSW photoelectron yield curves of the substrate XPS levels.	64
Table 5.1. Structural results for PTCDA in the first and second layer on the Cu(111) surface by Wagner <i>et al.</i>	68
Table 5.2. Structural results and proposed model parameters for PTCDA on the Cu(111) surface.	74
Table 6.1. Reported structural parameters for PTCDA on the Au(111) surface.	90
Table 6.2. Averaged effective transfer widths deduced from LEED spot profiles of the clean Cu ₃ Au(111) surface for different electron energies.	94
Table 6.3. Averaged vertical shifts for the Cu and Au atoms at the clean Cu ₃ Au(111) surface as obtained from XSW experiments.	107
Table 6.4. Averaged vertical shifts for the Cu and Au atoms at the PTCDA-covered Cu ₃ Au(111) surface.	117
Table 6.5. XSW results for the Cu and Au atoms at the PTCDA-covered Cu ₃ Au(111) surface for different times of x-ray beam exposure.	119
Table 6.6. Structural results and proposed model parameters for PTCDA on the Cu ₃ Au(111) surface.	122
Table 6.7. XPS fitting parameters for the C1s and O1s levels of PTCDA on the Cu ₃ Au(111) surface.	143
Table 6.8. Summary of the final XSW results for the adsorption configuration of PTCDA on the Cu ₃ Au(111) surface.	152

Table 6.9.	XSW results for the adsorption configuration of PTCDA on the $\text{Cu}_3\text{Au}(111)$ surface for subsequent acquisition of individual data points on fresh spots.	154
Table 6.10.	XSW results for the adsorption configuration of PTCDA on the $\text{Cu}_3\text{Au}(111)$ surface at different times of x-ray beam exposure on exposed spots.	155
Table 6.11.	Values for averaged vertical distances d of the carbon and oxygen atoms for PTCDA adsorbed on the $\text{Cu}_3\text{Au}(111)$ surface in comparison to PTCDA adsorbed on the $\text{Au}(111)$ and $\text{Cu}(111)$ surfaces.	169
Table 7.1.	Values for averaged vertical distances d of the carbon and oxygen atoms for PTCDA on different coinage metal surfaces.	185
Table 7.2.	Relative values for averaged vertical distances d of the carbon and oxygen atoms for PTCDA on different coinage metal surfaces.	186
Table 7.3.	Experimental and theoretical results for the adsorption geometry of PTCDA on the low-index Ag surfaces.	189
Table 7.4.	Expected vdW and covalent distances of metal atoms at the substrate surface and C and O atoms in PTCDA.	190
Table 7.5.	Reported work functions of the clean coinage metal surfaces and work function shifts induced by the adsorption of PTCDA (sub-)monolayers.	191
Table 7.6.	Peak shifts in XPS for the $\text{C}1s$ and $\text{O}1s$ levels of PTCDA in the (sub-)monolayer regime on various coinage metal surfaces.	203
Table 7.7.	Peak shifts in XPS for the $\text{C}1s$ and $\text{O}1s$ levels and metal-to-molecule charge transfer for PTCDA in the (sub-)monolayer regime on the low-index Ag surfaces.	207
Table 7.8.	Adsorption energies for PTCDA on the low-index Ag surfaces.	215
Table 7.9.	Electron densities at bond critical points for PTCDA on the low-index Ag surfaces.	217
Table 7.10.	Deviations from the planarity of the functional groups in PTCDA adsorbed on various coinage metal surfaces.	221
Table A.1.	List of abbreviations of the functions, parameters, and variables used for the calculation of the reflectivity $R(E)$ and the XSW photoelectron yield $Y_{Z,j}(E)$ as employed in the text of the present work.	247
Table A.2.	List of terms used in the XSW source code for the calculation of the reflectivity $R(E)$ and the XSW photoelectron yield $Y_{Z,j}(E)$ in alphabetical order.	248
Table B.1.	Structure factors and Debye-Waller factors of Cu_3Au and Si.	291
Table B.2.	Structure factors and Debye-Waller factors of Ag and Si in the case of PTCDA/Ag(100).	292
Table B.3.	Structure factors and Debye-Waller factors of Ag and Si in the case of PTCDA/Ag(110).	293
Table C.1.	Structural results and proposed model parameters for PTCDA on the Ag(100) and Ag(110) surfaces reported in the literature.	296
Table C.2.	Structural results from SPA-LEED measurements and proposed model parameters for the herringbone phases of PTCDA on the Ag(100) and Ag(110) surfaces.	302
Table C.3.	XPS fitting parameters for the $\text{C}1s$ and $\text{O}1s$ levels of PTCDA on the Ag(100) surface.	314

Table C.4.	XPS fitting parameters for the $C1s$ and $O1s$ levels of PTCDA on the Ag(110) surface.	315
Table C.5.	XSW results for the adsorption configuration of PTCDA on the Ag(100) surface.	325
Table C.6.	XSW results for the adsorption configuration of PTCDA on the Ag(110) surface.	326
Table C.7.	XPS fitting parameters for the $O1s$ level of PTCDA on the Ag(100) surface at lower photon energy.	328
Table C.8.	XSW results concerning the adsorption site of PTCDA on the Ag(100) surface, employing the (111) Bragg reflection of the substrate crystal.	331
Table D.1.	Structural results from SPA-LEED measurements and proposed model parameters for PTCDA plus K on the Ag(110) surface.	342
Table D.2.	XPS fitting parameters for the $C1s$, $K2p$, and $O1s$ levels of PTCDA plus K on the Ag(110) surface.	351
Table D.3.	XSW results for the adsorption configuration of PTCDA plus K on the Ag(110) surface.	356

Acknowledgments

At this point, I would like to wholeheartedly thank all those who have supported me during the experimental work behind this thesis:

- First of all, I would like to express my gratitude to my PhD mentor, Professor Dr. Moritz Sokolowski, for giving me the opportunity to work in his group. I am grateful for his abundant support during the last years, for many stimulating discussions, and for the many opportunities he has given me to grow further into the exciting field of surface science.
- I would like to thank Professor Dr. Christian Kumpf (Forschungszentrum Jülich, Jülich, Germany) for his interest in our work and for accepting to co-referee my PhD thesis. Furthermore, I am grateful to Professor Dr. Thomas Bredow (Rheinische Friedrich-Wilhelms-Universität Bonn, Bonn, Germany) and Privatdozent Dr. Carsten Busse (Universität zu Köln, Köln, Germany) who also agreed to be on the board of examiners.
- I am grateful to Giuseppe Mercurio, Martin Willenbockel, Dr. Serguei Soubatch, and Professor Dr. Frank Stefan Tautz from Forschungszentrum Jülich (Jülich, Germany) for the exciting and fruitful collaboration within the framework of our joint XSW research project on the adsorption configurations at metal/organic interfaces. Our profound and intense discussions may have brought us a lot further down the way towards a deeper understanding of interfacial bonding. In particular, the close and incentive collaboration with Giuseppe Mercurio is appreciated. Our working-in-parallel on the XPS fitting models and the XSW data evaluation in the cases of both PTCDA/Ag(110) and K + PTCDA/Ag(110), and also the parallel development of the necessary computational algorithms for the two evaluation routines Torricelli and XSWAVES as well as the cross-checking of their performances have put our structural results from XSW on a very firm foundation, eventually.
- I have also benefited from stimulating inputs concerning our XSW research project by Benjamin Stadtmüller, Ingo Kröger, and Professor Dr. Christian Kumpf (Forschungszentrum Jülich, Jülich, Germany), who are acknowledged at this point.
- I deeply appreciate the technical and intellectual support by Dr. Jörg Zegenhagen, Dr. Tien-Lin Lee, Dr. Blanka Detlefs, Dr. Yanyu Mi, and Dr. Julien Duvernay from the European Synchrotron Radiation Facility (ESRF) at Grenoble, France, during our beamtimes at ID32. Furthermore, my thanks go to Christoph Heinrich Schmitz, Benjamin Fiedler, and Maria Buchholz from Rheinische Friedrich-Wilhelms-Universität Bonn (Bonn, Germany) and also to Adam Lassise from Forschungszentrum Jülich (Jülich, Germany) for their assistance during our beamtimes at the ESRF.
- I highly acknowledge the warm and friendly atmosphere as well as the enjoyable collaboration with my dear colleagues from the Organic Films group over the last years. In particular, I acknowledge the fruitful and exciting collaboration with Dr. Julian Ikonov during the STM studies on PTCDA/Cu₃Au(111) as well as the countless and vivid discussions with Benjamin Fiedler, Mathias Müller, Christoph Schmitz, and Martin Specht on any issue one

may encounter when doing surface science and performing UHV experiments. Also, my thanks go to Abdessabour Ben Hamed and Ina Krieger for their assistance during the SPA-LEED investigations on PTCDA/Cu(111) and PTCDA/Ag(100), respectively.

- I am thankful to Dr. Werner Reckien and Professor Dr. Thomas Bredow (Rheinische Friedrich-Wilhelms-Universität Bonn, Bonn, Germany) for the close collaboration within our joint research project on surface bonding at the metal/organic interface. Their theoretical calculations on PTCDA/Ag(*hkl*) have shone more light on the interfacial bonding mechanism.
- My special thanks go to Manuel Marks from the group of Professor Dr. Ulrich Höfer at Philipps-Universität Marburg (Marburg, Germany) who has performed the UPS experiments on PTCDA/Ag(100). I have enjoyed sharing his enthusiasm on surface bonding at metal/organic interfaces a lot.
- I am grateful to all staff members of both the mechanics and the electronics workshop of the Institute of Physical and Theoretical Chemistry (Rheinische Friedrich-Wilhelms-Universität Bonn, Bonn, Germany), in particular to Heinz-Peter Königshoven and Martin Böhmer, for their support in any technical issue. Also, technical support by Knut Hintzen from the IT staff is acknowledged.
- I would like to thank Udo Linke from Forschungszentrum Jülich (Jülich, Germany) for polishing the Cu₃Au(111) substrate crystals.
- Financial Support by the Deutsche Forschungsgemeinschaft under the projects SFB 624 (Template – Funktionale chemische Schablonen), SFB 813 (Chemie an Spinzentren – Konzepte, Mechanismen, Funktionen), and SO 407/6-1 (Vertical Bonding Geometry of Pi conjugated Molecules on Surfaces) as well as by the ESRF are acknowledged.
- Finally, there are people outside the world of academia who have selflessly accompanied me along my way—not only as a graduate student. There are no words sufficient to express my deepest gratitude to those who have given me any support one could ever ask for, to those who have carried me in times when I was afraid to stumble, to those who have always brought a smile to my face, to those who have made me the person I am, to those I love. You know who you are!

List of publications

1. S. K. M. Henze, **O. Bauer**, T.-L. Lee, M. Sokolowski, and F. S. Tautz, *Vertical bonding distances of PTCDA on Au(111) and Ag(111): Relation to the bonding type*, Surface Science **601**, 1566–1573 (2007).
2. J. Ikononov, **O. Bauer**, and M. Sokolowski, *Highly ordered thin films of perylene-3,4,9,10-tetracarboxylic acid dianhydride (PTCDA) on Ag(100)*, Surface Science **602**, 2061–2068 (2008).
3. E. Le Moal, M. Müller, **O. Bauer**, and M. Sokolowski, *Misfit driven azimuthal orientation of NaCl domains on Ag(100)*, Surface Science **603**, 2434–2444 (2009).
4. A. Hauschild, R. Temirov, S. Soubatch, **O. Bauer**, A. Schöll, B. C. C. Cowie, T.-L. Lee, F. S. Tautz, and M. Sokolowski, *Normal-incidence x-ray standing-wave determination of the adsorption geometry of PTCDA on Ag(111): Comparison of the ordered room-temperature and disordered low-temperature phases*, Physical Review B **81**, 125432 (2010).
5. E. Le Moal, M. Müller, **O. Bauer**, and M. Sokolowski, *Stable and metastable phases of PTCDA on epitaxial NaCl films on Ag(100)*, Physical Review B **82**, 045301 (2010).
6. **O. Bauer**, G. Mercurio, M. Willenbockel, W. Reckien, C. H. Schmitz, B. Fiedler, S. Soubatch, T. Bredow, F. S. Tautz, and M. Sokolowski, *Role of functional groups in surface bonding of planar π -conjugated molecules*, Physical Review B **86**, 235431 (2012).
7. G. Mercurio, **O. Bauer**, M. Willenbockel, N. Fairley, W. Reckien, C. H. Schmitz, B. Fiedler, S. Soubatch, T. Bredow, M. Sokolowski, and F. S. Tautz, *Adsorption height determination of nonequivalent C and O species of PTCDA on Ag(110) using x-ray standing waves*, Physical Review B **87**, 045421 (2013).
8. G. Mercurio, **O. Bauer**, M. Willenbockel, B. Fiedler, T. Sueyoshi, C. Weiss, R. Temirov, S. Soubatch, M. Sokolowski, and F. S. Tautz, *Tuning and probing interfacial bonding channels for a functionalized organic molecule by surface modification*, Physical Review B **87**, 121409(R) (2013).
9. S. Gärtner, B. Fiedler, **O. Bauer**, A. Marele, and M. M. Sokolowski, *Lateral ordering of PTCDA on the clean and the oxygen pre-covered Cu(100) surface investigated by scanning tunneling microscopy and low energy electron diffraction*, Beilstein Journal of Organic Chemistry **10**, 2055–2064 (2014).